eman ta zabal zazu
Universidad del País Vasco
Euskal Herriko Unibertsitatea
FACULTY OF ENGINEERING BILBAO
UNIVERSITY OF THE BASQUE COUNTRY

Ph.D. Thesis

New methods for ferrous raw materials characterization in electric steelmaking

Author:

Asier Vicente Rojo

Bilbao, February 2020

Advisors:

Javier Jesús González Martinez

José Tomás San Jose Lombera

eman ta zabal zazu
Universidad del País Vasco
Euskal Herriko Unibertsitatea
FACULTY OF ENGINEERING BILBAO
UNIVERSITY OF THE BASQUE COUNTRY

Ph.D. Thesis

New methods for ferrous raw materials characterization in electric steelmaking

Author:

Asier Vicente Rojo

Bilbao, February 2020

Advisors:

Javier Jesús González Martinez

José Tomás San Jose Lombera

ArcelorMittal

Dedico este trabajo a Eli, por ser el aire bajo mis alas en el duro viaje de vivir

Y a Sara y June, ya que cada minuto dedicado a esta tesis ha sido un minuto robado

ABSTRACT

The use of recycled scrap steel in steelmaking processes -both in Electric Arc Furnaces (EAF) and in Basic Oxygen Furnaces (BOF)- has increased over the past few decades and the recycling of ever higher volumes are forecast in the future.

Once considered as waste, scrap has regularly been used as a raw material in steelmaking processes, which has led to its valorization and significant periodic price rises. A situation that levered open new (and in many cases, lower quality) ferrous scrap markets, broadening the sources and the diversity of the ferrous scrap that is currently recycled.

The various international Steel Scrap Specifications define a set of scrap categories (qualities) by the source of the scrap and its physical characteristics, as well as its content of undesirable elements and non-ferrous (sterile) materials.

Those specifications reflect a compromise between what steelmakers need (high density for productivity, low percentages of tramp elements for metallurgical purity, reduced costs of low sterile contents) and the grades of purity that the industrial treatments can deliver with the tools that are available at scrap recycling plants. However, the widely varying quality of the scrap that is delivered to steel mills and scrap cleaning plants means that suppliers will often provide materials below the minimum requirements defined in those specifications (mixtures of materials with different qualities, inadequate dimensions, hazardous elements, contamination with other constituents i.e. earth, slag, grease, and other impurities, …).

Bulk deliveries of scrap materials to steel mills and scrap recycling plants can be made by road, rail, and sea, where trained operators conduct a visual inspection of the delivery on the basis of the aforementioned specifications. The materials are then allocated to scrap piles, according to certain criteria such as type, quality, density, production scenarios, and scheduled scrap deliveries, constrained only by the size of the plant and its lay out.

Following an in-depth analysis of the global situation in the steelmaking sector and a thorough state-of-the-art study of modern scrap-management technologies, various tools and a general methodology will then be defined for assessing the quality of ferrous scrap, the main raw-material smelted in an EAF.

Having pointed out some of the main shortcomings of the scrap recycling process and its management in steel mill scrap yards and scrap recycling plants, the study will then focus on

the development of three novel methodologies, presented as on-site management support tools for automatic quality assessment of scrap deliveries, which are designed to assist decision-making operations.

Initially, a mathematical model is proposed that can, in economic terms, quantify the inevitable degradation of scrap quality throughout its storage in scrap piles, which is the interval between reception of the material at the steelmaking facility and its smelting in the electric arc furnace.

The other areas studied within the scope of this thesis will be focused on the development of new tools to assess the effects of the non-ferrous materials found in scrap metal. On the one hand, spectroscopic techniques for the chemical characterization of sterile material are proposed, knowledge of which can optimize EAF smelting processes. On the other hand, a new tool for automatic quantification of the non-ferrous materials contained in scrap samples will be outlined, greatly assisting quality control of ferrous slag deliveries from suppliers.

The tools under development are another step towards complete scrap yard automatization processes, well aligned with the new industry 4.0 paradigm and the digitalization of factory production processes.

ACKNOWLEDGMENTS

Firstly, I would like to start by expressing the deepest appreciation to my thesis directors, Prof. José Tomás San José Lombera and Prof. Javier Jesus Gonzalez Martinez for their continuous support, guidance and motivation. To both of you, sincerely, thank you for your involvement and commitment in every step of this research.

My gratitude to my superiors at ArcelorMittal during these 4 years; Iñaki Macaya first and Susana Peregrina after for proposing me the challenge of materialize this thesis, and for facilitating me to balance my daily duties with the research activities required for completing this work. Also, to all my colleagues in ArcelorMittal Basque Country Research Centre, who have given me their support

I would also like to thank the different people of ArcelorMittal who, in one way or another, have supported me during this work. Specifically, to Mark Atkinson and Philippe Russo, for their mentoring, support and the knowledge put at my disposal. Your contributions have been of great value throughout the entire process.

Finally, I would like not to forget that without the support and contribution of some regular collaborators (and friends) from Tecnalia, this thesis would not have come to end. Artzai Picon, Jose Antonio Arteche, Alberto Lago and Aitor Alvarez, I know that sometimes it is difficult to work with me, and for your infinite patience, Thank you.

I gratefully acknowledge the funding provided by the Basque Government to the "AURRERAB: Advanced and Useful REdesign of CSP process for new steel gRAdes" project through the Hazitek programme (ZE-2017/00009). An important part of the different researches included in the thesis has been carried out in the context of this project. Also, I wish to express my gratitude for funding through contracts RTI2018-097079-B-C31 (MCIU/AEI/FEDER, UE) and PPGA19/61 plus GIU19/029 (UPV/EHU), in addition, my thanks to Basque Government research group (IT1314-19).

Above all, I would like to thank my family. To my wife, Eli, and my daughters, Sara and June, for their personal support and love. My parents and parents in law for being always there offering me their morally support and patient

To all of them.

THANK YOU

Table of contents

Table of Figures

List of Tables

1

Preface

In this introductory chapter the basic objectives established at the beginning of the thesis are presented. The structure of the thesis is posed describing the contents of the different chapters composing the research work.

1.1 Introduction

Throughout the history of humankind, steel can be considered as one of the prime global industrial materials; it was initially produced from an abundant raw material (iron ore) with which it can be mass produced at low cost and it is easily transformed into specific products for further assemblage or final use.

Nowadays, steel recycling is of great importance to society, because it mitigates the environmental impacts associated with steelmaking. Recycling involves the substitution of the natural resources used in integrated steelmaking and the smelting down of steel scrap for new steel products. The Electric Arc Furnace, the main scrap-based steelmaking process, uses less energy and its CO_2 emissions are lower than the integrated steelmaking process.

However, the management of integrated steelmaking industries are keenly aware of current global environmental issues and are implementing practices that will reduce the hot metal ratio (CO_2 footprint), aiming to increase the recycling of high-quality scrap metal that in many cases is superior to pig iron.

Industrial trends likewise show an increase of obsolete scrap availability (both in quantity and in complexity), coupled with greater scrap processing capacity in the short term.

This new context places additional pressures on the electric steelmaking routes for two main reasons. On the one hand, the availability of high-quality scrap will be lower in the future, so in regions such as Europe where the market for alternative ferrous materials, such as Hot Briquetted Iron (HBI) and Direct Reduced Iron (DRI), is limited, scrap availability will be low. Also, the available scrap will be of poorer quality and more heterogeneous, which will require additional efforts when sorting it.

On the other hand, when a layperson with no technical knowledge of the siderurgical process considers scrap materials, the idea is usually one of reusing "old steel" to produce "new steel". However, its constituents are much more complex than may be thought. Both the physical and the chemical characteristics of steel scrap that can come from a wide array of sources (ship and car breaking, rail tracks, rebars, turnings, etc.) are immensely heterogeneous and it may have undergone several processing steps before delivery to the scrap recycling plant or steel mill.

Preface

In an ideal situation, the material introduced into the furnace should only be steel, due to the intrinsic nature of scrap as a recycled material. However, scrap materials are a mixture of steel with other types of materials that, in some cases penalize the steel smelting process (loss of metallic performance, increased slag volumes, ...) and in other cases benefit the smelting process (reduction of energy consumption, alloy materials, ...). However, optimal process management implies that the chemical composition of all the materials introduced into the furnace must be precisely controlled.

The concept of Value in Use (VIU) has proven to be very useful when relating scrap quality with the operating cost of Electric Arc Furnace operations. This concept includes a criterion for a comparative interpretation of the results generated by each scrap quality grade in the steelmaking process.

Apart from the purchasing costs, the VIU of a particular scrap grade will incur additional costs associated with extra energy consumption and other materials (electrode, refractories, fluxes …), due to the melting of non-ferrous materials included in regular scrap. Those elements or compounds present in scrap can be divided into four groups:

Fe (as high as possible).

Sterile elements (SiO_2, $CaCO_3$, MgO, Al_2O_3, H_2O, FeO …), usually associated with the source of the ferrous material and the pre- and post-processing methods of scrap.

Tramp elements (Cu, Sn, Ni, Cr, Mo, S, P …) which generally have a negative impact on the rolling or stamping processes.

Carbonaceous compounds, (Cl), heavy metals, which can saturate furnace emission filters, reducing their efficiency, with a negative impact on the steel plant environment.

Among all these compounds, the sterile fraction probably represents the most complex part in scrap and, the existing methodologies for on-site characterization of this fraction are still barely sufficient for full optimization of furnace performance. Thus, the focus of this study is to develop novel methodologies for characterizing scrap sterile, in both qualitative and quantitative terms, as well as proposing a new model for material quality assessment due to corrosion degradation over lengthy periods of storage.

1.2 Objectives

The overarching objective of this thesis is to develop new methodologies for easy assessment of scrap quality as soon as it is delivered to steelmaking facilities, for use as management support tools in the daily decision-making operations of Steel mills.

This research is guided by two key questions, corresponding to the two main phases of this thesis:

I. What is the state of the art of scrap processing and management in the steelmaking sector?

II. How can the present-day methodologies be improved for understanding scrap materials?

The specific objectives of the study were framed in an attempt to respond to those questions:

- To examine the scrap-management-related practices of the main scrap dealers.
- To define a proper method for assessing the quality of ferrous materials and its influence on the Electric Arc Furnace process.
- To identify existing needs for the efficient characterization of scrap material.
- To propose new methodologies for improving the state of the art of scrap material characterization

1.3 Thesis overview

The complex problem of gaining an in-depth understanding of ferrous scrap that is used as the main raw material for Electric Arc Furnace (EAF) steelmaking forms the central focus of this research. The basic aim of the research concerns the development of new tools and their associated methodologies, for an easy characterization of ferrous scrap materials that accumulate at scrap recycling plants and steel mills. Non-quality scrap strongly penalizes the metallurgical processes of an EAF and therefore its economic performance. The new methods proposed in this thesis can be used as management decision-making tools for optimizing the steelmaking process (not only from an operational point of view, but also for optimizing scrap purchasing strategies and steel purity).

The applied studies will be focused on the non-ferrous materials found in scrap -such as sterile (dirt, wood, slag), tramp elements, surface oxidation- and methods for their characterization (quality and quantity). The specific information for each batch will then be used for optimizing the EAF steelmaking production.

The thesis will be divided into 10 chapters, as shown in Fig. 1.1. In Chapters 1-3, an introduction and some background will be presented; a global review of the steelmaking sector will be outlined in Chapter 2; and, some insight into the treatment of scrap materials within the steelmaking sector, in Chapter 3. Value-In-Use (VIU) methodology, the scrap quality assessment method proposed for the evaluation of the research results, will then be explained in Chapter 4. In Chapters 5 and 6, current pre- and post-processing technologies will be outlined, with the purpose of explaining the starting point of the research in this thesis. These activities will be then described in detail in Chapters 7-9: a new model for the economic assessment of scrap quality degradation (Chapter 7), a novel approach towards the use of spectroscopy techniques for quality assessment of sterile present in scrap materials (Chapter 8), and a breakthrough methodology for automatic sterile quantification in scrap materials (Chapter 9). Finally, a discussion and some conclusions from the research work will be found in Chapter 10, as well as some reflections on future work.

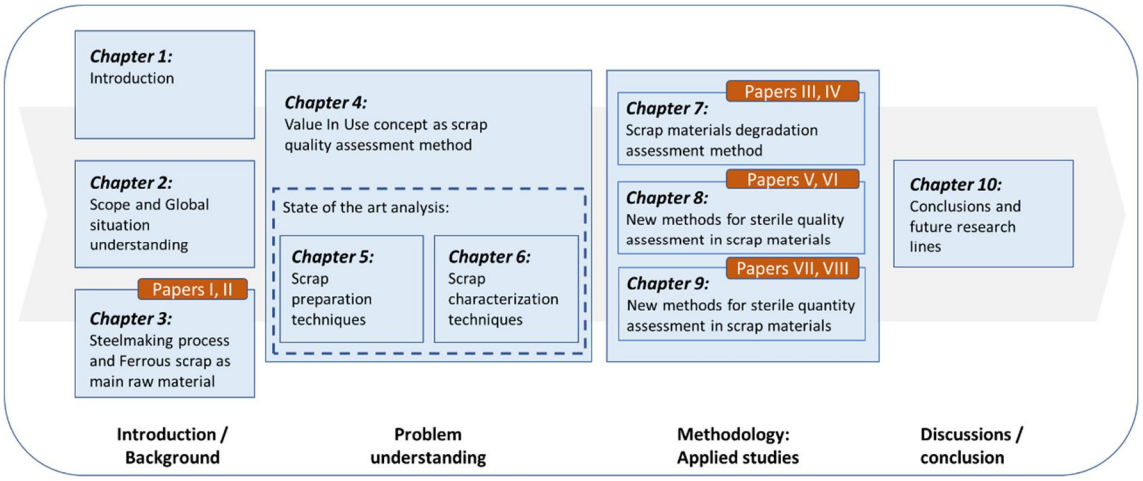

Fig. 1.1: Illustration of the Thesis structure

2

Scope and Global steelmaking situation understanding

In this chapter, a thorough analysis of the current situation of the global steelmaking sector is carried out. Likewise, scrap metal is presented as the main raw material of the steelmaking process, highlighting the paradigm shift from waste to raw material of this complex material, as a starting point for the work that will be presented in subsequent chapters

2.1 Steelmaking process overview

Steel is the world's most important industrial material, with over 1.8 billion tonnes produced annually. The development of mankind would have been impossible but for steel. The backbone of developed economies was laid on the strength and inherent uses of steel.

The main objective of steelmaking process is to produce the steel which is later manufactured to obtain the final product with very particular characteristics. In modern steelmaking, steel can be obtained by two different processes: ironmaking route (from iron ore) and electrical steel making route (from scrap metal) (1)

In the case of production from iron ore, the first step is the transformation of iron ore into pig iron. To so, iron oxide is reduced to hot metal in a blast furnace by combining iron ore and carbon inside the furnace.

Prior to its use in the blast furnace, iron ore is milled to give it an appropriate size. The iron ore that meets the required conditions in terms of iron law and granulometry goes to the furnace. The iron ore that does not meet the quality requirements is agglomerated together with fluxing materials, so that it can be used in the furnace later (sintering process).

Once the adding ore and sintering products are introduced into the blast furnace, the mixture is heated by coke addition and oxygen blowing. Together with this mixture, additional flux materials are added to trap all non-metallic impurities present in the mineral.

The complete combustion of the introduced materials is achieved by high pressured hot air injection. This allows holding the suspended materials while the transformation from solid to liquid is carried out.

Scope and Global steelmaking situation understanding

The final product of the blast furnace is hot metal. This is a material with an iron law of about 95% and about 3.5-4% of carbon. The remaining fraction consists of materials such as silicon, manganese, sulphur and phosphorus.

Among the by-products produced in the blast furnace process, besides the atmospheric emissions, slag products must be taken into consideration. Blast furnace slag agglutinates the leftover fluxes, the mineral gangue and the coke material ashes. This by-product is recovered to be used as raw material in civil roads and cement producer companies.

The key difference between pig iron and steel is the amount of carbon contained. If the carbon content is less than 1,7% it is considered steel. Thus, in order to transform the pig iron into steel, the product from the blast furnace continues its transformation process in the Basic Oxygen Furnace (BOF). This facility is responsible for removing the excess carbon through a refining process.

Once the oxidized steel is obtained, it is transferred to the next stage of the production process, the secondary metallurgy process. The main characteristics of this phase are the total deoxidation of the steel, the elimination of sulphur and the final adjustment of the chemical composition of the steel.

Subsequently, the steel is processed in the continuous casting machine. In this installation the liquid steel is poured from the ladle to the mould, where it starts to solidify in a very particular shape, such as slabs, beam blanks, blooms or billets.

All these products are then conformed in the rolling mill to give them the final shape and mechanical characteristics necessary for their use in the manufacturing industry. This process takes advantage of the deformation capacity (ductility) of the steel and can be performed both in hot and cold conditions.

Flat products (coils and plates) are destined, among others, to automobile and domestic appliance sectors. On the other hand, long products (wires, rods and profiles) are mainly destined to the construction sector.

On the other hand, the electric steelmaking route differs from the ironmaking route in two fundamental aspects: the main raw material is scrap instead of iron ore and the steel melting phenomena takes place thanks to the thermal energy released by an electric arc.

In its earliest beginnings, Electric Arc Furnaces (EAF) were used for manufacturing special steels. However, nowadays, this is considered a highly efficient process in which it is possible to produce almost any type of steel.

Fig. 2.1 shows the materials flows that occur in steelmaking:

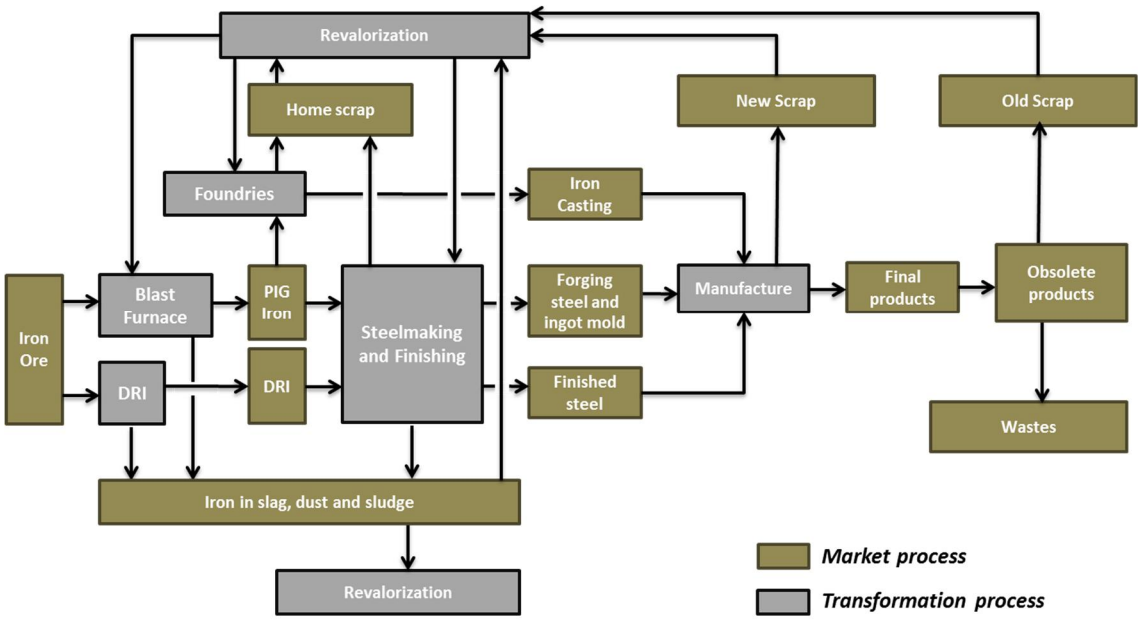

Fig. 2.1: Materials flows in steelmaking

Steel plays a fundamental role in today's society. In fact, it has been one of the materials (maybe the most) that has contributed most to the welfare of mankind. Its properties, which include low cost, ease forming, high resistance, long service life, variety of qualities and applications, assembly capacity and easy and comfortable recycling, make it irreplaceable.

In addition, steel can be considered a sustainable material due to its properties and also because of the abundance of iron in nature and the low nature resources required to process it.

Regarding the by-products generated during the steelmaking process, around 90-100% of electric steelmaking wastes and produced by-products are valued in different ways, as opposed to what happens in ironmaking. For example, slags are reused mainly as sand and gravel, in the construction of roads or the production of cement, and rolling scale is almost 100% recycled as raw material in the integral steel industry for other uses.

Regarding recycling matter, a deep knowledge of the intrinsic characteristics and the quality of the raw materials are crucial.

Being aware of that, major steel companies are devoting huge amounts of resources on research and development activities focused on raw materials characterization and within this scope, this thesis becomes important.

2.2 Brief analysis of the steel industry evolution during the 20th century

During the 20th century, the steelmaking process has faced many changes based on the political, social and technological trends evolution.

In the 1950s and 1960s, demand for high quality steel encouraged the steelmaking industry to produce large quantities of steel. Integrated steel plants producing steel by refining iron ore become popular. Using Ironmaking route for steel production was possible to produce very high quality steel with very well controlled chemical compositions to meet all product quality requirements.

The energy crisis of the 1970s made thermal efficiency in steel mills a priority. The furnaces used in integrated plants were very efficient; however, the common production practices needed to be improved. The large integrated plants of the 1950s and 1960s tended to produce steel in batches where iron ore was taken from start to finish. This causes some equipment to be idle while other equipment was in use. To help reduce energy use, continuous casting methods were developed. By keeping blast furnaces continually fed with iron ore, heat is used more efficiently.

As environmental concerns gained importance in the 1980s and 1990s, regulations have become more stringent, prompting further changes in the steelmaking industry. Competition also increased during this period due to decreasing local markets and increasing foreign steel production plants. The competition forced steelmaking facilities to reduce expenses and increase quality. To meet these changing needs, just-in-time technology became more prominent and integrated steel plants started to be replaced by mini-mills, that use steel scrap as raw material rather than ore. Mini-mills will never completely replace integrated steel plants because they cannot maintain the tight control over the chemical composition, and thus cannot consistently produce high quality steel. Mini-mills have a narrower production line and cannot produce the specialty products produced by integrated plants.

In the second decade of 21th century, due to the global economic situation, overcapacity became one of the main concerns from the point of view of industrial benefits. And this needs a major focus on innovation to face the new challenging scenario.

2.3 Current steelmaking worldwide situation

In order to properly define the research lines that will be further developed in this thesis, it is imperative to understand, not only the current situation of steelmaking sector, but also to estimate their prospects in the medium-long term.

2.3.1 Historic evolution

The first analysis to be done if we want to understand the steel market in recent years is to take a quick look at the behaviour of the worldwide steelmaking figures during the last 50 years. The figure below shows the global evolution in the period from 1960 to 2018:

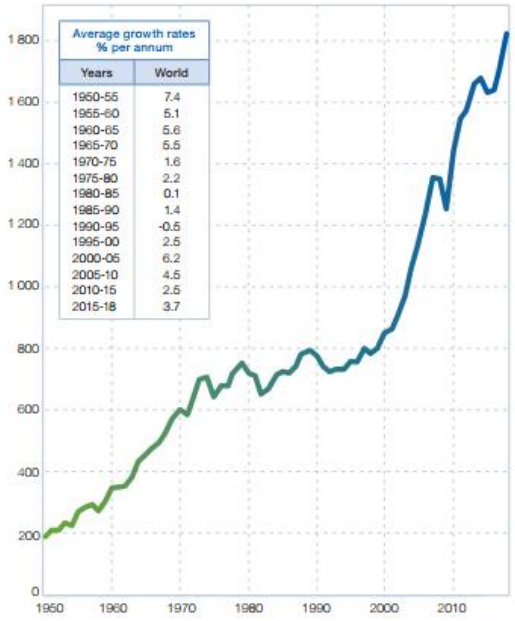

Fig. 2.2: Global Steel production for the last 50 years in millions of tones (2)

After a quick look at Fig. 2.2 and in line with what was presented in the previous section, the following observations can be made:

- From 1950 to 1973 there was a growth period with a mean annual rate of increase in production of 5.8%.
- Later on, there was a non-growth period that lasted 27 years (from 1974 to 2001) with a mean annual growth rate of 0.7%.
- In the first decade of the 21st century (from 2002 to 2007) the steel boom occurred, with average an annual growth rate of 8.4%.
- In 2008, with a global crude steel production of 1.343 billion tonnes, the global economic crisis prompted a readjustment of the productive capacities began at the global level.

Scope and Global steelmaking situation understanding

- The impact of the adjustments started the year after, becoming to be noticed on 2009, when the global production dipped to 1.239 billion tonnes, but rebounded quickly in 2010 to 1.433 billion tonnes.
- The production rate continued to rise the following years and reached a record high of 1.67 billion metric tons in 2014.
- Weak global demand for steel in 2015 caused a slight contraction in crude steel production worldwide, with a 2.8 % decrease from 2014.
- Since 2015, the steelmaking situation seems to start recovering slowly

By the time this analysis was done, the World Steel Association had forecasted relatively steady steel demand levels for the comings years, which would indicate that production may hold steady at current levels in the near future.

2.3.2 Current crude steel production by geographic distribution

Fig. 2.3 shows the worldwide distribution of the crude steel production among the top producing countries in 2018. It can be observed that 20 countries account for 92.8% of the total production, with China leading the ranking with nearly 50% of the total tonnage.

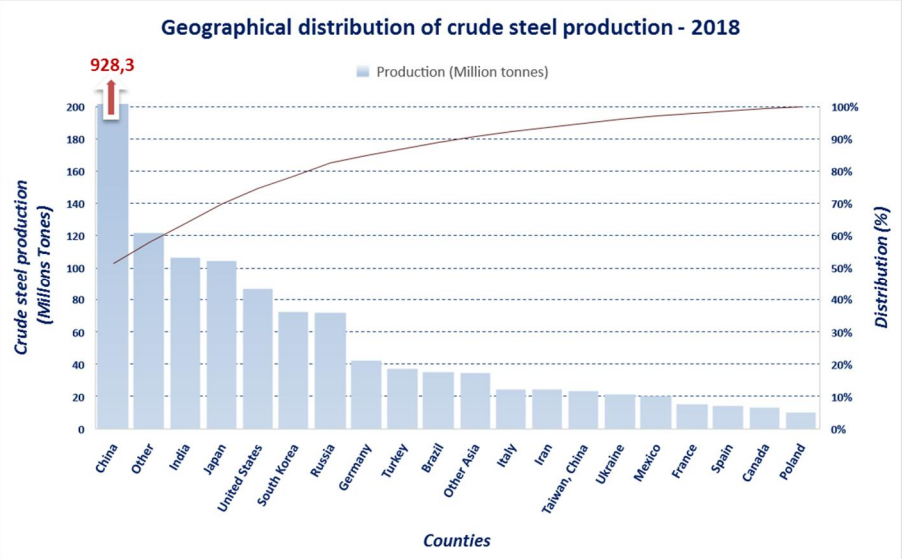

Fig. 2.3: Top steel producing countries 2018 (3)

Looking at the eight main world regions, Asia and Oceania produced 1.275 billion tons of steel in 2018, accounting for 70,6% of the global production. The European Union was the second-largest steel producing region in 2018 with a 9,3 % of the production (167,7 million tons), followed by North America with a 6,6 % (119,7 million tons) and the Commonwealth of

Independent States (CIS) with a 5,6 % (101,3 million tons). These figures, as well as the evolution trends since 2011, are illustrated in Fig. 2.4 and Table 2.1.

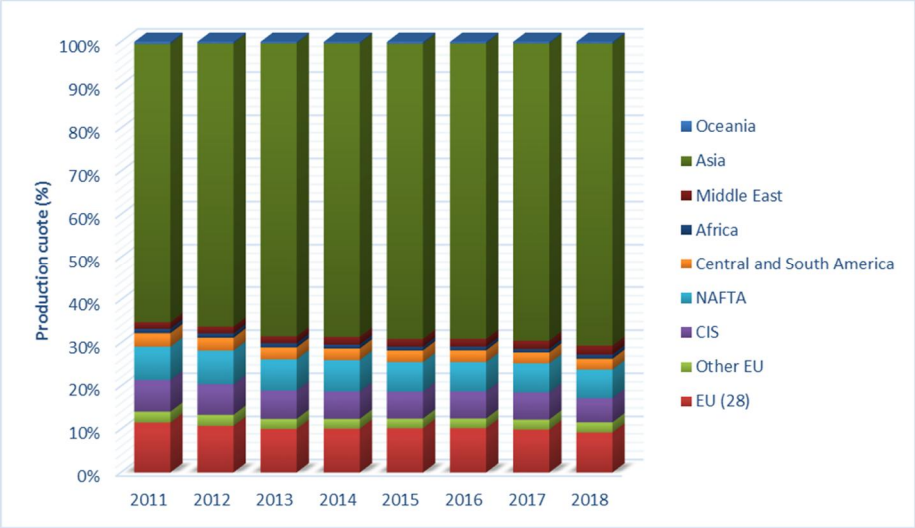

Fig. 2.4: Worldwide crude Steel production distribution in 2009-2018 (4)

PRODUCTION DISTRIBUTION (%)	2011	2012	2013	2014	2015	2016	2017	2018
EU (28)	11,6	10,8	10,1	10,1	10,2	10,3	9,9	9,3
OTHER EU	2,5	2,6	2,3	2,3	2,2	2,2	2,3	2,3
CIS	7,3	7,1	6,6	6,4	6,3	6,3	6,3	5,6
NAFTA	7,7	7,8	7,2	7,3	6,8	6,8	6,7	6,6
CENTRAL AND SOUTH AMERICA	3,1	3,0	2,8	2,7	2,7	2,7	2,5	2,5
AFRICA	1,0	1,0	1,0	0,9	0,8	0,8	0,8	1,0
MIDDLE EAST	1,5	1,6	1,6	1,8	1,8	1,8	1,9	2,1
OCEANIA	0,5	0,4	0,3	0,3	0,4	0,4	0,4	0,4
ASIA	64,7	65,8	68,1	68,2	68,7	68,7	69,1	70,2

Table 2.1: Crude Steel production percentage distribution worldwide (2)

The production distribution by region has changed markedly in the last decade. Between 2011 and 2018, most regions have seen their share of production decrease. Only “Other Europe” maintained its at around 2.3 % share. The Middle East and Asia increased their percentage of global production by 0.6% and 5,5% respectively.

In Fig. 2.5, the crude steel production share evolution along the last decade for Europe, NAFTA and Asia is shown.

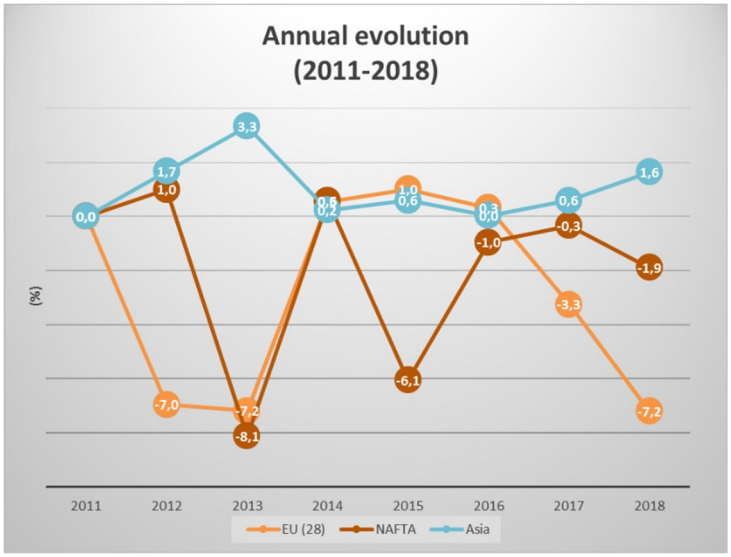

Fig. 2.5: Worldwide crude Steel production distribution evolution in EURO, NAFTA and Asia in 20011-2018 (4)

One conclusion reached looking at Fig. 2.5 is that, the global economic crisis hit Europe severely, systematically loosing production market share.

Nevertheless, Global production ratio distribution is useful for understanding global market trend evolution but, and since the total produced amount is changing every year, it does not reflect real activities inside each producer country. Table 2.1 highlights the evolution of the produced steel amount of each region for one year in comparation with the previous one.

	2006	2007	2008	2009	2010	2011	2012	2013	2014	2015	2016	2017	2018
EU (28)	6	1,4	-5,5	-29,8	24	2,8	-5,2	-1,3	1,7	-1,9	0,0	-2,5	3,5
OTHER EU	13	8,6	3,6	-8,2	15,9	16,1	2,0	-3,3	-0,5	-5,7	0,0	4,1	12,5
CIS	5,9	3,6	-7,9	-14,6	10,8	4,1	-1,8	-2,1	-2,1	-4,3	0,1	0,8	-1,1
NAFTA	3	0,9	-5,6	-33,1	33,2	6,4	2,4	-2,2	1,8	-8,4	-1,3	0,4	8,9
CENTRAL AND SOUTH AMERICA	-0,5	6,5	-1,5	-20,5	16,2	9,7	-3,7	-1,3	-1,5	-2,7	1,1	-7,9	10,3
AFRICA	4,1	-0,1	-9,1	-9,3	7,9	-5,6	-2,5	4,3	-6,6	-8,1	-0,7	-3,7	32,8
MIDDLE EAST	0,8	7	1,2	6,7	12,6	16,2	7,7	8,0	11,2	-1,6	-0,7	7,5	20,6
OCEANIA	12,5	12,2	3,3	3,2	13,3	8,2	3,0	9,4	1,4	-2,2	-0,4	1,3	12,8
ASIA	6	1,4	-5,5	-29,8	24	2,8	-5,2	-1,3	1,7	-1,9	0,0	-2,5	3,5
TOTAL	8,9	7,8	-0,3	-7,8	15,7	7,3	1,42	5,79	1,2	-2,87	-0,31	0,71	11

Table 2.2: Annual Steel production evolution of the main producer regions (2)

Until 2007, as shown in Fig. 2.2, virtually all world regions increased their annual production of tons of crude steel. In 2008 and 2015 occurred the two major crises of steel industry of the 21st century (linked to the global economic situation). Nevertheless, in view of the data, a recovery of the sector can be predicted. Assertion that is demonstrated looking at 2018 results, in which all regions have increased the steel production volume with respect to 2017.

On the other hand, when specifically looking at the situation of steel production in Europe (EU28) in 2018, Fig. 2.6 shows the crude steel production distribution by countries in millions of tons. According these figures, 9 countries account for 82% of the total crude steel production, Germany as the leading steel producer with one quarter of the total European

production volume. But it is also worth mentioning Italy, France, Spain and Poland as the mayor producers in Europe.

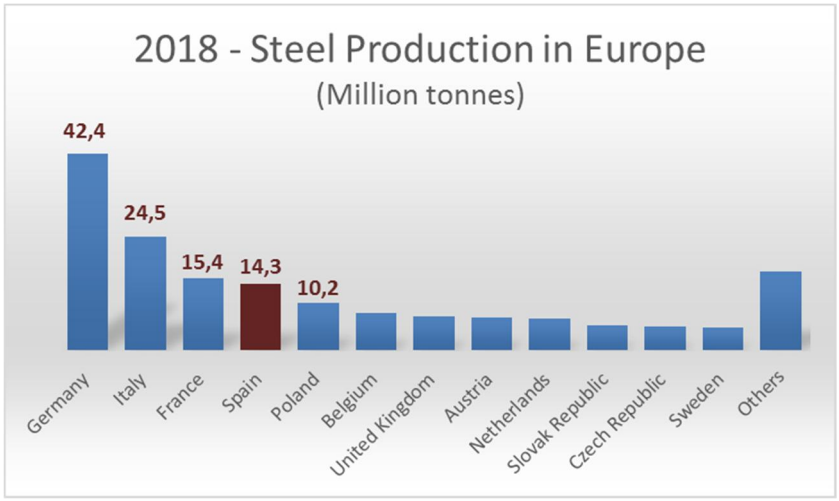

Fig. 2.6: European crude Steel production in 2018 (4)

2.3.3 Main steel producer companies

In 2018, 20 companies accounted for 37.2% of all world-produced steel. ArcelorMittal has been the world's largest Steel producing company for several years and produced 96.42 million tons of steel (5,3 % of global production) in 2018. China Baowu Group, ranked second with 67,43 million tons, followed by Japan's Nippon Steel and Sumitomo Metal Co., which merged in 2012, with 49.22 million tons. Five of the top 10 companies are headquartered in China, and nine of the top 10 are headquartered in Asia and Oceania. ArcelorMittal is the only company headquartered outside the Asia and Oceania region. These figures can be observed in Fig. 2.7.

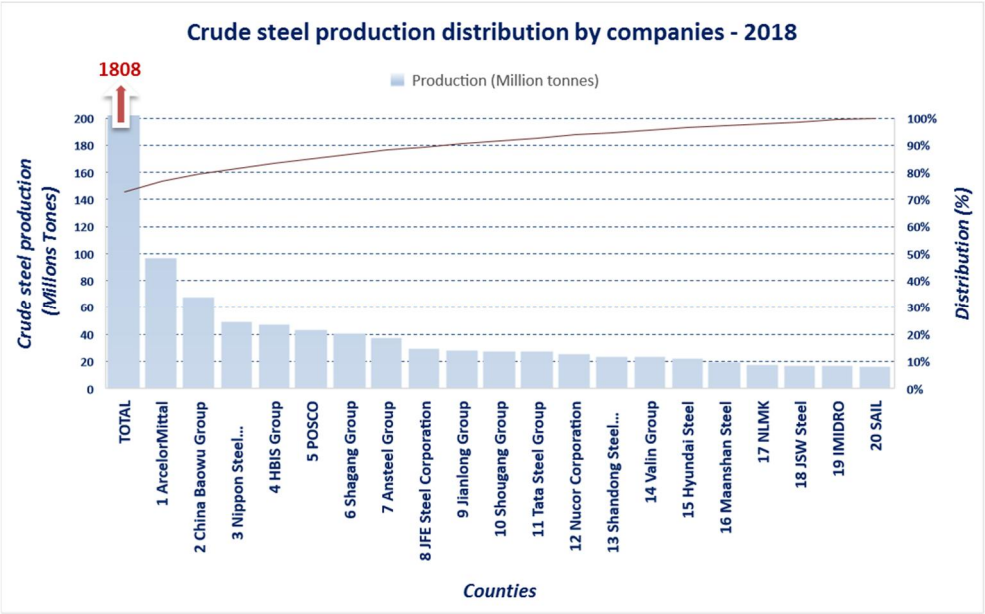

Fig. 2.7: Top steel producing companies 018 (4)

2.3.4 Steel production processes distribution

Looking at the historic evolution of the process along the 20th century, it is observed that since the 1950s, BOF and EAF processes started to gain industrial share, almost completely replacing the Open Hearth Furnace process at the beginning of the 21st century [5].

In 2018, 70.8% of the global steel production was made by BOF route and 28.8% was made by EAF route. Fig. 2.8 depicts the production process distribution by regions.

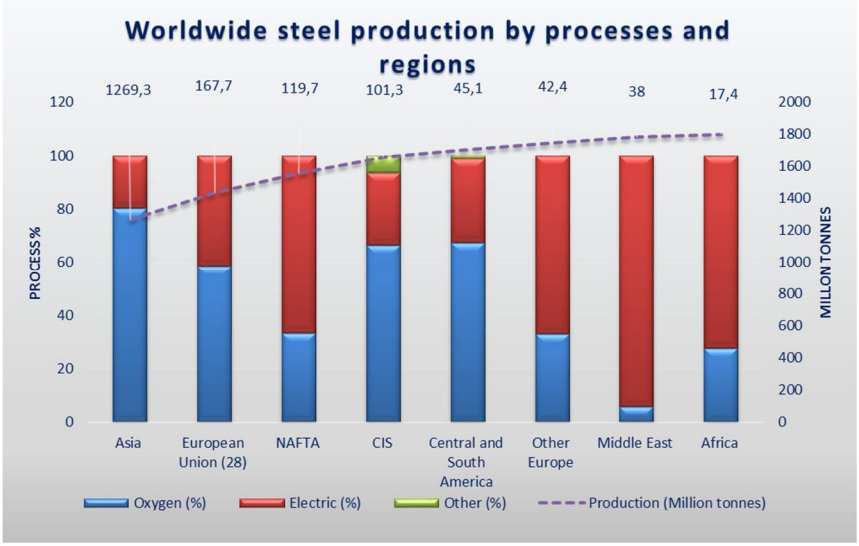

Fig. 2.8: Crude Steel production by processes (3)

Looking at these data, it can be said that Europe, NAFTA, Africa and overall Middle East are heavily dependent on scrap due to their dependency on EAF process. However, it is important to highlight that:

- The integrated steelmaking route uses, on average, 1,370 kg of iron ore, 780 kg of metallurgical coal, 270 kg of limestone, and 125 kg of recycled steel to produce 1,000 kg of crude steel. Around 70% of total global steel production (1.2 Gt in 2017) were produced in BOFs. It represents about 150 Mt of scrap.
- The electric arc furnace (EAF) route uses, on average, 710 kg of recycled steel, 586 kg of iron ore, 150 kg of coal and 88 kg of limestone to produce 1,000 kg of crude steel. In 2017, global EAF output accounted for about 30% of global steel production (around 480 Mt), which required 340 Mt of scrap.

EAF process is a massive scrap consumer process. However, considering that BOF process represents 70% of the total steel production, the overall scrap consumption by this process is also important and should not be belittled. Fig. 2.9 and Fig. 2.10 put the attention on the steel production values in Europe by countries for EAF and BOF processes.

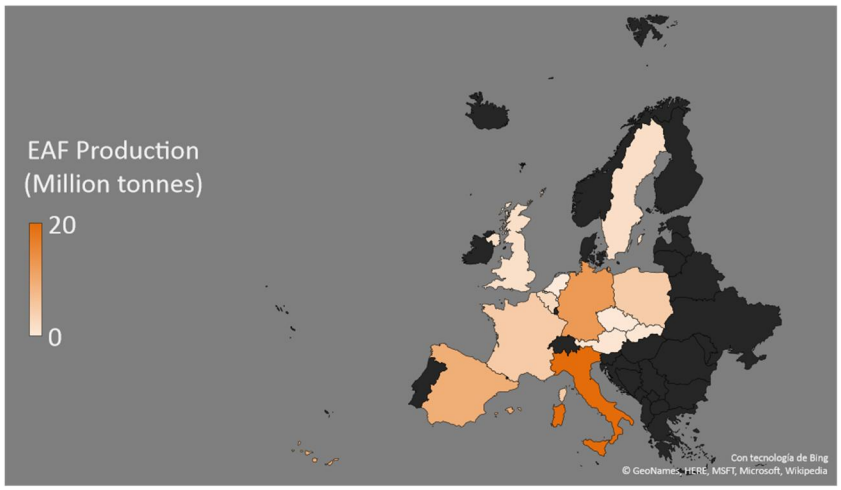

Fig. 2.9: EAF production in Europe

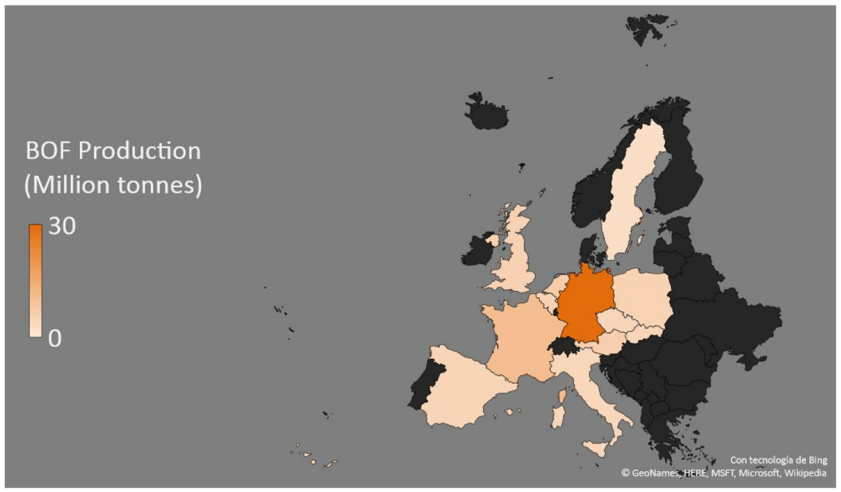

Fig. 2.10: BOF production in Europe

2.4 Steelmaking raw material; the steel produced today is the raw material tomorrow

Electric steelmaking requires about one-third of the energy used in ironmaking route, which could make the EAF the technology of choice for the future, considering the environmental footprint is one of the key criteria in the choice of technologies nowadays. However, the expansion of EAF will to be limited by the global availability of steel scrap.

According to (5), by 2050 Electric Arc Furnace production tonnage will be 2.1 times that of 2010, with a share increase from 29% in 2010 to 40% in 2050. BOF production in 2050 is expected to be 1.3 times that of 2010.

2.4.1 The importance of scrap as a sustainable material

The current importance of sustainability and the challenges imposed by the aggressive global economic situation developed since 2008, have pushed the steelmaking industry towards the continuous development of new grades with higher performance and lower environmental footprint.

Since 1900 the global steel industry has recycled over 22 billion tonnes of steel. This has reduced iron ore consumption by around 28 billion tonnes, as well as cutting coal consumption by 14 billion tonnes. The industry has also dramatically reduced the use of energy. Producing one tonne of steel today requires just 40% of the energy it did in 1960 (1).

In 2018 more than 1.8 Billion tons of crude steel were produced worldwide, and more than 520 million come from EAF technology. EAF technology uses less resources, auxiliaries and energy compared to BOF technology. As a consequence, impact to the environment is reduced, due to the endless cyclic use of scrap as raw materials in EAFs. This closed material loop is one of the most important characteristics from a sustainability point of view, and one of the strengths of steel. In fact, when recycling scrap, the new steel inherits the properties of the original materials and can be modified during the steelmaking process or through ulterior thermal processes. This recyclability makes steel play a very important role in the upcoming circular business model.

Fig. 2.11 shows the recyclability distribution of steel products.

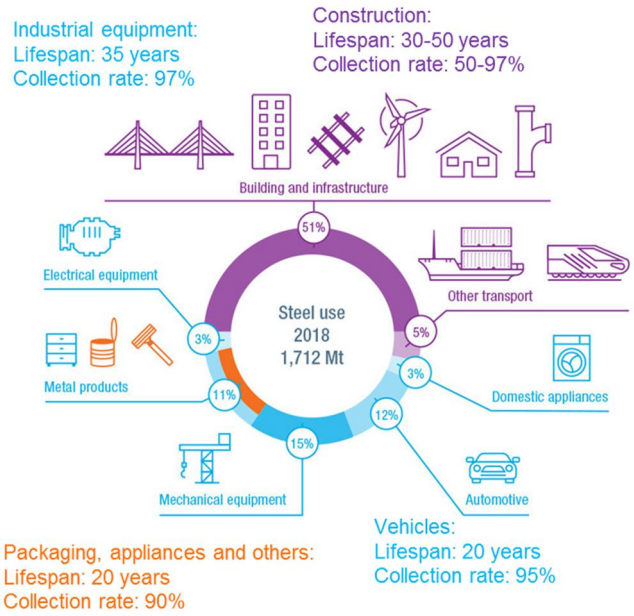

Fig. 2.11: Recyclability of Steel products (1)

A sustainable circular economy is one in which the stress over natural resources is reduced, ensuring resource availability for the future generations. Once the maximum value has been extracted from a particular product, the resources are recovered and reused, remanufactured, or recycled to create new products and continuing valorising this wasted product. As a permanent material which can be recycled over and over again without losing its properties, steel is fundamental to the circular economy.

However, steel will still have to be produced through BOF route, using iron ore, because the world's steel demand is too high to be satisfied with recycled steel.

The industrial material cycle basically consists on:

- Reducing the amount of material, energy and other resources used to produce steel as well as decreasing the weight of steel used in products by developing higher strength steels.
- Remanufacturing products by the process of restoring durable, used steel products to as-new conditions.
- Recycling is melting steel products at the end of their useful life to create new steels.

- Reusing materials again, either for its original purpose or for a similar one, without significantly altering its physical form. The goal of steelmakers is to use all raw materials to their full capacity, ensuring zero waste from steelmaking.

Electric Steel mills are probably the technology that plays the main role in the industrial society's material cycle:

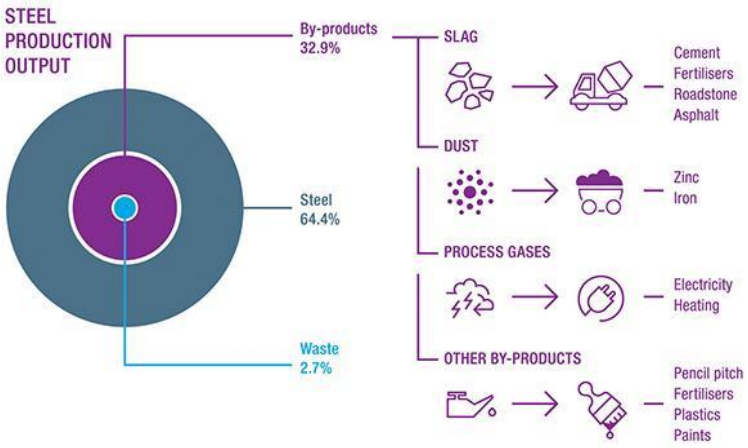

Fig. 2.12: Steelmaking recycling product distribution.

In the sustainable future, new economic models will maximize the value of raw materials, and under this approach is where the present research makes sense.

2.4.2 Forecast on scrap availability in future

Even though scrap based processes will be important, primary steel production (BF-BOF) will remain dominant. One of the main reasons for this trend is the fact that availability of scrap at a point in time is defined by the past production and the recycling rate at the moment under consideration. Currently, the steel recycling rate is around 85%, since there are some low quality scraps that are not going to be reused. Fig. 2.13 illustrate this concept.

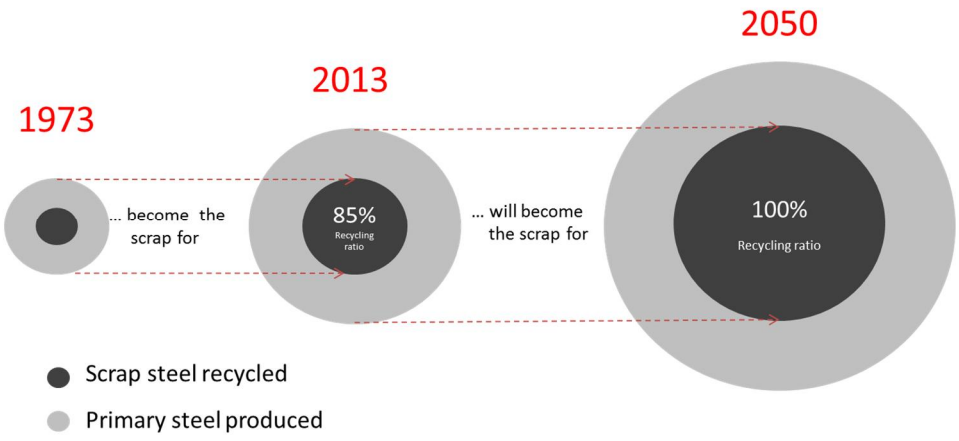

Fig. 2.13: Scrap Steel recycling rate analysis (6)

Scope and Global steelmaking situation understanding

The current recycling rate of ferrous material is an important parameter to define the future recycling strategies to maximize the natural resource availabilities. ArcelorMittal (7), proposed a very simple method for estimating the quantity of scrap that will be available in one particular year as obsolete scrap from the four main sectors of steel use (lifespans and collection rates are estimations):

- Construction: Construction is the main steel consumer sector and can be divided into 4 subsectors:
    - Cladding: estimated lifespan of 30 years and 85% collection rate.
    - Reinforcing steel in buildings: estimated lifespan of 40 years and 50% collection rate.
    - Infrastructure: estimated lifespan of 60 years and 80% collection rate.
    - Structural steel on buildings: estimated lifespan of 50 years and 97% collection rate.
- Industrial equipment: This sector presents an estimated lifespan of 35 years and 97% collection rate.
- Vehicles: This sector presents an estimated lifespan of 20 years and 95% collection rate.
- Packaging, appliances and others: This sector presents an estimated lifespan of 20 years and 90% collection rate.

The lifespan estimated for each of the different sectors allows obtaining the total Crude Steel Production (CSP) at the year when the steel was produced (Reference year) from the existing databases.

The model proposed by ArcelorMittal is represented by the following two equations:

$$SU_{ry} =\rightleftarrows \sum\left[\left((CSP_i \cdot Ylr_i) - (CSP_i \cdot Ylr_i \cdot PS_i)\right) \cdot DS_i\right] \quad \textbf{(2.1)}$$

$$OS_{ry} =\rightleftarrows \sum[SU_i \cdot ls_i] \quad \textbf{(2.2)}$$

Where:

- *SU_{ry}: Total Steel use in the production reference year (Mt).*
- *i: Each sector considered*
- *SU_i: Steel use per sector in the production reference year (Mt).*
- *CSP: Crude steel production in the production reference year (Mt) – From general Databases.*
- *Ylr: Global yield loss rate for crude & finished steel production in the production reference year (%) – From general databases.*
- *PS: Prompt scrap per domain at the reference year (%)– From general databases.*

Scope and Global steelmaking situation understanding

- *DS: Domains share in the production reference year (%) – From general databases.*
- *ls_i: Lifespan (years) – Assumption*

The minimum lifespan estimated is obtained in vehicles and packaging, appliances and other domains. Therefore, the proposed model allows calculating the obsolete scrap availability for the next 20 years.

One of the main objectives of this thesis is to provide new tools and methods of scrap characterization to increase the current recycling ratio through better understanding of the quality of the scrap.

2.5 Current scrap market worldwide situation

The world crude steel production reached 1.621 billion tonnes in 2015 (time at which this analysis was done), presenting a reduction of 2.9% when compared to the previous year. Following the same trend, global steel scrap use decreased in 2015 from 35% to 34.2% (between 0.6% and 10.4% depending on the analysed country). In most cases, the individual reduction in steel scrap usage was steeper than the drop in crude steel production for each particular country or region (4).

General statistics confirm that:

- The world's biggest steel producer, China (where the BOF route dominated the country's crude steel production accounting for 93.9% of the total) presented a steel scrap consumption of 83.3 million tonnes.
- The EU (28) steel scrap consumption in 2015 was 91.1 million tonnes with a scrap usage of 54.8% in steelmaking process. Its biggest steel scrap users were Italy (19.65 million tonnes), Germany (18.49 million tonnes), Spain (11.8 million tonnes) and France (7.38 million tonnes).
- In the USA, the steel scrap usage was 56.5 million tonnes with a scrap usage of 71.7% in steelmaking process.
- Japan's steel scrap usage was 33.6 million tonnes with a scrap usage of 31.9% in steelmaking process.
- The Republic of Korea recorded a scrap usage of 29.9 million tonnes (42.9% in steelmaking processes share).
- According to 2015 figures, Turkey's steel scrap consumption was about 26.06 million tonnes where the electric arc furnace route accounted for 65% of the total steel production.
- Finally, Russia's steel scrap usage was 17.3 million tonnes.

Despite the fact that 2015 was an atypical year, the global distribution of scrap import and export patterns among the different regions has not changed significantly over the last few years. The data from 2015, gives a good picture of ferrous scrap transit around the world:

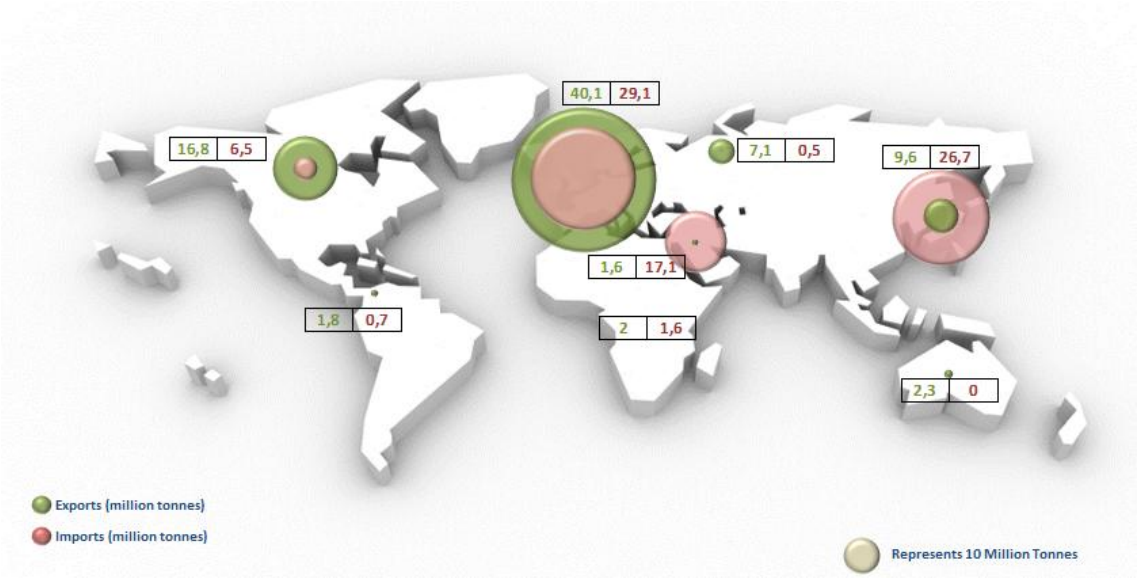

Fig. 2.14: Worldwide ferrous scrap trade balance in 2015

According to Fig. 2.14, Europe is the main driver of the scrap trade worldwide, both in export and import figures. After Europe, Asia leads the volume of global imports and North America leads the volume of global exports.

Table 2.3 compiles the main scrap trade among the different regions:

Exporting Region / Destination	EU (28)	Other EU	CIS	NAFTA	Central and South America	Africa & Middle East	China	Japan	Other Asia	Oceania
EU (28)	26,4	1,4	1,3	0,2	0,1	0,1	0	0	0	0
Other EU	8,9	0,1	3,2	4,2	0	0,5	0	0	0	0
CIS	0	0	1,8	0	0	0	0	0	0	0
NAFTA	0,3	0	0	5	0	0	0	0	0	0
Central and South America	0	0	0	0,5	0,2	0	0	0	0	0
Africa	1,2	0	0	0,3	0	0,1	0	0	0	0
Middle East	0,1	0	0	0,3	0	0,1	0	0	0	0,1
China	0,1	0	0	0,1	0	0		1,9	0,1	0
Japan	0	0	0	0	0	0	0	0	0,1	0
Other Asia	2,9	0,1	0,9	5,4	1,4	2,7	0	5,9	2,3	2,1
Oceania	0	0	0	0	0	0	0	0	0	0
Total Export	**39,9**	**1,6**	**7,2**	**16**	**1,7**	**3,5**	**0**	**7,8**	**2,5**	**2,2**
Total Import	**29,5**	**16,9**	**1,8**	**5,3**	**0,7**	**2,2**	**2,2**	**0,1**	**23,7**	**0**
Trade Balance	**10,4**	**-15,3**	**5,4**	**10,7**	**1**	**1,3**	**-2,2**	**7,7**	**-21,2**	**2,2**

Table 2.3: Ferrous scrap Worldwide trade figures in 2015 (3)

Turkey is the world's foremost steel scrap importer with 16.251 million tonnes. Other important countries to be mentioned are India (6.71 million tonnes), the Republic of Korea (5.758 million tonnes), the USA (3.513 million tonnes), Taiwan (3.373 million tonnes), China (2.328 million tonnes) and Canada (1.516 million tonnes).

On the other hand, the US export of steel scrap was about 12.976 million tonnes in 2015, followed by Japan (7.847m tonnes).

The most basic way to perform pre-characterization of scrap is in terms of its origin. If new scrap is obtained directly from its producer, before any quality mixing take place, it is easier to determine its chemical composition. So that the first output of the current research work is to identify the scrap sources and destinations among the UE (28) as shown in Table 2.4.

Exporting Region / Destination	Germany	France	Netherlands	United Kingdom	Cezch Republic	Poland	Belgium	Austria	Others
Germany	X		0,685		0,572	0,731		0,312	
Italy	1,357	0,535						0,575	
France	0,866	X					0,63		
Netherlands	1,659		X				0,278		
Cezch Republic					X	0,343			
Poland					0,342	X			
Belgium	1,061	1,293	0,579				X		
Luxembourg	1,182	0,733							
Portugal				0,529					
Spain		1,769		1,214					
Others	0,986	0,555	1,24	0,605	0,759	0,255	0,291	0,108	5,271

Table 2.4: EU (28) scrap trade market (4)

2.6 Chapter 2 recall and conclusions

There is no doubt that Steel is the world's most important industrial material, not only due to the abundance of iron in nature and the huge material volume produced every year, but also because Its properties, which include low cost, ease forming, high resistance, long service life, variety of qualities and applications, assembly capacity. And most important, due to steel capability to be easily recyclable.

On the other hand, steelmaking industry has proved its capability to adapt the manufacturing processes to the socioeconomic changes of society along the history

Looking at global steel production figures, several statement can be done:

- Since there are records, worldwide Steel production is always growing up, with specific exceptions during the global economic crises of the 90s and the first decade of the 21st century.
- Steel production is relatively localized: 20 countries account for more than 90% of the worldwide steel production. China is leading the ranking with about 50% of the total production.
- Europe is the main driver of the scrap trade worldwide, both in export and import figures. In Europe the main steel production is allocated in 5 countries: Germany, Italy, France, Spain and Poland
- Focusing on Europe, the global economic crisis hit the continent severely, systematically loosing production market share. Nevertheless, and looking at 2018 figures (new Steel production historical maximum of 1.8 Billion tons), the worldwide situation seems to be recovering slowly.
- Analyzing steel producing companies, the fragmentation of production is much more acute, being ArcelorMittal the largest producing company
- From the steel production processes point of view, in 2018, around 70% of the global steel production was made by BOF route (12,5% of the BOF raw material is scrap) and 30% was made by EAF route (71% of EAF raw material is scrap). These data confirm the importance of ferrous scrap metal as the main raw material of the current steelmaking processes.

In the medium and long-term, boosted by the social and environmental pressure, we can expect the steel industry to increasingly replace natural resources by steel scrap, thereby conserving raw materials, energy, and reducing CO2 emissions. Some authors propose that by 2050, Electric Arc Furnace production tonnage will increase significantly, reaching a production share of 40% in 2050.

Currently, Europe, NAFTA, Africa and overall Middle East are heavily dependent on scrap due to their dependency on EAF process. If the previous forecasts are met, studying scrap availability in the future is crucial to ensure the steelmaking process feasibility.

Within this context, the current recycling rate of ferrous material is an important parameter to define the future recycling strategies. Being aware of that, major steel companies are devoting huge amounts of resources on research and development activities focused on raw materials characterization and within this scope, this thesis becomes important.

3

Ferrous Scrap, such a complex material

This chapter presents Ferrous scrap as the main steelmaking raw material, describing the specifics of the scrap based on its origin, as well as the importance of the physical and chemical characteristics of the material. Two additional important concepts, in the context of the current thesis, are also introduced; the official scrap specifications as reference accepted standards and the Total Cost of Ownership (TCO) as the main criteria for assessing the real cost of the different scrap grades. Some of these concepts will be better detailed in subsequent chapters.

As it was described in the previous chapter, Ferrous scrap is the main raw material in the steelmaking process by Electric Arc Furnace (EAF) route and it is also an important raw material for Basic Oxygen Furnace (BOF) process in the case of integrated route.

Since the objective of steelmaking processes is just to transform “old” steel in “new” steel products, the main component of interest in scrap materials is the iron content. However, any material made of steel is prone to be used as primary raw material in steelmaking and this makes scrap an unreliable material in terms of chemical composition, pollutants, mixtures with other materials and physical characteristics.

3.1 The main steelmaking Raw material; Ferrous scrap

The first statement that should be clear before starting the descriptive analysis of the different types of ferrous scrap is that steel scrap comes from a wide array of sources, and therefore presents a great heterogeneity in both physical and chemical characteristics, even within scrap grades belonging to the same family.

In order to produce good quality steel with scrap, steelmakers require confidence in the quality and consistency of the scrap used. It must also be in the correct physical form for the steel making process.

Due to its wide range of physical forms and great variability of additional materials, an effective management and classification of steel scrap enhances the efficiency of the steelmaking process So that, general understanding of scrap families, according standard international classifications agreements, is the first step when proposing new characterization methods.

3.1.1 Sources of steel scrap

A simple, but most widespread classification of scrap is based on its source. According this classification criteria, three scrap types can be differentiated:

Home scrap (plant scrap): Home scrap is generated in steel mills during the production of steel and therefore depends on a conversion factor (production yield). Nevertheless, and due to improved efficiency in production, the quantities of home scrap have decreased over time. The amount of home scrap generated differs from mill to mill, but it typically represents around 10% of the total steel production.

This type of scrap requires no recovery process and rarely leaves the steel-making production area. Instead, it is returned to the furnace on site and melted again. The recovery of home scrap is managed within the steel mill and is not handled by the recycling industry.

It is relatively pure, and its chemical composition is known, so it can be easily characterized and recycled.

In terms of figures:

- Home scrap accounts for approximately 29% of total available scrap (8).
- The easiest way to estimate home scrap availability is:

Crude steel production (tonnes) x production yield (%)

Some examples of home scrap are as follows:

- Internal Scrap: Metallic scrap can be generated all along the steelmaking production process. It may be generated in large solidified shapes - such as large volumes of steel that have solidified in a ladle or pot, irregular sheets from spillages or pouring and waste from parts of slabs, blooms, billets rods, wire coil and off-specification materials. Large pieces of material must be processed into more manageable sizes for the handling system and furnace used for re-melting. This material is normally very high in metallic content. If the steel mill produces a limited number of grades it may not be worth segregating this material into different types. However, if there is a wide range of steel qualities produced - particularly if there are any special grades produced (with chromium, copper...) it may be worthwhile segregating some materials in order to maximize their value and / or minimize contamination.
- Metal Recovered from Slag: Magnetic fractions can be recovered from iron and steel slags. The iron recovered from de-sulphurisation slags has high sulphur content and should be kept separate. Since sulphur is difficult to remove at the steelmaking stage, this material is preferable to be recycled via Blast Furnace or used for steel grades that accept higher sulphur contents.

  The metal recovered from steel making slag is being of a similar composition to the grades of steel produced. If special grades are produced it may be worth evaluating the segregation of the slag from those heats.

Ferrous Scrap, such a complex material

New scrap: New scrap (also called prompt or industrial scrap) is generated in steel-product manufacturing plants when steel is fabricated into finished products and includes such items as turning, clipping and stamping leftovers.

This scrap is generally of high quality with well-known composition and is available for recycling relatively shortly time after its generation.

This material requires little processing and is typically sold to the scrap metal industry that processes it for sale to steel mills and foundries. New scrap with paint or coating (with the exception of cable which does need treatment prior to input into a furnace) does not generally need any waste-related pre-treatment before being sent to the furnace.

In terms of figures:

- New scrap accounts for approximately 23% of total available scrap (8).
- New scrap is a simple function of crude steel production and semi-products manufacturing, respectively. The easiest way to estimate new scrap availability is:

Finished steel consumption per sector (tonnes) x manufacturing process yield (%)

Examples of new scrap are:

- Fabrication Scrap: Scrap coming from fabrication will be the off-cuts, cuttings, punching, chips, turnings, and from the production of components and sub-assemblies. It may be possible to segregate this scrap into different categories at the fabrication shop.
- Manufacturing Scrap: Manufacturing scrap is usually be generated in lower volumes and consists of a higher proportion of finer material (swarf, grindings, polishing sludge, etc.).

There is something an overlap between scrap produced during fabrication and manufacturing stages.

Old scrap or obsolete scrap: This type scrap is generated from obsolete steel products that have come to the end of their useful lives, either separately or mixed, and it is often contaminated to a certain degree. For this reason, the chemical composition of obsolete scrap fluctuates widely depending on its origin and the collection systems used. The recycling industry is essential for the supply of old scrap.

Since the lifetime of many metal products is often longer than 10 years and sometimes longer than 50 years, for instance products for building and construction, when considering the availability of this type of scrap, it must be considered that there is an accumulation of metal in use since the beginning of the industry.

In terms of figures:

- Obsolete scrap accounts for approximately 48% of total available scrap (8).
- The easiest way to estimate Obsolete scrap availability is:

Ferrous Scrap, such a complex material

Finished steel consumption per sector (tonnes) x Recycling Rate (%) x life time (years)

Some examples of old scrap are given as follow:

- End of life vehicle scrap: One major source of steel scrap is end-of-life vehicles (ELVs). Approximately 9 million end-of-life vehicles are discarded every year (9). Assuming that each vehicle produces about one tonne of steel scrap, this gives an indication of the size of this market.

  Cars are primarily composed of metal (about 75%) and a range of other materials. The metallic parts are separated by physical processes and recovered as ferrous scrap (iron and steel, comprising 70% of the total vehicle waste) and non-ferrous metals (5%), all of which are recycled. The remaining 25% is the automotive shredder residue (ASR), which is composed mainly of plastics, contaminated with non-ferrous metallic and other parts that could not be separated.

- Construction: Steel has been used as beams, reinforcement bars and other structural parts in building and construction since its production. The amount of steel scrap generated during the demolition of a building varies greatly by type of building and geographical location. Almost all steel parts are recovered, with good quality beams for direct re-use or for recycling at steelworks.
- Large equipment and machinery: This category cover the industrial and agricultural machinery.
- Packaging material: Steel packaging includes food cans, beverage cans, aerosols, etc.

3.2 Simplistic approach to scrap quality

Use of recycled scrap steel in steelmaking processes has increased for the last decades, and this trend is expected to continue and grow in the future (10). As a result, levels of residual impurity elements entering the steel-making process from scrap are increasing with the growing obsolete scrap use and repeated recycling.

Apart from the general classification explained in the previous section, scrap can be further sub-classified into different groups. However, despite this sub-classification, the characteristics of the scrap within each sub-group tend to vary greatly. In order to keep control of the final quality of the steel products to be manufactured, good characterization of scrap must be performed.

Scrap trade associations worldwide have developed a number of systems for classifying the steel scrap recovered by commercial scrap processing companies. Most of them basically classify ferrous scrap according to several properties, most notably:

- **Chemical composition of metals**: In the case of iron and steel scrap, metal content would best be defined in a narrow sense. This would include other metals besides ferrous ones only if they form part of an iron or steel alloy. Defined in this way metal content would be 100 % minus the sterile content.

  The metallic content measured in terms of weight percentage of the total mass should be as high as possible and can be measured practically as the amount of material that can be unloaded with a magnet. However, if the iron and steel objects have coatings that cannot be neglected or other materials attached to them, these would have to be loosened.

  On the other hand, dust should not be counted towards metal content because it is undesired; scrap should not contain excessive ferrous oxide in any form, except for typical amounts arising from the outside storage of prepared scrap under normal atmospheric conditions. This requirement is used in order to avoid the inclusion of metal scrap with very low economic value due to the excessive metal's oxidation.

- **Level of impurity elements**: Elements in steel are considered as impurities or alloy elements depending on where in the process they are added or removed. Impurities worth noting are:

  - **Sterile**: Sterile materials in scrap include:

    - Non-ferrous metals and non-metallic materials such as earth, dust, insulation and glass;
    - Combustible non-metallic materials such as rubber, plastic, fabric, wood and other chemical or organic substances;
    - Large pieces (brick-size) which are non-conductors of electricity such as tyres, pipes filled with cement, wood or concrete;

        - By-products arising from steel melting, heating, surface conditioning (including scarfing), grinding, sawing, welding and torch cutting operations, such as slag, mill scale, baghouse dust, grinder dust, sludge.

    - **Tramp elements**: The elements that have lower oxygen affinity than iron, such as Cu, Sn, Co, Cr, or Ni remain in the final alloy. Utilisation of low quality scrap can result in the production of out of specification steel and impact the final quality of steelmaking products. There are basically three sources of tramp elements in scrap:

        - Tramp elements in pure state coexisting with pieces of steel scrap. The impurities are mixed with the ferrous portion of the scrap and are mechanically separable, e.g.: discarded electric motors (iron and copper coexist in pure state)

        - Tramp elements used as coating material for steel products. Iron and the non-ferrous metal of the coating build a series of layers consisting of different phases, e.g.: galvanised steel (zinc-rich layers on steel sheet)

        - Tramp elements used as alloying additions in certain steel grades. The impurity elements are dissolved in the bulk steel scrap and are separable only after scrap melt down, e.g.: Ni, Cr, Mo as alloying elements in steel.

    - **Other elements with environmental considerations**:

        - Pb and Zn contained in the scrap are emitted to a large extent, by the furnace as vapour or metal oxide particles and are collected by the Steelshop de-dusting systems.

        - PVC and other halogenated substances might lead to higher emissions of dioxins and other toxic substances from the steel furnaces.

        - Radioactivity: It is very important to detect the presence of radioactive materials as early as possible since the consequences of such incidents for the metal processing industry are always very serious.

- **Physical size and shape:** The size and shape of the scrap to be used at a plant may be limited by its technical limitations. In order to avoid process incident related the size and shape of scrap, these need to be controlled by the agreement between seller and buyer.

- **Homogeneity and consistency:** large variations in quality will result in the production of off-specification steel (or limit the quantity of scrap that can be utilised).

These scrap-quality criteria need to be checked, firstly to assess the potential environmental and health risks of scrap use and manipulation, and secondly to conclude whether the raw material is suitable as direct input to final use (steel work/foundry) or not. It should also allow

deciding if the metal in the scrap is sufficiently pure and has been separated effectively from other types of materials.

Based on these general properties, the scrap is acquired, and the mixture is designed. Given that a large amount of scrap is used in the steelmaking process, it is necessary to have a good characterisation in order to be able to counteract its negative impact during the melting and steel refining processes, which have a high impact on the plant operating costs.

The importance of scrap quality control concept lays on the necessity to optimize process variable costs.

Fig. 3.1 offers a full view of the EAF variable cost control through the scrap management point of view, showing the interrelations between the different aspects that have influence on scrap quality, including those associated with scrap market and the operating costs of the melting process.

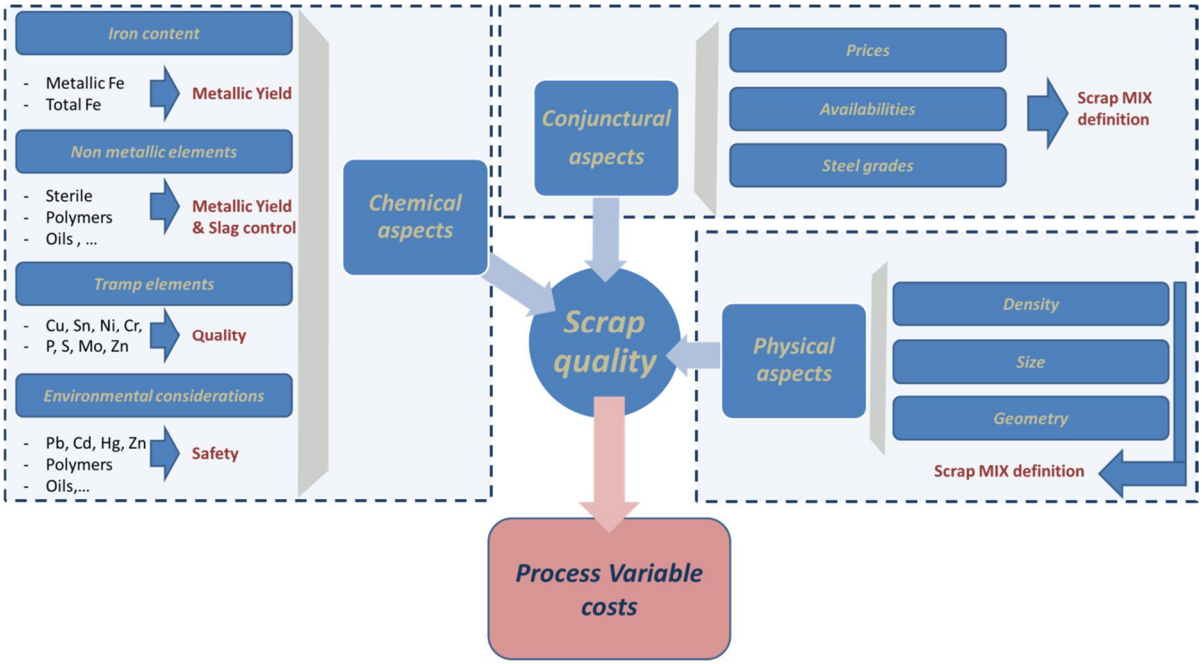

Fig. 3.1: Schematic representation of scrap quality influence on variable process costs

3.3 Scrap specifications and standards

At this point, it is clear that, not only for marketing and trading purposes but also for process optimization requirements, international standards and scrap specifications are needed to set the price and to be used as reference for classification and quality control in steelmaking facilities.

Specifications and standard classifications for ferrous metal scrap exist at international, and National levels, as well as between individual parties. A brief outline of the most representative references is given below:

European Steel Scrap Specification: There are several European entities which have contributed to the elaboration of the European Steel Scrap Specification, making it one of the world reference specifications. Among them, probably the most important are the European Ferrous Recovery & Recycling Federation (EFR) and the European Confederation of Iron and Steel Industries (EUROFER)

The European Steel Scrap Specification includes a first section with some general conditions applicable to all grades of scrap and covers the requirements from an environmental, as well as health and safety perspective. This specification also includes the chemical elements for all scrap grades that must be considered, from a cleanliness point of view, in terms of sterile, residual and other metallic elements. It also provides a detailed description of these specifications by category, which corresponds to the type of scrap, including dimensions and density (11).

ISRI specifications: The institute of scrap Recycling industry (ISRI) is the trade association from the USA that has developed a specification which classifies scrap as non-ferrous and ferrous materials. This specification is used internationally. ISRI's Scrap Specifications Circular is posted in at least once per year on the ISRI web site (12).

The American specification includes a codification for each material included in the document, as well as a description of each item.

National standard classification: Some countries have their own classifications for steel scrap developed by the national industry associations, for example The United Kingdom, Spain, Belgium, France or Germany.

Bilateral contract or Unilateral specification: Due to the great importance of the matter, there are also specifications made as agreements or contracts in trade between two parties or even unilateral definitions that scrap traders must accomplish to introduce scrap products in some particular steelmaking companies. Such specifications are usually based on a standard classification with additional requirements suitable for the desired production process or product. These specifications tend to be continuously reviewed and if necessary modified. Some examples are:

- ArcelorMittal: ArcelorMittal Scrap specifications in USA provide information to ensure that steel scrap materials that do not meet the design criteria enter the site. These

requirements are detailed for every scrap grade by site, including conformance criteria, chemistry, elements that must not be included, sampling criteria, among others.

- GERDAU: Similar to other companies, Gerdau North America publishes its own iron and steel scrap specifications, where different materials are classified into prompt, obsolete or unprepared scrap. The specification of each material includes a brief description, the expected chemistry and dimension restrictions for all steel plants.

3.4 The Real value of scrap

The real value of scrap does not only represent its iron content and price. Scrap represents between 55 and 65% of the total cost of the mini-mill plant. Around 85% of the total costs incurred by the plant are associated with the activities of the Steelshop (13).

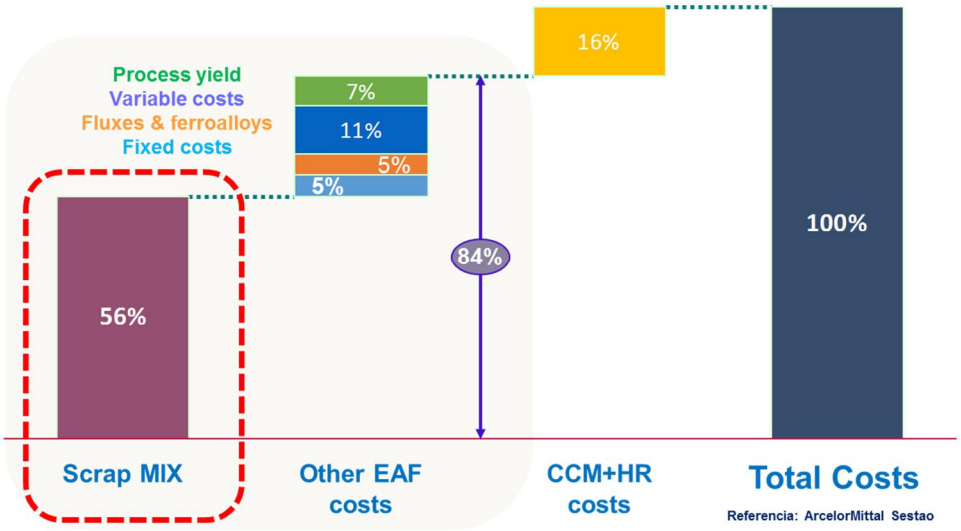

Fig. 3.2: Detailed description of the total cost in a mini-mill plant

Focusing on the Steelshop part, about 60% of the cost corresponds to the purchasing cost of metallic and 40 % of the cost is related to operational parameters, mainly metallic yield (14). Fig. 3.3 depicts the mentioned cost deployment.

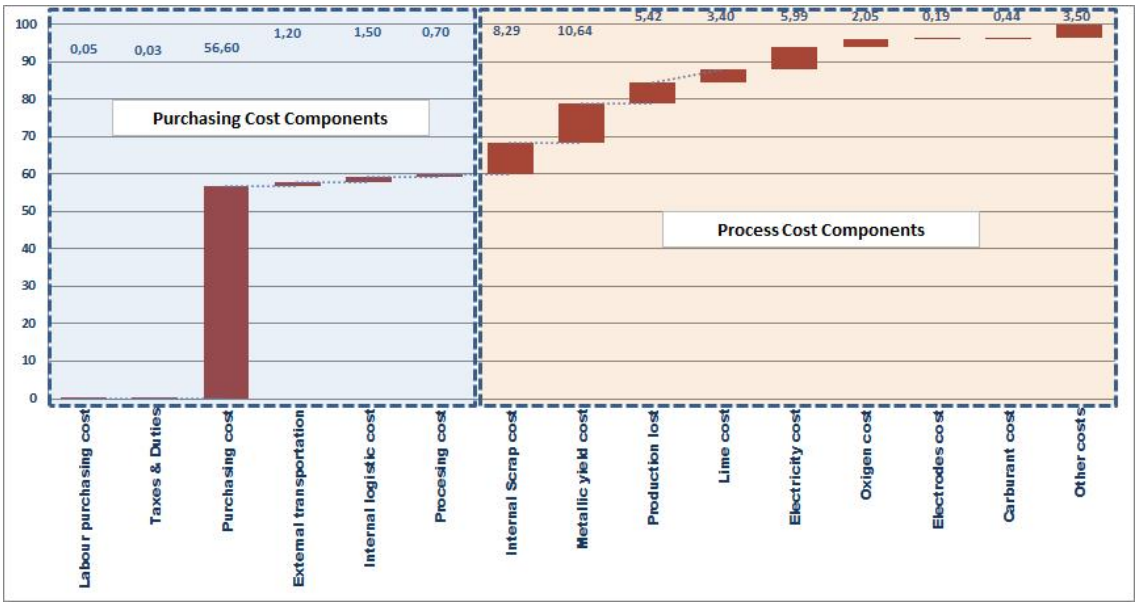

Fig. 3.3: Metallics Waterfall analysis in Electric Arc Furnaces

Thus, when the potential feasibility of using a particular scrap grade is analyzed, other factors apart from the purchasing price need to be looked at. Probably, the most widespread method to define the real value of a material is the Total Cost of Ownership concept (TCO).

Ferrous Scrap, such a complex material

According to ArcelorMittal (14), TCO is "*A holistic mindset and analytical approach to purchase goods and services that incorporates not just price, but all costs associated to acquisition, transport, storage, usage and disposal*". It allows the investigation and reduction of all associated costs of purchased goods by simultaneously pulling all levers: commercial (supplier consolidation, volume bundling, negotiations), demand (standardization, substitution, mix optimization) and process (inventory optimization and transport optimization).

Using a global TCO approach to analyze the EAF process, it is possible to split the individual cost contributions to the total TCO from purchasing to melting. This is very useful for identifying the economic potential of controlling scrap quality.

Fig. 3.4 shows an example of the TCO analysis:

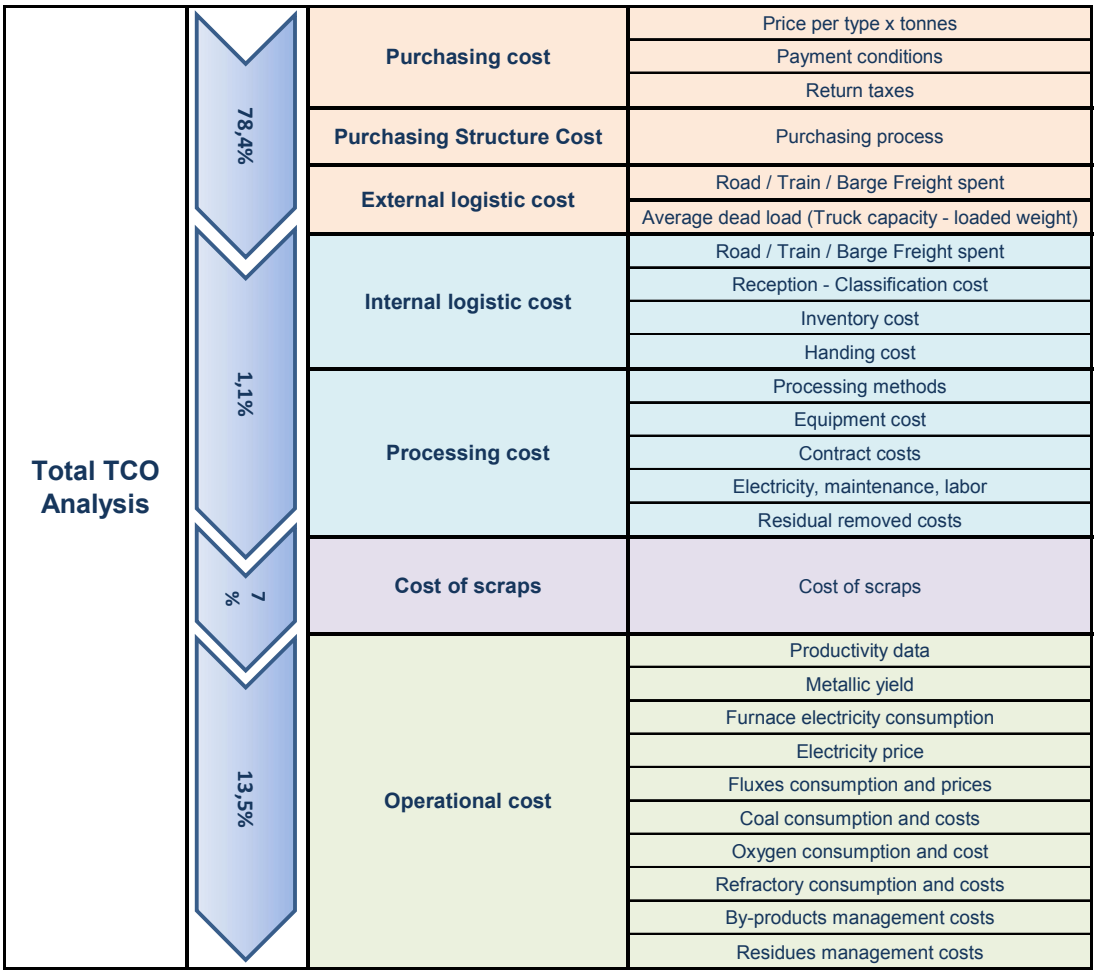

Fig. 3.4: EAF process TCO analysis.

3.5 Chapter 3 recall and conclusions

The main issue of using ferrous scrap as raw material in steelmaking processes is that steel scrap comes from a wide array of sources, and therefore presents great heterogeneity in both physical and chemical characteristics.

Aiming to put some order in the scrap classification, scrap materials can be allocated in three general families based on the origin; obsolete, new and home scraps. However, since Home scrap is generated in steel mills and New scrap is generated in steel-product manufacturing plants, their properties are well known for steelmakers, that why the main concern is to get the characteristics of obsolete scrap.

Around 85% of the total costs incurred by the plant are associated with the activities of the Steelshop, and the scrap non-quality has a strong influence over the steelmaking variable process costs like; metal chemical composition, level of impurities, physical aspect, homogeneity and consistency. Being aware of that;

- Specifications and standard classifications for ferrous metal scrap have been agreed at international and national levels, to ensure that all the entities involved in the scrap trade have a unique criterion for material quality assessment.
- In the steel manufacturing sector, the criterion based on the Total Cost of Ownership (TCO) concept has been established as a standard for the analysis of scrap quality. TCO is a method to define the real value of one particular material in the steelmaking process considering, not only the purchasing price, but also the influence of this material on the variable process costs.

4

Value In Use (VIU) concept; The real scrap value assessment method in steelmaking

This chapter start explaining the EAF process and offers some examples of non-quality in different grades of scrap. Also, the VIU concept is presented as a methodology for analysing the influence of scrap non-quality in the operational results of the EAF melting process. The chapter concludes by evaluating numerically the penalty that the main sterile (CaO, SiO_2 and FeO) have regarding a reference material.

4.1 Steel production in the Electric Arc Furnace (EAF)

In daily electric steelmaking operation, a mixture of different scrap grades is periodically defined as regular scrap mix. This mix selection is mainly based on the TCO concept approach, but always constrained by some physical and chemical conditions that must be accomplished by the whole of the scrap mixture and which are defined by the product's and the process's specifics (the Mix selection process was stabilised in Fig. 3.1).

Although in an ideal situation, the material to be introduced in the furnace should be only steel, due to the intrinsic nature of scrap as recycled material, Scrap is a mixture of steel with other type of materials that, in some cases penalize the steel melting process (loss of metallic performance , Increased volume of slag generated, ...) and in other cases benefit the melting process (reduction of energy consumption, alloys materials, ...). However, from an optimum process management point of view, it is necessary to exactly know the chemical composition of the materials mixture introduced into the furnace.

Focussing the attention on the EAF process, it can be said that three operations are carried out; Melting of scrap, oxidation of liquid steel (reduction of phosphorus and carbon) and temperature adjustment (15).

The efficiency of the melting process of scrap is mainly linked to physical aspects. However, besides the evidence loss of metallic yield produced by the substitution of part of the Iron by other materials, the chemical composition of scrap has a special influence in the other two mentioned processes:

- Oxidation of liquid steel (reduction of phosphorus):
  - The phosphorus removal operation in EAF process must be conducted under oxidizing conditions. The oxidation of phosphorus and its transfer to the slag (slag acts like a sponge) is done by producing phosphate ion. The P_2O_5 is in gaseous state and it does not present enough thermodynamic stability. In order to do the phosphorous removal, it is necessary to generate a stable oxide in the slag, this is

accomplished by generating a phosphate compound called tri or tetra-calcium according to the following reaction:

$$[P] + \frac{5}{2}(FeO) + \frac{3}{2}(CaO) \leftrightarrow \frac{1}{2}(Ca_3(PO_4)_2) + \frac{5}{2}[Fe] \qquad \textbf{(4.1)}$$

But to encourage this reversible chemical reaction, it should pay attention to the following rules:

- There should be an oxidizing medium: there must be present a significant amount of oxygen available (e.g. high FeO).
- There should be a large amount of available CaO, higher compared with the amount of C2S (high basicity index).
- It should be considered the partition coefficient (P) / [P] in equilibrium conditions; [amount of stabilized phosphorus in slag ($nCaO\text{-}P_2O_5$)] compared with (the phosphorus present in the steel).
- There should be a good contact between the slag and steel which favours the kinetics of phosphorous reduction reactions.
    - Slag fluidity (nearly 100% of the liquid phase, avoiding excessive saturation of MgO and CaO, and an early formation of FeO).
    - Efficient steel-slag stirring (gas flow produced during decarburization).
    - Time under favourable conditions.

- Temperature adjustment
    - Chemical energy input: When oxygen is injected into the EAF, it partially reacts with metallic elements contained in scrap generating oxides. Those oxidizing chemical reaction are highly exothermic and release a lot of energy.

reaction					energy of the reaction	
2 Al	+	1.5 O_2	→	Al_2O_3	- 8.61 kWh/kg_{Al}	-13.86 kWh/m^3O_2
Si	+	O_2	→	SiO_2	- 8.70 kWh/kg_{Si}	-10.92 kWh/m^3O_2
Mn	+	0.5 O_2	→	MnO	-1.95 kWh/kg_{Mn}	-9.56 kWh/m^3O_2
2 Cr	+	1.5 O_2	→	Cr_2O_3	-3.05 kWh/kg_{Cr}	-9.44 kWh/m^3O_2
S	+	O_2	→	SO_2	-2.75 kWh/kg_S	-3.94 kWh/m^3O_2
2 Fe	+	1.5 O_2	→	Fe_2O_3	- 2.03 kWh/kg_{Fe}	-4.74 kWh/m^3O_2
Fe	+	0.5 O_2	→	FeO	- 1.32 kWh/kg_{Fe}	-6.58 kWh/m^3O_2
C	+	O_2	→	CO_2	- 9.10 kWh/kg_C	-4.88 kWh/m^3O_2
C	+	0.5 O_2	→	CO	- 2.55 kWh/kg_C	-2.73 kWh/m^3O_2
CO	+	0.5 O_2	→	CO_2	- 2.81 kWh/kg_{CO}	-7.02 kWh/m^3O_2

Table 4.1: Ooxidizing reaction in EAF steelmaking

This new compound generation also presents an important drawback that must be taken into consideration and which is related to refractory consumption since those compounds are mostly acid compounds that react with the basic bricks used for building the refractory shell in the EAF.

- Electrical energy input (foaming slag practice): After scrap melting, the heating up of liquid steel to the desired temperature in the electric arc furnace is accomplished by heat transfer through the electric arc, so that the efficiency of this heat transfer is essential in the economic balance of the furnace. Currently, the most common practice to optimize the heat transfer is the permanent foamy slag practice of the slag in order to intend covering with slag the entire electric arc. There are four main factors which allow improving the capability of controlling slag foaming behaviour:
  - Decreasing the surface tension in the steel-slag interface: by controlling the basicity index of the slag and the presence of FeO in the slag.
  - Increasing the viscosity of the slag by controlling the temperature, the basicity index and the presence of MnO and FeO.
  - Generated slag volume.
  - Presence of the second phase particles in slag due to CaO (Ca_2SiO_4) and / or in MgO (Magnetowustite in solid solution) saturation.

It is important to point out that the chemical composition of slag along the process varies a lot, tending to reduce the amount of MgO and CaO and to increase the amount of FeO. However, to ensure the Phosphorus oxidation processes and to guarantee the energy efficiency of the liquid steel heating process, it is necessary to maintain the proper relationship between basic oxides and acids oxides (basicity index of the slag) at the different process stages. To ensure the proper evolution of steel and slag chemical composition along the melting process, it is necessary to know the amount of no ferrous elements introduced with the scrap and then to adjust Oxygen, Carbon, lime and dolomite addition during the melting process.

4.2 Understanding different scrap specifics

In Section 3.1.1, the different sources of steel scrap were generally allocated in three general families accepted worldwide (Home scrap, New scrap and Obsolete scrap) and described in a very general way.

In that section, some of the reference Steel Scrap Specifications were also presented. As it was previously described, these Steel Scrap Specifications define the scrap categories (qualities) not only by their origin or their shape but also by their content in residual elements, content in sterile and by also their density.

In this section, some of the most used scrap grades in the EAF steelmaking process are analysed in greater detail. This analysis will allow to better understand how the different scrap grades are generally defined according to their physical and chemical characteristics, as well as the way in which some of these scraps are sometimes received in the factory's scrap yards.

The "high residual" family includes E1, E3, E40, E46, EHRB and EHRM categories (European specification). The following lines describe the most common grades of this scrap family:

- **Shredded steel scrap (E40)** corresponds with Old steel scrap fragmentized into pieces not exceeding 200 mm in any direction for 95% of the total. No piece, in the remaining 5%, shall exceed 1000mm. It should be prepared in a manner to ensure direct charging. The scrap shall be free of excessive moisture, loose cast iron and incinerator material (especially tin cans). Must be free of metallic copper, tin, lead (and alloys), and sterile to meet the aimed analytical contents (11).

Fig. 4.1: E40 examples: Top-left) USA, top-right) Luxembourg, bottom-left) Spain and bottom-right) Belgium

Typical shredded scrap composition, in certain elements, allowed by some of the international scrap specifications, and also internally defined by several steelmaking companies are showed in Table 4.2: and Table 4.3:

	Cu	Ni	Sn	Sterile
EUROFER	<0,25		<0,02	<0,4
EFR	<0,25		<0,02	<0,4

Table 4.2: E40 Scrap chemical requirements according two international scrap specifications

	C	Mn	Si	P	S	Cu	Ni	Sn	Sterile
ArcelorMittal				0,03	0,04	0,2	0,1	0,1	<0,4
Gerdau			0,2	0,02	0,04	0,3	0,11		
SSM			0,3	0,05	0,05	<0,25	<0,15	<0,02	
Cascade Steel	0,25	1,5	0,5	0,05	0,05	0,22	0,1	0,015	<0,4

Table 4.3: E40 Scrap chemical requirements according three steelmaker internal scrap specifications

However, although the acceptance criteria of the different scrap are clearly defined, it is common to find high dispersions over the allowed chemical composition required. Fig. 4.2 shows some examples of non-fulfilments.

Fig. 4.2: Example of higher amount of dirt than allowed (left) and highly oxidized scrap (right)

- **Light structural steel scrap (E1)** corresponds with Old thin steel scrap (Old Light Scrap) with thickness < 6mm and dimensions ≤1.5 x 0.5 x 0.5 m. It should be prepared in a manner to ensure direct charging. Must be free of rebar and merchant bars, free of metallic copper, tin, lead (and alloys), mechanical pieces and sterile to meet the aimed analytical contents. May include light vehicles wheels (11).

Fig. 4.3: E1 examples: Top-left) Luxembourg, top-right) Spain, bottom-left) Spain import and bottom-right) Belgium

Typical E1 scrap composition, in certain elements, allowed by some of the international scrap specifications, and also internally defined by several steelmaking companies are showed in Table 4.4 and Table 4.5:

	Cu	Ni	Sn	Sterile
EUROFER	<0,4		0,02	<1,5
EFR	<0,4		0,02	<1,5

Table 4.4:E1 Scrap chemical requirements according two international scrap specifications

	C	Mn	Si	P	S	Cu	Ni	Sn	Sterile
ArcelorMittal	0,3	0,5	0,2	0,03	0,03	<0,4		<0,02	<1,5
Gerdau			0,25	0,04	0,04	<0,3	<0,15	<0,015	
SSM			0,5	0,06	0,05	<0,4		<0,02	
Cascade Steel	0,5	1,5	0,5	0,05	0,05	<0,2	<0,15	<0,015	<1,5

Table 4.5: E1 Scrap chemical requirements according three steelmaker internal scrap specifications

Fig. 4.4 shows some examples of non-fulfilments.

Fig. 4.4: Example of higher amount of dirt than allowed (left) and scrap grades mixing (right)

- **Structural steel scrap (E3)** corresponds with Old thick steel scrap (Old heavy scrap) with thickness ≥ 6mm and dimensions ≤1.5 x 0.5 x 0.5 m. It should be prepared in a manner to ensure direct charging. It may include tubes and hollow sections and exclude vehicle body and wheels from light vehicles. Must be free of rebar and merchant bars, free of metallic copper, tin, lead (and alloys), mechanical pieces and sterile to meet the aimed analytical contents (11).

Fig. 4.5: E3 scrap examples: Top-left) USA, top-right) Spain, bottom-left) rail and bottom-right) Belgium

Typical E3 scrap composition, in certain elements, allowed by some of the international scrap specifications, and also internally defined by several steelmaking companies are showed in Table 4.6 and Table 4.7:

	Cu	Ni	Sn	Sterile
EUROFER	<0,25		<0,01	<1,0
EFR	<0,25		<0,01	<1,0

Table 4.6: E3 Scrap chemical requirements according two international scrap specifications

	C	Mn	Si	P	S	Cu	Ni	Sn	Sterile
ArcelorMittal	0,4	0,5	0,2	0,015	0,014	<0,25		<0,01	<1,0
Gerdau			0,15	0,03	0,04	<0,15	<0,1	<0,01	
SSM			0,3	0,05	0,05	<0,25		<0,01	
Cascade Steel	0,7	0,75	0,025	0,025	0,035	<0,15	<0,15	<0,01	<1,0

Table 4.7: E3 Scrap chemical requirements according three steelmaker internal scrap specifications

Fig. 4.6 shows some examples of non-fulfilments.

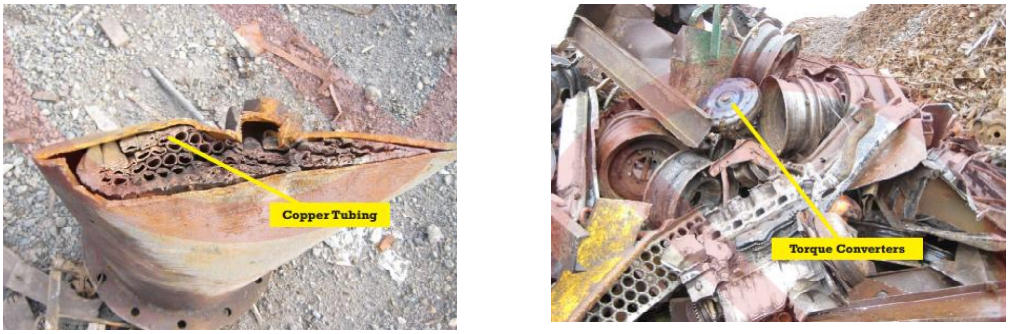

Fig. 4.6: Example of presence metallic Cu (left) and non-allowed elements in E3 scrap (right)

In “low residual” family, there are included scrap categories such as E2, E6, E8, E5H and E5M (European specification). The following lines describe the most common scrap in this category:

- **Bundled steel scrap (E6)** corresponds with New production thin steel scrap (less than 3mm thick), compressed or firmly baled in a manner to ensure direct charging. The steel scrap must be uncoated unless permitted by a joint agreement. Must be free of metallic copper, tin, lead (and alloys), mechanical pieces and sterile to meet the aimed analytical contents (11).


Fig. 4.7: E6 scrap examples: left) USA and right) Spain

Typical E6 scrap composition, in certain elements, allowed by some of the international scrap specifications, and also internally defined by several steelmaking companies are showed in Table 4.8 and Table 4.9:

	Cu	Ni	Sn	Sterile
EUROFER			<0,3	<0,3
EFR			<0,3	<0,3

Table 4.8: E6 Scrap chemical requirements according two international scrap specifications

	C	Mn	Si	P	S	Cu	Ni	Sn	Sterile
ArcelorMittal	0,07	0,32	0,07	0,01	0,012	<0,03		<0,007	<0,3
Gerdau			0,150	0,01	0,01	<0,1	<0,05	<0,005	
SSM			0,8	0,08	0,03				
Cascade Steel	0,1	0,75	0,5	0,03	0,03	<0,1	<0,1	<0,01	<0,3

Table 4.9: E6 Scrap chemical requirements according three steelmaker internal scrap specifications

Fig. 4.8 shows some examples of non-fulfilments.

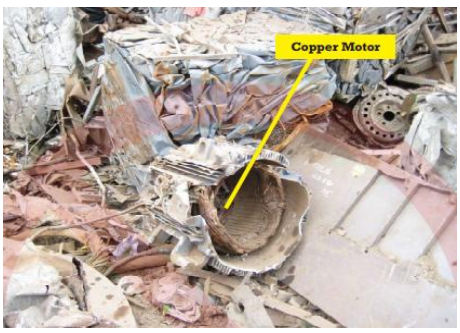

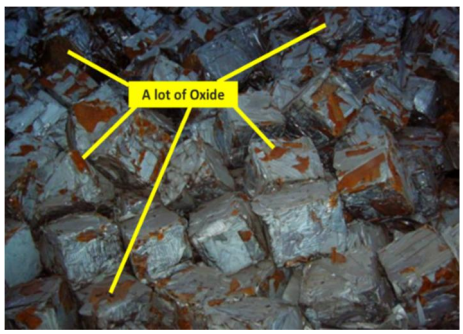

Fig. 4.8: Example of non-allowed elements in E6 scrap (left) and Highly oxidized scrap (right)

Value In Use (VIU) concept; The real scrap value assessment method in steelmaking

- **Busheling steel scrap (E8)** corresponds with new production thin steel scrap (less than 3mm thick) and dimensions ≤1.5 x 0.5 x 0.5 m. The steel scrap must be uncoated unless permitted by a joint agreement and be free of unbound ribbons. Must be free of rebar and merchant bars, free of metallic copper, tin, lead (and alloys), mechanical pieces and sterile to meet the aimed analytical contents (11).

Fig. 4.9: E8 scrap examples: left) USA and right) Luxembourg

Typical E8 scrap composition, in certain elements, allowed by some of the international scrap specifications, and also internally defined by several steelmaking companies are showed in Table 4.10 and Table 4.11:

	Cu	Ni	Sn	Sterile
EUROFER			<0,3	<0,3
EFR			<0,3	<0,3

Table 4.10: E8 Scrap chemical requirements according two international scrap specifications

	C	Mn	Si	P	S	Cu	Ni	Sn	Sterile
ArcelorMittal	0,07	0,32	0,07	0,01	0,012	<0,03		<0,007	<0,3
Gerdau				0,01	0,01	<0,1	<0,08	<0,005	
SSM			0,03	0,02	0,02				
Cascade Steel	0,15	1,5	0,5	0,05	0,05	<0,1	<0,1	<0,01	<0,3

Table 4.11: E8 Scrap chemical requirements according three steelmaker internal scrap specifications

Fig. 4.10 shows some examples of non-fulfilments.

Fig. 4.10: Example of tin coated busheling (left) and (right)

In addition to the two scrap families described previously (low and high residual scrap grades), there are also other "clean" raw materials that are normally used to complement the scrap mix. These materials are mainly HBI, DRI, Pig Iron, Beach Iron and own recovered scrap.

- **Beach Iron steel scrap** corresponds with Solid hot metal which has been cooled on the sand and broken into pieces.

Fig. 4.11: Beach Iron scrap examples: left) Spain and right) Belgium

Typical composition internally defined by several steelmaking companies are showed in Table 4.12:

	C	Mn	Si	P	S	Cu	Ni	Sn	Sterile
ArcelorMittal	4,5	0,23	0.7	0.065	0,02				<2,0
Gerdau	4			0,07	0,03	<0,02	<0,01	<0,002	
Cascade Steel	4,5	0,5	2,25	0,05	0,06	0,05	0,05	0,01	

Table 4.12: Scrap chemical requirements according three steelmaker internal scrap specifications

Fig. 4.12 shows some examples of non-fulfilments.

Fig. 4.12: Example of high slag content (left) and (right) big pieces of BI

- **Hot Briquetted iron (HBI)** corresponds with reduced iron ore briquetted at high temperature just after reduction in the rotary hearth furnace.

Fig. 4.13: HBI scrap example

Typical HBI composition are showed in Table 4.13:

	C	Mn	Si	P	S	Cu	Ni	Sn	Sterile
ArcelorMittal	0,9			0,09	0,011				<3
Cascade Steel	1,5	0,25	0,25	0,05	0,05	<0,1	<0,05	<0,01	

Table 4.13: HBI Scrap chemical requirements according three steelmaker internal scrap specifications

It should be clear that the final composition of the scrap is mainly defined by the origin of the raw material. However, it is important to note that scrap pre-treatment (see chapter 5) and post-treatment processes (see chapter 6) have an important influence on the final quality of scrap materials. So, the acceptance criteria of each factory are strongly conditioned by other aspects such as suppliers, local scrap market availability or market prices trends.

Thereby, it is easy to make a rough estimation of which are the predominant chemical elements in each of the scrap grades based on their origin and processing methods before arriving the Steelshop:

- **Shredded scrap (E40)** mainly comes from the recycling activities of vehicles after end of life. The Metallic recovered fraction is usually defined as the 75–85% of the vehicle mass remaining after de-pollution and dismantling (16). And due to its origin and processing methods it usually contains small portions of the elements removed in the pre-processing operations before fragmentation, such as plastics and painted elements (presenting high contents of Carbon and volatile materials) and electric wiring (leading to high copper levels). On the other hand, the high apparent surface of to this scrap results in high surface oxidation (The FeO content is also high).
- **Structural light scrap (E1)** usually comes from used and unserviceable goods (and partially from industry). This scrap category is characterized by a higher percentage of impurities than in other scrap grades (volatile, sterile materials and high oxidized superficial layer), as well as higher free metallic elements content (aluminium, Copper, chromium). It may also content coated (tinned or galvanized) or painted steel. Because of the way in which this type of scrap is collected and transferred to recycling plants, they usually contain high amounts of dirt (mainly SiO_2) and therefore, the metallic yield of this scrap is one of the lowest.
- In **Structural scrap (E3)** case, the recycling material comes from demolition work and industry. Steel manufactured for this type of applications are usually low-medium carbon steels, killed by silicon and alloyed with manganese (and / or niobium or vanadium) which will lead to high contents of C, Mn and Si in the steel. It might include concrete steel, mechanical parts, galvanized scrap.
- The steel from which **Bundled and Busheling** scrap comes corresponds normally with flat product manufactured by integral route (very low level of residual elements such as copper, tin or nickel). Some examples of pieces made with this steel are automotive parts, steel clipping, die-cutting or stamping products, presses, deep drawing products or pipes. Theoretically, it is free of metal which is coated, limed, vitreous enamelled, and electrical sheet (low carbon, silicon and sulphur). On the other hand, and since the material is collected from processing shops, this material is free sterile materials.

Value In Use (VIU) concept; The real scrap value assessment method in steelmaking

- The main raw material used to produce **Beach Iron** / Pig Iron in a blast furnace are iron ore, coke, sinter, and limestone. Iron ores are mainly iron oxides and include magnetite (72,4% of Fe), haematite (70,0% of Fe), Goethite (62,8% of Fe) or Siderite (48,3% of Fe) (17), However, it also contains other impurities that will be present in the produced Beach Iron such as sulphur, phosphorus and silicon. Lime is used to remove this large amount of the impurities in the ore and some of it may remain in the Blast Furnace's products. Finally, Coke is used as energy input due to Carbon oxidation reaction leading to high Carbon product.
- Finally, Iron Briquettes (**HBI**) are produced by reducing iron ore fines by any of several commercially proven direct reduction processes. Once the reduction process is completed, the hot iron is transferred to the briquetting machines, where it is compacted, and then passivated and cooled. The product obtained at the end of the process it is characterized by high density and metallization (including high FeO content), low residual content, high Carbon content and It may present significant values of acid gangue

In line with the concepts mentioned above, Table 4.14 shows the chemical composition of some grades of scrap according to the internal characterization of one ArcelorMittal site:

(%)	Feº	C	Mn	Si	P	S	Cu	FeO	SiO_2	Al_2O_3	CaO	MgO	volatiles
Shredded E40	**85,23**	**0,3**	**0,6**	0,20	0,03	0,04	**0,40**	**6,0**	**1,5**	0,80	0,50	0,4	**4,0**
Structural E1	**84,81**	**0,3**	**0,70**	0,30	0,04	0,05	**0,60**	**4,0**	**3,5**	**1,2**	1,0	0,5	**3,0**
Structural E3	**90,20**	0,16	**0,7**	0,20	0,02	0,02	**0,30**	**3,0**	**1,3**	0,6	1,0	0,5	2,0
Bundle E6	**93,85**	**0,05**	0,35	0,05	0,01	**0,01**	**0,08**	2,0	0,5	0,6	0,5	0,0	2,0
Bushelling E8	**92,54**	**0,05**	0,35	0,10	0,02	**0,02**	**0,12**	2,2	1,0	0,6	1,0	0,5	1,5
Beach Iron	86,20	4,0	0,5	**1,2**	**0,1**	**0,1**	0,0	2,5	**1,50**	0,8	2,0	1,0	0,1
HBI	87,48	**0,8**	0,08	0,01	**0,12**	0,02	0,0	**7,0**	**3,0**	0,5	0,5	0,3	0,2

Table 4.14: Example of characterization of scrap grades in one ArcelorMittal site

4.3 Scrap Value In Use Concept

The Value In Use (VIU) concept has proved to be very useful to relate scrap quality with the operating cost of the Electric Arc Furnace. This concept provides a criterion that allows the comparative interpretation of the results generated by each scrap quality uses in the steelmaking process.

There are several ways to obtain the VIU of scrap (18). All of them are based on a similar approach described as follows: "*The VIU of scrap in the Electric Arc Furnace is an estimation of the operating cost of melting this scrap compared to a reference cost, which is that of melting pure iron*".

It has been demonstrated that there is a clear relationship between the VIU of each scrap material with its process performance (mainly metallic yield). However, the nature of the non-metallic materials, as well as the Fe oxidation degree, also has a great influence on the material performance in the process.

The VIU of a particular scrap grade includes, besides the purchasing costs and metallic yield, the additional costs associated with extra energy consumption and other additional material consumption (electrode, refractories, fluxes …) incurred due to the melting of non-metallic materials included in regular scrap. Those elements or compounds present in scrap can be splinted in four groups:

- Fe; which must be as high as possible.
- Sterile elements (SiO_2, $CaCO_3$, MgO, Al_2O_3, H_2O, FeO …) which are usually associated to the ferrous material source and the pre and post processing methods of scrap.
- Tramp elements (Cu, Sn, Ni, Cr, Mo, S, P …) which have generally a negative impact on the rolling or stamping processes.
- Carbonaceous compounds, Cl, heavy metals, which can have a negative impact on the steel plant environment, if the furnace fumes treatment device is saturated or inefficient.

According to the method proposed by Sidenor (Spain) (19), the scrap VIU can be calculated as:

$$VIU\left(\frac{€}{kglst}\right) = \frac{\frac{€}{kg.scrap} + \left(\frac{kWh}{t.scrap} \cdot \frac{€}{kWh} \cdot \frac{1}{1000}\right) + \left(\frac{kg.CaO}{t.scrap} \cdot \frac{€}{kg.CaO} \cdot \frac{1}{1000}\right)}{\frac{MetallicYield(\%)}{100}} \qquad \textbf{(4.2)}$$

In this method, the VIU of the scrap, besides the metallic yield, is closely linked to the specific electric energy consumption and the theoretical desulphurization requirements.

The method used by ArcelorMittal (19) is a little bit more sophisticated, as it considers heat and mass balances, after setting several Electric Arc Furnace operation parameters according to some theoretical values of EAF process:

- Steel temperature: 1650°C

Value In Use (VIU) concept; The real scrap value assessment method in steelmaking

- Basicity of slag: $(CaO + MgO)/(SiO_2+Al_2O_3) = 2$
- Fe content in the slag (oxides + metal) = 25 %
- Additional losses of metal (in fumes for example): 15 kg/t
- Secondary combustion ratio:
    - $CO_2/(CO+ CO_2) = 0.1$
    - $H_2O/(H2 + H_2O) = 0.5$
- Electrical energy ratio: 70%
- Adjustment of oxygen and carbon mass balance is made by modulation of coal quantity (for example, the carbon carried by the scraps is removed and the iron oxides are reduced with coal)

ArcelorMittal´s method allows to obtain a so called Anti-value (A). In order to obtain this Anti-value, a complete characterization of a given scrap quality, in terms of chemical analysis, together with the output of the previous balances is conducted. The (A) value can be used to obtain the actual VIU of the analysed material according to the following equation:

$$VIU = r \cdot VIU_{PureFe} - A \quad \textbf{(4.3)}$$

Where:

- VIU is the VIU of scrap
- r is the metallic yield
- VIU_{PureFe} is the reference cost of melting pure iron
- A is the total Antivalue, and can be calculated as:

$$A = DQ \cdot E + DC \quad \textbf{(4.4)}$$

Where:

- DQ is the difference of electrical energy used to melt one tonne of scrap and the amount of energy used to melt one tonne of pure iron;
- E is the cost of electrical energy (including the consumption of graphite electrodes);
- DC is the difference of additional costs (lime, coal, refractory consumption and treatment of slag) used to melt one tonne of pure iron and one tonne of scrap.

4.3.1 VIU as effective tool for evaluating scrap quality

There are important discrepancies between the results obtained using the different methods for VIU analysis because the concepts considered in the analyses and the theoretical assumptions are different (18).

However, whatever the analytical method used, to establish a criterion for comparing different scrap grades, not only allows to evaluate the influence of scrap chemical composition over EAF steelmaking process, but also the pre-processing (dismantling, shredding...) and post-processing (storage, mixing...) techniques used for each scrap grade.

In this research work, the method proposed by ArcelorMittal will be adopted to evaluate the influence of the different scrap characterization method presented in this thesis. To carry out these analyses, it is available a dedicated Software called SVIU which has been developed internally by ArcelorMittal Global R&D department. A snapshop of the input data tab of SVIU software is shown in Fig. 4.14:

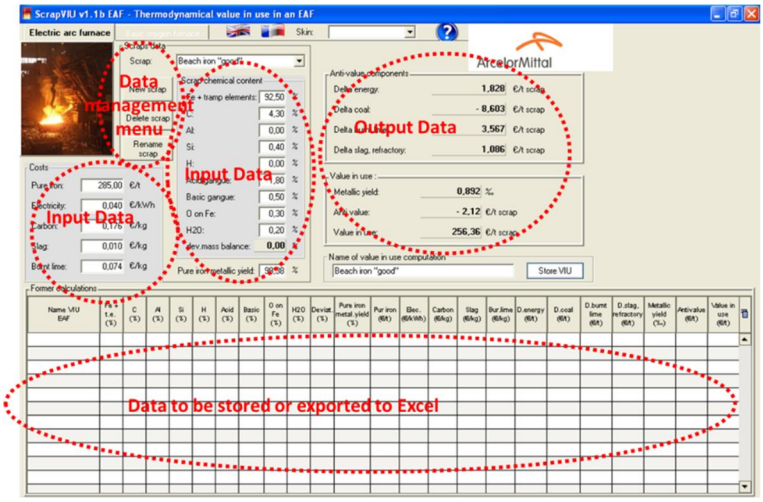

Fig. 4.14: Scrap VIU tool developed in ArcelorMittal Global R&D

SVIU tool requires two types of input data:

1. Cost data: it corresponds with unit cost data in €/unit of the main concepts to be evaluated, including the reference material purchasing cost.
2. Scrap chemical composition.

On the other hand, it provides as main outputs:

1. The Antivalue, in € / t scrap, of the process component consumptions (energy, coal, lime, refractory and slag)
2. Expected performance of each particular scrap grade in specific energy consumption and metallic yield
3. The real VIU of the analysed material.

4.4 Value In Use analysis for scrap characterization

The mass and thermal balances elaborated by ArcelorMittal and supported by different melting tests conducted in a 6 tm pilot EAF in France, allowed ArcelorMittal to quantify the influence of the different elements or compounds present in scrap over the final performance of the EAF steelmaking process. Table 4.15 represents, using colours intensities, how the presence of a certain material in the scrap benefits or harms the EAF steelmaking process for each of the different concepts evaluated by the SVIU tool proposed by ArcelorMittal; green colour represents positive influence and red colour represents negative influence on the process (metallic yield is an exception since the partial substitution of Fe by any other element will always penalize the metallic performance, so that intense green colour represents low negative influence and the intense red colour represents big negative influence).

		Metallic yield	Energy (kWh/t scrap)	Carbon (kg/t scrap)	Burnt Lime (kg/t scrap)	Slag, Refr. (kg/t scrap)
% Fe + tramp elements	Scrap with 100% Fe					
% C	+1% C -1%Fe					
% Al	+1% Al -1%Fe					
% Si	+1% Si -1%Fe					
% H	+1% H -1%Fe					
% acid gangue	+1% acid qangue -1%Fe					
% basic gangue	+1% basic gangue -1%Fe					
% O on Fe	+1% O -1%Fe					
% H2O	+1% H2O -1%Fe					

Table 4.15: Influence of different elements over EAF process performance

The colour distribution and its relationship with the additional specific consumptions included in the table are easily interpretable:

- %Fe + Tramp elements: This concept corresponds with the elements that will remain dissolved in liquid steel.
- %C: 1 additional percent of Carbon in scrap will directly reduce the metallic yield in 1%. It will slightly reduce Carbon requirement during the melting process too.
- %Al: Aluminium will highly penalize the metal yield since it forms acid gangue that should be counteracted later to ensure proper process conditions. To do so, additional burnt lime is required leading to the generation of higher slag volume (containing 25% of FeO. On the other hand, the aluminium oxidation reaction is highly exothermic (+8,61 kWh/kg Al), so it will reduce the amount of electrical energy and carbon addition required
- %Si: Silicon influence over the process is similar to aluminium's described above. For this particular case, the energy released during the oxidation reaction of Silicon is +8,70 kWh/kg Si.
- %H: Hydrogen is usually coming with plastics or hydrocarbons. The presence of this type of materials in scrap, will slightly increase the specific energy consumption associated mainly to the dissociation of the Hydrogen-Carbon bonds, which are

counteracted by the subsequent carbon oxidation reaction (+9,10 kWh/kg C for CO2 reaction and +2,81 kWh/kg C for CO reaction). On the other hand, the carbon contribution will reduce its addition requirement.

- % Acid Gangue: Regarding the acid gangue, it is known that Al_2O_3+SiO_2 are the most pernicious element to include with the scrap metal. As described in previous sections, in order to achieve the slag conditions allowing the process to be optimized, the acid gangue must be compensated for by basic materials, significantly increasing the consumption of lime and the slag generation. This high mass increase in the system causes an additional energy requirement in the process.
- % Basic Gangue: Being able to know the amount of basic elements present in the scrap allows to elaborate the whole system mass balance to adjust the additional lime required by the EAF process.
- % O on FeO: From a theoretical point of view, the presence of FeO in the scrap will not penalize the metallic yield of EAF process given that, according ArcelorMittal's criteria, it was established as a calculation criterion that the iron oxide will be reduced in the slag to a steady value of 25%. However, to reach this point, an additional amount of deoxidizer (carbon) is required. Thus, additional energy is necessary to promote the endothermic FeO reduction reaction (1,08 kWh/kg Fe).
- %H_2O: Basically, the presence of water in the scrap mix leads to an extra input of energy to heat it up to its evaporation point.

According the previous criteria, there are three main elements to be considered when analysing the EAF process penalties due to scrap chemical composition:

- Iron Oxides: Although iron oxide is mainly composed of Fe and it will not cause significant losses in metallic yield, its presence in scrap need to be closely controlled due to the extra energy and carbon that requires its processing.

  Fig. 4.15 depicts how the expected metallic yield evolves as a function of the iron oxide percentage present in the scrap:

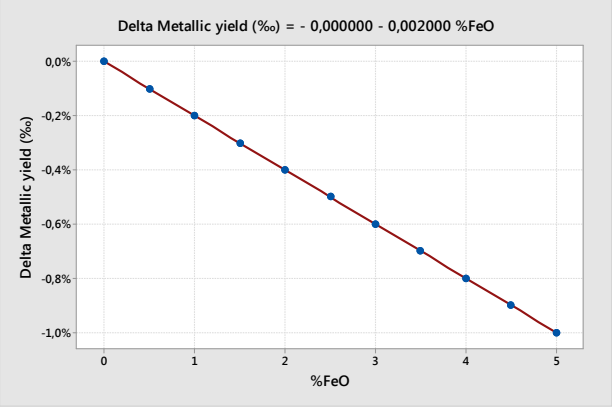

Fig. 4.15: Yield losses due to partial substitution of Fe by FeO

Fig. 4.16 depicts the influence of FeO content over the other specific consumptions considered in ArcelorMittal method for Value In Use calculation.

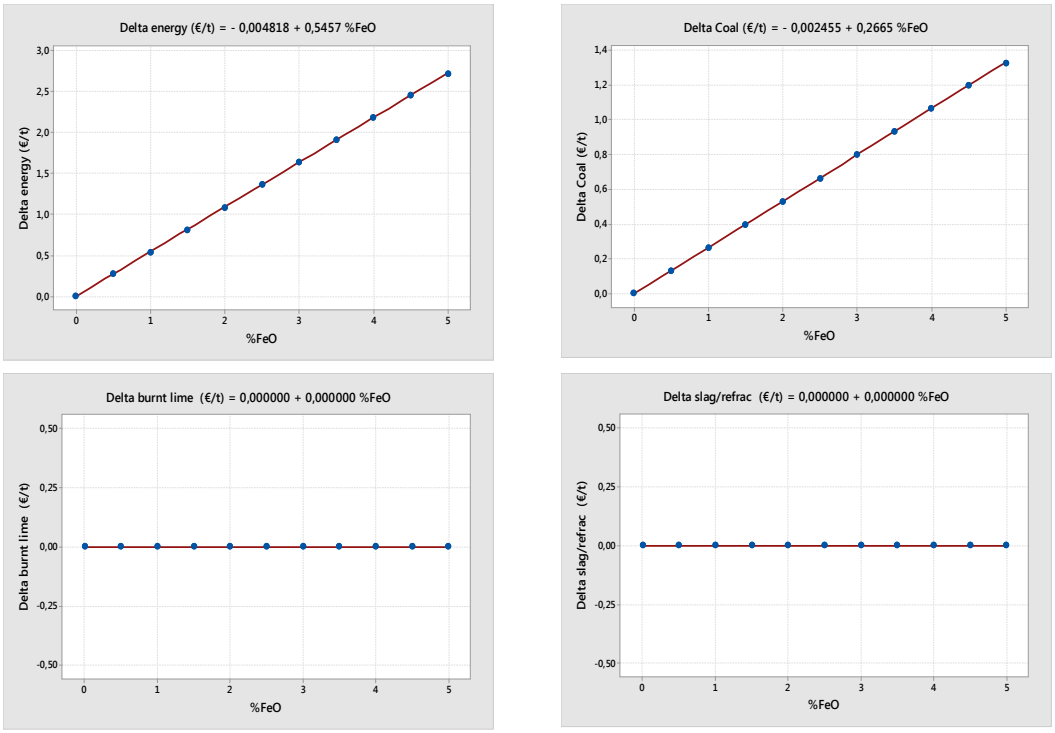

Fig. 4.16: Influence of FeO on furnace performance; Top-left) Energy, top-right) Coal, bottom- left) Lime and bottom-right) slag

Based on process performance shown in Fig. 4.15 and Fig. 4.16:, the total economic penalties with respect to FeO percentage contained in scrap has been calculated applying the VIU equation, and the results obtained are shown in the Fig. 4.17:

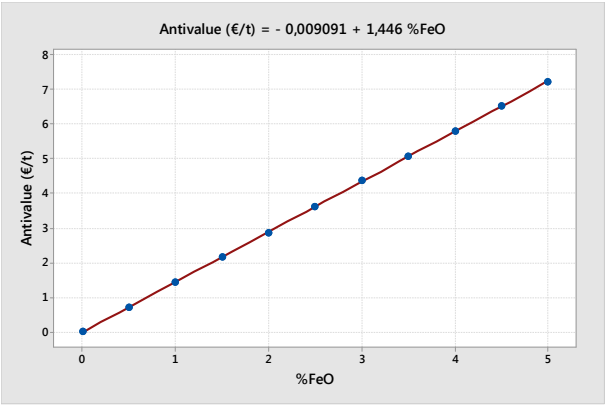

Fig. 4.17: Penalties in €/ton of scrap due to %FeO contained in scrap

- Acid gangue: It is probably the most harmful element in steelmaking process (as it can be seen in Fig. 4.20), and although certain quantities are necessary to provide the slag with the proper properties, its presence in the scrap must be minimized.

In Fig. 4.18, metallic yield evolution with respect to SiO_2 content is shown:

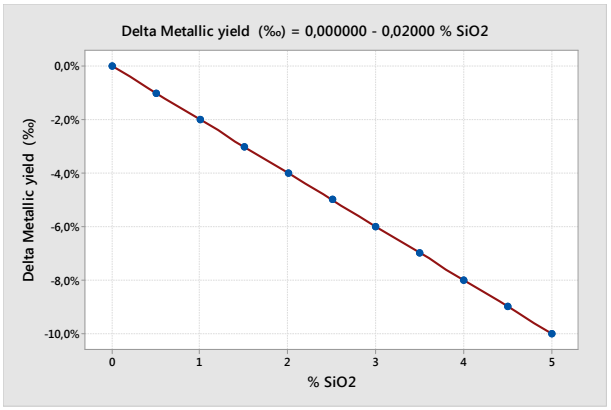

Fig. 4.18: Yield losses due to partial substitution of Fe by SiO_2

Fig. 4.19 depicts the influence of SiO_2 content over the other specific consumptions considered in ArcelorMittal method for Value In Use calculation.

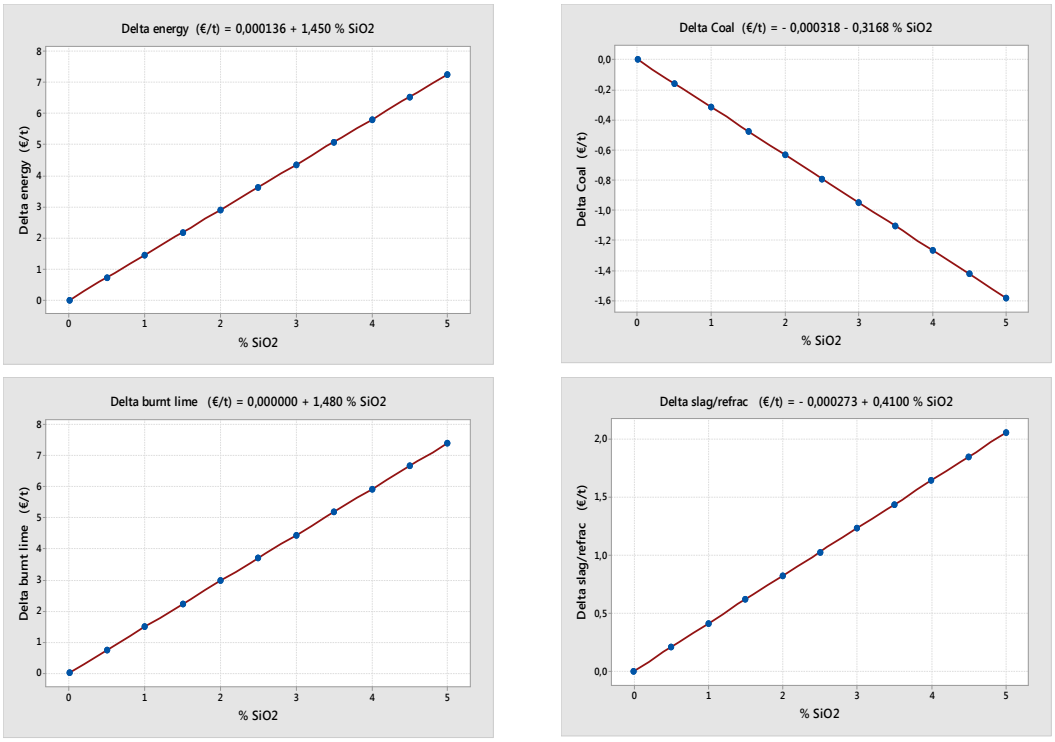

Fig. 4.19:Influence of SiO_2 on furnace performance; Top-left) Energy, top-right) Coal, bottom- left) Lime and bottom-right) slag

Based on process performance shown in Fig. 4.18 and Fig. 4.19, the total economic penalties with respect to SiO_2 percentage contained in scrap has been calculated applying the VIU equation, and the results obtained are shown in the Fig. 4.20:

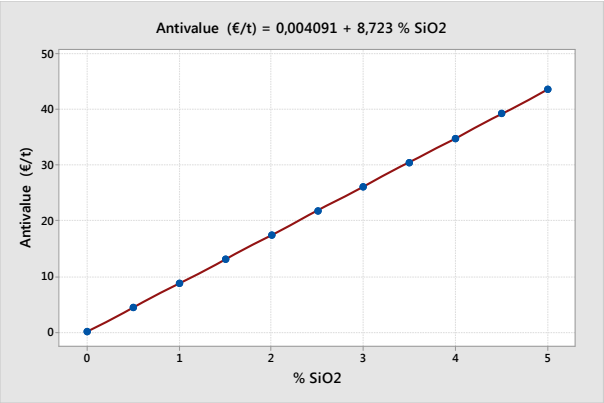

Fig. 4.20: Penalties in €/ton of scrap due to % SiO_2 contained in scrap

- Basic Gangue: Adding basic gangue to the scrap, besides the fact of paying CaO at the price of iron, does not have a significant influence on the value in use of the scrap.

  In this line, Fig. 4.21 depicts how the expected metallic yield evolves as a function of the CaO percentage present in the scrap:

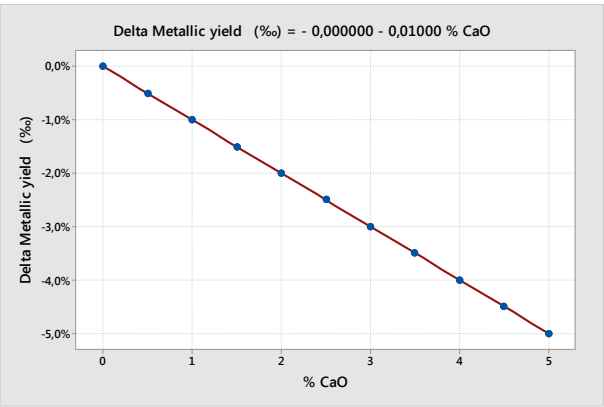

Fig. 4.21: Yield losses due to partial substitution of Fe by CaO

Fig. 4.22 depicts the influence of CaO content over the other specific consumptions considered in ArcelorMittal method for Value In Use calculation.

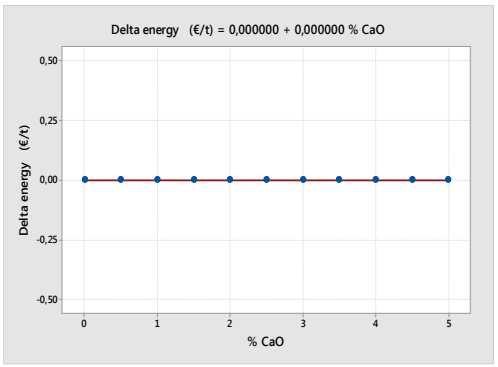

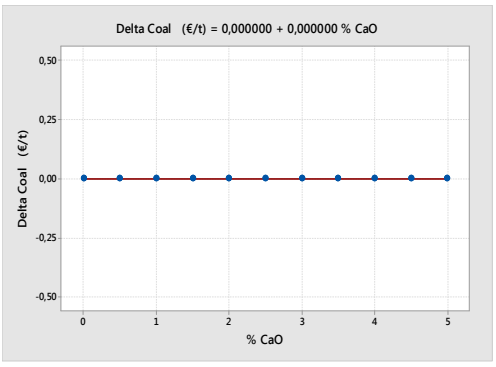

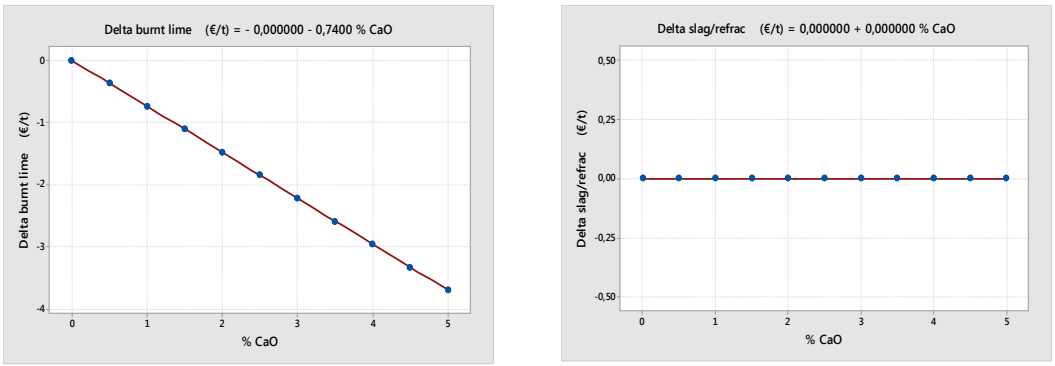

Fig. 4.22: Influence of CaO on furnace performance; Top-left) Energy, top-right) Coal, bottom- left) Lime and bottom-right) slag

Based on process performance shown in Fig. 4.21and Fig. 4.22, the total economic penalties with respect to CaO percentage contained in scrap has been calculated applying the VIU equation, and the results obtained are shown in the Fig. 4.23:

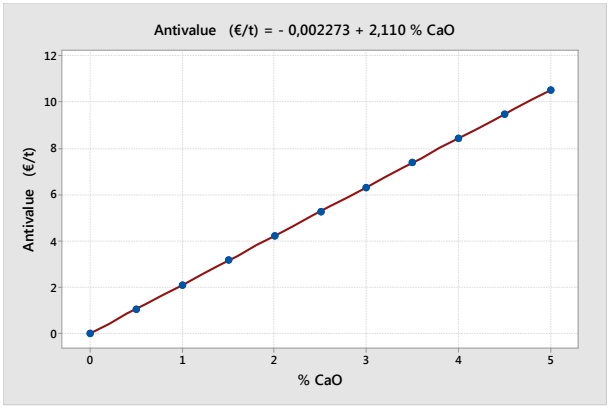

Fig. 4.23: Penalties in €/ton of scrap due to % CaO contained in scrap

4.5 Chapter 4 recall and conclusions

In previous sections, the different scrap grades were generally classified based on their origin. However, additional constrains when using ferrous scrap for producing new steel products are the presence of tramp elements, such Cu, Sn or Ni, that cannot be removed from liquid steel and the amount of sterile material contained. When preparing the scrap mix to be used in the furnace, it is necessary to consider that the individual copper contribution should not exceed the final product requirement in any of those tramp elements.

In this section, besides describing in detail the different scrap grades according the most known international classification standards, a new classification criterion is presented. This criterion is based on tramp elements levels present in the material. According this classification, the different scrap grades can be allocated in:

- "High residual" family includes E1, E3, E40, E46, EHRB and EHRM categories (European specification).
- "Low residual" family, there are included scrap categories such as E2, E6, E8, E5H and E5M (European specification).
- "Clean" raw materials that are normally used to complement the scrap mix. These materials are HBI, DRI, Pig Iron, Beach Iron and own recovered scrap.

On the other hand, TCO concept has been proved to be a useful methodology for defining the scrap purchasing strategies, but it presents some limitations in terms of optimizing the EAF process. To this end, several steelmakers have proposed a new analytical approach called Value In Use (VIU). This new approach claims that "*The VIU of scrap in the Electric Arc Furnace is an estimation of the operating cost of melting this scrap compared to a reference cost, which is that of melting pure iron*".

In this chapter, the method proposed by ArcelorMittal for measuring the VIU is described (including a homemade software for conducting the analyses). ArcelorMittal's tool was used for doing a basic analysis of the influence of the main sterile compounds in the VIU of scrap materials.

The following equations have been obtained from these analyses:

$$AntiValue\ (€|t) = -0{,}0091 + 1{,}446\ \%FeO \quad \textbf{(4.5)}$$

$$AntiValue\ (€|t) = 0{,}0041 + 8{,}723\ \%SiO2 \quad \textbf{(4.6)}$$

$$AntiValue\ (€|t) = -0{,}0022 + 2{,}11\ \%CaO \quad \textbf{(4.7)}$$

5

Scrap preparation techniques; State of the art.

This chapter presents a thorough analysis of the most widespread waste treatment techniques in the ferrous scrap recycling sector, as well as a market search of the different available schemes for scrap processing. Based on these analyses, the chapter concludes proposing an integrated processing scheme

Scrap pre-treatment is not a very widespread activity by steelmakers, and it is usually done directly by scrap dealer. However, in other sectors such as aluminium and copper recycling industries or highly valuable metals recovering industries, in which the economic potential lies in separating and identifying the materials of interest, complex routes of size reduction and sorting have been developed and implemented. Otua Group in Vitoria – Spain is a good example (20).

There are a great number of ferrous scrap types with huge different origins. The numerous sources and forms of ferrous scrap require the use of numerous scrap sorting and preparation techniques to remove the contaminants and/or recover other valuable materials (i.e. non-ferrous metals) prior to entering the steelmaking process.

In the past, scrap was considered a waste and not a raw material and, due to the high offer of this waste, the steelmakers took a very conservative approach. According to this approach, a series of families of scrap, of established origin and with a high content of iron, were defined in the different regulations, assuming that part of the non-ferrous material contained in it should be digested in the steelmaking process. This approach should have been questioned at the moment in which the demand for scrap as raw material increased in the decade of the 90s and it became a raw material (and therefore its price began to increase drastically)

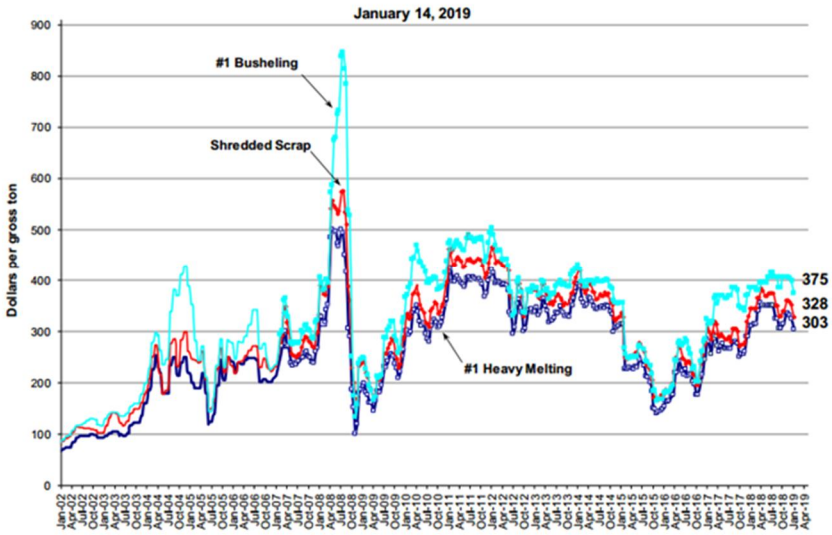

Fig. 5.1: Scrap prices evolution since 2001 (21)

New scrap pre-processing routes to upgrade scrap quality might be the firsts step toward identifying and testing new ferrous scrap market that are not currently in use due to poor quality specifics.

This chapter aims to analyse the different technical options for improving the quality of scrap streams according state of the art in physic mechanical commercial techniques.

5.1 Treatment scheme for ferrous scrap

When designing a scrap treatment strategy, it is necessary to optimize all the intermediate processing stages. These stages include the processes of crushing and separation, to later seek for the most efficient extraction technique of the ferrous fraction generated. To this end, it is essential to understand the macro characteristics of the material to be treated.

The generality of the scrap materials makes complicated the implementation of a single treatment line, basically because the scrap can contain complex structures with very different materials and / or very different and limiting dimensions when defining treatment processes.

One of the main problems that must be faced when defining mechanical treatment processes for size reduction and material separation is that it is difficult to think of a single line of treatment, basically because scrap can contain complex structures with very diverse materials and / or very different and limiting dimensions when defining treatment processes.

Mechanical recycling should include all processes; initial separation, fragmentation, crushing and grinding applied to release the different materials from each other and the separation processes that allow isolating and concentrating the different fractions in order to obtain secondary raw materials suitable for metallurgical treatment.

Scrap preparation techniques; State of the art.

Fig. 5.2 shows some schemes with the possible crushing and separation treatments, to which scrap and waste with high metallic content could be subjected in the recycling lines.

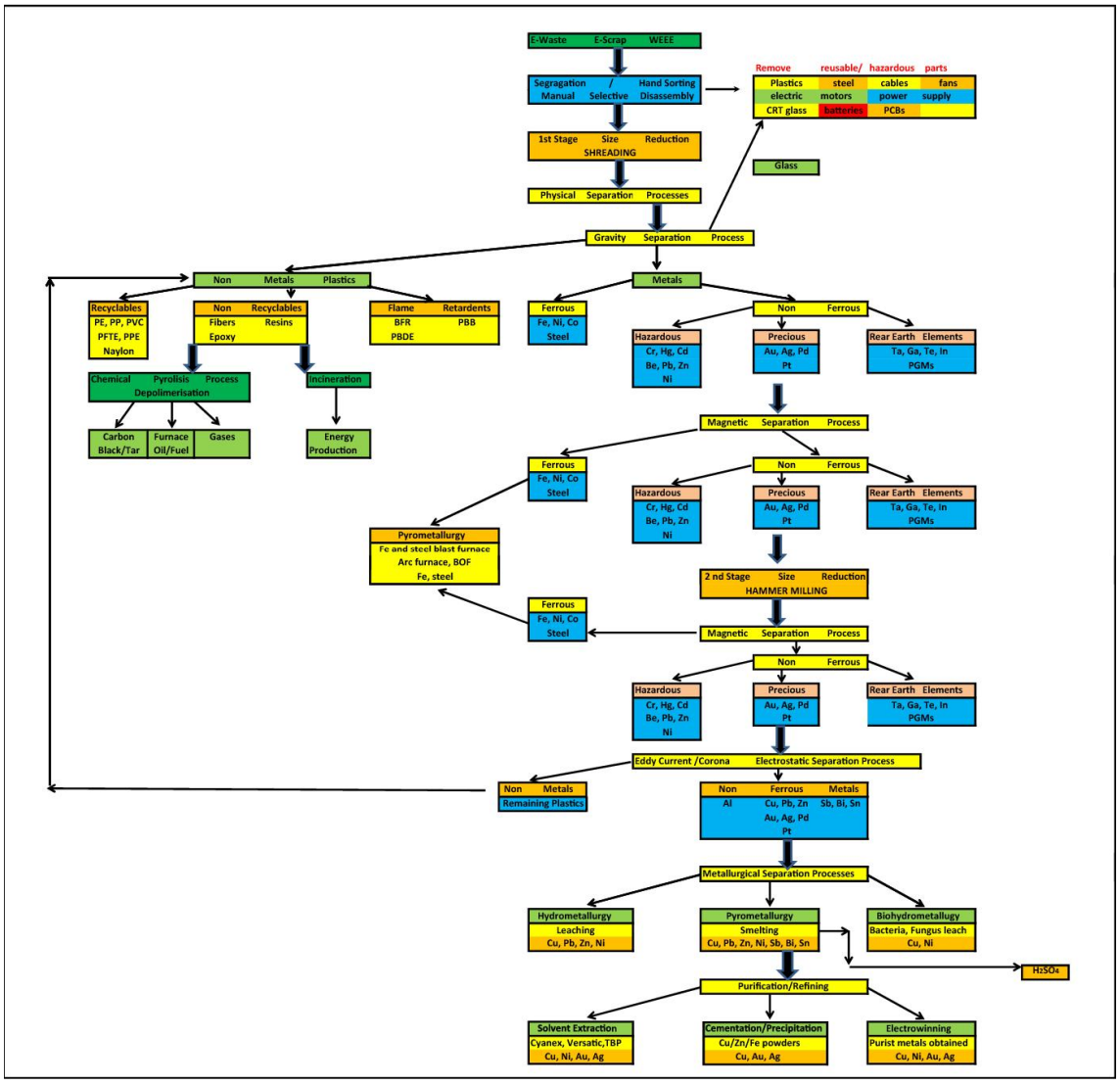

Fig. 5.2: Complete and generic physical-chemical treatment diagram of complex metallic wastes (22)

Thus, the most appropriate initial approach for the purpose of this research is to define various applications to separate and sort the different materials from each other and concentrate them according to their physical-chemical characteristics (magnetic behavior, conductivity, density, colour ...).

According to this, scrap pre-treatment processes could should be classified:

1. Manual Sorting and Preparation
2. Scrap Size Reduction Processes
3. Material Sorting Processes

5.2 Manual Sorting and Preparation

The main scrap supply for steelmaking comes from obsolete ferrous scrap. However, due to the huge amount of possible origins, only a small proportion of this material can be directly used by consumers, the vast majority of purchased iron and steel scrap is sorted and processed by the scrap recycling industry. In this sense, there are two main manual sorting and preparation operations:

5.2.1.1 Manual disassembling and sorting:

In the next session different materials treatment schemes are described in more detail, however, at this point it is important to highlight that the pre-treatment scheme for the reduction of size of the ferrous materials is closely linked to the ductile or fragile nature of the different materials that make up the mixture.

In the case of highly complex products of different nature an excessive reduction in size, without materials pre-separation, can lead to mixtures hard to separate or low-quality products for the steelmaking process. In such cases, a preliminary manual disassembly step is preferable, which allows for maximum recovery, release and separation before the automatic processing stages.

However, since manual disassembly requires high labor and therefore high operating costs, recycling stages with disassembly and manual selection are combined with size reduction processes, where disassembly is frequently limited to decontamination or separation of especially valuable components. In this way, lower costs are achieved in the release of materials contained in complex products

Fig. 5.3: Up) Hand picking after shredding. Down) No-Ferrous material sorted from the scrap stream

An appropriate disassembly step and the successive release by a size reduction stage significantly increases the efficiency of the separation processes to be applied subsequently and, therefore, the quality of the metal scrap products.

5.2.1.2 Manual size reduction:

There are dimensional restrictions of the materials to be charged into the electric arc furnace, mainly to preserve the process from incidents such as mechanical damage to the water-cooled panels for large pieces impact, electrode breaks during the scrap penetration phase or electric arcing to shell and roof.

Large metal pieces must be cut to allow them to ensure that the scrap fulfil the dimensional requirements. This can be done using shears, hand-held cutting torches, crushers and shredders.

5.3 Scrap Size Reduction Processes

In any proposed configuration, the different combinations of the size reduction and separation stages turn out to be the key to an efficient metal recovery scheme. and therefore, a thorough analysis of both the input waste and the requirements of the output residue is required

As mentioned above, the processes to be applied to each waste depend on the different materials contained, their format and layout, the way in which the different materials are joined together, so the exact process to be applied is particular to each residual flow stream. Fig. 5.4 shows a general configuration of a typical shredder and separation plant:

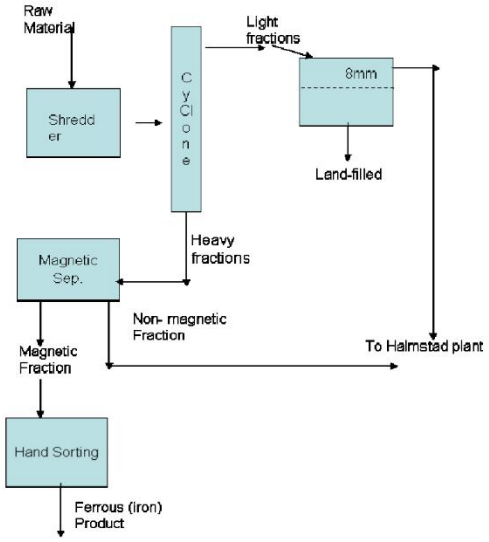

Fig. 5.4: Configuration of the generic shredding and separation plant proposed by Huddinge (23)

To be able to separate the materials from each other it is essential to release them using fragmentation, crushing and grinding processes, these being generally the first processes applied in all recycling schemes.

At this point, three concepts should be introduced for better understanding scrap size reduction processes; size reduction, failure mechanisms and particle release capability.

- **Size reduction:**

Size reduction when processing secondary raw materials, is applied with one of the following purposes:

- To release valuable or dangerous components. The objective is to release the different materials that are connected to each other.
- To promote a faster chemical reaction by increasing the reactant surface (spraying for dissolution or thermal treatment of plastics).
- Production of a material with certain properties depending on its use or storage (densification, appropriate particle size for feeding other processes ...).

Scrap preparation techniques; State of the art.

First consideration when talking about material size reduction is to differentiate between ductile and fragile materials.

The group of materials considered as ductile include mainly steel, non-ferrous metals, rubbers and many plastics. Certain fibrous materials and foams are also included in this category. Also, some combinations of fragile and ductile materials can be included (reinforced cement, cars with glass or washing machines with cement counterweights).

In the case of ductile materials, cutting and shearing are the main mechanisms of size reduction. Examples of size reduction equipment are automobile shredders, rotary shears and blade mills.

In the fragmentation of ductile materials, the energy consumption increases approximately with the second power of the particle size reduction:

$$\frac{P_1}{P_2} \approx \frac{d_2^2}{d_1^2} \qquad \textbf{(5.1)}$$

Thus, for example, the reduction of the final particle size from 50 mm to 10 mm means increasing the energy consumption by a factor of approximately 25. This does not only mean resizing the size reduction engine, but reconsidering the complete operation, since small changes in the size reduction strategy can have a strong influence on both the operational costs and the quality of the final products obtained.

On the other hand, for fragile materials, crushing is the main mechanisms of size reduction, and once subjected to size reduction operations, the fragile materials exhibit particle sizes several times smaller than those of the ductile materials, which makes it possible to separate them by screening.

- **Failure mechanisms:**

During the shredding, particles breakage occurs as a result of a complex combination of impact, tension, compression, shear, bending and torsion forces (24). The compression mechanisms can be basically divided two. These effects are shown in Fig. 5.5:

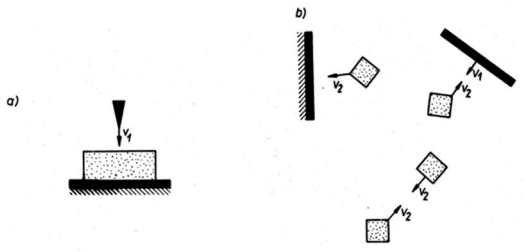

Fig. 5.5: a) The particle rests on the Junque and is hit by the hammer. b) the particle is accelerated by the movement of the rotor and hits the wall, the rotor or another particle

On the other hand, the bending stresses contribute to weakening the material by fatigue, provoking the appearance of cracks and their propagation. However, this effect is not especially important when fragmenting ductile materials.

Scrap preparation techniques; State of the art.

The main forces related to shredding ductile materials are the shear forces, which can be seen in the following figure:

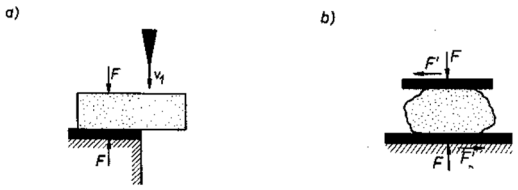

Fig. 5.6: Representative scheme of shear efforts; a) in crushers or blades mills, b) in hammers shredders

The shear mechanism is the majority in crushers and blade mills, so these mills tend to be used for those materials that include mixes of ductile materials.

However, hammer shredders also induce shear stresses in the material, although said efforts are combined with compaction and bending efforts too.

On the other hand, in the impact mills (contrary to blade mills), compression and bending mechanisms prevailing, with a minimal contribution of the shear mechanism in reducing the particle size of the treated material.

Depending on the combination of materials present in the waste to be treated, the different designs vary between these two main technologies (Blade mills and impact mills); In blade mills it is only advisable to introduce relatively soft and ductile materials since the premature wear of the blades associated with the presence of hard and fragile materials greatly reduces the efficiency of the mills. On the contrary, the introduction of ductile materials in impact mills results in a very inefficient reduction of the particle size, since these materials absorb the energy of the impact by deformation, with a low reduction of the particle size.

The shredders mills are in the middle of the two previous fragmentation systems, since this technology combines the different mechanisms for particle size reduction.

- **Particle release capability and particle size reduction:**

The size and morphology of the particles and the composition of the material to be treated are the fundamental properties to consider when designing the most convenient process for its treatment.

Thus, the composition of the particles resulting from the shredder process, depend on both, the particle size and its relationship with the releasing capability. During the fragmentation process of consumer goods, the design of the product itself and the combinations and junction mechanisms between their different materials determine the degree of the particle size reduction and the materials releasing degree. This will define the efficiency of the physical sorting process.

The "foreign" materials contained in the recovered material stream due to the incomplete release, in many cases become irreversible contaminants of this current, and must be considered. In steelmaking process, the contamination of steel with copper is a classic example. If the recovered materials are not pure enough to meet the needs of obtaining new

raw materials, it is necessary to use high purity materials (i.e.; HBI or DRI) to dilute the contamination, resulting in a lower efficiency in the use of resources and higher production costs.

Although a higher reduction in particle size can lead to a greater release degree, allowing a better separation, it should be considered with caution since it also presents some drawbacks; Fragmentation has a high cost, certain types of joints between materials are not releasable if the joint is stronger than the materials themselves, the plastic deformation of some pieces can reduce the degree of release of some metals by promoting complex physical connections between them. In addition, the smaller the particle size, the greater the material apparent surface, which favours the losses by oxidation.

The following diagram shows the typical joints types between materials:

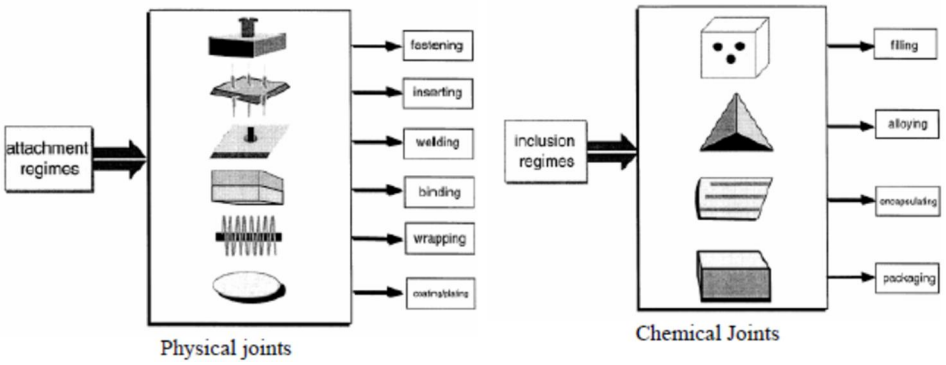

Fig. 5.7: Type of unions among materials (23)

The release of different materials joined by mechanical junctions (screwed, edged ...) is simple in principle, while the release of welded, encapsulated and glued materials is more complicated. In the case of end of life vehicles, the most difficult materials to be completely released from ferrous fractions are mainly related to copper. In the case of aluminium recycling, the most difficult materials to be completely released are related to iron (i.e. screws) and plastic materials (aluminium / polymer composites) (23). Some images of mixtures materials fragments coming from end of life vehicles are shown:

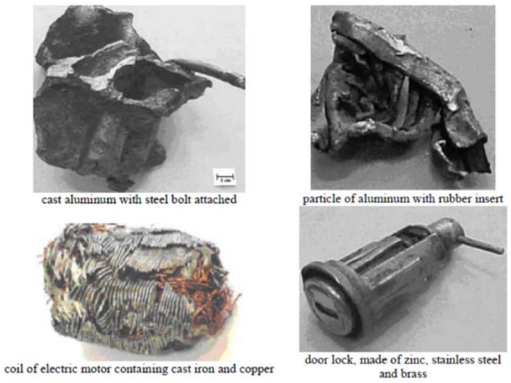

Fig. 5.8: Images of shredded scrap from cars whose components have not been totally released

Scrap preparation techniques; State of the art.

It is always important to note that different materials and different geometries lead to different failure mechanisms and hence different particle shapes.

Also, according (23), the analysis of the degree of particles release of both, ferrous and non-ferrous metals, based on the particle size resulting from shredding indicates that the smaller the particle size, the greater the degree of release, while larger fractions exhibit lower degrees of release.

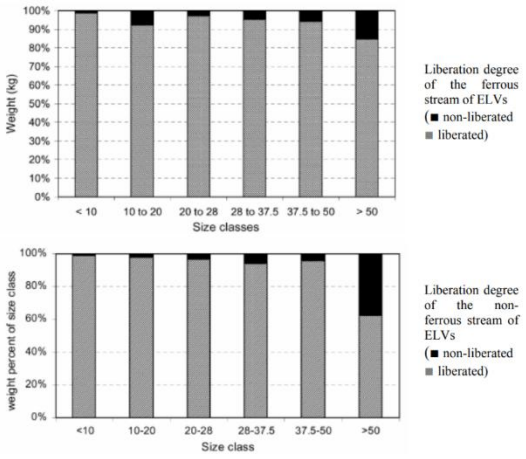

Fig. 5.9: Particles releasing of ferrous and non-ferrous metals according to the size of the particles resulting from the fragmentation process

Therefore, it can be concluded that the release of both ferrous and non-ferrous metals during size reduction process is affected not only by the degree of reduction in size but also by other parameters such as the type of joints used, the physical properties of the materials and the initial geometry of the product.

If the focus is put on the type of unions to joints materials, the "chemical" bonds are more significant in the smaller particle size fractions, while "physical" unions tend to be more significant in the larger particle size fractions (23).

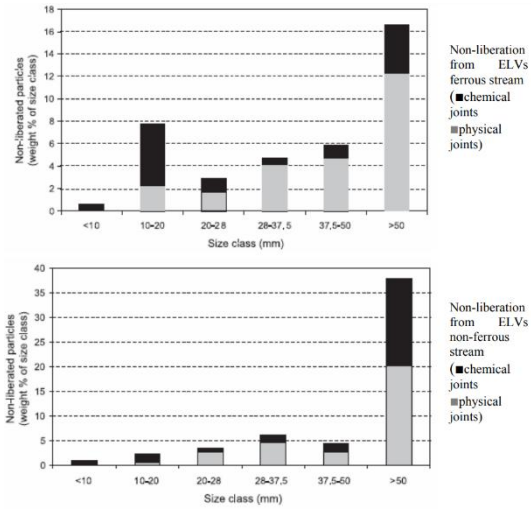

Fig. 5.10: Differences between chemical and physical joints based on the particles size fractions resulting from fragmentation processes

When the metal to be processed is attached to plastic or other foreign elements, it is necessary to considerably reduce the particle size. In these cases, the particle size is generally reduced below 15 mm (in some cases below 4 mm) to ensure a correct release of the metal from the non-metallic elements. These particle sizes guarantee a correct release of other physical bonds, although they do not usually allow the complete release of welded elements and / or coatings

5.3.1 Shredders

Shredders are an important size reduction equipment for those products composed mainly of low thickness steel, such as cars, white goods or small electrical appliances. However, they are not suitable for the fragmentation of massive pieces of steel.

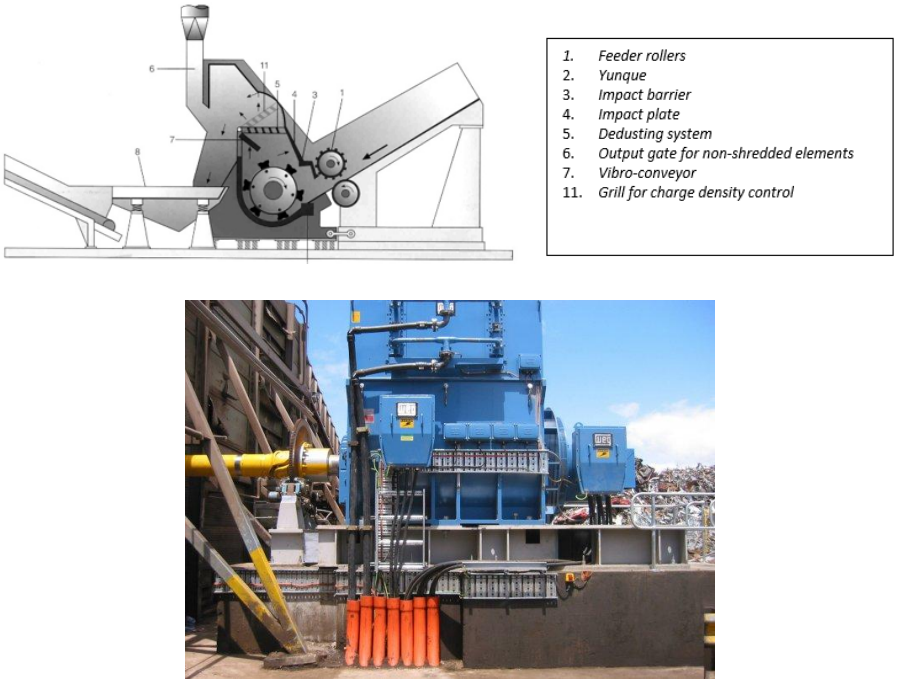

Fig. 5.11: Up) Description and Down) Example of a typical impact shredder mills (23)

The shredders are similar to impact mills but with some modifications (larger fragmentation chamber, greater distance between hammers and Junque, auxiliary output for massive parts and dosing control system) aiming to the reduction of particle size of light metal scrap. They consist of one or more cylinders, which rotate at high speed, equipped with hammers (the weigh is up to 100 kg per hammer). The material to be fragmented is, in some cases, flattened by rollers in the feeding area, which also allow the dosing of the material. The primary fragmentation of the fed material occurs in the entry area by the joint action of the rotating hammers and the Junque, which is stationary. The cutting action is more efficient when the material is struck between the Junque, located just at the entrance of the material to the fragmentation chamber, and the hammers. A second fragmentation effect occurs due to the repeated bending and shearing of the fragments inside the fragmentation chamber, until their particle size allows them to pass through the grate.

The product leaves the fragmentation chamber through the grate, which usually has openings that go from about 150 mm in the car shredders to 15 mm in the secondary grinding systems for waste derived from electrical appliances and electronics. However, the shredders can be equipped with grates with different dimensions depending on the type of material to be fragmented, the production capacity and the desired final particle size.

The shredders are equipped with dust collection systems in order to eliminate fines and other light materials that can be released during fragmentation, avoiding the formation of potentially explosive atmospheres and diffuse dust emissions. The fragmentation process generates a considerable amount of heat and the air flow forces by the dedusting system also allows the cooling down of the shredding equipment.

The shredders are usually classified according to the installed power. In general, it can be said that the installed power, in terms of horsepower (CV) or kilowatt (kW), determines the production capacity (for a defined chamber and rotor). Likewise, said power affects the maximum thickness of the processable material (which can reach 10 cm). Depending on the installed power, the shredders could be classified as follows (25):

- Mini-shredders (≤ 250 kW / ≤ 340 HP): Capacity <10,000 t/year. They are used for E5, packaging, electronic scrap ...
- Medium-sized Shredders (250-750 kW / 340-1,020 CV): Capacity: 10,000-40,000 t/year. They are used for pre-cut scrap, appliances or pre-cut cars without motor or transmission.
- Large Shredders (750-2,200 kW / 1,020-3,000 HP): Capacity 40,000-125,000 t/year. They are often used in the fragmentation of car and other scrap in Europe.
- Heavy and super-heavy shredders (2,200-7,500 kW / 3,000-10,000 hp): Capacity up to 600,000 t/year. They are often used in the fragmentation of old vehicles and other scrap in the USA.

In addition to the number of included rotors (which is usually 1 or 2), the shredders can be classified according to how the rotor is arranged in Horizontal shredders and Verticals shredders.

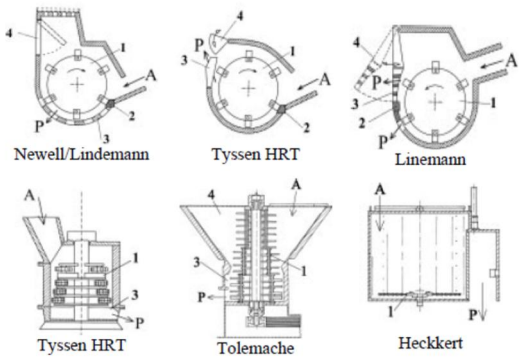

Fig. 5.12: Shredders classification based on the rotor arrangement. up) horizontal type, down): vertical type (23)

Scrap preparation techniques; State of the art.

Horizontal shredders are very flexible with respect to the types of scrap to be treated. The main element of these equipment is the rotor, equipped with several hammers that hang from their respective rotor axes, which "centrifuges" them while rotating. In this way, part of the impact energy is absorbed and the non-fragmentable material can pass.

The design of the horizontal axis shredders and their operational parameters are usually adjusted depending on the material to be fragmented: Some designs (24) can be seen in Fig. 5.13:

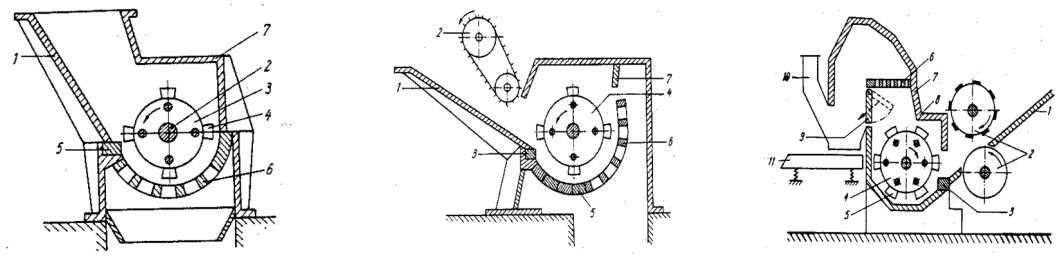

Fig. 5.13: Horizontal Shredders design. Left) provided with a bottom grate, Middle) provided with lateral grate and Right) provided with upper grate

The shredders with bottom and/or side grate are mainly used for light scrap, that is, pre-cut materials with low particle size. Shredders with superior discharge are often used in more demanding applications, such as in the case of out-of-use vehicles.

Alternative designs for fragmentation chambers include additional discharging grates. This "additional" grid at the bottom of the fragmentation chamber allows fragile materials to be evacuated from the fragmentation chamber.

In the case of the end of cycle vehicles, the width of the rotor is usually about 2.5 m, with a diameter up to 2.5 m including the trajectories of the hammers. Smaller rotors can be used in the fragmentation of bundles or pre-cut vehicles. The rotors rotate at speeds between 400 rpm and 1000 rpm, with tangent speeds of the hammers normally in the range 55-65 m/s.

The characteristics of the shredded product, in terms of particle size distribution, releasing degree and bulk density, are mainly affected by:

- The shape of the Junque and hammers
- Fragmentation chamber design.
    - Distance between Junque and Hammers
    - Distance between hammers and grate
    - Distance between Hammers and lateral walls
- Opening surface of the grate
- Tangential speed of the rotor
- Wear situation of the key elements

Although the horizontal rotor shredders are mainly used in the fragmentation of out of use cars and other scrap, it is worth mentioning the existence of vertical rotor shredders:

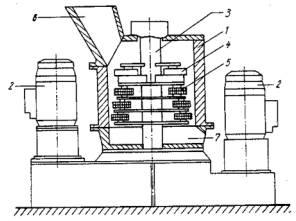

Fig. 5.14: Vertical shredder design (23)

Vertical shredders are used mainly with very light scrap (mainly turnings). Generally, the distance between the hammers and the walls of the shredder progressively narrow towards the bottom, so that the upper hammers release the components while the lower hammers compact and fragment the particles gradually. The product of these shredder machines consists of more or less spheroidal particles. The discharge occurs towards the bottom side, without the use of grates. The main characteristics of this design provide more densified materials (1.2-1.8 g/cm3) than in the equivalent horizontal rotor machines (0.7-1.1 g/cm3), although its productive capacity is usually significantly lower (normally between 5 and 10 t/h), which is the main reason why its implementation has been marginal in the recycling sector.

5.3.2 Blades mills

The blades mills have a similar design than shredders, with the difference that, in the rotor, there are not mobile hammers, but fixed blades. Those blades are adjusted closely to stationary blades placed in the structure of the machine.

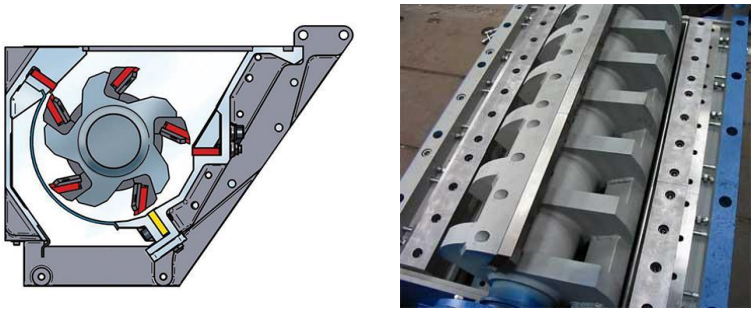

Fig. 5.15: left) rotor of a blades mill. right) fixed blades situated in the rotor of a blade mill

In addition to the blade mills, there are also blade crushers. The main differences between both technologies lie in the angular speed of the rotor, the shape and clamping of the blades, the cutting angle of the non-fixed blades with respect to the fixed blades and the separation between them. In this sense blade crushers, which operate at lower angular speeds, are more robust and resistant to wear than the blade mills blades.

Due to this, blade crushers are usually used for initial stages of cutting (up to 10 - 25 mm) and blade mills to the fine grinding of materials (up to 2 - 4 mm).

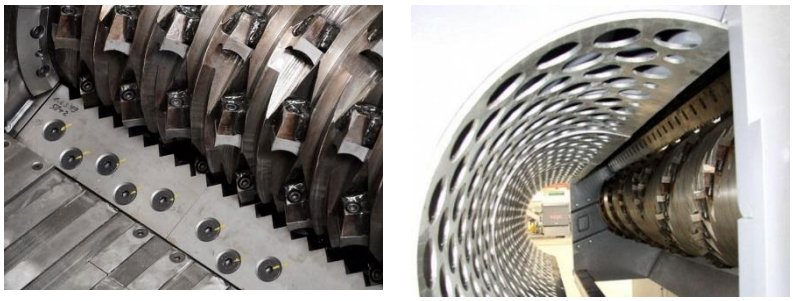

Fig. 5.16: Left) Detail of a blades crusher. Right) Blade crusher with perforated grill

Blade crushers can work with lower perforated grill or not, being the grid the element that determines the maximum particle size. The Blades mills include in all cases a perforated grid, since the friction induced in the material when passing between the blades and the grid contributes to the reduction of the particle size.

In the case of blade crushers there are designs with one, two, three and four rotors. In the design of a single rotor (known as shredder), it rotates at higher revolutions and the cutting mechanism is induced between the blade in the rotor and the stationary blade.

The blade crushers with more than one axis work normally at lower angular speeds of the rotor, rotating in opposite directions, so that the reduction of the particle size is produced by tearing. This type of crusher usually works without a lower grate, so the final particle size is given by the geometry of the rotors and the distance between them. Due to the lower angular speed, in many cases hydraulic drive systems are used instead of electric motors.

Blade mills with multiple axis are normally used as pre-grinding stage for high voluminous materials, to obtain smaller particle sizes (100 - 250 mm) suitable for feeding to single rotor crushers.

In all cases, and especially in the coarsest crushing stages, the design of the rotors and blades is made according to the characteristics of the material to be crushed and the durability and maintenance requirements applicable in each case. Table 5.1 shows different blade designs for a single rotor shredder.

Flat Blade	**Concave blade**	**High Performance blade**
		
General usage	Higher durability	Better cutting action without self-feeding effect
Carbide blade	**Hexagonal blade**	**Cross cut blade**
		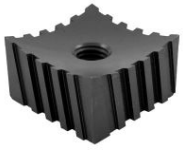
Improves wear resistance Greater fragility	For very demanding applications	Improve cutting, reduce energy consumption and increase the durability of the blades

Table 5.1: Different blades designs for single rotor shredders (26)

Scrap preparation techniques; State of the art.

5.3.3 Impact mills

Fragile materials (glass, stones, minerals ...) are usually processed in impact mills. In these mills, impact-induced compressive forces predominate as the main mechanism for reducing particle size.

Since these mills are used extensively in the extractive industry of minerals and aggregates, strong efforts have been done to reach high performance designs. These designs depend on the features of the material to be processed and the particle size of both, the input and output materials (27). This is shown in the following picture:

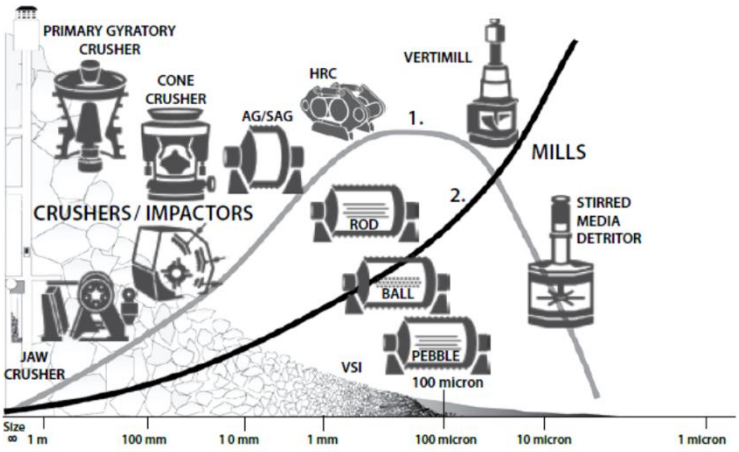

Fig. 5.17: Different designs based on the characteristics of the material to be processed, the size of input particle and the size of output particle

Among all the technologies mentioned in the previous picture, it is worth mentioning the jaw mills (Jaw Crusher) for a primary the particle size reduction (up to 20 - 200 mm), the impact mills (Crushers / Impactors) for an intermediate milling (up to 0.5 - 5 mm), roller mills (HRC) and ball and rods mills (Ball, Rod and Pebble) to obtain pulverulent materials (<0.1 mm).

These kinds of systems are also used for processing some fragile secondary non-metallic raw materials. Some examples are glass or steelmaking slag. These materials are usually processed using one of the following types of mills:

- Jaw mills (28): It is usually used as a pre-grinding stage admitting very large input materials (up to 1.2 m).
- Impact mills (29) (30): These mills are the most typical ones when processing materials such as metallurgical slags aiming to separate the metal retained in the slag
- Ball mills (29): In general, these crushing systems are not frequent in the operations of recovery of ductile metals, since the compression mechanisms are not appropriate to reduce the particle size of the same. So that, ball mills are used for processing fragile materials. They are used to reach particle sizes below 100 microns for some slag that must be subjected to subsequent chemical treatment where increased reactivity is required.

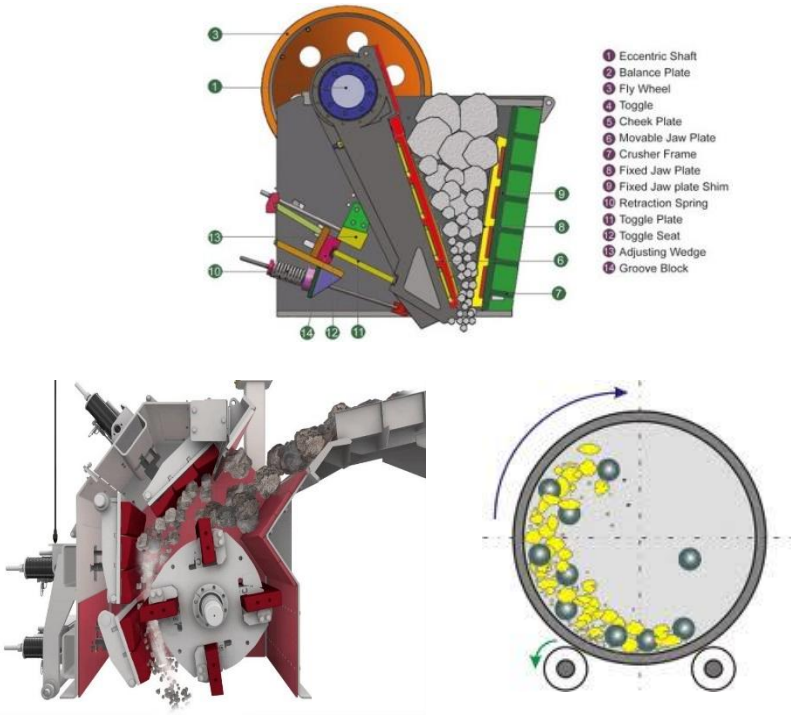

Fig. 5.18: Different impact mils designs. Up) General description of Jaw mill, Down Left) Impact mills for steelmaking slag processing and Down Right) Example of ball mills operation

5.4 Separation technologies

The resulting particle shape coming from the different size Reduction Processes, instead of having a uniform particle size, are inevitably composed of particles whose size is distributed within a certain range. This aspect is important because the efficiency of the subsequently separation processes depends remarkably on this particle size.

Thus, separation processes operate optimally with particles of uniform size, since in many processes this factor influences the separation itself. However, and given that we rarely encounter materials with a uniform particle size, it is important to limit, at least, the range of particle sizes of the material to be processed. This particle size separation is normally undertaken with screening systems or air classifiers. In addition, it must be kept in mind that separation is usually difficult when the particle size is reduced. Therefore, the number of fines must be reduced to a minimum, considering as fines the percentage of material with a particle size 10% smaller than the particle size required by the separation system.

Fig. 5.19 shows a classification of the different separators techniques according to the physical property that allows the separation and the particle range in which they are applicable:

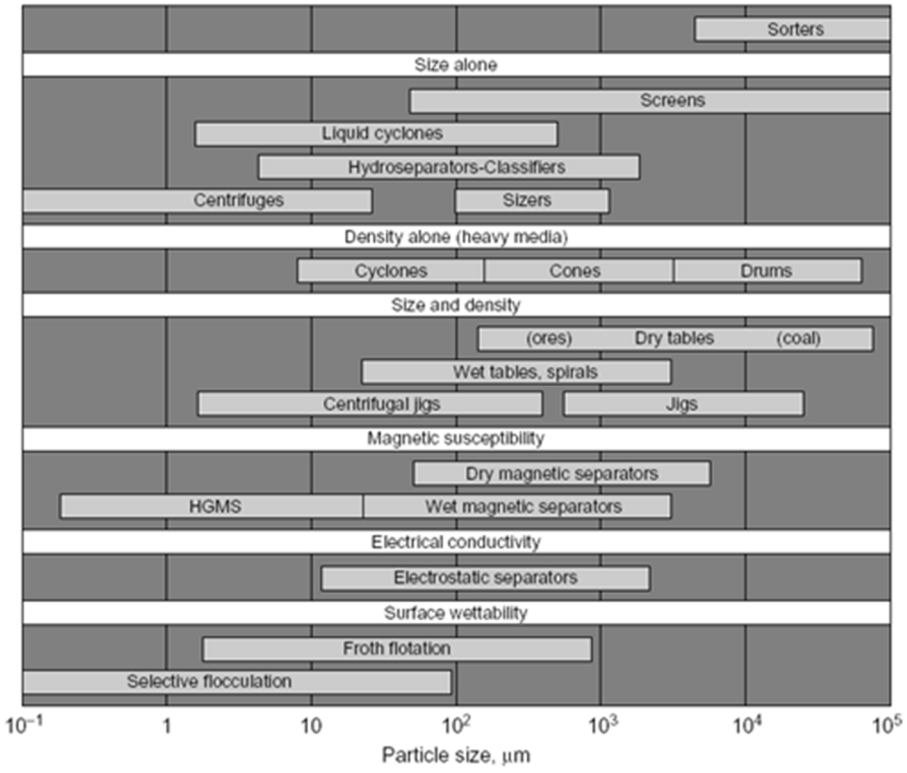

Fig. 5.19: Guide for the particle size range applicable to different industrial separation techniques (31)

When separating two materials from each other, It should be selected the technology capable of differentiating them from the property that distinguishes them. The most significant techniques are detailed below.

5.4.1 Separation by size difference:

The particle sizes distribution of a material stream is a key parameter when properly selecting the design and capacity of the equipment necessary for processing it.

Likewise, the size distribution conditions the quality of the resulting material streams, so its optimization also influences the economic viability of the treatment facility.

Screens, sieves and trommels, are the most common technologies capable of classifying materials in various particle sizes by dry route.

5.4.1.1 Screens and sieves

In screens and sieves, thanks to their screening grids with variable filtering dimensions, the material is guided through the inlet distributor to the screening grid that vibrates horizontally. The grids are integrated into the screening box and can be removed both from above and from the front of the machine, which greatly facilitates cleaning and maintenance. The configuration of the screening box is horizontal, and its operation depends on the input material, the inclination of the screening screen, the number of collisions between particles and their speed. All these variables can be controlled and modified looking for the most optimal classification for each input material. Also, the output material will be classified into different outputs, depending on its size. In the following pictures, two different designs are shown.

Fig. 5.20: Example of industrial screen for separating by sizes during metal waste processing (32)

5.4.1.2 Rotary screen or trommel

The rotary screen allows to treat a stream of material to achieve a granulometric classification of the particles that compose it. The rotating drum is perforated as a sieve, in which the holes are dimensioned according to the material to be separated. An example is shown in Fig. 5.21:

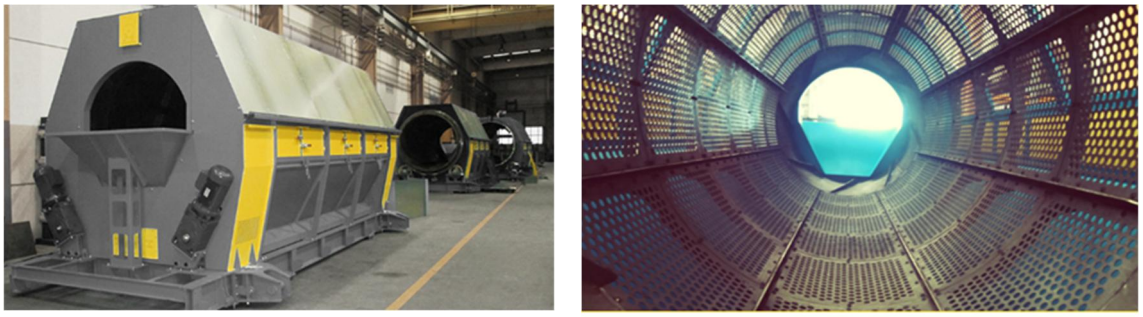

Fig. 5.21: Example of trommel for separating by sizes (33)

5.4.2 Separation by density difference

There is a family of equipment that classifies materials only by the density of their particles.

5.4.2.1 Cyclone:

The Cyclone is the most commonly equipment used for dust collection in recycling processes. It removes the particulate material from the gas stream, based on the inertial impaction principle generated by the centrifugal force. Fig. 5.22 shows the movement of the larger particles towards the walls of the cyclone due to the centrifugal force.

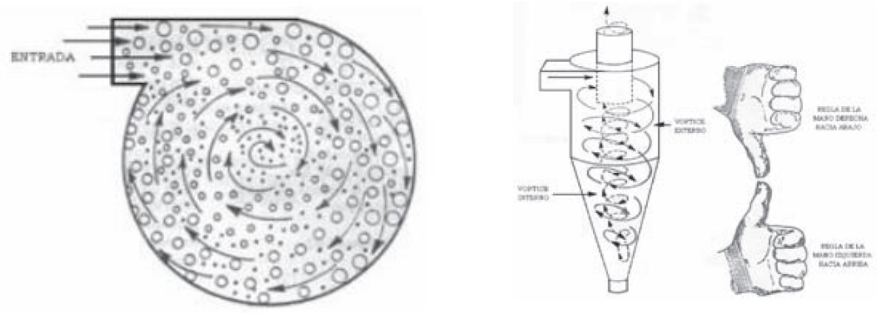

Fig. 5.22: Schematic representation of the particle collection mechanisms in cyclones (34)

This technology basically consists of a sedimentation chamber in which gravitational acceleration is replaced by centrifugal acceleration.

In cyclones, the gas path consists on a double vortex, where the gas follows a downward spiral on the outer side, and ascending, on the inner side. The gas enters tangentially by the upper chamber and descends in spirals to the conical section; then, it ascends in a second spiral, with a smaller diameter, and exits through a vertical centred duct at the top. The solids move radially towards the walls, they slide along the walls, and are collected at the bottom. As an alternative, Hydro cyclones follow the same operation using water instead of air.

Cyclone is one of the least expensive means of eliminating dust from waste material under recycling treatment, both from an operational and investment point of view. They are simple instruments, may be mobile and with easy maintenance.

5.4.2.2 Cone Separator

In the Cone Separator the feeding material is introduced in the upper part of the cone on the surface of the medium.

The pottant medium is introduced inside the cone at different levels by means of return pipes that allow the density gradient control. And the cone has mechanical stirrers to maintain the suspension of the medium.

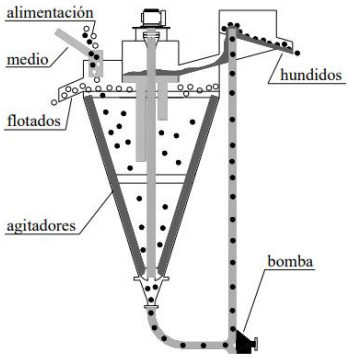

Fig. 5.23: Cone separator with pumping system

5.4.2.3 Drum separator

In the drum separator, the rotation effect lifts the sunk material until it is removed from the bath and deposited in an exit hopper located at a different level, the floating products decant into another exit hopper located at the opposite side of the drum feed channel.

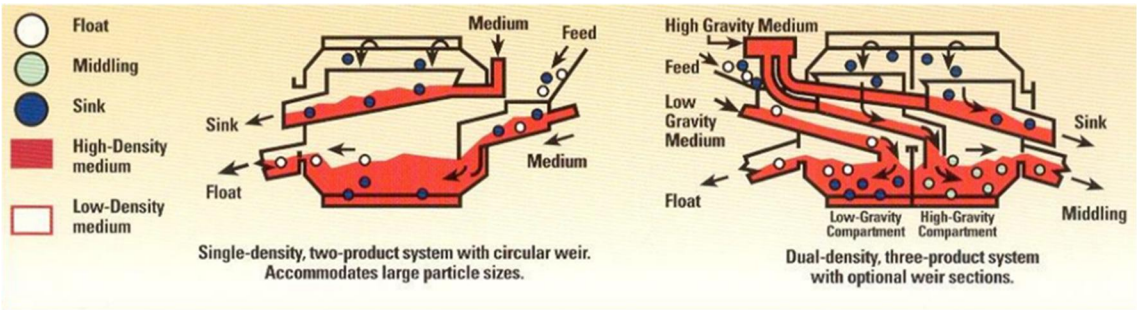

Fig. 5.24: Wemco model drum separators (35)

The drum separators can separate the products by means of a drum provided with two different compartments: the low density and the high density compartments.

The process is based on the use of the controlled density of an aqueous medium, so that materials with lower density float on the medium while materials with higher density sink. Theoretically, it can be considered as an absolute system, that is, the separation only depends on the density of the materials to be separated and the density of the medium. However, there are other factors that determine the degree of separation achievable due to the rate of sinking of the materials to be separated: particle size, morphology, wettability of the materials and viscosity of the medium.

To adjust the density of the medium (usually based on water) for the metals recovery operations, it is necessary to incorporate finely dispersed additives in the water. The particle size of these additives conditions the maximum solids content of the suspension, so that the smaller the particle size, the higher the solids content (and hence the density) of the resulting suspension. However, there is a physical limit in the solids content (and therefore there is a limit in the density of the medium).

In principle, densities higher than 4 g/cm^3 can be achieved. These densities ranges allow to separate the metallic elements from the non-metallic ones and even metallic elements from

each other. In fact, dense media separators are the fundamental means of separation traditionally applied in waste treatment plants by shredding.

However, dense media separation systems have relatively high operating costs, so their use is economically viable only on materials with minimal metal contents.

The drums can reach diameters up to 4.6 m and lengths up to 8 m. Their productive capacities can reach up to 800 t/h, and they are capable of separating particles with sizes between 6 mm and 30 cm.

5.4.2.4 Flotation separators:

Flotation technology is widely used for plastics separation within a base solution with reference density (usually water). Those materials with a higher density than the base solution sink while those with a lower density float. The elements resulting from the separation can be easily processed later.

Flotation technology is based on density differences between the different materials. In the graph shown in Fig. 5.25, the different densities for the polymers considered as "commodities" (PE, PP, ABS, PS) that have densities lower than 1.10 are depicted. Therefore, by using an appropriate configuration it is possible to separate them according to their density.

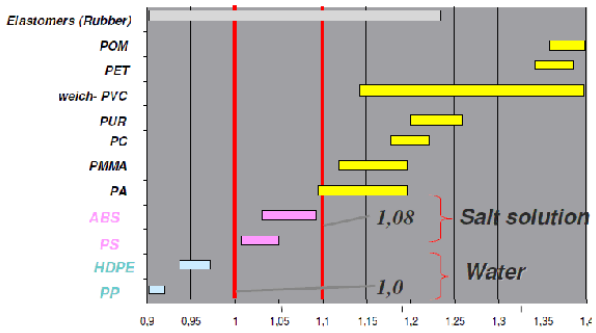

Fig. 5.25: Densities of the different polymers in reference to the aqueous environment (36)

It is a relatively cheap technology, but low selectivity. Therefore, it does not provide a solution to the heavy fractions (which are shown in yellow in Fig. 5.25). On the other hand, an additional drawback of the wet separation methods is that it generates an aqueous effluent that would require an extra treatment of the generated sludge.

This procedure was widely implemented in the early nineties, when large-scale plastic recycling began in Germany and since then, many companies have developed different treatment schemes based on the flotation principle:

- Hermion (37), Heith Group (38), Eurohansa (39) or Carlos Domench (40) Workshops, among others, offer flotation separation schemes to recycle plastics of different nature: PET (bottles, containers), PP (caps, batteries, boxes, bumpers, pots, fraction of light vehicle shredder -ASR-), HDPE (caps, drums, bottles), WEEE and PS/ABS (hangers, refrigeration plastics, household appliances and plastic waste appliances), PVC (wires) and others (plastic and metal or plastic and paper combinations).

Scrap preparation techniques; State of the art.

- Flottweg (41) specializes in plastic separation technologies for the chemical, pharmaceutical and food industries, proposing technologies capable of separating small fractions of less than one millimetre.
- Navarini (42) presents a highly effective flotation method. The method is used for plastic mixing plants in which PVC is recovered

5.4.3 Separation by density and size differences

Separation technologies by size and density allow to differentiate fractions of material according to the following classification:

- Heavy metals: Cu, Zn, Inox, Pb, Ti ...,
- Light metals: Al and Zn
- Heavy No-metals: glass, stones ...,
- Light No-metals: polymeric materials.

In the case of non-ferrous metals, densiometric separation methods are especially relevant since they allow separating heavy metals and their alloys (Cu, Zn, Inox, Pb, Ti ...) from light metals and their alloys (Al and Mg), and light metals from light non-metallic materials (polymeric materials) based on their different density.

In the case of high particle sizes (> 10 mm), wet flotation methods in controlled density media are usually used, while for smaller particle sizes (<10 mm), dry densiometric tables are usually used.

Densiometric Tables and dense separation media stand out among the industrial methods for the separation of materials with different density (dry and wet density separation, respectively). Densiometric tables are generally applied for separating materials with fine granulometries, while the dense media are usually applied on materials with medium grain sizes.

5.4.3.1 Densiometric Tables

In Densiometric Tables, the material is dosed on a vibrating porous surface through which air is blown. Denser materials remain longer in contact with the surface and are pushed forward, while less dense materials remain less in contact with the vibrating surface and tend to move back or remain static. The "threshold" density can be selected by adjusting the operational parameters of the table (vibration speed, air flow rate and table inclination).

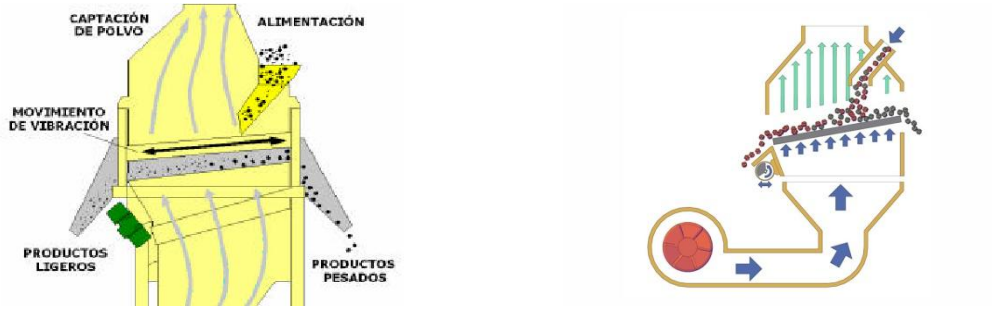

Fig. 5.26: Operating scheme of a dry densiometric table (43)

Densiometric tables are suitable for treating small particle sizes materials (usually lower than 20 mm), so they are used extensively in the recovery of copper contained in electrical and electronic equipment wastes and vehicles out of use. By the appropriate selection of certain process parameters (mesh size, air flow, table inclination, oscillation speed and amplitude and thickness of the layer of material to be separated over the table), densiometric tables can separate materials with particle sizes lower than 1 mm.

The greater is the difference in density and the more uniform the size and morphology of particles between the materials to be separated, the more is the efficiency of the separation process. However, the wider the granulometric distribution of the material treated on the table, the greater the proportion of fine particles of heavy metals will be carried by the light materials and vice versa.

Densiometric tables are very efficient separating heavy metals from light metals and non-metals, since the difference in density between both groups of materials is relatively high (6-8 g/cm^3 vs. <4g/cm^3).

Current trend in densiometric separation is to adjust the densiometric tables for metals separation (density > 2 g/t) and polymeric materials, although in these cases, inert materials (stones and glass) contaminates metal flow if they have not been previously removed. In a second stage, heavy metals must be separated from light metals and inert materials (if not previously removed).

5.4.3.2 Spiral classifiers

Spiral Classifiers are usually used in mining. The operating principle is very simple, they consist of a screw that acts as a lifting device. They have been widely used in wet milling facilities for closed-loop minerals. Currently they are being replaced by cyclones. Among the technologies used in mining are worth mentioning (32):

- The Jig, as gravity separation method, uses vertical currents for the concentration of minerals. It separates the heavy and light minerals according to the difference of the sedimentation speed in the vertical current.
- The Zig-Zag operates in the same line than the Jig. It separates materials based on their specific weight and It is commonly used to avoid dust and less dense materials that could increase complexity in the technical work within more complex separation schemes.

In a Zig-Zag, the material to be processed is introduced into the input channel and distributed throughout the cross section of the so-called classification channel. An air stream flows through the classifier from the bottom to the top, this allows the material to flow and separate easily from the attached dust particles. In each curve, due to the centrifugal forces generated by the air currents themselves, the material collides with the opposite wall of the channel. The particles with high densities fall and the light ones are collected by the dedusting system.

5.4.4 Separation by superficial wettability

Froth flotation and flocculation are the most used technologies when differentiating fractions according to their surface wettability.

5.4.4.1 Froth flotation

Froth flotation is a highly versatile method to physically separate particles based on differences in their wettability. Different parameters are interrelated during flotation operations: reagents used in the aqueous medium, pH value of the aqueous medium, cell design, stirring of the aqueous medium, air flow, feeding rate of the material to be processed, mineralogy, size of particle of the material in process or temperature of aqueous medium.

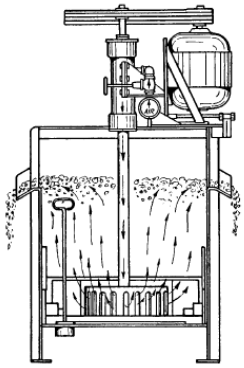

Fig. 5.27: Operating scheme of a froth floating system (44)

In these systems, in some cases the foam may be the medium in which unwanted impurities are removed, in other cases the desired product is extracted in the foams. It is important to maintain a good relationship between the volume physically stable and the foamed volume.

5.4.5 Separation by magnetic susceptibility

Due to its magnetic properties (ferromagnetic, paramagnetic and diamagnetic), in all crushing and separation processes, regardless of particle size, it is common to find magnetic separators in various configurations and with different magnetic strength. In this way, it is possible to easily separate ferromagnetic materials (and even some paramagnetic materials) from non-

ferromagnetic materials, reducing wear in the later stages of the process and separating materials that are normally metallurgically incompatible (Fe and Cu, for example).

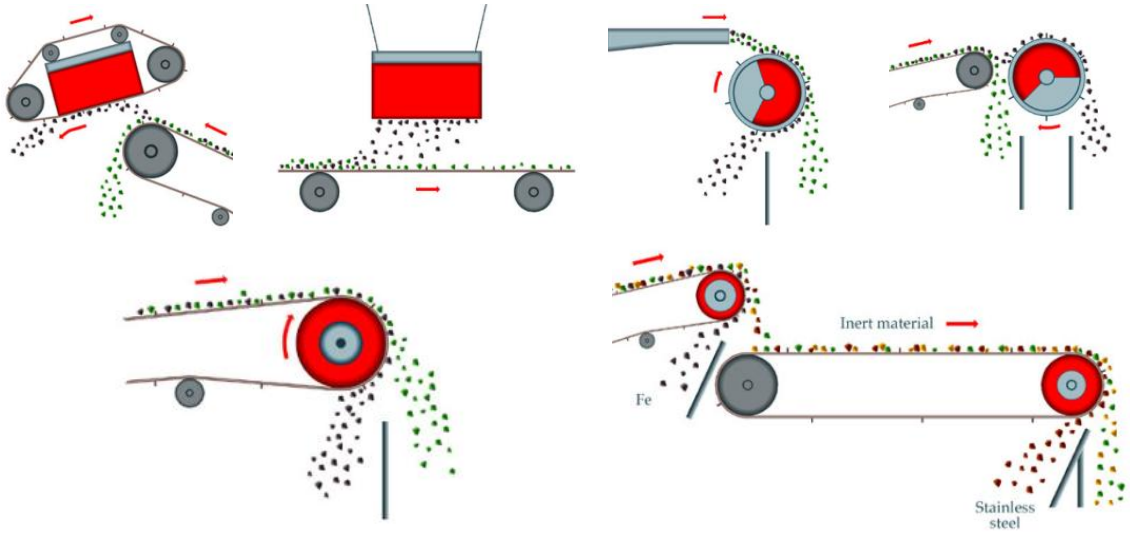

Fig. 5.28: Different operating schemes during separation of Ferromagnetic material (45)

Within this group of separation techniques are:

- Magnetic wet separators are used to separate magnetizable particles from process fluids, sludge and emulsions for sizes between 1µm and 3.000µm by using high intensity magnetic fields. The range of potential applications go from separation by float-sinking techniques in iron ore processing to the cleaning of industrial processing waters.
- High gradient magnetic separators: This separation equipment is designed to extract the weakly magnetic material that can be found in dry material with fine granulometry as impurities. This separator creates a high intensity magnetic field of high gradient capable of attracting very weak magnetic materials such as iron oxides and paramagnetic materials. This separator consists of a vibrating feeder that receives the product and distributes it evenly in a thin layer, over a special antistatic band. The drive roller is provided by permanent magnets of very high magnetic power (rare earths) and steel magnetic poles of high permeability.

  The material transported by the conveyor reaches the magnetic roller and is exposed to its magnetic field. The attracted magnetic particles accompany the roller in its rotation movement and detach behind the roller, in a different falling trajectory than the non-magnetic material which falls freely without being influenced by the magnetic field. Two small hoppers collect and evacuate the magnetic material and the clean product.
- Dry magnetic separators: It is designed to extract and retain ferromagnetic parts that occasionally are among the material that circulates on the conveyor belt.

5.4.6 Separation by electric conductivity

The separation technologies by electrical conductivity are mainly based on electric currents electromagnetic induced in a conductive material when it moves in a spatial region in which there is a variable magnetic field. Induced electrical currents (or Eddy currents) are caused by changes in the time of the magnetic induction that acts on a particle. They can be determined by the Faraday induction law:

$$\nabla \times \vec{j} = -\sigma_p \frac{\partial \vec{B}}{\partial t} \quad \textbf{(5.2)}$$

where:

$\vec{j}$ is the current density,

σ_p is the specific electrical conductivity of the material,

$\vec{B}$ is the magnetic induction.

These induced currents generate a magnetic field opposite to the external magnetic field (Foucault effect), being variable. Non-conductive materials do not develop Foucault effect and, therefore, the opposite magnetic field is not generated.

In the case of Eddy current separators, the opposite magnetic field produces the Lorentz force and this effect allows separation. Lorentz force magnitude in a linear conductor (ds) is expressed as follow:

$$\vec{F}_L = Id\vec{s} \times \vec{B} \quad \textbf{(5.3)}$$

Where I is the intensity of induced current

Since non-conductive materials do not undergo changes in their trajectory (as the magnetic field is not induced), it is possible to separate conductive particles from non-conductive particles.

In the case of electro-pneumatic electromagnetic induction separators, the magnetic field induced in the conductive particle generates an induced current in any conductor located in its radius of influence, which constitutes the detection system of the separator. The electrical signal generated by the detection solenoids allows locating the conductive particle in the separator and, by synchronized it with a pneumatic ejection system, is separated from the non-conductive particles.

A variable magnetic field can be generated in different ways; It can be generated by circulating alternating currents through solenoids, It can also be generated by means of electromagnets powered by alternating current or it can also be generated by the movement of particles through static or rotating non-homogeneous magnetic fields.

5.4.6.1 Eddy current separation (Foucault)

This separation method was developed as an efficient technique to separate non-ferrous metals contained in waste material streams.

The static eddy current can be considered as the first one to be developed using this magnetic principle and are composed of a long ramp (45°) consisting of permanent magnet bands of alternating polarity mounted on a steel plate. When dropping a stream of materials down the ramp, non-conductors descend through the branch without movement diversion, while the displacement of the conductive materials, under the influence of Lorentz's repulsive force (perpendicular to the magnetic bands) induced by Eddy currents is altered and the magnetic particles are separated from the non-conductive particles (see Fig. 5.29).

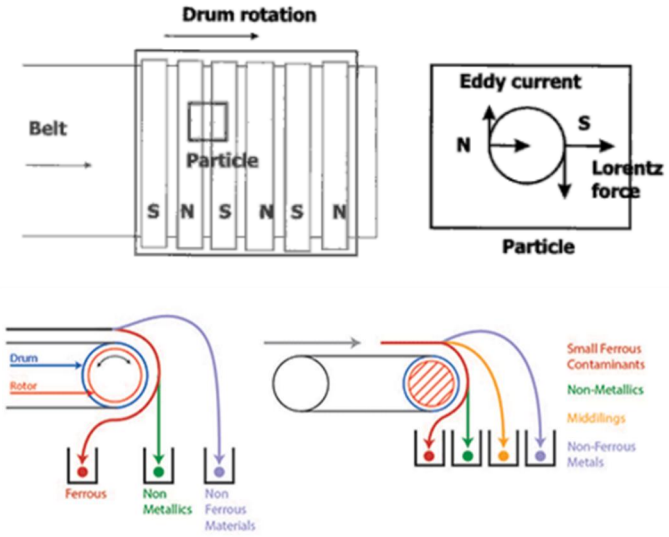

Fig. 5.29: Up) Conveyor belt with the magnetic rotor and summary of forces applied to each particle and Down) Material sorting by An Eddy current scheme (46)

Basically, the conductive materials, as a consequence of the Lorentz force generated by the induced currents, are displaced at a greater distance than the non-conductive materials that are only exposed to the forces of gravity, the force of inertia and the frictional force.

As shown in Fig. 5.30, both Lorentz's forces and rotational moment are directly proportional to the square of the magnetic field intensity (linked to the nature of the used magnets and the design of the magnetic rotor).

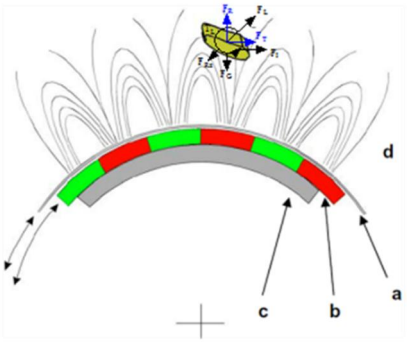

Fig. 5.30: Forces applied to the particles during the separation process by Foucault principle (47)

Other factors that must be taken into account, due to their influence on the forces mentioned above, are the size and shape of the particles, their orientation with respect to the inductive magnetic field, the electrical conductivity of the material, the size of the magnetic poles and the changing frequency of the magnetic field.

In addition to the induced forces described in Fig. 5.30, there are other forces that affect the trajectory of the particles. These include gravity, the inertial force and the friction force, as well as centrifugal forces and aerodynamic forces (magnus effect).

On the other hand, the inertia of the particles that are transported by the conveyor belt is mainly determined by the mass of the particles and by the linear speed of the belt. For this reason, adjusting the speed of the belt allows altering the trajectory of the conductive particles.

Finally, it is necessary to emphasize that the frictional force has a very significant influence depending on the particle size. At high particle sizes (> 20 mm) the incidence of frictional force in the displacement of the particles is lower. However, by reducing the particle size (<5 mm), the magnitude of this force determines the separability of the different materials. This occurs because the mechanisms that act in the separation of smaller particles are different from those that take place in larger particles.

Given the high number of forces involved in the separation by eddy currents principle and the many factors that affect them, determining the appropriate operating conditions to maximize separation efficiency is a problem of considerable complexity. Among the parameters that determine the effectiveness of the separator, the particle size and morphology are the most significant (planar particles exhibit greater displacements than the spheroidal ones) (48). This effect is shown in Fig. 5.31.

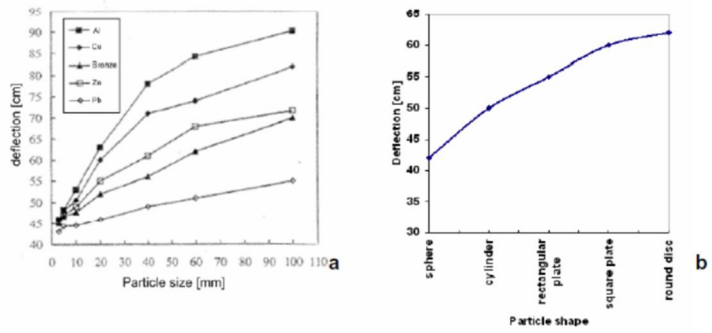

Fig. 5.31: Particle behavior within an eddy current separator and function of their nature (left) and shape (right)

The frequency of the inductive magnetic field, determined by the rotating angular speed, the width of the magnetic pole and the number of pairs of magnetic poles of the rotor (see Fig. 5.32), also plays a determining role in the efficiency of the separator. This operational parameter is much more significant by reducing the particle size (p1 and p2 in Fig. 5.32), since the differences between Lorentz forces, to which materials of different nature are subjected, are reduced.

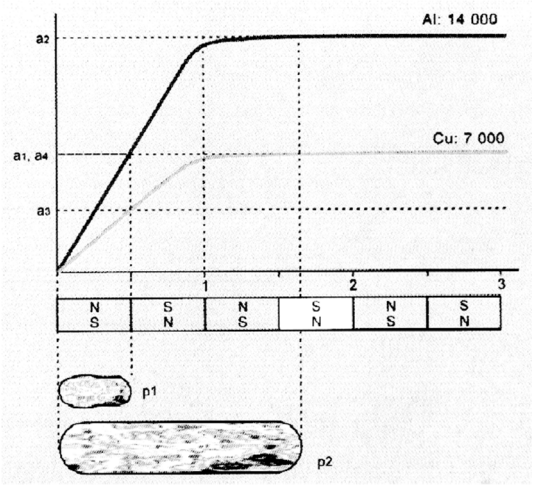

Fig. 5.32: Variation in the separability of the conductive metal particles: relationship between particles size (p1 and p2) regarding the alternation of the magnetic poles (48).

Therefore, to maximize the extraction of conductive metal particles in low granulometry materials, it is necessary to guarantee a high frequency of variation of the magnetic field (by reducing the size of the magnetic poles, increasing the number of them and/or increasing the rotational speed of the rotor).

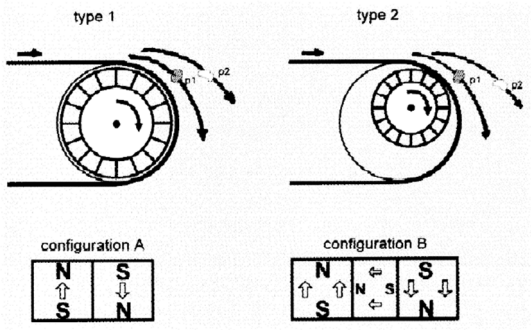

Fig. 5.33: Different Eddy current separators setups (49)

5.4.6.2 Electro-pneumatic separation by electromagnetic induction

Electro-pneumatic separation by electromagnetic induction is based on the same principles as Eddy current separation, although the operating procedure to get material separation is totally different (50).

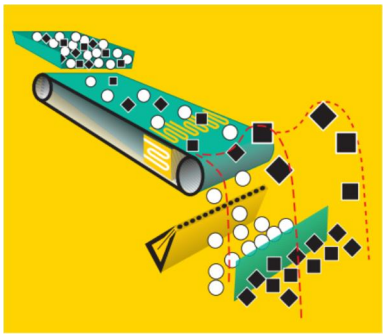

Fig. 5.34: Basic scheme of an electromagnetic induction separator

The magnetic field in the conductive particle generates an induced current in any other conductor located closed to it. By installing different conductive elements (solenoid) in the transversal direction to the particle's displacement, the electrical current induced in those elements allows to position the particles on the transversal axis of the conveyor belt. Once the position of the particle and the displacement speed of the conveyor belt are known, a data processing system drives a pneumatic ejection system, separating the conductive particle from its inertial trajectory, thus enabling its separation.

In these separators, the magnetic field induced in the particle does not act as a separation driving force, but it is only used to position the particles on the separator conveyor. Therefore, the separability of the materials in this type of separators does not depend on the conductivity/density ratio, as in the eddy currents separators, but only depends on the conductivity.

By reducing the metallic content of a particle (particle size, composite materials...) the intensity of the electric currents in the detection system is reduced, and this can condition the detection capability of the separation system. Similar than in Eddy current separators, the intensity and frequency of the inductor become a key parameter as the metallic content of a particle of the materials to be separated is reduced.

Another relevant aspect of these separation systems when working with complex materials is the number of channels that constitute the ejection and detection system. If the channels are wider than the particles sizes, in the same channel there can be both conductive and non-conductive particles at the same time and, therefore, they will be separated by the pneumatic system together, negatively affecting the separation efficiency. Therefore, to achieve acceptable separation degrees it is necessary to properly adjust the width of the detection channels to the particle size of the material to be treated. This is one of the main limitations when using this type of separators for treating low granulometry materials.

It can be said that these separators are more efficient when separating all kinds of conductive materials, while Eddy current separators are more efficient when separating those materials with a high conductivity / density ratio (aluminum, magnesium). These differences accentuate the complementarity of both types of separators despite being based on the same elementary principle, since the combination of both types of separators allows improving the separation efficiency.

5.4.7 Separation by physical superficial appearance (colour, reflectance, fluorescence and transmittance):

The sensor systems allow to separate, by automatic methods, materials that would otherwise only be detectable by expensive analysis or specific treatment schemes. Sensor separation systems are used in those cases where a high degree of separation is needed, and conventional separation techniques are not enough.

The sensor-based separators take advantage of all the useful properties of the materials to achieve the best separation results. In these separation schemes, every material that enters the separation machine is identified, classified and, if necessary, separated.

The most extended classification principle is based on sensor systems and, it works on the same basic principle as the one used in the classification techniques by electric conductivity. The input materials are driven by a conveyor belt through the sensors zone. The information obtained from the sensors is processed electronically so that, depending on the classification criteria setting, the detected materials can be selectively ejected from the material stream.

Among the main applications of this separation technology are:

- Steelmaking slag classification: Separation of various metals from a mixture composed of slag and metal.
- Aluminum Classification:
    - Separation of various impurities from metals (Cu, Zn, VA, brass, Pb, etc.).
    - Separation of various impurities from another source (wood, plastic) through image processing technologies.
    - Separation of aluminum alloys with high Zn and / or Cu content.
- Stainless steels classification:
    - Impurity separation (Cu, Zn. Brass, Pb, Sn), in pure form and of alloys.
    - Separation of carbon steel and stainless-steel mixtures.
    - Separation of stainless steels with Mo content.
    - Separation of stainless steels with Ni content.
- Classification of non-ferrous metals regardless of material's colour:
    - Separation of Cu, Zn, brass, etc., in pure fractions.
    - Pure classification of dirty / oxidized material is also possible.
- Classification of precious metals:
    - Separation of material with Au content.
    - Separation of material with Ag content.

Regarding the existing technologies for separating materials based on their superficial appearance, it is worth mentioning colour detection, Near infrared, X-ray, LIBs and electrostatic separation.

5.4.7.1 Colour detection separation

Modern colour separation technologies usually have linear scanning cameras and 3D recognition systems capable of differentiating different colour values. The information on the colour of the material to be separated is recorded and combined with the 3D information

obtained by laser triangulation. In this way, a colour topographic image of each of the objects located on the moving conveyor belt is achieved.

After detection, the different objects are separated by material classes according to the criteria specified previously.

Some common fields of application for colour separation are the separation of non-ferrous heavy metal (like copper, brass or grey metals), as well as the colour separation of industrial minerals.

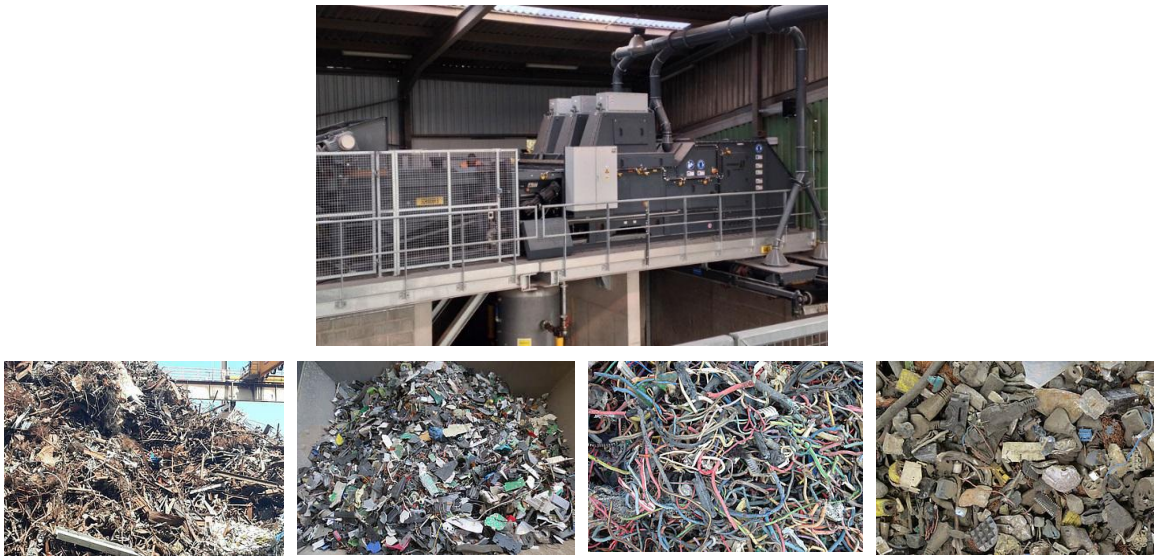

Fig. 5.35: Up) Color separation technology (51). Down) Different materials to treatment, from left to right: sheared scrap, electronic scrap, wire processing, shredder residue.

5.4.7.2 Sorting by Near infrared technologies (NIR)

NIR refers to the spectrum range, not visible to the human eye, between 760 and 2,500 nm. In this spectral range it is possible to detect specific patterns in some materials based on the vibration of the molecules after exciting them with light.

It has been more than 20 years since the first near-infrared (NIR) detection systems, originally developed for the food industry, were used in the field of polymer fraction recycling and it was a matter of time before camera-based systems were became a standard component of NIR separators.

Near infrared spectrometry is based on a device that radiates the sample with IR light. A diffuse reflectance occurs, in which the radiation penetrates through the surface of the particle layer, excites the vibration modes of the molecules and disperses it in all directions. The produced reflectance effect depends on the molecular composition of the material and it can be used as detector system for locating the exact location of the particles of interest and to trigger the particle extraction.

This technique allows the removal of both heavy and light elements, but it presents problems when separating metals and “black” materials, capable of absorbing almost all the IR light. Another drawback of this technology is that it is a relatively expensive technology

Scrap preparation techniques; State of the art.

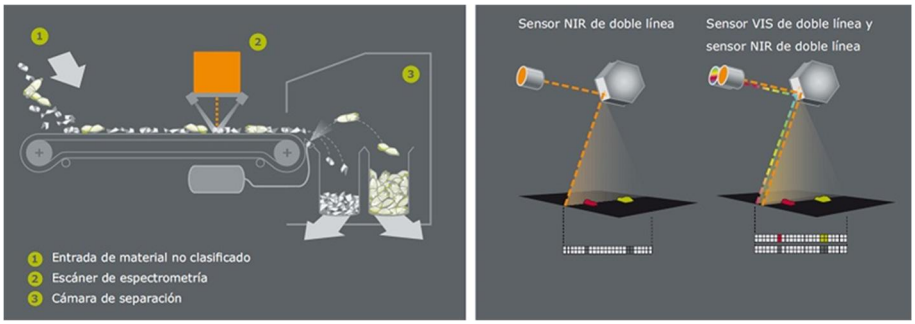

Fig. 5.36: Operating scheme of an infrared spectroscopy separator (52)

5.4.7.3 Separation by X-ray Technology

X-ray separation systems provides useful information to separate materials according to their characteristics, offering a decisive contribution to improve the recovery of recyclable materials and the use of resources.

Basically, there are two separation systems based on this technology:

- X-Ray Fluorescence technology (XRF). This system can separate materials analyzing their elementary composition.

  X-ray fluorescence technology allows detection and separation based on the elemental composition of the material to be separated. For example, it can differentiate between copper and brass or zinc by the elements that are present. Such detection is possible even when the surfaces are very dirty. It is also possible to detect metal scrap with metallic coatings.

  X-ray fluorescence (XRF) consists on the emission of secondary (or fluorescent) x-rays characteristic of a material that has been excited by being exposed with high-energy X-rays or gamma rays. The basis operation principle is to identify the wavelength or energy of each of the characteristic radiations, in this way it is possible to know the elements that compose the sample, if the intensities are measured, their respective concentrations would be known.

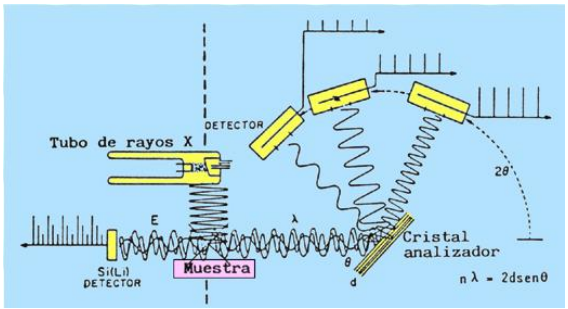

Fig. 5.37: Scheme of a classic x-ray fluorescence spectrometer (53)

In Fig. 5.37, the scheme of a classic X-ray fluorescence spectrometer or wavelength dispersion X-ray spectrometer, is shown. This technology receives this name because the polychromatic fluorescence spectrum emitted by the sample when excited by a radiation beam produced by an X-ray tube, is decomposed into its monochromatic components depending on its wavelengths, when diffracted into a known spacing

monocrystal. The diffracted beam for each angular position of the monocrystal reach the detector, which converts photons into electrical impulses.

According to Bragg's law ($n \cdot \lambda = 2 \cdot d \cdot \text{sen}\theta$), measuring the value of the angle θ at which each of the radiations constituting the spectrum emitted by the sample is diffracted, and since the spacing d of the analyzer crystal It is known, the wavelength λ of each can be calculated. By analyzing these wavelengths, the qualitative and the quantitative characteristics of the sample can be known.

- X-ray transmission technology (XRT): It is used to dry separation by material densities. In a transmission process, differences in X-rays absorption are detected. These differences are categorized and used to separate by densities.

  The X-rays absorption degree depends both on the density and on the thickness of the material. The higher the atomic mass and the thicker the piece of material, the more radiation is absorbed. To compensate for the influence of the thickness of the object, the absorption of the material to be separated is usually measured in several different energy phases, thus the specific absorption of the material is determined, and the density of the material is inferred with the help of a specific software.

  The most important advantage of X-ray transmission technique is that it is not sensitive to surface dirt and it can detect inclusions inside the material. For example, in mining, pyrite clusters can be found in pieces of ore, or, in the field of recycling, heavy metal inclusions in aluminum parts.

  Next figure shows an example of a separation scheme based on X-ray transmission technique as characterization method. The material to be separated reaches the system through a vibrating conveyor to an acceleration belt that spaces the material in the transportation direction, thus facilitating its separation. Then, the belt transports the material through the scanning area, where a radiation source located below the belt applies radiation to a small part of the conveyor belt. At the top of the material, detectors measure the proportion of the rays not absorbed by the material. The difference between the initial radiation and the measured radiation makes it possible to infer differences in density between objects or inside. This information is used for triggering the separation according to the specific criteria of the application.

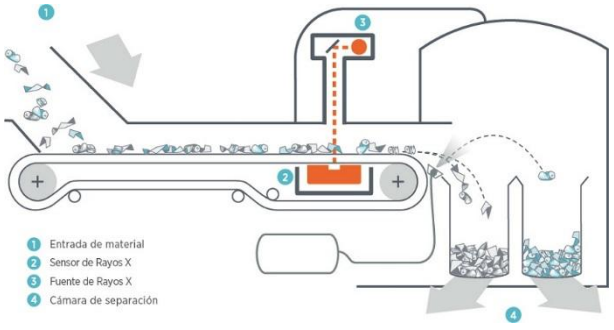

Fig. 5.38: Operating scheme of transmission x-ray technology (xrt) as a sensor technology to separate the material by atomic densities (54)

The main disadvantage of these technologies is the high cost. It also presents limitations when separating elements with atoms that shield X-rays and fractions of dense materials.

5.4.7.4 Laser Induced Breakdown Spectroscopy technology (LIBs)

In Laser Induced Breakdown Spectroscopy (LIBs) a high-energy radiation pulse of laser light is emitted on the sample to be analyzed. This evaporates tiny particles of material on the surface and a plasma is generated, in which the atoms, ions and molecules are in an excited state and emit light. These emissions are collected through the optical components and introduced into a spectrometer.

LIBs employ robust lasers that operate with a pulse frequency between 20 and 100 kHz with a constant laser power. By achieving very short measurement times, very small objects can be measured, analyzed and then separated at high belt speeds (up to 3 m/s without contact).

The Figure 46 shows a commercial automated separation system for scrap metal, specially developed for shredded stamping waste from the aluminum industry (55).

Fig. 5.39: LIBs Down) Different materials for treatment; Aluminum and non-ferrous metals recycling.

5.4.7.5 Electrostatic separation

Technologies based on electrostatic separators allow sorting on materials that cannot be achieved using manual sorting or other automatic methods.

There are two main separation systems based on this technology:

- Electrostatic crown separators are used for dry separation of metals (reaching metal particles <0.1 mm) and plastics or other non-conductive materials. It is an efficient system to recover metal fractions from metal/plastic mixtures or to clean plastics from metal parts before processing.

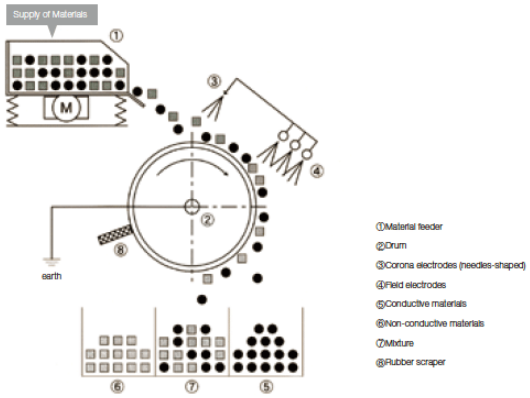

Fig. 5.40: Basic operating principle of an electrostatic corona separator (56)

In this separation scheme, the material enters to rotating drum connected to ground, also an electrode connected to a high voltage source is capable of generating an electrostatic field around the material that rotates on the drum, the material is electrically charged according to its conductivity; good conductors quickly separate from the drum, while bad conductors remain attached to the surface of the drum until a non-conductive obstacle forces them to detach.

- Electrostatic triboelectric separator: The system is based on a vibrating conveyor through which the plastic mixture passes to the so-called triboelectric charging unit. The different plastics are ionized depending on their composition, taking a positive or negative electric charge due to the effect produced by the passage of electrons from one particle to another. The ionized material is passed through a two flat-parallel plates design fed with high tension making cathode and anode. In its displacement, the components are electrostatically separated according to their different charges. Positive particles are attracted to the negative electrode, while negative particles are rejected and vice versa.

  The magnitude of the electric charge, as well as its sign, only depends on the composition of the material, allowing the materials to be separated according to their triboelectric behavior, regardless of their density and atomic charge. However, there is a limitation in terms of the size of the particles to be separated (<12mm), which makes necessary to incorporate additional crushing systems, increasing the cost of the process.

5.5 Market review on scrap pre-processing techniques

This section presents a review on the commercial scrap preparation solution available in the market

5.5.1 Size reduction systems

Together with the bibliographic work for assessing the state of the art on the size reduction available technologies, an exploration of the different commercial options that can be found in the market was carried out and presented in Table 5.2:

Type		Weight and dimensions				Reduction technique	Main application	Production
Supplier	Model	General dimensions (mm)	Total Weigh t (t)	Inlet size (mm)	Outlet size (mm)			
EDGE (Distribuidor : EMSA)	SLAYER	11200X2500X3200	22	0-800	0-40	Cutting	Electronic scrap, appliances, metal profiles	Linked to material
	SLAYER XL	13000X2500X3200	24	0-1000	0-40	Cutting	Electronic scrap, appliances, metal profiles	Linked to material
ELDAN (Distribuidor : Recycling Equipos)	SC1412 M	1700X3000X3500	15	2000	< 200	Cutting	Wires, aluminium, bulk materials, MSW	Up to 12
HUSMANN (Distribuidor : Reverter Industries)	HL I 1230	11035X2558X2695	20	1200X3020	200-250	Cut and tear	Electronic scrap, appliances, metal profiles	Linked to material
	HL II 1622	10200X2340X2650	22,5	1600X2200	200-250	Cut and tear	Electronic scrap, appliances, metal profiles	Linked to material
	HL UNI 75	7500X2460X2700	18	1750X1560	200-250	Cut and tear	Electronic scrap, appliances, metal profiles	Linked to material
HAMMEL	NZS 1000	10257X5208X4960	19			Cut and tear	Universal	Linked to material
	HEM 1250	14413X4689X3856	46			Cut and tear	Universal	Linked to material
	VB950DK	**2200X1400X5000**	**44**		**150**	Cut and tear	**Universal**	Linked to material
KOMPTECH (Distribuidor : Masias Recycling)	TM3400, TM3400 SD, TM5000, TM6000 SD	9120X2550X3360	23,9-24,9	3020X1800	10-100	Tearing	Electronic scrap	45/30 – 100/90
	CRAMBO 3400, 5000, 6000, 42000, 5200, 6200	9120X2550X3360	24-25,4	3000X1800	10-100	Tearing	Electronic scrap	45/35 – 120/100
LINDNER	Urraco 75D/DK	7000X2500X2900	22	1500X2500	< 150	Cut and tear	Universal	55 t/h
	Urraco 95DK	**9200X3000X3200**	**42**	**2500X3000**	**< 200**	Cut and tear	**Universal**	**120 t/h**
	Miura 1500	9300X2500X3300	24	1500X2500	< 150	Cut and tear	Universal	60 t/h
EUREC (Distribuidor : Maquinter)	S40	12000X2860X2990	34	2400X1980	< 250	Tearing	General scrap	Up to 230 t/h
	S24	10800X2440X2670	19,2	2100X2200	< 200	Tearing	General scrap	Up to 150 t/h

	S16	10415X2270X2680	16,5	1535X1440	< 200	Tearing	General scrap	Up to 80 t/h
METSO (Distribuidor: Recyprojects)	M&J Preshred 4000M	9350X2530X4005	35	5081X2535	< 125	Cut and tear	Bulk materials, Waste from electrical and electronic equipment, Urban solid waste	40 t/h < 300 mm
	M&J Preshred 6000M	10880X3830X3994	60	3461X2400	< 125	Cut and tear	Bulk materials, Waste from electrical and electronic equipment, Urban solid waste	24,5-27,7 t/h
SPR	RS100/130	4200X5100X4900	18	1100X1300	300	Cutting	Bulk materials, Urban solid waste	Up to 30
	RR2000	3900X1705X708	10	1890X1245	300	Tearing	Bulk materials, end of life cars	20
	PC2200/55	3060X2700X1810	11,5	2200X1500	300	Cut and tear	Bulk materials, end of life cars	10-15
LEFORT	MTP1100	--	147	2600X900		--	Universal	18-25 t/h
TANA (Distribuidor: EMSA)	220Deco	10530X2520X4030	24	500	50	Cut and tear	Aluminium, bulk materials, wood, urban solid waste	15 t/h
	220DTeco	10530X28300X4030	26	500	50	Cut and tear	Aluminium, bulk materials, wood, urban solid waste	15 t/h
	440Deco	10530X2520X4030	27	500	50	Cut and tear	Aluminium, bulk materials, wood, urban solid waste	15 t/h
	440DTeco	10530X28300X4030	29	500	50	Cut and tear	Aluminium, bulk materials, wood, urban solid waste	15 t/h
TEREX (Distribuidor: Carmaq)	TDS820	--	27		100	Tearing	Bulk materials, Waste from electrical and electronic equipment, Urban solid waste	Linked to material
	TDSV20	--	37		30	Cutting	Bulk materials, Waste from electrical and electronic equipment, Urban solid waste	Linked to material
	TSS390	--	30		100	Tearing	Bulk materials, Waste from electrical and electronic equipment, Urban solid waste	Linked to material
VECOPLAN	VMZ1800	6810X2440X2800	--	1700X1500	< 200	Tearing	Bulk materials, urban solid waste	5-15
	VMZ3600	9100X3700X2500	--	1700X1500	< 200	Tearing	Bulk materials, urban solid waste	15-60
	VMZ7700	10000X3700X2500	--	2100X1500	< 200	Tearing	Bulk materials, urban solid waste	30-100
UNTHA	XR MOBILE E	3805X2950X12710	37	2950X1560	30	Cutting	Bulk materials, Waste from electrical and electronic equipment, Urban solid waste	47 t/h
ZB GROUP	THOR-1521K	16000X3500X5400	87	1460X4800		Cutting	Light metal scrap and vehicles out of	10-15 t/h

							use	
	THOR-1720K	18600X3500X6100	104	1700X7000		Cutting	Light metal scrap and vehicles out of use	15-25 t/h
ZATO	BLUE SHARK					Cutting	Light metal scrap and vehicles out of use	5-60 t/h

Table 5.2: Comparative table; primary crushers

Next pictures show some of the commercial solution that can be purchased:

HAMMEL® Mobile crushers

LINDNER® Mobile crushers

EuRec® Mobile crushers

Lefort® Mobile crushers

Thor® serie Mobile crushers by ZB Group

Bano® Recycling Mobile crusher

Fig. 5.41: Examples of commercial crushers

5.5.2 Size difference separators

Together with the bibliographic work for assessing the state of the art on the available technologies for separating materials by size property, an exploration of the different commercial options that can be found in the market was carried out and presented in the next table:

Type		Technical specifications							
Supplier	Model	Number of Steps	Width (m)	Length (m)	Surface (m^2)	Holes size (mm)	Inclination (°)	Power (kW)	Weight (t)
BINDER+CO	BIVITEC	1-4	0,8-3,0	3,0-12,0	2,4-36,0	0,08-200	5-30	2-55	1-25
HEIN LEHMANN, GMBH	LIWELL	1-2	1-3	2,5-10,1	2,5-30,2	>0,4	15-30	5,5-55	2,1-18,2
SPALEK	(LF and KT)								

Type		Materials		
Supplier	Model	Operational performance (t/h)	Size (Density > 1,5 t/m3) (mm)	Size (Density < 1,5 t/m3) (mm)
BINDER+CO	BIVITEC	1000	80	200
HEIN LEHMANN, GMBH	LIWELL	5-80	0-80	0-80
SPALEK	(LF and KT)		0-120	0-120

Table 5.3: Comparative table; Size difference separators

Next pictures show some of the commercial solution that can be purchased:

LIWELL® Sieve

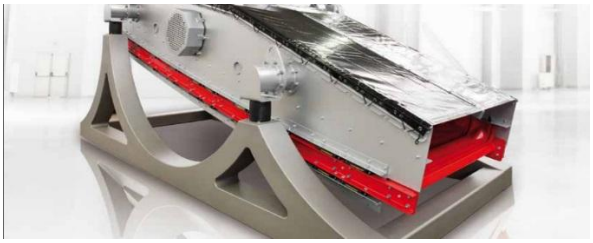

BIVITEC® by Binder+Co Sieve

SPALECK® Sieve

Fig. 5.42: Examples of comercial sieves

5.5.3 Magnetic susceptibility separators

Together with the bibliographic work for assessing the state of the art on the available technologies for separating materials by its magnetic properties, an exploration of the different commercial options that can be found in the market was carried out and presented in the next table:

Supplier	Type	Model	Dimensions and weights				Electrical power / electro-magnet (kW)	Conveyor speed (m/s)	Working distance (mm)
			General (mm)	Magnetic Width (mm)	Magnetic Length (mm)	Total weight (t)			
DRAGO ELECTRONICA		ODEP-7	1105X2320X665	900	900	1200	4	2	350
		ODEP-8	1304X2738X665	1000	1000	1600	5,5	2	400
		ODEP-9	1304X2720X665	1300	1300	2000	7	2	450
ERIEZ MAGNETICS EUROPE LIMITED	Permanent	CP20/80 SC2	2150X1208X391	832	526	0,83		2,2	250
	Permanent	CP25/80 SC2	2500X1300X455	836	520	1,35		2,2	300
	Electro-magnet	SE740SC 2	2768X1660X1132	1048	1048	2,5	4,5	2,2	350
	Electro-magnet	SE750SC 2	2920X1821X1145	1199	1199	3,6	5,6	2,2	425
IFE	Electro-magnet	MEQL 1201 Q	2664X1390X900	1200	1200	3,1	4,7		400
	Electro-magnet	MEQL 1401 S	3156X1634X981	1400	1400	4,5	6,1		450
	Electro-magnet	MEQL 1601 T	3300X2400X990	1600	1600	5,7	7,6		450
	Electro-magnet	MEQL 2201 V	3900X3050X1030	2200	2200	10,8	12,8		450
FELEMAMG	Electro-magnet	SF1-100-RC/100	2580X1495X575	970	1000	2450	6,2	2,3	320-400
	Electro-magnet	SF1-120-RC/120	2946X1705X590	1160	1200	3550	8,5	2,3	385-400
	Electro-magnet	SF2-100-RC/100	2420X1495X665	970	1000	2350	4,3	2,3	320-400
	Electro-magnet	SF2-120-RC/120	2785X1705X680	1160	1200	3450	5,9	2,3	385-400
GRUPO FEM	Overband	OPFEM 8.6	2300X1390X440	630	1030	1,4	--	1,5	220
	Overband	OOPFEM 12.1	2350X2060X550	1300	1085	1,5	--	1,5	320
	Overband	OFEM 13.2	2865X1850X790	1000	1310	3,9	7,6	1,5	250
	Overband	OFEM 14.2	2880X2100X790	1400	1400	4,7	12	1,5	300
	Overband	OFEM 20.1	3200X2300X790	1600	2000	5,5	18	1,5	300
REGULADOR-CETRISA	Overband	R-SKM 9 11	2510X1475X670	900	1100	2,4	4,4	Up to 3,7	370
	Overband	R-SKM 10 12	2790X1600X670	1000	1200	2,8	6,1	Up to 3,7	420
	Overband	R-SKM 12 13	3050X1815X760	1200	1300	4,2	7,6	Up to 3,7	530
	Overband	R-OMP 75 100	2260X1300X400	750	1000	1,4	Permanent magnet	Up to 3,7	280
	Overband	R-OMP 95 120	2450X1500X400	950	1200	2,1	Permanent magnet	Up to 3,7	340
STEINERT	Overband	UMP 90 100 WG	2489X1504X586	950	1126	1,8	--	1,7	360
	Overband	UMP 130 200 WG	3728X1904X716	1350	2126	5,9	--	1,7	460
	Overband	UME 75 90 C	1986X1364X760	750	900	1,6	3,1	2,1	350
	Overband	UME 95	2186X1564X770	950	1100	2,1	4,1	2,1	420

		110 C							
	Overband	UME 135 170 C	3246X2006X850	1350	1700	5,9	8,3	2,1	560

Table 5.4: Comparative table; Magnetic separators

Next pictures show some of the commercial solution that can be purchased:

Overband solution by FELEMAMG

Overband solution by Cetrisa

Permanent magnet solution by Steinert

Table 5.5: Examples of commercial magnet solutions

5.5.4 Electric conductivity separators

Together with the bibliographic work for assessing the state of the art on the available technologies for separating materials by electrical conductivity property, an exploration of the different commercial options that can be found in the market was carried out and presented in the next table:

Type		Dimensions and weights			Eccentricity (mm)	Inductor (kW)	Inductor speed (rpm)	Conveyor speed (m/s)	Main Application
Supplier	Model	General (mm)	Magnetic Width (mm)	Total weight (t)					
DRAGO ELECTRONIC	FC-FCF	3160X1390 X1340	800			2,2	3000	1-3	
	FC-FCF	3160X1390 X1340	1000			2,2	3000	1-3	
	FC-FCF	3160X1390 X1340	1200			2,2	3000	1-3	
ERIEZ MAGNETICS EUROPE LIMITED	UHF (Ultra High Frequency)	4880X2630 X2791	300-2000	6,6	608	15	6000	2,5	Ultra fine (1mm)
	RevX-E	1320X455X 1259 – 3170X2630 X903	300-2000	0,9-3,1	418	7,5	3000	2,5	+ 1mm
	LC	1320X455X 1259 – 3170X2630 X903	300-1500	0,9-3,1	296	5,5	2500	2,5	+50mm
IFE	INP 400X2000	4315X2340 X1250	2300	3100	-	11	600-2500	0,8-3,4	
	INP 400X2500	4315X2840 X1250	2800	3600	-	15	600-2500	0,8-3,4	
	INP 400X3000	4315X3340 X1250	3300	4100	-	18,5	600-2500	0,8-3,4	
	INPX 650X1500 Excéntrico	4200X1840 X1300	1800	3600	125	7,5	600-2500	0,8-3,4	0-50mm
	INPX 650X2000 Excéntrico	4200X2340 X1300	2300	4200	125	11	600-2500	0,8-3,4	0-50mm
FELEMAMG	SFME-29/1000	3370X1805 X1180	950	1360	110	4	3000	0-2,7	Residues plant
	SFME-29/1100	3370X1905 X1180	1050	1450	110	4	3000	0-2,7	
	SFME-29/1200	3370X2070 X1180	1150	1540	110	5,5	3000	0-2,7	
	SFME-29/1300	3370X2170 X1180	1250	1630	110	5,5	3000	0-2,7	
	SFME-29/1400	3370X2270 X1180	1350	1720	110	5,5	3000	0-2,7	
GRUPO FEM	SMFEM 800/14	3000X1950 X874	800	1,2	-	3	3000	0-2,5	25-200mm
	SMFEM 1000/14	3000X2150 X874	1000	1,3	-	4	3000	0-2,5	25-200mm
	SMFEM 800/20	3000X1950 X874	800	1,5	-	3	3000	0-2,5	3-60mm
	SMFEM 1200/20	3000X2350 X874	1200	1,4	-	5,5	3000	0-2,5	3-60mm
	SMFEM 1200/24	3000X2450 X874	1200	1,8	-	5,5	3000	0-2,5	3-150mm
REGULADOR-CETRISA	R-SPM 1800-E ADS	3600X2546 X653	1800	2,2	120	4	3000/4000	3	RSU
	R-SPM 1800-E AF	3600X2546 X653	1800	2,2	120	4	3000/4000	3	<60mm
	R-SPM 1800-E AM	3600X2546 X653	1800	2,2	120	4	3000/4000	3	<20mm
	R-SPM 1800-E AD	3600X2546 X653	1800	2,2	120	4	3000/4000	3	<300mm
	R-SPM XXX-YY	3600XZZZZ X653	500-1800	--	30	4	3000/4000	3	>300mm
	R-SPM XXX-E YY	3600XZZZZ X653	500-1800	--	120	4	3000/4000	3	>300mm

STEINERT	CanMaster 100	3700X1300 X1000	1000	1,2	105	2,2	2610	2,5	>50mm RSU
	CanMaster 150	3700X1800 X1000	1500	1,4	105	3	2610	2,5	
	NES 200 220 E 5012	4200X2630 X1345	2000	3,5	105	5,5	2610-3000	-	>4mm
	NES 200 220 E 6109	5200X3150 X1345	2500	5,3	94	7,5	2610	-	>5mm
	NES 200 210 E 6119 4T	4100X2630 X1345	2000	3,6	94	9,2	2610-4000	-	>0,5mm

Table 5.6: Comparative table; Electric conductivity separators

Next pictures show some of the commercial solution that can be purchased:

Several examples of Eddy current separators by Drago Electrónica

Eddy current separator by Eriez

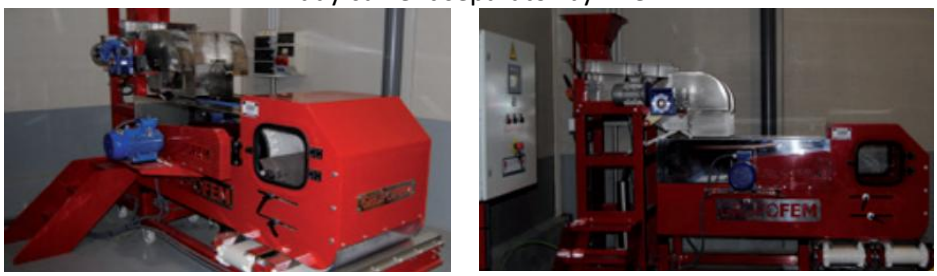

LCFEM compact line by FEM Group

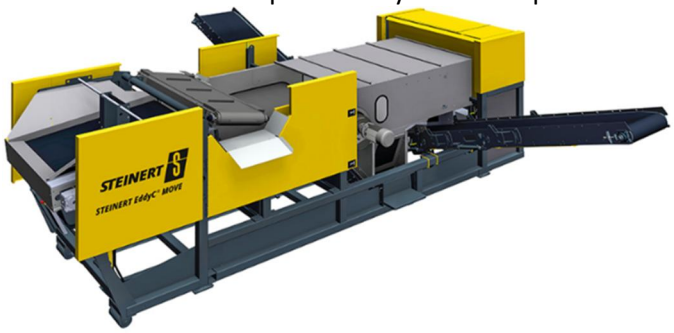

EddyC MOVE system proposes by STEINERT

Fig. 5.43: Examples of commercial Electric conductivity systems

5.5.5 Sensor based separators

Together with the bibliographic work for assessing the state of the art on the available technologies for separating materials based on sensors, an exploration of the different commercial options that can be found in the market was carried out and presented in the next table:

Type		Technology type of sensor	Materials to be detected	Minimum detectable size (mm)	Minimum object size for ejection (mm)	Resolution (Pixel/s)	lighting	Distance sensor-belt
Supplier	Model							
BINDER+CO	CLARITY	NIR/SWIR/VIS /X-ray-X/others	scrap	1mm	1mm	0,5mm/pixel	LED	700mm
MSS OPTICAL SORTERS	L-VIS	Colour (VIS)	scrap	Depends on application	Depends on application	0,4mm	LED	Depends on application
	CIRRUS	NIR/SWIR	Plastics, paper, CDR, RSU	Depends on application	Depends on application	¼''	Halogen	Depends on application
PELLENC ST	MISTRAL+	NIR/SWIR/VIS /X-ray/others	scrap	4x4mm	30mm	10x10mm	Halogens	900mm
	XPERT	NIR/SWIR/VIS /X-Ray/others	scrap					
PICVISA MACHINE VISION SYSTEMS	ECOGLASS	VIS/UV	wires	2mm	2mm	0,6mm/pixel	LED	700mm
	ECOSCRAP	VIS/NIR/EM	scrap	4mm	4mm	5mm	Halogen	89000mm
	ECOPACK	NIR/HSC	wires	8-16mm	8mm		Halogen	89000mm
TOMRA SORTING RECYCLING	AUTOSORT	NIR, VIS	Plastics and paper	17mm	11mm	640000	2 redundant lights integrated	500. 575, 915, 1375mm
	XTRAT	XRT	Scrap and RCD	6mm	3mm		X ray source	
REDWAVE	M	Identification by induction	scrap	--	--	Depends on material and size	--	--
	XRF-M	X-ray	scrap	--	--	Depends on material and size	--	--

Table 5.7: Comparative table; Sensor based separators

Next pictures show some of the commercial solution that can be purchased:

Complete Classification system MISTRAL +

Xpert system for scrap classification

Sorting system by TOMRA

Fig. 5.44: Examples of commercial material classification systems

5.6 Chapter 5 recall and conclusions

In this section, the most widespread waste treatment techniques in the recycling sector have been presented. Each of the different technologies presented in this section, were developed and optimized to solve very specific problem associated with a particular type of waste. However, the processing of iron scrap is much more complex than the simple implementation of any of the technologies described individually due to its high heterogeneity.

An example of a complete steel scrap treatment scheme may consist on an initial fragmentation process, followed by several cleaning and separating processes that allow upgrading the ferrous raw material to be used in steelmaking processes. These processes also give added value to the non-ferrous metal fractions contained in those materials that, otherwise, would not be used.

Basically, a scrap upgrading facility could be comprised by the following stages:

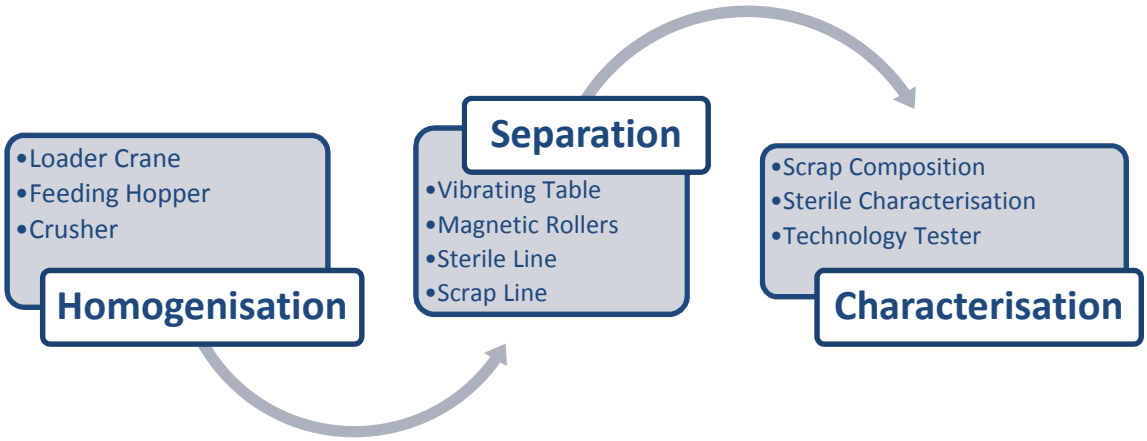

Fig. 5.45: Complete Ferrous scrap processing flow

- The size reduction schemes for current ferrous scraps require large and robust industrial facilities, and normally their design is very conditioned by the specificities of the type of scrap to be processed. Likewise, the exploitation of this type of equipment requires the availability of auxiliary machinery for logistics and material handling, both at the entrance and at the exit of the processing stage. For this reason, providing this technology with some mobility is a requirement that will be imposed in future developments.
- Subsequent separation steps by size and magnetic nature. In the case of ferrous scrap, and given the magnetic particularity of these materials, practically all separation technologies contain, in some of the intermediate steps, some separation technique based on that physical property
- Optical separation allows the classification of almost all types of waste. This option replaces the conventional means and allows to obtain fractions of high purity and constant quality, helping to reduce costs and increasing the profitability of the treatment plants.

Scrap preparation techniques; State of the art.

Based on the previous analysis, an integrated processing scheme proposal is presented in Fig. 5.46:

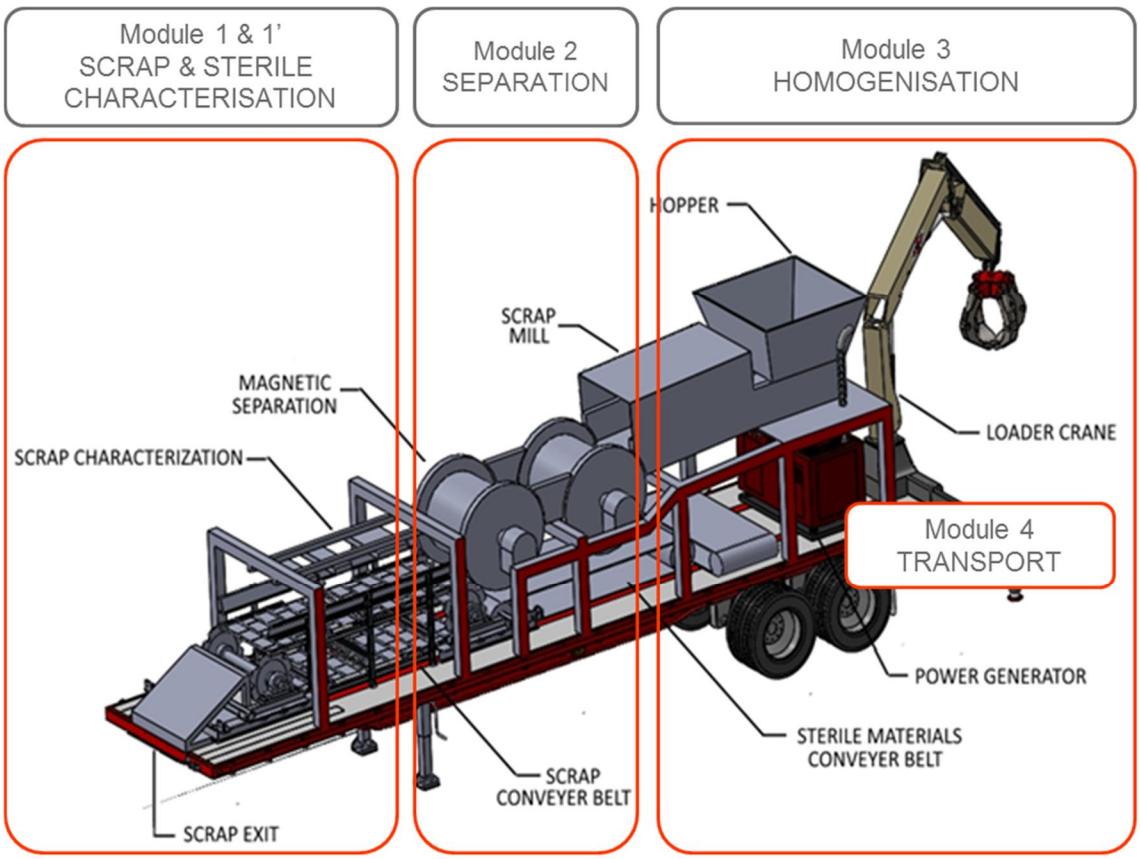

Fig. 5.46: Proposed integrated scrap processing unit

However, it is important to highlight that the first stages of size reduction and separation using magnetic techniques have been widely studied and there are, more or less, efficient industrial solutions for most of the ferrous materials morphologies. However, the characterization of the different materials contained in the ferrous mix remains being an important challenge, opening a world of possibilities to researchers in almost all scientific disciplines.

6

Scrap Characterization techniques; State of the art.

This chapter presents a thorough analysis of the current state of the art in ferrous scrap characterization methods applied in the steelmaking industry. This information about available technologies was discussed with several industrial steel producers for identifying, not only the fields of interest in scrap characterization, but also current technological lacks. The conclusions reached after the analysis allowed defining the new characterization methods to be developed in the subsequent chapters.

Usually the acquisition of ferrous scrap for a particular steelmaking site is done by the purchasing department. Regardless of the method used to select the scrap in the market, steelmakers need to closely control the quality of the scrap to achieve the maximum profit of the steelmaking process. The control of scrap quality is a key operation that has not been totally solved yet.

Carrying out a close control of scrap quality, both in origin and in destination is a very complicated task due to the high heterogeneity of this material; Large volumes, many origins, different pre-treatment processes before arriving at the factory, quality mixtures, cheating of some suppliers, make it difficult to control the characteristics of the scrap.

In the last decades, several methods have been developed to assess the scrap quality, in order to help all stakeholders standardized their scrap managing practices.

6.1 Scrap characterization

Steelmakers have always been aware of the great economic potential derived from an adequate characterization and management of the scrap in steelmaking process. In fact, several projects have been carried out in this respect in the last decades (57). However, despite the fact that different factories have developed or adapted existing methods to their own particularities, none of them has prevailed over the rest, which reveals the real difficulty of performing a correct characterization of scrap.

The easiest way to classify the existing methods or those under-developments for scrap characterization can be as illustrated in Fig. 6.1:

Scrap Characterization techniques; State of the art.

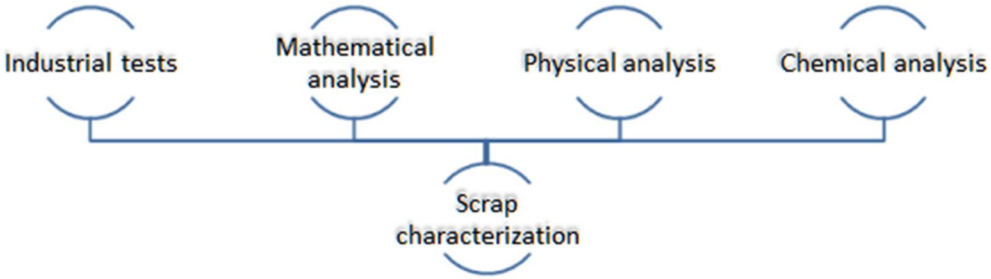

Fig. 6.1: General methods for scrap characterization

The scrap characterization techniques that are currently available in each of the selected methods are described in detail in the following sections

6.2 Industrial testing methods

Various industrial testing methods for material characterization are widely used in steelmaking for obtaining useful information of raw materials when analytical procedures cannot be used or when their use would result in a high consumption of time or resources. These tests provide the data required to make critical process decisions or meet regulatory compliance requirements.

It is possible to group the industrial testing methods in three main categories:

- Melting tests
- Concrete pad analysis
- Cleaning machine sterile content assessment

6.2.1 Melting tests

A melting test is a semi-industrial method for scrap quality assessment in which a close controlled raw material input is melted. It could comprise either 100% of the scrap grade to be tested, or mixed with other scrap of well-known composition, such as home scrap from a BOF shop, or prompt scrap.

There are several methodologies reported in bibliography, depending on the industrial capabilities of the research entity (R&D centres, Universities, steelmakers…). The most complete method consists of a melting test in real industrial conditions, in which complete mass and energy balances are performed. Steel, slag and fumes are monitored in terms of mass or flow rate and composition, with particular attention to iron, carbon, oxygen and tramp element metals.

A major question is to decide what the minimum size of the sample is to be melted and how big a furnace should be selected to carry out the test. Three test levels can be defined:

- **Laboratory scale:** In these kinds of tests, it is possible to characterize little amount of material (in the order of kilograms) under protected or non-protected atmosphere. The main advantage of these tests is its accuracy, due to the strict control of the quantities and conditions under which it takes place.

  Laboratory scale melting tests are a good solution for initial testing of new and uncommon materials considered for charging in the EAF, as well as for determining the variability within a delivery of scrap

  Some examples of equipment for conducting laboratory scale melting tests are shown in Fig. 6.2:

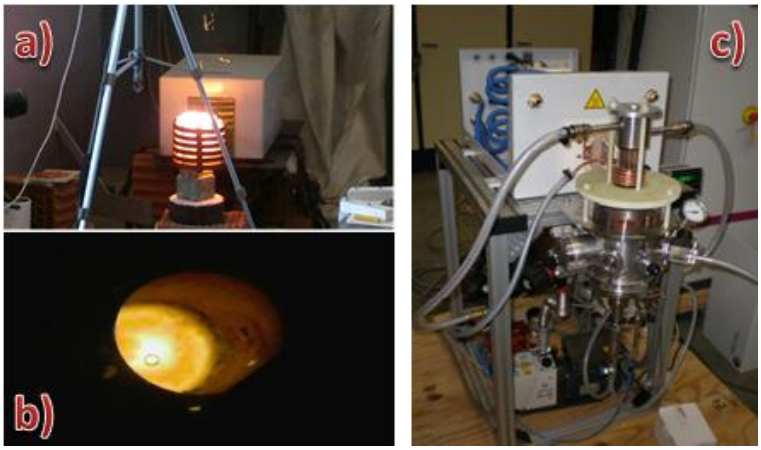

Fig. 6.2: a) and b) 8 kg laboratory induction furnace; c) 77 cm3 levitation furnace. Both equipment in Tecnalia Research Fundation in Zamudio (Spain)

The main drawback of this characterization method is that it is not representative of the real steelmaking process, so that it is only useful for very particular analyse, the high number of tests required to draw conclusions and high time consumption.

- **Pilot scale:** These kinds of tests are suitable for initial testing of new and uncommon materials considered for charging in the EAF or BOF, as well as for determining the variability within a delivery of scrap. This allows to design mechanisms for quality control of supplier compliance with grade specifications and to verify suspected deviations in quality.

  The methods available to perform this type of tests are mainly two: high-capacity induction furnaces and scaled industrial furnaces.

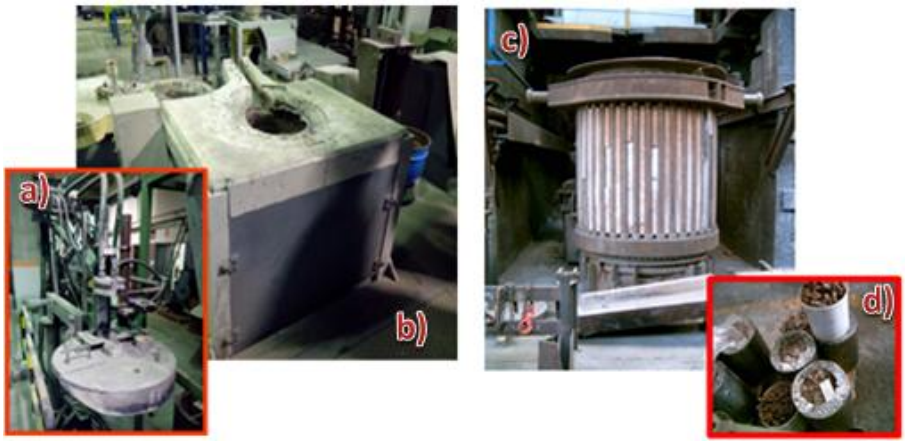

Fig. 6.3: a) and b) 700 kg industrial induction furnace with an electrode heating system in Tecnalia Research Fundation in Irun (Spain); c) and d) 300 kg induction furnace in ArcelorMittal Global R&D centre in Maizieres (France).

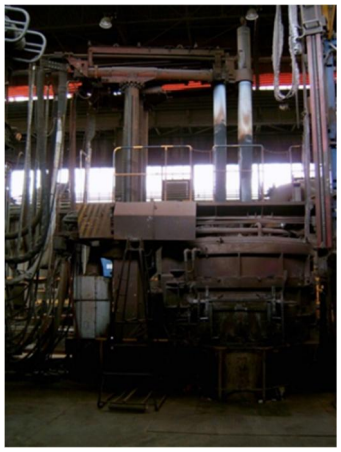

Fig. 6.4: Pilot Electric Arc Furnace (6 tones) in ArcelorMittal Global R&D center in Maizière (France).

The main advantages of these tests include very well controlled conditions during the experiment and high accuracy in the results.

However, there are several disadvantages: it is time consuming, and therefore has long response times, it is a highly costly method and the pre-treatment and cutting of heavy pieces may be necessary.

- **Industrial scale:** Industrial scale melting tests consists on controlling some parameters during the standard operation in industrial Electric Arc Furnaces. This method is usually used for determining the actual chemical composition of high alloyed scrap (stainless steel, special steels) or to carry out the confirmation or updating of scrap properties used by scrap mix optimizer tools or process models.

  Among its main advantages are the high accuracy and quick response of the method and the possibility to study a specific problem and apply the obtained conclusion directly at the steel plant.

  The main drawbacks are the risk of process disturbance and possibility of material downgrading due to the test heats.

In general, the behavior of different scrap grade categories exhibits a large scatter, even for those with "good" mean values. However, regarding individual results, where identical markers indicate a single supplier yard, the dispersion is much smaller between scrap deliveries from a single preparation yard.

Some usual operations associated to the melting test for scrap characterization operations are:

- Bulk density measurement weighing a known volume.
- Humidity estimation drying the sample in a furnace at high temperature until its mass remains stable.
- Hand sorting operations before the melting.

The data obtained by the melting tests constitute a very powerful tool to assess the quality of both, internal and external scrap. Nevertheless, the use of this kind of tests is gaining

popularity for the economic analysis of the potential use of other industrial residues and/or by-products in the steelmaking process.

6.2.2 Characterization of deliveries by concrete pad analysis

This method basically consists of unloading a scrap truck on a concrete surface at the scrap yard. Then the scrap is collected by magnetic means. The remaining material (nonmagnetic material) is finally sorted by hand and then weighed. It allows estimating the most general quality parameters in a very simple manner.

This method is probably the most extended one, due to its simplicity and the non-expenditure of additional resources. It has a clearly didactic utility, both for the scrap suppliers and for the scrap classification technicians.

Fig. 6.5 shows the quality control process and some examples of the output obtained using this method.

Fig. 6.5: Up) Quality control on concrete area. Down) Elements containing Cu (a), sealed elements that can explode in the furnace (b) and sterile remaining on the floor (c)

6.2.3 Cleaning machine sterile content assessment

The worldwide scrap metal recycling industry has developed sets of specifications and grading systems to ensure consistent quality of source scrap material for a given grade of metal scrap. These specifications generally set minimum and maximum content of certain metal impurities and restrict levels of certain hazardous metals and other substances.

Scrap yard personnel must know these criteria. This knowledge, together with the acquired experience, allows scrap yard specialists to estimate the amount of impurities in every scrap delivery.

In the most widespread way of proceeding, a very experienced scrap yard operator conducts a visual inspection of the discharge of each scrap delivery and estimates a quantity of sterile, which is subsequently used to penalize the supplier.

On the other hand, ferrous metals are magnetic and often collected in scrap yards by a large electromagnet attached to a crane, sweeping across piles of scrap to grab magnetic objects. This magnetic property of scrap has been used by different engineering companies that focus their business on the development of siderurgical equipment to develop scrap cleaning machines.

Scrap cleaning machines allow not only eliminating the undesired materials that come with the scrap (and penalize the performance of electric arc furnaces) but can also be used to track the quality of the material supplied by each scrap suppliers.

Fig. 8 shows a basic description of a scrap cleaning machine for E1 scrap type:

Fig. 6.6: Scrap cleaning machine description

Some steelmakers use scrap cleaning machines for the assessment of sterile content. The benchmark practice usually used to this end is described below:

1 Every scrap truck is registered at the factory arrival (plate number and weight).

2 Scrap is delivered at the scrap yard where it is discharged in the material receiving hopper of the cleaning machine (each scrap truck is processed separately).

3 The cleaning machine sorts non-ferrous materials from ferrous materials.

4 Non-ferrous material separated after the processing of each truck is collected with a backhoe provided with a scale.

5 The non-ferrous material is accumulated in a pile to be later sold.

6 Every scrap truck is registered at the factory departure (plate number and weight).

7 A report is generated.

Fig. 6.7 describes the practice followed for the assessment of sterile content:

Fig. 6.7: Sterile weight characterization at the scrap cleaning machine

Although the benefits of scrap cleaning machines have been clearly demonstrated, they also present several drawbacks, such as, the high cost of equipment, high maintenance requirements, dedicated personnel required to process the scrap and the fact that not all scrap can be cleaned.

6.3 Mathematical analysis methods

From an industrial point of view, and given that at plant level, there are extensive databases that allow a deep analysis of the process performance, along time different mathematical methodologies have been developed for the purpose of scrap quality estimation. The most extensive ones are statistical analyses for chemical composition and energy models.

6.3.1 Statistical analysis

Carrying out a statistical analysis of operating data from the Steelshop databases is probably the easiest and most extended method for scrap characterization, since it can be applied consistently almost everywhere with a small effort.

The most common method is based on a multilinear regression analysis of the elements of interest (whereby parameters relative to each heat are assumed to be linear functions of each scrap category constitutive of the charge) and the overall mass balance on the heat population. Some criteria must be taken into consideration when selecting the sample of heats to be analyzed:

- Large sample populations (>1000 heats)
- Charging schedules should be numerous, different and statistically independent
- Data must be carefully selected

The method itself gives trustworthy information on mean values of the main components of scrap quality: purity in tramp elements and iron content. It can also be used to follow up the evolution of scrap quality over time.

Careful testing of the method in three French Steelshop in a 2-year period during the nineties, showed that this method can be used to estimate the content in tramp elements, including Sulphur, and, under stricter conditions, the metallic yield (58).

6.3.1.1 Metallic yield estimation

In its simplest conception, the metallic yield of scrap can be calculated by a multi-linear regression analysis as follows:

$$Y_i = \sum_j Y_j \frac{W_{ji}}{Wi} \qquad \textbf{(6.1)}$$

Where:

Y_i **:** The scrap yield of heat i

Y_j **:** The scrap yield of scrap type j

W_{ij} **:** The weight of scrap j in heat i

W_i **:** The total weight of scrap in heat i

However, the hot heel has a great influence on the results obtained by this method. The hot heel can be assumed to be constant. It can be measured (some systems for automatic measurement of liquid steel level inside EAF have been found in the bibliography (59)) or can be estimated by using a tracer (Cu or Sn). The method used for estimating the hot heel could be critical on the correlation between calculated vs. actual values of yield.

Fig. 6.8 and Fig. 6.9 show some results obtained in ArcelorMittal, by using this technique for the analysis of the metallic yield associated with each scrap grade in monthly and a daily basis analysis.

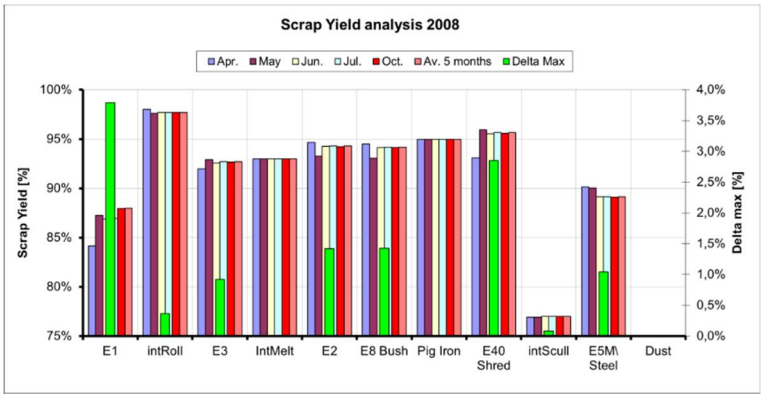

Fig. 6.8: Example of Monthly scrap analysis

September	Paq. 4A	Paq. 4C	Est. OA	Est. 1/2	Rec.	Propia	Fragm.	Lingote	Arrabio	D.R.I.	ERROR
Day	Yield										
1	1058	1132	1086	1251	1069	1215	1167	1092	1105	1251	2,23%
2	1104		1085	1228	1145	1219	1159	1093	1152	1161	1,56%
3	1126		1077	1216	1148	1220	1153	1095	1169	1169	1,34%
4	1110		1100	1230	1152	1219	1165	1094	1156	1177	2,18%
5	1081	1084	1116	1249	1146	1219	1177	1096	1141	1186	0,77%
6	1091	1083	1122	1260	1154	1224	1182	1096	1160	1231	1,96%
7	1082	1085	1095	1235	1137	1216	1165	1093	1143	1146	1,76%
8	1150		1083	1228	1181	1218	1148	1097	1148	1205	1,76%
9	1042		1078	1285	1116	1215	1183	1091	1142	1134	1,80%
10	1084		1099	1229	1147	1223	1160	1097	1140	1135	1,79%
11	1028		1081	1180	1116	1200	1160	1090	1101	1256	2,07%
12	1081		1102	1226	1134	1216	1167	1093	1143	1153	3,40%
13	1082		1107	1253	1134	1220	1179	1094	1151	1179	2,27%
14	1079		1102	1245	1132	1218	1173	1093	1143	1155	1,42%
15	1081		1105	1247	1133	1219	1175	1094	1147	1164	1,36%
16	1085		1103	1247	1136	1219	1173	1093	1148	1168	2,18%
17	1013	1074	1134	1363	1075	1216	1240	1094	1174	1168	1,42%
18	1197		1008	1177	1173	1196	1115	1096	1122	1162	1,53%
19	1106		1062	1334	1145	1218	1200	1095	1194	1161	1,28%
20	1080		1102	1246	1132	1218	1173	1093	1143	1153	2,31%
21	1084		1105	1248	1136	1220	1175	1094	1149	1172	3,42%
22	1182		1089	1158	1335	14	1168	1178	1110	1287	2,00%
23	1070	1090	1116	1245	1134	1224	1181	1099	1148	1194	2,24%
24	1085	1109	1099	1214	1153	1218	1160	1096	1144	1152	2,60%
25	1126	1098	1098	1211	1108	1216	1160	1093	1154	1153	4,68%
26	1093		1103	1241	1131	1220	1171	1094	1148	1163	1,00%
27	1165		1095	1200	1129	1219	1147	1099	1157	1166	0,70%
28	1086		1105	1253	1133	1221	1175	1094	1151	1183	1,88%
29	1087	1079	1106	1252	1132	1221	1174	1094	1154	1184	1,08%
30	1071		1093	1282	1114	1227	1201	1089	1162	1195	1,57%

Fig. 6.9: Daily scrap analysis (used Scrap / produced Steel x 1000)

Scrap Characterization techniques; State of the art.

Other modelling approaches have been published in the bibliography that tries to predict the metal performance of the process for a particular scrap mixture (57), among them:

- "Mefos approach", which corresponds with a Partial least squares (PLS) prediction model based on specific scrap grade consumptions (% of total scrap mix) for individual grades. This model allows updating the different scrap grades yield coefficients considering process a data from 20 heats in a row.
- "BFI approach", which correspond with a multiple linear regression prediction model based on weights of charged scrap (kg). This model allows predicting the yield for individual heats as well as estimating the remaining liquid steel inside the furnace after tapping operation (hot hell).

6.3.1.2 Tramp element estimation

The tramp element content can also be calculated by a multi-linear regression analysis. The model assumes that the composition of steel produced by melting a mixture of scrap of very different natures, follows a law of mixture without interaction, so that, the model relates the composition of the melt (output) to the linear composition of each scrap category used, with a ponderation directly related to the proportion of each scrap category and the yield of the heat and taking into account the hot heel (18):

$$\frac{e_{i\_output}}{u_i} - \frac{P_{hh} \cdot e_{i-1}}{\left(P_{input} + P_{hh}\right)} = \sum_j \hat{e}_j \times \frac{P_{ij}}{\left(P_{input} + P_{hh}\right)} \qquad \textbf{(6.2)}$$

Where:

e **:** a residual element (Ni, Sn, Cu, Mo)

i **:** index of heat

j **:** index of scrap category

$\hat{e}_j$ **:** content in element e in scrap j

$\hat{e}_i$ **:** content in element e in heat i

e_{i_output}: content in element e after melting

P_{ij}: weight of scrap j in heat i

P_{hh}: weight of hot heel

P_{input}: total weight of scrap charged for heat i

U_i: yield of the heat i

Scrap Characterization techniques; State of the art.

On the other hand, one of the main missions of the scrap yard is to manage the logistics of raw materials to ensure continuous feeding to the steel mill. To do this, and in order to increase the operation of the scrap yard, it is usual to prepare several scrap piles with scrap grades from the same family (usually when the scrap yard has several basket loading sites). Fig. 6.10 shows an example of a scrap yard lay-out:

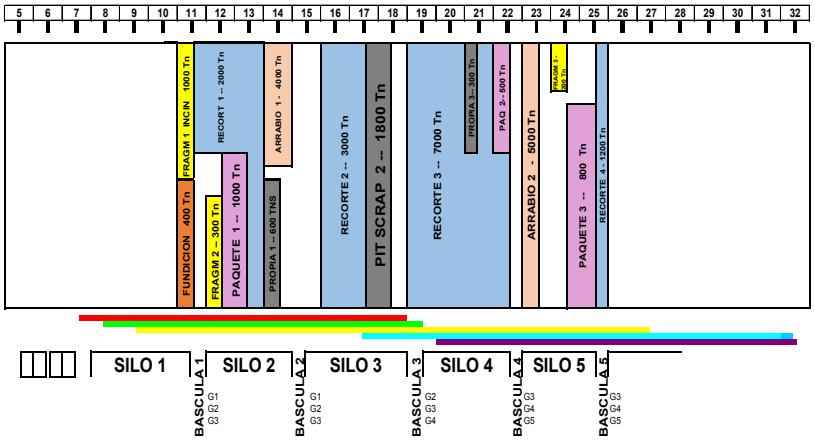

Fig. 6.10: Example of scrap distribution in one ArcelorMittal site scrap yard

When the multi-linear regression method is used to estimate the metallic yield of different scrap grades, scrap from the same family turns out in similar results (within reasonable upper and lower limits). However, this is not so clear when tramp element content is analyzed. Given that for each scrap family the residual content varies greatly depending on the origin, the scrap pre-treatment methods and intermediate scrap mixtures, the best way to carry out the tramp element characterization is to classify the inputs by scrap piles in the scrap yard rather than by scrap grade families. Fig. 6.11 shows an excel tool for multi-linear regression analysis based on scrap allocation in piles in the scrap yard instead of scrap grades for residual elements estimation.

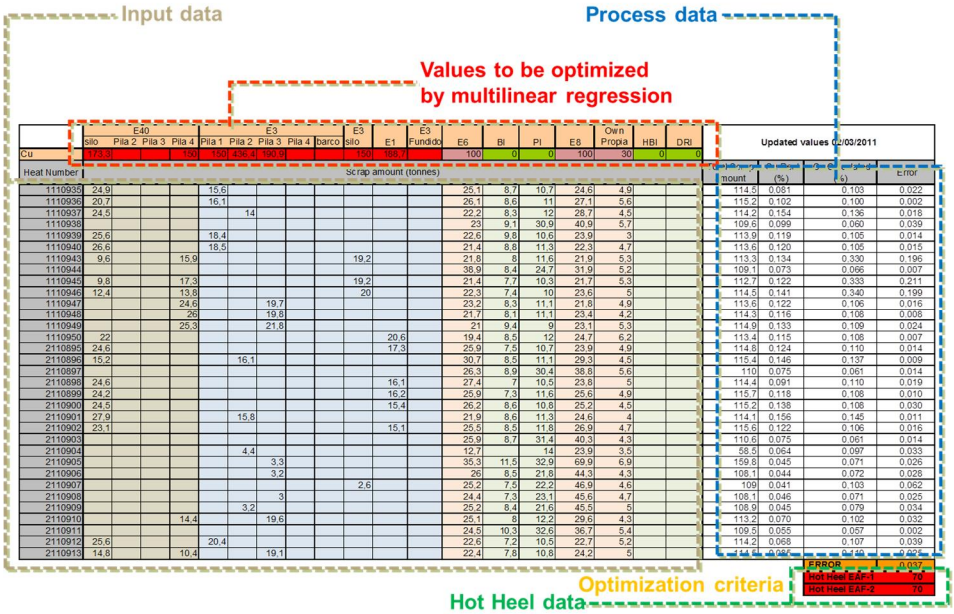

Fig. 6.11: Cu content estimation method by classifying inputs by scrap piles in the scrap yard

6.3.1.3 Acid gangue content estimation

Probably the most extended mathematical analysis method applied to acid gangue estimation of the different scrap grades is comprised by a combination of the total EAF mass balance with multi-linear regression analysis. Thereby, the acid gangue content in every scrap grade can be back-calculated from slag analysis, where CaO, MgO, SiO_2, Al_2O_3 balances must be done.

According to this approach, the acid gangue (AG) weight is defined as:

$$\mathrm{AG} = SiO2_{(S)} + Al2O3_{(S)} \quad \textbf{(6.3)}$$

The total SiO_2 heat input is derived from the total CaO and MgO inputs and the slag basicity (IB):

$$SiO2_{(T)} = (CaO_{(T)} + MgO_{(T)}) \,/\, \mathrm{IB} \quad \textbf{(6.4)}$$

The slag volume (V_s) is calculated from the total added CaO and CaO content in the slag:

$$V_s = CaO_{(T)} \,/\, \%\ \mathrm{CaO} \quad \textbf{(6.5)}$$

The total Al_2O_3 heat input is derived from the slag volume and the Al_2O_3 content in the slag:

$$Al2O3_{(T)} = V_s \cdot\ \%\ \mathrm{Al2O3} \quad \textbf{(6.6)}$$

The total added CaO is the sum of CaO coming from lime (1), dolomitic lime (2), dust (3) and scrap (4):

$$CaO_{(T)} = CaO_{(1)} + CaO_{(2)} + CaO_{(3)} + CaO_{(4)} \quad \textbf{(6.7)}$$

The total added MgO is the sum of MgO coming from the refractory (5), dolomite (2), dust (3), and scrap (4):

$$MgO_{(T)} = MgO_{(5)} + MgO_{(2)} + MgO_{(3)} + MgO_{(4)} \quad \textbf{(6.8)}$$

The MgO coming from the scrap is calculated as follows:

$$MgO_{(4)} = (V_{(s)} \cdot\ \%\ \mathrm{MgO} \,/\, 100) - MgO_{(5)} - MgO_{(2)} - MgO_{(3)} \quad \textbf{(6.9)}$$

where subscripts (s) and (t) refer to the content of the compound in scrap and total respectively.

With the total SiO_2 input and the total Al_2O_3 input, the acid gangue included in each scrap grade is calculated by minimizing a so-called cost function which depends on the scrap grade use per heat and per mix, total scrap use per mix and number of produced heats per mix, using a similar multi-linear regression approach to previous methods.

Fig. 6.12 shows some results obtained in one ArcelorMittal site using the explained methods for scrap acid gangue characterization:

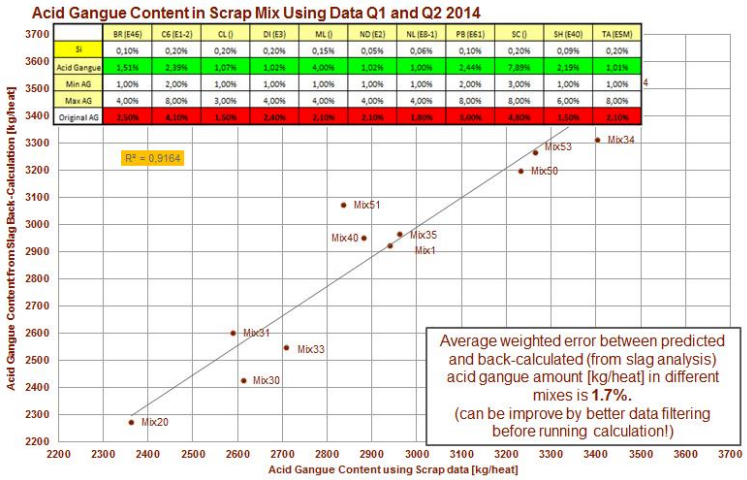

	BR (E46)	C6 (E1-2)	CL ()	DI (E3)	ML ()	ND (E2)	NL (EB-1)	PB (E61)	SC ()	SH (E40)	TA (E5M)
Si	0,10%	0,20%	0,20%	0,20%	0,15%	0,05%	0,06%	0,10%	0,20%	0,09%	0,20%
Acid Gangue	1,51%	2,39%	1,07%	1,02%	4,00%	1,02%	1,00%	2,44%	7,89%	2,19%	1,01%
Min AG	1,00%	2,00%	1,00%	1,00%	1,00%	1,00%	1,00%	2,00%	3,00%	1,00%	1,00%
Max AG	4,00%	8,00%	3,00%	4,00%	4,00%	4,00%	4,00%	8,00%	8,00%	6,00%	8,00%
Original AG	2,50%	4,10%	1,50%	1,40%	2,10%	2,10%	1,80%	3,00%	4,80%	1,50%	2,10%

Fig. 6.12: Calculation results on scrap acid gangue content in ArcelorMittal

6.3.2 Energy estimation

Energy consumption represents an important part in the production costs in an EAF. It may represent around 15% of the total production cost. Each type of scrap, due to its main physical properties (size, thickness, density ...) and its chemical properties (coatings, apparent surface ...), has an intrinsic energy requirement for being melted. Actually, the energy requirement of a particular scrap turns out to be higher due to the effect of scrap non-quality (see the concept of VIU developed in previous sections).

A very general way of performing the partial characterization of scrap is to model the energy behaviour of the EAF process. This is why energy modelling has become a topic of concern for many years. In order to control this, different methods for modelling the energy performance of the furnace have been developed:

- **Empirical models of energy demand**: Most empirical models are based on linear regression of variables of very different nature along the process. In these models, these variables are used to feed a regression model to estimate the change of electric energy demand when process parameters are modified.

  The main drawback of this type of models is that they do not allow characterizing energy requirements for each scrap grade individually. Instead, they tend to gather scrap families with similar behaviours from an energetic point of view.

  The most known empirical model was proposed by S. Köhle for quantifying the influence of various process parameters on the electrical energy demand based on linear relations (60).

Scrap Characterization techniques; State of the art.

$$\frac{W_R}{kWh/t} = 300 + 900 \cdot \left[\frac{G_E}{G_A} - 1\right] + 1600 \cdot \frac{G_Z}{G_A} + 0.7 \cdot \left[\frac{T_A}{°C} - 1600\right] + 0.85 \cdot \frac{t_S + t_N}{min} - 8 \cdot \frac{M_G}{m^3/t} - 4.3 \cdot \frac{M_L}{m^3/t} \quad (1)\ 1992$$

$$\frac{W_R}{kWh/t} = 300 + 900 \cdot \left[\frac{G_E}{G_A} - 1\right] + 1600 \cdot \frac{G_Z}{G_A} + 0.7 \cdot \left[\frac{T_A}{°C} - 1600\right] + 0.85 \cdot \frac{t_S + t_N}{min} - 8 \cdot \frac{M_G}{m^3/t} - 4.3 \cdot \frac{M_L}{m^3/t} - 2.8 \cdot \frac{M_N}{m^3/t} + 80 \cdot \frac{G_{DRI/HBI}}{G_A} - 300 \cdot \frac{G_{HM}}{G_A} - 15 \cdot CON \quad (2)\ 1999$$

$$\frac{W_R}{kWh/t} = 391 + 450 \cdot \left[\frac{G_E}{G_A} - 1\right] + 800 \cdot \frac{G_Z}{G_A} + 0.35 \cdot \left[\frac{T_A}{°C} - 1600\right] + 0.43 \cdot \frac{t_S + t_N}{min} - 2.1 \cdot \frac{M_L}{m^3/t} \quad (3)\ 2001$$

$$\frac{W_R}{kWh/t} = 375 + 400 \cdot \left[\frac{G_E}{G_A} - 1\right] + 1000 \cdot \frac{G_Z}{G_A} + 0.3 \cdot \left[\frac{T_A}{°C} - 1600\right] + 1.00 \cdot \frac{t_S + t_N}{min} - 8 \cdot \frac{M_G}{m^3/t} - 4.3 \cdot \frac{M_L}{m^3/t} - 2.8 \cdot \frac{M_N}{m^3/t} + 80 \cdot \frac{G_{DRI/HBI}}{G_A} - 350 \cdot \frac{G_{HM}}{G_A} - 50 \cdot \frac{G_{Shr}}{G_A} + NV \cdot \frac{W_V - W_{Vm}}{kWh/t} \quad (4)\ 2002$$

CON	continuous (+1), discontinuous (-1) operation	M_N	Specific post-combustion oxygen [m^3/t]
G_A	Furnace tap weight [t]	NV	Furnace specific factor (0.2 to 0.4)
G_{DRI}	Weight of DRI (Direct Reduced Iron) [t]	T_A	Tapping temperature [°C]
G_E	Weight of all ferrous materials [t]	t_N	Power-off time [min]
G_{HBI}	Weight of HBI (Hot Briquetted Iron) [t]	t_S	Power-on time [min]
G_{HM}	Weight of hot metal [t]	W_R	Specific electric energy demand
G_{Shr}	Weight of shredder [t]		(from regression analysis) [kWh/t]
G_Z	Weight of slag formers [t]	W_V	Energy losses (if measured) [kWh/t]
M_L	Specific lance oxygen [m^3/t]	W_{Vm}	Mean value of W_V [kWh/t]
M_G	Specific burner gas [m^3/t]		

Fig. 6.13: Köhle model

These models remain widely used nowadays as they allow for the direct comparison of the performance of furnaces with very different technical characteristics or operating regimes.

- **Static models based on mass and heat balances**: Several static models are described in the literature for estimating the mass and energy balances applied to BOF steelmaking processes. Most of these models seek to calculate the energy profile based on output steam unknowns. To do so, all heat oxidation reactions and heat capacities are used in order to calculate the temperature of the liquid steel at the end of the blow and the amount of scrap that should be added to cool the path (61) (62) (63) (64).

  Despite the fact that most energetic models have been developed for BOF steelmaking route, it is also possible to find several works dedicated to EAF. However, for these models, the chemical composition of the scrap grades included in the used MIX is an input, and the output corresponds to the total energy consumption of the process as it was set.

  In a simpler way, it is possible to obtain the general energetic model of an EAF using the average values of the most representative process parameters. Three easily implementable methods exist: complete method (energy input and output calculations), direct method (based on the energy input calculations) and indirect method (based on energy output estimations obtained by experience) (65).

- **Dynamic models based on mass and heat balances**: Dynamic models and simulators became popular in the first decade of the 21th century for EAF, since Steelshop engineers could work with them to optimize these processes. The main efforts are

focused on obtaining a model that is appropriate for closed-loop control system simulation and initial controller verification. This kind of models needs to approximate the physical process in terms of its dynamic response to control and disturbance input changes, aiming to obtain the same type of response, with the same order of magnitude as is found in an industrial EAF.

There are only limited references to dynamic EAF models in the literature, since most of them were developed for a particular plant.

- **More sophisticated models of energy demand**: Starting from previously developed linear and statistical EAF process models, for appraising the electric energy demand and end-point of the heat elaborations, in recent time, multivariable data analysis and artificial neural networks have become important tools for process monitoring and control of industrial processes.

6.4 Physical analysis methods

In previous sections, it was presented the interrelations between scrap specifics and its influence over the EAF process variable costs. So far, several methods for estimating chemical characteristics of the different scrap grades have been discussed.

In terms of physical considerations, the most relevant characteristic are physical shape, homogeneity and consistence.

Several research works have been reported, implemented with greater or lower success in the industrial field, to offer solutions that allow obtaining information of these physical characteristics.

6.4.1 Machine vision techniques for scrap online characterization

Currently several physical analyses can be carried out by very specialised technicians on site, mainly based on subjective criteria and their own experience. This has led thinking that there may be certain image features which allow to describe the scrap for classification. These extracted features can be used to build a machine vision system for steel scrap characterization.

However, and since we are referring to severe industrial processes, some problems need to be solved related to changing light conditions, high variability on operation temperatures for the site and changing distances between inspected objects and cameras. These problems require a thorough image processing in order to extract objects for analysis from the images. Some common algorithms are: edge detection binary large object analysis image segmentation and gauging

Several systems based on machine vision for physical characterization of scrap materials have been reported in literature. Among them:

A system for classification of steel scrap during charge bucket operation based on image processing during basket was published in 2008 (66). This system consists of detecting the location of the basket and electromagnet by pattern matching algorithms. This information is used as a calibration pattern of the system and thus it is possible to transform a pixel coordinate to physical measurements. After separating the scrap from the surrounding background and image noise filtering, a scrap volume assessment algorithm was implemented. This algorithm was based on the removal of the magnet and the segmentation of the image, assuming a cylindrical shape.

When the weight carried by the magnet is known, the scrap density calculation is immediate. The 2D colour image processing allows extracting additional information such as oxidation degree, degree of heterogeneity, compactness and other relevant properties.

Scrap Characterization techniques; State of the art.

In 2008, J.C. Baumert and other (67) also presented a system for conducting the automated assessment of scrap quality before loading it into an Electric Arc Furnace. This system was installed in the scrap yard gantry cranes at one ArcelorMittal EAF plant in Luxembourg.

The importance of monitoring the scrap charging process into the baskets relies on the fact that a good scrap density layering within the basket is crucial for allowing rapid formation of liquid at the first stages of the melting process in the EAF, while providing protection to the cooled panels from arc radiation, which lead to an improvement in the global energetic efficiency of the melting process.

The proposed scrap monitoring system allows extracting information related with the visual aspect and granulometry of the scrap used (imaging system), as well as the height distribution of the scrap layers deposited in each basket (laser scanners). Combining all this information, it is possible to make the scrap density classification of the scrap and calculate the basket filling ratios.

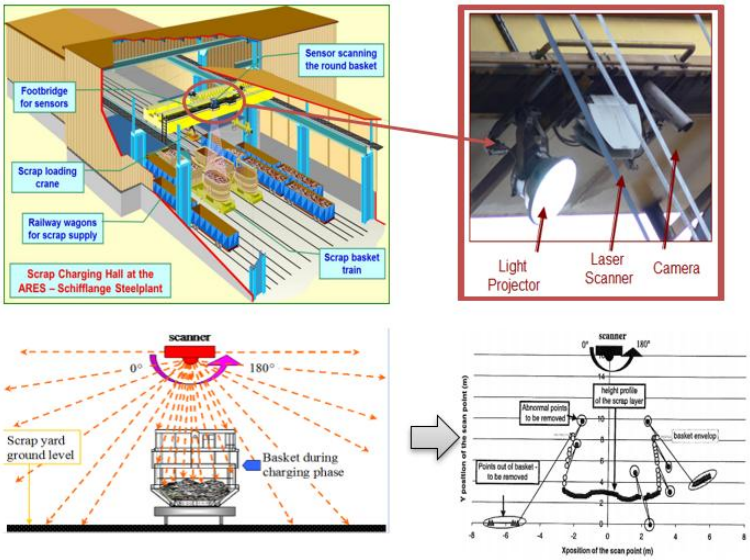

Fig. 6.14: Up) Detail on data acquisition system and Down) Scanner operation during basket charging

The system, as shown in Fig. 6.14, is basically composed of:

- A data acquisition system: Composed by four medium resolution digital colour digital cameras combined with four high precision laser distance scanners and a powerful light projector.
- Scrap layering image processing: digital image processing is applied to extract information about scrap size distribution and granulometry.
- Automated charged scrap classification: after image processing, artificial neuronal network classifiers allow the automatic identification of the charged scrap types
- Height scan processing for scrap density assessment: the scrap level distribution in the basket is assessed by means of laser-based scanner measurement.

In the two cases presented, the attention was focused on the basket charging operation. Nevertheless, the proposed methodologies can be applied to other operations in the scrap yard to control the quality of the scrap directly in the trucks or trains at the factory entrance or to make the automatic scrap inventory of the different scrap piles in the scrap yard.

6.4.2 Characterization of skulls using water displacement method

The most accurate method to determine the steel content in reverts is the melting test of a representative sample, which can be considered as the “reference method”. Nevertheless, the melting test requires the use of a dedicated furnace and high manpower resources for the operation of the furnace, an accurate weight of the steel and slag generated, and the preparation and analyses of the steel and slag samples.

The water displacement method is less accurate than the melting test but is easier to carry out. It requires less investment and it is faster to obtain a rather good estimation of the steel content of the skulls. So, it is typically a test that can be developed in any industrial site. Once the volume of skulls is determined, it is possible to evaluate the steel content, using the densities of the steel and slag fractions: the main difficulty is to use a correct density value for the slag fraction, which may vary depending on the skull grain size or the chemistry and porosity of the slag.

Steelmakers use the water displacement method to evaluate quickly, without melting, the iron content of the reverts coming back from the EAF process (slag pits, slag pots, ladles and tundish bottom).

This method is supported on the theoretical concept that a submerged object displaces a volume of liquid equal to the volume of the object.

The general procedure used to conduct the water displacement test, is to use of a weighed container with standard dimensions. Once the container is filled in with the material to be characterized and with water up to a previously defined level, it is possible to use bulk density and true density concepts to obtain the iron content.

Fig. 6.15: Water displacement method

The water displacement method for skulls or reverts is based on the definition of density as the mass per volume unit. For a given value of the density of skulls (7874 kg/m^3) and non-iron elements (2200-3000 kg/m^3), the iron content can be estimated as follow:

$$V_{skull} = V_{iron} + V_{non-iron} \quad \textbf{(6.10)}$$

Where:

- V_{skull} is the volume of the material to be characterized
- V_{iron} is the volume of iron
- $V_{non-iron}$ is the volume of elements that are not iron

Since $\rho = m/V$ and $m_{skull} = m_{iron}$ *ecu+* $m_{non-iron}$, it can be said that:

$$\%Fe = \frac{m_{iron}}{m_{skulls}} = \left(\frac{\rho_{non-iron} - \rho_{skulls}}{\rho_{non-iron} - \rho_{iron}}\right) \cdot \frac{\rho_{iron}}{\rho_{skulls}} \quad \textbf{(6.11)}$$

Fig. 15 shows the correlation between the Fe content measured by melting test and the density measured in reverts using water displacement method obtained by the ArcelorMittal Global Research and Development center at Maizieres in France.

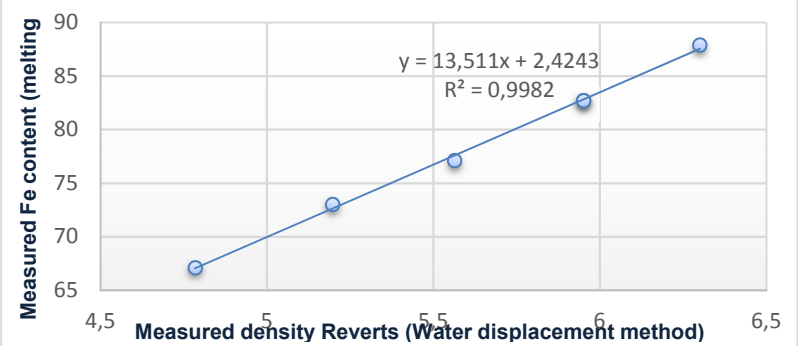

Fig. 6.16: Correlation analysis between melting test and water displacement method (19)

However, if several references of the use of this method are consulted, some dispersion is observed in the reported results (68) (69).

This disparity might be due to several fundamental flaws in the industrial method. First, the iron contents and densities of the pure metallic phase and the pure non-metallic phase are often determined by slag processors using their preferences. The calculated total iron contents in steelmaking slags are quite different if different values of the iron contents and densities for the ‘‘pure’’ metallic phase and the ‘‘pure’’ non-metallic phase are assumed.

The second issue with the industrial method is the water displacement density. Water can only penetrate large open pores. Steelmaking slag particles can have closed pores and microspores (impermeable voids) through which water cannot penetrate. Number of the closed pores and microspores in the steelmaking slag particles can change with slag composition, cooling rates and particle size.

Therefore, water displacement density cannot be directly related to the iron content in the slags. In other words, water displacement density and total iron content depend on the particular sample porosity, slag chemistry (FeO content, slag basicity, etc.), and actual steel chemistry.

Scrap Characterization techniques; State of the art.

Naiyang Ma et others (70) have published a second order polynomial equation able to fit the correlation of the measured total iron contents in the steelmaking slag samples to the measured water displacement densities of the slag samples that guarantees reliable results of this method:

$$F_S = \frac{2253.8}{\rho_S^2} - \frac{1712.6}{\rho_S} + 343.24 \quad (R^2 = 0.9319) \tag{6.12}$$

Where:

- F_s is the total iron content slag sample
- ρ_s is the slag density

6.4.3 Radioactive analysis

Despite the fact that radioactive scrap control may not be considered as a scrap quality characterization method for the process optimization purpose, radioactive properties are also a requirement of scrap quality, and must be taken into consideration during the scrap purchasing operations and factory material management processes.

Radioactive elements, when introduced in the steelmaking production, pollute steel products, by-products and process wastes. This contamination also affects the production equipment as well as the surrounding environment.

On the other hand, increasing globalization of scrap markets and production site locations introduces an additional risk from less regulated regions.

Fig. 6.17 shows the material flow inside the factory, indicating, through colour coding, the potential risk of finding radioactive materials. Also, the most common radiation control points are represented.

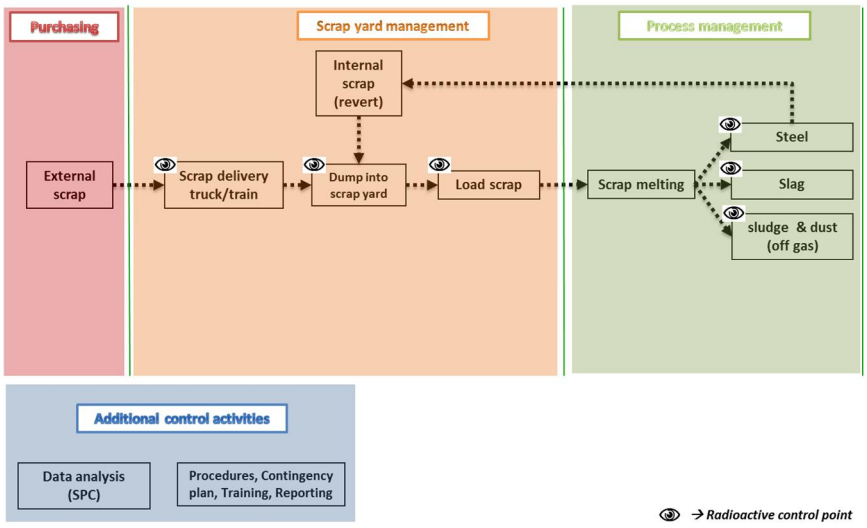

Fig. 6.17: Radiation detection flow chart

Scrap Characterization techniques; State of the art.

The radioactive contamination is a really important topic for the steel industry, and it is carefully monitored due to the relevant impact from both ecological and economical aspects. The systems currently used in the steel industry are based on the radiation detection: sensors are placed at the reception of scrap metal cargos or during first operations on the scrap metal inside the steel plant.

Such equipment are based on radiation presence and, unfortunately, in case of shielded sources can rise an alarm only once the shielding has been opened (e.g. melted) and/or the production plant contaminated. Fig. 22 to Fig. 24 show some pictures of these controls mechanisms:

Fig. 6.18:Diferent radioactive controls: Up) Portal control for Scrap delivery by truck and by train, mid) Scrap and dust on line control and Down) punctual analyses

This detection mechanisms are sometimes not enough and this generalized concern is reflected in a RFCS European project called “Muons scanner to detect radioactive sources hidden in scrap metal containers” which aimed to develop a muon based portal for the identification of shielded orphan sources in order to avoid accidental melting in the steel industries, as well as to determine the minimum inspection time needed to discover the presence of a source hidden in the scrap metal, as a function of the source size (71).

6.5 Chemical analysis methods

From the chemical analysis point of view, there are several methods to be applied depending on the purpose of the characterization activity.

6.5.1 Conventional laboratory analytical methods

A summary of conventional laboratory analytical techniques is shown in Fig. 6.19. Given that they are widely known, no further explanation is considered necessary in this review

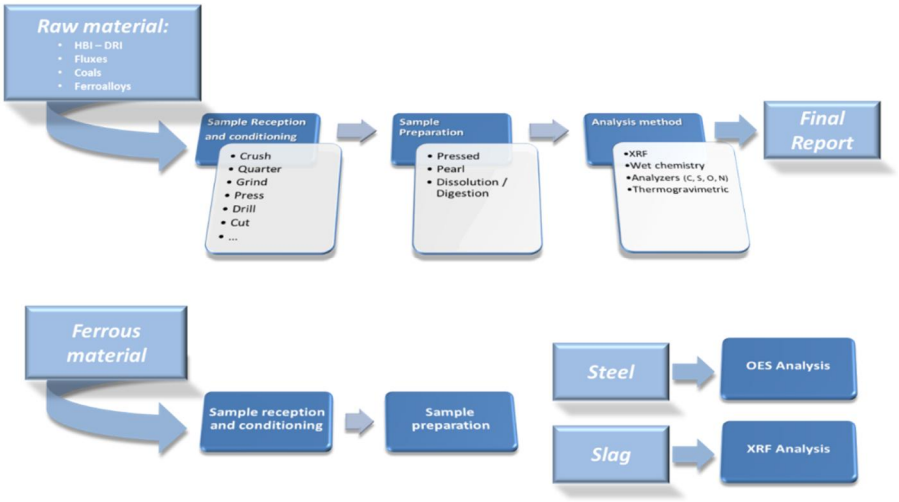

Fig. 6.19: Laboratory analytical Flow (72)

6.5.2 Hyperspectral techniques

Hyperspectral techniques allow obtaining the emission spectrum or reflection of an element remotely. This allows estimating the reflectivity or emissivity of one element in relation to its wavelength. The reflectivity or emissivity depends on several factors, including the chemical composition.

The early developments of this technology focused on wood, plastic and the paper industry, and it was used for material classification purpose and to remove unwanted and easily identifiable materials of the manufacturing process (67) (73). However, when materials to be sorted cannot be identified by classical procedures due to their colour, weight and shape similarities more complicated data processing algorithms are required (74).

In the recycling industry it is also possible to find some developments for industrial inline material sorting which use the spectral imaging technique as classification technique (75). One experimental set up is shown in Fig. 6.20.

Scrap Characterization techniques; State of the art.

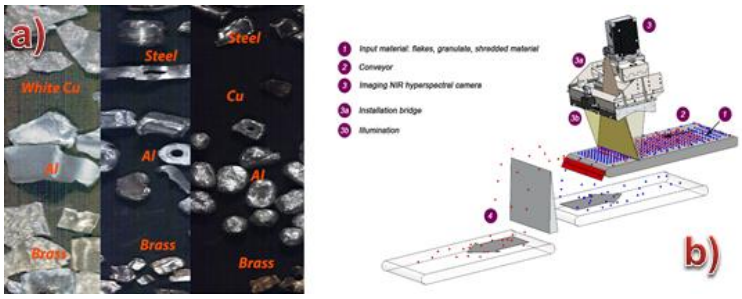

Fig. 6.20: a) Materials used in the experiments; b) Experiment configuration

Besides material sorting, some hyperspectral techniques have also been developed for material characterization. These developments have a direct application in scrap characterization for non-quality definition in terms of slag/sterile contents or rusted surface characterization. Some examples are given below:

- ArcelorMittal Global R&D Basque Country applied for a patent consisting on a new method of determining a chemical composition of a slag portion using hyperspectral techniques (76), which could be useful for sterile content analysis present in ferrous scraps.

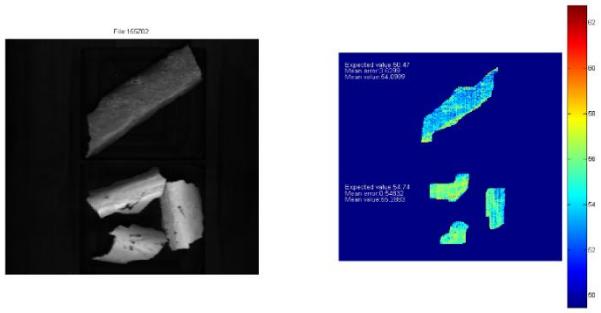

Fig. 6.21: Results of the estimate of the chemical analysis of the samples

- O-chess RFCS project dedicated to the online chemistry of the steel surfaces (77) which could be applied for analysing the scrap corrosion evolution associated with material storage, and therefore, its influence on the scrap quality in the phase prior to its use in the steelmaking process.

However, the use of hyperspectral techniques for scrap classification is still a technology at a very early stage of development and therefore it presents several disadvantages, such as:

- Hyperspectral systems are highly dependent on calibration and very specific signal processing algorithms. Therefore, changes on the used sensor and variations on the light make it impossible to transfer algorithms trained at one plant to another without a new dataset generation for calibration.
- The analytical capacity in the hyperspectral processing is limited to the surface of the analysed material, so it is only useful if scrap is scattered to be analysed on a sampling surface.

Scrap Characterization techniques; State of the art.

- In the current state of the art, scrap pieces with surface coatings (tinned, galvanized, paints ...) are discriminated by the analysis equipment as non-ferrous materials

6.5.3 Gamma ray

Prompt-gamma neutron activation analysis (PGAA) is a very widely applicable technique for determining the presence and amount of many elements simultaneously in samples ranging in size from micrograms to many grams. It is a non-destructive method, and the chemical form and shape of the sample are relatively unimportant.

The technique can be described as follows: the sample is continuously irradiated with a beam of neutrons. The constituent elements of the sample absorb some of these neutrons and emit prompt gamma rays which are measured with a gamma ray spectrometer. The energies of these gamma rays identify the neutron-capturing elements, while the intensities of the peaks at these energies reveal their concentrations. The amount of analyse element is given by the ratio of count rate of the characteristic peak in the sample to the rate in a known mass of the appropriate elemental standard irradiated under the same conditions.

Neutrons are effective probes for matter since they are highly penetrative, are not affected by electromagnetic forces and possess large interaction probabilities with many different elements.

Currently, there is a commercial system for scrap characterization based on PGAA technology. It was developed by Gamma Tech and is capable to measure Cu, Cr, Ni and Mn. This system is equipped in 20 shredders in the USA and in 2 shredders in Europe (78).

However, Neutron analysers developed by Gamma Tech can only be used with scrape grades of small size fragments and cannot be used on sheared scrap which is the major scrap grade purchased.

On the other hand, in steelmaking, there is also a great interest on knowing the scrap composition in other elements such as Mo, Sn, C, Ca, Mg, Al, O,… and these are the reasons why a collaborative project called Scrap Probe and involving Cetto Industries, University of Liverpool, CRM and ArcelorMittal R&D was initiated in 2008 (78).

Scrap Probe project included three main activities:

1 The design of the analyser through modelling and simulation

2 Laboratory developments of the scrap analyser

3 Construction of industrial scale scrap analyser

Scrap Characterization techniques; State of the art.

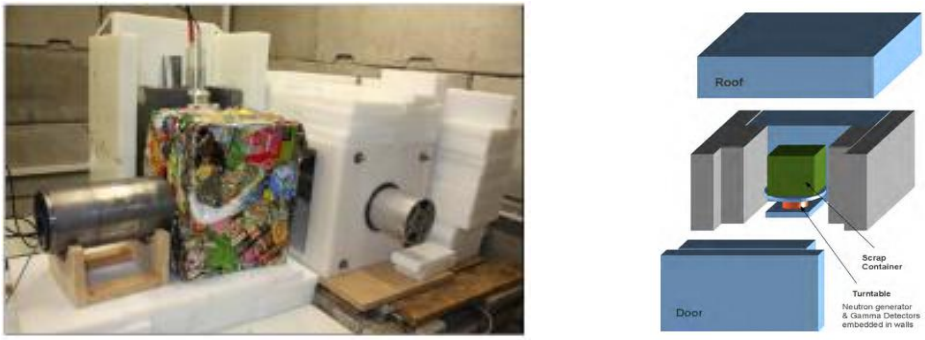

Fig. 6.22: Industrial configuration developed within Scrap Probe project

The main conclusions can be summarized as follows:

- The energy resolution became the crucial parameter in the sensitivity of the analyser, so that depending on the detector used, different detection limits were achieved.
- The kinds of detectors required are very expensive.
- Neutron analysers can only be used with scrap grades of small size fragments and cannot be used on large fragments and heavy scrap deliveries. It should be more effective to get clean scrap deliveries to detect fragments containing copper, using XRF or LIBS, and to remove them mechanically.
- As main advantage, during this project is was proven that the proposed method is one of the few methods currently able to measure in bulk as well as ideally suited for conveyor belts

6.5.4 Laser Induced Breakdown Spectroscopy (LIBS)

Laser-induced breakdown spectroscopy (LIBS) is a type of atomic emission spectroscopy which uses a highly energetic laser pulse as the excitation source. The laser is focused to form a plasma, which atomizes and excites samples. The formation of the plasma only begins when the focused laser achieves a certain threshold for optical breakdown, which generally depends on the environment and the target material.

In principle, LIBS can analyse any matter regardless of its physical state, be it solid, liquid or gas. Due to the fact that all elements emit light of characteristic frequencies when excited to sufficiently high temperatures, LIBS can (in principle) detect all elements, limited only by the power of the laser as well as the sensitivity and wavelength range of the spectrograph and detector. This capability allows LIBS technique to be used as a powerful tool for scrap composition analysis in real time. Probably the most representative developments of the industrial application of LIBS technology to scrap characterization field in steelmaking are two European projects within the European program Research Fund for Coal and Steel:

IPRO (2010 – 2013) project (79) and LCS (2006 – 2009) project (80) aimed to do Inline elemental characterisation of scrap, in EAFs with continuous charging of scrap through a conveying system that connects the scrap yard to the EAF and in crap recycling industry

respectively, for improved EAF charging control and internal scrap recycling. The main output of the proposed system is a guidance of scrap charging operation for EAF in order to stabilize process conditions and optimise internal scrap recycling. Fig. 6.23 shows the experiment configuration used in LCS project.

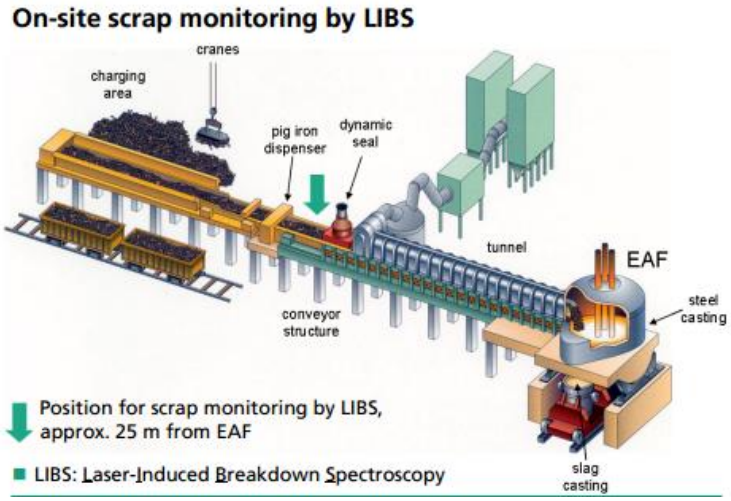

Fig. 6.23: Theoretical configuration of in line system for scrap characterization during continuous scrap charging processes (80)

Fig. 6.24 shows some pictures related to the industrial installation of LIBS system as outcomes of IPRO project.

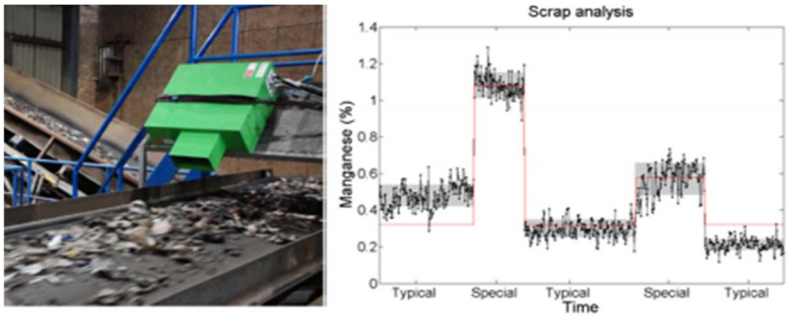

Fig. 6.24: Measurement campaign at Stena Recycling's scrap yards in Sweden (79)

In 2008-2011, in an RFCS (78), CRM (Belgium) tested Prompt Gamma Neutron Activation Analysis (PGNAA) as a potential technique for conducting on-line bulk composition analysis of steel scrap. Within this analysis, and aiming for having a comparative criterion of the results, CRM published some experiment they did using LIBS technique. Fig. 6.25 shows the experimental set up and some results obtained from the data analysis.

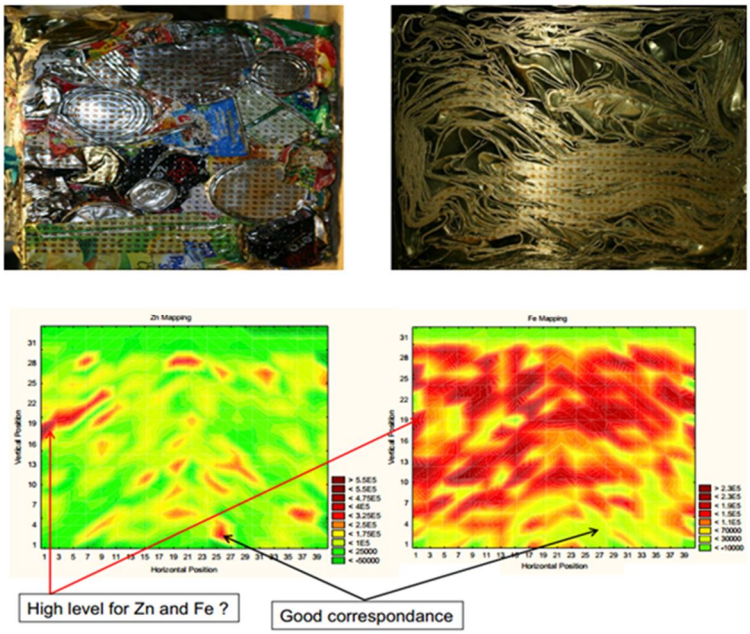

Fig. 6.25: Examples of analyzed bundles

In all cases, the research reached similar conclusions:

- LIBS system is a superficial analysis technique, and it does not seem to be reliable to analyse big pieces of material
- Elements spread unevenly in the scrap charge in the case of conveyor feeding, because of the physical impossibility for the device to scan the whole scrap flow on the current conveyor setup (when the scrap is piled on top of each other).
- It is not possible to analyse bundled scrap, since the inlet part can present large heterogeneities.
- In terms of accuracy, the measuring operation requires time for conducting a good measurement, in the case of highly heterogeneous materials there could be a worsening of the measurement accuracy. On the other hand, there are some materials that are out of measuring range such as plastics, paper or organics

In general, the concept of using laser analysers for inline elemental characterisation of scrap pieces transported on conveyor lines is assessed to be suitable for improved EAF charging. Nevertheless, the industrial implementation of this technique needs to be further investigated.

6.5.5 Portable Analysers

The primary objective of portable instruments is to, either qualitatively or quantitatively, analyse a material on site. In the particular case of scrap characterization, portable versions of these instruments simplify the operation of complex spectrometers into point-and- shoot tools that can be used with minimal training or understanding of the instrument's inner workings.

Scrap Characterization techniques; State of the art.

Portable analysers are becoming important tools for the on-site sorting and identification of scrap in scrap yards. Their analytical accuracy, while not as good as laboratory systems, seems to be more than adequate for sorting mixes and most grade verification requirements.

The most extended portable technologies for scrap metal analysis are Optical emission spectroscopy, X-Ray fluorescence and Laser Induced Breakdown Spectroscopy

6.5.5.1 Optical Emission Spectrometer (OES)

Optical Emission Spectroscopy (OES) is a well trusted and widely used analytical technique used to determine the elemental composition of a broad range of metals. The part of the electromagnetic spectrum which is used by OES includes the visible spectrum and part of the ultraviolet spectrum

Every element emits a series of spectral lines corresponding to the different electron transitions between the different energy levels. Each transition produces a specific optical emission line with a fixed wavelength or energy of radiation.

For a typical metallic sample containing iron, manganese, chromium, nickel, vanadium, etc., each element emits many wavelengths, leading to a line-rich spectrum. For example, iron emits just over 8000 different wavelengths so choosing the optimum emission line for a given element in a sample is important.

The characteristic light emitted by the atoms in the sample is transferred to the optical system where it is split into its spectral wavelengths. Next the individual spectral line peak signals are collected by detectors and processed to generate a spectrum showing the light intensity peaks versus their wavelengths.

The peak wavelength identifies the element, and its peak area or intensity gives an indication of its quantity in the sample. The analyser then uses this information to calculate the sample's elemental composition based on a calibration with certified reference material. The whole process, from pressing a start button or a trigger to getting the analysis results, can be as quick as 3 seconds or it can take up to 30 seconds for a full accurate quantitative analysis, it all depends on the analyser used, the range of elements measured and the concentrations of those elements.

The elements and concentrations that OES analysers can determine depend on the material being tested and the type of analyser used.

Compared to other analytical techniques, OES is fast and relatively easy to use, it measures a wide range of elements and concentrations in many different types of materials and it's fairly low-cost compared to other techniques.

Another important point to highlight is that OES is also currently the only method which can analyse carbon and nitrogen on site, out of the laboratory.

Different element detection thresholds for portable OES are shown inTable 6.1 (similar detection threshold are achieved with LIBS and HHXRF):

	Low allow steel		Stainless steel		Ni steel		Cr steel		Tool steel		Fe-Orientation		Fe Overview	
	Min	Max	Min	Max	Min	Max	Min	Max	Min	Max	Min	Max	Min	Max
Si	0,01	1,6	0,01	2	0,01	0,6	0,01	3,3	0,01	1,5	0,01	3	0,01	3
Mn	0,015	2,5	0,01	11	0,01	1	0,01	12	0,01	2	0,015	13	0,015	13
Cr	0,015	5,5	4	30	0,01	0,6	6	33	0,01	20	0,01	33	0,015	33
Mo	0,005	2	0,005	4,5	0,01	6	0,01	2,4	0,01	11	0,01	11	0,005	11
Ni	0,01	5,5	2	40	10	50	0,01	7	10	7	0,01	50	0,01	50
Al	0,005	1,2	0,01	0,35	0,01	0,3	0,01	0,2	0,01	0,35	0,01	1,2	0,005	12
Co	0,01	1	0,01	1,2	0,01	13	0,01	0,2	0,01	12	0,01	13	0,01	13
Cu	0,005	0,8	0,005	0,5	0,01	0,35	0,01	1	0,05	0,6	0,01	1	0,005	1
Nb	0,01	0,9	0,01	1,1	0,01	0,15	0,01	3	-	-	0,005	3,3	0,005	3,3
Ti	0,01	0,35	0,01	2,3	0,01	1,5	-	-	-	-	0,01	2,3	0,01	2,3
V	0,005	1,5	0,01	0,6	0,01	0,6	0,01	1	0,01	10	0,01	10	0,01	10
W	0,05	1,5	0,01	4	-	-	-	-	0,05	22	0,05	22	0,005	22
Zr	0,01	0,5	-	-	-	-	-	-	-	-	-	-	0,05	0,5
Pb	0,01	0,25	-	-	-	-	-	-	-	-	-	-	0,01	0,25
Sn	0,01	0,2	-	-	-	-	-	-	-	-	-	-	0,01	0,2

Table 6.1: Portable OES detection threshold for different elements (81).

6.5.5.2 X-RAY fluorescence analysers

XRF Fluorescence is a method in which the radiation produced by a miniature X-ray tube strikes the sample surface and causes ionizations of the inner shell of the atoms constituting the sample. The resulting vacancies in the inner shell of the atom are filled by electrons from higher shells and thereby photons specific to the element are emitted and detected with a detector.

XRF analysers allow analysing almost all elements present in metallic materials. The main detecting limitations are light elements (lighter than Mg). These elements have energy levels that are low enough that they struggle to escape from the sample without being absorbed. For the fluorescent x-rays that do escape the sample, some of them will not be able to penetrate the air between the sample and the instrument to reach the detector.

So essentially, light elements are difficult to measure by portable XRF because their fluorescence struggles to reach the instrument and then to calculate how much of that element is present. This also explains why the lightest elements that the instruments measure has higher detection limits, often 0.5-1%, because they need that higher concentration to produce enough energy that can be recognised.

The effective element range and limit of detection (LOD) varies between analysers, depending mainly on tube and detector specification, analyser geometry and with sample matrix composition. Higher abundance of heavier major elements, especially iron, negatively affects trace element detection. The best instruments are now capable of LOD in the 5 to 100 mg/kg range for elements with Z between 19 (K) and 68 (Pb). LOD vary between elements with emission lines and possible interferences. Each instrument has therefore its own specific element range, to be considered before selecting an analyser for a specific application (82).

Other important limitations of this technique are:

Scrap Characterization techniques; State of the art.

- XRF is a surface measurement method in which the penetration depth is less than 50 µm.
- XRF uses radiation. Due to this, some industries may require health and safety control certification or a license to handle such radiation emitting equipment.
- XRF cannot detect carbon

6.5.5.3 Laser Induced Breakdown Spectroscopy

LIBS is an atomic emission technique whereby the instrument's laser fires a series of nanosecond-long pulses through a small focusing lens onto the sample. The focused beam ablates a tiny amount of the sample's surface and subsequently ionizes the removed material to create a plasma. The plasma expands as it is bombarded by the laser and excites electrons in the plasma's constituent atoms. As electrons relax and atoms return to a stable state, they emit photons that are characteristic of the element and electron transitions.

Portables LIBS devices have advantages over portable XRF devices, such as sensitivity to the light elements. Generally, elements from laser induced plasma emit a lot of lines in the UV, VIS or NIR region and provide a possibility to avoid or minimize interference from different spectral lines.

On the other hand, OES and LIBs share similarities on the detection side as both are atomic emission techniques. Where LIBs uses a laser to create the plasma in which the elements are excited, OES uses an arc or spark between an electrode and the sample. Because of this, OES requires a conductive sample and is constrained to metal analysis only, while LIBs spectrometers can be used for other kinds of materials.

Other advantages of portable LIBs devices are the high spatial resolution and the possibility to distinguish between different layers of the sample.

Probably the main important disadvantages are:

- Portable solution is not a mature technology and it presents some limitation for most of the tramp elements (trace levels)
- It can't quantify C at 200-300 ppm
- High LODs for S, P.

Scrap Characterization techniques; State of the art.

For elemental analysis in scrap yards, XRF, OES and latest addition LIBS each have their strengths and limitations.

*** - Excellent	** Good	*Poor

Table 6.2 shows a comparative analysis among different portable techniques:

Portable technique	LIBS	XRF	OES
Have a small, lightweight and portable analyser	***	***	*
Accurately determine the full chemical composition	*	**	***
Analyse penalty and trace element down to <0,1% level	***	**	***
Analyse samples with minimal sample preparation	**	***	*
Bring the analyser to the sample	***	***	*
Have minimum hassle with certifications and approvals	***	*	***
*** - Excellent	** Good	*Poor	

Table 6.2: Comparative analysis among different portable techniques

These portable techniques have numerous advantages:

- There is no need of sampling or surface preparation.
- Quick analytical technique that offers instantaneous results
- It may be considered as non-destructive technique; the measurement will only affect locally the sample.

However, the main limitation of this type of analysis is due to the spot analysis approach, so that only information about metallic elements content in the analysed piece is obtained. In summary, there is no complete characterization of the material (sterile, coatings, quantity of oils ...).

6.6 Industrial interest on scrap characterization methods

In previous chapters, a complete overview of the available techniques for residues recycling were presented. Although understanding size reduction and separation technologies are of high interest for steelmakers, these activities are usually covered by scrap dealers. On contrary, in site material characterization, both ferrous and nonferrous portions, is still a non-solved issue for daily scrap yard operation.

Up to this section, this chapter analyzed the current state of the art in ferrous scrap characterization reported in literature. However, and since this thesis aims to identify technical needs in scrap management operations and to proposed novel solutions for covering potentials steelmaking demands, the literature search done was discussed with 8 different EAF plants (in ArcelorMittal). The results of this survey of interest will be used for defining the next research lines of the current work.

Based on the questioner answers, Fig. 6.26 depicts the degree of plants interest classifying them in Low interest, medium interest and high interest:

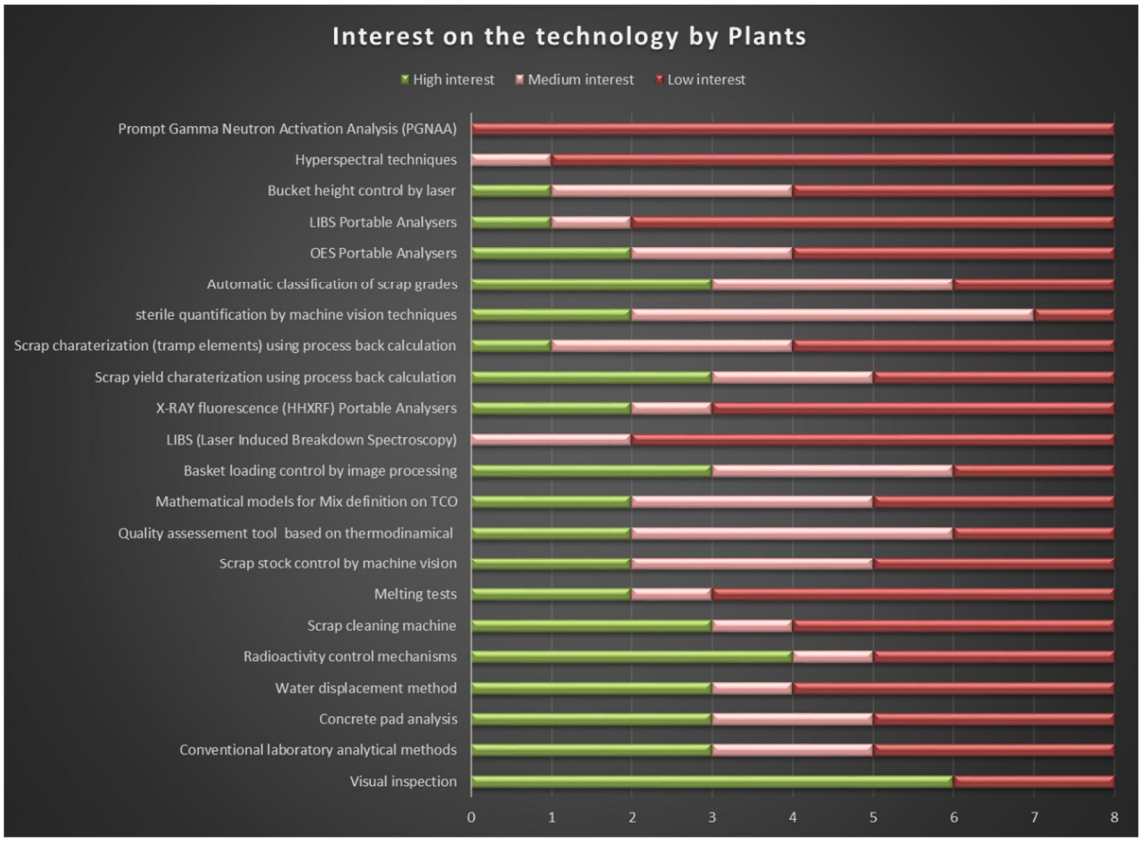

Fig. 6.26:Interets of EAF plants in the different scrap characterization methods

Once the industrial interest on the different technologies is reported by the final user, another criterion that must be considered is the usage degree. The direct comparison between these two concepts allows understanding where there is a gap for proposing new characterizing solutions. The exercise is shown in Fig. 6.27:

Scrap Characterization techniques; State of the art.

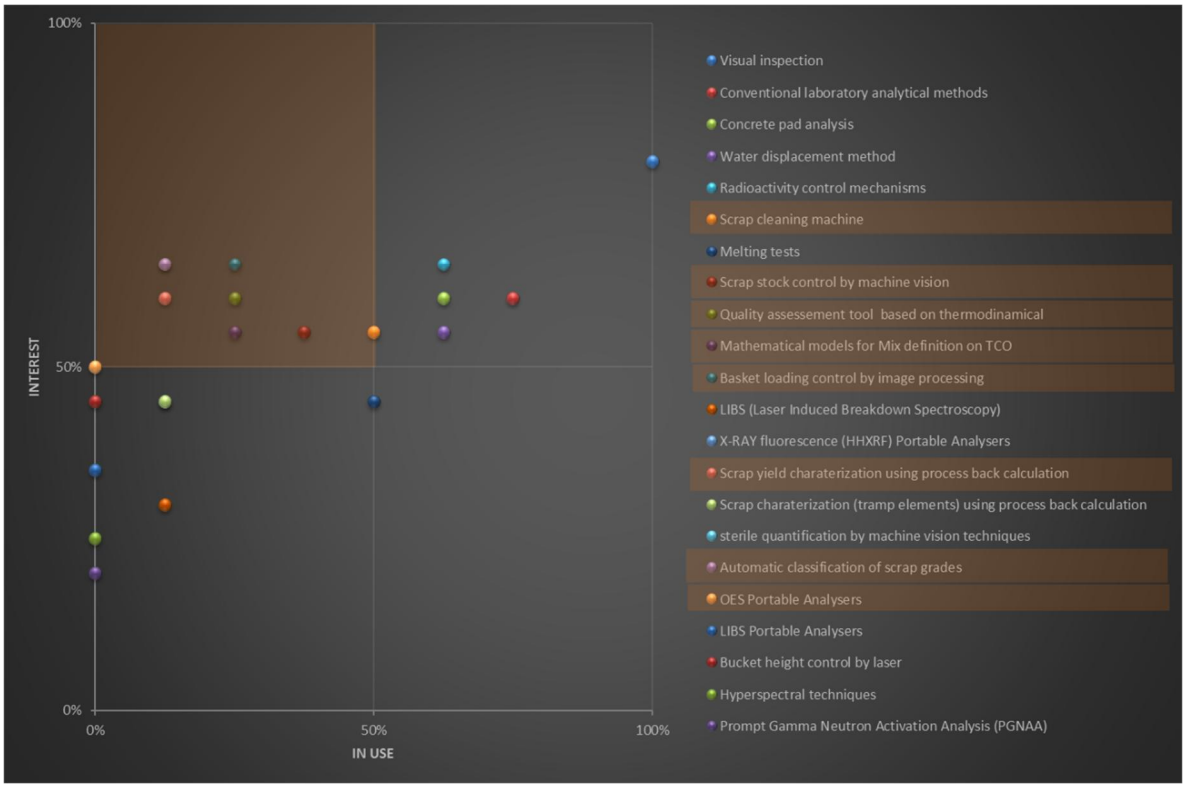

Fig. 6.27: Interest of EAF plants on characterization solution vs. degree of utilization

Looking at the results presented in Fig. 6.27, special attention should be put in low used/high interesting quadrant (in red), which are:

- Scrap Cleaning technologies
- The application of image processing for automatic scrap control
- Methodologies for scrap management optimizing (TCO, purchasing and mix definition)
- Scrap yard automatization – Industry 4.0
- Portable analysers for sterile characterization

6.7 Chapter 6 recall and conclusions

Ferrous scrap products are extremely complex materials since, beside a ferrous matrix composed by Iron and other metallic elements, they are composed by coatings, dirt, sterile, foreign attached materials (plastics, wood, glass) and oxidized layers.

In order to optimize the overall EAF process, it is necessary to have detailed information about the input raw materials. In this sense, the different available technologies currently on application in steelmaking for characterizing ferrous materials, can be grouped in four main categories; Industrial methods, mathematical methods, chemical analyses and physical analyses

This chapter presents the state of the art of the aforementioned characterization methods. The literature survey was also used to discuss with 8 different EAF steelmaker about the current situation of the methods usage and its real industrial interest.

Looking at the questioner's analysis results, the topics of most interests for steelmakers are; Scrap Cleaning technologies, automatic scrap control, methodologies for scrap management optimization and sterile characterization.

The work carried out in this section permitted to assess the novel scrap characterization methods developed in the doctoral thesis:

1. New empirical method for estimating VIU lost due to storage degradation
2. New method for chemical characterization of sterile material in scrap
3. New method for sterile quantification in scrap deliveries.

These methods development work is described in the next chapters

7

New method proposal for estimating VIU lost due to storage degradation.

Due to regular steelmaking scrap yard operative methodologies, EAF ferrous raw materials are purchased in high volumes and can be stored for long period before being used. This chapter proposes a new analytical methodology for estimating how the material degradation due atmospheric corrosion affect to the quality of ferrous materials and the material VIU.

At this point in the document, it seems recurrent to insist that ferrous scrap is the main raw material in steelmaking process by electric arc furnace route, and as such, it represents a high percentage of the total factory manufacturing costs. It makes necessary to dedicate a specific installation in the Steelshop for material management and storing.

The basic purpose of a steel plant scrap yard is to have enough scrap (of each grade used in the furnace) to make the furnace running without any stoppage due to lack of scrap. To this end, several important aspects must be kept in mind:

- The Steel-shop daily scrap consumption in regular operation
- Scrap grades/alternatives to reach final product requirements
- Scrap availabilities in local and global markets
- Scrap delivery time from initial purchase
    - Local:
        - Truck (2 - 7days)
        - Rail (7 -14 days)
        - Barge (7 – 14 days)
    - Remote
        - Rail (14 – 20 days)
        - Barge (14 – 28 days)
        - Vessel (30 – 42 days)

The scrap yard replenishment rate will determine the minimum scrap yard capacity:

- If all scrap deliveries arrive by vessels, the minimum scrap yard capacity would be 6 to 8 weeks of inventory.

New method proposal for estimating VIU lost due to storage degradation.

- If all scrap arrives by truck, the minimum scrap yard capacity would be 7 to 10 days of inventory.

All abovementioned concepts are used to define the general rules for Scrap Yard Layout design at any steel site. This steelmaking general Lay-Out is basically composed by these elements:

- A scrap receiving and inspection station, usually located at entrance.
- Scrap storage area in well-defined piles
- Scrap basket loading location stations

In Fig. 7.1 several examples of steelmaking scrap yard are shown:

Fig. 7.1: Examples of EAF scrap yards

However, once the scrap yard Lay-Out is defined, most of the steel plant managers must focus on maximizing the economic profitability of the overall facility. Probably, the most extended practice is to use the scrap yard as a scrap storing facility; purchasing high volumes of scrap when the market price is low and consume the stored materials when the market prices are high.

This strategic procedure for scrap management presents one drawback that is not usually considered by steelmakers; the material quality degradation due to long storing period by atmospheric corrosion

This chapter proposes an analytical procedure for obtaining empirical equations which allow estimating the cost worsening of ferrous material due to the degradation produced by the atmospheric corrosion.

7.1 Atmospheric corrosion

Metallic atmospheric corrosion may be considered as a type of corrosion resulting from the interaction between a metallic material and the natural atmosphere. Generally, it can be understood as the general tendency of metallic materials to look for their most stable form (lower internal energy state).

Atmospheric corrosion can be classified into three categories (83);

- Dry: In the absence of moisture, many metals corrode very slowly at room temperature. Accelerated corrosion under dry conditions is achieved at high temperatures and generally occurs on metals which have a negative free energy of oxide formation and then rapidly form a thermodynamically stable film in the presence of oxygen.
- Damp: This type of corrosion requires the presence of moisture in the atmosphere and its aggressiveness increases with the moisture content. When moisture exceeds a critical value (which is about 70% in terms of relative humidity), an invisible thin film of moisture is formed on the surface of the metal, providing an electrolyte to transfer current. The critical value depends strongly on surface conditions such as cleanliness conditions, corrosion products produced or the presence of hydroscopic contaminants (which can absorb water in very low relative humidity).
- Wet: It occurs when water droplets or visible water films are formed on the surface of the metal due to sea breeze, rain or dewdrops.

These corrosion processes have been reviewed and analysed in detail in the past and several mathematical models have been developed to predict the corrosion damage of metals in the atmosphere (84) (85) (86) (87). (88) These activities are related to the durability analysis metallic structures, mainly for determining the economic costs associated with this degradation phenomenon. However, in the scope of this research, the analysis of the atmospheric corrosion on metallic materials has the only purpose of assessing the cost of the loss of quality in the scrap induced by the degradation of the material subject to atmospheric corrosion.

7.1.1 General mechanism of atmospheric corrosion

A fundamental requirement for electrochemical corrosion processes is the presence of an electrolyte. Thin-film "invisible" electrolytes tend to form on metallic surfaces under atmospheric exposure conditions, after a certain critical humidity level is reached. In the case of a completely uncontaminated atmosphere, at a constant temperature, a perfectly clean metal surface would not be expected to undergo corrosion damage at a relative humidity below 100%. However, in practice, due to the presence of hygroscopic surface species, impurities in the atmosphere and small temperature gradients between the atmosphere and

metallic surfaces, a microscopic surface electrolyte tends to form at significantly lower humidity levels. The critical humidity level is not constant (70% can be used as reference). It depends on the corroding material, the tendency of corrosion products and surface deposits to absorb moisture and the presence of atmospheric pollutants.

In the presence of thin-film electrolytes, atmospheric corrosion occurs by balancing anodic and cathodic reactions. The anodic oxidation reaction involves the dissolution of the metal, while the cathodic reaction is often assumed to be the oxygen reduction reaction. These reactions are illustrated schematically in Fig. 7.2. It should be noted that corrosive contaminant concentrations can reach relatively high values in thin electrolyte films, especially under conditions of alternate wetting and drying. Oxygen from the atmosphere is also readily supplied to the electrolyte, under thin-film corrosion conditions.

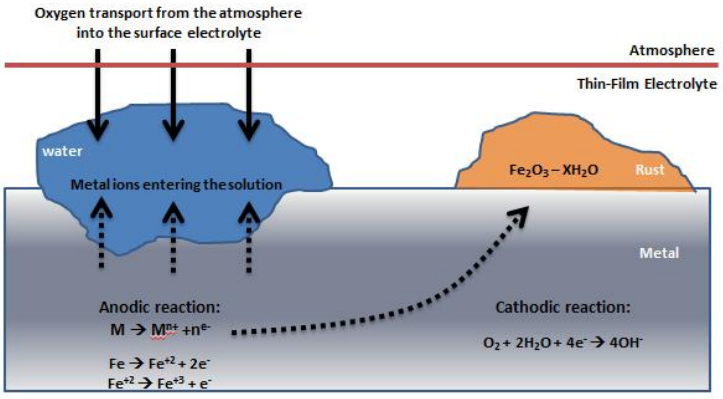

Fig. 7.2: Simplified mechanism of atmospheric corrosion (89)

However, it is important to note that the corrosion process is a discontinuous process and the intensity of the corrosive phenomenon is strongly dependent on the duration of electrolyte film presence on the surface of the metallic material.

7.1.2 Factors of influence in the severity of atmospheric corrosion

Through the numerous studies carried out both in laboratory and in field conditions, the most relevant factors that cause corrosion have been identified and classified (83). The two most important ones are meteorological conditions and pollution. These two factors determine the intensity and nature of corrosive processes.

Other factors such as metal composition and properties of the oxide formed are also important. However, exposure conditions represent the most important factor regarding meteorological corrosion. The main factors of influence are listed below:

Wetting time:

The most important atmospheric characteristic directly related to the corrosion process is humidity, since it is the origin of the electrolyte needed in the electrochemical process.

The time in which the electrolyte is present is called wetting time. The wetting time determines the duration of the electrochemical process. The thickness and chemical composition of the water film are important. Fig. 7.3 shows the relationship between atmospheric corrosion and the thickness of the electrolyte layer on the metal surface.

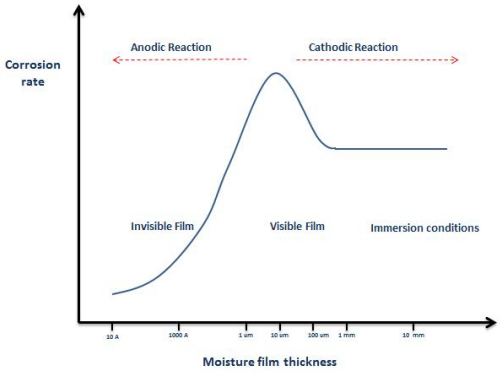

Fig. 7.3: Relationship between electrolyte film and corrosion rate (90)

The diffusion of oxygen through the thin-film of electrolyte is usually the controlling factor of the corrosion rate. The corrosion rate increases with the aqueous layer and reaches its maximum value at intermediate thicknesses.

The clustering of individual water droplets to produce relatively thick layers of electrolyte reduces the corrosion rate by reducing the oxygen diffusion process.

Likewise, an excessive reduction in the thickness of the moisture layer slows down the corrosion effect due to the high ohmic resistance of the extremely thin films and the inhibition of the ionization and dissolution reactions of the metal. Therefore, the climatic variations in non-rainy periods have a great influence on the corrosion rate. These aspects are depicted in Fig. 7.4:

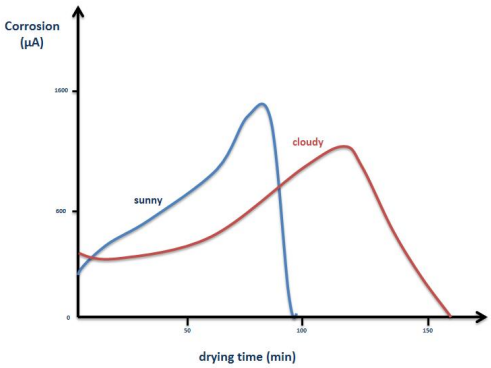

Fig. 7.4: Variation of the corrosion rate during the drying cycle after rainfall (84)

The wetting time as defined in ISO 9223 “Corrosion in metals and alloys” does not cover all aspects of climate. The wetting time can be estimated by determining the number of hours in a given time interval, when the relative humidity (RH) exceeds 80% and the temperature exceeds 0ºC. Its estimation is based on the characteristics of the atmosphere humidity and has nothing to do with the level of pollutant and the nature of the metallic materials.

New method proposal for estimating VIU lost due to storage degradation.

Relative humidity of air:

The relative humidity of the air determines the percentage of moisture from which the condensation phenomenon (necessary for the formation of an electrolyte film on the metal surface) will occur.

This condensation theoretically occurs at relative humidity of 100%. However, under certain conditions, it can occur at lower humidity levels.

This may particularly occur when the temperature of the metal is lower than the air temperature, when the surface is porous (caused by the surface tension phenomenon, which decreases the saturation pressure within the pore), or when the surface contains deposits of some hydroscopic contaminants.

Temperature:

The effects of temperature in the corrosion rate are twofold. On one hand, as the temperature rises, the rate of electrochemical reactions increases. On the other hand, as the temperature increases, the evaporation of water on the metal is accelerated and the concentration of oxygen and other corrosive gases dissolved in the metal decreases.

Usually, the corrosion of a metal in contact with a large volume of liquid increases with temperature. This effect is produced due to the fact that the diffusion coefficient of many substances in aqueous solution increases with temperature since the diffusion layer lowered by the effect of the evaporation. Therefore, even though the solubility of oxygen decreases with temperature, the rate of corrosion of processes controlled by the cathodic reduction of this gas is multiplied several times before reaching a maximum.

Winds:

The direction and speed of the wind have a great influence on the atmospheric corrosion rate. Wind carries pollutants, which settle on metals and directly influence the measured corrosion figures.

Pollution effect

The main pollutants contained in the atmosphere are sulphur dioxide (SO_2), different nitrogen oxides (NO_x), chlorates and solid particles that are deposited on the metal surface. From the corrosion point of view, chlorates (mainly present in marine regions) and SO_2 (from burning fossil fuels, such as coal from volcanic activity) are the most important species

7.1.3 Atmospheric corrosion in steelmaking

The analysis of atmospheric corrosion on metallic materials within steelmaking scrap yards has the only purpose of assessing the cost of scrap non-quality induced by the degradation of the material subject to atmospheric corrosion. The evolution of corrosion in ferrous materials

New method proposal for estimating VIU lost due to storage degradation.

results in loss of metallic yield, increase of slag generation and worsening of the main specific consumption of the process.

In this section several real examples of corrosion effects on steelmaking raw materials are shown.

Hot Briquetted Iron (HBI):

Hot Briquetted Iron is the product of reducing iron ore with natural gas. The direct reduction process is a complex process, which, explained in simple terms, consists of the following steps:

- Raw material: Iron ore pellets are fed into the reactor
- Natural gas is converted into reducing gas and then injected in a closed system
- The direct reduction process occurs: Hot reducing gas flows through the iron ore, from the bottom to the top (according to the counterflow principle). The Oxygen content is reduced, producing the "sponge iron", which is pressed into briquettes

Direct reduction processes associated with hot briquetting can be grouped as follow:

- Gas based reduction of pellet and lump ore. These processes include mainly Midrex, Hyl and Purofer
- Gas based fine ore reduction, which includes Fior, Finmet and Circored
- Coal based reduction, which includes Fastmet or Iron dynamics

These direct reduction processes generated HBI material with well bounded chemical characteristics. Table 7.1 shows an example of it.

	Min.	Max.
Metallization	92%	
Fe (Total)	88%	94%
Fe (Metallic)	83%	90%
C	0.5%	1.6%
S	0.001%	0.03%
P2O5	0.005%	0.09%
Gangue	4%	9%
Size (typical)	(90x48x32) mm	(140x58x34) mm
Fines	-	5%
Apparent Density	5 t/m^3	
Buck Density	2.5 t/m^3	3.3 t/m^3

Table 7.1: Example of typical HBI general characteristics (91)

Since the HBI production technology is known, when purchasing, the final consumer has a clear idea of the expected material chemical composition. In spite of that, there is usually a double check of this information by spot sampling analysis in both, supplier site and consumer site.

New method proposal for estimating VIU lost due to storage degradation.

However, due to high lead times of this product material (more than 2 months in most cases), the steelmakers that systematically use this material, tend to acquire HBI in large quantities. And so that, HBI might be stored for months in the scrap yard (in most cases outdoors)

Fig. 7.5 shows the state of two different pieces of HBI from the same delivery subject to different storage times:

Fig. 7.5: HBI specimen with different atmospheric exposure times

The visual inspection of these images leads to the following conclusions; The two samples are not visually the same any more. However, from a TCO approach point of view, the steel mill is still considering them as the same materials when defining the scrap MIX, since there is no method available to quantify the worsening of quality with time.

Direct Reduced Iron (DRI):

Direct reduction of iron is the removal of oxygen from iron ore or other iron bearing materials in the solid state, i.e. without melting, as in the blast furnace. The reducing agents are carbon monoxide and hydrogen, coming from reformed natural gas, syngas or coal. Iron ore is used mostly in pellet and/or lumpy form.

There are several processes for direct reduction of iron ore:

- Gas-based shaft furnace processes (Midrex® and Energiron being the main ones). This process accounts for about 80% of total production
- Coal based rotary kiln furnaces (mainly in India) - accounting for around 20% of total production.

	Min.	Max.
Metallization	92%	96%
Fe (Total)	86%	94%
Fe (Metallic)	81%	88%
C	1%	4.5%
S	0.001%	0.03%
P2O5	0.005%	0.09%
Gangue	4%	9%
Size (typical)	4 mm	20 mm
Apparent Density	3.4 t/m^3	3.6 t/m
Buck Density	1.6 t/m^3	1.9 t/m^3

Table 7.2: Example of typical DRI general characteristics (91)

New method proposal for estimating VIU lost due to storage degradation.

From the storage point of view, DRI suffers a similar process as HBI. In this case, the storage period is usually much lower and the DRI is carefully protected from exposure to the weather due to its high self-combustion risk in the presence of moisture.

DRI is highly susceptible to oxidation and rusting when stored unprotected

As explained in section 6.3.1.1, a regular operation performed by some steelmakers for characterizing scrap is the systematic linear regression analysis of the furnace performance with respect to the Ferrous input materials in daily basis, in order to estimate, for each scrap grade, the metallic yield and specific energy requirements associated to this material.

Fig. 7.6 and Fig. 7.7 show the data obtained for DRI using the mentioned methodology from May 2011 to October 2011 in one specific ArcelorMittal site.

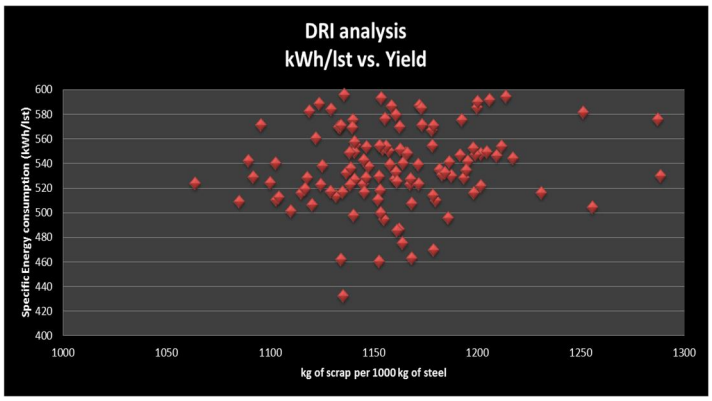

Fig. 7.6: Metallic yield vs. specific Energy data calculated for DRI based on EAF performance

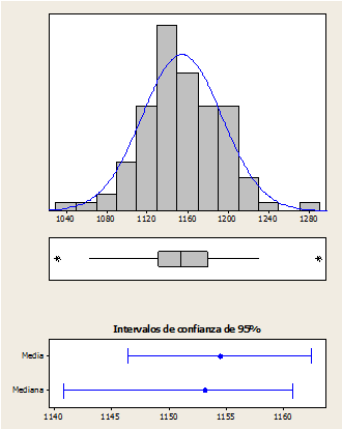

- Number of samples: 95
- Mean: 1154,4
- Standard deviation: 39,2
- Variance: 1536,6
- Bias: 0,08363
- Kurtosis: 1,16661

Fig. 7.7: DRI Metallic yield statistical data from EAF performance

Attention is drawn to the fact that, although DRI came from the same supplier through the whole period, the behaviour of the material was very unpredictable. This variability seems to be associated with the effect of environmental oxidation.

Other Ferrous materials:

Same that happens with the HBI or DRI, also occurs with the other ferrous scrap. References of a research activity has been found in ArcelorMittal, which analysed the evolution of

New method proposal for estimating VIU lost due to storage degradation.

incinerated shredded scrap quality as well as the impact of temporally outside storage period in its value in use.

According these reports, as it is shown in Fig. 7.8, 1 tonne of incinerated shredded scrap (E46) was sampled directly at the output of the shredded producing incinerated shredded scrap in 2009. This sample was then divided into 2 homogenous subsamples: the first one was directly melted in a 300 kg induction furnace in ArcelorMittal and the second one was stored outside in an opened basket, weighted every week and then melted in the induction furnace three months later.

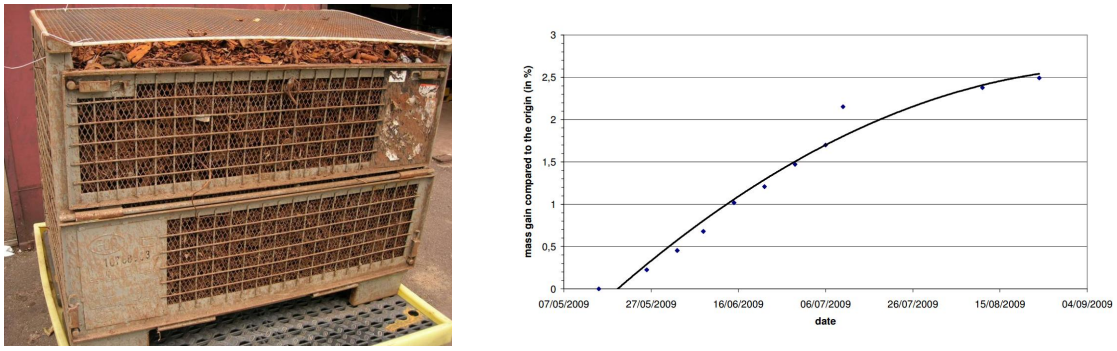

Fig. 7.8: E46 scrap analysis: Left) E46 stored in an opened basket and Right) Mass evolution in the sample stored outside for 3 months (in %)

After the characterization of the two scrap samples ("fresh" and "aged") through melting tests analyses, their thermodynamic value in used were calculated (using as reference pure iron cost in July 2009). It showed that the "aged" scrap VIU was 10.1 €/t less than "fresh" scrap.

This experiment confirms that it is really important to avoid long storing period to the outdoors.

The atmospheric degradation effect observed for observed for HBI and DRI also occurs with other scrap materials like E46. Demonstrating that atmospheric corrosion has an important impact on the VIU of the steelmaking materials. This is where the need to work on designing new methods to assess the worsening of quality for different types of ferrous scrap arises.

7.2 Experimental Set up for assessing the influence of atmospheric corrosion in steelmaking raw materials

The simplest form of direct atmospheric corrosion measurement is by specimen exposures. Subsequent to the exposure, the specimens can be subject to weight loss measurements, pit density and depth measurements, and also visual and microscopic examination for evaluation purposes.

The analytical method proposed in this section consists of the empirical analysis of the degradation by corrosion that certain materials present when exposed to weather conditions, in order to associate it with the additional costs that this degradation generates (Value In Use approach).

7.2.1 Specimens selection

The most widespread way of classifying the different grades of scrap within the scrap yard is based on its content in tramp elements (Cu, Sn, Ni). The final content in these elements in steel is one of the main constraints when deciding the scrap mixture, even more important than price.

Based on this criterion, scrap can be classified into 3 large groups:

- Low residual scrap
- High residual scrap
- Pre-reduced iron

Keeping in mind this classification criteria, and for the analysis proposed in this section, It have been selected as materials to be tested, one type of scrap for each of the three defined groups; Busheling (E8) as low residual scrap, Shredder (E40) as high residual scrap and Hot Briquetted Iron (HBI) as pre-reduced iron. Fig. 7.9 shows the selected specimens.

Fig. 7.9: Selected specimens. Left) Busheling scrap (E8), middle) Shredder scrap (E40) and right) HBI samples

7.2.2 Exposure of the specimens

The selection of the exposure location of the specimens is an important aspect to consider and it should be defined mainly by considering three factors;

Location: In order to simulate the natural degradation process of storing the material outdoors, the exposure location selected corresponds with the scrap yard of a real Steelshop in Spain close to the sea. However, and since exposure to marine and windy environments is one of the factors that accelerates the oxidation process, the selected location aimed to protect the samples from a direct exposure to these factors. Fig. 7.10 indicates the experiment location detail.

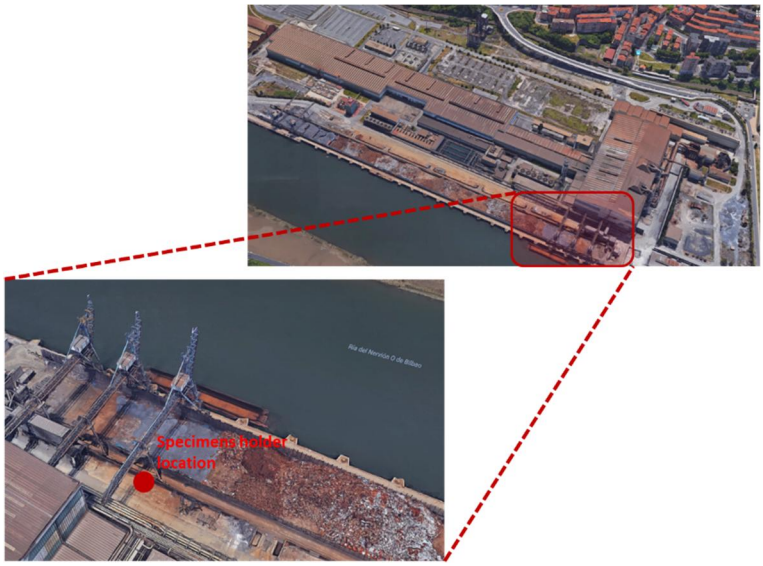

Fig. 7.10: Tests site location in ArcelorMittal Sestao factory (Spain)

Exposure configuration: Particular attention should be paid to the way in which the specimens are exposed to atmospheric conditions, ensuring that there is no accumulation of water or other elements after long periods of exposure. To do so, a specific exhibition panel was built for this experiment whose design is shown in the following figure.

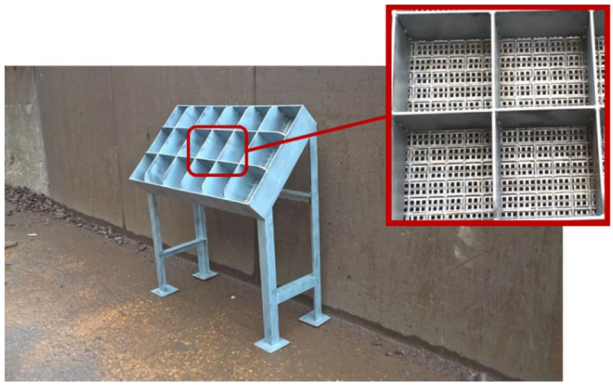

Fig. 7.11: Dedicated holder for the experiment

New method proposal for estimating VIU lost due to storage degradation.

Sample exposure time: In order to analyse the evolution of corrosion phenomena along time for a specific location, some samples from the same scrap delivery for the selected scrap types were exposed to the weather, part of these specimens were progressively recovered and analysed at the laboratory after 1 month, 2 months, 3 months, 6 months, 9 months and one year of exposition. Fig. 14 show the experimental setup.

Fig. 7.12: Exposure set up

7.2.3 Laboratory resources for Specimens analysis

Before any analysis, it was defined the characterization protocol considering the following:

- Weight loss was determined by measuring the difference of weight before and after the exposure time.
- Oxidation layer thickness evolution was determine analysing the samples in an optical microscope.

The available laboratory equipment for this end is listed below:

- PG5001 balance by METTLER TOLEDO, whose main characteristics are listed in the following figure:

Readability:	0,1 g
Maximum Capacity:	5100 g
Taring range:	0-5100g
Repeatability (s):	0,08g
Linearity:	+/- 0,1g
Stabilization time:	1-2 s
Sensibility: - Tª drift - Long-term drift	 +/- 10 ppm/ºC +/-0,007%
Weighing pan:	240x240mm

Table 7.3: PG5001 balance description

- LEICA MEF4M Widefield Inverted Metallograph, whose main characteristics are listed below:

Equipment Details:	
List of Equipment:Brightfield, Darkfield, Polarized Light, Polarization Contrast, Differential Interference Contrast, Interferometry, Video port, PC	
Objectives:	
Plan Fluor:	2.5x/0.075 (∞/-)
Plan Fluor LWD:	5x/0.10 Epi (∞/0)
Plan Fluor LWD:	10x/0.20 Epi lK (∞/0)
Plan Fluor XLWD:	20x/0.40 Epi lK (∞/0)
Plan Fluor:	50x/0.80 Epi lK (∞/0)
Plan Apo:	150x/1.25 W lK (∞/0)

Table 7.4: LEICA MEF4M microscope

- Buehler Simplimet 2000 metallurgical mounting press for the encapsulation of metallographic samples.

Mould size:	25 mm
Operating mode:	Automatic
Type of resins:	Thermosetting Thermoplastic
Dry air requirement:	5,5 – 6 bar
Cooling water requirements:	2 l/min 1 - 2 bar

Table 7.5: System for Encapsulation of metallographic samples details

- Wet chemistry lab for conducting the chemical analysis

Fig. 7.13: Wet chemistry Laboratory

7.3 New method for assessing atmospheric corrosion penalties in steelmaking raw materials

Section 7.2.1 described the selected specimens for the proposed research activity, using as main selection criteria their content in residual elements:

- Low residual scrap: Busheling scrap (E6 – according European scrap specification)
- High residual scrap: Shredded scrap (E40 – according European scrap specification)
- Pre-reduced iron: HBI

Once selected, the specimens were characterized in laboratory and exposed to atmospheric conditions according the set up described in section 7.2.2. Then, different fractions of each selected material were recovered periodically along one year of exposition and the degradation was measured. To ensure the coherency on results this analysis was done twice; in 2017 and 2018.

On the other hand, and since the most important factors influencing material degradation due to atmospheric corrosion process are related to humidity and temperature, it is important to monitorize these two factors along the experimental period to establish the experimental references. In Fig. 7.14 and Fig. 7.15 the daily average temperature and rain data during the experimental periods are depicted. These meteorological data were obtained from meteorological station that the State Meteorological Agency in Spain (AEMET) (92) has at Bilbao airport (the closest official meteorological station to the site)

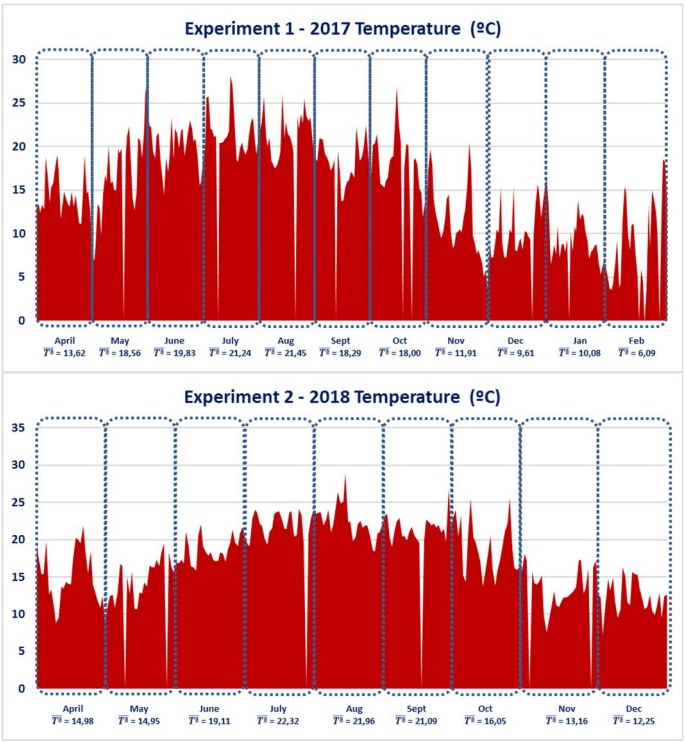

Fig. 7.14: Annual temperature evolution during experiment 1 (2017) and experiment 2 (2018)

New method proposal for estimating VIU lost due to storage degradation.

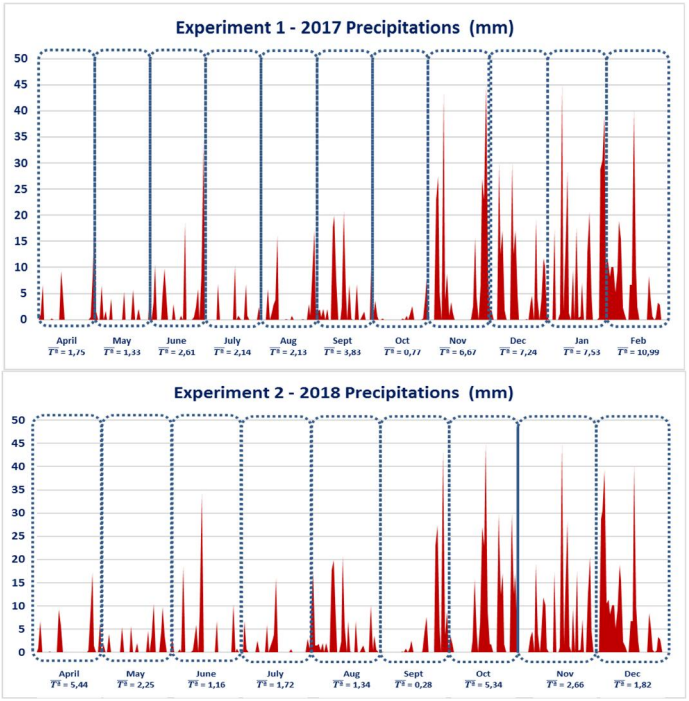

Fig. 7.15: Annual raining rate evolution during experiment 1 (2017) and experiment 2 (2018)

According the information presented in Fig. 7.14 and Fig. 7.15, the average annual temperature values were 15,3ºC (2017) and 17,6ºC (2018), and the average annual raining ratio values were 4,1 mm (2017) and 2,5 mm (2018).

New method proposal for estimating VIU lost due to storage degradation.

7.3.1 Hot Briquetted Iron (HBI)

This section focuses on Hot Briquetted Iron (HBI). The motivation for this lies on that, HBI production technologies are well-known and the variability on HBI composition is low. For each purchasing order, the steelmaker has a precise quantification of the raw material chemical composition although, there is usually a double check of this information by spot sampling analysis in both, supplier and consumer sites.

However, due to the high lead times of this material deliveries (more than 2 months in most cases), the steelmakers, tend to acquire HBI in large quantities (thousands of tons per order). And so that, HBI can be stored for months in the scrap yard (in most cases outdoors). This large storing period produces progressive degradation of the material, worsening its VIU.

As shown in Fig. 7.5, a very basic visual analysis of these HBI samples clearly shows that the two samples (before and after long storing periods) present different chemical and physical properties. However, current TCO methods does not take into account their degradation and still consider their VIU and properties equal to the VIU that was calculated when defining the scrap mixture. Currently, there is no other method to estimate the VIU degradation as a function of time. The motivation of this work is to develop a novel methodology for easily recalculating the VIU of HBI material in relation with the storing periods in the steelmakers scrap yards.

The analytical method proposed is based on the empirical analysis of the degradation by corrosion that HBI presents when exposed to weather conditions. In order to measure how atmospheric corrosion affects to the additional costs associated to this degradation (VIU approach), several pieces of material coming from the same deliver were selected and exposed to atmospheric conditions. Then by measuring the chemical evolution for different exposure period, the selected VIU methodology is used for obtaining generalized equation for measuring the material cost penalties induced by atmospheric exposure.

7.3.1.1 Laboratory methodology for material Chemical control

Wet chemistry analysis for HBI scrap was used for obtaining the chemical composition of the main iron compounds in samples as established quality criteria for HBI and DRI materials (Total iron, Metallic iron, % FeO in sample and % Fe_2O_3). The laboratory protocol was followed according the normalized methodology proposed by the Basque Country Association of iron and steel chemical analyses (72) and described below:

- **Total Fe:**
    - 0.5 g of sample is weighed
    - Addition of 50 ml of concentrated HCl
    - Slow heating until the total attack occurs

New method proposal for estimating VIU lost due to storage degradation.

- Addition of 6-8 drops of concentrated FH
- Heat up to dryness
- Cooling down
- Addition of 20 ml of concentrated HCl
- Boiling until having 10 ml
- Cooling down
- Reduction with Stannous Chloride
- Addition of 200 ml of H_2O (cold)
- Addition of 10 ml of Mercury Chloride
- Addition of 30 ml of Sulphophosphoric solution and a few drops of Diphenyl Amino Sodium Sulfonate
- Assessment with $Cr_2O_7K_2$ until violet coloration
- Calculous and results expression:

$$\% \text{ Fe} = \text{Solution expenditure (cc)} \times \text{f of solution} \quad \textbf{(7.1)}$$

- **Metallic Fe:**
  - 0.5 g of sample is weighed
  - Addition of 5 g of Cl_2Hg and 0.5 g of Ammonium Citrate
  - Addition of 50 ml of hot water
  - Boiling for 2 minutes to attack only metallic Fe
  - Filtering of Fe oxide
  - Solution Washing
  - Calcination at low temperature (650 ° C)
  - Same procedure followed for Total Fe calculation
  - Calculous and result expression:

$$\% \text{ Fe } (FeO + Fe_2O_3) = \text{Solution expenditure (cc)} \times \text{f of solution} \quad \textbf{(7.2)}$$

- **FeO and Fe_2O_3:**
  - 0.5 g of sample is weighed
  - Addition of 40 ml of concentrated HCl and 0.5 g of Co_3Na_2
  - Heat up to dryness
  - Cooling down

New method proposal for estimating VIU lost due to storage degradation.

- Addition of 50 ml of carbonated water, 30 ml of sulfophosphoric and 1 ml of indicator
- Assessment with $Cr_2O_7K_2$ until violet coloration
- Calculous and results expression:

% FeO = (Solution expenditure (cc) x f of solution x 0,9) / 0.7 **(7.3)**

Wet chemistry results over HBI samples on Fe contents were:

Sample ID	Collecting Date.	Fe_{Total}	$Fe_{Metallic}$	FeO	Fe_2O_3
Experiment 1	22/03/2019	90,25	85,72	5,17	0,72
Experiment 2	04/04/2018	90,97	80,18	13,54	0,36

Table 7.6: Initial HBI chemical composition for experiment 1 and experiment 2

7.3.1.2 Experimental results over HBI samples

The exposed specimens to the outdoor environmental conditions as shown in Fig. 7.10 and Fig. 7.12 were progressively recovered from the expositing holder after 1 month, 2 months, 3 months, 6 months, 9 months and one year of exposition. After recovery, they were analysed at the laboratory. This procedure was repeated twice (in 2017 and 2018) to confirm the coherence of the results. Progressive degradation due to corrosion, due to environmental exposure, is clearly seen in Fig. 7.16:

Fig. 7.16: Visual appearance after different exposure periods of samples in experiment 1

It was assumed that corrosion effect over the chemical composition HBI is only linked to the iron oxides based compounds, but not alteration on the rest of component are expected (CaO,

New method proposal for estimating VIU lost due to storage degradation.

SiO_2, MgO, Al_2O_3, or C. The experimental results (Total iron, Metallic iron, % FeO and % Fe_2O_3) after analysing the exposed samples are showed in Fig. 7.17:

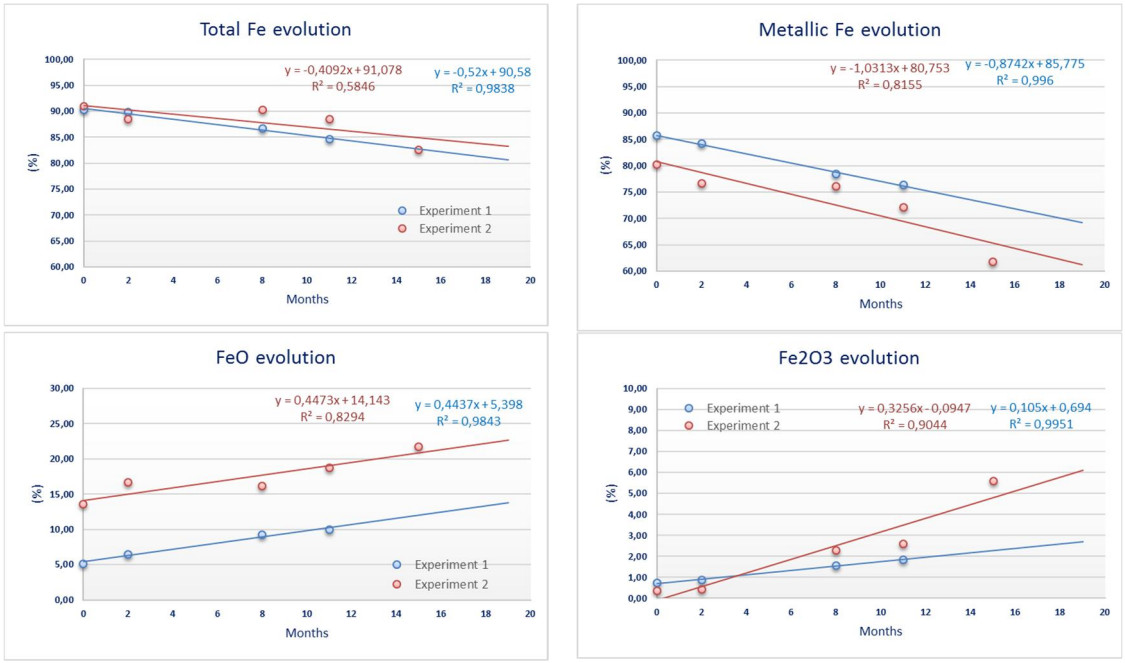

Fig. 7.17: Iron based compounds evolution in HBI samples along 1 year of exposure. Two experiments (2017,2018) are shown.

Since the initial chemical composition is highly variable and strongly depends on the HBI supplier, the material production process and the manipulation procedures from material manufacturing processes to its consumption, we normalize the initial chemical composition data for allowing direct comparison among different deliveries. Next picture shows the chemical evolution after normalization:

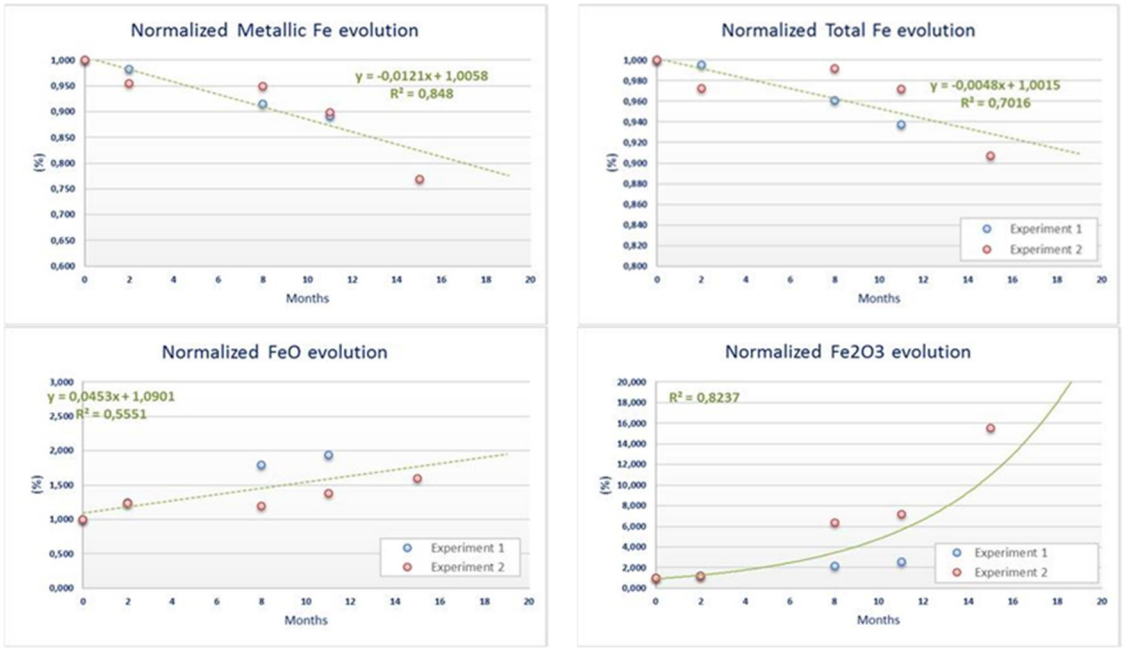

Fig. 7.18: **Normalized data for iron-based compound evolution in HBI samples along 1 year of exposure**

New method proposal for estimating VIU lost due to storage degradation.

The evolution of the Fe, FeO and Fe_2O_3 is then fitted based on the normalized data. The metallic Iron shows a linear decrease, while the FeO percentage in samples increases linearly. For Fe_2O_3 case, the composition evolution shows an exponential increase with exposure time.

Three different models are adjusted for the three components and general degradation equations of the mentioned components are extracted:

$$Fe^{f}_{Total} = (-0{,}0048\ t \cdot Fe^{i}_{Total}) + Fe^{i}_{Total} \quad (R^2=0{,}7016) \tag{7.4}$$

$$Fe^{f}_{Metallical} = (-0{,}0121\ t \cdot Fe^{i}_{Metallic}) + Fe^{i}_{Metallic} \quad (R^2=0{,}8480) \tag{7.5}$$

$$FeO^{f} = (0{,}0453\ t \cdot FeO^{i}) + FeO^{i} \quad (R^2=0{,}5551) \tag{7.6}$$

$$Fe2O3^{f} = \frac{Fe2O3^{i}}{0{,}9121 \cdot e^{0{,}1659t}} + Fe2O3^{i} \quad (R^2=0{,}8237) \tag{7.7}$$

Where:

- Fe_{Total}, $Fe_{Metallic}$, FeO and Fe_2O_3 are the total % in those compounds in HBI sample
- ***i*** represents the initial value of the analysed compound
- ***f*** represents the final value of the analysed compound
- ***t*** represents the exposure time in months

Equations (7.4), (7.5), (7.6) and (7.7) allow estimating the HBI chemical composition evolution taking into consideration the degradation process caused by the storage period from a known chemical composition (conventional wet chemistry analysis in lab) when the material is delivered to the scrap yard.

These calculated current HBI composition due to degradation allow determining the penalties over the Value-In-Use motivated for the storage of the material along time. The general equation aforementioned can be used for estimating the evolution of chemical composition of HBI -

	Fe+t.e. (%)	C (%)	Acid gangue (%SiO_2+%Al_2O_3)	Basic Gangue (Cao+MgO)	Oxygen on Fe
HBI – i	90,25	0,8	5	1,16	2,76
+1 Month	89,77	0,8	5	1,16	4,88
+2 Month	89,29	0,8	5	1,16	7,02
+3 Month	88,81	0,8	5	1,16	9,17
+4 Month	88,33	0,8	5	1,16	11,35
+5 Month	87,85	0,8	5	1,16	13,54
+6 Month	87,37	0,8	5	1,16	15,76
+7 Month	86,89	0,8	5	1,16	18,02
+8 Month	86,41	0,8	5	1,16	20,31
+9 Month	85,93	0,8	5	1,16	22,65
---	---	---	---	---	---

Table 7.7: Estimated temporal evolution of HBI Chemical composition

On the other hand, the costs of the different consumables are needed for estimating the VIU associated to each of the chemical compositions. The costs values used for this study are listed below:

New method proposal for estimating VIU lost due to storage degradation.

Cost Pure Iron (€/t)	Cost Electricity (€/kWh)	Cost of Carbon (€/kg)	Cost of slag (€/kg)	Cost of lime (€/kg)
285	0,05	0,176	0,01	0,074

Table 7.8: Main EAF process costs

According to the proposed VIU methodology, the main contributors to the scrap Value in Use are Electrical energy and Metallic Yield. Fig. 7.19 and Fig. 7.20 depict the temporal evolution of those two concepts according the estimated evolution of HBI chemical composition showed in Table 7.7:

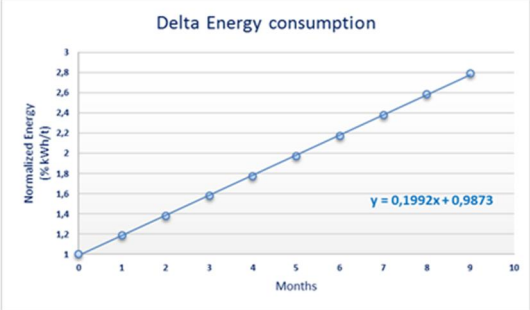

Fig. 7.19: Energy temporal evolution for calculated HBI chemical composition along time

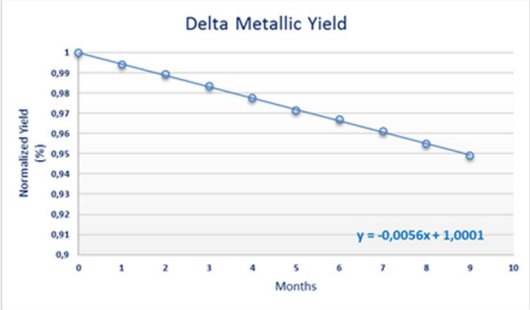

Fig. 7.20: Metallic yield temporal evolution for calculated HBI chemical composition along time

Besides metallic yield and electrical energy consumption, other extra consumptions must be considered for calculating the Antivalue (A), necessary for estimating the total Value in Use (VIU) when the scrap degrades (such as extra coal consumption, extra refractory wear and extra slag generation).

Table 7.9 shows the results in terms of Antivalue (A) and Value In Use (VIU) got for the analytical period:

VIU EAF	Antivalue (€/t)	Value in use (€/t)
HBI - i	22,91	218,28
+1 Month	30,65	209,18
+2 Month	38,45	200,01
+3 Month	46,29	190,80
+4 Month	54,24	181,48
+5 Month	62,23	172,13
+6 Month	70,32	162,66
+7 Month	78,56	153,05
+8 Month	86,92	143,34
+9 Month	95,45	133,43

Table 7.9: (VIU) and (A) temporal evolution

New method proposal for estimating VIU lost due to storage degradation.

These values of (A) and (VIU) showed in Table 7.9 are linked to the initial chemical composition used. In order to offer a standard methodology for analysing these values for any initial composition, it is necessary to normalize the data. In Fig. 7.21 and Fig. 7.22, the normalized response of (A) and (VIU) got according the previously postulated Value In Use methodology is shown.

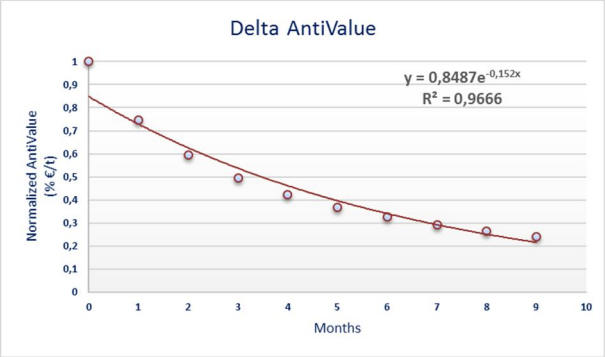

Fig. 7.21: Variation of HBI (A) due to storage period

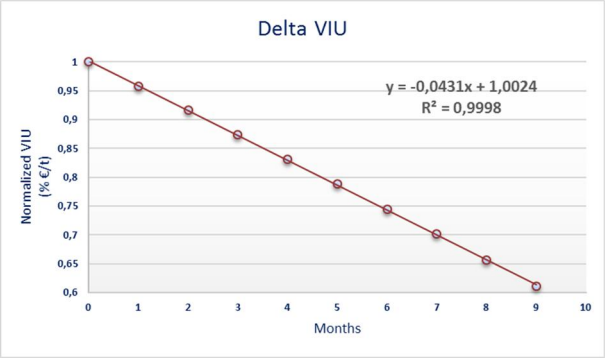

Fig. 7.22: Variation of HBI VIU due to storage period

From the previous data, it is possible to deduce the general equations that allow to estimate the evolution in the value in use of the HBI as EAF raw material, and thus be able to calculate how the storage periods affect the quality of the material.

$$VIU^f = (-0{,}0431\ t \cdot VIU^i) + VIU^i \quad \textbf{(7.8)}$$

$$A^f = A^i \cdot (0{,}8487 \cdot e^{-0{,}152t}) \quad \textbf{(7.9)}$$

From a purchasing point of view, steelmakers currently determine the amount of material to be purchased based on three main concepts; purchasing price, market availability and material quality at the moment to be purchased. However, as demonstrated in this research work, HBI material suffers a degradation process due to oxidation during the storing period that should be measured and incorporate to regular purchasing process and stocking strategies. The general equations posed in (7.8) and (7.9) will allow rethinking the purchasing strategies of the Steelshop based on, not only the three concepts previously mentioned, but also the storing period.

New method proposal for estimating VIU lost due to storage degradation.

7.3.1.3 Conclusion on HBI samples

Knowing how the chemical composition of the HBI evolves over time allows estimating the economic penalty that the loss of quality of the material will cause in the EAF melting process for producing steel.

However, current methodologies include spot sampling and subsequent analysis in the laboratory using conventional analytical techniques. Also, there are currently no methodologies that allow conducting this analysis in quickly and easily manner and there is no procedure to quantify how the lost in quality affects the process from economical point of view either.

In this work we have estimated the chemical composition changes of HBI along time caused by atmospheric corrosion, and it was proposed a methodology for Fe, FeO and Fe_2O_3 variation in composition along storing period. This analysis has permitted defining general equations for estimating the evolution of iron-based compound in HBI material linked to material stock operations in the scrap yard.

We have extended the VIU model with the proposed methodology, two general equations have been proposed for calculating the real Value In Use and the economic Antivalue of HBI with regard the storing time in the scrap yard in relation to a reference initial chemical composition. These two equations allow defining the purchasing strategies of the Steelshop in terms of material purchasing volume, considering that, the larger the storing period, the higher are the process costs associated to the ferrous material quality degradation.

This work represents the first step towards the definition of new strategies for the management of ferrous materials in scrap yards for the production of steel by electric steel mill route

New method proposal for estimating VIU lost due to storage degradation.

7.3.2 Ferrous scrap materials

In the previous section, an analytical methodology for estimating the HBI material quality loss as raw material for the electric arc furnace (evolution of the Value In Use during storage periods) has been proposed. For HBI, the material physical shape is standard, and the main differentiation among material suppliers lays on the initial chemical composition.

When analyzing Low Carbon non alloyed scrap, material´s chemical composition can be considered similar for all of them (only considering the ferrous fraction). However, the physical shape of the material is determined by the material preprocessing phase (shredded, bundled, stamping or sheared). So that, the material apparent surface turns to be one of the most important factors affecting to atmospheric degradation.

For ferrous material, the analytical method proposed is based on the analysis on the superficial iron oxide layer thickness evolution when the ferrous specimens are exposed to weather conditions, and its relationship with the estimated apparent surface of the material.

7.3.2.1 Laboratory methodology for material Chemical control

In order to do the initial characterization of the selected specimens and to ensure that the weights and surface appearance analysis is the same at the started point for all pieces tested, it was necessary, before any exposition, to expose all specimens to some initial cleaning and characterization treatments according the following treatment:

1. Cleaning of initial sample using standard water
2. Degreasing using detergent
3. Pickling of the sample by acid prior to sampling in order to remove surface dirt and corrosion products. To do so, the samples were soaked in acid (described in Table 7.10) for a short time interval (30 seconds), obtaining the results show in Fig. 7.23:

Metal	Solution	Temperature
Steel	1 l. HCL + 20gr Sb2O3 + 50gr SnCl2	25ºC

Table 7.10: Chemical cleaning solution for corrosion removal.

Fig. 7.23: Appearance of samples after pickling

New method proposal for estimating VIU lost due to storage degradation.

4. The samples are rinsed using distilled water
5. A final rinse is performed using industrial alcohol
6. Then sticky surface layers were removed using a soft brush.
7. Finally, the samples are dried with a hair dryer.
8. Once the preparation process of samples is completed, specimens are identified

After sample preparation process, optical metallography analysis of the pieces was conducted just to confirm that there is not oxide scale in the surface of the specimens. In Fig. 7.24 and Fig. 7.25, the total absence of oxide crust at the beginning of the experiment is demonstrated.

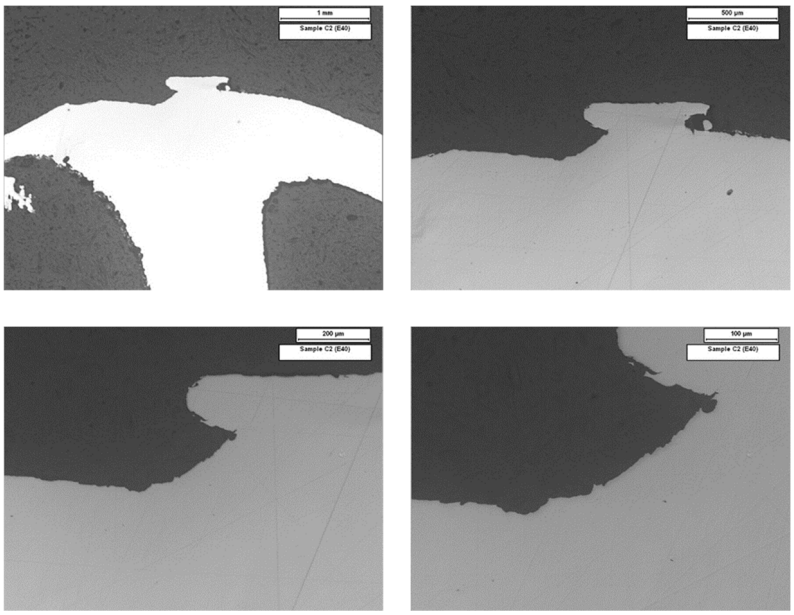

Fig. 7.24: Example of E40 specimens after pickling at x25 (upper left), x50 (upper right), x100 (bottom left) and x200 (bottom right) in the microscope

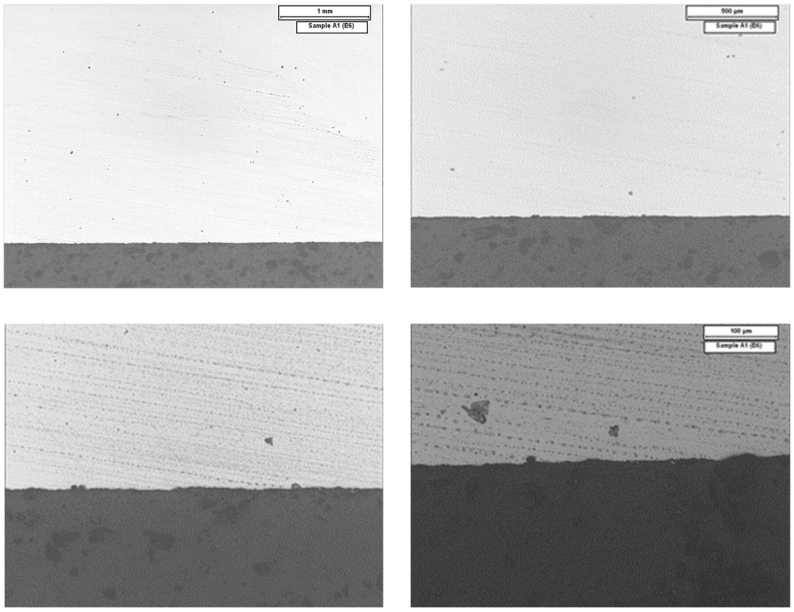

Fig. 7.25: Example of E6 specimens after pickling at x25 (upper left), x50 (upper right), x100 (bottom left) and x200 (bottom right) in the microscope

New method proposal for estimating VIU lost due to storage degradation.

As shown in Fig. 7.24: and Fig. 7.25, before the samples were exposed to the environment, and since they have been pickled and conveniently prepared, Oxide layer were not observed at the microscope. This confirm that all weighted material is steel.

The final step in the preparation process corresponds with specimen's characterization. This includes material weighing and chemical composition assessment:

- Material Weighting: Weight information is used, after specimen recovery, to determine how much steel has been transformed into Iron oxide (based on the apparent surface of the material tested) by the effect of atmospheric corrosion.
- Chemical composition of the selected materials after pickling was got by Optical Emission Spectroscopy (OES) technique. The chemical composition of the samples for the two experiments are shown in Table 7.11:

Sample ID	Feº	C	Mn	Si	P	S	Cu	FeO	SiO_2	Al_2O_3	CaO	Mg0
Experiment 1	98,43	0,30	0,60	0,2	0,04	0,04	0,40	0	0	0	0	0
Experiment 2	98,10	0,34	0,50	0,2	0,03	0,02	0,25	0	0	0	0	0

Table 7.11: Chemical composition of E40 specimens

Sample ID	Feº	C	Mn	Si	P	S	Cu	FeO	SiO_2	Al_2O_3	CaO	Mg0
Experiment 1	99,25	0,06	0,50	0,05	0,01	0,01	0,12	0	0	0	0	0
Experiment 2	99,30	0,04	0,50	0,02	0,01	0,01	0,08	0	0	0	0	0

Table 7.12: Chemical composition of E6 specimens

Once the material is recovered from the exposure holder, the weighting operation is repeated, before and after sample pickling to calculate the amount of iron oxide removed. And the average iron oxide layer thickness is measured by using optical microscopy. These data are used for measuring the degradation of each exposed sample.

7.3.2.2 Numerical approach for exposure results understanding

The physical shapes of ferrous materials are highly variable (as shown in Fig. 7.23) and the chemical composition is quite similar (as shown in Table 7.11 and Table 7.12). Those facts make no possible to apply same methodology than the one proposed for HBI Materials which were based on the chemical evolution the whole material. For ferrous scrap, the procedure proposed for assessing the quality loss is based on determining the amount of Fe that is transformed into iron oxide compounds. This procedure is graphically described in Fig. 7.26:

New method proposal for estimating VIU lost due to storage degradation.

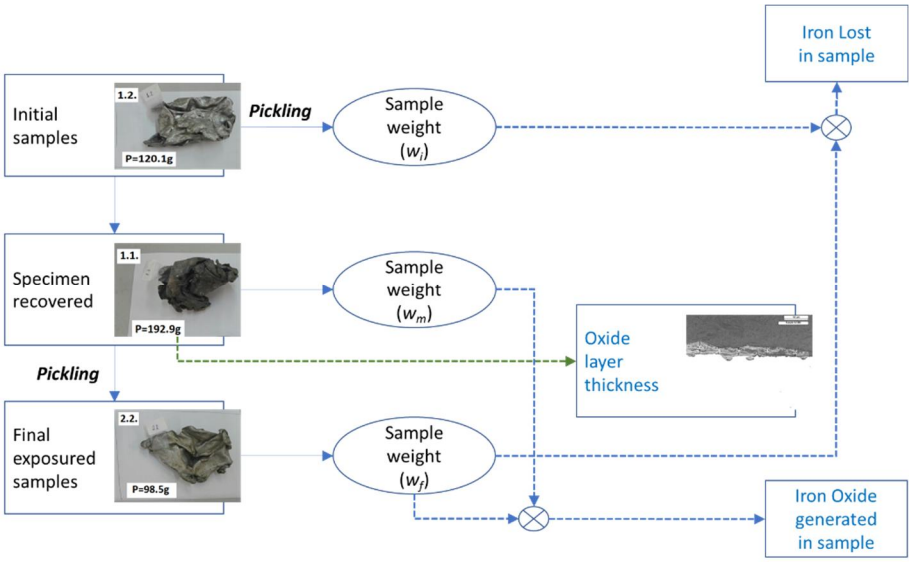

Fig. 7.26: Sample analysis workflow proposed

The main data of interest for material degradation analysis is the metallic iron weight loss due to the superficial degradation. According the methodology proposed in Fig. 7.26, the weight loss can be easily obtained by applying the following equation:

$$w_{Fe} = w_i - w_f \tag{7.10}$$

Where:

$\boldsymbol{w_{Fe}}$ represents the actual Fe weight loss due to corrosion process

$\boldsymbol{w_i}$ represents the weight of the specimen at the initial moment prior to exposure

$\boldsymbol{w_f}$ represents the weight of the specimen after pickling

Once the exposed specimens are recovered, the amount of iron oxide present in the material surface is obtained by comparing the weight of the scrap piece before and after the pickling process.

$$w_{Fe2O3} = w_m - w_f \tag{7.11}$$

$$P_{Fe2O3} = \frac{w_m - w_f}{w_m} x100 \tag{7.12}$$

Where:

$\boldsymbol{w_{Fe2O3}}$ is the total Iron Oxide generated due to the corrosion process

$\boldsymbol{P_{Fe2O3}}$ is the % of total Iron Oxide generated due to the corrosion process

$\boldsymbol{w_m}$ represents the weight of the specimen when recovered after exposure

$\boldsymbol{w_f}$ represents the weight of the specimen after pickling

New method proposal for estimating VIU lost due to storage degradation.

By knowing the average thickness of iron oxide layer in the exposed specimen (***e***), measuring it with the optical microscope, and considering an iron (III) oxide density ($\boldsymbol{\rho_{Fe2O3}}$) equal to 5250 kg/m3, the total Iron Oxide generated due to the corrosion process got by using equation (7.16) is used for calculating the apparent surface (***A***)

$$A = \frac{w_{Fe2O3}}{\rho_{Fe2O3} \cdot e} \tag{7.13}$$

Then, the specimen apparent surface data can be used for obtaining the material weight lost due to corrosion (***L***) per unit area

$$L = \frac{\boldsymbol{w_{Fe}}}{A} \tag{7.14}$$

Finally, the daily material weight lost due to corrosion or corrosion severity ($\boldsymbol{L_{day}}$) can be estimated by applying equation (7.20)

$$L_{day} = \frac{L}{(month\ x\ 30)} \tag{7.15}$$

7.3.2.3 Analysis on Shredded scrap (E40 – European specification)

Scrap metal shredders are often used to recycle items containing a variety of other materials in combination with steel. The types of scrap metals that are sent to metal shredding facilities include end-of-life products that are primarily composed of metal, such as vehicles, appliances, construction and demolition materials. These items are labor-intensive to manually sort things like plastic, copper, aluminum, and brass. By shredding into relatively small pieces, the steel can easily be separated out by any of the processing techniques described in Chapter 5.

Shredded scrap represents a large part of the recycling industry worldwide and an important source of raw material for steelmaking. The shredded scrap grade consists of homogeneous pieces of steel scrap not exceeding 200 mm in any direction, which is magnetically separated to ensure low presence of dirt mixed with the material

7.3.2.4 Experimental results over Shredded samples

Several randomly selected pieces of E40 scrap were collected and exposed according the methodology described in 7.2.2.

The exposed specimens to the outdoor environmental conditions, as shown in Fig. 7.23, were progressively recovered from the expositing holder after 1 month, 2 months, 3 months, 6 months, 9 months and one year of exposition. After recovery, they were analyzed at the laboratory. This procedure was repeated twice (in 2017 and 2018) to confirm the coherence of

the results. Progressive degradation due to corrosion, motivated by the environmental exposure, is shown in Fig. 7.27:

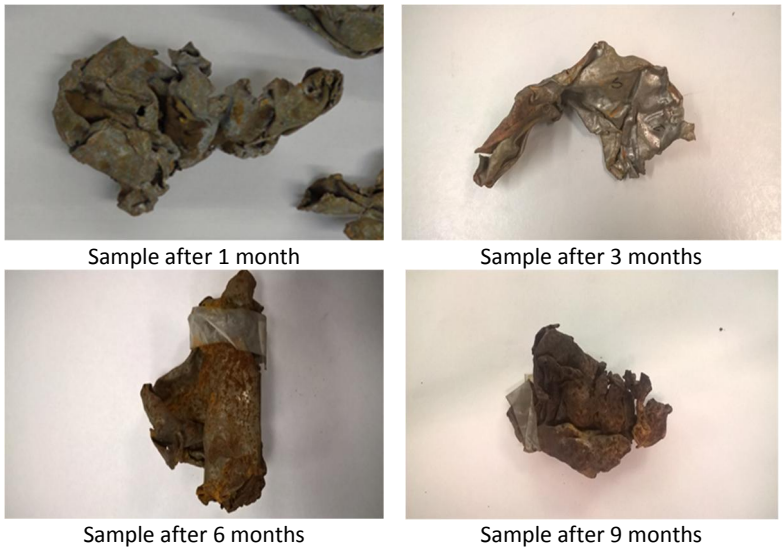

Fig. 7.27: Visual appearance of E40 after different exposure periods of samples in experiment 1

Similar than in HBI material analysis, it was assumed that corrosion effect over the chemical composition ferrous materials is only linked to the iron oxides-based compounds, but not alteration on the rest of component are expected (CaO, SiO_2, MgO, Al_2O_3, or C).

In the case of ferrous scrap, wet chemistry methodology cannot be used. For analyzing the degradation of scrap samples due to corrosion effect, the proposed methodology consisted on understanding the evolution of the oxide rust thickness evolution along time according the methodology described in Fig. 7.26

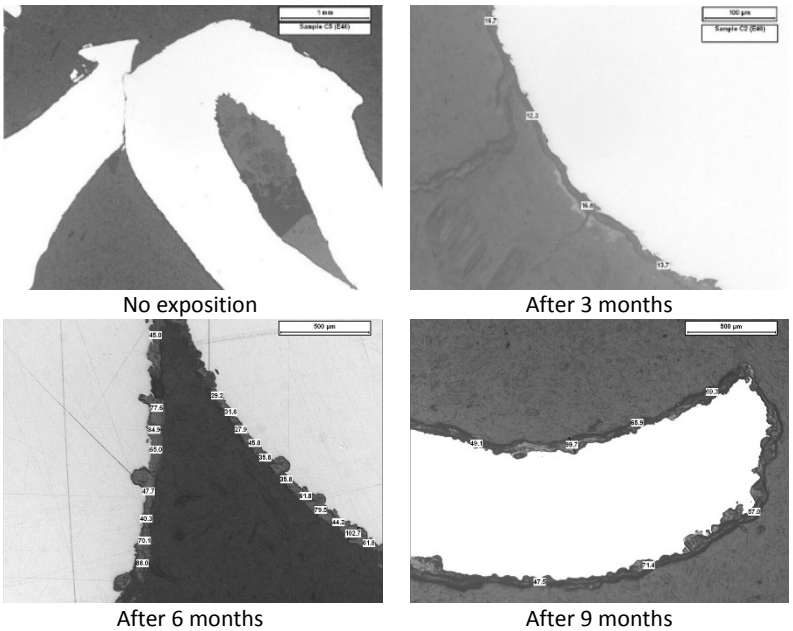

New method proposal for estimating VIU lost due to storage degradation.

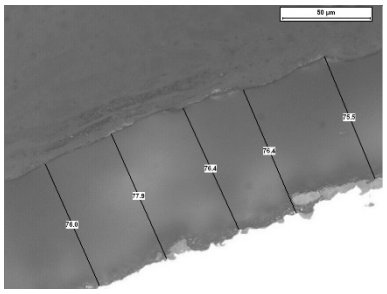

After 12 months

Fig. 7.28:Microscope images of iron oxide layer temporal evolution for E40 in experiment 2

The average value of the rusted layer was obtained by measuring it thickness in 30 points along the sample surface using an optical microscope. Fig. 7.29 shows the oxide layer measurement results got for experiment 1 and 2:

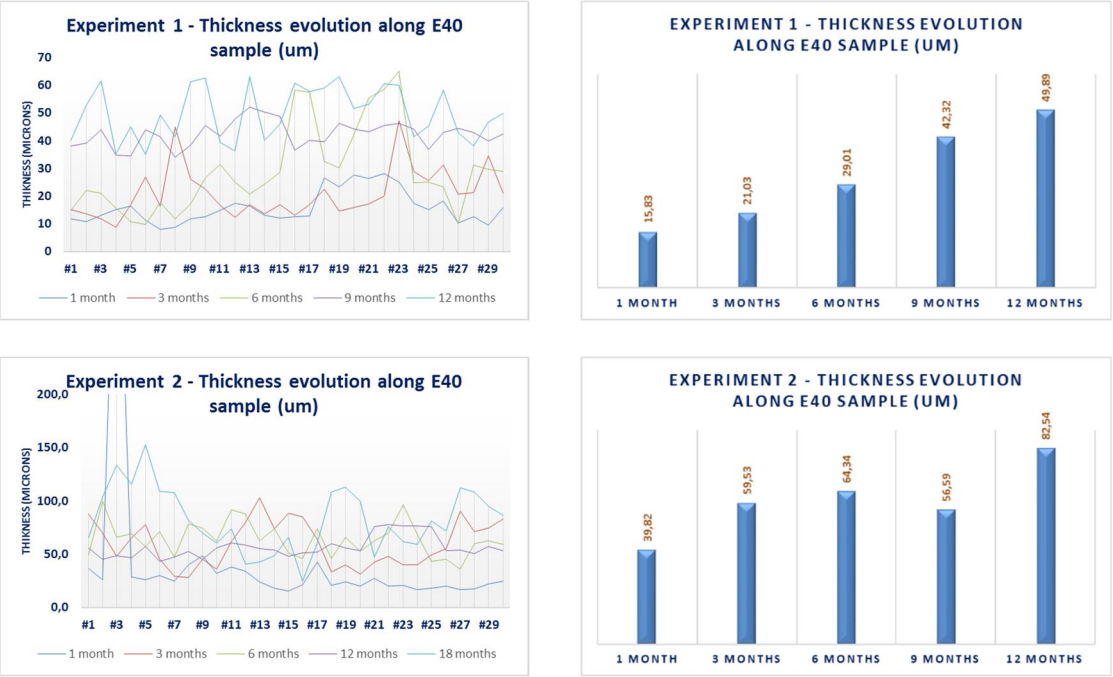

Fig. 7.29: Iron Oxide layer temporal evolution of E40 for experiment 1 and 2

Then, applying equations (7.11) and (7.13) it is possible to estimate the apparent surface of scrap samples. In the case of shredded scrap samples, the average apparent surface value for all exposed samples was 0,019 m^2.

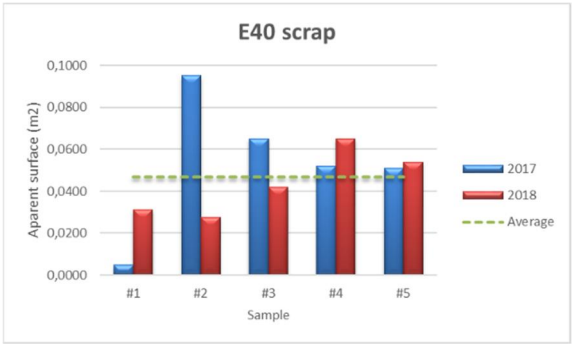

Fig. 7.30: Apparent Surface of E40 scrap samples

New method proposal for estimating VIU lost due to storage degradation.

Known the apparent surface of the sample, equation (7.14) can be used for calculating the evolution of the exposed samples weight lost due to corrosion in mg/m^2. Fig. 7.31 graphically present these data:

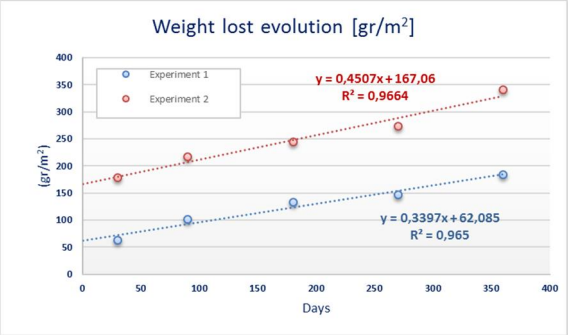

Fig. 7.31: E40 Weight lost evolution due to corrosion

As previously described in 7.1.2, the corrosion degradation phenomenon is mainly linked to atmospheric conditions (temperature, humidity, rain ration...) during the exposure period. However, there are intrinsic aspects to the sample that also condition the degradation phenomenon (such as the chemical composition of the exposed steel and the exposed surface), however, for this experiment, only Low Carbon non allowed scrap materials are considered, so the influence of the chemical composition in the degradation process was not considered in this research work.

Fig. 7.31 shows that the degradation presents a linear trend over time with a similar slope for the two experiments, but it can also be observed that there is an important gap between the two experiments in terms of weight lost value magnitude, probably this is linked to differences in the two experiments in both the intrinsic (material shape) and atmospheric aspects.

After analyzing the data, as shown in Fig. 7.32, it is also possible to assess that the corrosion severity decreases with the exposing time

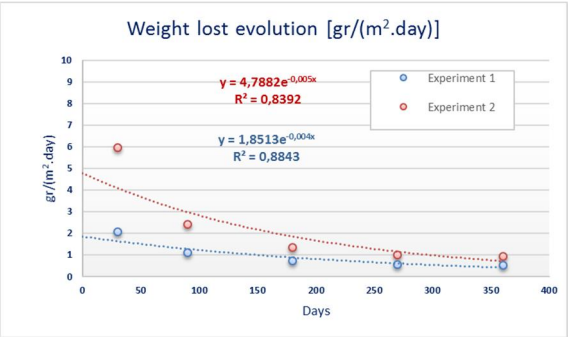

Fig. 7.32: E40 Relative temporal degradation

The normalization of the data allows confirming that there is a clear correlation in the degradation process for both experiments.

New method proposal for estimating VIU lost due to storage degradation.

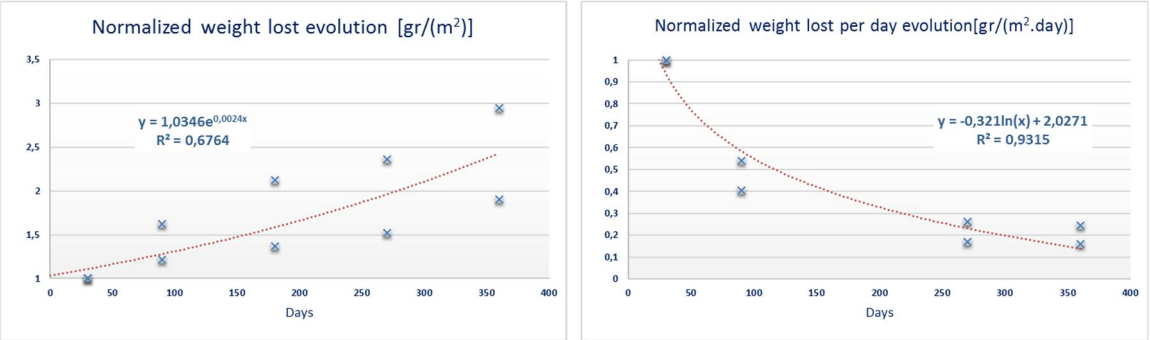

Fig. 7.33: Normalized data on the temporal degradation of E40

7.3.2.5 Analysis on busheling scrap (E6 – European specification)

Similar than for E40 analysis, several randomly selected pieces of E6 scrap were collected and exposed according the methodology described in section 7.2.2.

The exposed specimens to the outdoor environmental conditions, as shown in Fig. 7.23, were progressively recovered from the expositing holder after 1 month, 3 months, 6 months, 9 months and one year of exposition. After recovery, they were analyzed at the laboratory. This procedure was repeated twice (in 2017 and 2018) to confirm the coherence of the results. Progressive degradation due to corrosion can be observed in Fig. 7.34:

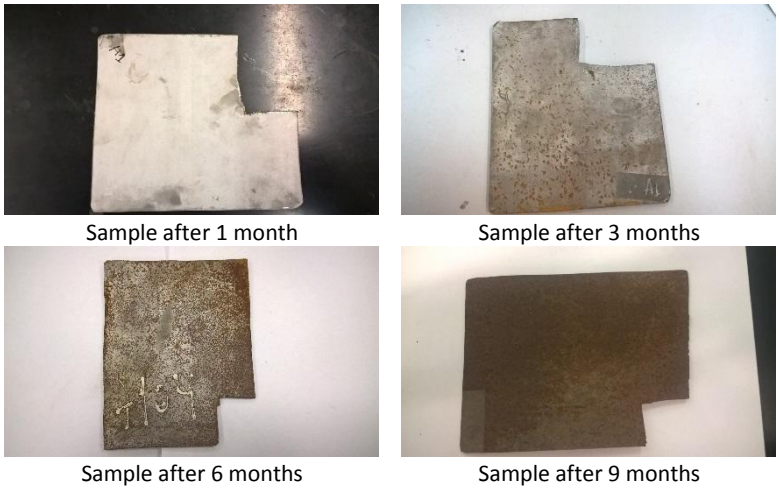

Fig. 7.34: Visual appearance of E6 after different exposure periods of samples in experiment 1

Again, it was assumed that corrosion effect over the chemical composition ferrous materials is only linked to the iron oxides-based compounds, but not alteration on the rest of component are expected (CaO, SiO_2, MgO, Al_2O_3, or C).

For analyzing the degradation of scrap samples due to corrosion effect same methodology than the one used for shredded scrap was used. Fig. 7.35 shows some examples of the E6 scrap oxide layer thickness measurement results got by optical microscopy techniques along the exposure time of specimens.

New method proposal for estimating VIU lost due to storage degradation.

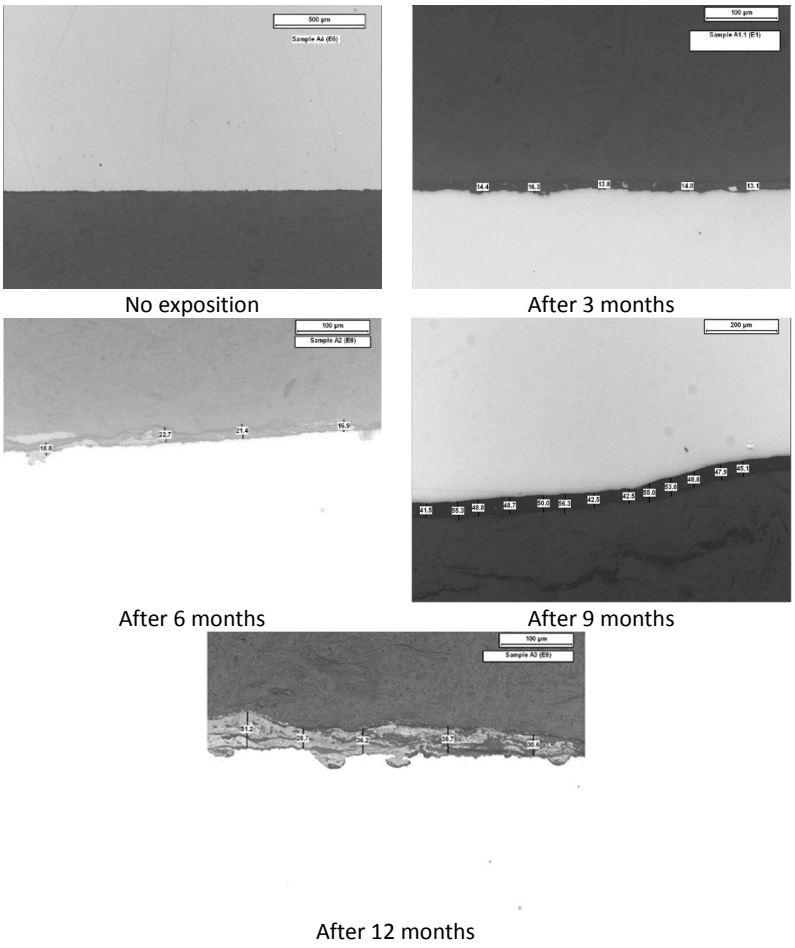

Fig. 7.35:Microscope images of iron oxide layer temporal evolution for E6 in experiment 2

The average value of the rusted layer was obtained by measuring it thickness in 30 points along the E6 scrap samples surface.

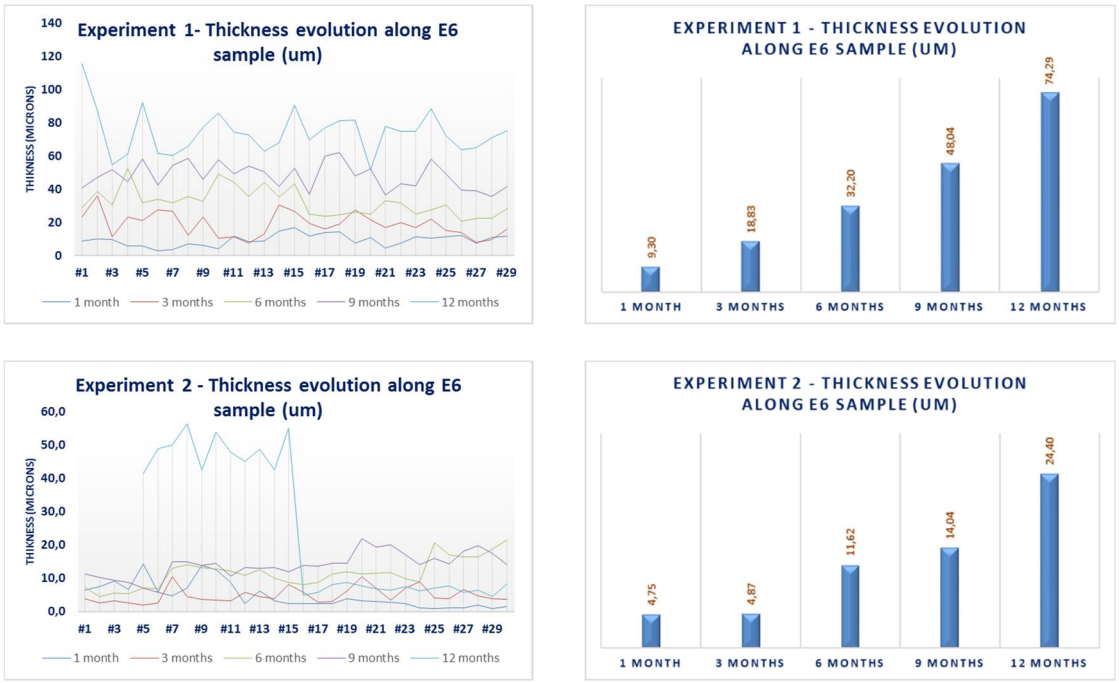

Fig. 7.36: Iron Oxide layer temporal evolution for experiment 1 and 2

New method proposal for estimating VIU lost due to storage degradation.

Then, applying equations (7.11) and (7.13) it is possible to estimate the apparent surface of scrap samples. In the case of E6 scrap, the average apparent surface value for all exposed samples was 0,047 m^2.

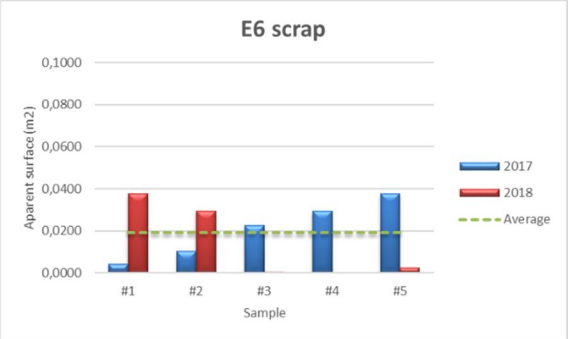

Fig. 7.37: Apparent Surface of E6 scrap samples

Known the apparent surface of the sample, equation (7.14) can be used for calculating the evolution of the exposed samples weight lost due to corrosion in mg/m^2. Fig. 7.38 graphically presents these data:

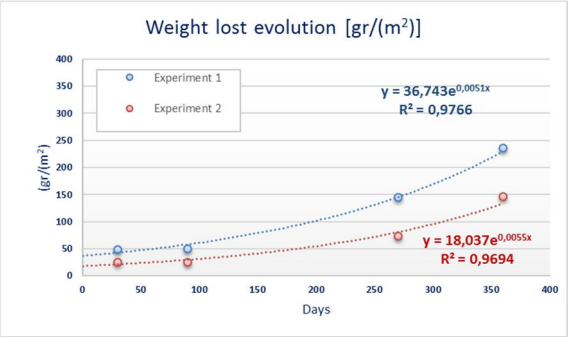

Fig. 7.38: E6 Weight lost evolution due to corrosion

As previously described in 7.1.2, the corrosion degradation phenomenon is mainly linked to atmospheric conditions (temperature, humidity, rain ration...) during the exposure period. However, there are intrinsic aspects to the sample that also condition the degradation phenomenon (such as the chemical composition of the exposed steel and the exposed surface), however, same than in previous experiment, only Low Carbon non allowed scrap materials are considered.

Fig. 7.38 shows that the degradation presents an exponential trend over time similar for both experiments.

By analyzing the data, as shown in Fig. 7.39, it is also possible to assess that the corrosion severity decreases with the exposing time

New method proposal for estimating VIU lost due to storage degradation.

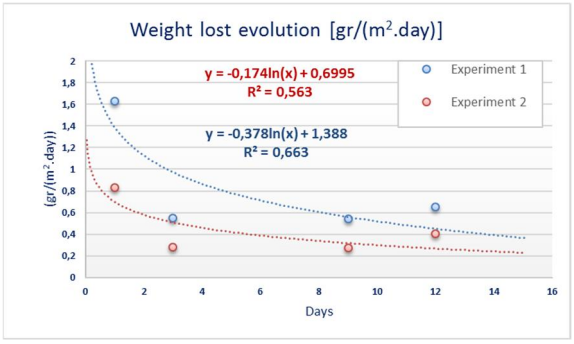

Fig. 7.39: E6 Relative temporal degradation

Similar than in the case of shredded scrap, the normalization of the data allows confirming that there is a clear correlation in the degradation process for both experiments.

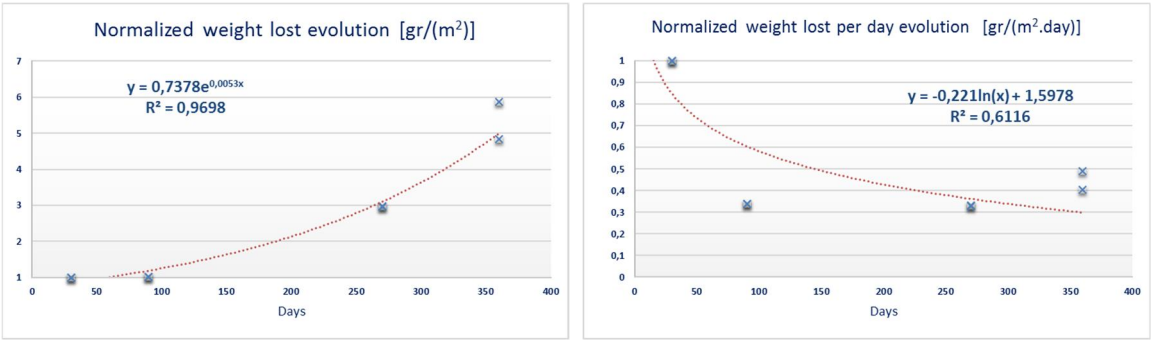

Fig. 7.40: Normalized data on the temporal degradation of E6

7.3.2.6 General VIU degradation model for Ferrous scrap materials

In the previous sections, two different materials with different shapes but similar chemical composition were studies, identifying similar degradation behaviors strongly associated with the apparent surface.

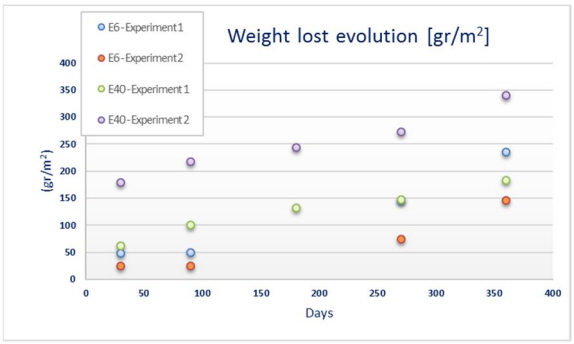

Fig. 7.41: Weight lost evolution for all analyzed samples

New method proposal for estimating VIU lost due to storage degradation.

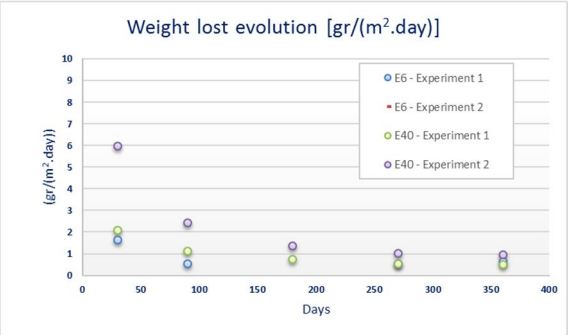

Fig. 7.42: Degradation severity for all analyzed samples

Up to this point, the degradation process of several ferrous materials has been analyzed separately. However, the purpose of this work is to offer general equations for assessing the economic penalties induced in ferrous scrap material due to the degradation process after long storing periods in the steelmakers scrap yard.

By normalizing all these data together with respect to the degradation produced at the beginning of the experiment (after one month of exposition), it is possible to independentize the specific results obtained on each of the samples from the apparent surface of each specimen (given the heterogeneity in the physical shape of ferrous materials) and from the chemical nature of the sample (corrosion intensity), and thus to extract a general degradation equations applicable to any proposed case of use.

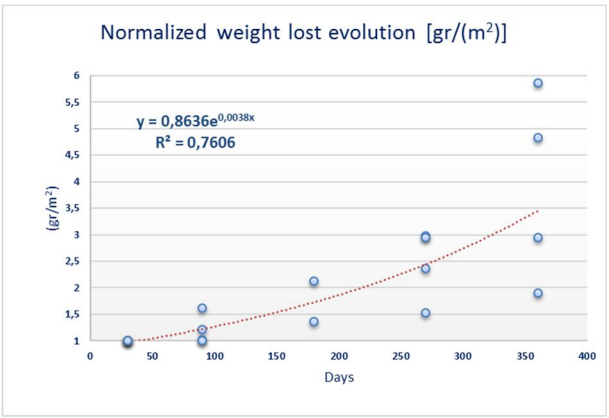

Fig. 7.43: Normalized data on scrap degradation

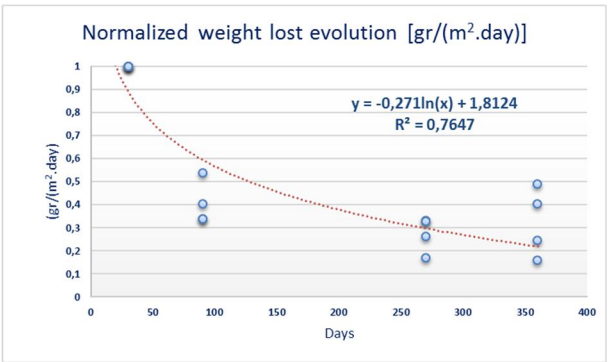

Fig. 7.44: Normalized data on scrap degradation severity

New method proposal for estimating VIU lost due to storage degradation.

From the normalized data presented in Fig. 7.43 and Fig. 7.44, two general equations, describing the weight loss and the degradation severity due to Fe → Fe_2O_3 transformation, are extracted:

$$L_f = L_i \cdot (0{,}8636e^{0{,}0038 \cdot t}) \quad (R^2=0{,}7606) \tag{7.16}$$

$$L_f^{Day} = L_{t1}^{Day} \cdot (-0{,}271Ln(t) + 1{,}8124) \quad (R^2=0{,}7647) \tag{7.17}$$

Where:

$\boldsymbol{L_f}$ is the material weight lost at time $\boldsymbol{t}$ due to corrosion in gr/m^2

$\boldsymbol{L_i}$ is the material weight lost due to corrosion in gr/m^2 at the reference time (1 month).

$\boldsymbol{L_f^{Day}}$ represents the corrosion severity rate at time $\boldsymbol{t}$ in gr/(m^2 day)

$\boldsymbol{L_{tDay}^{R}}$ is the corrosion severity rate in gr/(m^2 day) at the reference time (1 month)

$\boldsymbol{t}$ is the time of analysis in days

On the other hand, equations (7.16) and (7.17) are not enough to conduct a complete analysis on ferrous samples degradation. To this end, one of the most critical data affecting the corrosion phenomena is the apparent characteristic surface of each material associated with its morphology. Two different methods can be proposed for estimating the apparent surface of the material under study:

- The laboratory methodology described in previous sections (7.3.2.2) and based on iron oxide thickness measurement and weight differences before and after sample picking.
- Apparent surface estimation based on material density (according Table 7.13), piece weight and piece thickness

Material	E3	E1	E8	E6	E40
density (kg/m^3)	600	500	400	1000	900

Table 7.13: Standard density for different ferrous scrap (8)

For example; one metal piece of 1kg with a thickness of 5 mm (except for the E8 that a side of the cube equal to 500mm is used for the calculation) that losses 10 gr of iron after 30 days of exposition, the apparent surface can be calculated as reported in Table 7.14:

Material	E3	E1	E8	E6 (0,5m in 1D)	E40
Apparent surface (m^2)	0,0333	0,040	0,050	0,20	0,0222

Table 7.14: Apparent Surface estimated by material density

Checking the estimated values presented in Table 7.14, with the experimental apparent surface measured in laboratory during E40 and E8 tests (0,019 m^2 and 0,047 m^2 respectively). it is shown that both methodologies offer similar results

New method proposal for estimating VIU lost due to storage degradation.

Continuing with same example proposed above (one metal piece of 1kg with a thickness of 5 mm), by dividing the normalized weight lost evolution (7.16) by the apparent surface of the scrap material under analysis, it is possible to calculate not only the Fe weight lost for any exposure period, but also the Fe_2O_3 generated in the sample surface due to the Fe oxidation (using atomic number of Oxygen and Iron).

Fig. 7.45: Weight lost evolution for different scrap materials according initial material characterization data for the selected example

The main assumption that has been taken for this experiment is that the chemical composition is the same for all ferrous materials, so the effect of degradation is determined primarily by the exposed surface. Transforming the data in Fig. 7.45 by dividing each curve by the apparent surface of each material, it is possible to obtain not, only the generic Fe losses and Fe_2O_3 generation due to corrosion effect, but also the amount of oxygen incorporated to the sample due to this oxidation effect

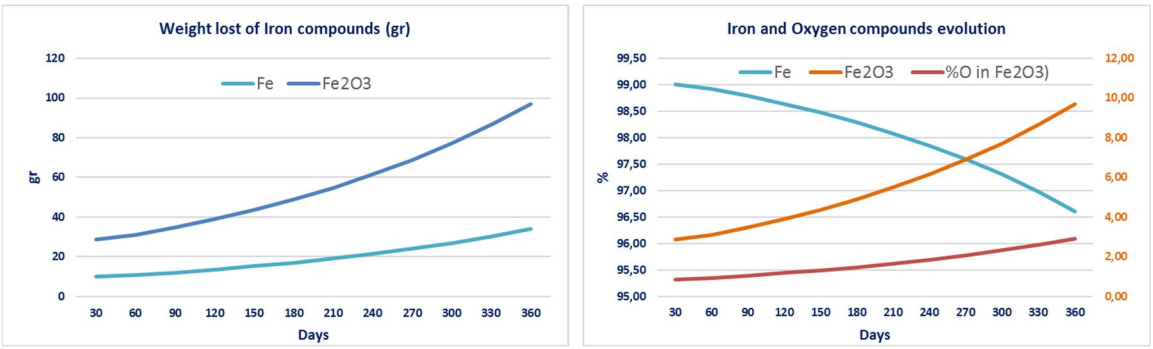

Fig. 7.46: Iron compounds evolution due to degradation of ferrous material

The data shown in Fig. 7.46 are used, first to generate the temporal evolution of the chemical composition of ferrous scrap materials presented in Table 7.15 and then, to obtain the general Antivalue equation (Fig. 7.47) that represents the economic penalties of the EAF process linked to the scrap degradation. This equation will be used later on for calculating the Value In Use evolution when ferrous scrap are stored in uncovered scrap yards.

New method proposal for estimating VIU lost due to storage degradation.

	Fe+t.e. (%)	Acid gangue (%Fe_2O_3)	Basic Gangue (Cao+MgO)	Oxygen on Fe
Ferrous scrap	100	0	0	0
+30 days	99,00	2,86	0	0,86
+60 days	98,92	3,10	0	0,93
+90 days	98,78	3,48	0	1,04
+120 days	98,64	3,90	0	1,17
+150 days	98,47	4,37	0	1,31
+180 days	98,29	4,89	0	1,47
+210 days	98,08	5,48	0	1,65
+240 days	97,85	6,15	0	1,85
+270 days	97,59	6,89	0	2,07
+300 days	97,30	7,72	0	2,32
+330 days	96,97	8,65	0	2,60
+360 days	96,61	9,70	0	2,92

Table 7.15: Estimated temporal evolution of Low Carbon non allowed scrap materials Chemical composition

The costs values used for this study are the same than the ones presented in Table 7.8.

As described in section 4.4, incorporating oxygen to the sample (by Fe_2O_3 generation in sample) affect to the Antivalue as follow:

- By increasing 1% the amount of oxygen, the electrical energy consumption is increased by 49 kWh/t of steel.
- By increasing 1% the amount of oxygen, the coal consumption is increased by 6,8 kg/t of steel.

The data shown in Table 7.15 can be normalized for obtaining a general ANTIVALUE equation for Low Carbon Low alloyed steel scrap

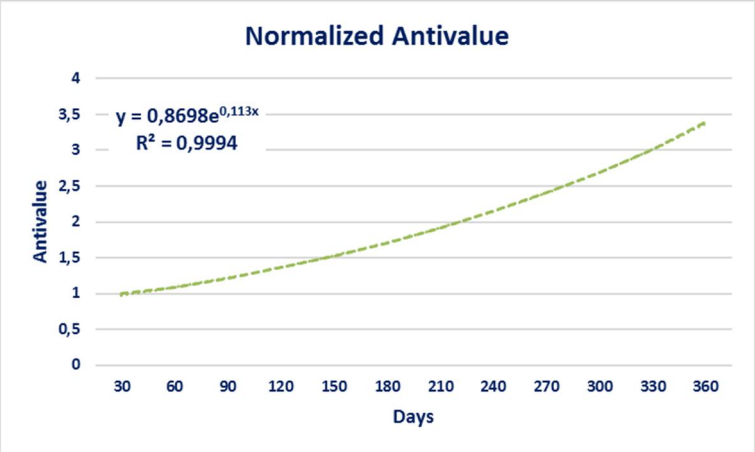

Fig. 7.47: Normalized antivalue for Low Carbon Low alloyed steel scrap

From previous figure, the general ANTIVALUE equation for Low Carbon Low alloyed steel scrap is extracted:

$$A^f = A^i \cdot (0{,}8698 \cdot e^{0{,}113t}) \quad \textbf{(7.18)}$$

Where:

New method proposal for estimating VIU lost due to storage degradation.

A^f represents the ANTIVALUE at time ***t***,

A^i represents initial Antivalue after one month of exposition

t represents the exposition time in days

Also, according to the proposed VIU methodology, the main contributors to the scrap Value in Use are Electrical energy demand and Metallic Yield. Fig. 7.48 and Fig. 7.49 depict the temporal evolution of those two concepts according the estimated evolution of sample chemical composition for three different scenarios (the one showed in Table 7.15, one sample of 1 kg with a weight lost after one month of 50 gr and 0,5kg sample with a weight loss of 10 gr).

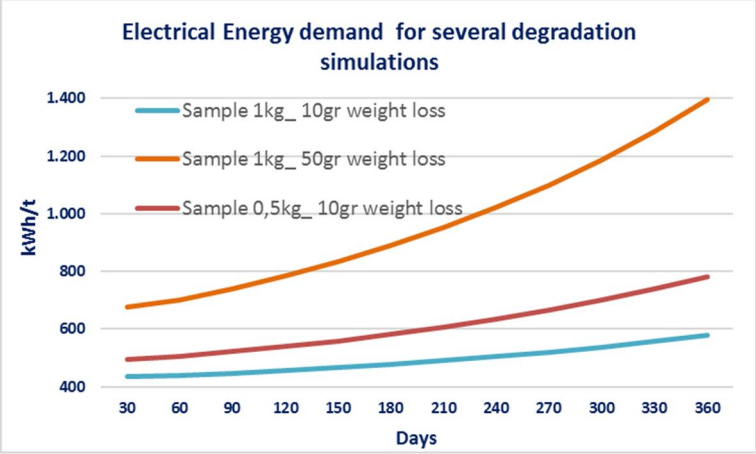

Fig. 7.48: Electrical Energy demand for the three studied cases

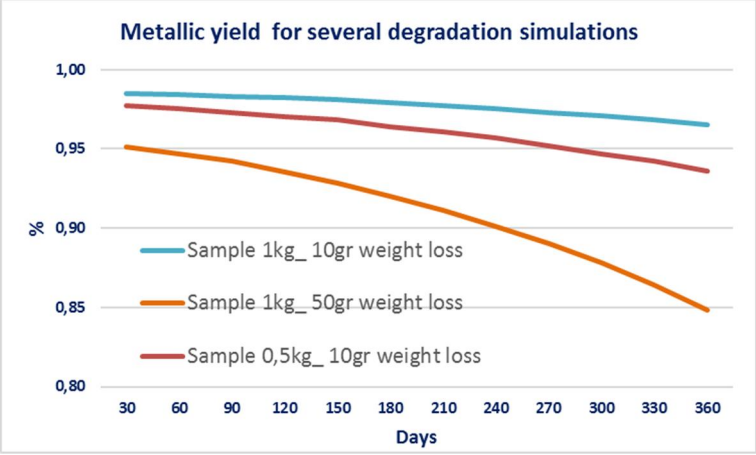

Fig. 7.49: Metallic yield for the three studied cases

Finally, by combining the general Antivalue Equation (7.18) with the general material weight lost equation L_f (7.16), and the weight sample data after 30 days of exposure, it is possible to calculate the Real Value In Use evolution of any Low Carbon Low Alloyed ferrous scrap material when exposed to atmospherically for a certain period of time.

Based on the equations posed, the quality assessment methodology (VIU) proposed consists on the steps described in Fig. 7.50:

New method proposal for estimating VIU lost due to storage degradation.

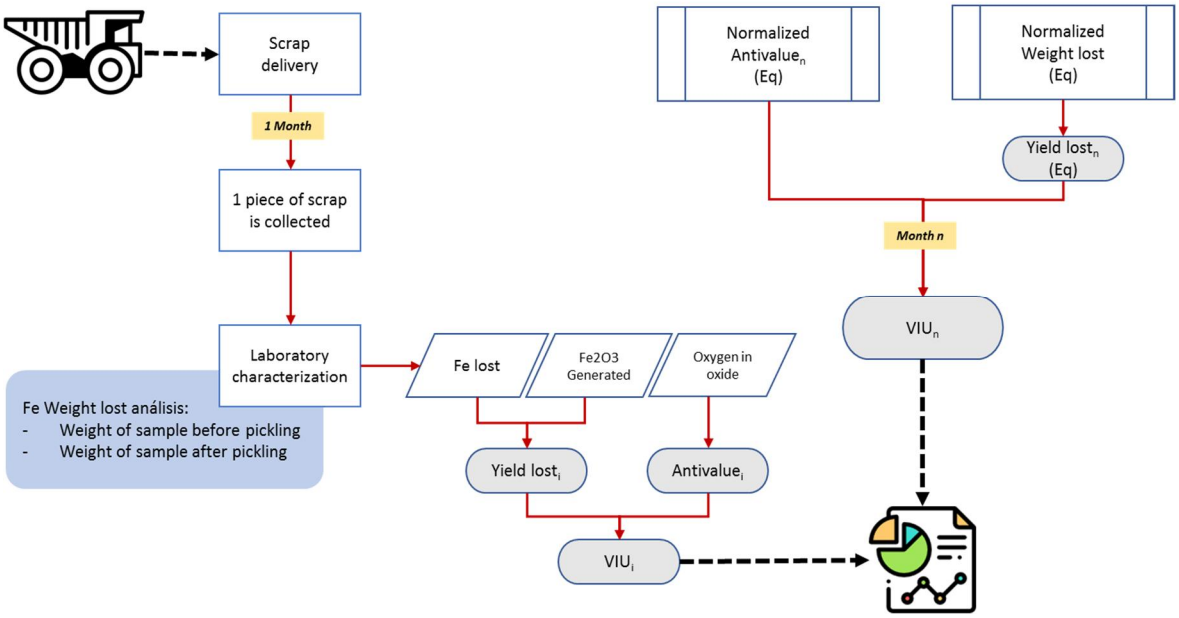

Fig. 7.50:Proposed methodology for initial degradation assessment and VIU evolution linked to material nature

In chapter 4, the General Value In Use equation (4.3) was described. By applying the methodology described in Fig. 7.50 to the VIU general concept, the VIU equation for ferrous scrap materials that describes the quality losses for material degradation can be define as follow:

$$VIU = \left(\left[100 - \frac{L_f \cdot 100}{w_i}\right] \cdot C_{€}\right) + A^f \qquad \textbf{(7.19)}$$

Same as proposed for HBI materials, this research work demonstrates the ferrous scrap material suffers a degradation process due to oxidation when storing in scrap yards. This effect should be measured and incorporate to regular purchasing process and stocking strategies. The general equation posed in (7.19) will allow rethinking the purchasing strategies of the Steelshop based on, not only the three concepts previously mentioned, but also the storing period.

7.3.2.7 Conclusion on ferrous scrap samples

Knowing how the chemical composition of the Low Carbon Low Alloyed steel scrap evolves over time allows estimating the economic penalty that the loss of quality of the material will cause in the EAF melting process for producing steel.

The current state of the art does not allow measuring the degradation of ferrous scrap materials. Even doing spot materials sampling and subsequent laboratory analyses, the obtained information would not be representative of the whole scrap pile. Similarly, than in the case of HBI material, there is no procedure to quantify how the lost in quality affects the process from economical point of view either.

New method proposal for estimating VIU lost due to storage degradation.

This work presents a model for estimating the temporal evolution in Fe and Fe_2O_3 in Low Carbon Low alloyed steel scrap based on simple equations.

The new proposed model allows to extend the well-established VIU methodology to be applied for a novel approach which incorporates material quality penalties due to storing period at scrap yard in steel plants in general Antivalue and VIU equations.

The new available information permits defining the purchasing strategies of the Steelshop in terms of material purchasing volume, considering that, the larger the storing period, the higher are the process costs associated to the ferrous material quality degradation.

This work represents the first step towards the definition of new strategies for the management of ferrous materials in scrap yards for the production of steel by electric steel mill route

New method proposal for estimating VIU lost due to storage degradation.

7.4 Chapter 7 recall and conclusions

Since around 60% of the EAF steel production costs correspond to ferrous raw materials, the scrap yards turn to be one of the most critical elements in the steel production factories. However, the scrap yard is probably one of the less automatized facility in the steelmaking shop acting mainly as a material storing area (high volumes of scrap are purchased and stored when the market price is low, and the stored materials are consumed when the market prices are high) to ensure a continuous flow of raw material to the Electric Arc Furnace that avoids discontinuities in factory productivity.

The quality control of ferrous materials is usually done only when the material is purchased at the scrap dealer facility and when the material arrives at steel site. This poor quality approach presents one drawback that is not usually considered by steelmakers; the worsening of material quality due to long storing period in the scrap yard induced by the atmospheric corrosion.

The atmospheric degradation process of ferrous material has been widely reported in the literature, but it mainly focuses on metallic structures integrity analysis. In the case of ferrous scrap as main steelmaking raw material, the degradation process affects to the material quality being of great influence on the EAF operative performance through the Scrap's Value In Use concept.

This material degradation process has been extensively studied in this work by grouping ferrous materials in two categories; HBI and ferrous scrap.

The research done in this section has concluded by proposing an analytical procedure for obtaining empirical equations which allow estimating the cost worsening of ferrous material due to the degradation produced by the atmospheric corrosion.

The following equations have been obtained from these analyses:

- For HBI materials:

$$VIU^f = (-0{,}0431\ t \cdot VIU^i) + VIU^i \quad \textbf{(7.08)}$$

$$A^f = A^i \cdot (0{,}8487 \cdot e^{-0{,}152t}) \quad \textbf{(7.09)}$$

- For Ferrous scrap materials:

$$VIU = \left(\left[100 - \frac{L_f \cdot 100}{w_i}\right] \cdot C_{€}\right) + A^f \quad \textbf{(7.19)}$$

$$A^f = A^i \cdot (0{,}8698 \cdot e^{0{,}113t}) \quad \textbf{(7.18)}$$

8

New method proposal for chemical characterization of sterile material in scrap.

The chemical distribution of sterile fraction in Ferrous scraps have a significant impact on the economical results of the steelmaking process. This chapter presents the experimental analyses of several spectroscopy techniques in laboratory conditions, including laboratory set ups, acquisition configurations and samples preparation. The conclusion on this research will allow assessing the potentiality of each studied technologies for being used for in-site sterile characterization technique.

As described in previous chapters, the different referent technical steel scrap specifications group the scrap categories (qualities), not only by their origin or their shape, but also by other aspects like their content in residual elements or presence of certain sterile materials.

Putting the attention, only on the sterile present in the scrap, it is important to take into account that the quantity and the chemical composition of sterile materials in ferrous scraps are closely linked to the origin of the scrap, as well as to the previous collecting processes and scrap pre-processing. Some examples are listed below;

- Recycling of vehicles (shredders): In average 78.5% of vehicles weight are recycled (about 75% are both ferrous and non-ferrous metals and the rest are plastics, glass, part of Tires, etc.) (93).
- Recycling of construction and demolition waste: In addition to the ferrous material to be recovered, this type of scrap can present high percentages of arid and iron oxide (94).
- Metal Recovered from steelmaking process could present high percentages of slag from EAF (If it is recovered from the EAF deslagging pits or pots) or from LF or refractory materials (If it is recovered from the Ladles or tundish).

According the Institute of scrap recycling industry (ISRI), for example, “All grades shall be free of dirt, nonferrous metals, or foreign material of any kind, and excessive rust and corrosion”. However, the terms “free of dirt, nonferrous metals, or foreign material of any kind” are not intended to preclude the accidental inclusion of negligible amounts where it can be shown that this amount is unavoidable in the customary preparation and handling of the particular grade involved (8)

In the case of EU-27 Steel Scrap Specification given by the European Ferrous Recovery and Recycling Federation (EFR), the ferrous material cleanliness is defined by a combination of constrains: “All grades shall be free of all but negligible amounts of other non-ferrous metals and non-metallic materials, earth, insulation, excessive iron oxide in any form, except for nominal amounts of surface rust arising from outside storage of prepared scrap under normal

atmospheric conditions", "All grades shall be free of all but negligible amounts of combustible non-metallic materials, including, but not limited to rubber, plastic, fabric, wood, oil, lubricants and other chemical or organic substances", "All scrap shall be free of larger pieces (brick-size) which are non-conductors of electricity such as tyres, pipes filed with cement, wood or concrete" and "All grades shall be free of waste or of by-products arising from steel melting, heating, surface conditioning (including scarfing) grinding, sawing, welding and torch cutting operations, such as slag, mill scale, baghouse dust, grinder dust, and sludge" (95).

Category	Specification	Sterile
Old scrap	E3	**≤ 1%**
	E1	**< 1,5%**
New scrap	E2	**< 0,3%**
	E8	**< 0,3%**
	E6	**< 0,3%**
Shredder	E40	**< 0,4%**
Steel turnings	E5H	*Non clear method*
	E5M	*Non clear method*
High residual scrap	EHRB	**< 1,5%**
	EHRM	**< 0,7%**
Fragmentized from incineration	E46	**Fe content ≥ 92%**

Table 8.1: Maximum contents in sterile allowed according to EFR Specification (95)

There are different techniques and methods that allow to separate the sterile from the scrap. According data obtained through the application of some of these methods, when the material delivers to the scrap yard, much higher contents in sterile have been reported by some steelmaking sites than the maximum allowanced in the scrap technical specifications. Table 8.2 shows the chemical composition of sterile estimated for the scrap grades in one ArcelorMittal site in Spain:

	Input A - Metallic Charge	Contents					Total
		FeO	SiO2	Al2O3	CaO	MgO	
1	Imported Bundle E6	2,00	0,50	0,60	0,50	0,00	**3,60**
2	National Bundle E6 (4C)	2,40	0,50	0,60	0,50	0,00	**4,00**
3	Buy Back Bundle E6	0,90	0,50	0,20	0,50	0,10	**2,20**
4	Imported Bushelling E8	2,20	1,00	0,60	1,00	0,50	**5,30**
5	National Bushelling E8	3,50	1,00	0,60	0,50	0,20	**5,80**
6	Buy Back Bushelling E8	2,00	1,50	0,50	0,83	0,11	**4,94**
7	Structural E3 (OA + 3A)	3,00	1,30	0,60	1,00	0,50	**6,40**
8	Structural E1 (1/2 + 1)	4,00	3,50	1,20	1,00	0,50	**10,20**
9	Shredded E40	6,00	1,50	0,80	0,50	0,40	**9,20**
10	Pig Iron (Brasil, Zenica)	1,00	0,40	0,20	0,20	0,10	**1,90**
11	Group Beach Iron	2,00	0,60	0,10	1,50	0,50	**4,70**
12	Beach iron import	2,50	1,50	0,80	2,00	1,00	**7,80**
13	Beach iron import poor	4,00	2,00	1,40	2,20	1,20	**10,80**
14	Venezuelan HBI	7,00	3,00	0,50	0,50	0,30	**11,30**
15	Lybian HBI	10,00	2,00	1,00	0,50	0,20	**13,70**
16	Russian HBI	8,00	4,00	1,00	1,50	0,50	**15,00**
17	Point Lisas DRI	6,00	2,20	0,50	1,20	0,40	**10,30**
18	Pit scrap/skulls 85%	3,90	2,00	1,50	2,50	2,00	**11,90**
19	National E3	3,00	1,30	0,60	1,00	0,50	**6,40**
20	Own	4,00	2,00	0,60	6,00	3,00	**15,60**

Table 8.2: Sterile content estimation in the scrap grades used in one AM site

On the other hand, Fig. 8.1 shows the result of sterile characterization of a sheared scrap (E1) delivery in another ArcelorMittal site in Luxembourg after concrete pad test of one random

scrap delivery. This analysis gives a clear idea of how different elements are distributed in scrap sterile

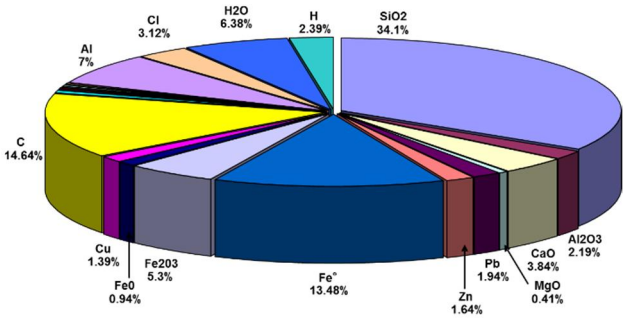

Fig. 8.1: Example of chemical content of the sterile sample after concrete pad analysis

For obtaining this scrap sterile chemical distribution, the most extended analytical procedure used (analysis of an unknown mixture of materials) is based on the X-Ray fluorescent technology, which allows a basic analysis of multiple elements to be carried out in a wide range of materials, being highly precise, quick and non-destructive.

One of the main drawbacks of this procedure lays on the necessity of transporting the samples to laboratory facilities and preparing the sample before analysing it (high time consuming).

Also, this type of characterization methods are spot methods and so that they are used mainly for scrap supplier tracking. However, It is important to keep in mind that the basic purpose of the scrap yard in the steel plant is to have enough scrap (of the different types) to make the furnace running without any stop due to lack of scrap. So the only way to ensure this function is doing scrap mixtures in the scrap yard grouping scrap by similarities in terms of ferrous specifications, where aspects like scrap origin, pre-treatment process, oxidation degree or sterile quantity or quality are not taken into consideration. And that is why these characterization methods are not suitable for the systematic control of the scrap quality allocated in the scrap yard in the daily management operations.

Nowadays, there is no industrial method to keep characterized the sterile in scrap on site. However, there is no doubts among steelmakers that it is necessary to develop new techniques that allow fast qualitative characterization of sterile contained in scrap piles.

In this line, characterization methods based on spectroscopy techniques (the study of interaction of electromagnetic radiation with matter) have got a great potential.

Different spectroscopic methods are frequently used for the characterization of a wide range of samples from different nature. These methods are used for qualitative and quantitative analysis of samples. The qualitative analysis is performed to establish the identity of sample while quantitative analysis is performed to estimate the constituent compounds of in sample. Some of the spectroscopic methods (e.g. UV–Vis Spectrophotometry) are used as a screening method since it gives the tentative identification of sample and are not specific in nature while other spectroscopic methods (e.g. Infrared Spectroscopy and Mass Spectrometry) are used as a confirmatory method since they give the reliable identity of sample and are specific in nature.

New method proposal for chemical characterization of sterile material in scrap.

In this research activity, the capability of three analytical methods, based on spectroscopy technology, for scrap sterile characterization have been analysed:

1. Raman spectroscopy
2. FTIR spectroscopy
3. Hyperspectral imaging

8.1 RAMAN Spectroscopy

The Raman scattering effect arises from the interaction of the incident light with the electrons of an illuminated molecule. In Raman spectroscopy, the energy of the incident light is not enough to excite the molecule to a greater electronic level of energy. Thus, the result of the Raman scattering is the change in the vibrational state of the molecule.

Raman spectroscopy technique involves shining a monochromatic light source (i.e. laser) on a sample and detecting the scattered light. The scattered light having a frequency different from that of incident light (inelastic scattering) is used to construct a Raman spectrum. Raman spectra arise due to inelastic collision between incident monochromatic radiation and molecules of sample. When a monochromatic radiation strikes at sample, it scatters in all directions after its interaction with sample molecules. Much of this scattered radiation has a frequency which is equal to frequency of incident radiation and constitutes Rayleigh scattering. Only a small fraction of scattered radiation has a frequency different from frequency of incident radiation and constitutes Raman scattering. When the frequency of incident radiation is higher than frequency of scattered radiation, Stokes lines appear in Raman spectrum. But when the frequency of incident radiation is lower than frequency of scattered radiation, anti-Stokes lines appear in Raman spectrum.

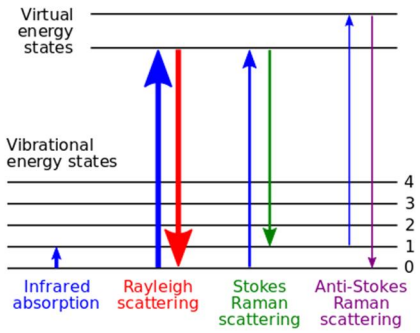

Fig. 8.2: Energy-level diagram showing the states involved in Raman spectra (96)

The energy difference between the incident and scattered photons is represented by the arrows of different lengths in Fig. 8.2. Numerically, the energy difference between the initial and final vibrational levels, V, or Raman shift in wave numbers (cm^{-1}), is calculated through (8.1) in which λ incident and λ scattered are the wavelengths (in cm) of the incident and Raman scattered photons, respectively.

$$v = \frac{1}{\lambda incident} - \frac{1}{\lambda scattered} \qquad (8.1)$$

When the energies of these transitions are plotted as a spectrum, they can be used to identify the molecule as they provide a “molecular fingerprint” of the molecule being observed.

New method proposal for chemical characterization of sterile material in scrap.

8.1.1 Literature survey about Raman spectroscopy

This research activity proposes to analyse the potential of developing a new in-line analytical technique for the characterization of sterile materials contained in scrap by Raman spectroscopy. To this end, it is proposed the adaptation of conventional Raman spectroscopy laboratory techniques to industrial steelmaking processes.

Before defining any experiment, it is necessary to review the existing knowledge to define the starting point of this research, as well as, to define the trials conditions, in terms of equipment to be used, sensors calibration and mathematical processing of the spectral data acquired.

This initial definition phase will guarantee that the conclusions obtained after laboratory tests are extrapolated to real industrial conditions.

Even though a Raman system is conceptually simple, the Raman effect is weak. The selection of each instrumental components that will compose an integrated system for substances chemical characterization is critically important. Only an optimized system can be capable of producing the greatest measurement potential, over the widest range of same types, and able to measure the lowest concentration of species in the shortest amount of time possible.

Fig. 8.3 shows a diagram of the different components that compose a Raman spectrometer

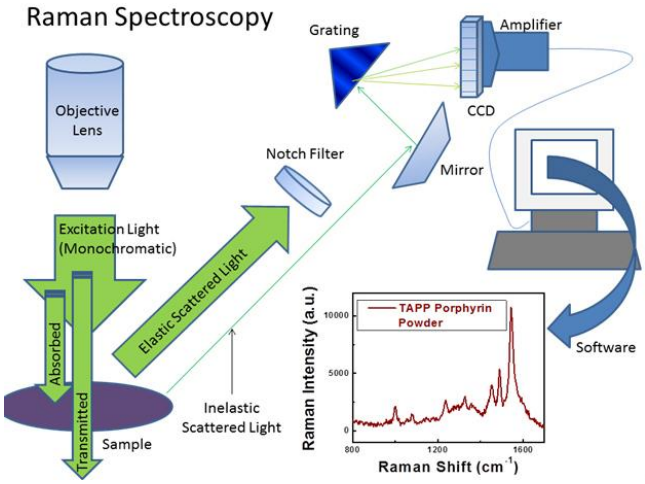

Fig. 8.3: Description of component in Raman spectroscopy (97)

The main components of an analytical system based on Raman technology are the Spectrograph and the Excitation Laser. Next, the main aspects to be considered when selecting the most appropriate elements for a particular application are detailed:

- Spectrograph:
    - Spectral Range: Raman shift range is specified in wavenumbers (cm^{-1}). Most spectrographs cover at least the "fingerprint region" from 400 - 1800 cm^{-1}; this is where the majority of vibrational bands occur. Below 400 cm^{-1}, there are vibrations associated with heavier atoms, such as C-halogen and metal oxide stretches. Other bending modes can occur at these lower frequencies as well.

On the other end, C-H stretches occur between 2900 - 3100 cm^{-1}, and the O-H/N-H stretches are visible up to 3600 cm^{-1}. There is little between 1800 and 2900 cm^{-1}, except for nitrile (CN) bands occurring near 2200 cm^{-1}. For many applications, the fingerprint region is sufficient for both quantitative and qualitative analysis.

- Spectral Resolution: The resolution of the spectrograph determines how well individual bands can be separated in the spectrum. Resolution should be specified as full width at half height (FWHH) of a measured band. Raman bands of solids are typically 2-6 cm^{-1} wide, and those of liquids can be 4-10cm^{-1} wide. Having a spectrometer that can measure close to the natural linewidths of the vibrational bands provides the most information. For simple applications, lower resolution spectrographs may be applicable.
- Spectral Throughput: Corresponds with the numbers of photons that will pass through to the detector. However, a complete Raman system is a sum of its parts, from the laser, to the sampling optics, to the spectrograph, to the detector. Throughput values are relevant, but overall performance is more important when comparing systems.
- Detector Sensitivity: Most dispersive Raman spectrographs employ CCD (charge coupled device) detectors. These are one- or two-dimensional arrays of silicon elements. In general, the dark noise of the CCD is reduced by 50% with every 5 degree drop in operating temperature. Most research-grade spectrographs employ vacuum-sealed arrays operating between -50 and -90C for highest sensitivity. Less expensive detectors can be used for applications that can afford less sensitivity.

- Excitation Laser
  - Excitation Wavelength: Raman scattering intensity is proportional to v4, where v is the excitation frequency. Therefore, higher excitation frequencies (i.e. shorter wavelengths in the visible and UV regions) provide higher Raman intensity than longer wavelengths. Unfortunately, shorter wavelengths can also excite fluorescence backgrounds in many samples, obscuring the Raman bands. For many general applications, near-IR excitation at 785 nm is preferred.
  - Laser Characteristics: There are many types of lasers available to the Raman spectroscopy. Traditional gas lasers provide stable, narrow lines, but are becoming less commonly used.
    - Diode lasers differ widely in the marketplace.
    - Single-mode diode lasers provide narrow linewidths but are usually low in power and require temperature stabilization to prevent mode hopping.

New method proposal for chemical characterization of sterile material in scrap.

- Multi-mode diode lasers can provide very high power, but the output can be as wide as 30 cm^{-1}. Multi-mode lasers can also be stabilized to produce a single-mode output; these lasers are usually associated with higher cost.

Raman spectroscopy is a versatile method for analysis of a wide range of samples, resolving most of limitations of other spectroscopic techniques (98). It can be used for both qualitative as well as quantitative purpose;

- Qualitative analysis can be performed by measuring the frequency of scattered radiations.
- Quantitative analysis can be performed by measuring the intensity of scattered radiations: The spectra are very specific, and chemical identifications can be performed by using search algorithms against digital databases since band areas are proportional to concentration.

8.1.1.1 Industrial Application of Raman spectroscopy

Numbers of papers describing the utility of Raman spectroscopy are available in the literature. Raman spectroscopy has been proved to be valid in different fields; applications in materials detection/identification in agriculture like soil characterization (99) (100) (101), agricultural products identification, (102) pesticide residues detection on fruit (103) or soil organic matter quality assessment (104) (105) (106). In pharmaceuticals industry for detecting counterfeit and adulterated pharmaceuticals (107). In geology for mineral identification (108) (109).

Maybe the sector in which the highest application boom has undergone developments based on Raman portable spectroscopy for the chemical identification of substances is law enforcement/first responders, associated with the rapid identification of drugs (110).

From an industrial point of view, Raman spectroscopy has been mostly used in recycling industry (i.e. to identify plastics for recycling (111)).

As regards the steel industry, the main references of Raman techniques application for materials characterization have been found in the field of coals characterization. In 2011 was published a RFCS project that aimed to optimise reductant utilisation in the blast furnace in order to minimise environmental emissions and allow more stable and efficient operation at high injection levels. To do so, Raman technique was used for determining the nature and origin of the carbon directly in the exhaust gases raceway (112). Later, in 2015 another RFCS project was published in which the work was concentrated on optimizing the coal blends composition and prediction of coke quality and in which Raman spectroscopy was used for evaluating the coke structure in relation to its optical texture (113).

In spite of the high potential of the application of Raman spectroscopy to the rapid characterization of materials (i.e. chemical composition of the sterile materials contained in the scrap), no previous bibliographic references of this approach have been found. This may be

New method proposal for chemical characterization of sterile material in scrap.

because process control and real-time on-site monitoring of chemical analyses in the field under severe industrial conditions require the use of portable and robust equipment.

8.1.1.2 Prior spectra knowledge

It is not necessary to start from scratch for defining the main requirements when developing a new sensor based on RAMAN technology; from acquiring spectra to train the data analysis models. There are several resources contained Raman spectra data bases that can be helpful to define the starting point of this investigation:

1. Handbook of Minerals Raman Spectra (114)
2. RRUFF Project: website containing an integrated database of Raman spectra, X-ray diffraction and chemistry data for minerals (115)
3. Spectral Database for Organic Compounds SDBS (116)
4. Raman Spectra of Carbohydrates (117)

From these data bases, it is possible to extract the spectral Raman responses of interest. As shown in Fig. 8.1, the main oxides present in scrap sterile are FeO, Fe_2O_3, SiO_2, CaO, MgO and Al_2O_3.

8.1.1.2.1 CaO Raman spectra data

Raman spectroscopy is a fully consolidated laboratory technique for the characterization of carbonated minerals. As regards lime, its use has been reported mainly for:

- Characterizing and differentiating calcite minerals from dolomite minerals.
- Determining the mineral structure; The conversion of lime to calcium hydroxide and its subsequent carbonation to various calcium carbonate polymorphs
- Allowing the detection of all three $CaCO_3$ polymorphs (calcite, aragonite and vaterite) phases
- Analysing the degree of calcination in the external and the internal volume of the samples

The $(CO3)_2$ group is characterized by four prominent Raman vibrational modes:

a. The symmetric stretching of CO3 group (v1)
b. The asymmetric deformation (v2) – This vibration mode does not appear
c. Asymmetric stretching mode (v3)
d. Symmetric deformation mode (v4)

New method proposal for chemical characterization of sterile material in scrap.

Also, it is important to clarify that some differences have been found in the position of the characteristic bands reported by the different authors. These differences can be justified by the fact that both the configurations of the experiments and the characteristics of the equipment used vary from one to another.

For convenience, the study of Raman spectra for lime materials are divided into three spectral range sections (108) (118);

- 1700–1200 cm^{-1} attributed to (*v1*): The Raman spectra of calcite in the 1700–1200 cm^{-1} region is shown in Fig. 4.

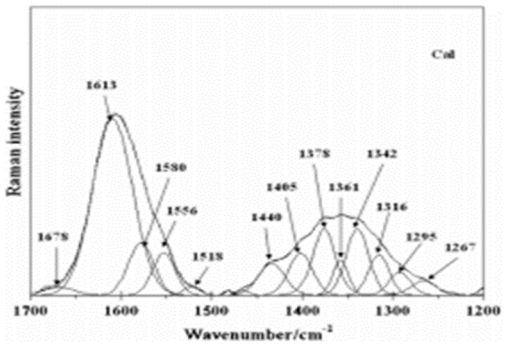

Fig. 8.4: Raman spectra of the calcite in 1700–1200 cm^{-1} region

In this wavenumber region the following can be observed;

  - The bands observed at 1678 cm^{-1} are assigned to the water bending mode.
  - The bands observed at 1613, 1580, 1556 and 1518 cm^{-1} may be regarded as the combination band of the asymmetric stretching in this region
  - The observed splitting at 1440, 1378, 1342, 1316, 1295 and 1267 cm^{-1} suggests that the carbonate groups are slightly distorted and are in the amorphous state. It is proposed that this splitting also indicates the prevalence of low pressure during the formation of the mineral. For calcite, the $(CO_3)_2$ asymmetric stretching modes are observed at 1440, 1405, 1378, 1361 and 1342 cm^{-1}.

In the case of Aragonite, the Raman lines attributed to the v3 asymmetric stretching mode can be observed at 1461 and 1573 cm^{-1}.

In general, the bands discussed above seem to be characteristic of the carbonate minerals.

- 1200–600 cm^{-1} attributed to (v3): The Raman spectra of calcite in the 1200– 600 cm^{-1} regions are shown in Fig. 8.5.

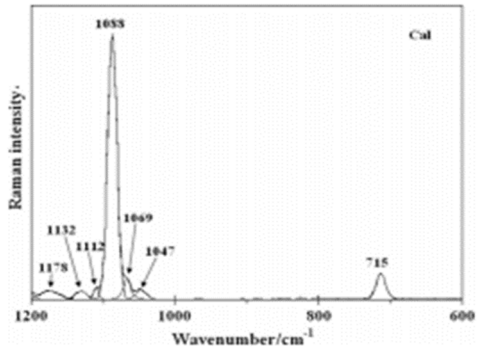

Fig. 8.5: Raman spectra of the calcite in 1200–600 cm^{-1} region

In this region, an intense sharp Raman band at 1088 cm^{-1} is observed for calcite. This band is assigned to the v1$(CO_3)_2$ symmetric stretching mode. It is reported that the position of this band is a function of the crystal structure of the carbonate mineral

For Aragonite, the strong Raman line attributed to the v1 symmetric stretching mode of the carbonate group can be found at 1083 cm-1, and there are some Raman bands at 693, 700 and 701 cm^{-1} assigned to the v4 normal mode.

- 500–100 cm^{-1}assigned to (v4): The Raman spectra of calcite in the 500– 100 cm^{-1} region are shown in Fig. 8.6.

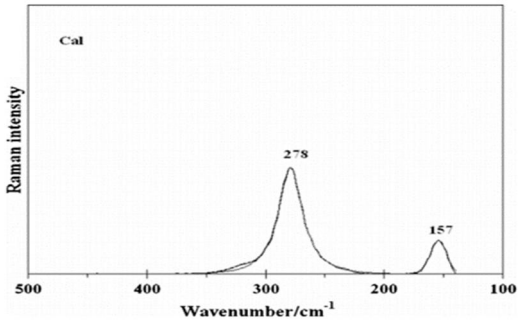

Fig. 8.6: Raman spectra of the calcite in 600–100 cm^{-1} region

In the low wavenumber region of the Raman spectra of calcite, two bands at 278 and 157 cm^{-1} are observed. These two lower wavenumbers bands arise from the external vibrations of the $(CO_3)_2$ group that involve the rotatory and translatory oscillations of those groups.

The Raman bands due to the external vibration mode for Aragonite can be found at 250 cm^{-1}

It is also possible to found in bibliography some references related to the spectral behaviour of fresh lime mineral when expose to moisture, that can be also interesting within the scope of this investigation (119).

According these sources, Raman spectroscopy has been proved to be a suitable technique for those material characterizations.

New method proposal for chemical characterization of sterile material in scrap.

Raman spectra of the CaO samples exposed to different relative humidity are presented in the next Figure:

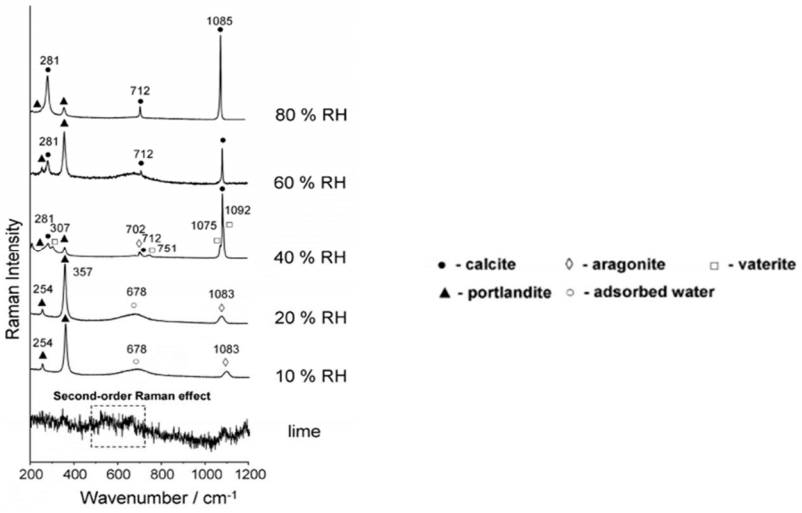

Fig. 8.7: Raman spectra of fresh and exposed CaO to moist air showing the formation of different hydration and carbonation products (119)

8.1.1.2.2 MgO Raman spectra data

All mentioned in the previous section for analysing the Raman spectra of Lime also applies when magnesium oxides are analysed.

The difference between calcite and dolomite is explained on the basis of the structure variation of the two minerals. Calcite has a trigonal structure with two molecules per unit cell, and dolomite has a hexagonal structure. This is more likely to cause the splitting and distorting of the carbonate groups. Another cause for the difference is the cation substituting for Mg in the dolomite mineral.

So that, as occurs with lime, the Raman spectra of MgO samples are divided into three spectral range sections (108) (120) (121);

- 1700–1200 cm^{-1} attributed to (v1): The Raman spectra due to MgO in the 1700–1200 cm^{-1} region are shown in Fig. 8.8.

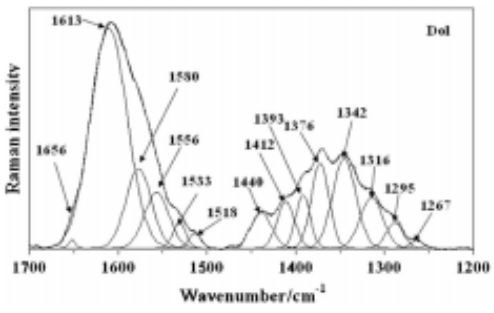

Fig. 8.8: Raman spectra of Dolomite in 1700–1200 cm^{-1} region

New method proposal for chemical characterization of sterile material in scrap.

- 1200–600 cm^{-1} attributed to (v3): The Raman spectra of Dolomite in the 1200–600 cm^{-1} region is shown in Fig. 8.9. In this region, dolomite minerals show an intense sharp Raman band at 1092 cm^{-1} is accompanied by two satellites having values of 1098 and 1088 cm^{-1}.

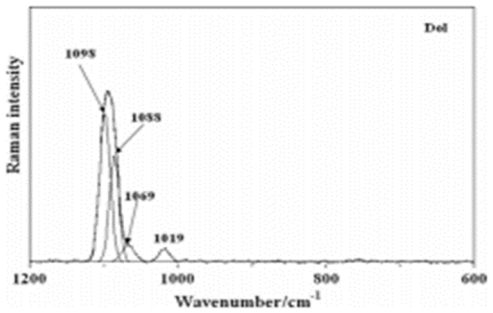

Fig. 8.9: Raman spectra of the Dolomite in 1200–600 cm^{-1} region

- 500–100 cm^{-1}assigned to (v4): The Raman spectra of Dolomite in the 500– 100 cm^{-1} region are shown in Fig. 10.

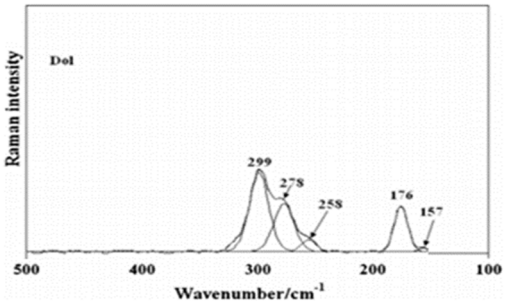

Fig. 8.10: Raman spectra of the Dolomite in 500–100 cm^{-1} region

The three lower wavenumber bands at 299, 258 and 176 cm^{-1} are observed in the Raman spectrum of dolomite:

- The relatively intense band at 299 cm^{-1} is attributed to the MgO symmetric stretching vibration.
- The low intensity band observed at 258 cm^{-1} is probably due to a function of the cation substituting for Mg in the dolomite mineral.
- The band at 176 cm^{-1} may be attributed to O-Mg-O bending modes.

Two additional bands at 278 and 157 cm-1 are also observed in the Raman spectrum of dolomite.

It is also possible to found in bibliography some references related to the transitions in Raman spectral signature from pure calcite mineral to pure magnesite (going through different dolomite compositions). This information can also be useful to understand the experimental results of the present research (108)

New method proposal for chemical characterization of sterile material in scrap.

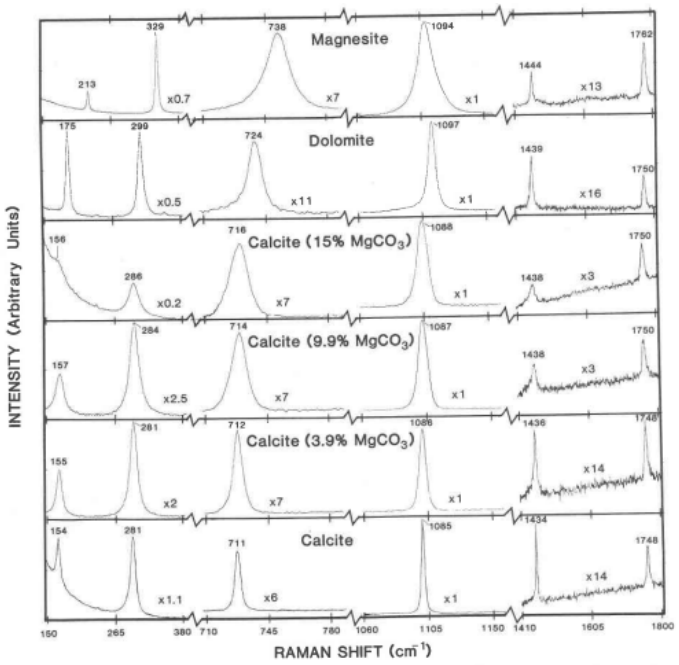

Fig. 8.11: Raman spectra of calcite, synthetic magnesian calcites, dolomite and magnesite

8.1.1.2.3 SiO_2 Raman spectra data

Silicates have as structural unit the tetrahedral molecule. These tetrahedral can share each of their vertices (oxygen atoms) and in this way it is possible to build a vast array of structures such as chains, planes and infinite three-dimensional networks. These structures essentially form giant molecules.

When silicon atoms are replaced by other types of atoms, the diversity of such structures increases (crystalline silicates)

In structures where each of the four vertices of the tetrahedron is connected to another tetrahedron, an infinite three-dimensional network is built. The chemical formula is known as SiO_2 (Silicon dioxide) and since each oxygen atom is shared by two silicon atoms, the stoichiometry is $SiO_{(4.2)} = SiO_2$.

It is possible to find several crystalline structures other than SiO_2 (quartz, Cristobalite, Coesite, Tridimine and Stishovite). The non-crystalline (amorphous) form of this structure is known as silicate glass.

So that the first study when analysing the Raman behaviour of SiO_2 is whether it presents a crystalline or amorphous state.

Fig. 8.12 shows typical silicon spectra from samples that range from pure crystalline top (strong band at 521 cm^{-1}) to those containing significant amounts of amorphous material bottom (broad band centred at 480 cm^{-1}) (122).

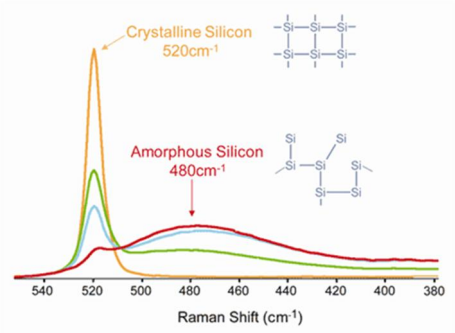

Fig. 8.12: Raman spectra of calcite, synthetic magnesian calcites, dolomite and magnesite

Some considerations must be taking into account when Using Raman Spectroscopy for Silicon Analysis (123):

- Laser power: some experiments show that as the power of the excitation laser is increased above a threshold, amorphous silicon is converted to the crystalline form.
- Laser wavelength: There are three potentially important effects of excitation laser wavelength on this application: Raman efficiency, sample penetration depth and fluorescence.
    - Since Raman scattering efficiency is proportional to 1/λ4, the signal is much stronger using short wavelength lasers.
    - Penetration of the laser into the silicon also diminishes with shorter excitation laser wavelengths.
    - Fluorescence is also excitation wavelength-dependent. Fluorescence is potentially capable of overwhelming the Raman scattering signal and should be avoided. Silicon fluoresces much more strongly at 780 nm than it does at 532 nm.

When the Raman spectrum of the crystalline structures of SiO_2 need to be understood, it is easy to find the characteristic spectrum associated to those structures from the general data bases of Raman spectra commented in previous sections

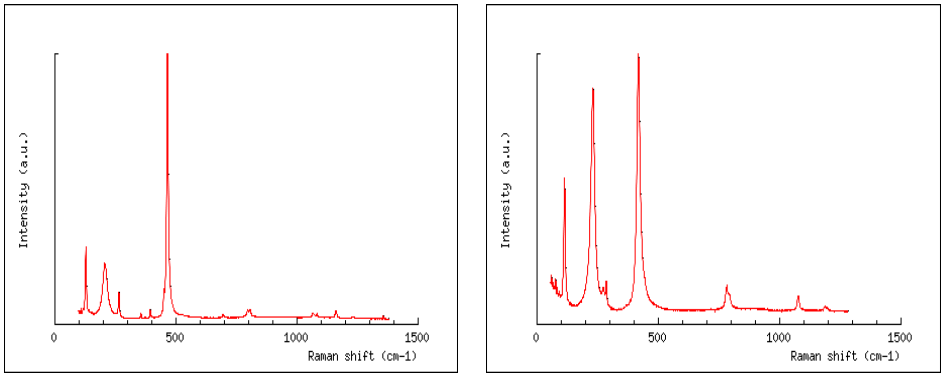

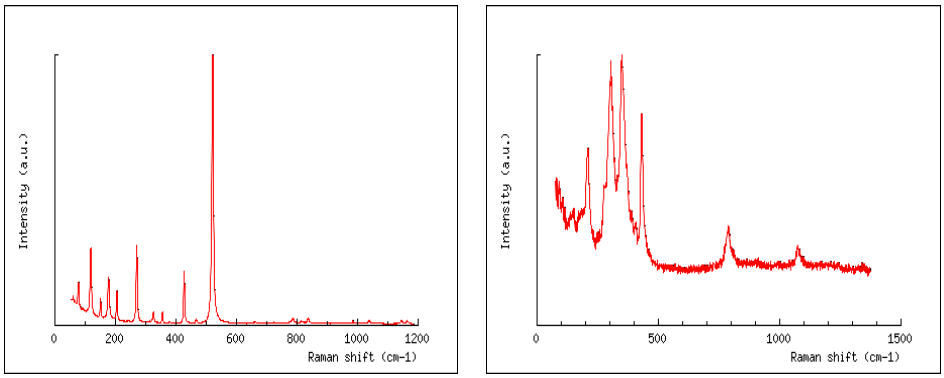

Fig. 8.13: Raman spectrum at 514.5 nm: Up-Left) quartz, Up-Right) Cristobalite, Down-Left) Coesite and Down-Right) Tridymite

In the particular case of amorphous structures of SiO_2, it is characterized by three prominent Raman vibrational modes (124):

- The symmetric stretching mode; this vibrational mode is mainly manifested in the range 400-600 cm^{-1}. In this region, three peaks can be found, a broad band at 450 cm^{-1}, and two narrow peaks closed to 495 cm^{-1} and 600 cm^{-1}.
- The symmetric bending mode; This mode appears in this same spectral region than TO1 and also in 800 cm^{-1}.
- Asymmetric stretching mode: This vibrational mode causes the most prominent peak, which is located around 1075 cm^{-1}, where a main peak appears at 1075 cm^{-1} and a shoulder about 1200 cm^{-1}

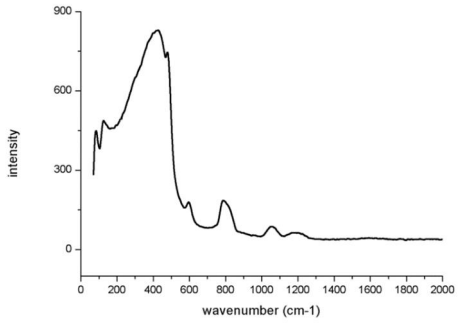

Fig. 8.14: Raman Spectra of amorphous SiO_2

8.1.1.2.4 Iron oxides Raman spectra data

Although during the corrosion of the steel several products such as hydroxides (white rust), carbonates and sulphates (black rust) are produced, in this section only the different iron oxides generated are analysed.

The main products of iron corrosion are iron oxides, which strongly absorb infrared radiation but are usually poor light scatters. So that, standard methods for the identification and

New method proposal for chemical characterization of sterile material in scrap.

characterization of iron oxides have traditionally been X-ray diffraction (XRD) and/or Mössbauer spectroscopy (MS). Due to the complexity of steel corrosion products, normally a combination of analytical techniques including Raman and infrared spectroscopies are commonly used.

In the particular case of Iron oxides compounds with one or many strong covalent-bonded vibrational units, Raman signature characterized can be separated in four groups (125):

- Symmetric stretching modes, for instance Fe_2-O and/or Fe_3-O modes peaking in the 400-700 cm^{-1} region for oxides, 300-600 cm^{-1} for chlorides, 200-400 cm^{-1} for sulphides. In symmetric modes, the strongest ones, only oxygen atoms move and thus the peak wavenumber mainly depends on the Fe-O distance. These modes are very sensitive to oxygen vacancies that broaden the peaks.
- Bending modes peak at lower energy, namely 400-500 cm^{-1} range for oxides or less for chlorides, sulphides. They are very sensitive to the short range disorder in the first neighbouring shell (1-5 nm around the chemical bond) and their broadness can be very informative on the short-range (dis)order. Because the mean symmetry often broke the symmetry of the vibrational units, many components are frequently observed.
- Vibrational (orientational oscillations, 150-400 cm^{-1} range) and lattice modes (<200 cm^{-1} range):
    - Vibrational modes are very sensitive to the short range disorder of the vibrational entities (i.e. FeO_4 tetrahedron);
    - Lattice modes reflect the long range crystalline order, like X-ray diffraction, and strongly depend on atom mass.
- Additional features (combination, harmonics…) consisting bands between 1000 and 1500 cm^{-1}: their origin lies in the interaction between electronic (and magnetic) levels and the light because the laser beam wavelength interacts with the electronic levels.

The analysed iron oxides in this section are:

- Red iron oxide (Haematite, α-Fe_2O_3):

  The most representative bands of hematite are around 225 cm^{-1} and 290 cm^{-1}. These bands of hematite are two of the seven Raman most representative bands. These two bands were taken for quantitative analysis by some authors (126). The remaining five characteristics bands at about 245, 300, 410, 495 and 610 cm^{-1}. From the literature (125) (126) (127), characteristic band at 225 and 495 cm^{-1} are attributed to the Fe-O symmetric stretching vibrational mode and bands at 245, 290, 410 and 610 cm^{-1} may be attributed to Fe-O symmetric bending modes. There is another characteristic band at about 1317.8 cm^{-1} which is close to the magnetite at approximately 1304.9 cm^{-1}. This causes an overlapping in vibrations when these two phases are mixed, making difficult their identification by using those bands.

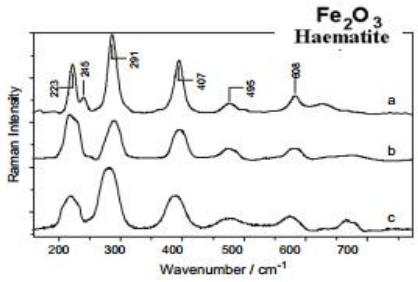

Fig. 8.15: Raman spectra of hematite from various sources: (a) commercial hematite; (b) hematite from pure starting material and (c) hematite from mill scale (128).

- Yellow iron oxide (Goethite, α-FeOOH):

  Goethite is one of the most widespread forms of iron oxides in terrestrial soils, sediments and ore deposits, as well as a common weathering product in rocks of all types.

  The band of goethite that stands out over other active modes in Raman spectra can be found at around 390 cm^{-1}, and it corresponds with symmetric stretching vibrational mode provokes with Fe-O-Fe / -OH structure. On the other hand, characteristic band at 297 cm^{-1} is attributed to the Fe-O symmetric bending modes. Some authors (127) attribute bands at 565 and 1000 cm^{-1} to Fe-OH asymmetric stretching vibrational mode. The band at about 560 cm^{-1} does not appear in other iron oxides, therefore, it could be used for the quantification of goethite in unknown materials.

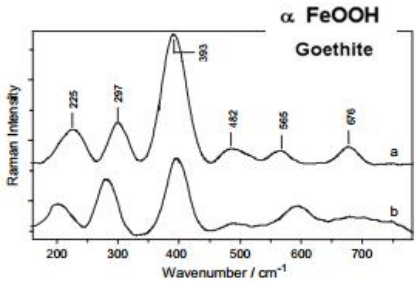

Fig. 8.16: Raman spectra of goethite from (a) pure starting material and (b) mill scale (128).

- Brown iron oxide (Maghemite, γ-Fe_2O_3):

  The most representative bands of hematite due to symmetric stretching vibrational mode of Fe-O are around 360, 665 and 721 cm^{-1} and 290 cm^{-1}. The characteristic band at 499 cm^{-1} is attributed to the Fe-O asymmetric bending modes.

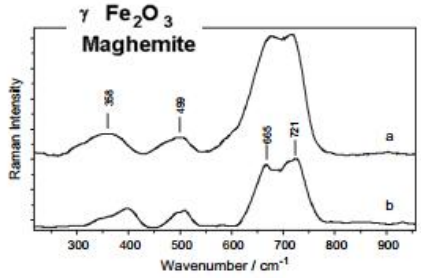

Fig. 8.17: Raman spectra of maghemite from (a) pure starting material and (b) mill scale (128).

New method proposal for chemical characterization of sterile material in scrap.

- Black iron oxide (Magnetite, Fe_3O_4):

  In the case of Magnetite, there are two bands related to the Fe-O asymmetric bending mode at 298 and around 530 cm^{-1}. The most representative bands are located at 667cm^{-1} and are attributed to the symmetric stretching vibrational mode of Fe-O. The characteristic band at about 310 cm^{-1} is attributed to the Fe-O symmetric bending.

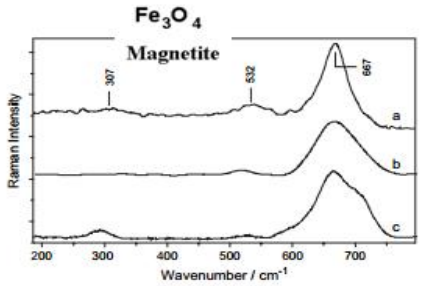

Fig. 8.18: Raman spectra of magnetite from various sources: (a) commercial magnetite; (b) magnetite from pure starting material and (c) magnetite obtained from mill scale (128).

8.1.2 Laboratory equipment for spectral analysis

As it was explained before, the key elements in a Raman system are the Spectrograph, the Excitation Laser and the optical elements. The equipment used for conducting the analysis proposed in this section were:

- **Wavelength Stabilized Laser by Innovative Photonic Solution**: This laser corresponds with a 785 nm stabilized Raman Laser and it allows high output power with narrow spectral bandwidth.

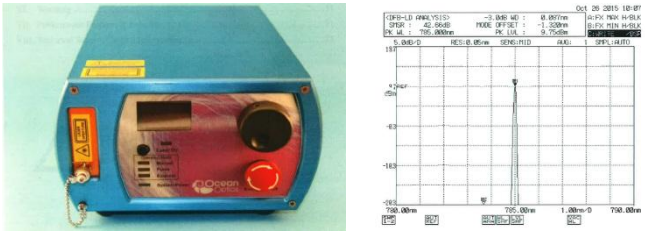

Fig. 8.19: Laser device and typical 785 nm Stabilized Laser Spectrum

- **QE Pro Ocean Optics spectrometer**: The Ocean Optics QE Pro Spectrometer is a scientific-grade spectrometer ideal for researchers. Its broadband sensitivity, from UV to NIR, makes it suitable for a wide range of applications, while its high sensitivity and thermo electric cooler enable effective measurements at very low light levels.

Detector:	
Type:	Hamamstsu scientific grade, back-thinned,
Range:	185-1100 nm
Spectroscopy:	
Wavelength range:	780-1000 nm
Raman shift:	0-2800 cm^{-1}
Resolution:	7 – 11 cm^{-1}
Integration time:	8 ms to 60 min
Dynamic range:	85000:1
Signal-to-noise-ratio:	1000:1

Fig. 8.20: Spectrometer technical characteristics

- **Ocean Optics Raman RPB probe:**

Probe Specifications:	
Excitation wavelengths:	532, 638, 785 and 1064 nm
Spectral range:	300 – 3900 cm-1
Sampling head:	Anodized aluminium
Probe length / diameter:	107 mm - 12.7 mm
Working distance:	7.5 mm
Fiber configuration:	Excitation and collection fibers; 0.22 NA
Fiber connectors:	FC and SMA 905

Fig. 8.21: Capturing equipment (probe)

New method proposal for chemical characterization of sterile material in scrap.

- **Renishaw's InVia Raman** equipped with a green laser of 514 nm wavelength as excitation sources and a CCD detector

Probe Specifications:	
Spectral range:	200-2200 nm
Laser compatibility:	229-1064 nm
Spectral resolution:	0.3 cm-1 (FWHM)
Lower wavelength threshold:	5 cm-1
Higher wavelength	30000 cm-1
Detector size:	1024 x 256

Fig. 8.22: InVia Raman Spectrometer technical characteristics

- For the capture, the visualization and the processing of the spectra, a PC equipped with **OceanView software** by OceanOptics was used. This software allows performing absorbance, reflectance and emission analysis, as well as absolute irradiance and Raman. Other signal-processing functions such as electrical dark-signal correction, boxcar pixel smoothing, and signal averaging were also available

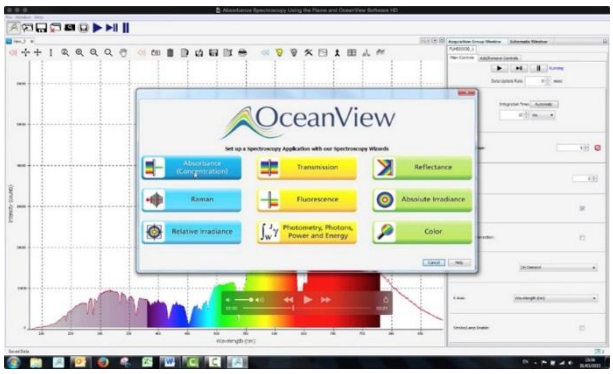

Fig. 8.23: OceanView software snapshot

8.1.3 Data processing algorithms

For analysing the acquired Raman signals and to extract the maximum spectral information, as well as to stablish the comparative criteria between different samples, two types of algorithms were used:

- **Signal processing algorithm**: The purpose of this processing algorithm is to improve and normalize the acquired signal to extract the maximum available information from it and to allow comparing spectra form several sampling campaigns. This algorithm consists of several processing levels:
    - Removal of the continuous component of the signal; This processing allows filtering the fluorescence of the acquired signal and it basically consists on:
        - Low-pass spectrum calculation using high-sigma Gaussian convolution filter.
        - Elimination of the calculated low-pass signal.
    - Signal smoothing: filtering noise by the convolution of a Gaussian filter (Savitzky-Golay filter (129)).
    - Desaturation (subtracting the minimum to start at 0)
    - Standardization (dividing by standard) (130)

Fig. 8.24 shows spectral signal transformations after each mentioned processing step:

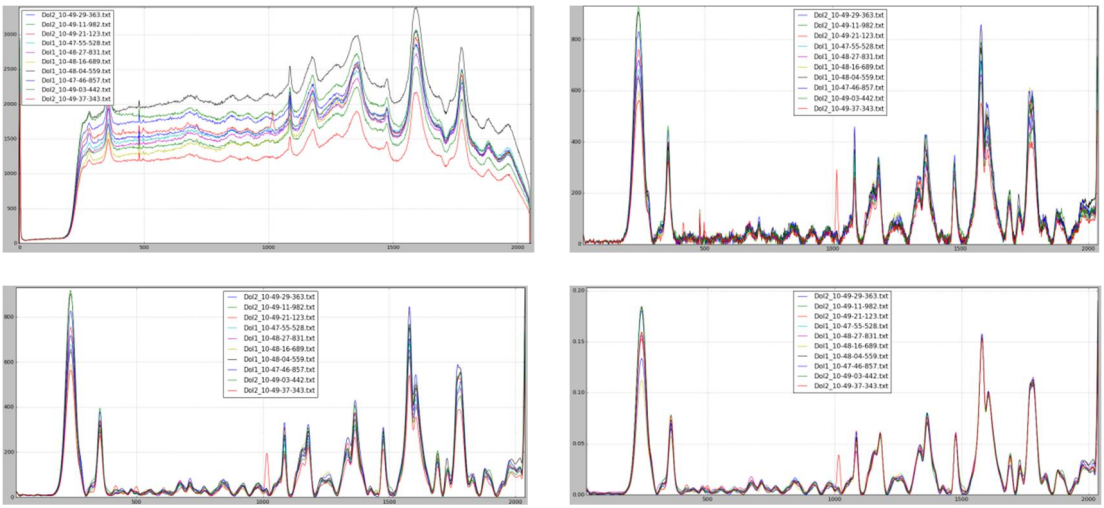

Fig. 8.24: Spectra processing steps: Top-Left: raw signal, Top-Right: continuous component removal, Bottom-Left: Signal smoothing and Bottom-Right: Signal Standardization

- **Chemical composition estimation** assuming a linear mixture model to calculate the percentage (abundance) of each base spectrum (endmember) in the observed Raman spectrum of the mixture.

New method proposal for chemical characterization of sterile material in scrap.

Due to signal complexity and high overlap between classes, classical unmixing methodologies based on linear methods do not yield appropriate results. To overcome this problem the Dobigeon Bayesian algorithm (131) (132) is adapted as a Bayesian generalization of a linear unmixing model on the normalized hyperspectral images of the different samples.

$$y = \sum_{r=1}^{R} m_r \alpha_r + n \tag{8.2}$$

Where; ***y*** is the observed spectrum, ***m*** is each endmember (base) spectrum and each ***α*** value is related to the spectral abundance of each endmember and ***n*** represents the noise.

The ***α*** set follows the following constraints:

$$\forall r \in \{1, \dots, R\}, \alpha_r \geq 0 \; and \sum_{r=1}^{R} \propto_r = 1. \tag{8.3}$$

Based on this model, a set of statistical variables were defined:

Variable	Distribution	Notes
Alpha	Dirichlet distribution	This assure positivity and sum=1
Sigma	Half Normal	Sd=1
M	Observed data	Observed pure reflectance desaturated vectors

Table 8.3: Statistical variables in the linear mixture model

The probability is defined as a normal distribution between the observed and the reconstructed spectra by the statistical variables

$$f(y \mid \alpha^+, \sigma^2) = \left(\frac{1}{2\pi\sigma^2}\right)^{\frac{L}{2}} \exp\left[-\frac{\|y - M^+\alpha^+\|^2}{2\sigma^2}\right] \tag{8.4}$$

In order to calculate the statistical distribution of the observed variables, the Bayesian Markov chain Monte Carlo algorithm (MCMC) is applied. The MCMC estimation method allows to obtain the most probable probability of abundance and its statistical distribution. Also, the distribution of the different abundances is calculated.

8.1.4 Capturing procedure – Experimental set up

The laboratory phase aims to determine the most suitable capturing conditions under controlled laboratory conditions (lighting, temperature, environmental pollution, sample preparation). For this purpose, artificially prepared samples with well-defined chemical compositions are used, so that, and supported by previous bibliographical references, it will be possible to establish the processing and analysis patterns of the spectral signatures obtained, which will then be applied under real industrial conditions.

In this section, the different method used for spectral acquisition during laboratory tests are described, but, before going further, there are some considerations that must also be considered to define the experimental set up of the analytical instruments during laboratory tests:

Laser power: This parameter affects the shapes and intensities of the bands resulting from the sample under investigation. The increase in laser power may result in band broadening and shifts. The increase in laser power may destroy the sample or transform it into a different chemical phase. The laser power may range from a few milliwatts (0.1 mW) to several hundreds. As the laser power is increased the Raman band intensities may increase but the baseline starts to increase at high Raman shift because of the effect of sample heating. Therefore, it must be careful to select the appropriate laser power to maximise the signal-to-noise ratio and minimise black-body radiation caused by the sample heating.

Sample recording time: Some compounds, i.e. silicates, are weak Raman scatters and short time recordings may not yield any peaks. However, with longer recording times the results improve. Therefore, the extension of recording time increases the efficiency and sensitivity of Raman spectroscopy. However, for heat sensitive samples degradation may occur as the recording time is lengthened.

Number of scan accumulations: The number of scan accumulations is closely linked to the recording time. When the sample recording is accompanied by more accumulations, there is an increase in efficiency and sensitivity. One distinct advantage that stems from the increased accumulations is the increase in the signal-to-noise ratio. The recordings using more accumulations result in more pronounced Raman peaks. However, increasing the number of accumulations can result in a different spectrum.

The used experimental set up are described below and shown in Fig. 8.25 and Fig. 8.26:

- **Capturing through pipette:** The first experimental set up consisted on acquiring spectra information from the different materials contained in a pipette. With this capturing procedure the spectral information of the sample is acquired through pipettes, so that for a fixed configuration between the Raman probe and the pipette, the operation consists only in exchanging the different pipettes filled with the samples looking for guarantying the repeatability of the analyses. This experimental configuration allows setting the capturing distance.

  For this proposal set up, the capturing parameters were:

New method proposal for chemical characterization of sterile material in scrap.

- Acquisition time: 800 ms
- Spectral averaging: 3 samples

- **Direct capture over sample contained in pipette:** The second experimental set up tested in laboratory trials was based on filling the pipette tubes to a predefined height and introducing the Raman probe into the tube, so that it is close enough to the sample and without interferences of the glass over the Raman signal.

  For this proposal, the captures were made in the darkness to avoid that the signal captured by the probe is affected by environmental lighting. On the other hand, the capturing parameters were:

  - Acquisition time: 800 ms
  - Spectral averaging: 3 samples

- **Direct capture over compressed powder:** This experimental set up was based on direct analysis over pressed pellets prepared with the material to be tested. This sample preparation method is one of the most common methods used for XRF analysis as it produces high quality results, relatively quick and at low cost.

  The process of making pressed pellets includes grinding the sample to a fine particle size, mixing it with a binder aid in mixing vessel, pouring the mixture into a pressing die and pressing the sample at high pressure.

  On the other hand, and in order to standardize capturing conditions, the Raman probe was fitted with a "cap" that rests on the pressed sample and allows:

  - Ensure fixed distance between the probe and the sample for all experiments.
  - Avoid that the signal captured by the probe is affected by environmental lighting.

Fig. 8.25: Samples of sterile to be analyzed: Left) pipette and Right) pressed pellet

New method proposal for chemical characterization of sterile material in scrap.

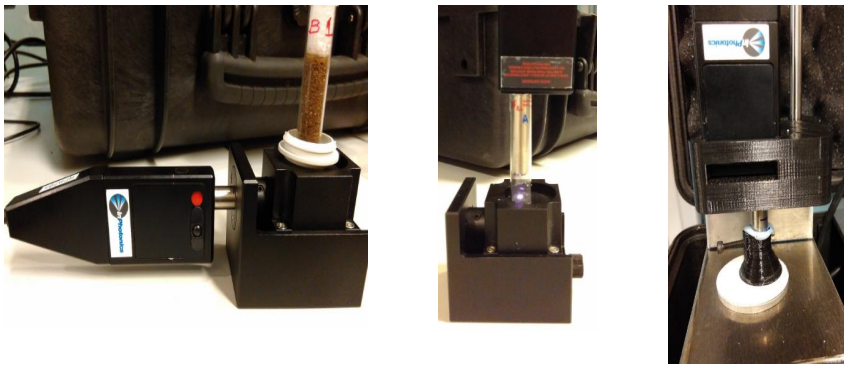

Fig. 8.26: Proposed capturing set ups: Left) through pipette, Middle) directly over sample and Right) pressed pellet

8.1.5 Samples selection and preparation

As it has already mentioned in previous sections, the main compound present in sterile materials are CaO, MgO, SiO_2, Al_2O_3, Fe_2O_3, FeO. Most of them are available as raw materials n several industrial activities and can be used for this research purpose.

- SiO_2; A material based on calcined rice husk has been selected as SiO_2 samples. This material is used in steelmaking as coverage material to prevent thermal losses of the steel during the casting process. The chemical composition (according the supplier) is about 92% of amorphous SiO_2, 1% of CaO, 1,5% of Al_2O_3 and 1% of Fe_2O_3
- MgO; The sample of this material is obtained from calcined dolomite stone. This material is used in steelmaking as adding material in electrical Arc Furnaces for refractory protection purposes. The chemical composition (according the supplier) is about 38% of MgO and 61% of CaO.
- CaO; This material is obtained from calcined calcite stone. Lime is required in steelmaking for phosphorous removal in the electrical Arc Furnaces process. The chemical composition (according the supplier) is about 1,5% of MgO and 97% of CaO.
- Fe_2O_3: For obtaining Fe_2O_3 compound, scale material from the rolling mill process was dried and prepared.

These materials allow analysing the capacity of the proposed laboratory configuration to obtain the spectral information identified in the bibliography.

On the other hand, in order to analyse real sterile materials in the proposed laboratory set up and to associate the spectral information obtained from pure components to real process conditions, 2 samples of sterile from two E1 scrap grade deliveries were collected.

Fig. 8.27: Raw material used for experimental tests; Left) Pure compounds (Lime, Dolomite and SiO_2 and Right) real sterile

To be sure that the chemical compositions of the pure compounds correspond to the compositions supplied by the supplier, as well as to have the complete chemical distribution of the two sterile samples, SEM-EDS analysis (Energy-dispersive X-ray spectroscopy for the elemental analysis of a sample) of all collected sample were performed. The results of these analyses are shown in Table 8.4:

New method proposal for chemical characterization of sterile material in scrap.

Spectrum	C	O	Mg	Al	Si	P	S	Ca	Ti	Mn	Fe	Zn
Sterile A	16.38	39.95	0.38	2.44	9.43	0.12	0.26	4.45	0.66	0.28	22.94	0.98
Sterile A 2	16.25	40.91	0.36	2.52	9.16	0.14	0.19	4.40	0.39	0.22	23.13	0.92
Sterile B	17.17	40.56	0.63	2.10	7.56		0.80	7.13	0.91	0.36	20.53	1.57
Sterile B 2	19.79	39.74	0.53	1.89	7.30	0.18	0.60	6.63	0.90	0.39	19.33	1.68
SiO_2		54.05	0.27		39.62	0.48	0.42	0.78				
SiO_2 2		53.87	0.23		39.82	0.51	0.34	0.93				
CaO+MgO		50.66	12.02					37.32				
CaO+MgO 2		50.10	11.30					38.61				
CaO	11.90	53.23	0.67	0.21	0.35			31.97			1.67	
CaO 2	10.63	58.48	0.69	0.24	0.14		0.13	28.80			0.89	

Table 8.4: Elemental analysis of collected samples (wt%)

The manner in which the samples were prepared for the proposed experiments consisting on mixing the pure compounds inside the pipette and by pressed pellet. Table 8.5 summarizes the material distribution used which are shown in Fig. 8.28:

Sample ID	% CaO	% Dolomite	%SiO_2
Sample 1	75	25	0
Sample 2	50	50	0
Sample 3	25	75	0
Sample 4	0	70	30
Sample 5	0	50	50
Sample 6	0	30	70
Sample 7	75	0	25
Sample 8	50	0	50
Sample 9	25	0	75
Sample 10	33,3	33,3	33,3

Table 8.5: Pure compounds distribution for mixing analysis

Fig. 8.28: Samples prepared on pipettes and on Pressed pellets

8.1.6 Experimental results

The objective of these laboratory experiments was to gain knowledge and expertise in defining the best optical configuration of the Raman spectrograph, as well as the definition of the key capture parameters to get a clear spectral signature in relation to the analysed components. The development of these tests, under controlled laboratory conditions, will guarantee subsequently better results in industrial conditions where there will be a greater number of uncontrolled variables (light and temperature, greater degree of heterogeneity, presence of unknown components or different degrees of humidity). In this section, the results obtained during laboratory tests are described

8.1.6.1 Capturing through pipette glass

Before conducting any experiments on samples of interest and aiming to evaluate whether the equipment available in the laboratory are valid to extract spectral signatures for this research purpose, a first experiment was performed over a pure material with a well-known Raman signature obtained from Ocean Optic database. In this sense, sugar was selected as testing material whose spectrum is available in public databases.

However, with this capture configuration, it is necessary to consider that the pipette itself has influence over Raman captured signal, since the laser must pass through the glass altering its characteristics. To eliminate the influence that the glass has on the captured signal, prior to the capture campaign, a capture with an empty glass tube is carried out. The collected spectrum will be used as background noise signal and subtracted from the captured spectrum of each sample.

Fig. 40 shows the methodology followed for background signal acquisition and two images comparing the acquired Raman spectra of sugar samples in raw and the result after subtracting the background signal:

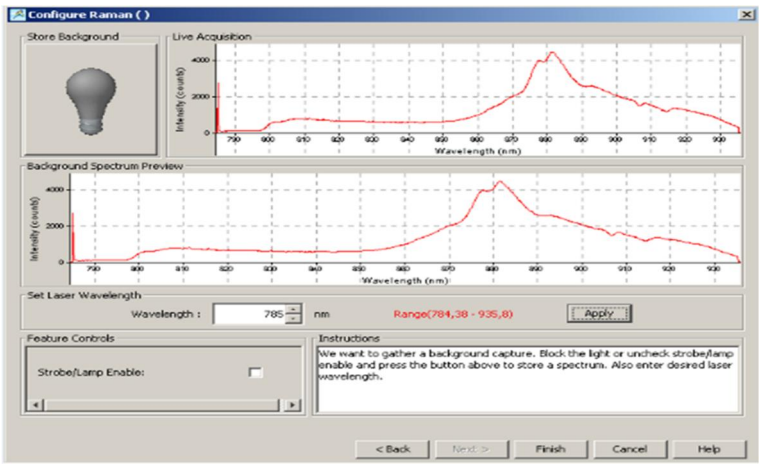

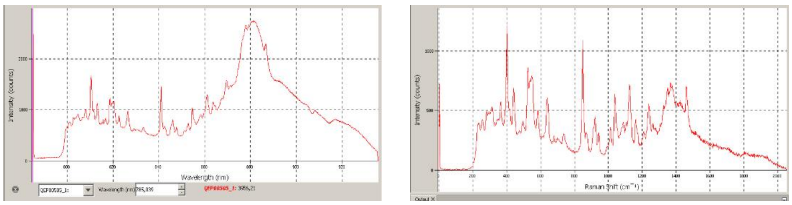

Fig. 8.29:Sugar spectra analysis: Up) Background signal and Down) Raw sugar Raman signal (left) and sugar signal after subtracting background (right)

Fig. 8.30 shows the unprocessed scanned signal after subtracting the background spectra produced by the glass (in red). This spectrum is compared with the Raman signature found the Ocean Optics general database for sugar. Looking at the results, it is proved that, despite some "noise" in the signal, the characteristic peaks detected correspond very well with the theoretical one.

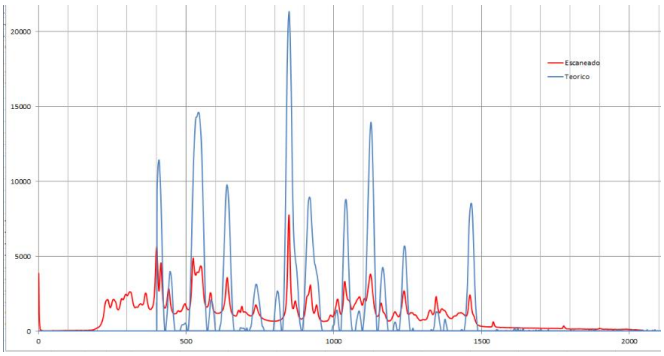

Fig. 8.30: Theoretical and obtained spectra of sugar

In view of the results, new pipettes of the same material (Borosilicate) were acquired, and according to the defined procedure, the capture of the spectrum generated by the glass of the empty pipettes were recorded.

After analysing the generated background spectra of several pipettes, it was demonstrated that the intensity of the signature obtained with the new tubes is much higher than the intensity obtained with the previous pipettes, possibly due to structural differences of the material induced in the manufacturing process. The mentioned effect can be seen in Fig. 8.31.

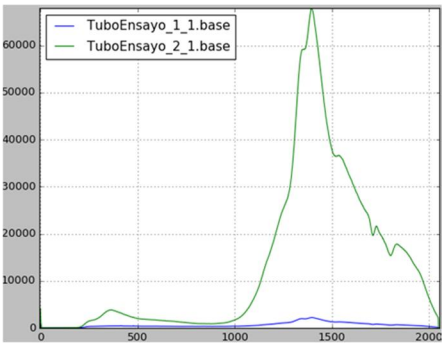

Fig. 8.31: Raman spectra of two different pipettes

It is concluded that this lab setting is not feasible to achieve consolidated results over time in real industrial conditions. For this reason, this acquisition set up is discarded.

New method proposal for chemical characterization of sterile material in scrap.

8.1.6.2 Direct capture over sample contained in pipette

With this spectra acquisition set up, three experimental analysis have been done:

- Direct capture over pure sample contained in pipette
- Direct capture over controlled material mixtures contained in pipette
- Direct capture over sterile contained in pipette

8.1.6.2.1 Direct capture over pure sample contained in pipette

In this laboratory set up, two samples (named as A and B) of each selected pure material (lime, Dolomitic lime and Silica) were selected. These 6 pipette tubes are filled to a predefined height and the Raman probe is introduced into the tube. For each sample, several spectra acquisitions are done for each pipette.

Fig. 8.32 shows the Raman spectral raw data without processing

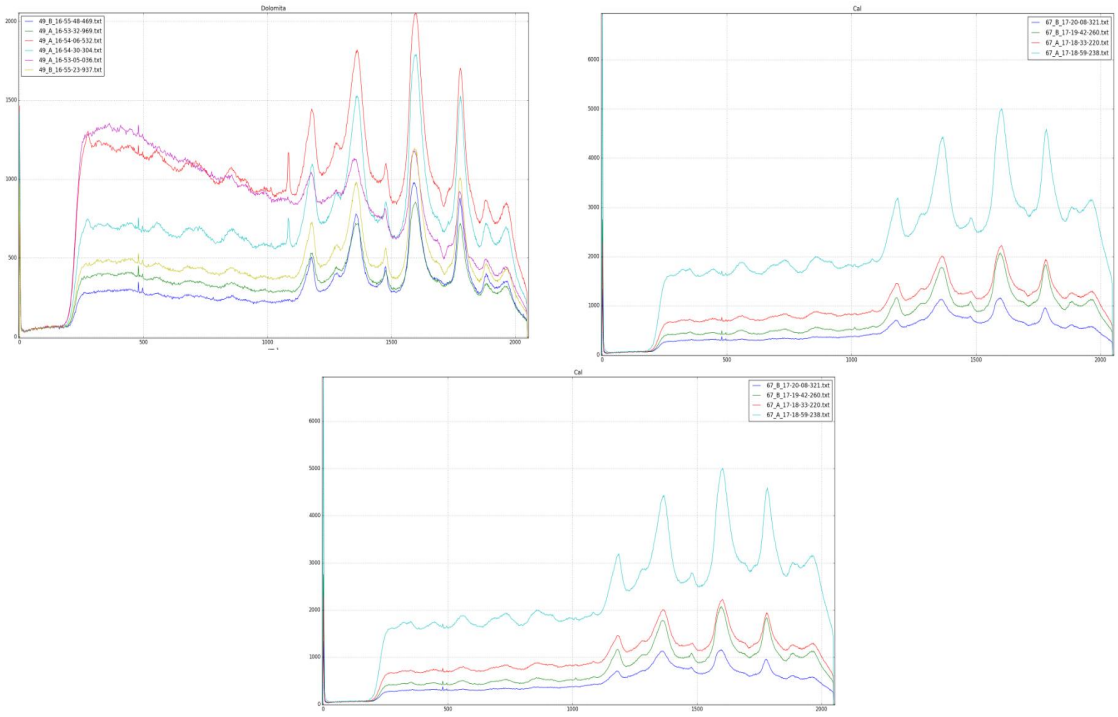

Fig. 8.32: Acquired spectral data from Dolomitic, lime and Silica before processing

After analyzing the results, there are two conclusions worth mentioning:

- There is a high repeatability in the characteristic peaks found in the captures of different samples of the same material.
- Under the same capture conditions and on different fractions of the same raw material, spectra with different intensity levels were obtained. At this investigation stage the causes of these differences are unknown yet.

New method proposal for chemical characterization of sterile material in scrap.

After this preliminary analysis, the next step consisted on processing spectra signatures according to the stabilised methodology for eliminating the continuous component of the acquired signal (see Fig. 8.33)

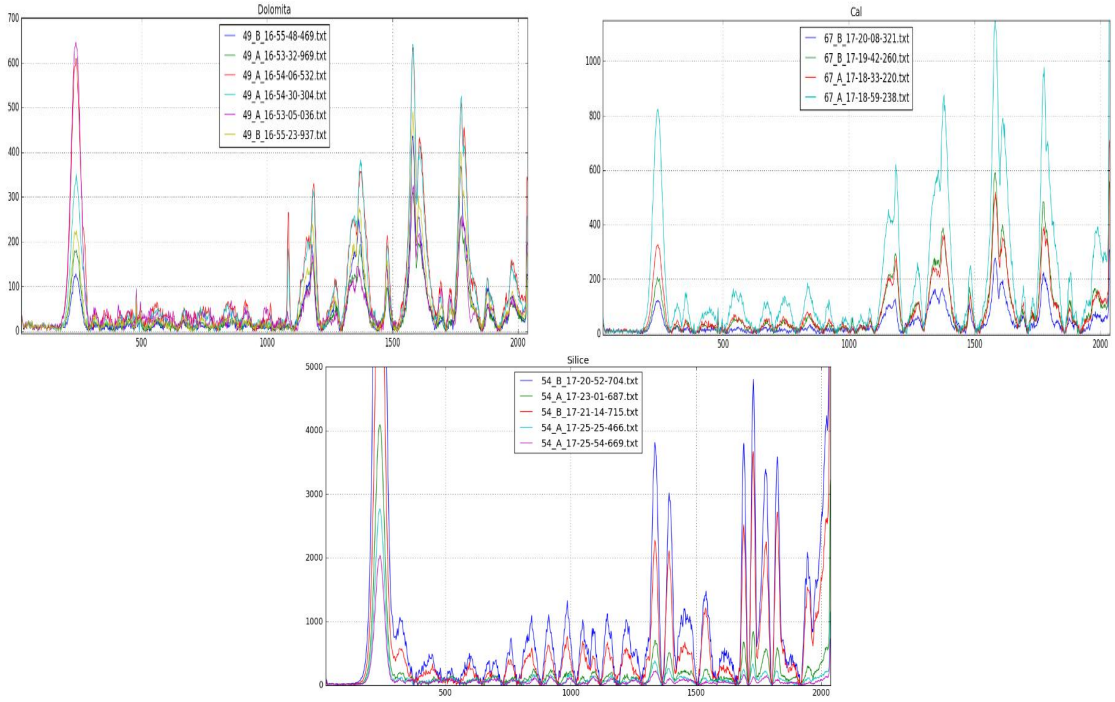

Fig. 8.33: Acquired spectral data from Dolomitic, lime and Silica after processing

An averaging of the spectral information obtained for each one of the samples in the different components is performed. Looking at the similarity of the results obtained for different samples captured, this averaging process serves to validate the capture procedure Those results also allow obtaining the position of the characteristic peaks for the defined catch conditions.

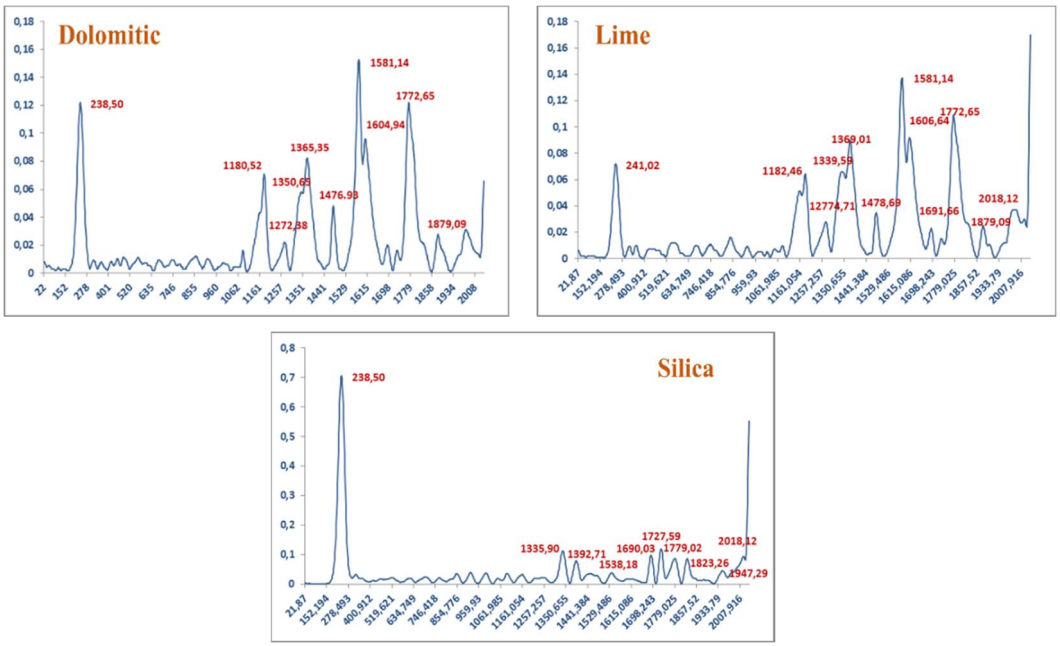

Fig. 8.34: Averaged spectral data and characteristic peaks from Dolomitic, lime and Silica after processing

New method proposal for chemical characterization of sterile material in scrap.

When the spectra information of each analysed component after processing raw data is compared with the information reported in the different bibliographic references, It is possible to state the following:

- Calcite: Similarities were observed in some of the peaks found in 1200-1600 cm^{-1} region; at 1581 (1580), 1365 (between 1378 and 1361), 1350 (1342) and 1272 (1267) cm^{-1}, where numbers in brackets represent characteristic peaks from literature. Also, in the lower region, it was expected to obtain a characteristic peak at 278 cm^{-1} and nevertheless it has been found at 238 cm^{-1}. Finally, in the region 200-1200, it was expected to find a clear peak at 1080-1090 cm^{-1} but nothing was observed.
- Dolomite: As it was the case with calcite, some similarities were observed in some of the peaks found in 1200-1600 cm^{-1} region; at 1606 (1613), 1581 (1580), 1369 (1376) and 1339 (1342) cm^{-1}, where numbers in brackets represent characteristic peaks from literature. In the lower region, several peaks were expected be found between 150 and 300 cm^{-1}, however it was found a unique peak at 241 cm^{-1}. Finally, in the region 200-1200, it was expected to find some clear peaks at 1080-1090 cm^{-1} but nothing was observed.
- Silica: At this point, only one Raman laser at 785 nm was available for these experiments. Also, it should be mentioned that, Silicon fluoresces is much stronger at 780 nm than it is at 532 nm, so most the bibliographical references are referred to analysis in the range of 500-550 nm. However, it was expected to find a strong peak at 520 cm^{-1} in the case of pure crystalline silica (Quartz, Cristobalite, Coesite, Tridymite or Koetita) or at 480 cm^{-1} in the case of amorphous material (silicate glass).

8.1.6.2.2 Direct capture over controlled material mixtures contained in pipette

In line with what was done previously on pure materials, the analysis of mixed materials was done using the same experiment configuration. In this case, after grinding and mixing the materials composing the mixtures, three different compositions were prepared:

- 50% lime and 50% Silica
- 70% lime and 30% Silica
- 90% lime and 10% Silica

In terms of sample preparation, three different spectral processing algorithms combination were tested:

a. Removing the continuous component of the signal, signal smoothing and Standardization (dividing by standard)
b. Spectra smoothing and Standardization (dividing by standard)
c. Only spectra smoothing

New method proposal for chemical characterization of sterile material in scrap.

The spectral signatures obtained for 50% lime and 50% Silica, after applying the three proposed spectral processing, are shown below:

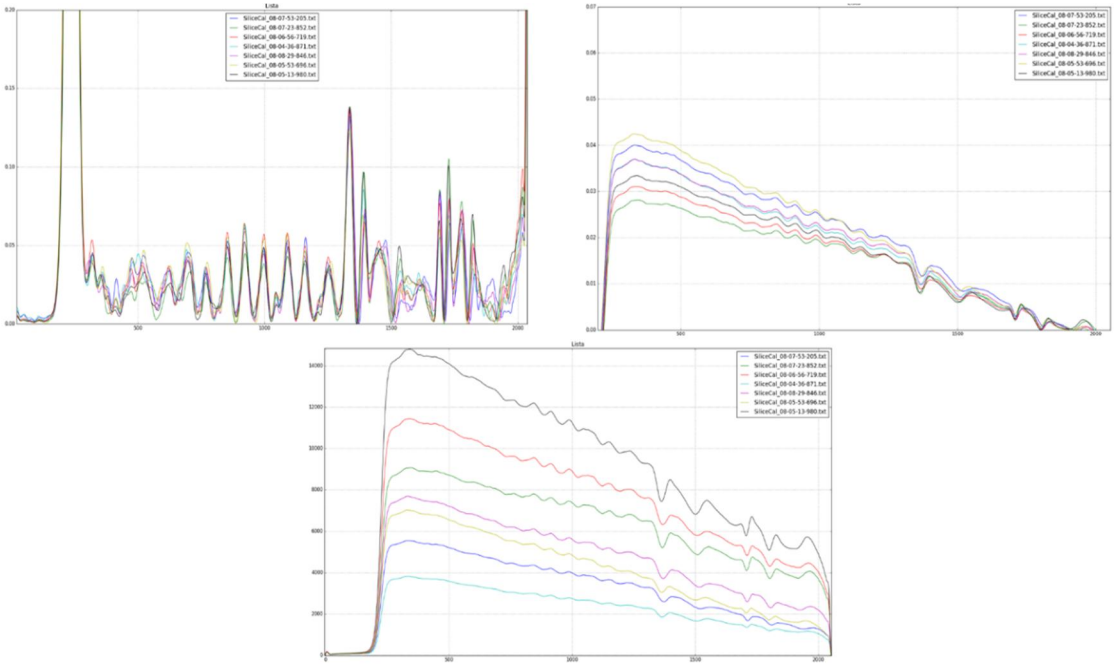

Fig. 8.35: 50% lime -50% Silica applying Up-Left) a methodology, Up-Right) b methodology and Down) c methodology

The spectral signatures obtained for 70% lime and 30% Silica, after applying the three proposed spectral processing, are shown below:

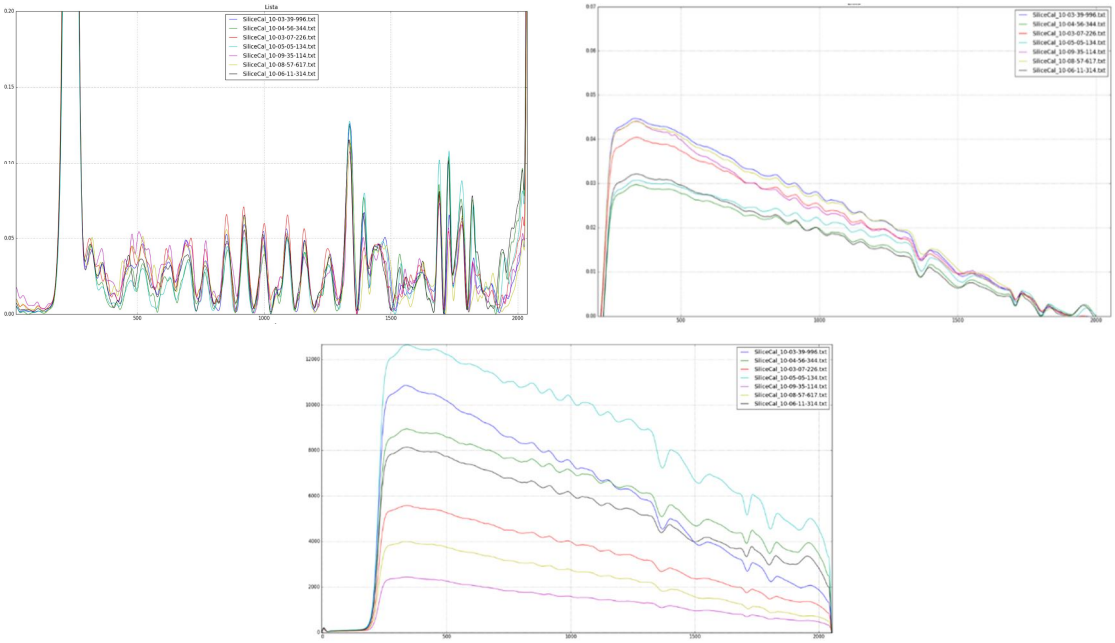

Fig. 8.36: 70% lime -30% Silica applying Up-Left) a methodology, Up-Right) b methodology and Down) c methodology

New method proposal for chemical characterization of sterile material in scrap.

The spectral signatures obtained for 90% lime and 10% Silica, after applying the three proposed spectral processing, are shown below:

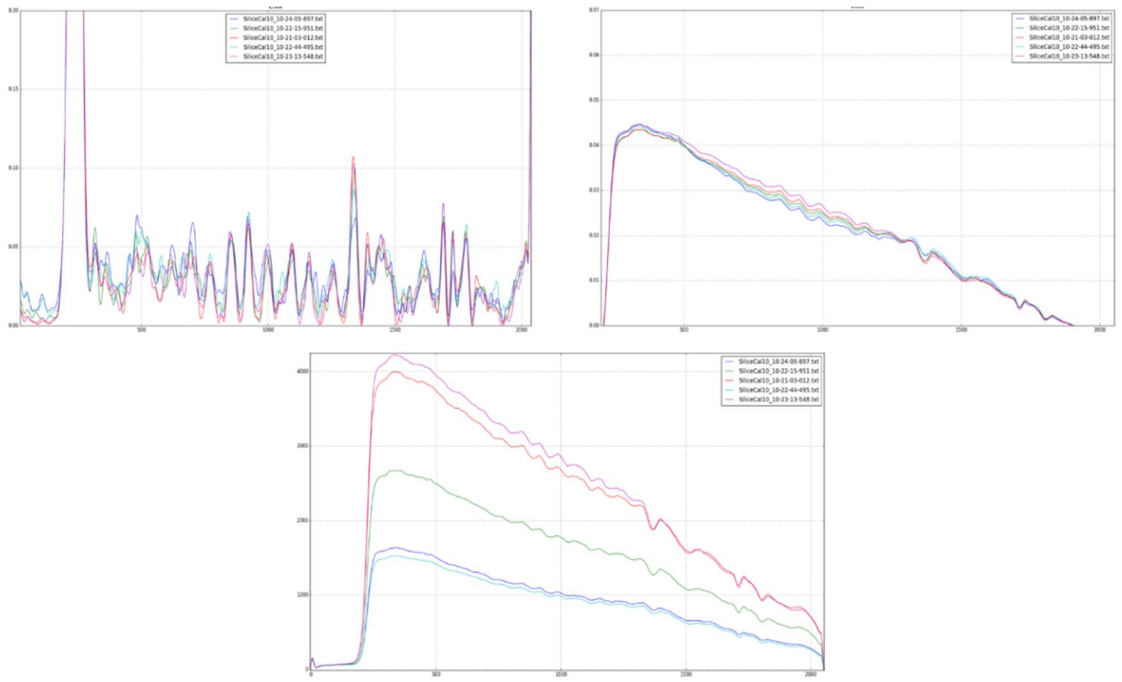

Fig. 8.37: 90% lime 10% Silica applying Up-Left) a methodology, Up-Right) b methodology and Down) c methodology

The data obtained from spectral averaging allowed quantifying, from the linear mixture model described in section 8.1.3, the similarity of the mixture with respect to the pure components, calculating both the abundance and its standard deviation of each component in the mixture. The results are shown in Table 8.6:

		Removing continuous component, Spectra smoothing and Standardization (a)	Spectra smoothing and Standardization (b)	Only spectra smoothing (c)
Case (50%-50%) [Silica; Lime]	$\bar{X}$	**[0.9518; 0.0481]**	**[0.9989; 0.0010]**	**[0.4504; 0.5495]**
	σ	[0.0138; 0.0138]	[0.0010; 0.0010]	[0.0001; 0.0001]
Case (30%-70%) [Silica; Lime]	$\bar{X}$	**[0.9449; 0.0550]**	**[0.9992; 0.0007]**	**[0.3859; 0.6140]**
	σ	[0.0126; 0.0126]	[0.0007; 0.0007]	[0.0004; 0.0004]
Case (10%-90%) [Silica; Lime]	$\bar{X}$	**[0.8906; 0.1093]**	**[0.9981; 0.0018]**	**[0.0871; 0.9128]**
	σ	[0.0261; 0.0261]	[0.0010; 0.0010]	[0.0871; 0.9128]

Table 8.6: Mean abundance and Std abundance data obtained

The main conclusion obtained after this experiment is basically that, with the defined capturing configuration for pure components mixtures, in terms of abundance only good results were obtained with the simplest method for processing the spectrum. This method corresponds with only signal smoothing by means of a noise filter. It could be due to the fact that some spectral processing method can remove some important spectral responses.

New method proposal for chemical characterization of sterile material in scrap.

8.1.6.2.3 Direct capture over sterile contained in pipette

In this laboratory set up two samples (named as A and B) of collected sterile material from the scrap yard were selected and split in two samples each. With the resulting samples, 4 pipette tubes were filled to a predefined height and the Raman probe was introduced into the tube. Several spectra captured were done for each pipette after mixing the material.

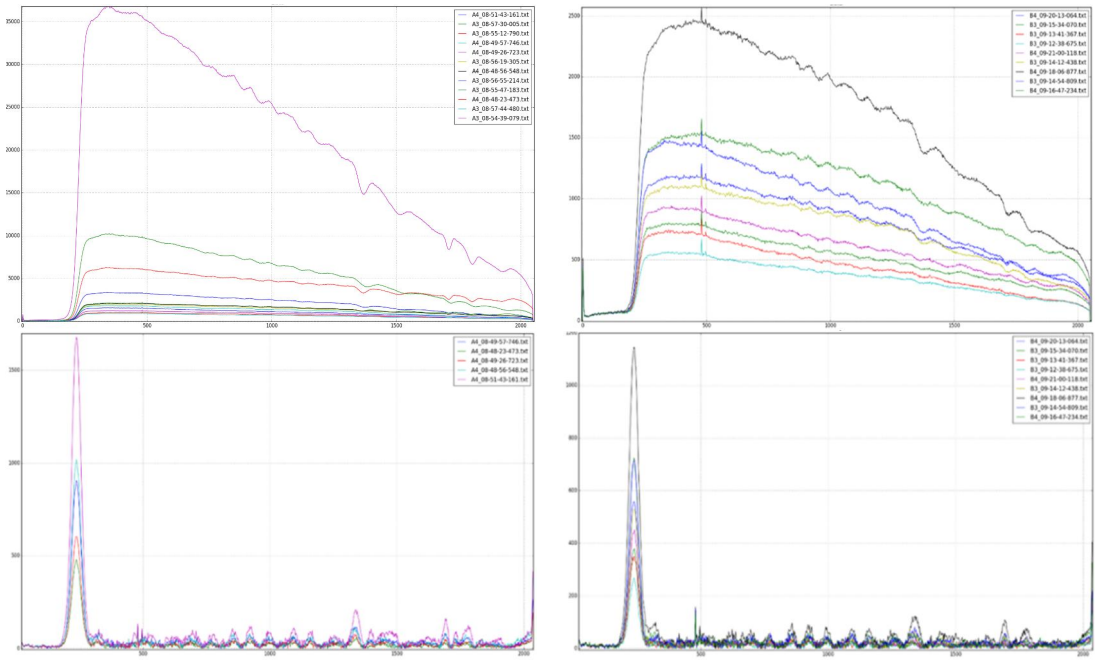

Fig. 8.38: Up) Raw spectra data of Sterile A (left) and B (right) without spectral processing and Down) Processed spectra data of Sterile A (left) and B (right)

In this case, the raw spectral data were processed by removing the continuous component of the signal, signal smoothing and Standardization (Processing algorithm referenced as A in previous sections).

Fig. 8.39 depicts spectral averaging for the data obtained from sterile A and B after signal smoothing:

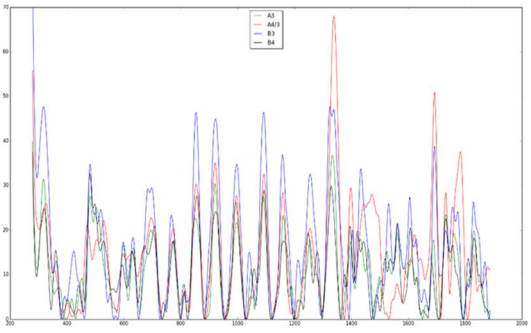

Fig. 8.39: Mean values obtained from each sterile sample

The obtained mean spectra are processed trying to determine what proportion of "pure components" are in the sterile analysed. Initially, to compare the pure and sterile signals, the

averaging spectra normalized on the maximum and on the standard values are calculated of each spectrum for both, the pure components and the two sterile samples.

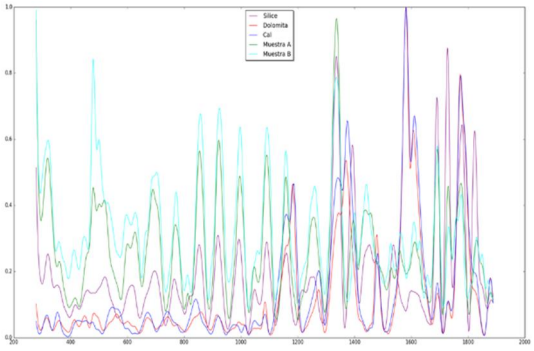

Fig. 8.40: Sterile and pure samples normalized to the maximum

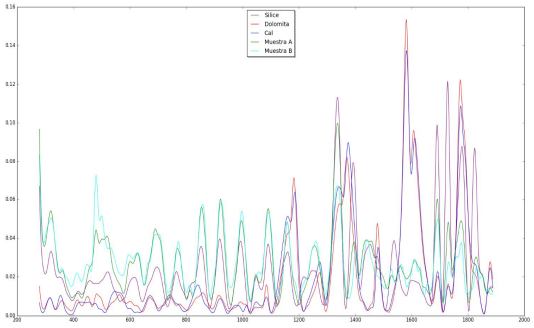

Fig. 8.41: Sterile and pure samples normalized to the standard

Looking at the graphical analysis results, it is concluded that the spectra signature got from the sterile samples are very similar to each other, and much more similar to silica samples (especially in the central part 600-1350 spectral range) than to dolomite or lime samples.

When calculating the abundance of each pure component contained in sterile according to the processing methodology described before, the similarity of sterile spectral signature with silica signature is confirmed. Abundance results obtained for each sample are the following:

Sterile		% Silica	% Dolomite	% lime
normalized to the maximum	Sample A	0.973	0.012	0.014
	Sample B	0.978	0.011	0.010
normalized to the standard	Sample A	0.870	0.061	0.067
	Sample B	0.892	0.075	0.031

Table 8.7: Abundance analysis on raw sterile

These results on abundance do not mean that the sterile contain the calculated percentage in weight of silica, but it looks much more like silica than dolomite or lime, which is in line with the chemical elemental distribution shown in Table 8.4. It is also important to consider that the sample has other components that have not been considered in this analysis.

The main conclusion got from these “direct capture over sample contained in pipette” experiments is that when sampling is performed without any previous sample preparation, there are a large number of variables that are not being evaluated, such as the heterogeneity of the material, the roughness of the surface, the illumination conditions of experiment ... Those experimental variables have a great influence on the acquired signal quality.

New method proposal for chemical characterization of sterile material in scrap.

Before thinking about continuing with the development of the methodology to be used to obtain the spectral information of sterile samples without sample pre-treatment in real industrial conditions, it is necessary to test and validate, under well controlled conditions, the management of other capture variables such as the configuration of the laser to use be and the most appropriate signal processing algorithms. These variables can only be tested over carefully prepared samples in order to minimize the capturing process uncertainties.

8.1.6.3 Capture over pressed pellets of samples

The experimental set ups of these analyses can be grouped in categories:

- Capture over pressed pellets of pure compound samples
- Capture over pressed pellets of mixed compound samples
- Capture over pressed pellets of sterile samples

The analyses over these categories were done using two different Raman Laser source at 785 nm and at 514 nm.

8.1.6.3.1 Capture over pressed pellets of pure compound samples

For this analysis, 2 samples of each pure component (Silica [SiO_2], Dolomite [$CaMg(CO_3)_2$], Calcite [$CaCO_3$] and Iron Oxide [Fe_2O_3]) were prepared in pressed pellets as shown in Fig. 8.42:

Fig. 8.42: Samples of pure compounds

Similar to the work done in previous analysis, two different spectral processing algorithms were tested:

a. Removing the continuous component of the signal, signal smoothing and Standardization (dividing by standard)

b. Spectra smoothing and Standardization (dividing by standard)

<u>Analyses over dolomite samples:</u>

The first analysis proposed over dolomite pressed pellet samples are conducted using a stabilized Raman Laser at 785 nm

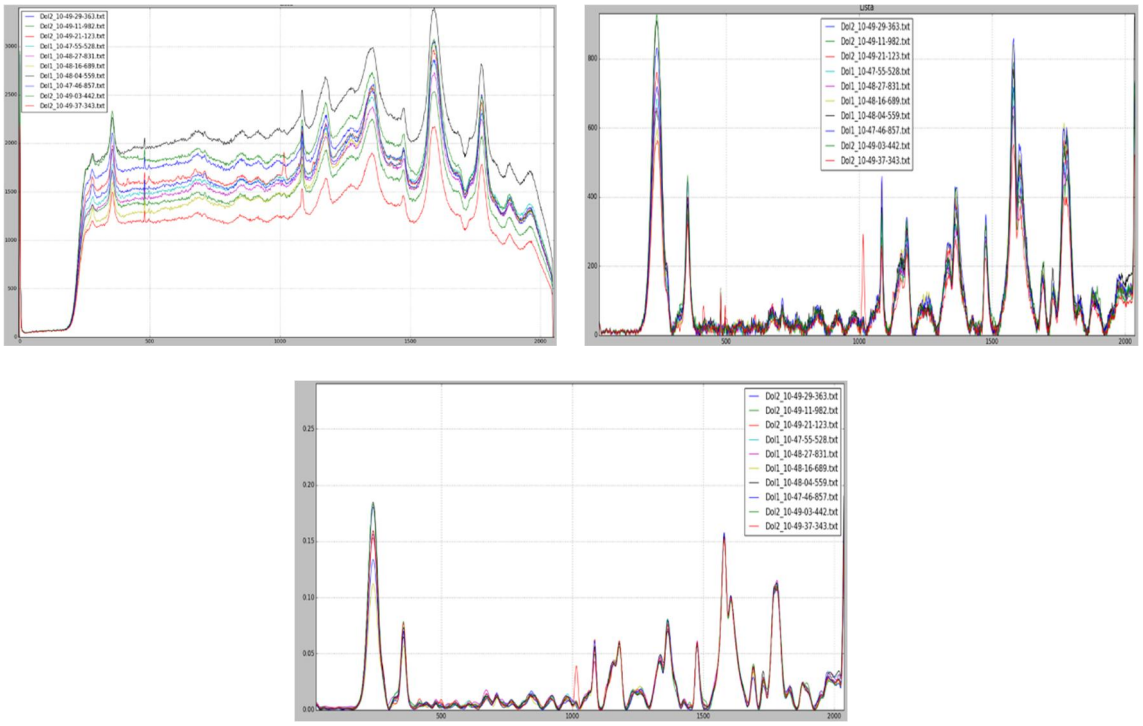

Fig. 8.43: Dolomite Spectral data at 785 nm. Up-Left) without processing, Up-Right) A methodology and Down) B methodology

In order to be able to compare the results obtained from the direct capture in pipette with the results got from the capture over pressed pellets, the average value of the spectral signatures after applying the processing algorithm B for both cases are drawn

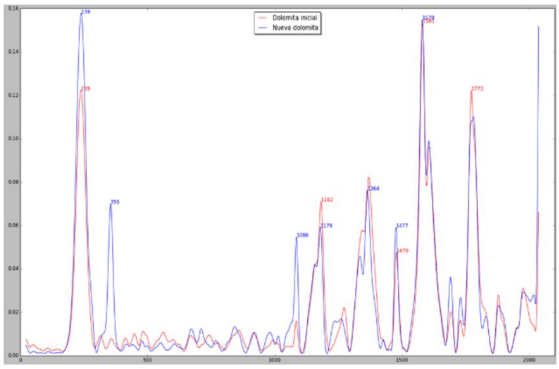

Fig. 8.44: Comparative analysis of dolomite between spectral data coming from direct capture in pipette and over pressed pellets

After analyzing these results, it can be concluded that the spectral signatures got from pressed pellets are more regular than the same spectral signals extracted from direct capture in pipette.

As far as characteristic peaks are concerned:

- With this experiment setup, a new peak is observed at 355 cm^{-1} (significant). According to the literature, a peak is expected around 299 cm^{-1} in dolomite, which is located far from the peak found.

New method proposal for chemical characterization of sterile material in scrap.

- On the other hand, small peaks (wide) are detected at 674 cm^{-1} and 711 cm^{-1}. According to the literature a peak is expected around 724 cm^{-1}
- The main characteristic peak at 1086 cm^{-1} is clearer than in the initial captures. According to initial bibliographical studies, a peak was expected around 1097 cm^{-1} in dolomite
- Finally, for> 1100cm^{-1}, the spectrum is similar to the initial captures, additional undocumented peaks were detected (1179, 1364, 1477, 1579, 1773).

As previously discussed, laser power affects the shapes and intensities of the resulting bands. However, the laser power must be carefully selected to maximize the signal-to-noise ratio and minimizing black-body radiation caused by the sample heating. Also, the extension of the exposure time will increase the efficiency and sensitivity of Raman spectroscopy. In order to analyze how these variables, influence on the obtained spectral signature, several sampling of Dolomite's pressed pellets were carried out varying both the laser power (between 300 and 950 mW) and the exposure time (between 3 and 900 sec).

Fig. 8.45 shows the results of the tests conducted testing different laser power and exposure time:

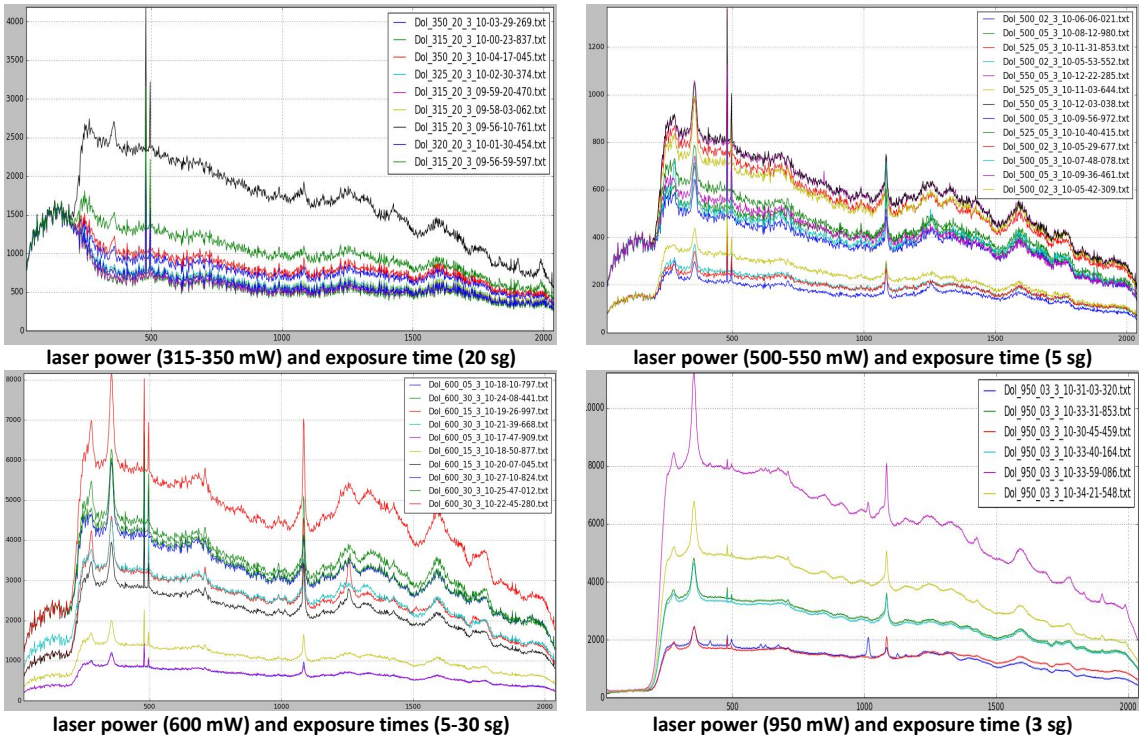

Fig. 8.45: Dolomite response to different laser power and exposure time at 785 nm

In order to evaluate the spectral response of dolomite materials to Raman Laser at 514 nm, the selected samples are exposed to green Raman Laser. The acquiered spectrum is shown in Fig. 8.46

New method proposal for chemical characterization of sterile material in scrap.

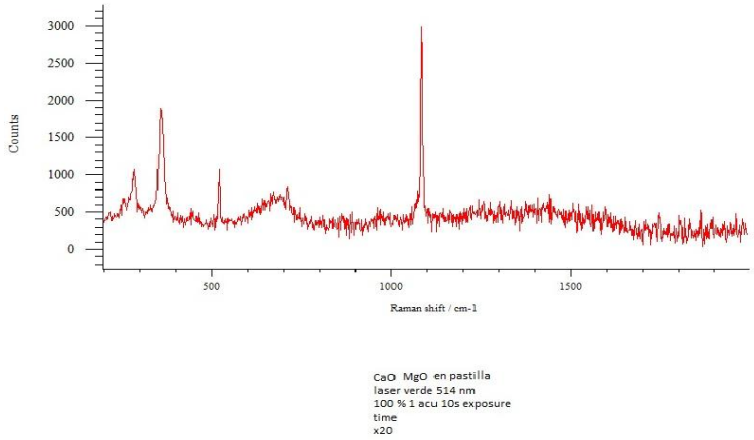

Fig. 8.46: Dolomite response at 514 nm

The spectrum collected with the green laser shows peaks around 290, 370, 510 and 1100cm^{-1}, and one wider peak around 700 cm^{-1}.

The most significant difference with respect to 784 nm laser is that the peak at 510 nm "moves" since 2 peaks are usually detected just under 500 nm.

In this case, the results obtained with the laser at 514 nm are comparable to the results obtained with the laser at 784 nm.

Analyses over Calcite samples:

As done before, the first analysis proposed over calcite pressed pellet samples are conducted using a stabilized Raman Laser at 785 nm

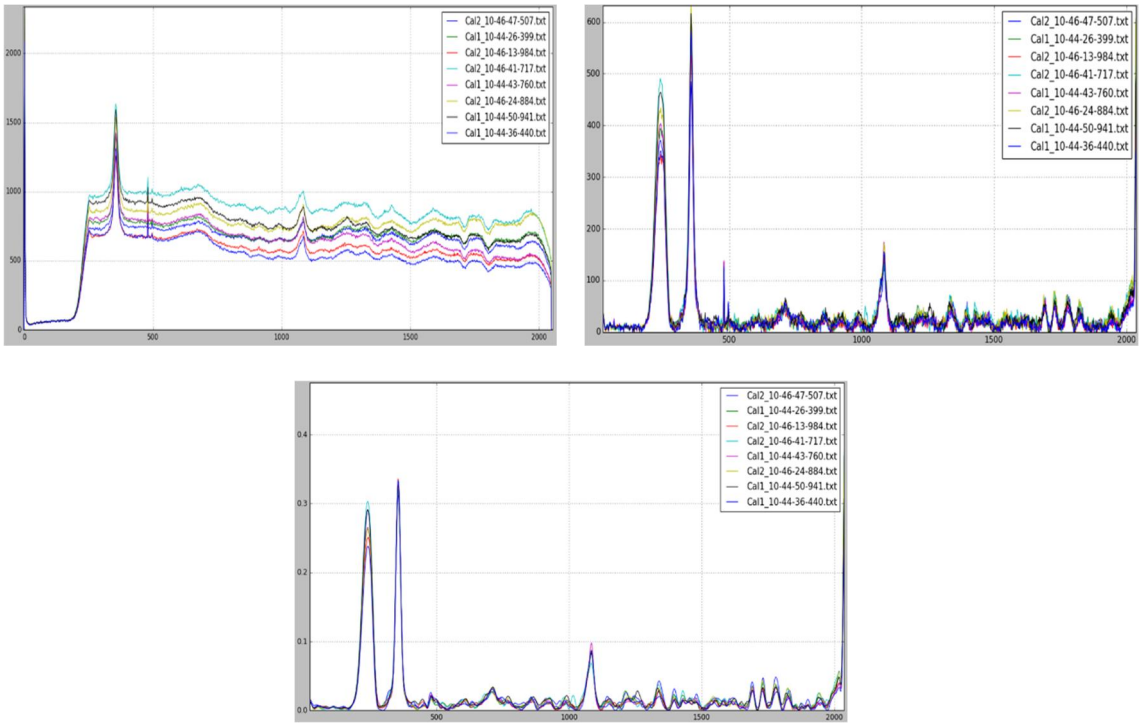

Fig. 8.47: Calcite Spectral data at 785 nm. Up-Left) without processing, Up-Right) A methodology and Down) B methodology

New method proposal for chemical characterization of sterile material in scrap.

After analysing the results, similarly to the results obtained in dolomite analysis case, the spectral signatures got from pressed pellets are more regular than in the direct acquisitions over the material contained in the pipette. The spectral signatures obtained with the new experimental configuration differ from the signatures obtained previously.

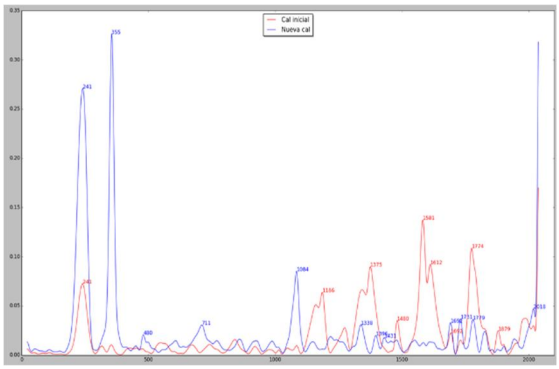

Fig. 8.48: Comparative analysis of calcite between spectral data coming from direct capture in pipette and over pressed pellets

Analysing the characteristic peaks, the following statements can be highlights:

- With this experiment setup, same peak than observed in dolomite case at 355 cm^{-1} (significant) is got. According to the literature, a peak is expected around 281 cm^{-1} in calcite, which is located far from the peak found.
- Relatively wide peak is found at 480 cm^{-1}. In the literature no reference was found referring to it.
- On the other hand, small wide peak was detected at 711 cm^{-1}, which corresponds closely with those found in the literature. Thus, the main characteristic peak of calcite at 1085 cm^{-1} is now clearly identify at 1084 cm^{-1}.
- For wavelengths greater than 1100cm^{-1}, The "large" peaks observed before are not observed any more. Now there are smaller and wider peaks at 1338, 1396, 1692, 1731, 1779 and 1825 cm^{-1}.

For Calcite case, similar conclusions than for dolomite material are reached. So that it does not seems worthy to repeat the experiments for assessing the laser power and the exposure time. In this particular case, several experiment for analysing the influence of laser focus over the sample are carried out. In order to identify the distance between the Raman optic and the sample that offers the clearest spectral signature, the sensor is placed manually at different distances from the sample. The results of this experimental tests are shown is Fig. 8.49:

New method proposal for chemical characterization of sterile material in scrap.

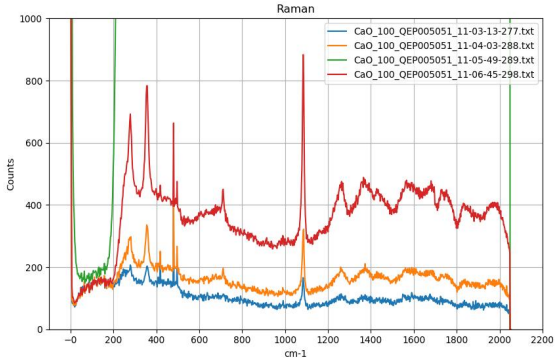

Fig. 8.49: Analysis on Laser focus tests for CaO

In order to evaluate the spectral response of calcite materials at 514 nm, the selected samples are exposed to green Raman Laser. The detected spectrum is shown in Fig. 8.50

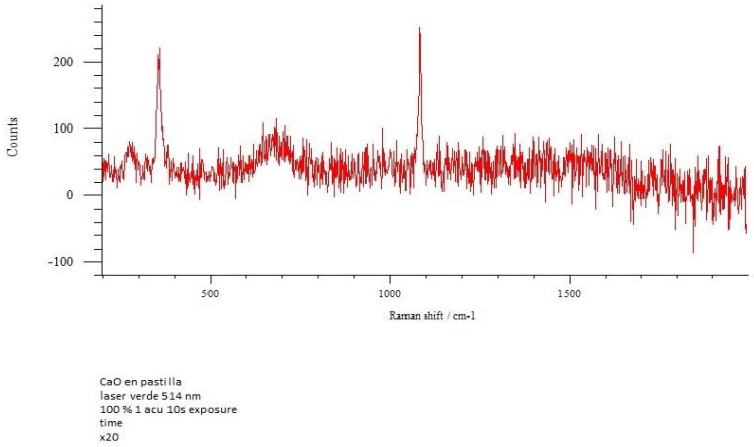

Fig. 8.50: Calcite response at 514 nm

The spectrum collected with the green laser shows peaks around 370 and 1100cm^{-1}, and one wider peak around 700 cm^{-1}.

Similarity to Dolomite case, the most significant difference with respect to 784 nm laser is that one peaks is detected just under 500 nm.

In this case, the results obtained with the laser at 514 nm are comparable to the results obtained with the laser at 784 nm.

Analyses over Silica samples:

When analysing samples composed by SiO_2 with Raman Laser at 785 nm, the following spectral signatures are got for the different processing methodologies proposed:

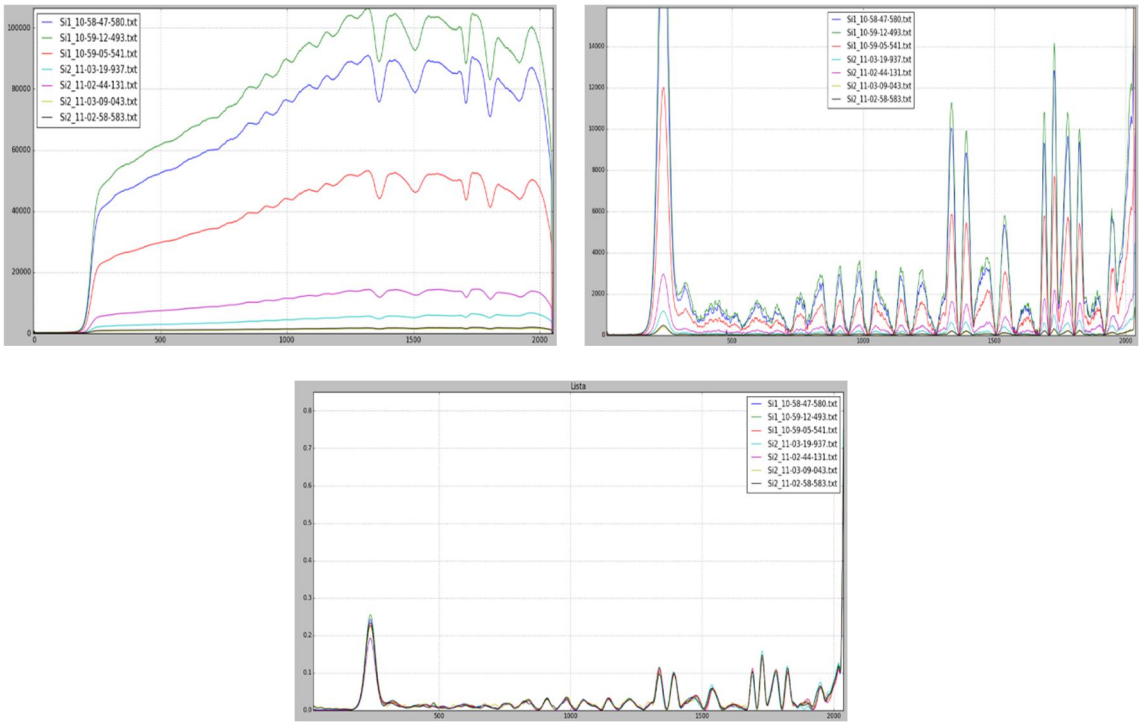

Fig. 8.51: Silica Spectral data at 785 nm. Up-Left) without processing, Up-Right) A methodology and Down) B methodology

As shown in Fig. 8.51, the results from pressed pellet samplings experiment were like the previous ones over direct capture in pipettes. No peaks comparable to those documented on SiO_2 were detected; neither in the crystalline structure (quartz, Cristobalite, Coesite, Tridimine and Stishovite), nor in the amorphous form.

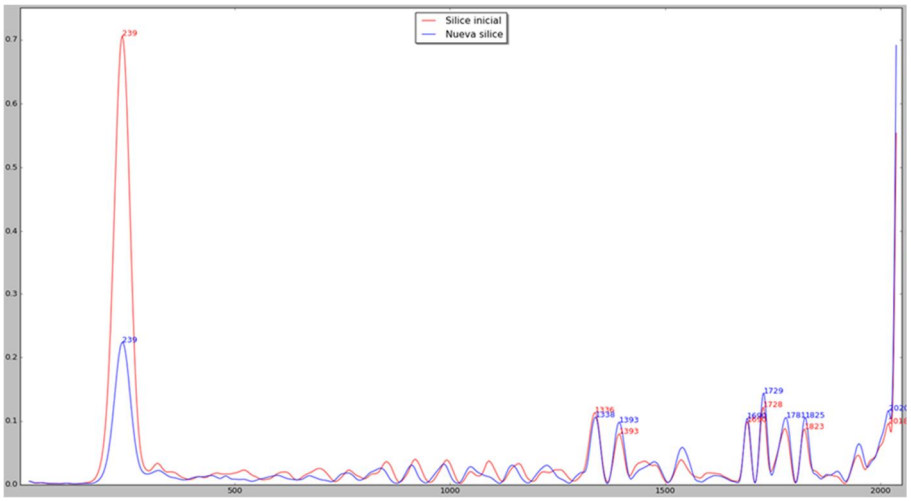

Fig. 8.52: Comparative analysis of Silica between spectral data coming from direct capture in pipette and over pressed pellets

As it was already mentioned in section 8.1.1.2.3, when using Raman Spectroscopy for Silicon Analysis some considerations related to the laser (power and wavelength) and the acquisition exposure time must be carefully taken into account, as well as Fluorescence effect that is potentially capable of overwhelming the Raman scattering signal. This last effect may justify the absence of characteristic peaks in the previous tests for SiO_2 samples.

New method proposal for chemical characterization of sterile material in scrap.

In order to analyse how these variables, influence on the obtained spectral signature, several sampling of silica pressed pellets were carried out varying both the laser power (between 300 and 950 mW) and the exposure time (between 3 and 900 sec).

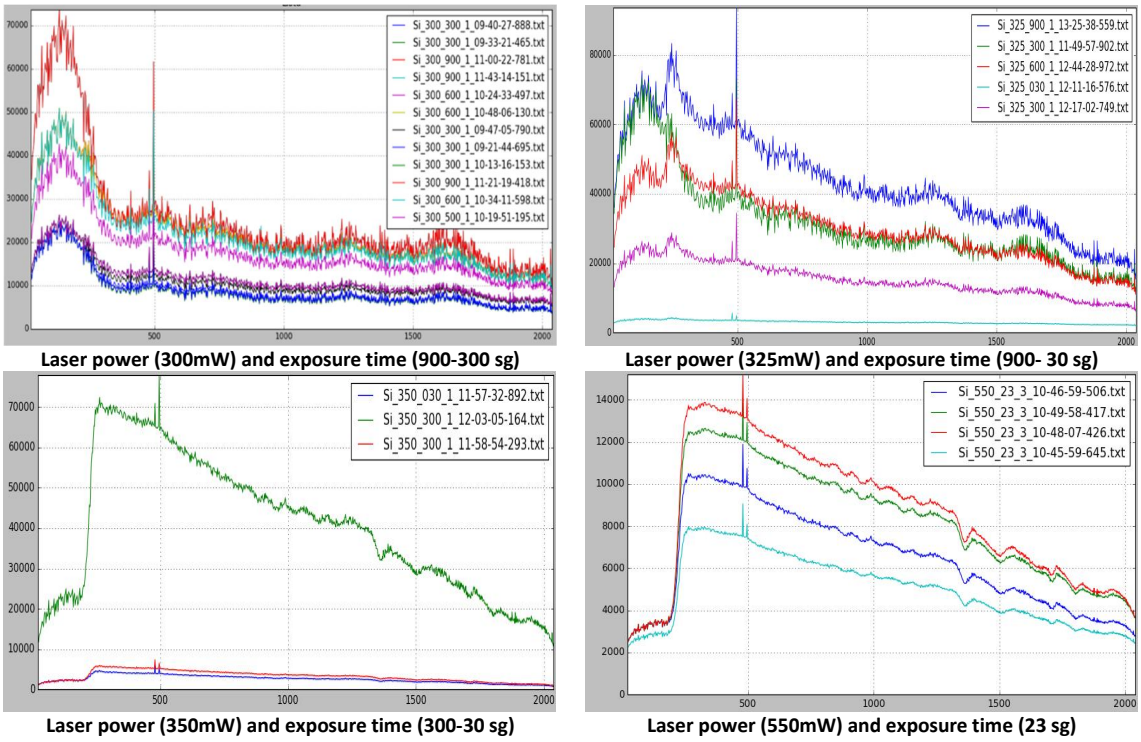

Fig. 8.53: Silica response to different laser power and exposure time at 785 nm

The following figure shows the average values of the normalized spectra of the samples taken with the different laser power and exposure time configurations

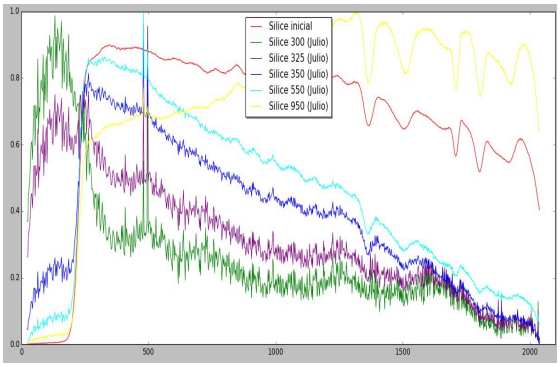

Fig. 8.54: Average spectra (normalized) with different laser power and exposure time configurations

Beside the influence of the laser set up (power and exposure time) on the quality of the acquired signal, an analysis on the influence of the focus distance between the sensor and the SiO_2 samples is conducted following same methodology than used for calcite.

In this case, with similar focus distances than used with CaO, the signal is saturated.

New method proposal for chemical characterization of sterile material in scrap.

As shown in Fig. 8.55, using closer positions, the signal is intense and with a positive slope (green graph). With lager distances the signal is less intense and with a negative slope (orange and blue graphics).

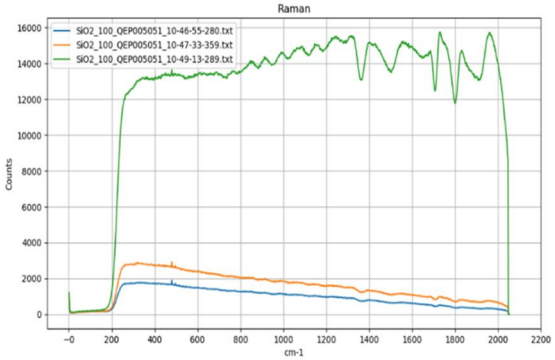

Fig. 8.55: Laser focus analysis for SiO_2

Finally, Fig. 8.56 shows the spectral response of silica-based materials at 514 nm is analyzed.

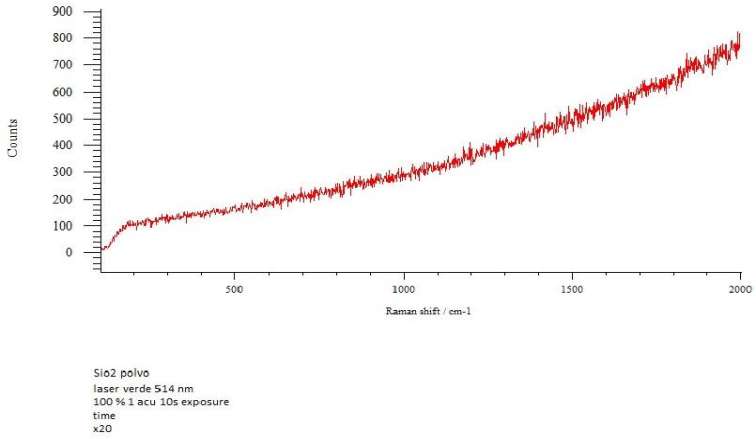

Fig. 8.56: Silica response at 514 nm

The collected spectrum using green laser does not shows clear peaks to identify the composition of the sample.

<u>Analyses over Iron oxide samples:</u>

As done with the other samples, Fe_2O_3 is analysed using Raman laser at 785 nm by placing the sensor at different distances from the sample, first slightly out of focus and then focusing it better (at an intermediate distance from the initial captures).

In this case, with good focus, the signal is saturated. In closer positions, the signal is intense and with a positive slope (green curve). In more distant positions (closer or further away than the focused one) the signal is less intense also with a positive slope (orange and blue curves).

New method proposal for chemical characterization of sterile material in scrap.

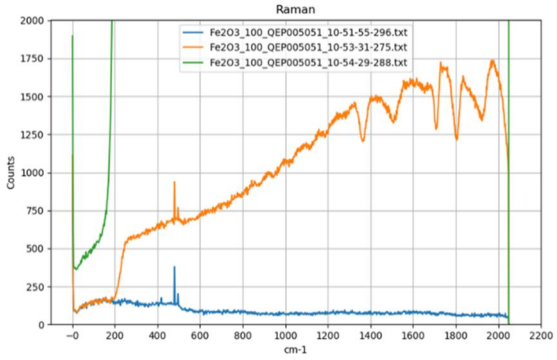

Fig. 8.57: Laser focus analysis for Fe_2O_3

After analysing the spectral information generated in the previous tests at 785 nm, no characteristic peaks reported in the literature are identified. However, if same experiments are conducted with a Raman at 514 nm, the iron oxide sample is clearly identified as a mixture of iron oxide in the form of hematite and goethite.

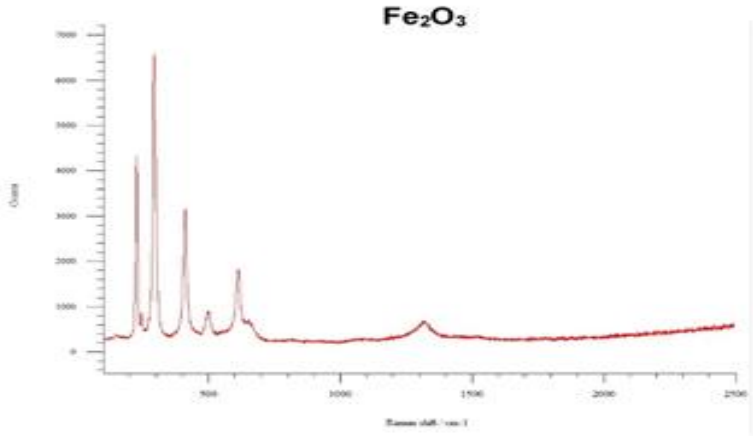

Fig. 8.58: Fe_2O_3 response at 514 nm

8.1.6.3.2 Capture over pressed pellets of mixed compound samples

For this analysis, samples of the different pure components selected earlier (Silica [SiO_2], Dolomite [$CaMg(CO_3)_2$], Calcite [$CaCO_3$] and Iron Oxide [Fe_2O_3]) were mixed to prepare pressed pellets as shown in Fig. 8.59.

In this case, and based on the conclusions reached in previous sections, the most convenient capturing parameters have been identified and set as follow:

- Laser power: 750 mW
- Integration time: 2 seconds
- Distance between sensor and sample individually adjusted for each case

New method proposal for chemical characterization of sterile material in scrap.

Sample ID	CaO (%)	Dolomite (%)	Fe2O3 (%)	SiO (%)$_2$
Sample 1	25	0	75	0
Sample 2	25	0	75	0
Sample 3	25	0	0	75
Sample 4	25	0	0	75
Sample 5	33	0	33	33
Sample 6	33	0	33	33
Sample 7	50		50	0
Sample 8	50	0	50	0
Sample 9	50	0	0	50
Sample 10	50	0	0	50
Sample 11	75	0	0	25
Sample 12	75	0	0	25
Sample 13	75	0	25	0
Sample 14	75	0	25	0
Sample 15	0	0	75	25
Sample 16	0	0	75	25
Sample 17	0	0	25	75
Sample 18	0	0	25	75
Sample 19	0	0	50	50
Sample 20	0	0	50	50

Fig. 8.59: Chemical composition of Mixed compounds pellets

Note that Dolomitic line was not used any more due to the similarity of the spectral signature with lime.

CaO / SiO_2 Mixtures:

Fig. 8.60 describes the result obtained over the analysis of the samples identified as sample 3, sample 4, sample 9, sample 10, sample 11 and sample 12 in Fig. 8.59.

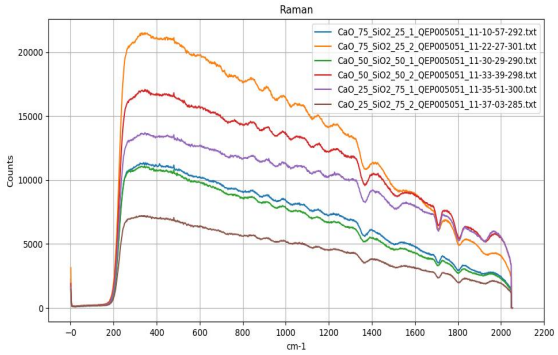

Fig. 8.60: Mixtures of CaO and SiO_2 in different proportions

Throughout the whole spectral range analysed, there is no relationship between the chemical composition of the pellets and the Raman signal intensity acquired for the different samples. Also, the spectral signatures obtained are quite similar to the curves previously identified for pure SiO_2 samples and no characteristic peaks or traces identified in the pure CaO pellets analysed before are detected.

CaO / Fe_2O_3 Mixtures:

Fig. 8.61 describes the result obtained over the analysis of the samples identified as sample 1, sample 2, sample 7, sample 8, sample 13 and sample 14 in Fig. 8.59

New method proposal for chemical characterization of sterile material in scrap.

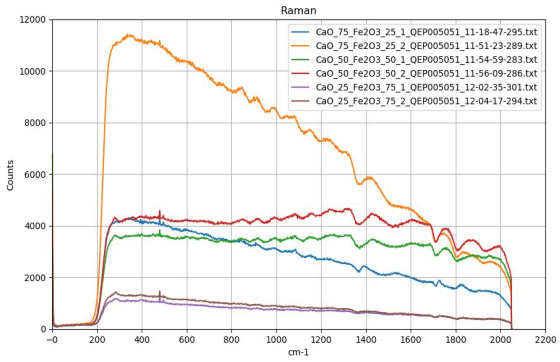

Fig. 8.61: Mixtures of CaO and Fe_2O_3 in different proportions

For this case, the spectral signatures obtained are quite similar to the curves previously identified for pure Fe_2O_3 samples and no characteristic peaks or traces identified in the pure CaO pellets analysed before are detected. However, samples with less content of CaO have a lower signal intensity level (except the sample identified as sample 8), which is in good agreement with the signal intensity generated by both pure components when analysed separately

SiO_2 / Fe_2O_3 Mixtures:

Fig. 8.62 describes the result obtained over the analysis of the samples identified as sample 15, sample 16, sample 17, sample 18, sample 19 and sample 20 in Fig. 8.59

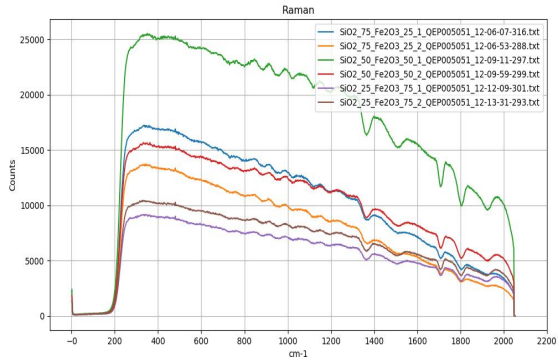

Fig. 8.62: Mixtures of SiO_2 and Fe_2O_3 in different proportions

For the lower wavelength range, the signal intensity, when high values Fe_2O_3 are present, shows coherence but, as the SiO_2 content increases, this coherence disappears. However, throughout the whole spectral range analysed, there is no relationship between the chemical composition of the pellets and the Raman signal intensity acquired for the different samples. Also, as happened for SiO_2/CaO mixtures case, the spectral signatures obtained are quite similar to the curves previously identified for pure SiO_2 samples and no characteristic peaks or traces identified in the pure Fe_2O_3 pellets analysed before are detected.

CaO / SiO_2 / Fe_2O_3 Mixtures:

Fig. 8.63 describes the result obtained over the analysis of the samples identified as sample 5 and sample 6 in Fig. 8.59

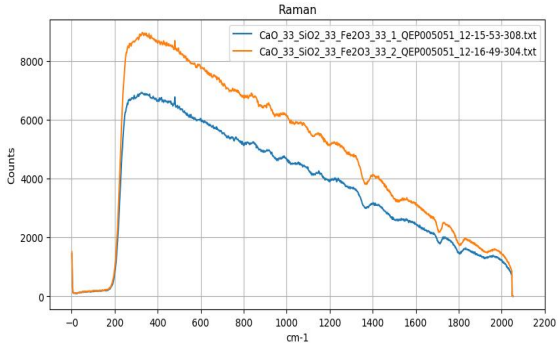

Fig. 8.63: Mixtures of CaO, SiO_2 and Fe_2O_3 in different proportions

Again, the spectral signatures obtained are quite similar to the curves previously identified for pure SiO_2 samples and no characteristic peaks or traces identified in the pure Fe_2O_3 nor CaO detected.

The abundance analysis was done, defining as endmembers (base components) the samples made on the pure components, for each compound per sample according the methodology described in section 8.1.3. The calculation procedure for abundance estimation was performed as follow:

- A pre-processing of each spectra has been carried out. According this pre-processing, the beginning and end of the spectral signature was removed, analysing only the spectral information contained in 250 - 2000 cm^{-1} range.
- On the resulting signal, the minimum is subtracted, so that the minimum signal for each of the spectra is equal to 0
- Finally, each of the spectra resulting from the previous step has been normalized with respect to its maximum to facilitate the comparison between different acquisitions.

The results obtained are shown in the following table:

	Real			Estimated		
	CaO	SiO_2	FeO	CaO	SiO_2	FeO
CaO 33% + SiO2 33% + Fe2O3 33%	33	33	33	0,01	99,97	0,01
CaO 25% + Fe2O3 75%	25	0	75	1,93		98,07
CaO 50% + Fe2O3 50%	50	0	50	0,37		99,63
CaO 75% + Fe2O3 25%	75	0	25	1,34		98,66
CaO 25% + SiO2 75%	25	75	0	0,03	99,97	
CaO 50% + SiO2 50%	50	50	0	0,04	99,96	
CaO 75% + SiO2 25%	75	25	0	0,02	99,98	
SiO2 25% + Fe2O3 75%	0	25	75		99,95	0,05
SiO2 50% + Fe2O3 50%	0	50	50		99,94	0,06
SiO2 75% + Fe2O3 25%	0	75	25		99,97	0,03

Table 8.8: Abundance estimation for spectra information acquired with Raman spectroscopy

From Table 8.8, It can be concluded that all samples containing SiO_2 are identified. However, for all of them the estimated SiO_2 amount is higher than 99% regardless of the actual amount of SiO_2 contained in the sample.

On the other hand, those samples that do not contain SiO_2, are identified as Fe_2O_3, also regardless of the amount of Fe_2O_3 in the mixture.

New method proposal for chemical characterization of sterile material in scrap.

Looking at these results, it is concluded that it is not possible to calculate abundances through the acquired spectral signatures. The main reason is that the spectra response obtained do not identify the composition when certain compounds are in the mixture analyzed

8.1.6.3.3 Capture over pressed pellets of sterile samples

For this analysis, the two sterile samples, identified as sample A and sample B, were also prepared in pressed pellets.

As in the previous analysis, two different spectral processing algorithms were tested for carrying out this analysis:

a) Removing the continuous component of the signal, signal smoothing and Standardization (dividing by standard)

b) Spectra smoothing and Standardization (dividing by standard)

Fig. 8.64 shows the results after Raman spectra analysis:

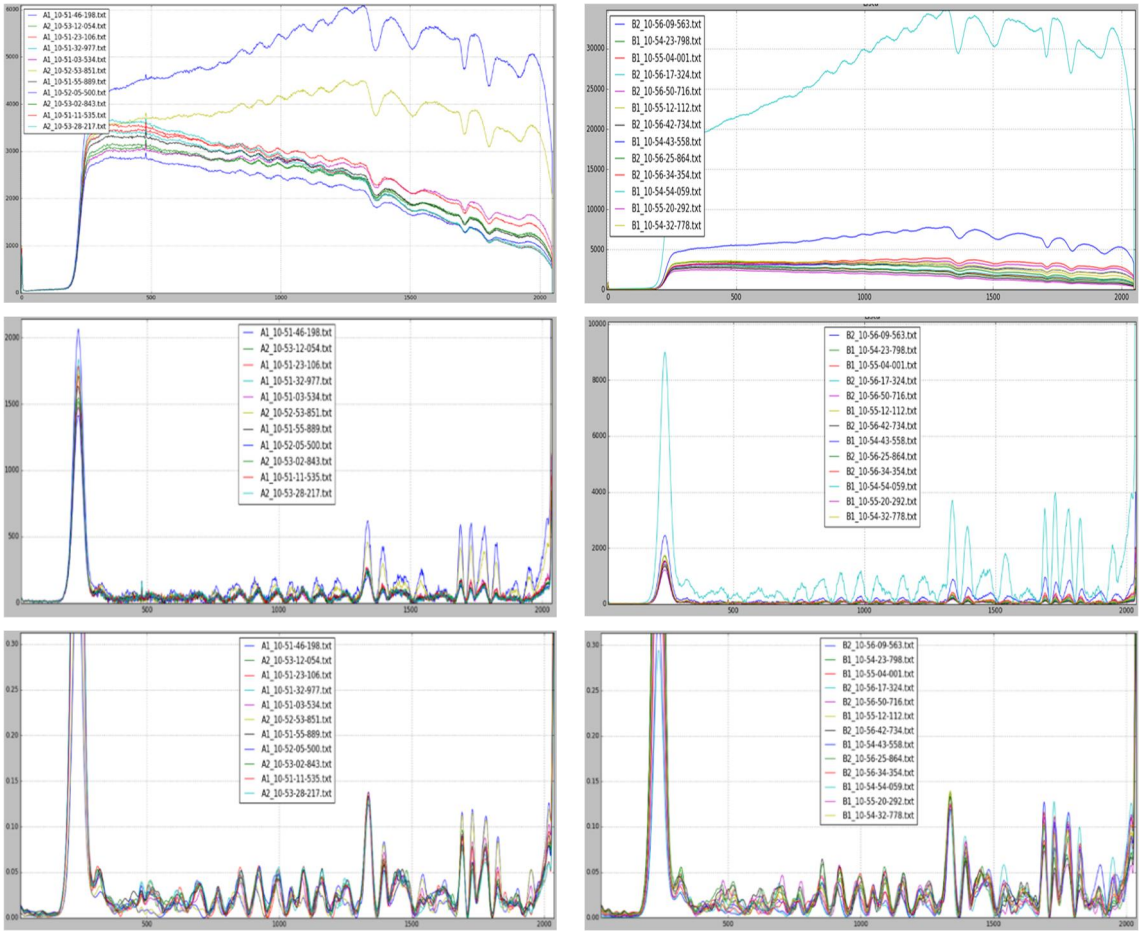

Fig. 8.64: Sterile A (Left) and B (Right) Spectral data; Up) without processing, Midle) after removing continuous component and Down) after spectra smoothing and standardization

Fig. 8.65, the averaging of the spectral data from different captures for each material, using processing algorithm B, are compared with the results obtained after same data processing of the samples captured directly from the pipettes.

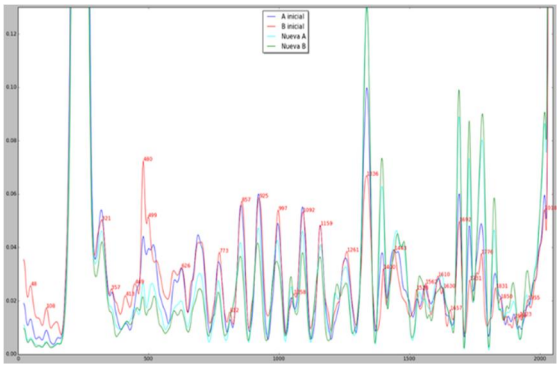

Fig. 8.65: Comparative analysis between Sterile A and B and silica from pressed pellect set up

Also, and given the similarities observed between the silica and sterile signals, the following figure draws together these signatures to allow a quick comparative analysis

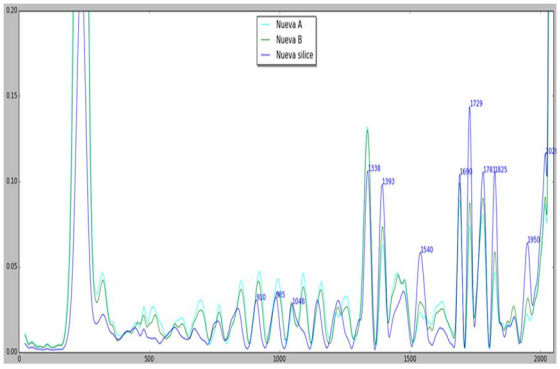

Fig. 8.66: Comparative analysis between Sterile A and B and silica from pressed pellet set up

In view of the results, the conclusion that can be drawn is that the Raman spectra signature got from sterile is basically the same as the silica's signature. This might indicate that silica gives a higher signal than calcite, dolomite or Iron oxide and masks these components.

8.1.7 Main conclusions on the use of Raman spectroscopy for the characterization of sterile

In Raman spectroscopy, the energy of the incident light is not enough to excite the molecule to a greater electronic level of energy, but it produces change in the vibrational state of the molecule. The analysis of these vibrational behaviors has proved to be valid for surface characterization of materials in different fields using laboratory equipment.

In steelmaking industry, where hard environment conditions are present, those kinds of laboratory system cannot be applied. However, recently, there have been significant improvements in Raman technology (stabilized, small, inexpensive laser sources, optical filter technology, and charge-coupled device (CCD) detectors) that could allow being used directly in site.

In this work several Raman systems have been tested, modifying the samples preparation techniques and the system parameters configuration. Based on these analyses, the following conclusions are reached in relation to compound analysis capabilities of Raman technology:

- Dolomite: It is possible to easily identify some characteristic peaks reported in the bibliography associated with this material; One small peak close to the theoretical at 724 cm^{-1} and the main characteristic peak at 1086 cm^{-1}.

  On the other hand, it is possible to produce same results with both laser at 785 nm and at 514 nm

  In the case of Dolomitic materials, laser power and sensor exposure time do not affect too much to the obtained results.

- Calcite: It is possible to identify some characteristic peaks reported in the bibliography associated with this material; small wide peak was detected at 711 cm^{-1}, which corresponds closely with those found in the literature. Thus, the main characteristic peak of calcite at 1085 cm^{-1} is now clearly identify at 1084 cm^{-1}.

  In this case, the results obtained with the laser at 514 nm are comparable to the results obtained with the laser at 784 nm.

  Like Dolomitic materials, laser power and sensor exposure time do not affect too much to the obtained results over Calcite materials.

- Silica: In the case of silica, with the laser at 784 nm (green laser) no significant information was obtained.

  Also, the results are quite dependable to the laser configuration at 514 nm; the best results were obtained at 350 mW and with an exposure time of 300 sg

- Fe2O3: Although it is not possible to get useful spectral information from Iron oxide samples at 785 nm, when using Raman at 514 nm, different iron oxide components can be clearly identified in the sample

New method proposal for chemical characterization of sterile material in scrap.

- Sterile: In view of the results, the conclusion that can be drawn is that the Raman spectra signature got from sterile is basically the same as the silica's signature. This might indicate that silica gives a higher signal than calcite or dolomite and masks these components.

  Since the main component in the sterile present in scrap is compose by silica (amorphous SiO_2 do no present Raman signal), Raman spectroscopy has been proved not to be a useful technique for quick analysis of nonferrous components present in scrap.

As summary, using Raman spectroscopy, well defined spectra for Iron and calcite compounds are obtained. However, when amorphous SiO_2 is present in the sample, the spectral signature is totally saturated by SiO_2 signal. This effect makes not possible to analyses sterile material composed by silica.

Besides SiO_2 effect, it was also identified some challenges in the capturing procedure definition related to the sample preparation and high variability in the optimal laser parameter depending on the compound to be analyzed. This makes not possible to propose a portable solution for ferrous scrap sterile analysis using only Raman spectroscopy.

8.2 Hyperspectral Imaging

Nowadays, one promising approach for quick characterization of unknown materials is based on hyperspectral imaging.

Hyperspectral analysis techniques make possible to obtain the emission and reflection spectrum of an element remotely by estimating the emissivity or reflectivity of the element to be analyzed, in terms of it wave length. This spectral behavior of each material at different wavelengths depend on various factors, including the chemical composition. However, the spectral information contained in the signal presents great variability and it is affected by other factors such as lighting, noise or low atomic excitation. For this reason, the main challenge when applying this hyperspectral approach is to build robust algorithms to obtain the spectral information inherent to that signal as well as the statistical techniques for performing robust data regressions.

8.2.1 Literature survey about Hyperspectral imaging

Light is composed of a bean of photons, associated to different frequencies (energies). The electromagnetic spectrum of an object can be defined as the distribution of the energetic intensity emitted, reflected or absorbed at a given range of wavelengths. This way, an incident light ray (L) is defined by the intensity of that ray in each one of the associated wave lengths. When this ray encounters a surface, part of it is absorbed, another one is transmitted and a third one is reflected. The reflected part is determined by the spectrum of the incident ray, the geometry of the body, the degree of mirror or Lambertian (diffuse) behavior of the object and its reflectivity (Fig. 8.67). This reflectivity is determined by its molecular characteristics and it is different depending on its Chemicals composition. As a result, for example, a red object will reflect the rays of wave length close to red, while it will absorb other wave length rays (e.g. blue) (133).

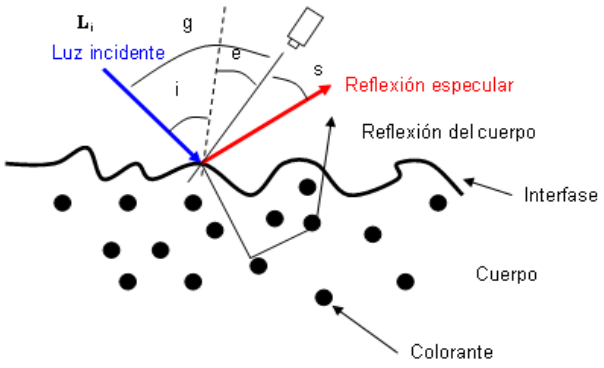

Fig. 8.67: Dichromatic reflection model

Based on these parameters and considering a known set of conditions, it is possible to estimate the real reflectivity of the object, assuming several lighting hypotheses. The

New method proposal for chemical characterization of sterile material in scrap.

reflectivity data of an object represents its behavior for different wave lengths, which will be used to infer some aspects related to its chemical properties.

Hyperspectral imaging, also known as imaging spectroscopy, is concerned with the measurement, analysis and interpretation of spectra acquired from a given scene (or specific object). More precisely, hyperspectral instruments acquire electromagnetic energy scattered within their instantaneous field view in hundreds of spectral channels with high spectral resolution, covering selectively, and according to the acquisition device technology, the visible and the different infrared ranges (IR) of electromagnetic spectrum. The signal recorded by a hyperspectral sensor at a given band and from a given pixel is often a mixture of the light scattered by the constituent substances located in the respective pixel spatial coverage.

In simple terms, a hyperspectral image is an extended image in which, instead of having three RGB colour channels (red, green, blue), there are available a number N of channels each of which is associated to a length of wave. This is a combination of a spectrograph and a digital camera.

There are numerous methods to obtain these images; one of the most used is based on diffraction net or a prism in which the system captures all spectral bands simultaneously. To this end, the variability between refraction angle and wavelength is used. Thus, after capturing a line of an image, the spectral information is extracted through a prism which disperses each of the wavelengths of the image. Thus, the image obtained contains; in abscissa, the captured line position and, in ordinates, each of the spectral frequencies. To obtain the complete image the system combines multiple snapshots of the same image.

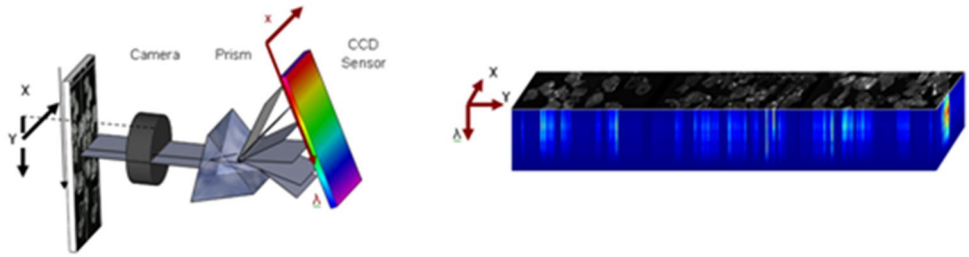

Fig. 8.68: Principle of hyperspectral imaging by refraction

Hyperspectral techniques allow obtaining the emission spectrum or reflection of an element remotely. This allows estimating the reflectivity or emissivity of one element in relation to its wavelength, and this information is dependent on several factors, including the chemical composition.

The selection for an application of the spectral range of the camera as well as the exact number of spectral channels (which can be typically between 256 and 1024 bands) and the spectral resolution (which can be typically of 10 nm) depends on the physical properties of the phenomena to be studied and induces very different costs of the device. This versatility allows the systems to detect, classify and identify different material, thus overcoming some of the limitations of the colour cameras which operate only in the range of visibility with low spectral resolution

New method proposal for chemical characterization of sterile material in scrap.

As opposed to standard images observed by the human eye, hyperspectral images contain complete spectral information of each spatial point of the image. This image is known as hyperspectral cube (Fig. 8.68) and consists of a three-dimensional matrix, in which two dimensions represent the spatial position of the point and the third dimension represents each spectral band. From a different point of view, a hyperspectral image can simply be considered as a vectorial extension of a monochrome image. This approach allows using the same tools as for a monochrome (grey) image, but from a vectorial perspective.

In hyperspectral images, each pixel of the image is represented by a vector, whose components correspond to one of the wave lengths captured, offering not only information related to the colour associated to the scene, but also information related to its molecular properties, as seen previously. Similarly, by selecting a given wave length, the two-dimensional image associated to that wave length can be determined, obtaining spectral and spatial information at the same time.

In short, the analysis by using hyperspectral technology in hard environments is based on the design of a mathematical function that relates the values of reflectivity captured by the hyperspectral camera with the real physical and chemical values of the element by a set of samples to generate a mathematical function to perform this transformation (regression). This technique is known in spectroscopy as calibration.

Many of the algorithms for hyperspectral analysis were developed for remote sensing applications (134) (135) (136) (137) (138) (139). Although they can be conceptually similar there are differences on the application that precludes the use of standard hyperspectral algorithms on every kind of application. We are going to focus on the algorithms and techniques related to material characterization applications:

1. Image capture and spectra selection: Using the adequate sensor that should be related to the materials to be characterized, their emission spectra and their emission lines.
2. Image normalization: The acquisition system must be calibrated. Indeed, using a simple polynomial calibration over a known spectrum (e.g. fluorescent tube or a laser) is a very precise calibration way. Besides the camera calibration another characterization must be done in order to correct the effect of lightning.

8.2.1.1 Previous applications of Hyperspectral technique in industrial applications

The number of published works which have studied the potential interest of hyperspectral imaging for steel industry applications is extremely limited. However, there are several researches done for using this kind of technologies in industrial sectors different form steel sector. Here is a brief description of some of them:

- The application of hyperspectral in steel industry can be inspired from the more developed case of wood and paper industry (140). A very interesting study on the

industrial application of inline paper sorting (according to the nature of the cellulose fiber) in recycling plants using a NIR hyperspectral camera was presented in 2005 (141). The proposed algorithm is basically composed of a pre-processing step (white and dark correction), dimensionality reduction (using PCA or LDA) and classification using k-NN. From this study, we can conclude that the (quasi) real-time requirements of inline quality control involves that the image analysis algorithms should be carefully optimized.

- On the other hand, wavelengths in the near infrared (NIR) range can be used for materials classification. However, sorting paper according to quality is a very difficult task due to the close similarities between the materials. Therefore, we have also found a development of a unique industrial inline material sorting system which uses the spectral imaging technique (141).

- Another application for the technology studied in this report is the nonferrous waste materials sorting. This kind of materials cannot be sorted by classical procedures due to their colour, weight and shape similarities. The experimental results obtained reveal that factors such as the various levels of oxidization of the waste materials and the slight differences in their chemical composition preclude the use of the spectral features in a simplistic manner for robust material classification. To address these problems, the proposed FUSSER (Fuzzy Spectral and Spatial classifier) algorithm merges the spectral and spatial features to obtain a combined feature vector that is able to better sample the properties of the nonferrous materials than the single pixel spectral features when applied to the construction of Multivariate Gaussian Distributions (74).

  The experimental results indicate that the proposed algorithm increased the overall classification rate from 44% using RGB data up to 98% when the spectral-spatial features are used for non-ferrous material classification

- The application of Hyperspectral Imaging systems is now well introduced for bulk sorting of materials. Since the work with the complex nature of information of Hyperspectral Imaging systems and the huge data volumes generated are recognized to be quite developed yet. It has been done some work in the application technology for the inline quality control of potatoes on the example of Sugar-Ends detection is presented (142)

- Another industrial sector where the multivariate imaging has been already used for quality control is the pharmaceutical industry, see the review (143), with as typical applications the measure of coating thickness and the counterfeit drug identification. However, this kind of “chemometrics” systems requires spectroscopic technologies, such as Raman or vibrational NIR spectroscopy, which are not compatible with the requirements of the inline quality control of steel products.

8.2.1.2 Prior spectra knowledge

Spectral reflectance in the visible and near infrared (0.35 to 2.55 µm) offers a rapid, inexpensive, non-destructive technique for determining chemical features of certain materials.

In this section some information obtained after a literature survey are presented. Previous laboratory works may be used as starting point of the current research line for identifying the main reflection characteristic of the different components present in ferrous scrap sterile.

8.2.1.2.1 Calite ($CaCO_3$) and Dolomite ($CaMg(CO_3)_2$)

Regarding Calcite and Dolomite materials, several studies have been found in the literature reporting two strong bands at 2.340 µm and 2.537 µm in the particular case of calcite and at 2.323 µm and 2.515 µm in the case of dolomite (144) (145) (146).

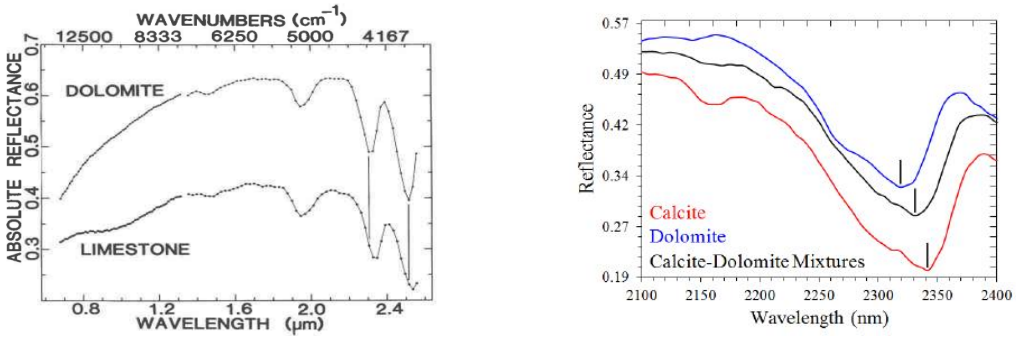

Fig. 8.69: Spectral signature of Calcite and dolomite reported by (144) left and by (145) right

As shown in Fig. 8.69. the spectra signature of carbonate minerals containing no transition metal cations are nearly straight lines near unity reflectance at wavelengths shorter than 1.6 µm. However, the presence of ferrous iron in calcite and dolomite can produce a broad absorption effect near 1.0 µm that can be useful for material identification purposes. This effect is shown in Fig. 8.70:

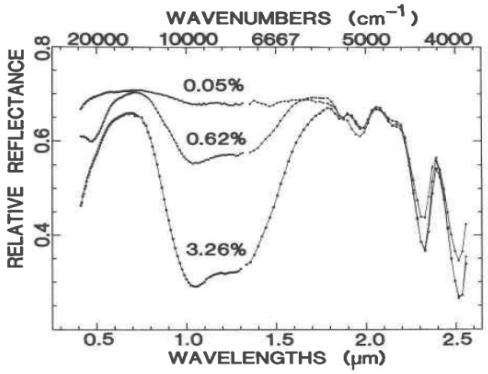

Fig. 8.70: Absorption band in carbonate materials due to the presence of Fe2+ (144)

New method proposal for chemical characterization of sterile material in scrap.

8.2.1.2.2 Silica (SiO_2):

As far as the analysis of silica is concerned, several studies have been found focusing on the characterization of rice husk ash (material used in the present study), as amorphous silica material by means of other technologies such as SEM (147), XRD (148) and FTIR (149). However, bibliographic references on the analysis of this type of material using hyperspectral techniques have not been found.

So that, the findings of this research work will allow to settle the foundations for future research works on the use of hyperspectral techniques for the analysis of Silica in other fields

8.2.1.2.3 Iron Oxides (FeO / Fe_2O_3)

Several studies have been found with regards the characterization of ferric iron minerals (hematite and goethite) (150) (151) (152).

In (150), distinct spectral curves in the visible near-infrared (VNIR) have been identified at about 465 nm, 650 nm and 850–950 nm.

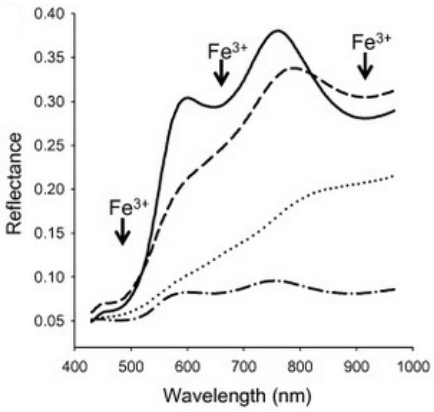

Fig. 8.71: Reflectance analysis and absorption bands of Ferric iron (Fe^{3+})

However, the shape or magnitude of the spectral curve of iron oxides can change due to numerous factors that need to be further investigated in the current work.

Also, (151) analyzed different absorption features in VNIR and SWIR reflectance spectra of several mineral species that can be used in this study. The characteristic absorption features for these materials correspond to specific molecular bonds such as OH, H_2O, CO_3 and other components of hydrous silicate minerals including AlOH, MgOH and FeOH bonds.

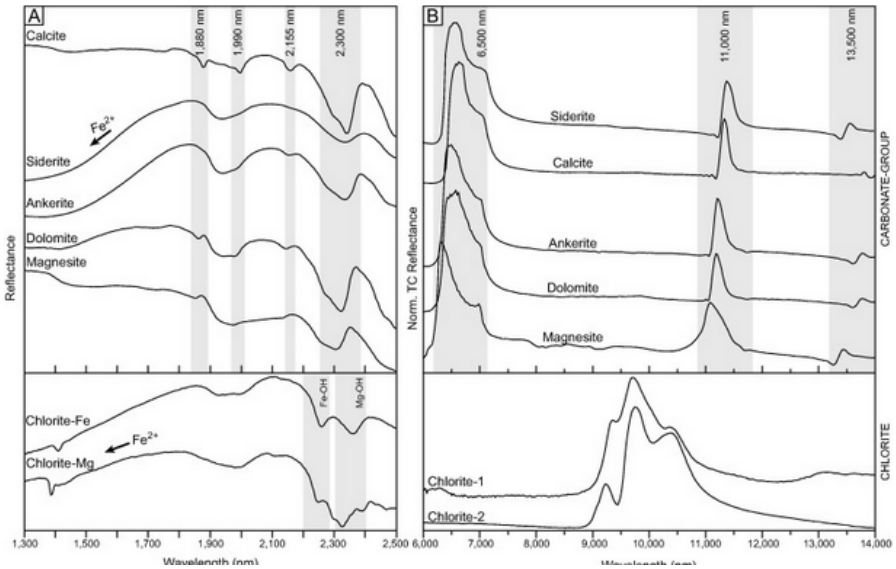

Fig. 8.72: (A) Short wave infrared (SWIR) reflectance spectra for reference library samples of carbonate and chlorite minerals. (B) Long wave infrared (LWIR or TIR) reflectance spectra for carbonate-group minerals and the positions of key spectral features used for diagnosis.

8.2.2 Laboratory equipment for spectral analysis

In the case of Hyperspectral processing, there are two key elements to consider; the Hyperspectral sensor (spectral range, sensibility, spectral resolution) and the lighting system used for exiting the sample.

The equipment used for conducting the proposed analysis were:

- Hyperspectral sensor: The hyperspectral optical sensor receives the light reflected from the material's surface and gets the intensity in each of the wavelengths analyzed. For this research activity, two sensors were tested:
    - Linear hyperspectral optical sensor in the VNIR range (400 - 1000nm): The sensor is composed by a spectrometer (Specim V10_04204) combined with a scientific CMOS camera (JAI-TM-1327GE)

Optical Characteristics:	
Type:	Specim V10_04204
Range:	400-1000 nm
Spectral resolution:	3.0 nm (30 um slit)
Spectral sampling:	0.78-6.27 nm/pixel
Spatial resolution:	RMS spot size < 9 um
Electrical Characteristics:	
Detector:	CMOS
Spatial Pixels:	1312
Spectral Bands:	768
Pixel size:	8 x 8 um
Camera Control:	CameraLink

Fig. 8.73: VNIR Spectrometer technical characteristics

    - Two-dimensional hyperspectral optical sensor in the SWIR range by sisuCHEMA (1000-2500nm)

Optical Characteristics:	
Type:	Specim sisuCHEMA
Range:	970-2500 nm
Spectral resolution:	10 nm
Spectral sampling:	6.3 nm/pixel
# Spatial pixel/line:	320
Other Characteristics:	
Illumination:	Diffused line
Data Format:	BIL file format, Evince end ENVI
Calibration:	Internal standard reference target

Fig. 8.74: SWIR Spectrometer technical characteristics

- Lighting system: The light is provided by wide spectrum illumination lamp that assures there is enough intensity on the wavelength range. The lighting system is based on a halogen bulb of 2218 lumens and forms 60º with the camera axial axis to reduce the effect of specular illumination.

8.2.3 Data processing algorithms

For analyzing the acquired spectral signature obtained by hyperspectral imaging and to extract the maximum spectral information as possible, as well as to stablish the comparative criteria between different samples, two types of methodologies are proposed:

First, for interpreting the acquired spectra three types of data processing are necessary:

- **Spectra acquisition**: The acquired spectral data is represented by an image where each element at column ***j*** represents a spatial point of the linear camera and each row element ***i*** corresponds to the radiance received at a wavelength ***λi***.. In Fig. 8.75 the imaging processing method is depicted.

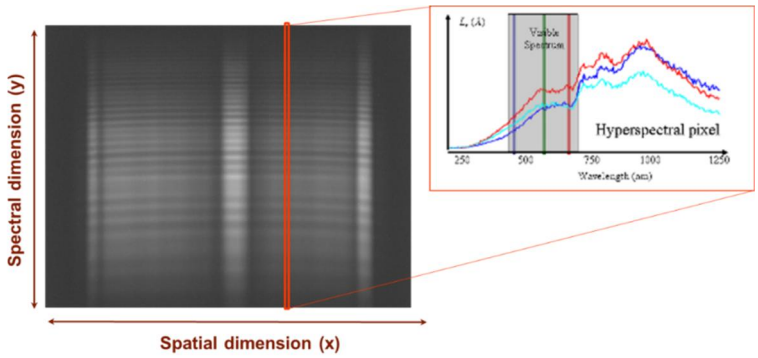

Fig. 8.75: Imaging processing method description (153)

Let ***Lj*** be the vector representation of the spectrum defined by the intensity responses of the ***M*** wavelengths at a spatial column ***j*** of the image represented as:

$$\boldsymbol{L}_{raw\,j} = \{L_1, L_2, \ldots, L_M\}^T \tag{8.5}$$

- **Signal processing**: In order to extract as much information from the spectral signature as possible, several signal processing techniques are proposed:
    - Median: It represents the value of the central position variable in a set of ordered data. In the case of multispectral analysis, for each wavelength, the reflectance value of 5 different spectra are taken and sorted, and the third value in the row (which is in the middle) is chosen.
    - Signal Smoothing: This processing technique consists on filtering the noise through convolution of a Gaussian filter. Each value of the spectrum is replaced by a weighted average of the nearby points using as weighting factors those corresponding to a Gaussian bell according the following equation:

$$G(x) = \frac{1}{\sqrt{2\pi}\sigma} e^{-\frac{x^2}{2\sigma^2}} \tag{8.6}$$

    - Signal normalization: This signal processing technique consists on performing the desaturation of the signal (subtracting the minimum so that it starts at 0)

and normalizing the resulting spectrum (dividing by the maximum) so that the new available data is between 0 and 1 and allows direct comparison.

- **Calibration algorithm**: The illumination system is based on a halogen lamp that is subject to temporal degradation. This causes incident radiance to change among different systems and to decay through lamp lifetime. The Spectralon (154) based calibration plate is used to calculate a polynomial correction method that calculates the lamp spectral radiance and compensates for the spectral light radiance changes (155). The calibration plate is made of four diffuse Spectralon tiles with 2%, 50%, 75% and 99% nominal reflectance. This reflectance level defines the calibrated working range reflectivity of the samples. A second-degree calibration polynomial is calculated pixel-wise to map each image intensity pixel (***i***=spectral wavelength, ***j***=spatial position) to the theoretical radiance of the Spectralon tiles at the calibration plate as shown in Fig. 8.76 and represented by equation (8.7).

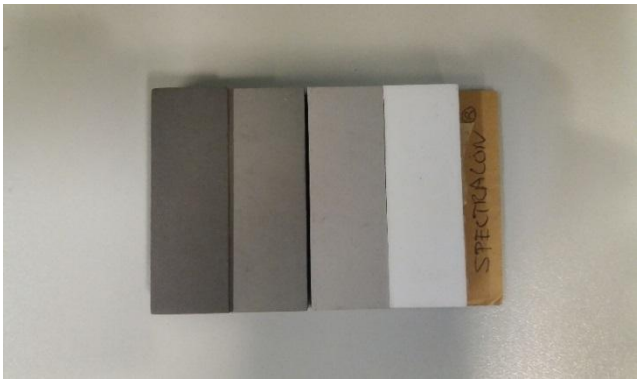

Fig. 8.76: Spectralon based calibration plate

$$L_{i,j} = a_{i,j} \cdot L_{raw}{}^{2}_{i,j} + b_{i,j} \cdot L_{raw_{i,j}} + c_{i,j} \quad \textbf{(8.8)}$$

Where $a_{i,j}$, $b_{i,j}$ and $c_{i,j}$ are the pixel-wise polynomial coefficients obtained by least-squares optimization which map the perceived intensity with the theoretical reflectance of the Spectralon tiles. This procedure decorrelates the perceived radiance with the lamp spectral radiance. Calibration parameters are calculated weekly in order to correct lamp degradation over time.

Second, the Chemical composition is estimated as following:

- Chemical composition estimation is done assuming a linear mixture model to calculate the percentage (abundance) of each base spectrum (endmember) in the observed Raman spectrum of the mixture.

  Due to signal complexity and high overlap between classes, classical unmixing methodologies based on linear methods do not yield appropriate results. To overcome this problem the Dobigeon Bayesian algorithm (131) (132) is adapted as a Bayesian generalization of a linear unmixing model on the normalized hyperspectral images of the different samples.

New method proposal for chemical characterization of sterile material in scrap.

$$y = \sum_{r=1}^{R} m_r \alpha_r + n \tag{8.9}$$

Where; ***y*** is the observed spectrum, ***m*** is each endmember (base) spectrum and each ***α*** value is related to the spectral abundance of each endmember and ***n*** represents the noise.

The ***α*** set follows the following constraints:

$$\forall r \in \{1, \dots, R\}, \alpha_r \geq 0 \; and \sum_{r=1}^{R} \propto_r = 1. \tag{8.10}$$

Based on this model, a set of statistical variables were defined:

Variable	Distribution	Notes
Alpha	Dirichlet distribution	This assure positivity and sum=1
Sigma	Half Normal	Sd=1
M	Observed data	Observed pure reflectance desaturated vectors

Table 8.9: Statistical variables in the linear mixture model

The probability is defined as a normal distribution between the observed and the reconstructed spectra by the statistical variables

$$f(y \mid \alpha^+, \sigma^2) = \left(\frac{1}{2\pi\sigma^2}\right)^{\frac{L}{2}} \exp\left[-\frac{\|y - M^+\alpha^+\|^2}{2\sigma^2}\right] \tag{8.11}$$

In order to calculate the statistical distribution of the observed variables, the Bayesian Markov chain Monte Carlo algorithm (MCMC) is applied. The MCMC estimation method allows to obtain the most probable probability of abundance and its statistical distribution. Also, the distribution of the different abundances is calculated.

8.2.4 Capturing procedure – Experimental set up

In this section, the two experimental configuration method used for spectral acquisition during laboratory tests are described.

In the very initial phase of the present work (hyperspectral imaging for sterile characterization), the laboratory set up used is shown in Fig. 8.77. This set up corresponds to the linear and static analysis of the selected samples in Visual + Near IR spectral range (400-1000 nm). The research was carried out using an existing equipment developed in ArcelorMittal for the chemical analysis of white slags originated in the steel treatment in the ladle process (76) (156) and under the patent application PCT/IB2015/053453.

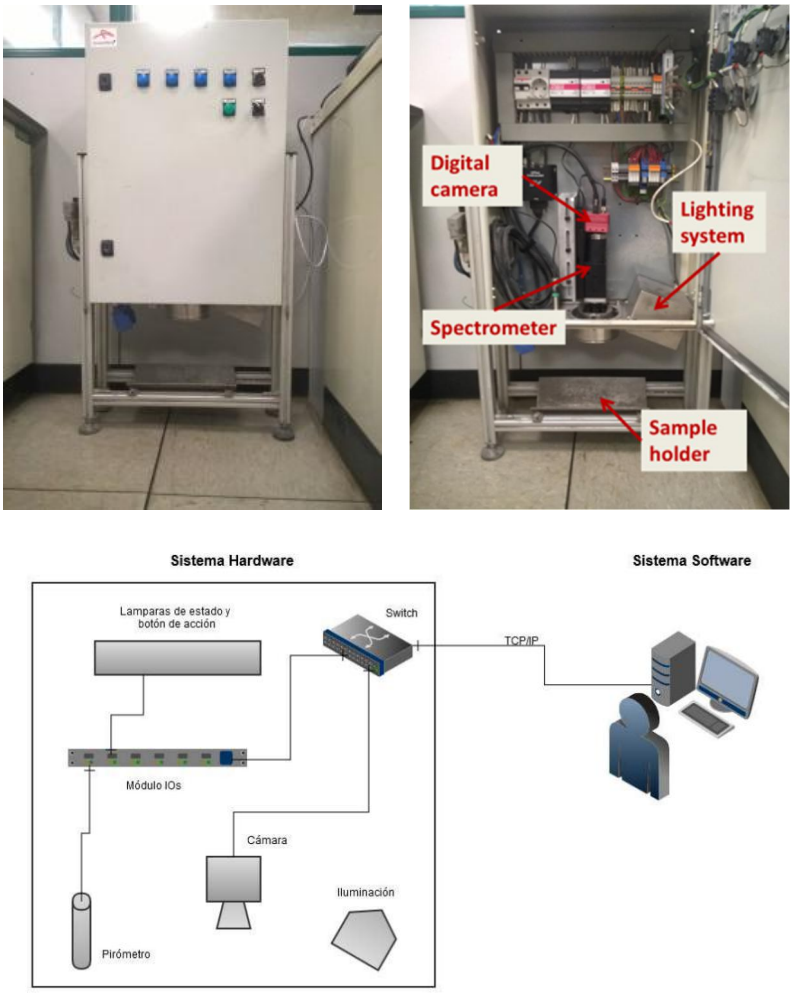

Fig. 8.77: Detail of the CARESBLOMETER system used by AM for LF slag analysis

The second laboratory configuration tested in this PhD thesis corresponds with a dynamic analysis of the selected samples. A new laboratory set up has been specifically developed for this experiment and consists on a conveyor belt driven by a servomotor and controlled by a FESTO CMMP-AS system. The system has got a programmed starting and ending point for the displacement of a tray placed on the belt. This tray carries the sterile samples to be analyzed. In the zenith position of the conveyor belt, two linear hyperspectral sensors (SisuCHEMA SWIR by SPECIM and PFD-65-V10E by SPECIM) have been placed to cover the spectral range among

400-1000 nm and 900-2500 nm. The two hyperspectral sensors were adjusted in such a way that the collected data from both sensors corresponds with the same spatial line. Thus, to ensure the control on lighting environmental conditions, the system is provided by an illumination system composed by two 50W halogen lights. Fig. 8.78 and Fig. 8.79 show the described system:

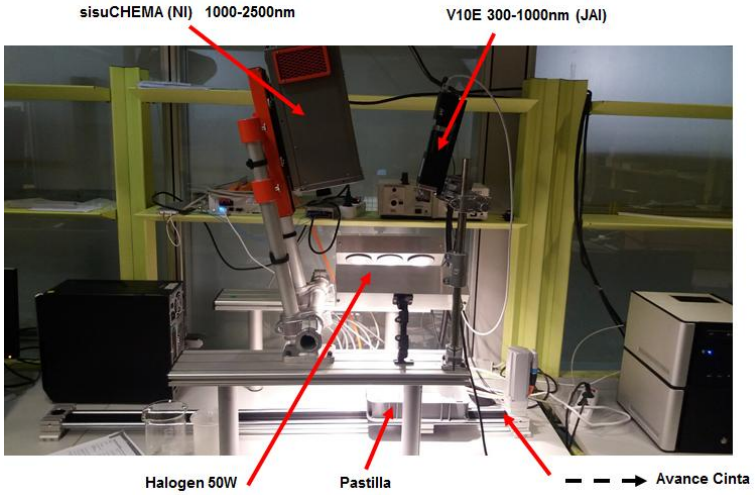

Fig. 8.78: Snapshot of the system installed in the laboratory

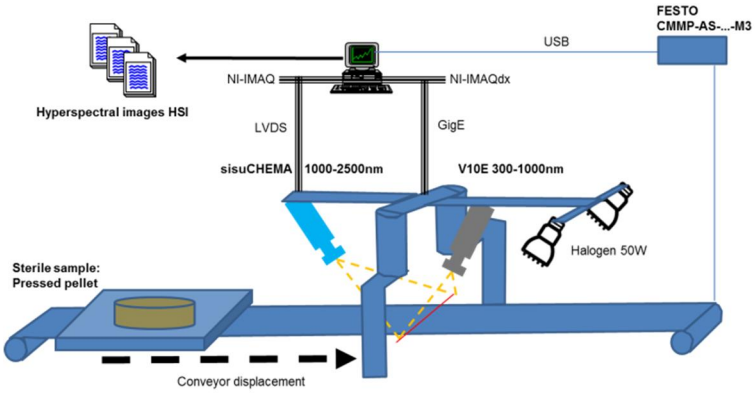

Fig. 8.79: Schematic representation of the laboratory set up

New method proposal for chemical characterization of sterile material in scrap.

8.2.5 Sample selection and preparation

Similarly, to previous experiments, the compounds selected to simulate real sterile in scraps were CaO, MgO, SiO_2.and Fe_2O_3 (same sources than before). In the case of hyperspectral processing, different samples combinations were prepared using the pressed pellet technique as shown in Fig. 8.80. For each mix, 2 samples were prepared.

Fig. 8.80: Pressed pellet of pure compound mix to simulate scrap sterile

8.2.6 Experimental results

Similarly, to the other tested technologies within this work, the objective of this novel activity is to evaluate whether hyperspectral imaging is suitable for implementing a new in situ analytical technique for the characterization of sterile materials contained in scrap.

The activities explained in this section aim to determine the most suitable capturing conditions under controlled laboratory conditions (lighting, temperature, environmental pollution, sample preparation). To this end, artificially prepared samples with well-defined chemical compositions will be used, so that, and supported by previous bibliographical references, it will be possible to establish the processing and analysis patterns of the spectral signatures obtained, which will then be applied under real industrial conditions.

8.2.6.1 Initial calibration procedure

The main challenge when proposing hyperspectral imaging lies on the fact that the trained models extracting features are not generalizable from one site to other. Also, when big changes in the environmental conditions occur, these analytical solutions are hardly generalizable. To solve these issues, the first step is to define a robust calibration methodology.

Given the importance of the calibration process in this type of technologies it is worth dedicating a complete section focus on defining the calibration methodology used during the current activity.

The sensor calibration pipeline in a hyperspectral sensor for chemical analysis should be composed by three main blocks that will correct all the possible sources of noise in the illumination. These blocks are; Initial calibration, Spectral normalization and Irregular reflection correction.

Hyperspectral device's sensors proportionally transform the incoming luminous energy (radiation) of each point of a scene into an electrical signal. During this process noise is added to the signal. Theoretically, in dark conditions the electrical signal generated by the image should be equivalent to zero. However, this is not the case due to the dark current. The dark current consists of a constant part (readout noise) and a non-constant part depending on the detector's temperature and the integration time (thermal noise). The first block is the initial calibration of the complete camera system including Dark calibration. This calibration has the objective of remove irregularities produced by hardware elements in the camera (static effects). The set composed by the camera sensor and the prism will be calibrated during the assembly of the hyperspectral camera and this is the initial calibration. To this end, the manufacturer of the camera provides a calibration polynomial that relates the wavelengths of the spectra. This polynomial is required to have a camera invariant model, as all the spectra will be defined in terms of its wavelengths and not in terms of its pixel position in a particular camera.

New method proposal for chemical characterization of sterile material in scrap.

On the other hand, Dark calibration consists on measuring the dark current by obscuring the light entrance to the detector and the subtracting it from the sensor's raw digital current values. In order to do the dark calibration, a dark scene was captured before every capturing campaign to be used as reference dark signal

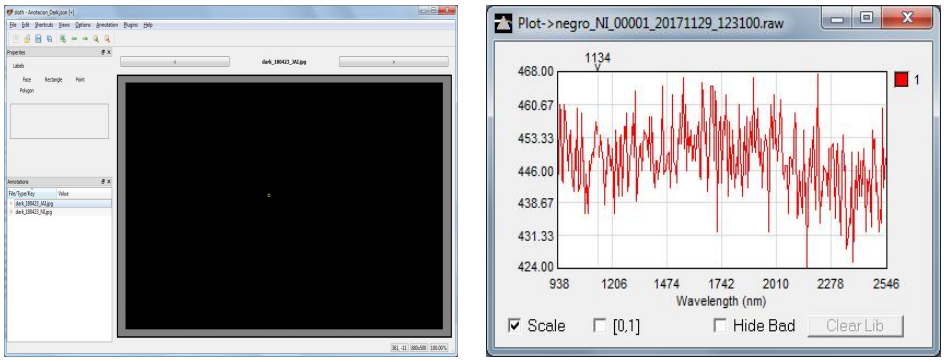

Fig. 8.81: Dark reference

Regarding dynamic effect corrections (changes in illumination along time), a periodic calibration must be implemented. A relative reflectance calibration is required.

As it was described previously, when any image processing technique is used for analyzing a scene, it is necessary to define the procedures that ensure system reliability along time at different environment conditions such as light, temperature variation or optic cleanliness.

The spectral calibration element selected to calibrate the hyperspectral sensors and to ensure the robustness of the acquisition results is based on 4 reflectance patterns provided by Spectralon (154). These reflectance patterns present known diffuse reflectance of 12%, 25%, 50% and 99%. Along the whole spectral range Then a second-order calibration polynomial is calculated pixel-wise to map each image intensity pixel to the theoretical radiance of the Spectralon (154) tiles at the calibration plate and so that, the "state" of illumination at every moment can be estimated.

- Calibration of the laboratory set up for static analysis (Visual + Near IR).

For the hyperspectral sensor covering 400-1000 nm spectral range (Specim V10_04204), the reflectance information obtained after acquiring the 4 reflectance patterns are shown in Fig. 8.82

Captured Image		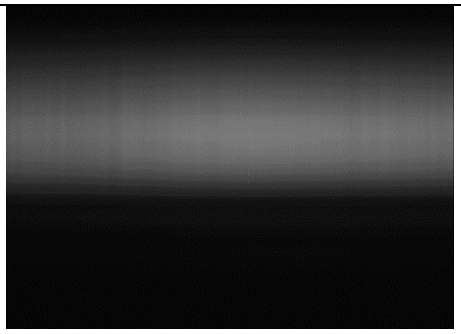
Reference	99%	50%

Captured Image	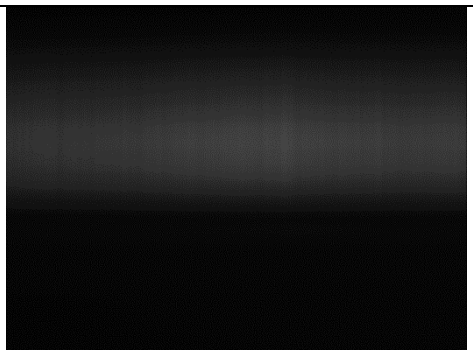	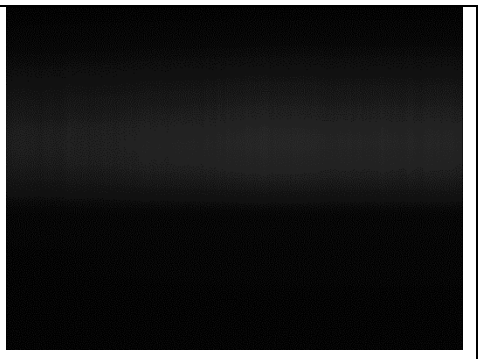
Reference	25%	12%

Fig. 8.82: Calibration references images captures by Specim V10 camera

Since in this laboratory set up a linear sensor is used, the reflectance information for calibration is obtained placing manually each of the 4 reflectance patterns in front of the camera and acquiring one line of the scene (note that X axis represents the space and the Y axis the reflectance intensity at every sensitive wavelengths).

Subsequently, to obtain the real reflectance value corresponding to each pixel of a capture, a polynomial equation generated by the 4 points of the reference patterns is calculated.

Since each wavelength could present a different behavior, it is necessary to calculate the polynomial equation for each wavelength independently. Then, the polynomial equations are applied to the captured reflexion value of every pixels at each particular wavelength using the Wavelength calibration equation provided by the spectrograph supplier represented as:

$$y = 3.66e^{-5} \cdot x^2 + 0.60131 \cdot x + 368.3846 \quad \textbf{(8.12)}$$

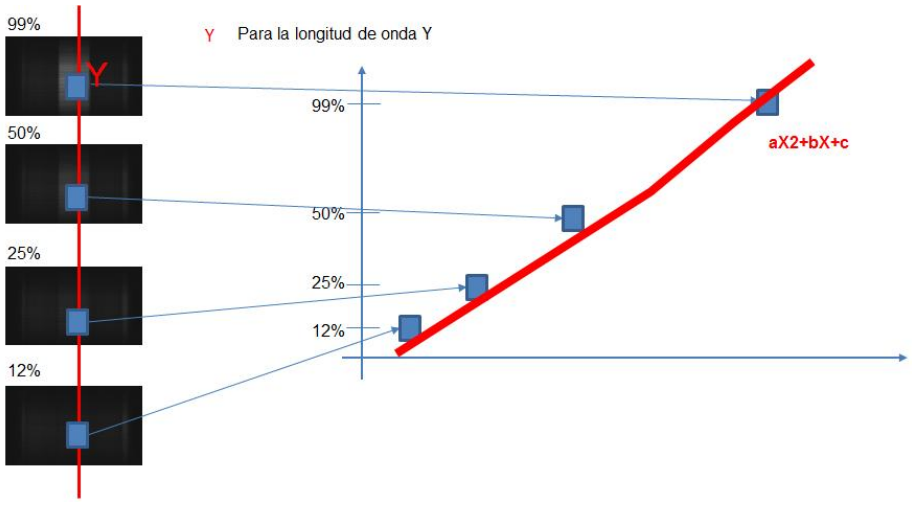

Fig. 8.83: Schematic representation of the calibration process for one specific wavelength

Fig. 8.84 depicts the spectral transformation after applying the mentioned calibration process based on reflectance patterns. Where the picture on the left side of the image shows the acquired values for each of the 4 plates and the picture on the right side shows the linearization of the data after applying the calibration polynomial equations.

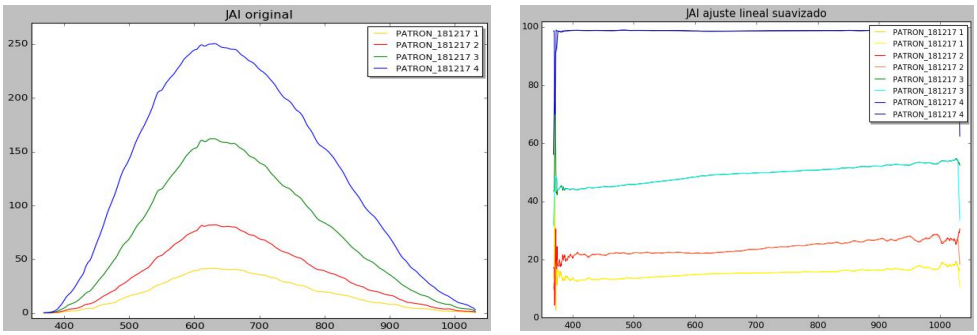

Fig. 8.84: Calibration process; (left) raw acquired data and (right) calibrated response

- Calibration of the laboratory set up for Dynamic analysis (VNIR + SWIR).

For the Dynamic analysis, two different sensors were used; V10_04204 sensor by Specim (400-1000 nm) and Sisuchema sensor by Specim (970-2500 nm). For this set up, instead of the static capturing, the samples are displacing in front of the sensor on a conveyor belt, and the whole surface of the sample is acquired by reconstructing line by line the scene.

As it was done with the VINIR sensor in the static set up, first thing to be done before every capture campaign was the relative reflectance calibration to be applied later to every acquired hyperspectral images. This step aims to correct the significant signal variations, which are caused by the non-uniformity of the illumination and the focal plane array of the camera, known as pattern noise.

From the spectral processing point of view, the methodology followed for calibrating the sensors in the dynamic set up is the same followed for calibrating the sensor in the static set up. However, with the dynamic set up there is available spatial information that can be used to improve the calibration.

As shown in the Fig. 137, the reflectance information of the 4 references are now available in the same image, in which for each element there are numerous pixels providing the same reflectance value.

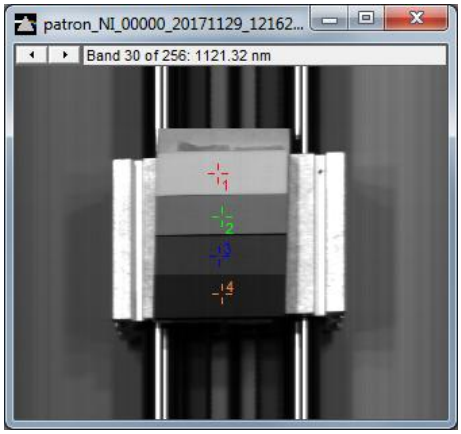

Fig. 8.85: Known Reflectance patterns acquired in the dynamic set up

One of the main advantages offered by the dynamic set-up is that, during the calibration process, it allows eliminating the non-uniformities that the sensor produces in the different wavelengths. For example, the sisuCHEMA camera does not generate the same spectrum for

all points of each reference target. In the following image a very intense peak is observed for another wavelength (1854 nm).

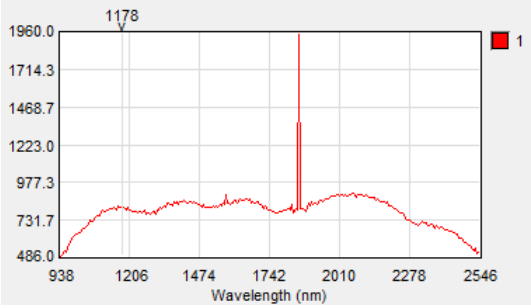

Fig. 8.86: Individual spectra acquired for reflectance 12%

The methodology used to avoid spectral non-uniformity problems consists of acquiring, for each reference, 5 nearby points and calculating the median of those 5 spectra. Fig. 8.87 shows all the individual spectra for the 12% reflectance target, as well as the median of them.

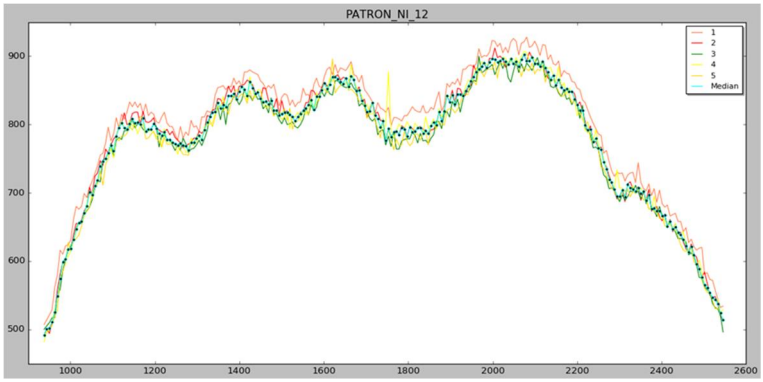

Fig. 8.87: Methodology for spectral non-uniformity correction

Once the actual reflectance information for each pixel obtained for the four patterns is available, the constants of the polynomial that fits these values with the theoretical value associated with each of the references patterns were calculated (for each wavelength). This procedure is shown in Fig. 8.88:

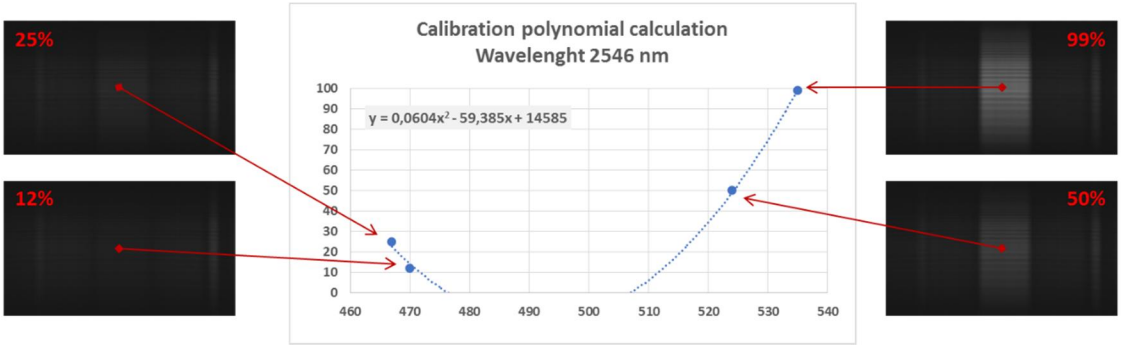

Fig. 8.88: Calibration polynomial constants calculation (example for 2546 nm)

In Fig. 8.89, several wavelengths have been selected randomly and the theoretical value of reflectance against the real value provided by the calibration polynomial has been represented. As seen, the curve fit is almost perfect.

New method proposal for chemical characterization of sterile material in scrap.

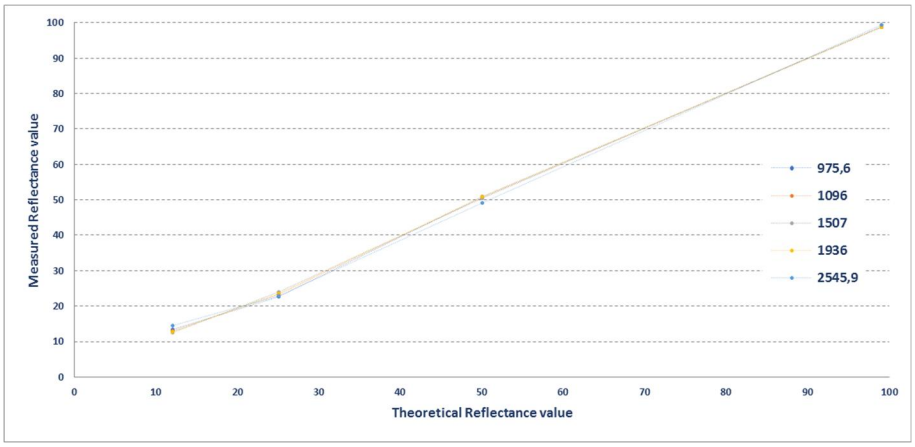

Fig. 8.89: Calibration polynomial fitting

With the second order polynomial constants obtained separately for each wavelength in the selected spectral range, the normalized reflection data for the Spectralom patterns and dark for the two cameras and the whole spectral range are shown in:

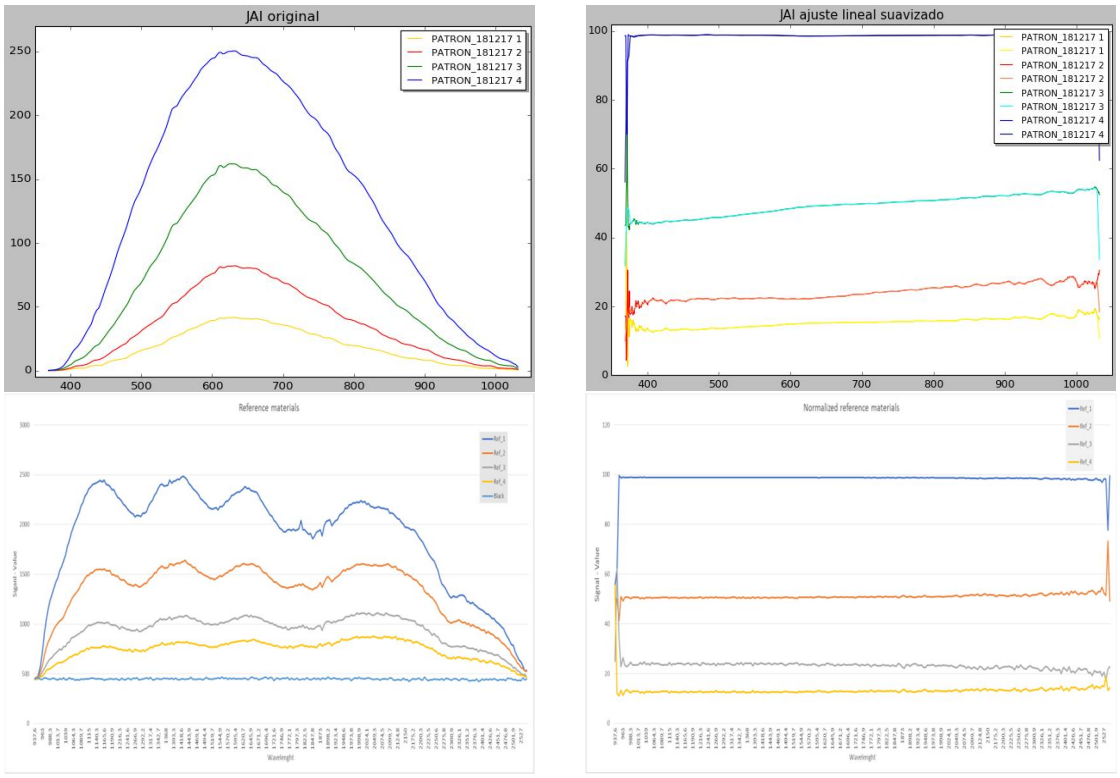

Fig. 8.90: Application of the linear adjustment on the reference patterns; Up) JAI camera and Down) sisuCHEMA camera

8.2.6.2 Static analysis of the selected samples in Visual + Near IR spectral range (400-1000 nm)

The initial analysis of Hyperspectral processing for quick characterization of scrap sterile was carried out using an existing equipment developed by the Global Research and development

centre that ArcelorMittal has in the Basque Country. This system, under patent application PCT/IB2015/053453 has proved its capabilities as a tool for quick analysis of the slag produced during Ladle furnace treatment of steel.

The principle used by this system to generate the spectral signature by reflection in the samples is the following:

- A well-known lighting system illuminates the sample to be analyzed
- The reflection response of the light on the sample varies depending on certain physical and chemical parameters of the sample to be analyzed
- The linear spectral sensor acquires the signal generated by the surface of the sample and a dedicated software generates the spectra dataset.

Fig. 8.91 depicts the sample processing process described above:

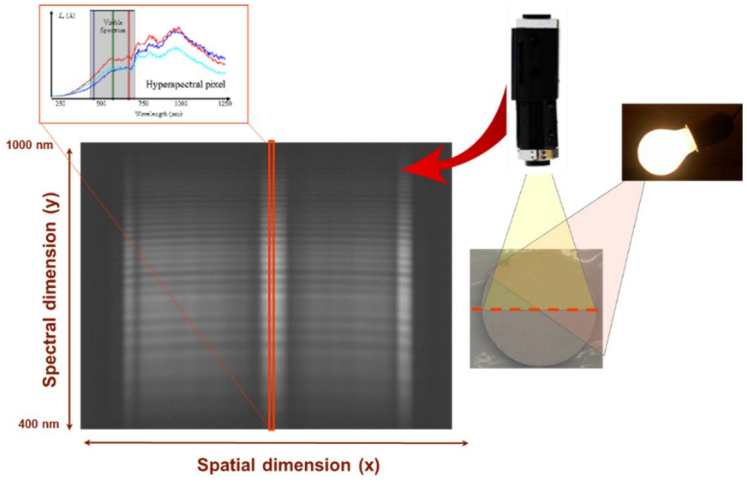

Fig. 8.91: Description of Samples processing

According this procedure, the different materials analyzed are listed below:

Sample ID	% FeO	% CaO	%SiO_2
Sample 1	50	50	0
Sample 2	0	50	50
Sample 3	50	0	50
Sample 4	50	25	25
Sample 5	25	50	25
Sample 6	25	25	50

Table 8.10: Pure compounds distribution for mixing analysis with hyperspectral

To determine the feasibility of this detection approach, several discs have been prepared (five per composition) with the mixed distributions listed in Table 8.10. The objective of the analysis is to capture the information for evaluating whether these kinds of technologies can detect the chemical mixtures. The acquired spectral signatures are showed below.

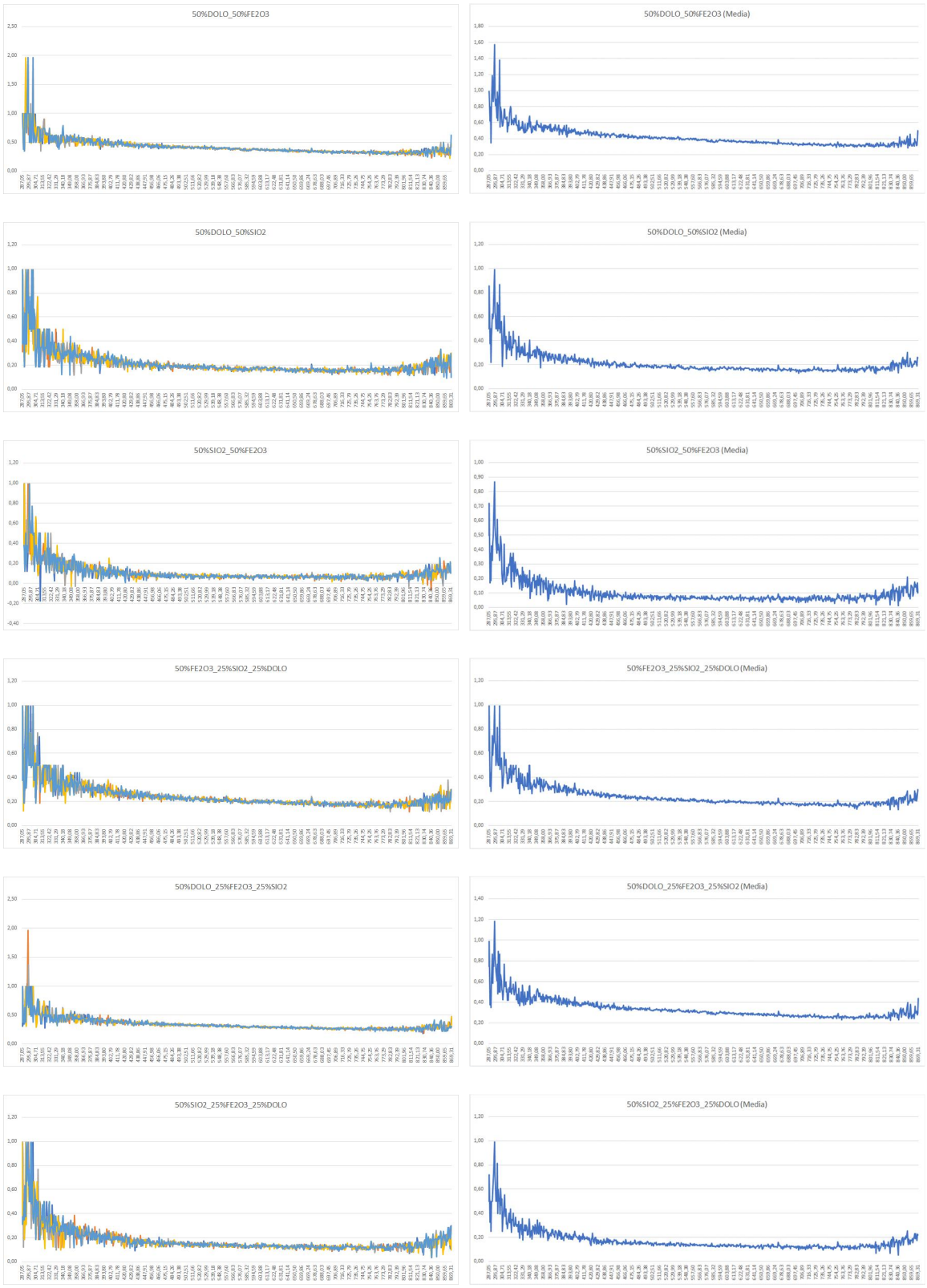

Fig. 8.92: Acquired spectral signatures for the 6 samples. Right) Raw data from 5 samples and Left) average data

Fig. 8.93 shows the comparative reflectance analysis over two compound mixtures:

New method proposal for chemical characterization of sterile material in scrap.

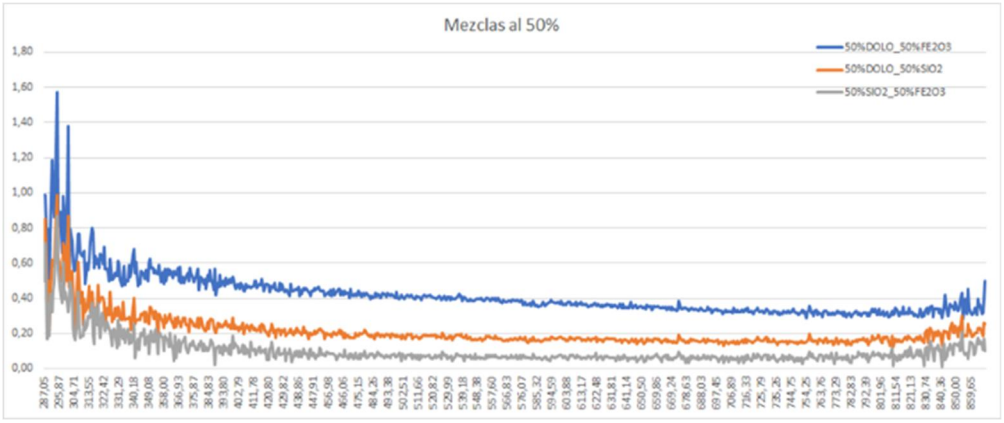

Fig. 8.93: Comparation among two compound mixtures

And Fig. 8.94 shows the comparative analysis results on three materials mixtures:

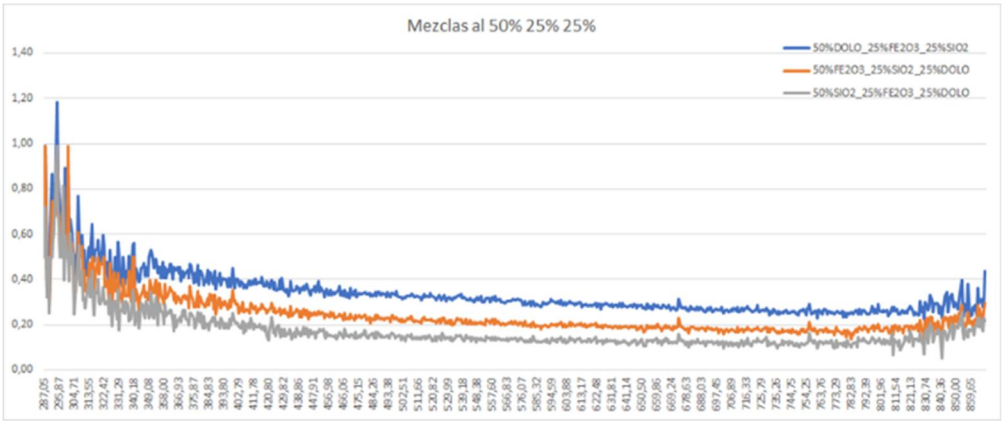

Fig. 8.94: Comparation among three compound mixtures

Looking at these analyses, it can be intuited that the presence of dolomite increases the reflectance of the sample along the whole wavelength range. However, as shown in Fig. 8.95, the presence of SiO_2 modifies the response of lime

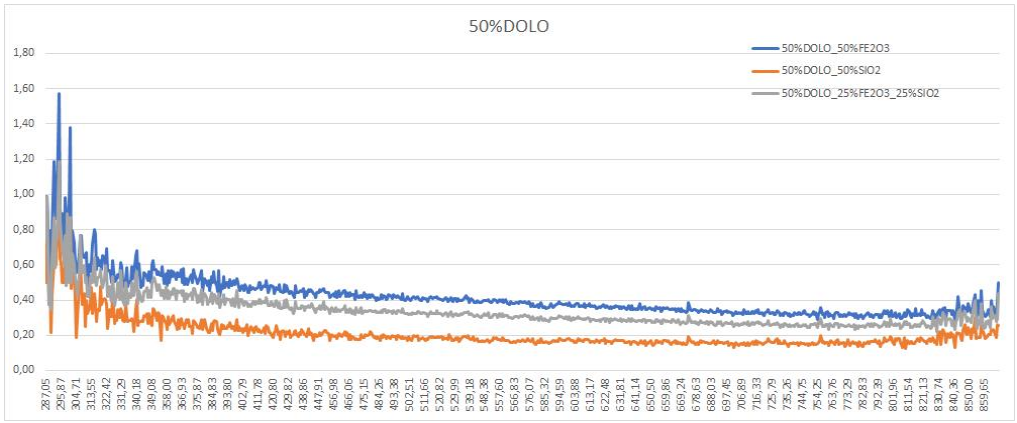

Fig. 8.95: Comparative analysis of all samples containing dolomite

The main conclusions to be highlighted after the preliminary analysis of the capacity of the hyperspectral imaging technique for sterile characterization are:

- There are no valleys nor characteristic peaks in the graphics displayed.

New method proposal for chemical characterization of sterile material in scrap.

- There are certain patterns in the spectral signature that can be exploited:
    - The higher the percentage of dolomite, the more reflectance.
    - The higher the percentage of silica, the less reflectance.
    - As expected, the results are consistent with the color (lighter or darker) of the samples.

It seems worthy to keep going on with more technical feasibility analyses.

8.2.6.3 Dynamic analysis of the selected samples in Visual + Near IR (400-1000 nm) and in SWIR (900-2500 nm) spectral ranges

The main disadvantage of the static approach using a linear camera is that there are not references of the material surface that is being analyzed. So that the pressed pellets must be carefully manipulated, as some aspects like material heterogeneities or dirt on the material surface influence on the results.

Once proven that it is possible to extract useful information by means of hyperspectral techniques and aiming to ensure the knowledge generation which is the final purpose of the present thesis work, it is necessary to extract the information from the entire surface to be analyzed. There are two different options for extracting 2 dimensional images of the sample surface:

- The use of linear sensors: the main advantage of this technology is a high spectral resolution which allows to have an enormous amount of information of the captured image. On the other hand, Linear sensors present as main disadvantage the necessity of moving the scene in front of the camera to reconstruct a 2D image.
- The use of matricial sensors: This technology offers the possibility of generating quick snapshots of the region of interest but, its main drawbacks are the low number of spectral channels available and the higher cost.

For this particular case, the option chosen was the use of linear sensors due to the high spectral resolution that these sensors offer. However, it was needed to develop a more technical laboratory set up for generating the required push broom effect for reconstructing 2D images. The developed laboratory set up was already described in section 8.1.4.

As described previously, the proposed laboratory set up consists of a conveyor belt driven by a servomotor which generates the displacement of the samples in front of the hyperspectral sensors:

- On one side, the system PFD-CL-65-V10E-OEM 1312x1024-65i / s-VNIR-CMOS-CL is a combination of a spectrograph and a monochrome camera. It generates an image whose Width corresponds to the spatial resolution of the camera (1312 pixels) and the

Height corresponds to the frequency spectrum associated with the corresponding pixel according the Wavelength calibration equation provided by the supplier.

- On the other hand, SPECIM: SisuCHEMA SWIR is a compact sensor that generate images with a spatial resolution of 320 pixels.

The samples to be analyzed are placed inside the tray and, due to the movement produced by the conveyor with respect to the cameras (shown Fig. 8.96), two complete images of the tablet are obtained (one for each camera).

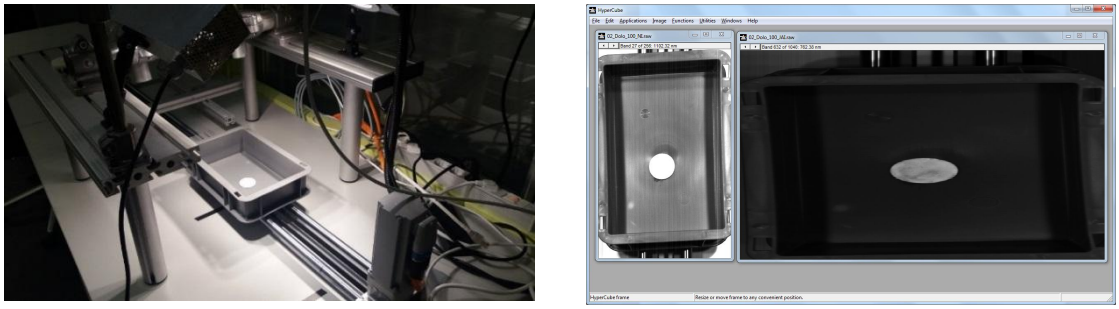

Fig. 8.96: Sample placement in front of cameras for analysis (Left) and 2D images Re-constructed from the information collected by each sensor (Right)

Using the presented laboratory set up, several capturing campaigns were carried out.

8.2.6.3.1 Capturing Campaign 1:

In the first capturing campaign, 15 samples with different pure compound mixture were prepared.

Sample ID	% FeO	% Dolo	%SiO_2
Sample 1	0	0	100
Sample 2	0	100	0
Sample 3	100	0	0
Sample 4/5	50	25	25
Sample 6/7	25	50	25
Sample 8/9	25	25	50
Sample 10/11	50	50	0
Sample 12/13	0	50	50
Sample 14/15	50	0	50

Fig. 8.97: Pure compounds distribution for mixing analysis with hyperspectral in campaign 1

For the analysis of each sample, the following procedure was carried out:

- The spectral patterns of the reference targets were obtained and, using the "theoretical reflectance spectra", the coefficients of the polynomial (for each wavelength) to be used in the linear adjustment were calculated.
- From each sample, the information of some selected pixels is extracted (median of 5 nearby points), the information is smoothed.
- The spectral signature is normalized by dividing itself by its maximum value.

New method proposal for chemical characterization of sterile material in scrap.

Pure component analyses:

Fig. 8.98 shows the raw spectral signature got from the SiO_2, FeO and dolomite pure compounds for both hyperspectral sensors:

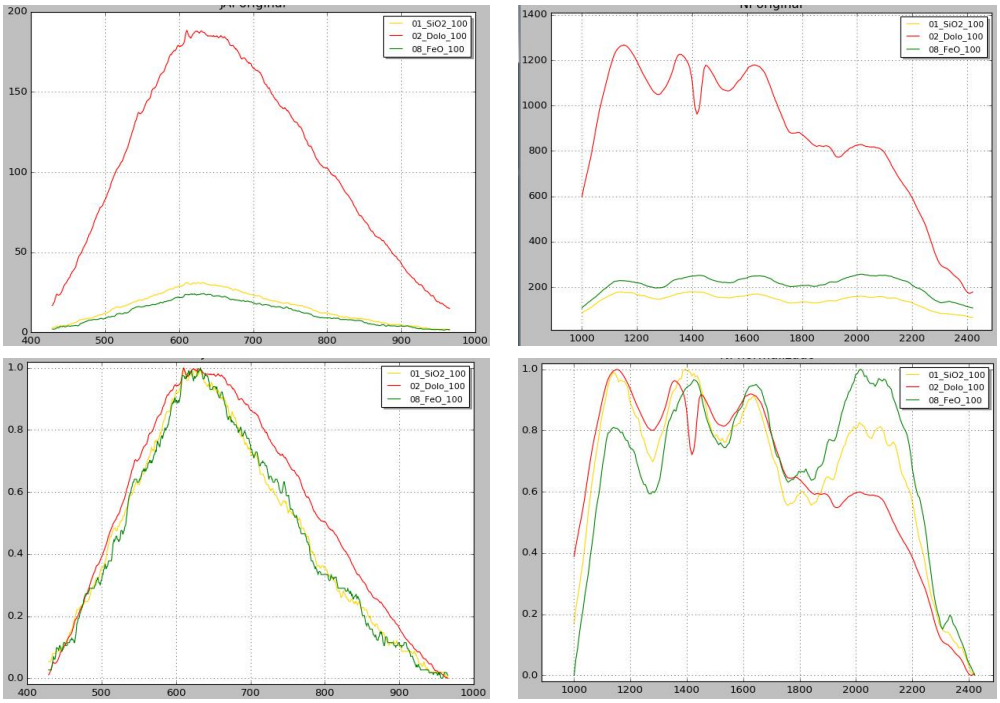

Fig. 8.98: Spectral signature of pure compounds with no processing (Up) and after normalization (Down) for JAI sensor (left) and for sisuCHEMA sensor (right)

show the spectral signature after linear adjustment got from the SiO_2, FeO and dolomite pure compounds for both hyperspectral sensors:

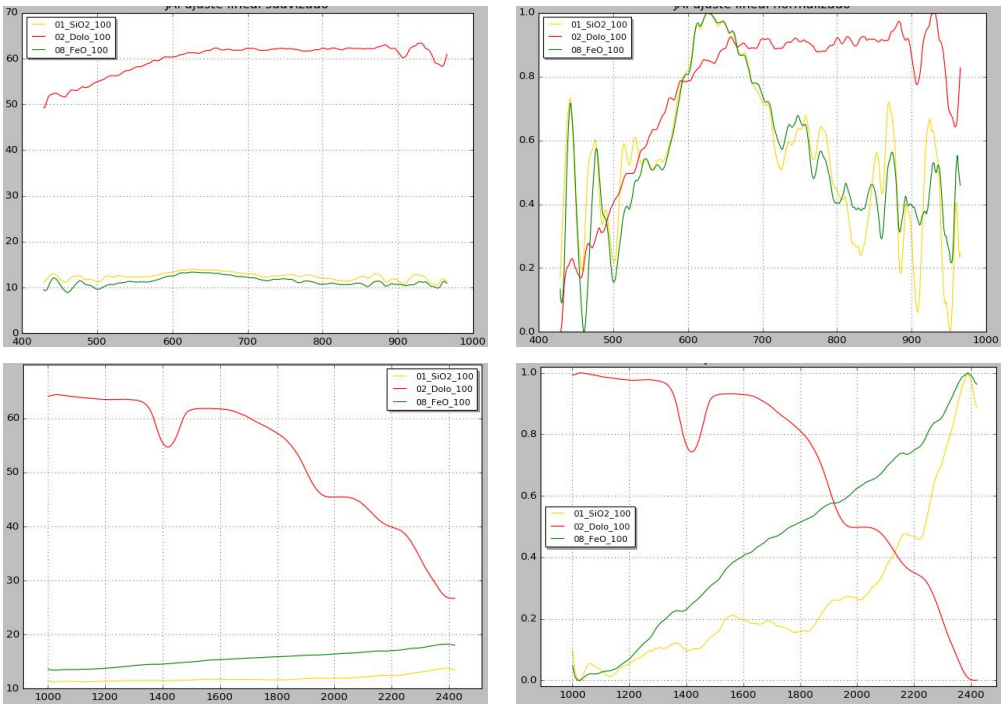

Fig. 8.99: Linearized Spectral signature with no processing (Up) and Linearized spectral signature after normalization (Down) for JAI sensor (left) and for sisuCHEMA sensor (right)

New method proposal for chemical characterization of sterile material in scrap.

Analyses over Mixture materials (4, 6, 8, 10, 12, 14):

Fig. 8.100 shows the raw spectral signature got from the mixed materials pellets for both hyperspectral sensors:

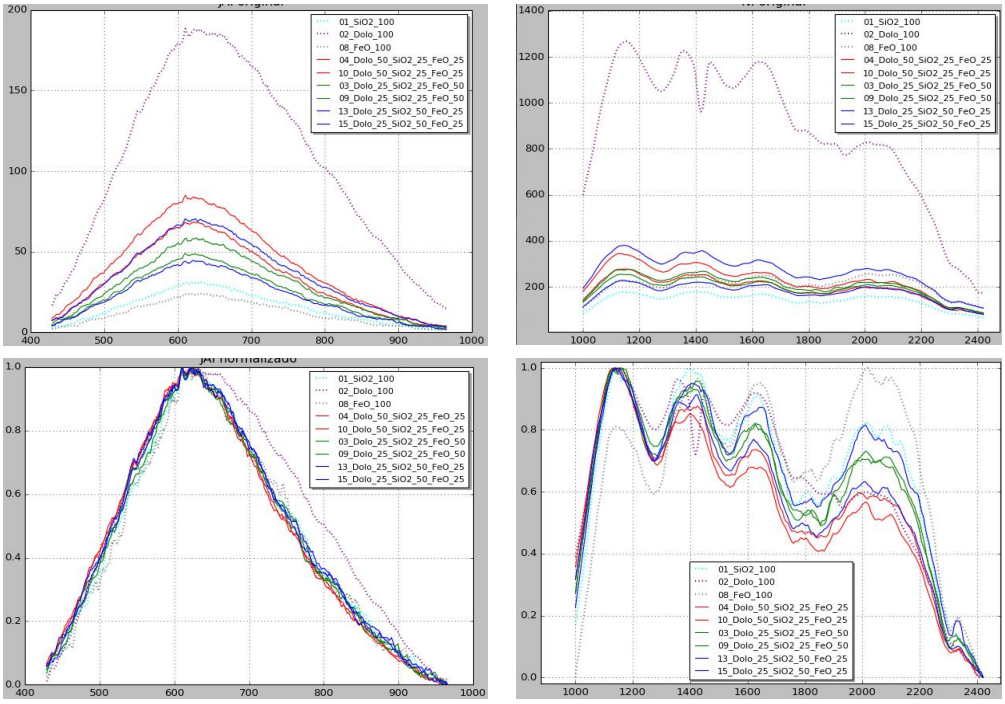

Fig. 8.100: Spectral signature of mixed materials pellets with no processing (Up) and Spectral signature of mixed materials pellets alter normalization (Down) for JAI sensor (left) and for sisuCHEMA sensor (right)

Next pictures show the spectral signature after linear adjustment got from mixed materials:

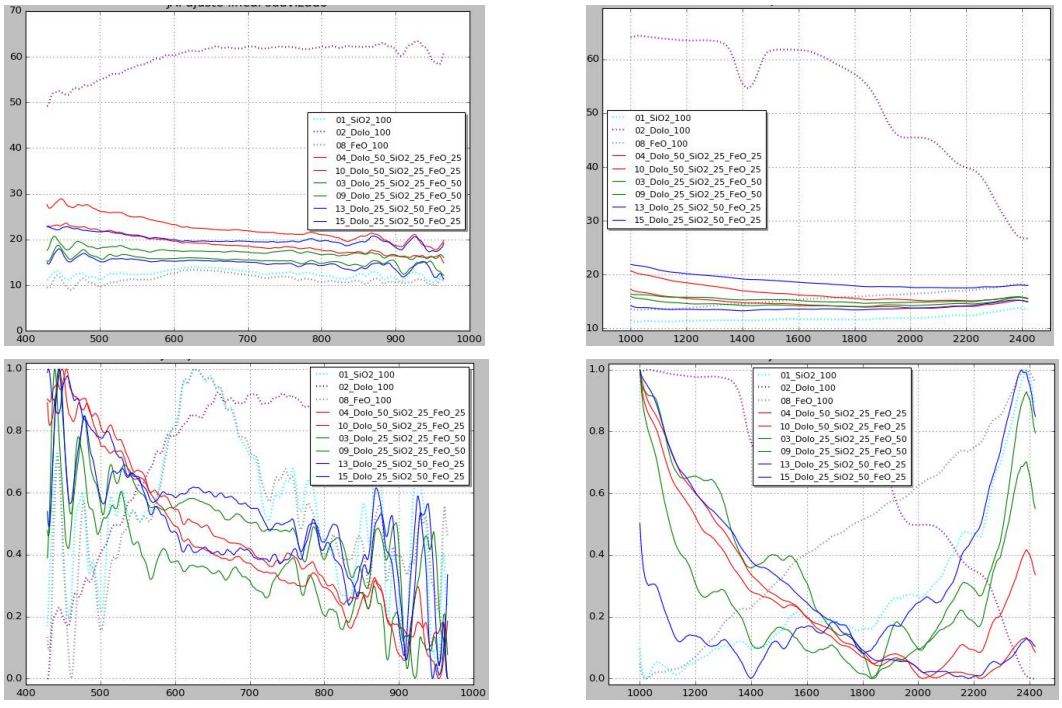

Fig. 8.101: Linearized Spectral signature with no processing (Up) and Linearized spectral signature after normalization (Down) for JAI sensor (left) and for sisuCHEMA sensor (right)

New method proposal for chemical characterization of sterile material in scrap.

Analyses over Mixture materials (5, 7, 9, 11, 13, 15):

Fig. 8.102 shows the raw spectral signature got from the mixed materials pellets for both hyperspectral sensors:

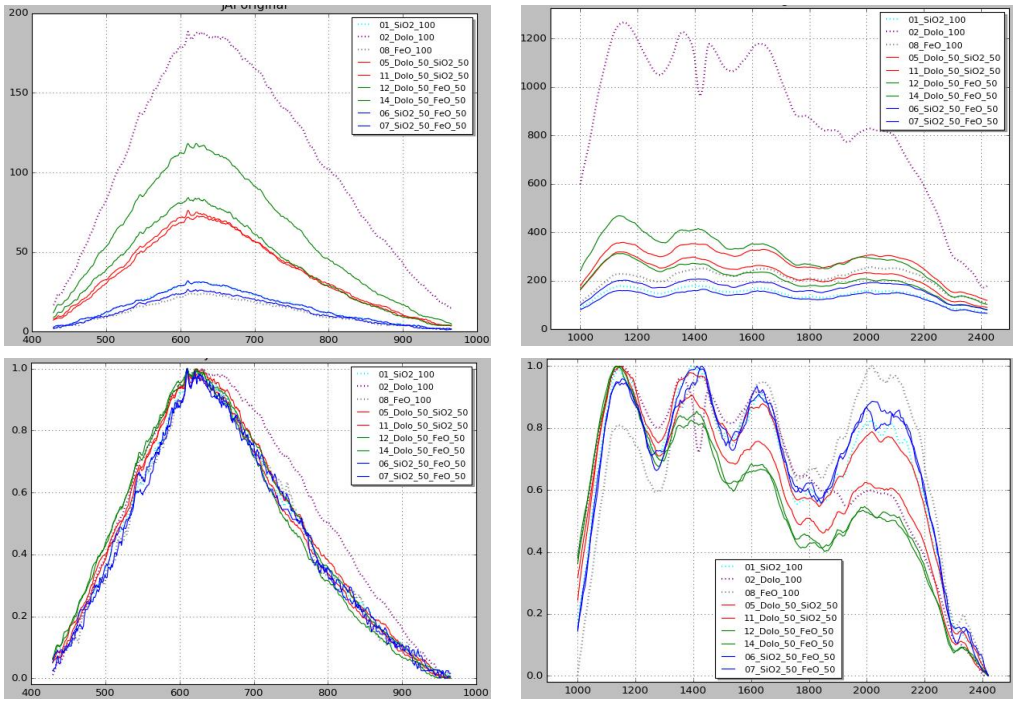

Fig. 8.102: Spectral signature of mixed materials pellets with no processing (Up) and Spectral signature of mixed materials pellets alter normalization (Down) for JAI sensor (left) and for sisuCHEMA sensor (right)

Fig. 8.103 shows the spectral signature after linear adjustment got from mixed materials:

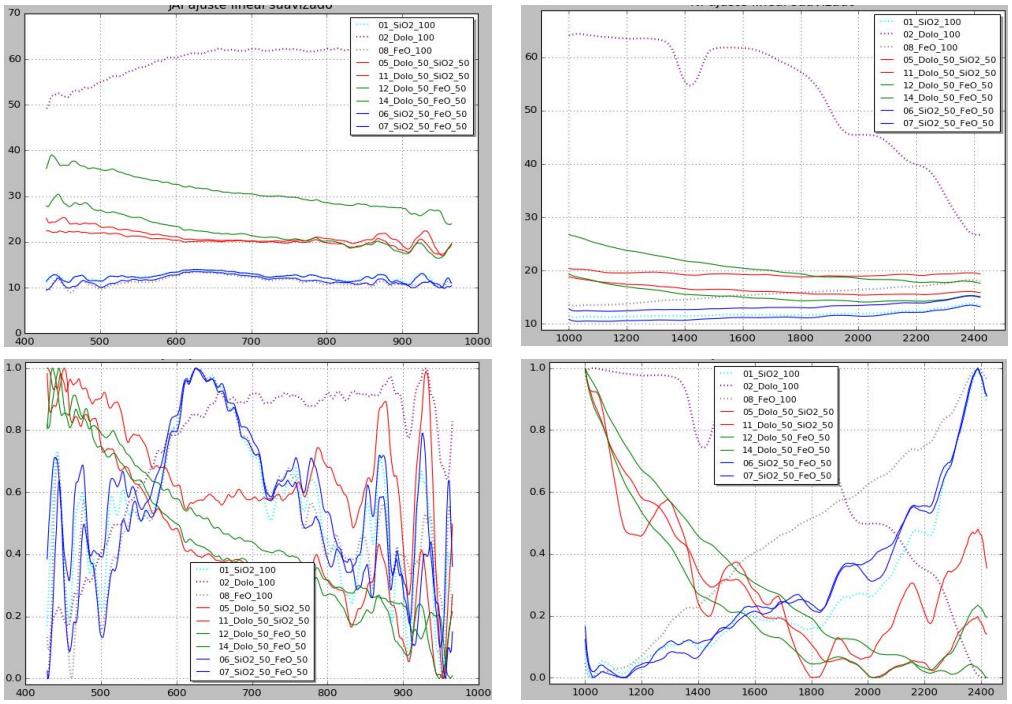

Fig. 8.103: Linearized Spectral signature with no processing (Up) and Linearized spectral signature after normalization (Down) for JAI sensor (left) and for sisuCHEMA sensor (right)

New method proposal for chemical characterization of sterile material in scrap.

Calculation of compound abundances:

The abundance was done, defining as endmembers (base components) the samples made on the pure components, for each compound per sample according the methodology described in section 8.1.3. The calculation over the spectral information acquired by each sensor was performed in the aforementioned conditions:

- Raw spectra information without normalizing.
- Normalized raw spectra information.
- The linear adjustments (without normalizing) of each spectral signature.
- The normalized linear adjustments of each spectral signature.

The results obtained are shown in the following figures:

Fig. 8.104 shows Raw spectra information **without normalizing** (VIS + NIR spectral range):

Real			Estimated		
Dolo	**SiO_2**	**FeO**	**Dolo**	**SiO_2**	**FeO**
50	50	0	24,97	74,50	0,53
50	50	0	24,14	75,40	0,47
25	25	50	9,77	89,92	0,31
25	25	50	15,39	83,82	0,78
25	50	25	7,81	91,81	0,39
25	50	25	22,65	76,50	0,85
50	25	25	30,09	66,28	3,63
50	25	25	20,56	78,93	0,50
50	0	50	29,35	70,20	0,45
50	0	50	50,24	49,53	0,23
0	50	50	0,09	28,98	0,00
0	50	50	0,01	99,15	0,84

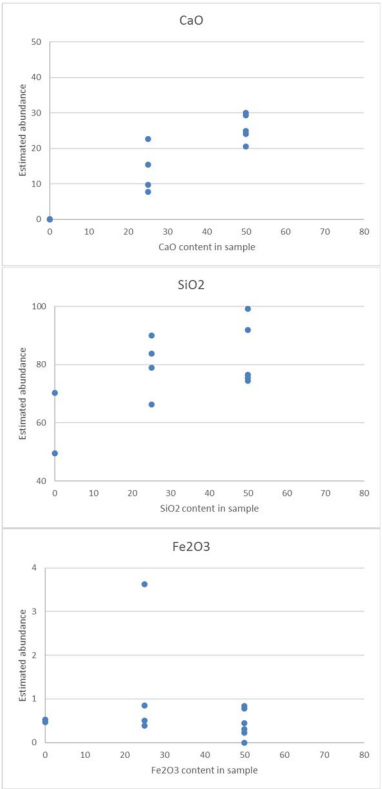

Fig. 8.104: Abundance estimation for raw spectra information without normalizing (JAI sensor)

Looking at these results, the proposed method can estimate the percentage of lime in the mixture. However, the algorithm is only capable to see trend in the SiO_2 estimation and is not able to identify FeO content in the sample.

For Raw spectra information **without normalizing** (SWIR spectral range), same analysis is depicted in Fig. 8.105:

Real			Estimated		
Dolo	SiO_2	FeO	Dolo	SiO_2	FeO
50	50	0	11,25	88,51	0,24
50	50	0	13,18	30,67	56,15
25	25	50	6,08	89,13	4,79
25	25	50	8,36	90,71	0,93
25	50	25	3,50	84,24	12,27
25	50	25	16,51	79,44	4,05
50	25	25	11,96	88,01	0,03
50	25	25	7,15	92,39	0,46
50	0	50	9,03	90,76	0,21
50	0	50	22,06	77,70	0,23
0	50	50	0,00	99,93	0,06
0	50	50	0,76	71,33	27,91

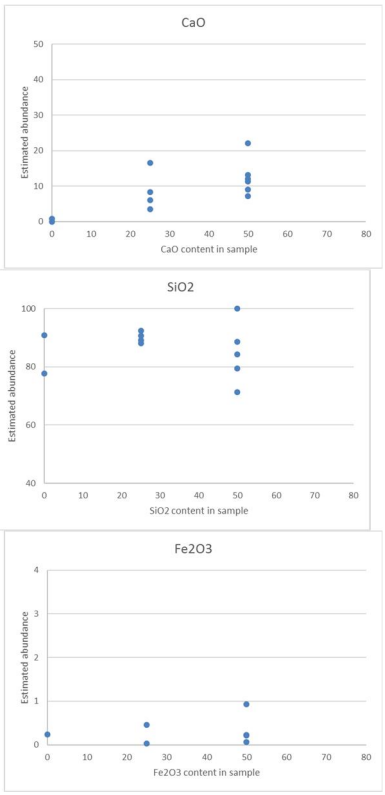

Fig. 8.105; Abundance estimation for raw spectra information without normalizing (sisuCHEMA)

Looking at these results, the proposed method cannot estimate the percentage in SiO_2 nor FeO and it only can do the qualitative interpretation of CaO content in the samples.

Regarding the result got from **Normalized raw spectra** (VIS + NIR spectral range:

Real			Estimated		
Dolo	SiO_2	FeO	Dolo	SiO_2	FeO
50	50	0	0,27	99,15	0,58
50	50	0	20,69	78,80	0,50
25	25	50	0,77	92,24	6,99
25	25	50	3,22	87,92	8,86
25	50	25	9,69	88,45	1,86
25	50	25	14,22	85,33	0,45
50	25	25	0,48	98,81	0,71
50	25	25	0,23	99,20	0,57
50	0	50	0,31	98,91	0,78
50	0	50	18,55	80,62	0,83
0	50	50	0,15	32,30	67,56
0	50	50	0,04	97,29	2,67

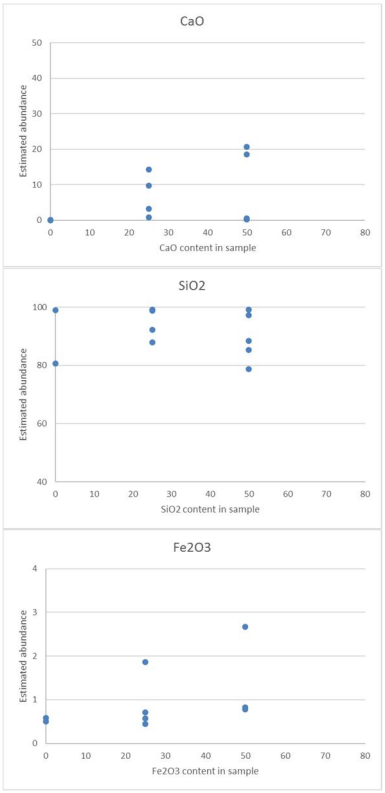

Fig. 8.106: Abundance estimation for normalized raw spectra (JAI sensor)

New method proposal for chemical characterization of sterile material in scrap.

Looking at these results, the proposed method cannot estimate the percentage in SiO_2. However, after data normalization clearer qualitative estimation of CaO and Fe_2O_3 contents in the samples can be done.

Fig. 8.107 shows the analysis on abundance for **Normalized raw spectra** in SWIR spectral range:

Real			Estimated		
Dolo	**SiO_2**	**FeO**	**Dolo**	**SiO_2**	**FeO**
50	50	0	66,24	32,63	1,13
50	50	0	16,65	83,17	0,18
25	25	50	33,52	65,62	0,86
25	25	50	40,63	59,13	0,23
25	50	25	14,44	84,84	0,73
25	50	25	65,42	33,81	0,77
50	25	25	89,23	9,51	1,26
50	25	25	72,05	27,07	0,88
50	0	50	88,90	9,57	1,53
50	0	50	92,88	6,07	1,05
0	50	50	2,28	71,01	26,71
0	50	50	0,35	73,32	26,33

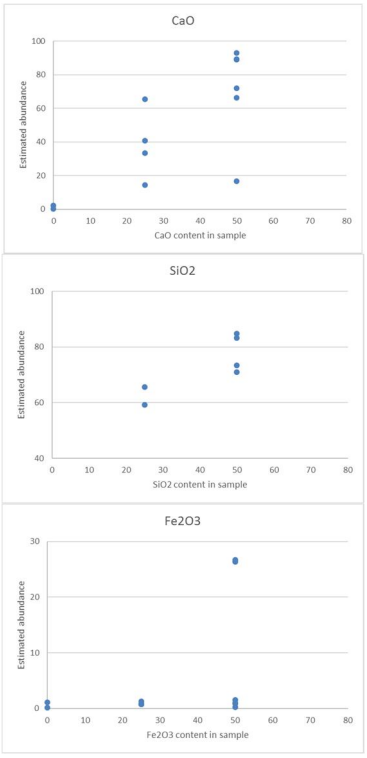

Fig. 8.107: Abundance estimation for normalized raw spectra (sisuCHEMA sensor)

For this case, the proposed method seems to be capable to estimate the percentage of CaO and SiO_2 in the mixture. However, the algorithm does not to see Fe_2O_3 in the sample.

The **linear adjustments without normalizing** (VIS + NIR spectral range) is shown Fig. 8.108:

Real			Estimated		
Dolo	**SiO_2**	**FeO**	**Dolo**	**SiO_2**	**FeO**
50	50	0	19,63	80,32	0,06
50	50	0	19,35	78,86	1,79
25	25	50	7,40	91,51	1,09
25	25	50	11,70	87,13	1,16
25	50	25	6,07	92,13	1,80
25	50	25	17,83	81,55	0,62
50	25	25	23,73	74,03	2,24
50	25	25	15,67	83,16	1,17
50	0	50	22,49	76,92	0,60

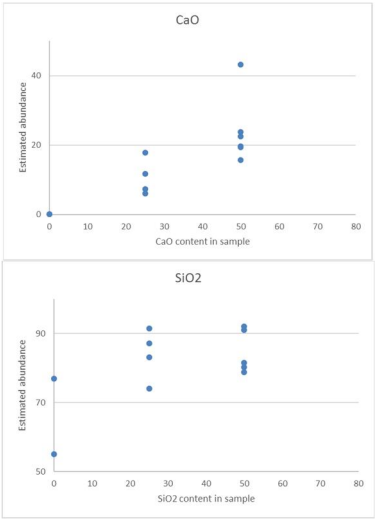

50	0	50	43,15	55,08	1,77
0	50	50	0,18	16,84	82,98
0	50	50	0,05	91,05	8,91

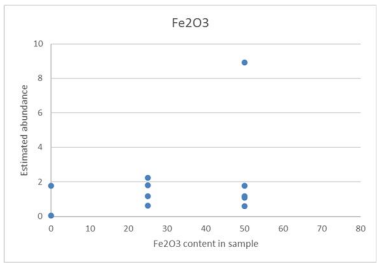

Fig. 8.108 Abundance estimation for raw spectra after linear adjustments without normalizing (JAI)

Looking at these results, the proposed method can estimate the percentage of lime in the mixture. However, the algorithm is not able to identify FeO nor SiO_2 content in the sample.

For the **linear adjustments without normalizing** in SWIR spectral range:

Real			Estimated		
Dolo	**SiO_2**	**FeO**	**Dolo**	**SiO_2**	**FeO**
50	50	0	10,73	89,20	0,07
50	50	0	13,70	41,19	45,11
25	25	50	6,42	92,77	0,81
25	25	50	7,89	90,24	1,86
25	50	25	2,98	79,29	17,73
25	50	25	15,63	80,43	3,94
50	25	25	11,35	88,11	0,54
50	25	25	6,77	92,39	0,84
50	0	50	8,52	90,33	1,15
50	0	50	20,99	77,92	1,09
0	50	50	0,01	99,90	0,09
0	50	50	0,73	71,29	27,98

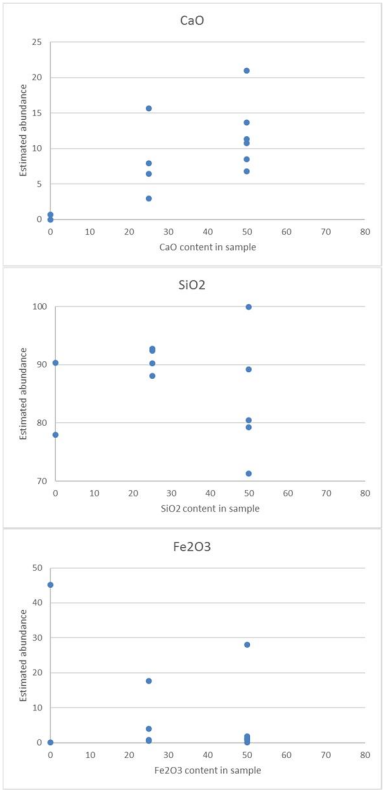

Fig. 8.109; Abundance estimation for raw spectra after linear adjustments without normalizing (sisuCHEMA)

Looking at these results, the proposed method cannot estimate the percentage in SiO_2 nor Fe_2O_3 nor Lime content in the samples.

The abundance analysis applying the last proposed spectral processing (**Normalized linear adjustments**) for VIS + NIR spectral range is shown in Fig. 8.110:

Real			Estimated		
Dolo	SiO_2	FeO	Dolo	SiO_2	FeO
50	50	0	0,89	91,71	7,40
50	50	0	2,17	97,36	0,47
25	25	50	0,67	95,96	3,37
25	25	50	0,53	48,26	51,21
25	50	25	1,51	96,49	2,00
25	50	25	0,80	97,28	1,92
50	25	25	0,94	6,86	6,70
50	25	25	0,97	95,60	3,43
50	0	50	0,90	82,10	17,00
50	0	50	1,20	96,42	2,39
0	50	50	0,07	4,23	95,70
0	50	50	9,32	90,42	0,25

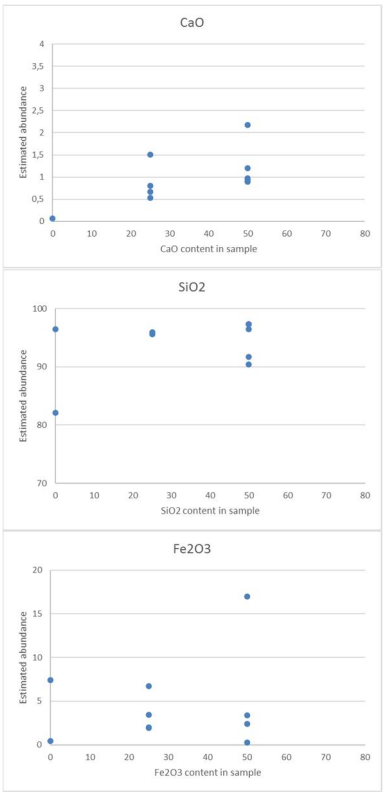

Fig. 8.110: Abundance estimation for normalized linear adjustments (JAI)

Looking at these results, the proposed method cannot estimate the percentage in SiO_2 nor Fe_2O_3 nor Lime content in the samples

For **Normalized linear adjustments** in SWIR spectral range, the results on abundance are:

Real			Estimated		
Dolo	SiO_2	FeO	Dolo	SiO_2	FeO
50	50	0	26,54	71,41	2,05
50	50	0	32,65	66,34	1,01
25	25	50	15,91	83,27	0,82
25	25	50	38,43	59,44	2,13
25	50	25	2,47	97,10	0,42
25	50	25	26,75	70,71	2,54
50	25	25	24,52	73,81	1,67
50	25	25	25,88	72,08	2,04
50	0	50	22,59	76,23	1,19
50	0	50	32,45	65,78	1,77
0	50	50	0,01	79,52	20,47
0	50	50	0,04	76,29	23,67

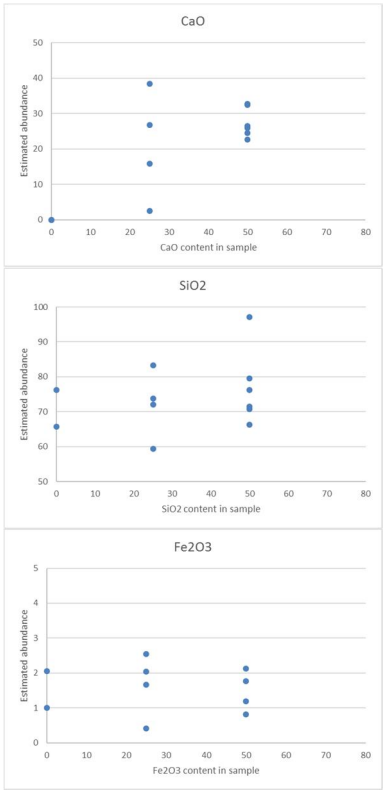

Fig. 8.111: Abundance estimation for normalized linear adjustments (sisuCHEMA)

New method proposal for chemical characterization of sterile material in scrap.

With the proposed method cannot estimate the percentage in none of the analyzed components in the samples.

The main conclusions reached after analyzing the data got during capturing campaign 1 are summarized below:

- In the case of Raw spectra information without normalization of pure compounds, the reflexion intensity of Dolomite lime is higher than for the rest of compounds. It also observed a specific spectral behavior of dolomite between 1200 and 1400 nm. For Fe_2O_3 and SiO_2, there are small differences in the signal intensity along the whole spectral range (being higher for SiO_2).
- For compound mixtures when analyzing Raw spectra information;
    - Samples composed by two compounds: There is a good grouping of signal associated to the compound mixtures, but the intensity of the signals does not correspond with the expected order. Sorting from high intensity (Dolomite) to lower intensity (FeO), it was expected to have the higher signal in the mixture composed by Dolomite+SiO_2 but this effect does not occur.
    - Samples composed by three compounds: the coherency with regards pure compounds is meet (the higher the Dolomite, the higher the intensity of the mixture, the higher the SiO_2, the lower the intensity of the mixture.
- For normalized raw spectra information, between 1900 and 2200 nm the three pure compounds are clearly identified, and the three mixtures are coherent in term of signal intensity sorting. Also, material mixtures signals seem to be in accordance with expected values.
- The results coming from the linear adjustments (with and without normalization) the observations are quite similar than the ones got before in case of VIS+NIR spectral range. For sisuCHEMA's sensor spectral range, no clear pattern is observed.
- When applying the components abundance estimation algorimths over the different spectral processing methodologies proposed:
    - The individual abundance estimation algorithm is offering some qualitative information for SiO_2 and CaO in the case of raw spectral data without and with normalization, but not useful information is extracted for linearization processing methods.
    - Fe_2O_3 content in the samples is not estimated using any abundance calculation method.
- Finally, some punctual incoherencies where found is few samples. The method selected for data acquisition (median of only 5 nearby points) could be questioned.

New method proposal for chemical characterization of sterile material in scrap.

8.2.6.3.2 Capturing Campaign 2:

In the second capturing campaign, 12x2 samples with different pure compound mixture were prepared.

Sample ID	% Fe_2O_3	% Dolo	%SiO_2
Sample 1/2	0	0	100
Sample 3/4	0	100	0
Sample 5/6	100	0	0
Sample 7/8	25	75	0
Sample 9/10	50	50	0
Sample 11/12	75	50	0
Sample 13/14	25	0	75
Sample 15/16	50	0	50
Sample 17/18	75	0	25
Sample 19/20	0	25	70
Sample 21/22	0	50	50
Sample 23/24	0	75	25

Fig. 8.112: Pure compounds distribution for mixing analysis with hyperspectral in campaign 2

Sine one of the main conclusions reached in capturing campaign 1 was that the method selected for data acquisition based on median of 5 nearby points could generate some incoherencies, for this second capturing campaign a new sample processing method is proposed:

- The dark signal of the hyperspectral cameras is obtained (by occluding the optic path) and the median of all the pixels is calculated.
- The reference patterns are acquired, and the median value of all pixels is obtained. The Dark signal is subtracted to this value and the polynomial coefficients (for each length wave) to be used in linearization process are got.
- Since the result of the previous processing step offers a highly noise-signal ratio and discontinuities between consecutive wavelengths, a Gaussian smoothing is applied.
- Finally, to make a comparative analysis of spectra, it is normalized by dividing each spectra signature by its maximum.
- A new method for spectral information extraction is implemented. The new procedure consists on defining a ROI inside the sample area to obtain the mean intensity value of every pixel inside this ROI:

New method proposal for chemical characterization of sterile material in scrap.

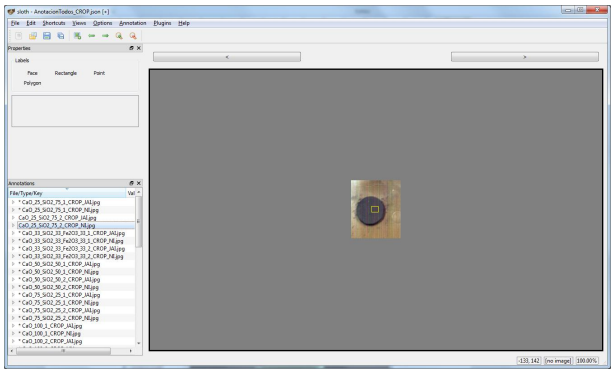

Fig. 8.113: Example of the new spectral information extraction method

Pure component analyses:

Like the study carried out in the capture campaign 1, the first analysis was made on pressed pellets composed of pure components of CaO, SiO_2 and Fe_2O_3

Fig. 8.114 shows the raw spectral signature, linearized and normalized signal got from the pure materials for both hyperspectral sensors:

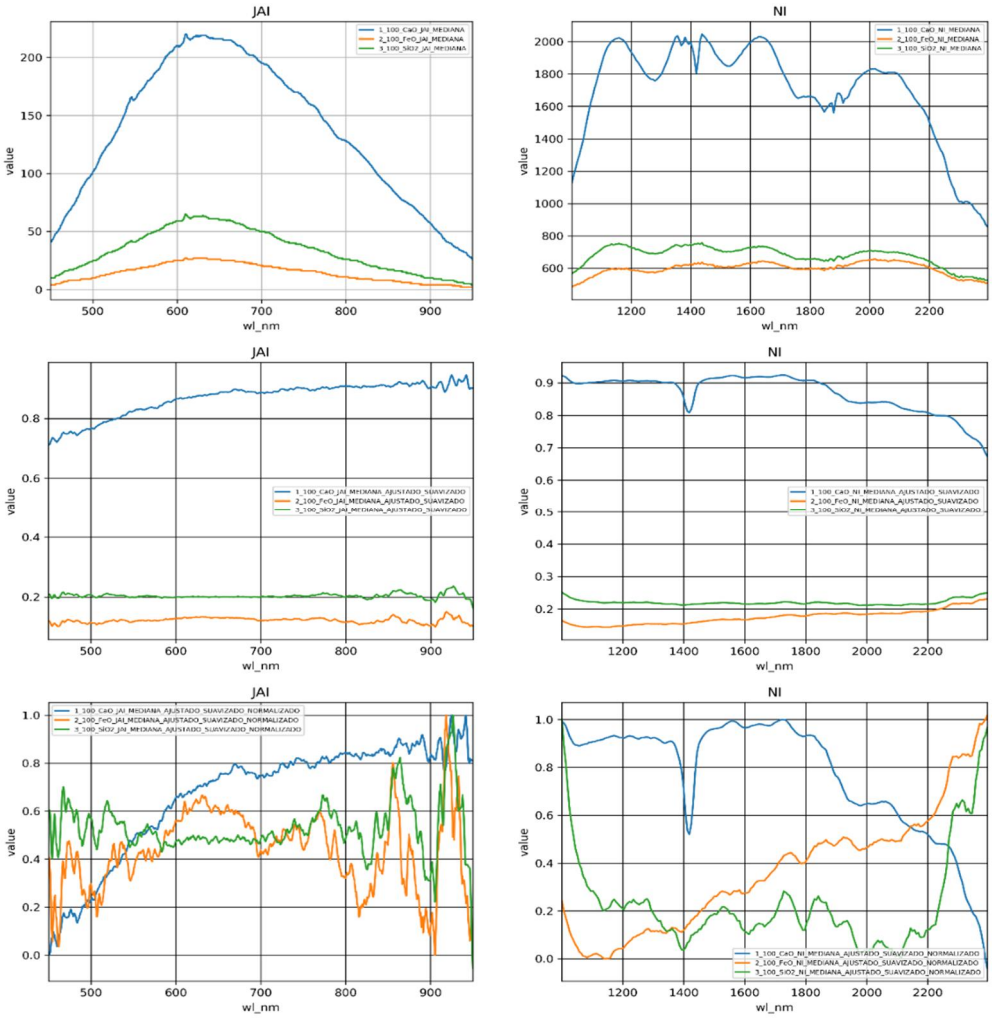

Fig. 8.114: Spectral signature of pure compounds with no processing (Up), linearized Spectral signature with signal smoothing (Mid) and linearized Spectral signature with signal normalization (Down) for JAI sensor (left) and for sisuCHEMA sensor (right)

- **Analyses over Mixture materials (3, 4, 5, 6, 7, 8, 9, 10, 11, 12):**

Fig. 8.115 shows Fe_2O_3/Dolomite mixtures raw spectral signature, linearized and normalized signals got from the pure materials for both hyperspectral sensors:

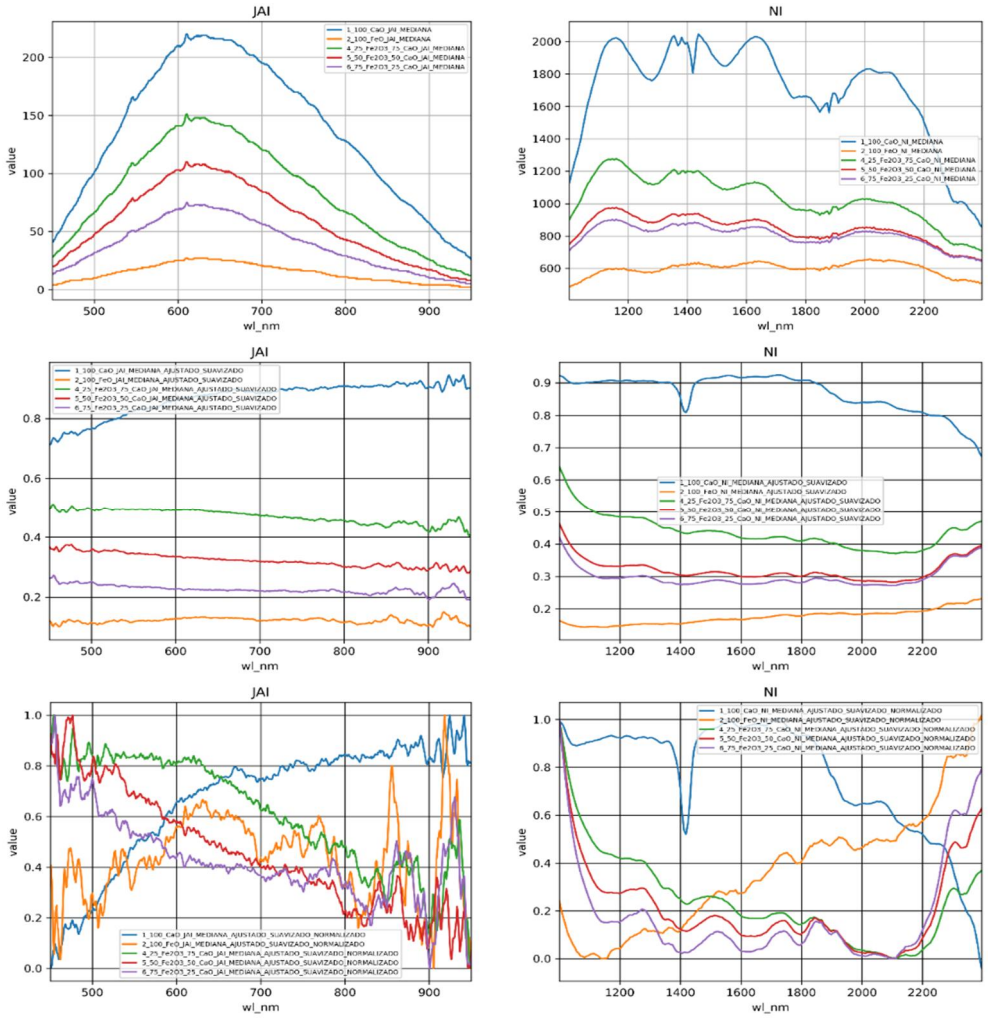

Fig. 8.115: Spectral signature of Fe_2O_3/Dolomite with no processing (Up), linearized Spectral signature with signal smoothing (Mid) and linearized Spectral signature with signal normalization (Down) for JAI sensor (left) and for sisuCHEMA sensor (right)

Analyses over Mixture materials (1, 2, 5, 6, 13, 14, 15, 16, 17, 18):

Fig. 8.116 shows Fe_2O_3/SiO_2 mixtures raw spectral signature, linearized and normalized signals got from the pure materials for both hyperspectral sensors:

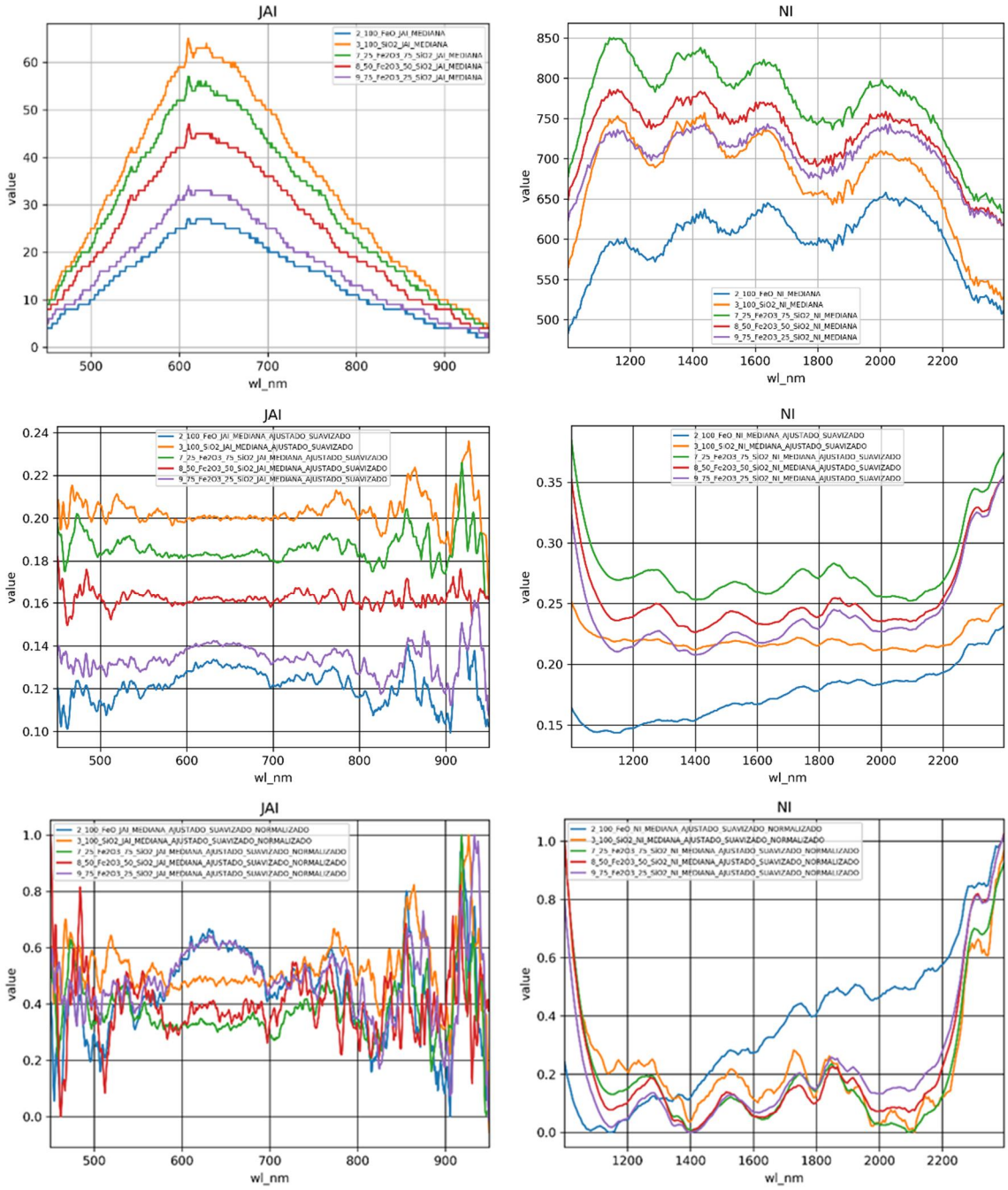

Fig. 8.116: Spectral signature of Fe_2O_3/SiO_2 mixtures with no processing (Up), linearized Spectral signature with signal smoothing (Mid) and linearized Spectral signature with signal normalization (Down) for JAI sensor (left) and for sisuCHEMA sensor (right)

Analyses over Mixture materials (1, 2, 3, 4, 19, 20, 21, 22, 23, 24):

Fig. 8.117 shows CaO/SiO_2 mixtures raw spectral signature, linearized and normalized signals got from the pure materials for both hyperspectral sensors:

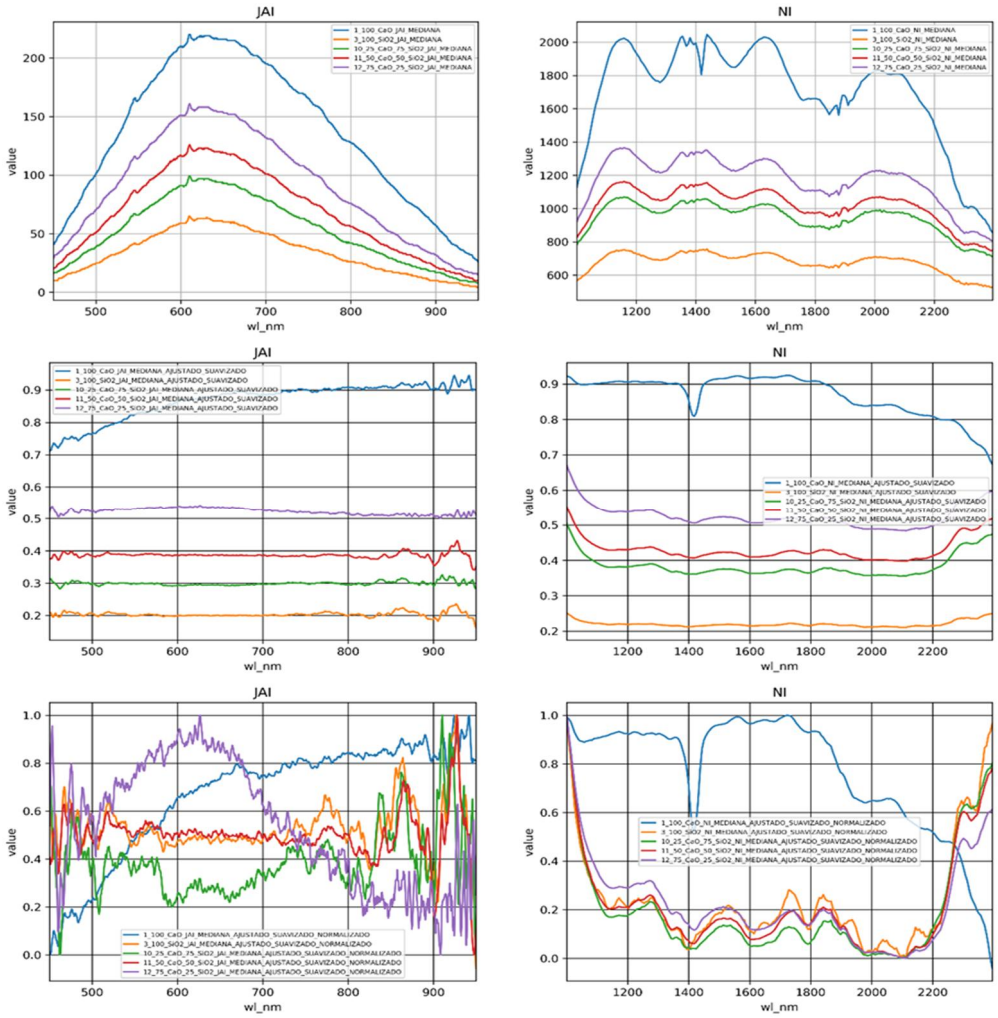

Fig. 8.117: Spectral signature of CaO/SiO_2 mixtures with no processing (Up), linearized Spectral signature with signal smoothing (Mid) and linearized Spectral signature with signal normalization (Down) for JAI sensor (left) and for sisuCHEMA sensor (right)

The main conclusions reached after analyzing the data got during capturing campaign 2 are summarized below:

- For pure components, same conclusions than in measurement campaign 1 were reached.
- In the case of Fe_2O_3 / CaO mixtures, for VIS+NIR spectral range, an increase in the reflection signal intensity is observed as the CaO content in the samples increases for all the cases in which the raw signal is analyzed. This clear relationship of signal intensity with the CaO content is maintained when analyzing the information obtained after spectra linearization.

  In the SWNIR spectral range, it is observed that between 1100 and 1300 nm as the CaO content of the sample increases, the signal intensity is greater. Also, in the spectral range between 2300 and 2400 nm, the higher the content of Fe_2O_3 higher is the signal intensity required.

New method proposal for chemical characterization of sterile material in scrap.

- For Fe_2O_3 / SiO_2 mixtures, The JAI sensor offers expected correlations between intensity signal and composition for pure compounds and mixed samples. This signal correlation is also maintained after spectra linearization.

  In the spectral range of the sisuCHEMA sensor, and after signal normalization process, it is observed that between 1100 and 1300 nm previous observed relationships are still clear. In the spectral range between 2300 and 2400 nm, those relationships are inverted

- Finally, in the case of CaO / SiO_2 mixtures, similarly to previous cases, an increase in the reflection signal intensity is observed as the CaO content in the samples increases for raw and linearized data. This clear relationship of signal intensity with the CaO content is maintained when analyzing the information obtained after spectra linearization.

  For this particular case, the normalization process does not offer any useful information.

- Finally, the new method for spectral information extraction based on ROI definition offers better results than the methods used in campaign 1

8.2.6.3.3 Capturing Campaign 3:

In the second capturing campaign, some pure compounds spectral features characteristics were observed in mixed pressed pellets samples. However, several inconsistencies were also found (mainly associated with the presence of SiO_2 in the sample). In the third capturing campaign 13x2 samples with different pure compound mixtures were prepared to validate the conclusions reached in campaign 2.

Sample ID	% FeO	% Dolo	%SiO_2
Sample 1/2	100	0	0
Sample ¾	0	100	0
Sample 5/6	0	0	100
Sample 7/8	1/3	1/3	1/3
Sample 9/10	0	75	25
Sample 11/12	0	50	50
Sample 13/14	0	25	75
Sample 15/16	75	25	0
Sample 17/18	50	50	0
Sample 19/20	25	75	0
Sample 21/22	75	0	25
Sample 23/24	50	0	50
Sample 25/26	25	0	75

Fig. 8.118: Pure compounds distribution for mixing analysis with hyperspectral in campaign 1

For the spectral signature analysis of each sample, same procedure than in campaign 2 was followed.

New method proposal for chemical characterization of sterile material in scrap.

Pure component analyses:

Similar than in previous capturing campaigns, the first analysis was made on pressed pellets composed of pure components of CaO, SiO_2 and Fe_2O_3

Fig. 8.119 shows the raw spectral signature, linearized and normalized signal got from the pure materials for both hyperspectral sensors:

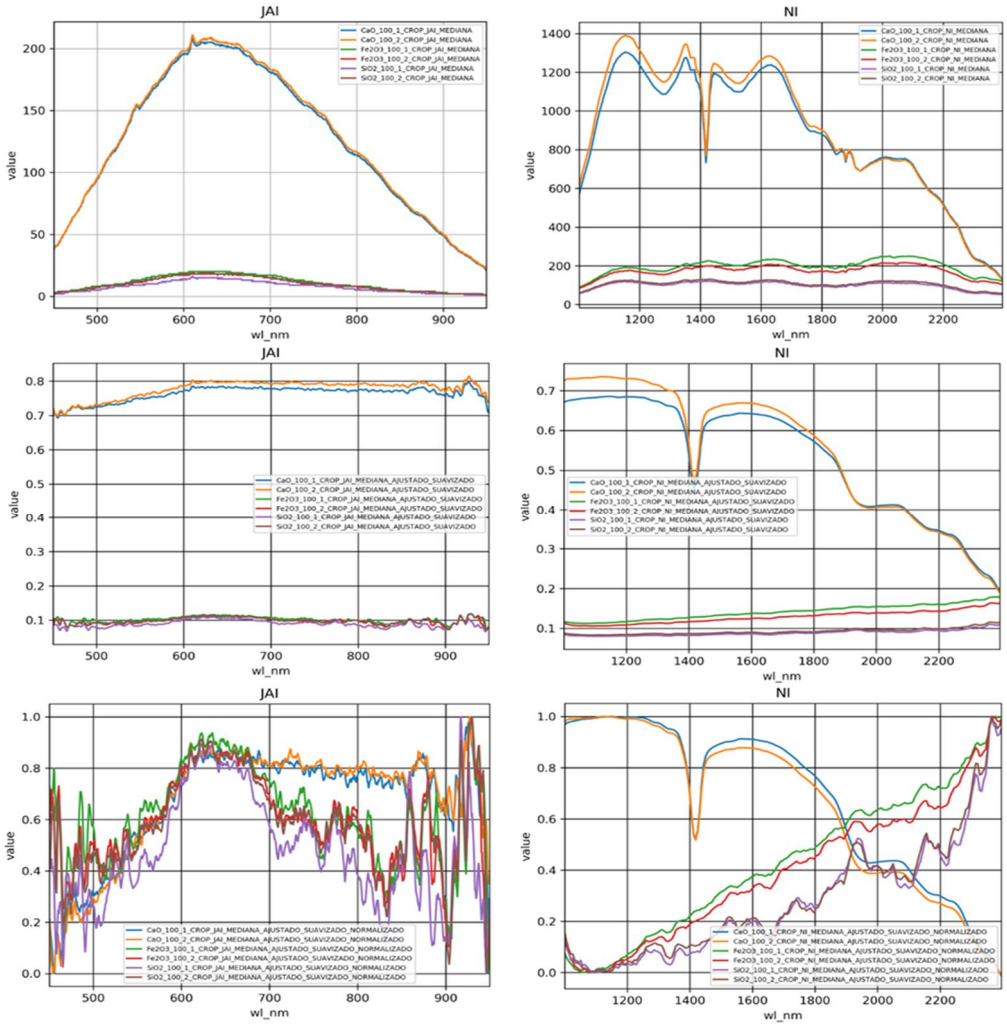

Fig. 8.119: Spectral signature of pure compounds with no processing (Up), linearized Spectral signature with signal smoothing (Mid) and linearized Spectral signature with signal normalization (Down) for JAI sensor (left) and for sisuCHEMA sensor (right)

Analyses over Mixture materials (1, 2, 3, 4, 15, 16, 17, 18, 19, 20):

Fig. 8.120 shows Fe_2O_3/Dolomite mixtures raw spectral signature, linearized and normalized signals got from the pure materials for both hyperspectral sensors:

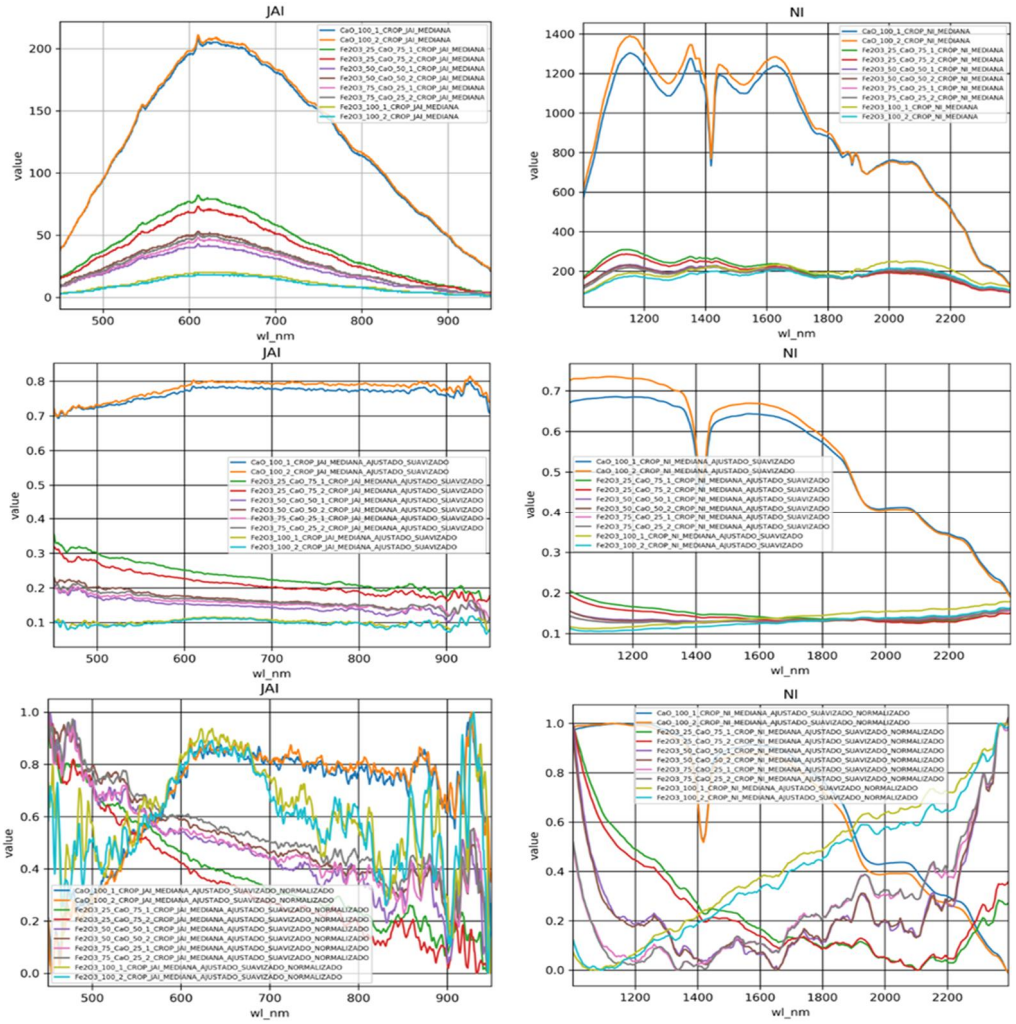

Fig. 8.120: Spectral signature of Fe_2O_3/Dolomite with no processing (Up), linearized Spectral signature with signal smoothing (Mid) and linearized Spectral signature with signal normalization (Down) for JAI sensor (left) and for sisuCHEMA sensor (right)

Analyses over Mixture materials (1, 2, 5, 6, 21, 22, 23, 24, 25, 26):

Fig. 8.121 shows Fe_2O_3/SiO_2 mixtures raw spectral signature, linearized and normalized signals got from the pure materials for both hyperspectral sensors:

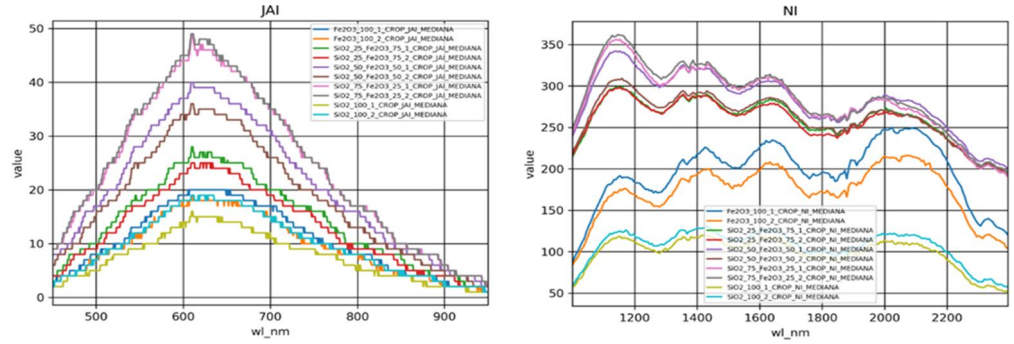

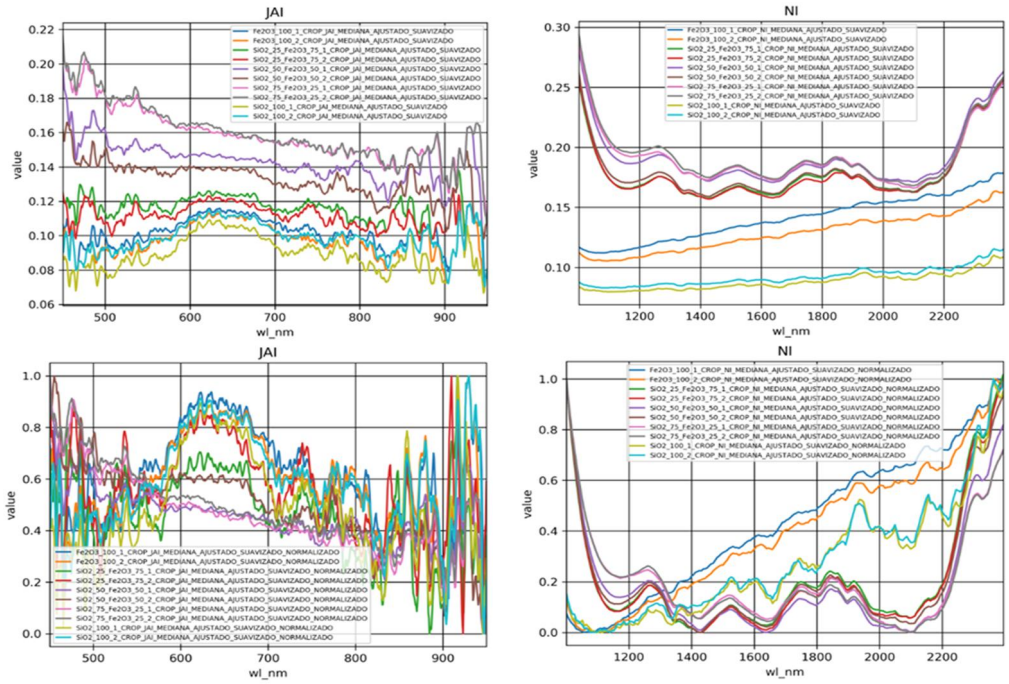

Fig. 8.121: Spectral signature of Fe_2O_3/SiO_2 mixtures with no processing (Up), linearized Spectral signature with signal smoothing (Mid) and linearized Spectral signature with signal normalization (Down) for JAI sensor (left) and for sisuCHEMA sensor (right)

Analyses over Mixture materials (3, 4, 5, 6, 9, 10, 11, 12, 13, 14):

Fig. 8.122 shows Dolomite/SiO_2 mixtures raw spectral signature, linearized and normalized signals got from the pure materials for both hyperspectral sensors:

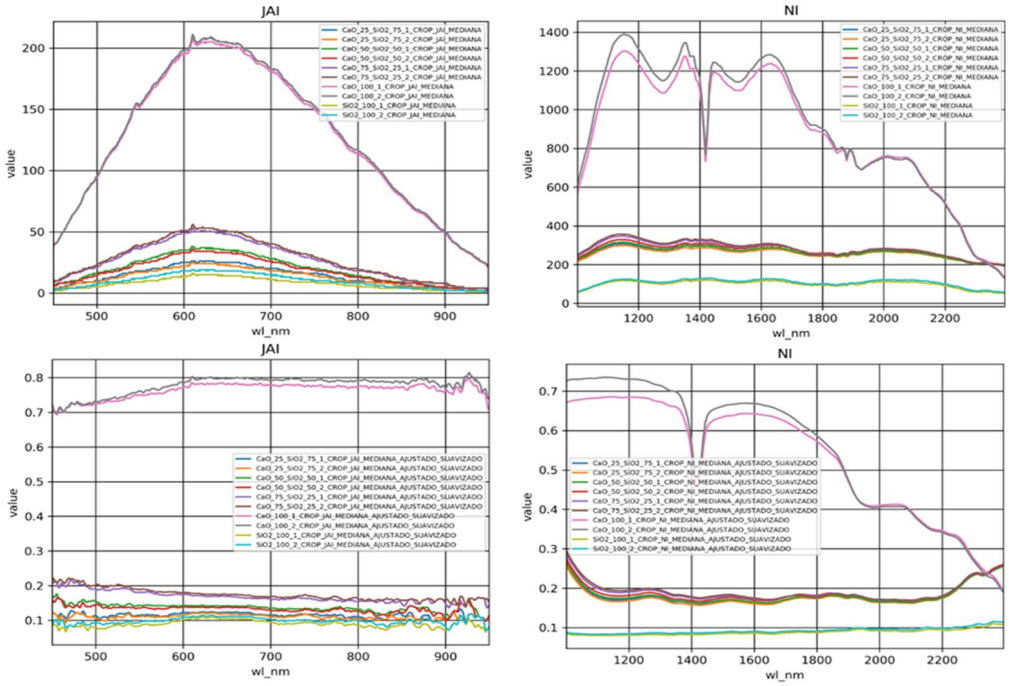

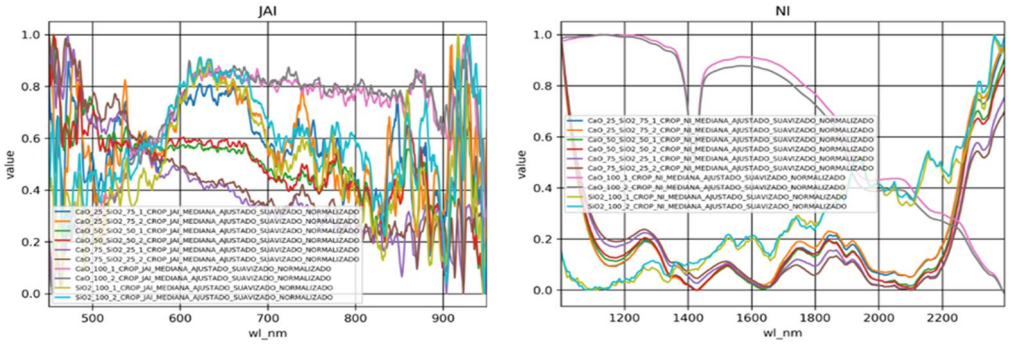

Fig. 8.122: Spectral signature of Dolo/SiO_2 mixtures with no processing (Up), linearized Spectral signature with signal smoothing (Mid) and linearized Spectral signature with signal normalization (Down) for JAI sensor (left) and for sisuCHEMA sensor (right)

Analyses over Mixture materials (1, 2, 3, 4, 5, 6, 7, 8):

Fig. 8.123 shows Fe_2O_3/SiO_2/Dolo mixtures raw spectral signature, linearized and normalized signals got from the pure materials for both hyperspectral sensors:

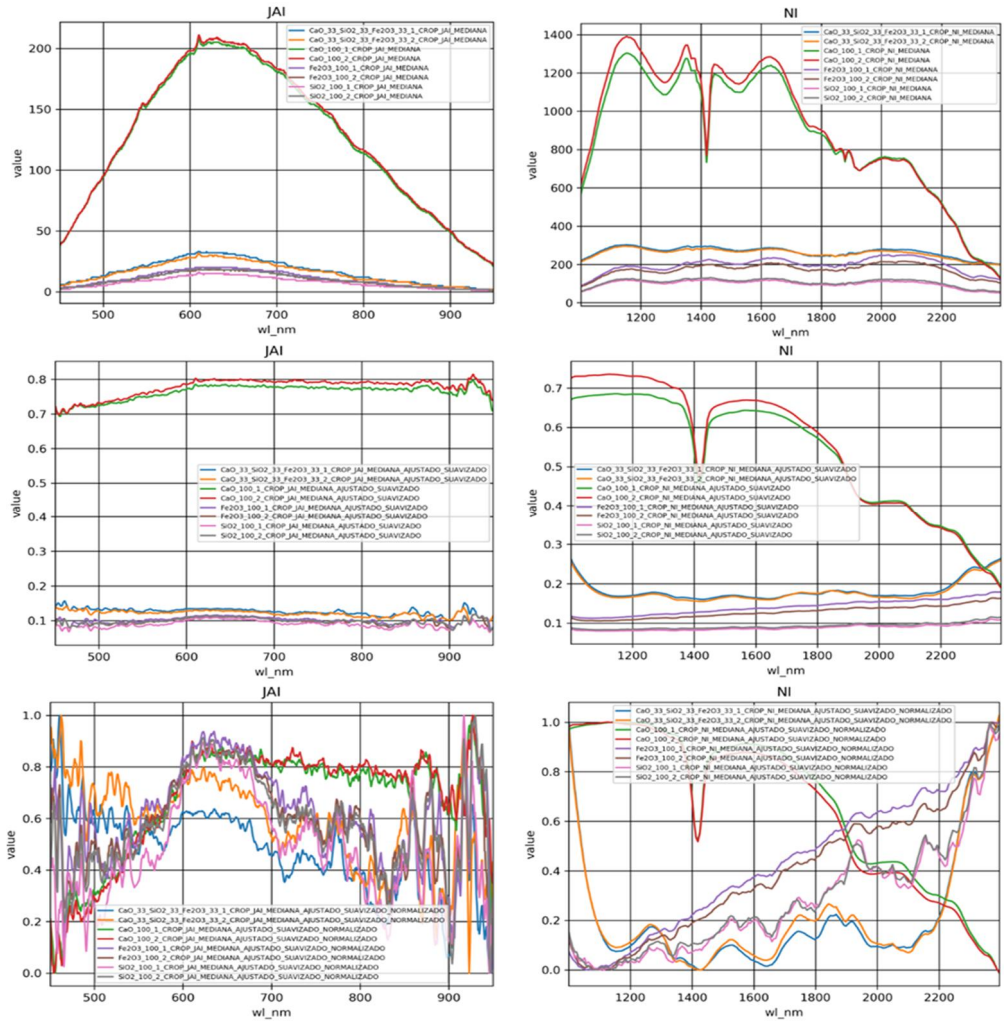

Fig. 8.123: Spectral signature of Fe_2O_3/Dolo/SiO_2 mixtures with no processing (Up), linearized Spectral signature with signal smoothing (Mid) and linearized Spectral signature with signal normalization (Down) for JAI sensor (left) and for sisuCHEMA sensor (right)

New method proposal for chemical characterization of sterile material in scrap.

Calculation of compound abundances:

Similar than in previous analysis, the abundance was done, defining as endmembers (base components) the samples made on the pure components, for each compound per sample according the methodology described in section 8.1.3

In the previous analysis, the abundance estimation algorithms were tested for several processing methodologies; raw unprocessed spectra, normalized raw spectrum, smoothed linearized spectrum and normalized linearized spectrum. However, the only analysis offering some qualitative information for SiO_2 and CaO (not for Fe_2O_3) was for the case of raw spectral data without and with normalization. This may be due to the fact that the spectra linearization process can lead to the loss of relevant information.

The results obtained are shown in the following images.

Fig. 8.124 shows Raw spectra information **without normalizing** (VIS + NIR spectral range):

Real			Estimated		
CaO	SiO_2	FeO	Dolo	SiO_2	FeO
33	33	33	3,56%	5,97%	90,47%
25	0	75	9,76%		90,24%
50	0	50	9,47%		90,53%
75	0	25	19,75%		80,25%
25	75	0	2,74%	97,26%	
50	50	0	5,98%	94,02%	
75	25	0	12,65%	87,35%	
0	25	75		0,34%	99,66%
0	50	50		0,91%	99,09%
0	75	25		1,89%	98,11%

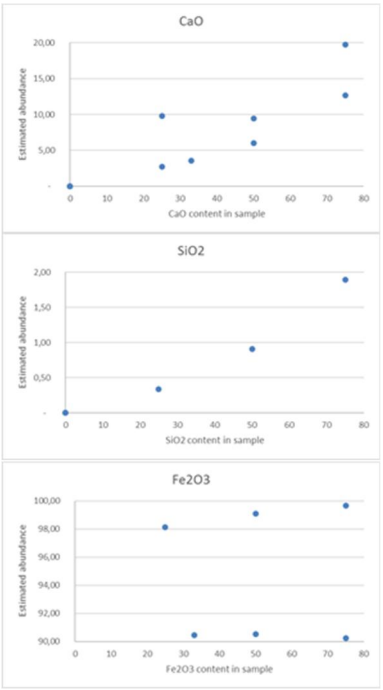

Fig. 8.124: Abundance estimation for raw spectra information without normalizing (JAI sensor)

Looking at these results, with a hyperspectral sensor in the VIS+NIR range is it possible to estimate quantitatively the presence of CaO contained in the sample. However, when analyzing the rest of the components, the algorithm behaves differently (The trends of SiO_2 and Fe_2O_3 are different) if there is CaO in the mixture.

Raw spectra information without normalizing (SWIR spectral range):

Real			Estimated		
CaO	SiO_2	FeO	Dolo	SiO_2	FeO
33	33	33	12,53	8,66	78,81
25	0	75	2,26		97,74
50	0	50	3,32		96,68
75	0	25	5,46		94,54
25	75	0	16,27	83,73	
50	50	0	18,24	81,76	
75	25	0	19,67	80,33	
0	25	75		0,63	99,37
0	50	50		0,67	99,33
0	75	25		0,45	99,55

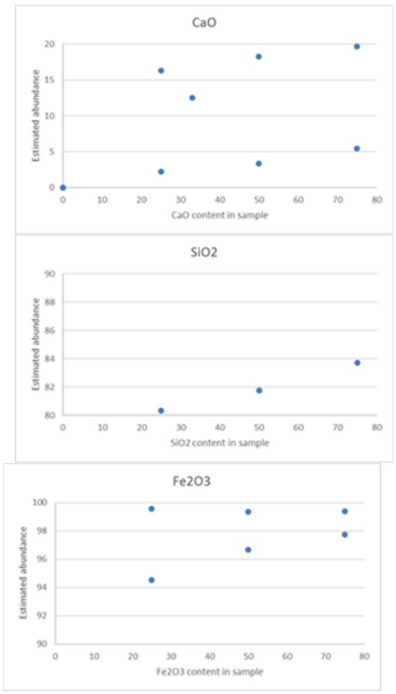

Fig. 8.125: Abundance estimation for raw spectra information without normalizing (sisuCHEMA)

Looking at these results, with a hyperspectral sensor in the VIS+NIR range is it possible to estimate quantitatively the presence of CaO contained in the sample. However, when analyzing the rest of the components, the algorithm behaves differently (The trends of SiO_2 and Fe_2O_3 are different) if there is CaO in the mixture

The main conclusions reach after analyzing the data got during capturing campaign 3 are summarized below:

- For pure components, same conclusions than in measurement campaigns 1 and 2 were reached.
    - In the VIS + NIR range (JAI sensor), CaO clearly stands out from the other two in the case of raw spectra, adjusted.
        - No relationship was observed for normalized spectral information.
        - Fe_2O_3 and SiO_2 are very similar to each other
    - For SWIR range (sisuCHEMA sensor), all pure compounds are clearly differentiable for the spectral data, with and without processing:
        - CaO: peak absorption at 1420 nm
        - Fe_2O_3: Clear slope and greater signal than SiO_2
        - SiO_2: Gradient slope that is accentuated at the end

    In the case of the normalized spectrum, there is a strange behavior between SiO_2 and Fe_2O_3 at high wavelengths.

New method proposal for chemical characterization of sterile material in scrap.

- In the case of Fe_2O_3 / CaO mixtures, for the case using the JAI sensor, as the Fe_2O_3 content increases, the signal intensities associated with the spectra for different compositions are confused.

  On the other hand, for sisuCHEMA sensor, an increase in the reflection signal intensity is observed as the CaO content in the samples increases for all the cases in which the raw signal is analyzed. This clear relationship of signal intensity with the CaO content is maintained when analyzing the information obtained after spectra linearization.

  - It is observed that between 1100 and 1400 nm as the CaO content of the sample increases, the signal intensity is greater.
  - Also, in the spectral range between 1800 and 2300 nm for the normalized spectra, the higher the content of Fe_2O_3 higher is the signal intensity required.
  - In no case (except for pure CaO) the characteristic absorption peak of CaO at 1400 nm is observed.

- For Fe_2O_3 / SiO_2 mixtures, when analyzing the raw spectra and the adjusted spectra acquired data, the spectral signatures for all the pure components with the JAI sensor offer similar signal intensities throughout the whole spectral range (no differentiation between pure SiO_2 and pure Fe_2O_3). Nevertheless, the signals of the mixtures do show an order of intensity depending on the composition of the sample (the higher the SiO_2, the greater the intensity of the acquired signal).

  In the case of sisuCHEMA sensor, the pure samples associated with each component are clearly differentiated. Likewise, the mixture samples are clearly grouped according to their composition (as a remarkable fact, the acquired signal intensity for the mixed samples is greater, for all the cases, than for each of the individual pure components).

  In the case of normalized spectra, there is no relationship between the composition of the mixtures and the shape of the graphs. Apart from the spectral range 1100 - 1300 nm, where it is observed that the greater the proportion of SiO_2, the greater the intensity of the acquired signal.

- In the case of CaO / SiO_2 mixtures, similar than in previous cases, an increase in the reflection signal intensity is observed as the CaO content in the samples increases for raw and linearized data for JAI sensor. However, in the case of SWIR spectral range, it is not possible to differentiate mixed materials.

  The normalization process only offers useful information for sisuCHEMA sensor

- Finally, when analyzing mixed composed by a 1/3 part of each compound (SiO_2, Fe_2O_3, CaO), in the case of the raw and adjusted spectral signature, consistency is observed between the signals intensities response for mixing of three components with respect to the pure components for both sensors.

  When the standardized spectral information is analyzed, for the JAI case, there is no identified relationship between the composition of the mixtures and the shape of the

signatures. On the other hand, for sisuCHEMA case, a clear relationship between the composition of the mixtures and the shape of the graphs:

- At lower wavelengths (1100 and 1600 nm) the more CaO the mixture has, the higher the signal.
- At higher wavelengths (between 1800 and 2100 nm) the more CaO in the mixtures, the lower the signal.

8.2.7 Main conclusions on the use of Hyperspectral spectroscopy for the characterization of sterile

Hyperspectral imaging analysis techniques seem to be a good solution for quick characterization of unknown materials, since it allows estimating the emissivity or reflectivity of the element to be analyzed, in terms of its wavelength.

The spectral behavior of one material at different wavelengths depend on various factors, including the chemical composition. However, the spectral information contained in the signal presents great variability and it is affected by other factors such as lighting, noise or low atomic excitation. And the research work proposed aimed to assess the capability of this technique for quick sterile scrap characterization in steelmaking sector.

The starting point of this work was a deep analysis of the state of the art in terms of spectra knowledge. Then two different experimental set ups for spectral acquisition were defined and built in laboratory; Static analysis of the selected samples in Visual + Near IR spectral range and Dynamic analysis of the selected samples in Visual + Near IR and in SWIR spectral ranges. Finally, calibration procedures were established for each of the laboratory set up.

Regarding the methods tested for spectral data acquisition, two different approaches were tested:

- Selection of 5 random point on the samples and spectral averaging: several inconsistencies were detected in the results which can be associated to samples manipulation, surfaces deteriorations, dirt. Those effects are not under control in laboratory conditions, so that this is not a valid method for industrial conditions.
- Defining of a Region Of Interest inside the sample area to obtain the mean intensity value of every pixel inside this ROI. This method for spectral information extraction based on ROI definition offers better results.

The straightforward analyses of the acquired spectral information, allow reaching the following conclusions in relation to hyperspectral technology capabilities for quantitative estimation of sterile compounds:

- In the case of Static analysis in Visual + Near IR spectral range (linear sensor), certain patterns in the spectral signature that can be exploited, however, nor characteristic peaks were identified.
- On the other hand, for Dynamic analysis in Visual + Near IR + SWIR spectral ranges (matricial sensor), the main conclusion can be summarized as follow:
    - Pure compounds analysis:
        - Reflexion intensity of calcite materials in bigger than for the rest of compounds in the whole spectral range (expected spectral response was got at 1200-1400 nm).

New method proposal for chemical characterization of sterile material in scrap.

        - For Fe_2O_3 compound showed a specific spectral slope (greater signal than SiO_2 was reported)
        - In SiO_2 compound also showed a specific spectral slope (being accentuated at the end).
        - The best spectral range for distinguish between Fe_2O_3 and SiO_2 is 2300-2400 nm for all spectra processing methodologies tested. However, for normalized raw spectra information, between 1900 and 2200 nm the three pure compounds are clearly identified.
    - CaO / SiO_2 compounds (two compound mixtures):
        - VIS+NIR sensor offers expected correlations of intensity signal in the case of CaO and SiO_2 mixtures (It is observed that between 1100 and 1400 nm as the CaO content of the sample increases, the signal intensity is greater)
        - Using SWIR sensor, it is not possible to differentiate mixed materials.
    - Fe_2O_3 / SiO_2 compounds (two compound mixtures):
        - In the spectral range between 1800 and 2300 nm for the normalized spectra, the higher the content of Fe_2O_3 higher is the signal intensity required.
    - Fe_2O_3 / CaO compounds (two compound mixtures):
        - No clear information in VIS+NIR range were observed.
        - For SWIR spectral range, carbonate compounds (higher signal intensity) were identified in 1100-1400 nm spectral range. Also, at 1800-2300 nm Fe_2O_3 content can be observed.
    - Fe_2O_3 / CaO /SiO_2 compounds (three compound mixtures):
        - The coherency with regards pure compounds is meet (the higher the Dolomite, the higher the intensity of the mixture, the higher the SiO_2, the lower the intensity of the mixture)
- Finally, when analyzing the output of the proposed methodology for abundance estimation from spectral information, the following conclusion can be highlighted:
    - The individual abundance estimation algorithm is offering some qualitative information for SiO_2 and CaO in the case of raw spectral data without and with normalization, but not useful information was extracted for any of the linearization processing methods proposed.
    - Fe_2O_3 content in the samples is not estimated using any abundance calculation method.

As summary, using hyperspectral imaging spectroscopy, could be possible to identify the presence of CaO, Fe_2O_3 (in VIS+NIR range) and SiO_2 (in SWIR range). For quantifying the

amount of those compounds in the mixture, the proposed abundance estimation algorithm offers some qualitative information for SiO_2 and CaO when analyzing raw spectral data. But Fe_2O_3 content cannot be estimated.

New method proposal for chemical characterization of sterile material in scrap.

8.3 FTIR Spectroscopy

In previous investigations, RAMAN spectroscopy technologies and Reflexive hyperspectral imaging were studied for assessing the capabilities of these techniques for qualitative analysis of the chemical composition of the sterile in scrap.

In this section we propose the use of reflection Fourier Transform InfraRed spectroscopy (FTIR) for sterile characterization purpose. In FTIR technique, interferometry is used to record information about the material to which the infrared beam is applied.

8.3.1 Literature survey about FTIR spectroscopy

8.3.1.1 Fundamentals and physic principles

Like other spectroscopy techniques, FTIR is composed by source, a sample and a detector. As shown in Fig. 8.126, FTIR technique consists on sending the generated energy of the source through an interferometer and onto the sample. In every scan, all source radiation gets to the sample. The light passes through a beam-splitter, which sends the light in two directions at right angles. One beam goes to a stationary mirror then back to the beam-splitter. The other goes to a moving mirror. The motion of the mirror makes the total path length variable versus the one taken by the stationary-mirror beam. When the two signals meet up again at the beam-splitter, they are recombined. The difference in path lengths creates constructive and destructive interference (interferogram). The recombined beam passes through the sample. The sample absorbs all the different wavelengths characteristic of its spectrum, and this subtracts specific wavelengths from the interferogram. The detector now reports variation in energy versus time for all wavelengths simultaneously. A laser beam is superimposed to provide a reference for the instrument operation. Then, a Fourier transform function allows to convert an intensity-vs.-time spectrum into an intensity-vs.-frequency spectrum.

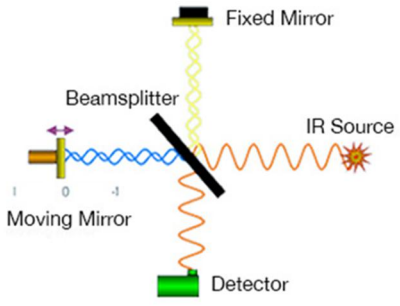

Fig. 8.126: General structure of Fourier Transform InfraRed spectroscopy

The resulting signal in the detector is a spectrum that represents the molecular "footprint" of the sample. Infrared spectroscopy could be useful since different chemical structures (molecules) produce different spectral signatures.

New method proposal for chemical characterization of sterile material in scrap.

One of the major advantages FTIRs, with regards other infrared spectrometers is their ability to measure spectra with high signal-to-noise ratios (157), however, an important aspect to consider when proposing an analysis using FTIR spectroscopy is the sample manipulation technique to be used. Certain sample handling techniques are more effective than others for specific types of samples, so to obtain a high-quality spectrum quality, it is important to know which manipulation technique works best for the type of sample to be analyzed. There are four main sampling techniques for FTIR (158):

- **Transmission**: The sample is placed directly into the infrared (IR) beam. As the IR beam passes through it, the transmitted energy can be measured, and a spectrum is generated. The transmission technique can be used to analyze organic and thermoplastic powders, some type of polymers, several liquids and gases
- **Total attenuated reflectance (ATR)**: An IR beam is directed onto an optically dense crystal with a high refractive index at a certain angle. This internal reflectance creates an evanescent wave that extends beyond the surface of the crystal into the sample held in contact with the crystal. This technique is commonly used for liquid analysis and it also fits well for homogeneous solid samples, surface layer analysis of a multi-layered solid or coating analysis
- **Diffuse Radiance (DRIFTS)**: This method operates by directing the IR energy into a sample cup filled with a mixture of the sample and an IR transparent matrix (such as KBr). The IR radiation interacts with the particles and then reflects off their surfaces, causing the light to diffuse, or scatter, as it moves throughout the sample. Diffuse radiance technique is commonly used for the analysis of both organic and inorganic samples that can be ground into a fine powder (less than 10 microns) and mixed in a powder matrix such as potassium bromide (KBr)
- **True Specular Reflectance:** This is a surface measurement technique that works on the principle of reflective efficiencies. Specular reflectance is commonly used for the analysis of both organic and inorganic samples having large, flat, reflective surfaces

8.3.1.2 Previous applications of FTIR spectroscopy technique in industrial applications

Fourier transform infrared spectroscopy (FTIR) is a fast and non-destructive analytical method, associated with chemometrics, it has become a powerful tool for the pharmaceutical industry (159) (160) (161) (162) (163). Also, in the general chemistry field several works can be found dealing with the use of spectroscopic characterization of polymers (164) (165) (166) and biological materials (167). Some research with FT-IR spectroscopy can be found in literature applied to inorganic minerals and pigments characterization (168), surface Analysis (169), characterization of optical behavior of certain materials like highly reflective materials [81] or characterization of the emittance behavior of materials (170).

New method proposal for chemical characterization of sterile material in scrap.

There are several researches done for using this kind of technologies in industrial steel sectors mainly in residues/by-product characterization;

- Understanding of EAF or LF slag chemistries, both during the processing phase or for subsequently application as by-product (171) (172) (173) (174).
- Characterization of EAF dust characterization for valuable material recovery (175) (176).

8.3.1.3 Prior spectra knowledge

The main advantages of FTIR spectroscopy are simplicity, practically no sample preparation and a superior speed of more than 100 spectra per second. In addition to this, the flow through setup means that continuous, real-time monitoring is possible

In this section some information about spectra characteristic peaks of some materials, obtained after a literature survey, are presented. Previous laboratory works may be used as starting point of the current research line for identifying the main reflection characteristic of the different components present in ferrous scrap sterile.

8.3.1.3.1 Calite ($CaCO_3$) and Dolomite ($CaMg(CO_3)_2$) materials

Regarding the use of FTIR spectroscopy as analytical technique applied to characterize and understand Calcite and Dolomite materials spectral behavior, several studies have been found in the literature (177) (178) (179) (180).

According the literature, each carbonate shows characteristic absorption bands. The most common groups have been widely reported as calcite, dolomite, and aragonite groups, and the spectral difference may be related to crystal structure. In this sense, carbonates have a strong and broad asymmetric absorption peak at 1300-1500 cm^{-1} due to the *v3* asymmetric stretching vibration mode of CO_3^{-2}. They also present a lower amplitude peak at 850– 880 cm^{-1} due to the v2 asymmetric vibration mode of CO_3^{-2}, which is characterized by a notch on the falling limb. It can be found another relevant peak at 700–746 cm^{-1} due to the v4 symmetrical in plane bend vibration mode of CO_3^{-2}.

Fig. 8.127 graphically describes the above mentioned:

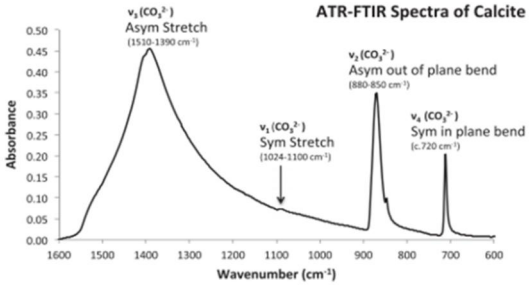

Fig. 8.127: Vibrational modes of CO_3^{-2} (181)

In Fig. 8.127, it is also observed that there is an absorption band at 1081 cm^{-1} for calcite groups (in the other carbonates ranging from 1000–1100 cm^{-1}), but they are less obvious and therefore they are not usually taken into consideration.

Another consideration to be taken into consideration when analyzing carbonate materials is that the increase in Mg content moves the *v4* peaks to the left. This effect is shown in Fig. 8.128:

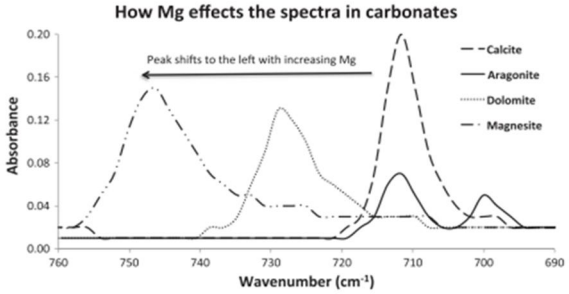

Fig. 8.128: Effect of Mg in Carbonate materials (181)

8.3.1.3.2 SiO_2 materials

Concerning silica, several studies have been found focusing on understanding its spectral behavior (181) (149) (182), however it is worth mentioning that silicates are more complex than carbonates minerals due to the complicated tetrahedron SiO_4 structures that can form and complex chemistries.

Similar than with other materials, the positions of the peaks help identify the mineral nature and the peak heights can be used for developing the calibration curves using the constant ratio method (CRM) (181). The CRM works by finding the relationship between a chosen peak and the peak of another mineral present as shown in Fig. 8.129 according (8.13)

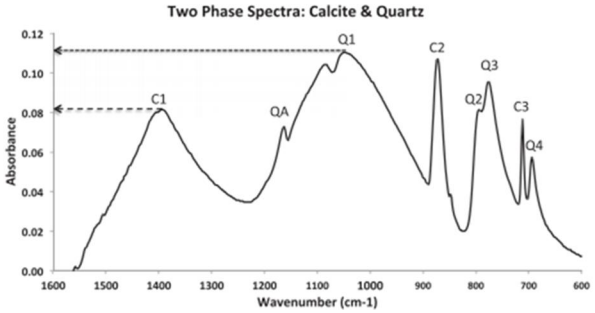

Fig. 8.129: ATR-FTIR spectrum of a known sample with 50% calcite and 50% quartz

$$CRM = \frac{C1}{(C1 + Q1)} \quad \textbf{(8.13)}$$

Where;

- ***C1*** is the Calcite absorption peak height
- ***Q1*** is the chosen analyte peak

New method proposal for chemical characterization of sterile material in scrap.

Beyond the CRM method described above for estimating material presence from spectral comparison with regard a reference mineral (Calcite), it is known that Silicon minerals show strong broad absorption bands at 1030 cm^{-1} and 800 cm^{-1}, which correspond to the stretching vibrations of *Si-O* and *Si-O-Si* respectively. Similarly, the absorption peaks at 530 cm^{-1}, 725 cm^{-1} and 1417 cm^{-1} can be assigned to *Si-O* asymmetrical bending (*Si-O* symmetrical bending and *Si=O* stretching vibration). In addition, the crystallinity may be calculated by comparing the ratio of intensity of the characteristic peaks at 766 and 700 cm^{-1} (149) (182). Also, an absorption band near 1083 cm^{-1}, assigned to *Si–O* vibrations of amorphous silica has been reported by some authors (182)

In previous tests for analyzing Hyperspectral and RAMAN spectroscopy techniques, the raw material used for simulating Silica presence in scrap sterile was Rice Husk Ash (RHA). Fig. 218 shows some transmittance FTIR spectra of RHA reported in literature (149):

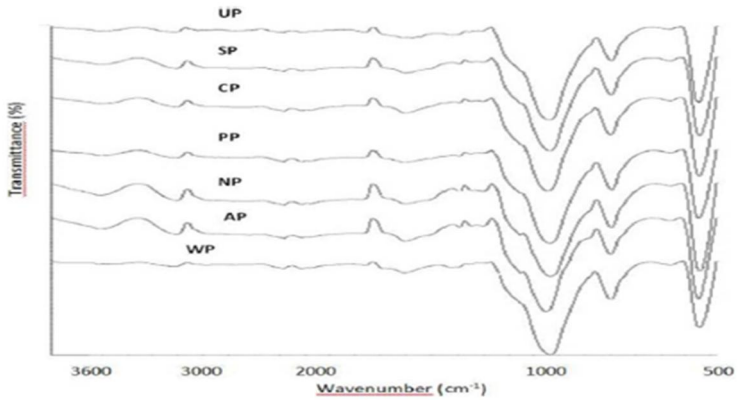

Fig. 8.130: FTIR spectra of RHA samples

8.3.1.3.3 FeO / Fe_2O_3 materials

Several studies have been found with regards the characterization of ferric iron minerals

FTIR spectra of iron oxides are well established (183) (184) (185) (186). According the information reported in literature the main absorption band associated to *Fe–O* lattice vibration can be found at lower wavenumber.

In the case of magnetite (Fe_3O_4), FTIR spectrum exhibits two strong infrared absorption bands at 570 cm_{-1} (*Fe–O* stretching mode of the tetrahedral and octahedral sites for the *υ1*) and 390 cm^{-1}(*Fe–O* stretching mode of the octahedral sites for the *υ2*). At this wavelength range, two other absorption bands at 268 cm^{-1} and 178 cm^{-1} are present.

For Maghemite (γ-Fe_3O_4), the main absorption bands can be found at 630, 590, and 430 cm^{-1}. And at 1018 cm^{-1} and 750 cm^{-1} for *OH* stretch for lepidocrocite (γ-FeOOH)

In the case of Hematite (α-Fe_3O_4), the main absorption bands can be found at 540, 470, and 352 cm^{-1}. And at 1124 cm^{-1}, 890 cm^{-1} and 810 cm^{-1} for *OH* stretch for lepidocrocite (α -FeOOH)

New method proposal for chemical characterization of sterile material in scrap.

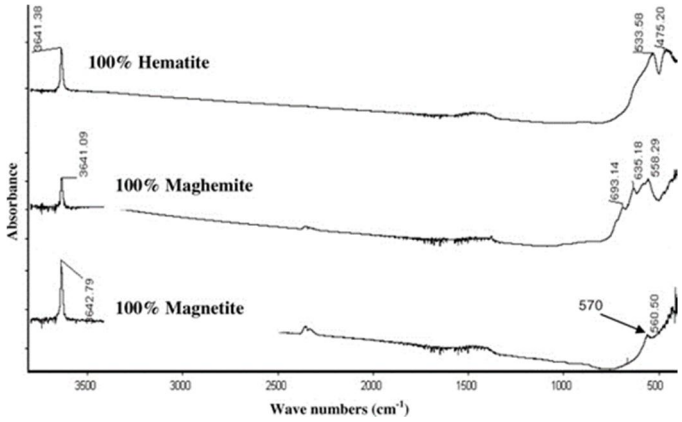

Fig. 8.131: FTIR spectra, over 400–4000 cm^{-1} spectral range showing IR bands of hematite, kaolinite, sulphate, quartz and nitrates

On the other hand, similar to what was found for Silicates minerals, calcium oxide (lime) is usually added to Fe_2O_3 samples as a standard reference in obtaining the calibration curves (183).

8.3.2 Laboratory equipment for spectral analysis

The equipment used for conducting the proposed analysis were:

- VERTEX 70v FTIR spectrometer: permanently aligned RockSolid TM interferometer, which is equipped with gold-coated optics and has a 30° angle of incidence for maximum efficiency and sensitivity as well as minimum polarization effects. Digital electronics ensure optimal interferometer control, highest sensitivity and long-term stability.

Performance:	
Spectral range:	Mid-IR, NIR, Far-IR/THz, Visible/UV 10 cm $^{-1}$ to 28,000 cm $^{-1}$ (360 nm)
Spectral resolution:	< 0.4 cm $^{-1}$
Optical Bench:	
Optics Housing:	Standard vacuum or purgeable, includes dry vacuum pump
Input / Ouput Ports:	2 / 5
Sample compartment:	Vacuum
Components & Electronics:	
Interfermeter:	RockSolid™
Detectors internal:	Up to two 24 bit dual-channel ADC DigiTect™
Detectors external:	Four, multiplexed up to 16
Dedicated Techniques:	
Rapid Scan:	>70 spectra/sec at 16 cm $^{-1}$ spectral resolution
Slow Scan **& Step Scan:**	100 Hz (0.0063 cm/sec), Phase modulation and internal demodulation, Temporal resolution 6 µsec/2.5 nsec

Fig. 8.132: FTIR Spectrometer technical characteristics

New method proposal for chemical characterization of sterile material in scrap.

- For the capture, the visualization and the processing of the spectra, a PC equipped with the integrated OPUS spectroscopy software. OPUS is the leading spectroscopy software for the advanced measurement, processing and evaluation of IR, NIR and Raman spectra.

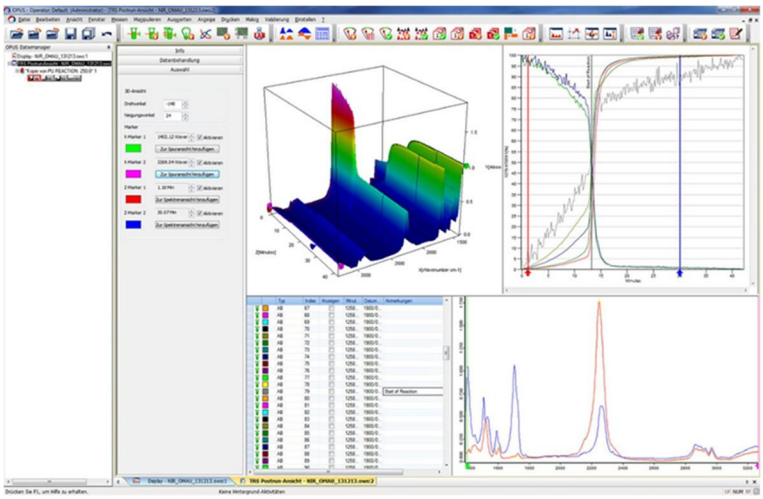

Fig. 8.133: OPUS spectroscopy software snapshot

New method proposal for chemical characterization of sterile material in scrap.

8.3.3 Laboratory tests

Similarly, to the other tested technologies within this work, the objective of this activity is the development and implementation of a new in situ analytical technique for the characterization of sterile materials contained in scrap.

The activities explained in this section aim to determine the most suitable capturing conditions under controlled laboratory conditions (lighting, temperature, environmental pollution, sample preparation). To this end, artificially prepared samples with well-defined chemical compositions will be used, so that, and supported by previous bibliographical references, it will be possible to establish the processing and analysis patterns of the spectral signatures obtained, which will then be applied under real industrial conditions.

8.3.3.1 Samples selection and preparation

As it was already mentioned in previous sections, the main compound tested were CaO, MgO, SiO_2, Al_2O_3, Fe_2O_3. In this sense, CaO, Fe_2O_3 and SiO_2 are easily obtainable materials in industrial activities.

- SiO_2; A material based on calcined rice husk has been selected. This material is used in steelmaking as coverage material to prevent thermal losses of the steel during the casting process. The chemical composition (according the supplier) is about 92% of SiO_2, 1% of CaO, 1,5% of Al_2O_3 and 1% of Fe_2O_3
- CaO; This material is obtained from calcined calcite stone. This material is required in steelmaking for phosphorous removal in the electrical Arc Furnaces process. The chemical composition (according the supplier) is about 1,5% of MgO and 97% of CaO.
- Fe_2O_3: This material can be easily found in different parts of the steelmaking process. In order to get a product with the higher iron Oxide as possible, mill scale will be used as reference material. Rolling Mill scale present a percentage of iron oxides up to 84%, presenting mostly Wuestite, Hematite and Magnetite.

In order to conduct FTIR analysis, it was necessary to prepare pressed pellet with a mixture of the sample with potassium bromide (KBr is not visible to FTIR). In this case and after testing several concentrations (since we are working with dark samples), the most convenient mixture corresponds with 1 mg of sample and 300 mg of KBr.

Once the manufacturing process and the mixtures requirements are set, 8 pressed pellets samples were made mixing the pure components to analyze the position of the absorption bands and their relationships with the actual chemical composition (using CaO absorption bands as calibrating reference).

Fig. 8.134: summarizes the material distribution used in this section:

Sample ID	% CaO	% Fe2O3	%SiO_2
Sample 1	100	0	0
Sample 2	0	100	0
Sample 3	0	0	100
Sample 4	50	50	0
Sample 5	20	80	0
Sample 6	50	0	50
Sample 7	0	50	50
Sample 8	0	80	20

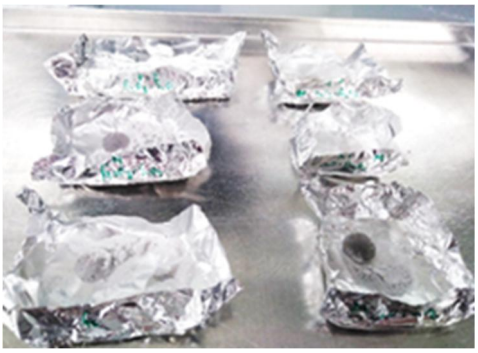

Fig. 8.134: Pressed pellets of pure compounds mixings

8.3.3.2 Capturing procedure

The capturing procedure consisted on exposing the different samples to a source of infrared light. The FTIR spectrometer makes a scanning from 4000 cm^{-1} to 600 cm^{-1} wavelengths. The intensity of the light transmitted through the sample (infrared spectrum of the sample) is measured at each wavenumber. This measurement allows calculating the amount of light absorbed by the sample by analyzing the difference between the intensity of the light before and after passing through the sample cell.

8.3.4 Laboratory tests results

The objective of the laboratory experiments proposed in this section was to gain knowledge and expertise in defining the best optical configuration, material manipulation and mastering spectral signature processing when FTIR spectrometers are used for oxides characterization present in Scrap dirt.

The development of these tests under controlled laboratory conditions will guarantee subsequently better results if this technique is proposed for industrial conditions where there will be a greater number of environmental uncertainties, material heterogeneities, presence of unknown components and/or different degrees of moistures in the samples. In this section, the results obtained during laboratory tests are described

Pure compounds analysis:

As mentioned before, three pure compounds have been tested:

CaO compound: A tablet containing 1 mg CaO sample in 300 mg KBr was prepared. In Fig. 8.135 FTIR spectra for CaO compound is shown:

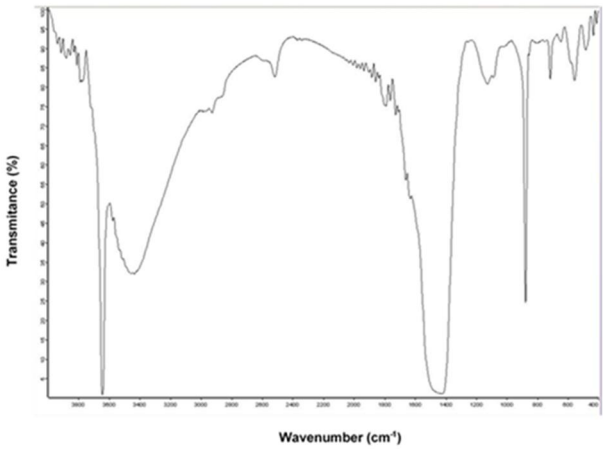

Fig. 8.135: FTIR spectra for CaO compound

Two main absorption bands are clearly observed at 1400 and 900 cm^{-1}. The commercial Software for spectrum identification includes identifies this spectrum with calcium carbonate ($CaCO_3$). These main bands will be used to identify this compound in samples containing mixtures.

On the other hand, the bands above 2600 nm are associated with the moisture contained in the sample and with environmental CO_2.

SiO_2 compound: A tablet containing 1 mg SiO_2 sample in 300 mg KBr was prepared. In Fig. 8.136, the FTIR spectrum obtained for the mixture is shown:

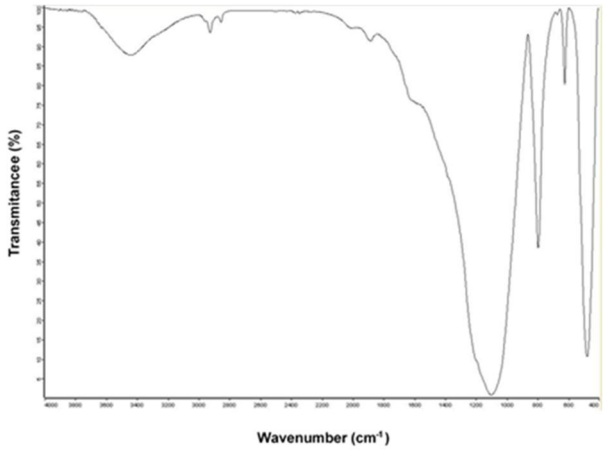

Fig. 8.136: FTIR spectra for SiO_2 compound

The main absorption bands identified in the acquired spectra due to the presence of SiO_2 in the sample were located at around 1100, 800 y 500 cm^{-1}.

According the literature survey done, In Silicon minerals an absorption band near 1083 cm^{-1}, assigned to *Si–O* vibrations of amorphous silica should be found. Also, a strong broad absorption band at 800 cm^{-1} corresponding to the stretching vibrations of *Si-O-Si* should be present. Regarding the band identified at 500cm^{-1}, it could be associated to the absorption peaks at 530 cm^{-1} (*Si-O* asymmetrical bending) reported by some authors.

Fe_2O_3 compound: A tablet containing 1 mg Fe_2O_3 sample in 300 mg KBr was prepared. In Fig. 8.137 the FTIR spectrum obtained for the mixture is shown:

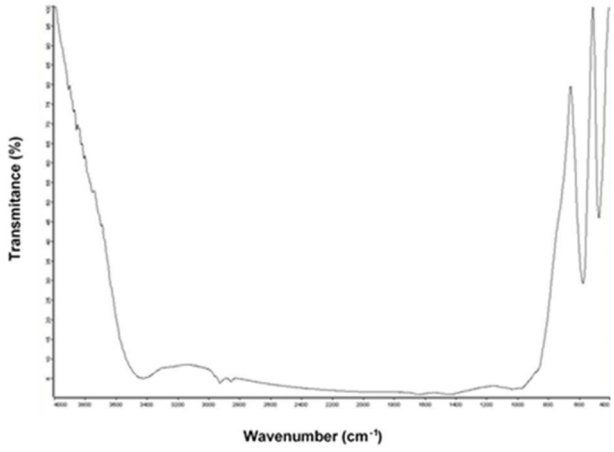

Fig. 8.137: FTIR spectra for Fe_2O_3 compound

For Fe_2O_3 materials, two Sharp bands are observed in 600 - 400 cm^{-1} spectral range. This shows coherence with the expected absorption band reported for magnetite (at 570 cm^{-1} and 390 cm^{-1}), for Maghemite (at 590 cm^{-1}, and 430 cm^{-1}) and for Hematite (at 540cm^{-1} and 470 cm^{-1}).

Mixed compounds analysis:

As described before, the selected pure compounds were mixture and analyzed using FTIR technologies.

Mixture based on **Fe_2O_3 / CaO** compounds: Two different mixtures were prepared; One mixture containing 0,5 mg Fe_2O_3 + 0,5 mg CaO sample in 300 mg KBr, and a second mixture containing 0,75 mg Fe_2O_3 + 0,25 mg CaO sample in 300 mg KBr.

Fig. 8.138 shows FTIR spectrum obtained for the mixture is shown:

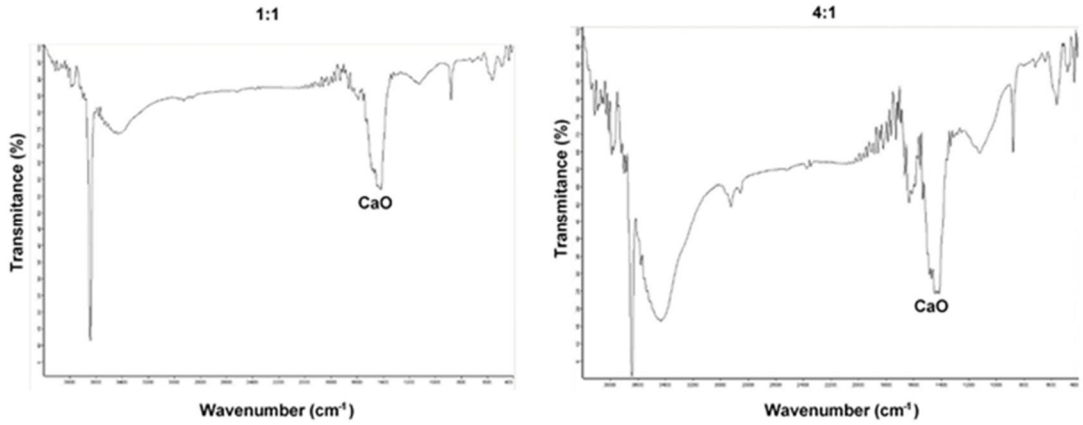

Fig. 8.138: FTIR spectra for Fe_2O_3 / CaO mixtures. Left) 1:1 and right) 4:1

In the spectra signatures obtained from CaO/Fe_2O_3 mixtures, no band corresponding to iron oxides compound were observed. This spectral response seems to be completely blocked by the CaO signal.

Mixture based on **SiO_2 / CaO** compounds: One mixture containing 0,5 mg SiO_2 and 0,5 mg CaO together with 300 mg KBr was prepared.

Fig. 8.139 shows FTIR spectrum obtained for the mixture is shown:

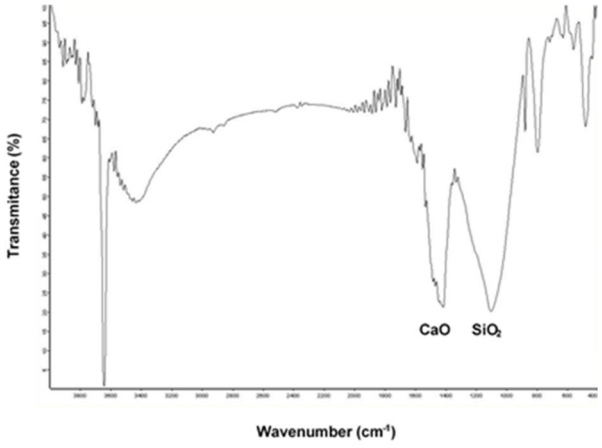

Fig. 8.139: FTIR spectra for SiO_2 / CaO mixtures (1:1 mixture)

New method proposal for chemical characterization of sterile material in scrap.

In this case, the main characteristic band of each component is clearly observed, so it would be possible to make an approximation to quantitative analysis based on the FTIR spectrum obtained from a mixture.

Mixture based on **Fe_2O_3 / SiO_2** compounds: Two different mixtures were prepared; One mixture containing 0,5 mg Fe_2O_3 + 0,5 mg SiO_2 sample in 300 mg KBr, and a second mixture containing 0,75 mg Fe_2O_3 + 0,25 mg SiO_2 sample in 300 mg KBr.

Fig. 8.140 shows FTIR spectrum obtained for the mixture is shown:

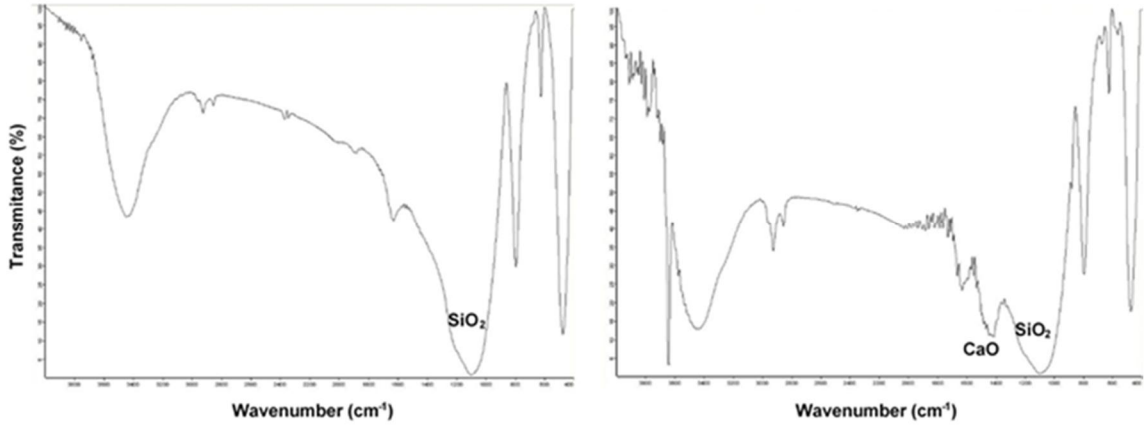

Fig. 8.140: FTIR spectra for Fe_2O_3 / SiO_2 mixtures. Left) 1:1 and right) 4:1

After analyzing the obtained spectral signature, the absorption band associated with the presence of SiO_2 can be easily identifiable. However, no band associated with iron oxides compounds is observed.

On the other hand, in the mixture composed of a higher content of Fe_2O_3, some contamination with CaO can be observed.

It can be concluded that the signal produced by the presence of Fe_2O_3 is totally blocked by the presence of other compounds

8.3.5 Main conclusions on use of FTIR for sterile characterization

In the present work, a laboratory FTIR spectrometer (VERTEX 70v model, supplied by Bruker) was used to evaluate the capability of the proposed technology to do a fast analysis of the different compounds present in ferrous scrap.

The following conclusions have been obtained:

- In the case of pure compounds, FTIR technology allows identifying clearly individual compounds according to their spectral signature reported in literature. The materials used for the tests were identified as:
    - Iron Oxide sample: Hematite and Goethite
    - Calcium sample: CaO and carbonates
    - SiO_2 sample: amorphous silica
- CaO and SiO_2 present very clear and well-defined spectral absorption signals well aligned with the bibliographic work done. So they could be quantified in mixtures containing both compounds, even in the presence of ferrous oxides compounds.
- The signal produced by the presence of Fe_2O_3 is totally blocked by the presence of other compounds. This makes not possible to estimate the presence of iron oxides in the samples using FTIR technique.

8.4 General conclusions about the use of spectroscopy technologies for sterile characterization

Since Ferrous scrap comes to many different origins, the nature of the non-ferrous materials contained in scrap materials is very variable, and therefore it is very complicated to have reliable information on the chemical distribution of the scrap mixtures. On the other hand, there are other circumstances that increase the dispersion in the chemical distribution of the sterile such as mixtures of scrap classes, contamination during manipulation or cheating attempts by the scrap dealer, and that should be measured to tune up the subsequent steel manufacturing processes allowing to maximize the efficiency of them.

To dispose of accurate information on chemical composition and amount of sterile materials contained in each type of scrap involves an important technological advance for the steelmaking sector.

In the current state of the art, the regular procedure to determine the chemical composition of sterile materials is based on X-Ray fluorescent technique. However, XRF technology present some limitation for massive analysis if huge piles of scraps need to be characterized; tests need to be done in laboratory conditions, laborious sample preparation is required for spot analysis.

During this work, several well-known spectroscopy techniques have been tested aiming to evaluate their capabilities to be used for estimating the chemical composition of the dirt present in ferrous scraps in a quick and simple manner.

In the case of Raman spectroscopy, well defined spectra for Iron Oxides and Calcite compounds are obtained, presenting clear characteristic peak easily identified at the different Raman spectral ranges (785 nm and at 514 nm) with not regard the laser power nor sensor exposure time. Those compounds have been widely studying in mineralogy studies and the findings obtained in the present work are well aligned with the information got from literature.

On the other side, when amorphous SiO_2 is present in the sample, the spectral signature is totally saturated by SiO_2 signal. This effect makes not possible to analyses sterile material composed by silica.

For Hyperspectral spectroscopy, and since a passive (non-artificially excited samples) approach was used, the very first conclusion reached was that for extracting useful information of one sample, high number of points on the sample must be analyzed at the same time, minimizing the variability effect of capturing environment such as light or dirt.

Secondly, it was demonstrated that SWIR sensor (2300-2400 nm) could be used for roughly estimating the presence of iron oxide Fe_2O_3 in sterile samples, VIS+NIR sensor offer quantitative information of the presence of CaO in the samples. Spectral information about the presence of Silica can be extracted from both VIS+NIR and SWIR ranges.

One important disadvantage of using hyperspectral spectroscopy for chemical analysis of unknown samples is that the more complex the composition of a sample, the more complex its

spectrum becomes, and the more difficult it is to disaggregate the individual compound spectral features for estimating the whole chemical composition of the sample.

When applying FTIR spectroscopy, individual compounds of CaO and SiO_2 present very clear and well-defined spectral absorption signals well aligned with the bibliographic work done. So they could be quantified in mixtures containing both compounds.

However, similar to what happened with silica when analyzed with Raman technology, the signal produced by the presence of iron oxides is totally blocked by the presence of other compounds, making not possible to estimate the presence of iron oxides in the samples using FTIR technique.

Sterile materials in Ferrous scraps are a complex mixture of residues like rubber, glass, wood and plastics with oxides materials. Those oxides are mainly CaO, Fe_2O_3 and SiO_2. According the findings achieved in this work, there is none analytical method capable to get information for all these compounds at the same time.

The subsequent step to this research activity should be to prepare an analytical portable station composed by the different spectrographs that have proved capabilities for extracting chemical information from the sample of sterile. A set up similar to the one shown in Fig. 8.141 could be proposed:

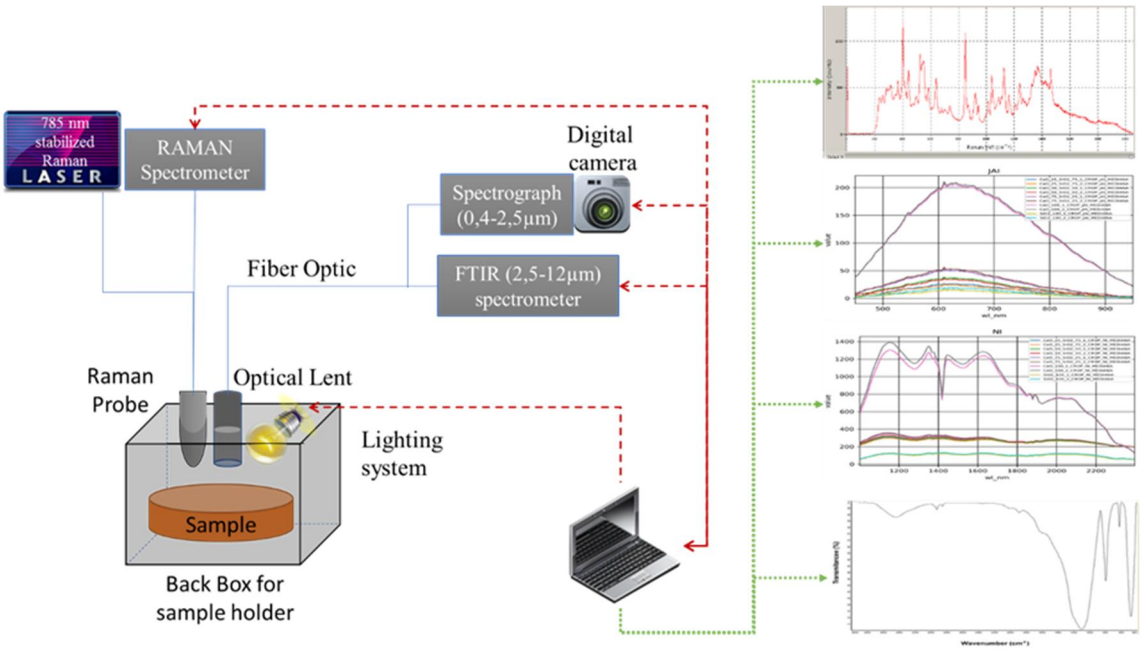

Fig. 8.141: Proposed analytical portable station

Since the main compound of interest in scrap sterile, from steelmaking process optimization point of view, are SiO_2, CaO and Fe_2O_3 the methodology proposed could be as follow:

New method proposal for chemical characterization of sterile material in scrap.

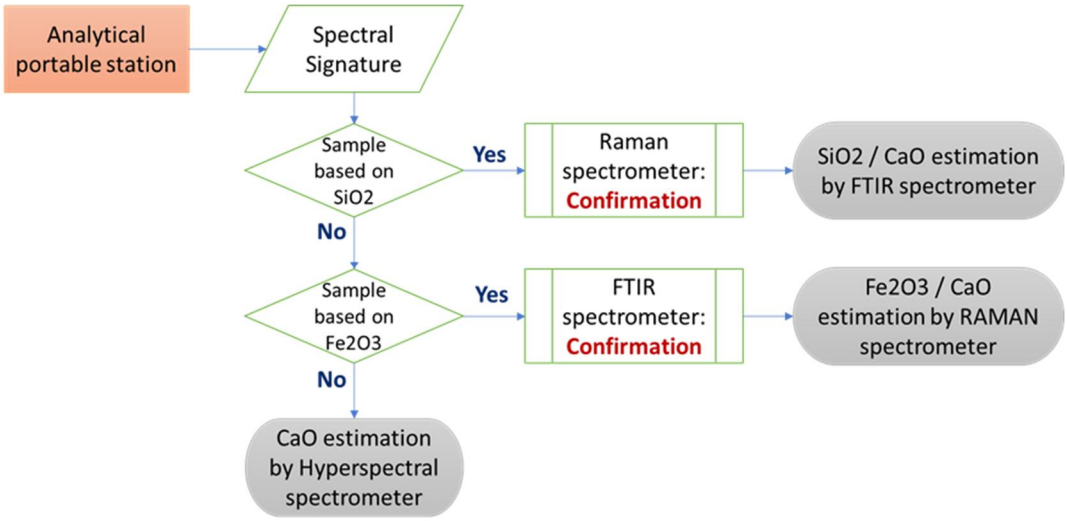

Fig. 8.142: Proposed analytical method

The proposed analytical method depicted in Fig. 8.142 would allow to quickly identify the main compound present in the unknown sterile material. It could be done depending on the response of the different spectrometers. Once the main compounds are identified, the spectral signatures coming from the right spectrometers could be analyzed looking for the spectral features. Then new processing algorithms must be developed for extracting quantitative information from the new proposed analytical portable station.

9

New method proposal for sterile quantification in scrap deliveries.

For understanding the economic affection of sterile materials in Electric Arc Furnace performance, besides its chemical distribution, the total amount dirt contained in scrap is necessary to be known. This chapter presents a novel tool for automatic quantification of the sterile contained in scrap materials. Although the proposed solution has been developed and validated in laboratory conditions, its industrial application would lead to great technological advance in steelmaking scrap yard facilities due to the automatization of key daily operations at material reception area.

In previous chapters, some of the most known steel scrap specifications were presented. The different international Steel Scrap Specification defines the scrap categories (qualities) not only by their origin or their shape but also by their content in residual elements, content in sterile and by also their density.

Those specifications are compromises between what steelmakers need (high density for productivity, low tramp elements for metallurgy, low sterile content for cost), and what scrap dealers can reach with their treatment tools. However, what is actually observed in the scrap reception processes at the steel mills, it is that the supplied material quality varies widely, and in many cases, scrap suppliers do not meet the minimum requirements defined in those specifications (Mixture of materials with different qualities, inadequate dimensions, Forbidden elements, contamination with other elements such as earth, slag or grease, cheats, …). Fig. 9.1 shows several examples:

Fig. 9.1: Examples of non-compliance with the scrap quality specifications

It is therefore necessary to find techniques which allow to check at reception in scrap yards the good belonging of the batches to the announced categories.

New method proposal for sterile quantification in scrap deliveries.

9.1 Current available techniques for sterile quantification

Nowadays, the most extended practice for sterile quantification consists on the visual inspection of each scrap delivery. Then a very experienced scrap yard operator, based on subjective criteria, estimates the quantity of sterile present as well as other possible non-compliance with the scrap quality specifications. Subsequently the scrap yard operator applies an economic penalization the supplied.

Periodically, and in order to verify the good judgment of the scrap yard operator or to analyse a particular supply, concrete tests are carried out. This method basically consists on unloading a scrap truck on a concrete surface at the scrap yard. Then the scrap is collected by magnetic means. The remaining material (nonmagnetic material) is finally sorted by hand and then weighed (see section 6.2.2 for more information). It allows to estimate the most general quality parameters in a very simple manner.

Besides the material purchasing price, and due to the high influence that the scrap quality has on aspects such as the overall efficiency of the steelmaking process, the final quality of steelmaking products, productivity or variable transformation costs, there is a growing awareness of the necessity of using higher scrap quality although this leads to an increase in raw material costs. One alternative that is becoming more and more booming is the installation of scrap cleaning machines in the scrap yards. Fig. 9.2 depicts one example of the industrial layout of these kinds of installations.

Fig. 9.2: E1 Scrap cleaning machine at one ArcelorMittal site in Spain

According scrap cleaning machine suppliers, the main benefits of cleaning scrap are listed below (187):

- Saving EAF energy: 12-18 kWh/steel ton.
- Saving Graphite Electrodes: 0.05 kg/steel ton.
- Saving Lime: 3 kg/steel ton.

New method proposal for sterile quantification in scrap deliveries.

- Increase productivity: 27,000 ton/year.
- Higher steel quality, lower presence of Cu, Ni, Zn, etc.
- Do not pay for non-ferrous or get value from them.
- Reduce the slag amount.
- Minimize dust emissions and filter replacement.
- Increase the life of your EAF refractory lining.

Besides the scrap quality enhance after cleaning operation, these cleaning facilities can be used for checking, at reception in scrap yards, the quality compliance of each scrap deliver. In this sense, the benchmark situation for those installations could be the use of the information provided by the scrap cleaning machine to measure the amount of non-ferrous material mixed with the scrap and apply direct quality penalties to the scrap suppliers truck by truck. The aforementioned practice can be described as follow:

1. Every scrap truck is registered at the factory arrival (plate number and weight).
2. Scrap is delivered at the scrap yard where is discharged in the material receiving hopper of the cleaning machine (each scrap truck is processed separately).

Fig. 9.3: Scrap discharge in the receiving hopper of the cleaning machine

3. The cleaning machine sorts no-ferrous materials from ferrous materials.

Fig. 9.4: Non-ferrous material pile

4. Non-ferrous material separated after the processing of each truck is collected with a backhoe provided with scale.

New method proposal for sterile quantification in scrap deliveries.

Fig. 9.5: Non-ferrous material weighting

5. The non-ferrous material is accumulated in a pile to be later on sold.
6. Every scrap truck is registered at the factory departure (plate number and weight).
7. A report is generated.

Despite the high potential of scrap cleaning machines, this equipment presents several drawbacks worth mentioning;

1. Installing a cleaning machine requires high CAPEX (around 0.5 M€)
2. Only allow to clean certain scrap grades (E1, E5, E40) depending on the initial design. The machine design is done for a very particular scrap specification, and once defined it is only valid for processing scrap material with the initially selected specification
3. The processing capacity of these machines is less than the scrap delivery rate to the scrap yard, so they cannot be used for the sterile amount assessment truck by truck. Also, high maintenance resources must be allocated to ensure high productivity of the cleaning facility.

These disadvantages make the visual examination done by the scrap classificator and the estimation of the sterile content based on subjective criteria to continue being the most widespread methods in the steelworks during the scrap reception process.

The reflexion done at this point is that, if an experienced person is able to estimate the sterile content present in every scrap truck by visual analysis during the discharge operation, there must be sufficient visual information in the scene to obtain objective data on the scrap quality when the proper machine vision techniques are applied for information extraction. The innovative activity presented in this section aims to:

- Explore the possibility of combining machine vision techniques with Hyperspectral imaging as a new method for extracting quantitative information of the sterile present in Ferrous scrap under laboratory conditions. This first phase allows, not only to evaluate the potential of the proposed system, but also to build the basic architecture and to do the network parameters tuning to extrapolate meaningful information from one scrap grade for others.
- Demonstrate the technical feasibility of the proposed solution in industrial conditions. To do so, the new system is installed in a real scrap cleaning machine for evaluating the output of the system against real process data.

9.2 State of the art on Machine Learning

9.2.1 Basic about machine learning

Machine Learning is one of the key elements of Artificial Intelligent which is nowadays a trendy subject in the research or industry fields. Companies and universities devote many resources to advance their knowledge in this field. Recent advances offer very solid results for different tasks, comparable to human performance.

To understand the evolution of machine learning techniques till today, we must go back to 1642, when one of the first mechanical adding machines was designed by Blaise Pascal. It used a system of gears and wheels similar to those found in odometers and other counting devises. Pascal's adder, known as the Pascaline, could both add and subtract and was invented to calculate taxes

In 1694, Gottfried Wilhelm Von Leibniz produced a similar machine to the Pascaline, that was more accurate and could perform all four basic arithmetic operations (addition, subtraction, multiplication and division). Leibniz also created the binary number system used by all modern computers.

Storing data was the next challenge to be met. In 1801, the first use of storing data was in a weaving loom invented by Joseph Marie Jacquard that used metal cards punched with holes to position threads. A collection of these cards coded a program that directed to loom. This allowed for a process to be repeated with a consistent result every time.

Logic is a method of creating arguments or reasoning with true or false conclusions. George Boole created in 1847 a way of representing this using Boolean operator (AND, OR, NOR) and having responses represented by true or false, yes or not, and represented in binary as 1 or 0. Web searches still use these operators today.

Later on, in 1890, Herman Hollerith created the first combined system of mechanical calculation and punch cards to rapidly calculate statistics gathered from millions of people.

An important milestone took place in 1945 with the development of The Mark I. This was built at IBM and designed by Howard Aiken and it was the first combined electric and mechanical computer. The Mark I could store 72 numbers and it could perform complex multiplications in 6 seconds and divisions in 16. While Mark I is far from current computer, this is still faster than most humans.

One year later, the first fully electronic computer was built by John Mauchly and John Eckert and named ENIAC (Electronic Numerical integrator and Computer). ENIAC was a thousand times faster than the Mark I. This computer weighed about 30,000 kilograms and fit on wall 3 meters high and 24 meters across.

Arthur Samuel was an IBM scientist who used the game of checkers to create the first learning program in 1952. His program became a better player after many games against itself and a

New method proposal for sterile quantification in scrap deliveries.

variety of human players in a “supervised learning mode”. The program observed which moves were winning strategies and adapted its programming to incorporate those strategies.

In 1957, Frank Rosenblatt designed the perceptron which is a type of neuronal network. A neuronal network acts like a brain. The perceptron connects a web of points where simple decisions are made that come together in larger program to solve more complex problems.

The first programs able to recognize patterns began to be developed in 1967. These programs were designed based on a type of algorithm called the nearest neighbour. When the program is given a new object, it compares this with data from the training set and classifies the object to the nearest neighbour, or most similar object in memory.

Gerald Dejong introduced Explanation Based Learning (EBL) in a journal article published in 1981. In EBL, prior knowledge of the world is provided by training examples which make this a type of supervised learning. The program analyses the training data and discards irrelevant information to form a general rule to follow.

In the 1990’s we began to apply machine learning in data mining, adaptive software and web applications, text learning and supervised and unsupervised learning. As well, reinforcement learning algorithms were developed.

The new millennium brought an explosion of adaptive programming. Anywhere adaptive programs are needed, machine learning is there. These programs are capable of recognizing patterns, learning from experience, abstracting new information from data, and optimizing the efficiency and accuracy of its processing and output.

In terms of machine learning techniques development evolution, Fig. 9.6 offers a good picture of the relationship between the moment when each one of the main techniques used arises and its evolution in popularity of use

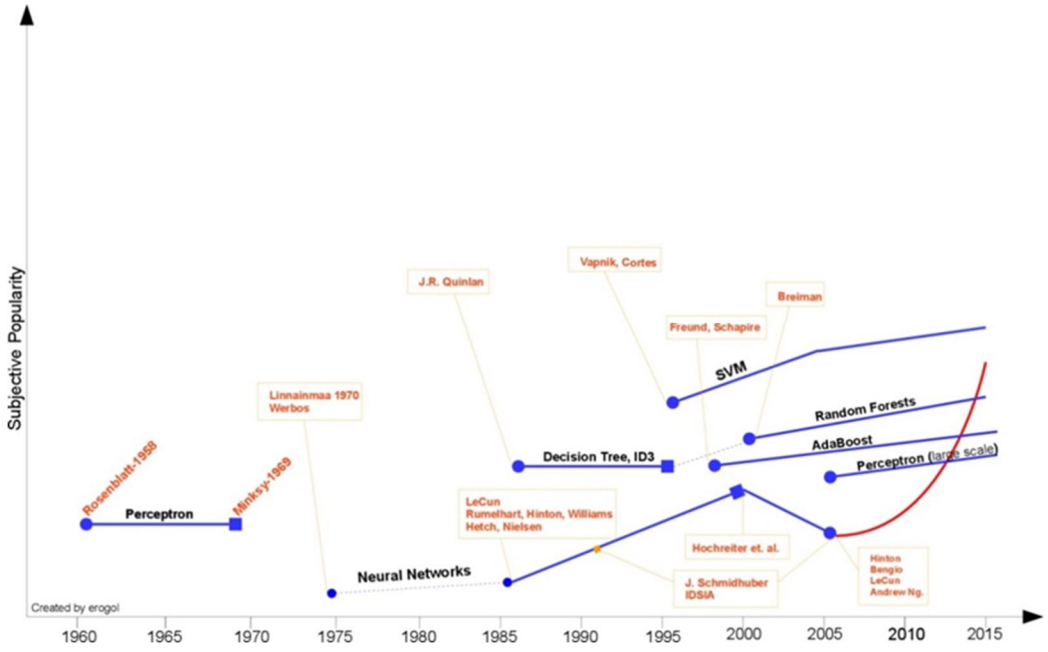

Fig. 9.6: Machine learning development timeline (188)

New method proposal for sterile quantification in scrap deliveries.

9.2.2 Machine learning as general Artificial intelligent approach

Machine learning is an artificial intelligence (AI) discipline geared toward the technological development of human knowledge. Machine learning allows computers to handle new situations via analysis, self-training, observation and experience. So basically, it studies computer algorithms for learning to do particular things.

Doing a basic comparison between conventional programming methods and new machine learning techniques, it can be said that:

- Traditional Programming: Data and program are run on the computer to produce the output.
- Machine Learning: Data and output are run on the computer to create a program. This program can be used in traditional programming.

The learning process is always based on observations or data, such as examples, direct experience, or instruction. So, and according previous classification, machine learning is about learning to do better in the future based on what was experienced in the past.

Machine learning tasks are typically classified into three broad categories, depending on the nature of the learning "signal" or "feedback" available to a learning system. These are (189) :

- Supervised learning: The computer is presented with example inputs and their desired outputs, given by a "teacher", and the goal is to learn a general rule that maps inputs to outputs. Example problems are classification and regression.
- Unsupervised learning: No labels are given to the learning algorithm, leaving it on its own to find structure in its input. Unsupervised learning can be a goal in itself (discovering hidden patterns in data) or a means towards an end (feature learning). Example problems are clustering, dimensionality reduction and association rule learning.
- Reinforcement learning: A computer program interacts with a dynamic environment in which it must perform a certain goal. The program is provided feedback in terms of rewards and punishments as it navigates its problem space. Example problems are classification and regression

In Machine Learning there are many algorithms which help discover the underlying physical process under the available data. The choice of an algorithm depends on the characteristics of the data. Perhaps the most useful way to group algorithms is based on its similarity in terms of their function (how they work).

- In classification, inputs are divided into two or more classes, and the learner must produce a model that assigns unseen inputs to one or more (multi-label classification) of these classes. This is typically tackled in a supervised way. Spam filtering is an example of classification, where the inputs are email (or other) messages and the classes are "spam" and "not spam".

New method proposal for sterile quantification in scrap deliveries.

- In regression, also a supervised problem, the outputs are continuous rather than discrete.
- In clustering, a set of inputs is to be divided into groups. Unlike in classification, the groups are not known beforehand, making this typically an unsupervised task.
- Density estimation finds the distribution of inputs in some space.
- Dimensionality reduction simplifies inputs by mapping them into a lower-dimensional space. Topic modelling is a related problem, where a program is given a list of human language documents and is tasked to find out which documents cover similar topics.

According previous classification, Fig. 9.7 shows the Machine Learning Algorithms Mind map.

Fig. 9.7: Machine Learning Algorithms Mindmap (190)

New method proposal for sterile quantification in scrap deliveries.

9.2.3 Deep Learning approach

Deep learning is an automatic learning technique that teaches computers to do what people does naturally (learn by experience). With deep learning, a computer model learns to perform classification tasks directly from images, text or sound. Classification models based on these technologies can achieve cutting-edge precision that sometimes exceeds human performance. The models are trained using a huge number of tagged data and neural network architectures that contain many layers.

Although the first theories about deep learning were developed in the eighties, there are two main reasons why it has only recently become useful:

- Deep learning requires large amounts of tagged data.
- Deep learning requires significant computing power. High-performance GPUs with parallel architecture, in combination with clusters or with cloud computing, allow reducing the time needed to train a deep learning network from weeks to hours or even less.

The latest advances in this field, together with higher computational capabilities, have led the state of the art to a point at which could exceed human's performance in some classification tasks; for example, in the classification of objects contained in images.

Fig. 9.8 shows the best yearly performance on image classification (ILSVRC challenge) (191). According to ILSVRC, since 2014 classificator based on neuronal networks architectures overcome human performance on image classification tasks

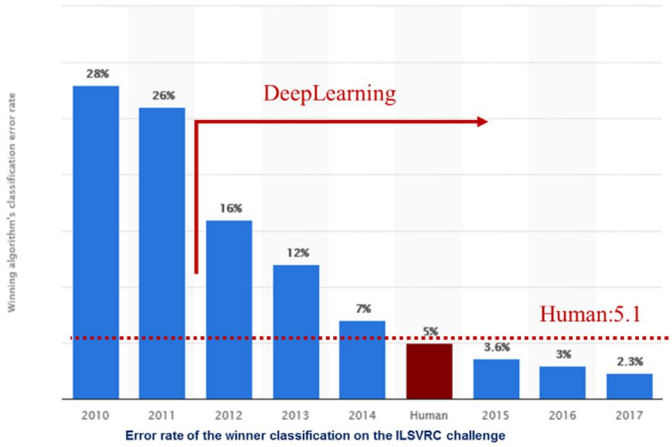

Fig. 9.8: Error rate of the winner classification on the ILSVRC challenge

There are several industrial sectors where Deep learning applications are being used more and more.

- Autonomous driving: Researchers in the automotive field use deep learning to automatically detect objects such as stop signs and traffic lights. In addition, deep learning is used to detect pedestrians, which helps to reduce accidents (192) (193).

New method proposal for sterile quantification in scrap deliveries.

- Aerospace and defence sector: Deep learning is used to identify objects from satellites that locate areas of interest (194) and identify safe or unsafe areas for troops deployment (195).
- Medical research: Cancer researchers use deep learning to detect cancer cells automatically (196) (197). Some UCLA teams have built an advanced microscope that produces a multi-dimensional data set used to train a deep learning application to accurately identify cancer cells (198).
- Industrial automation: Deep learning is helping to improve the safety of workers in environments with heavy machinery, thanks to the automatic detection of people or objects when they are at an unsafe distance from the machines (199) (200) (201).
- Electronics: Electronic learning is used in automated listening (202) and speech translation (203). For example, home help devices that respond to the voice and know their preferences are based on deep learning applications.

However, and despite the great potential demonstrated, these technologies are not being exploited yet in raw material classification activities in steelmaking industry.

9.2.3.1 Most advanced Deep Learning architectures

As it was mentioned before, in recent years, the structure and topology of deep neural networks have attracted significant research interests, since them have achieved huge success in a wide range of tasks of computer vision.

Although they were originally introduced over 20 years ago, improvements in computer hardware and network structure have enabled the training of truly deep CNNs only recently. Moving from traditional computer vision techniques to CCN architectures.

This section aims to give a snapshot of the main Computer Vision architectures evolution over the last few years:

In the 90s the first successful applications of Convolutional Networks were developed to recognise hand written digits. The best known was LeNet (204) which contained 5 layers in its more advanced form.

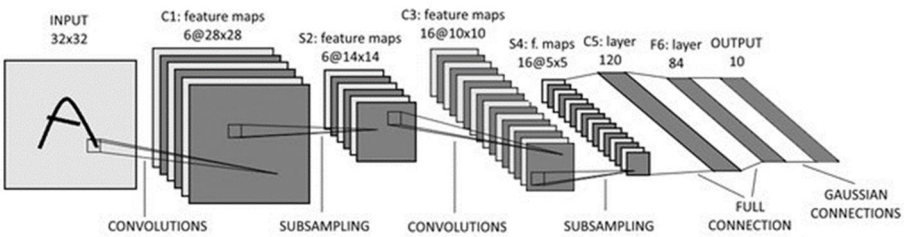

Fig. 9.9: Detail on LeNet5 architecture (204)

New method proposal for sterile quantification in scrap deliveries.

To find the next relevant milestone in the development of neural networks it is necessary to move forward in time. In 2012 AlexNet (205) CCN architecture was submitted to the ImageNet ILSVRC Challenge. This network had a very similar architecture to LeNet, but was deeper, bigger, and features convolutional stacked on top of each other. AlexNet contains 5 convolutional and three fully-connected layers, and it introduced ReLU non-saturating nonlinearity f(x) = max(0, x) which later on became gold standard choice for activation functions.

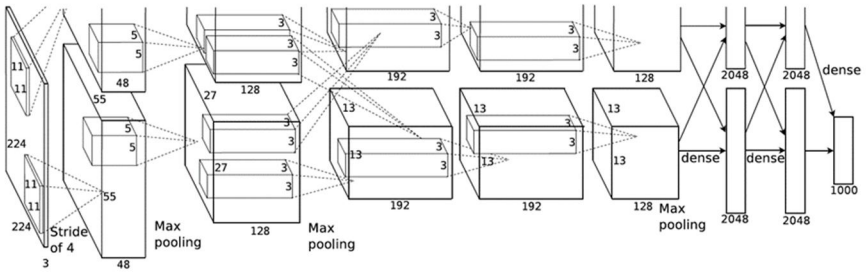

Fig. 9.10: Detail on LeNet5 architecture (205)

In 2103, an improvement of AlexNet called ZFNet (206) appeared. This new convolutional Network expanded the size of the middle convolutional layer and made the stride and filter size on the first layer smaller.

Later on, in 2014 VGGNet (207) demonstrated that the depth of the network is a critical component for good performance. It contained 16 Convolutional / Fully connected layers and an extremely homogeneous architecture (3x3 convolutions and 2x2 pooling from the beginning to the end). The spatial resolution is preserved after convolution by padding the image. A stack of conv layers is followed by FClayers. All hidden layers are equipped with ReLU.

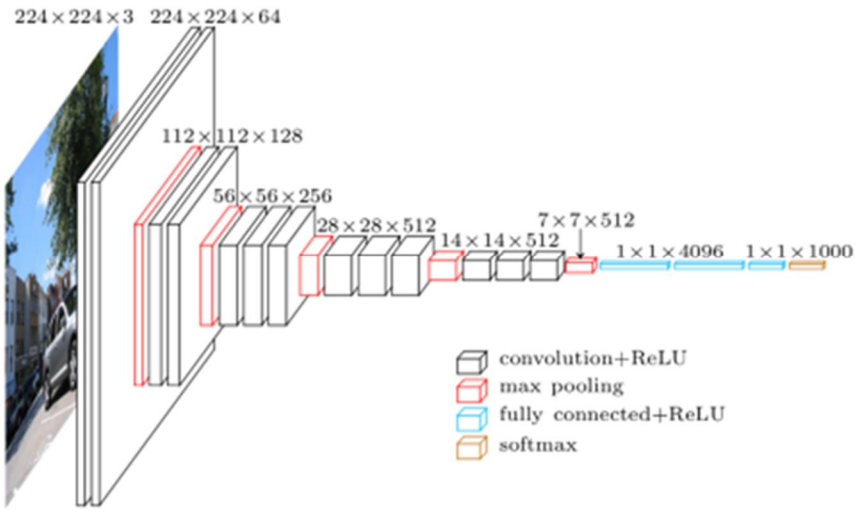

Fig. 9.11: Details on VGGNet architecture (207)

By this time, the general understanding was that having larger nets improved the performance of the models. It is possible to increase size; either by depth (Number of network levels) or width (number of units at each level). However, Network depth substantially increases the

number of parameters, and with limited training sets, this leads to over-fitting. The main contribution of GoogleLeNet (208) convolutional network was the dramatical reduction of the number of parameters (from 60M in AlexNet to 4M)

The most well-known architecture with this structure is ResNet (209) which won the ILSVRC-2015 classification.

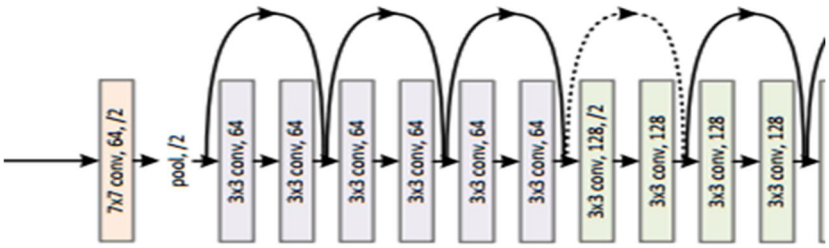

Fig. 9.12: Deatils on ResNet architecture (209)

The residual block structure in ResNet also inspires a series of ResNet variations, including ResNext, WRN and PolyNet.

ResNets like architectures bypass signal from one layer to the next via identity connections maintaining many short paths in the network. This randomly dropping layers during training allow better information and gradient flow. Although these different approaches vary in network topology and training procedure, they all share a key characteristic: they create short paths from early layers to later layers

However, all recent variations of ResNets showed that many layers contribute very little and can in fact be randomly dropped during training. This makes the state of ResNets similar to recurrent neural networks, but the number of parameters of ResNets is substantially larger because each layer has its own weights

DenseNet (210) was a newly proposed structure, where any layer in a block is the output of all preceding layers, and the input of all subsequent layers. This allows obtaining significant improvements over most of the previous presented architectures, whilst requiring less computation to achieve high performance.

Besides better parameter efficiency, one big advantage of DenseNets is their improved flow of information and gradients throughout the network, which makes them easy to train. Each layer has direct access to the gradients from the loss function and the original input signal, leading to an implicit deep supervision. This helps training of deeper network architectures.

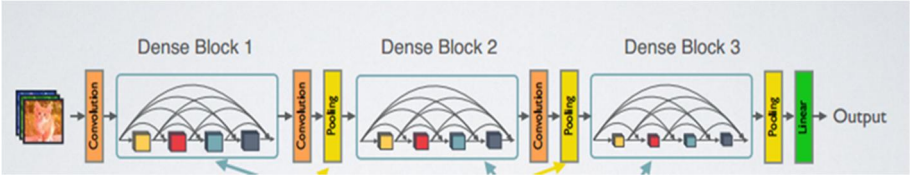

Fig. 9.13: Deatils on DenseNet architecture (210)

Several observations can be made from the DenseNet architecture described in Fig. 9.13:

1. All layers spread their weights over many inputs within the same block. This indicates that features extracted by very early layers are, indeed, directly used by deep layers throughout the same dense block.
2. The weights of the transition layers also spread their weight across all layers within the preceding dense block, indicating information flow from the first to the last layers of the DenseNet through few indirections.
3. The layers within the second and third dense block consistently assign the least weight to the outputs of the transition layer, indicating that the transition layer outputs many redundant features. This is in keeping with the strong results of DenseNet-BC where exactly these outputs are compressed.
4. Although the final classification layer, shown on the very right, also uses weights across the entire dense block, there seems to be a concentration towards final feature-maps, suggesting that there may be some more high-level features produced late in the network

In this way, the deep residual network is treated as a long sequence and hidden units are linked by skip connections. While this recurrent structure benefits feature re-usage and iterative learning, the residual information is restricted among neighbouring layers and cannot be considered across multiple layers, because the recurrence only happens once at each single layer.

9.3 General approach for sterile Estimation

The innovative activity shown in this chapter proposes the development of a new industrial tool able to do an online estimation of the quantity of sterile (low Scrap quality) present in the scrap deliveries to the scrap yards in steelshops. The main benefit provided by this new approach is the objectivity of the analysis that could substitute the subjective estimation of the scrap classification personnel.

For the complete development of the proposed tool, three phases of development should be carried out:

1. Laboratory analysis (work to be developed within the scope of this thesis): This task looks for understanding the capabilities of DeepLearning methodology for the selected application. Laboratory analysis will allow to well understand the real problem, define the most convenient network architecture and hyperparameters tune up. To this end, a laboratory testing station was built in which the conditions of the experiment are perfectly controlled (lighting, systems calibration, static scene and control over the weights and chemical compositions of analysed materials)
2. Semi-Industrial analysis under controlled conditions (To be proposed in this Thesis): Once the first DeepLearning network architecture is available, this second phase was carried out under well controlled industrial conditions. To do so, the prototype developed in the laboratory stage is adapted to semi-industrial conditions. For this purpose, a regular scrap cleaning machine for E1 scrap type processing will be used (E1 scrap may represent between 20-40% of the total ferrous scrap processed in a conventional steelshop scrap yard for structural long product manufacturing). This approach allows implementing an image features extraction methodology, which together with the hyperspectral images acquired, will allow to optimize the classifier developed in the previous phase.
3. Industrial development and proof of concept (posed as next step to the thesis): In this final phase, the DeepLearning architecture implemented in the previous phase is adapted to real industrial conditions. So that after a training period, the new system would be able to estimate the amount of sterile present in any scrap delivery, no matter the scrap quality

For reaching the final goals set in the aforementioned phases, it is needed to well define the following aspect of the proposed technology:

- Sensor
- Data processing algorithms

New method proposal for sterile quantification in scrap deliveries.

9.3.1 Hyperespectral sensors

Up to now, it is clear that the automated feature extraction made by the Convolutional Neuronal Networks makes deep learning models very accurate for machine vision tasks. Also, another important consideration to be done when building an image classificator is the vision sensor.

When the objective of the classificator is to perform the classification of certain classes likely present in the image data set, a conventional RGB camera could be enough. However, the challenge proposed in the present work tries to extract hidden information from enormous heterogeneous images in which the differentiation between scrap and sterile is not always clear.

Fig. 9.14: Examples of Scrap types: Up left) Old Light scrap, Up right) Old heavy scrap, Down left) Old fragmentized scrap, Down right) New production thin scrap

In order to dispose as much information as possible, the hyperspectral approach is sensed to be most suitable. So that, the first thing to do is the selection of the most convenient hyperspectral sensor for covering Visual, Near Infrared and Short-wave infrared spectral ranges.

9.3.1.1 Analysis on the available Commercial sensor

The objective of this section, in addition to exploring the different options in terms of spectral range available in the market for the vision equipment, is to analyse the commercial options between linear and matricial sensors in order to select the most convenient one for each of the three phases defined in the previous section.

New method proposal for sterile quantification in scrap deliveries.

Linear sensors:

The first phase of the proposed solution consisted on the development of laboratory experiments that will allow to, firstly demonstrating the applicability of the joint approach of hyperspectral imaging and data classification through DeepLearning, and secondly, establishing the basic requirements of a system that must subsequently be functional in extreme industrial conditions.

For a laboratory set up, in which it is relatively easy to manipulate the scrap/sterile samples by push broom methods, it is clear that the linear sensors are the most convenient. These Hyperspectral cameras would provide huge amount of spectral information facilitating a better understanding of the scene.

In the case of linear sensors, considering the high price of this type of equipment in far infrared ranges on one side, and the good results already obtained in similar experiments (according suppliers' recommendations) on the other side, SisuCHEMA sensor by SPECIM and V10E by SPECIM were the selected sensors for this activity.

Below, the technical characteristics of the aforementioned equipment are presented:

- Linear hyperspectral optical sensor in the VNIR range (400 - 1000nm): The sensor is composed by a spectrometer (Specim V10_04204) combined with a scientific CMOS camera (JAI-TM-1327GE)

Optical Characteristics:	
Type:	Specim V10_04204
Range:	400-1000 nm
Spectral resolution:	3.0 nm (30 um slit)
Spectral smpling:	0.78-6.27 nm/pixel
Spatial resolution:	RMS spot size < 9 um
Electrical Characteristics:	
Detector:	CMOS
Spatial Pixels:	1312
Spectral Bands:	768
Pixel size:	8 x 8 um
Camera Control:	CameraLink

Fig. 9.15: VNIR Spectrometer technical characteristics

- Two-dimensional hyperspectral optical sensor in the SWIR range by sisuCHEMA (1000-2500nm)

New method proposal for sterile quantification in scrap deliveries.

Optical Characteristics:	
Type:	Specim sisuCHEMA
Range:	970-2500 nm
Spectral resolution:	10 nm
Spectral smpling:	6.3 nm/pixel
# Spatial pixel/line:	320
Other Characteristics:	
Illumination:	Diffused line
Data Format:	BIL file format, Evince end ENVI compatible
Calibration:	Internal standard reference target (auto)

Fig. 9.16: SWIR Spectrometer technical characteristics

Matricial sensors:

Based on the findings made in the laboratory phase, a semi-industrial set up is proposed to demonstrate the usefulness of the proposed solution.

However, contrary to what happened with the analytical methodology followed in the laboratory, in such an extremely aggressive environment as the scrap yard in a steelshop mill (outdoor systems, high machinery activity, dust, temperature variations, vibration…), a sensor based in linear technology is not applicable. The system proposed for the final industrial application must be based on a matricial sensor that captures the scene of the scrap unloading in a static way (since the PushBrom effect that was easily generated in laboratory conditions will not occur).

The main disadvantage of this proposal is that the spectral resolution of matricial sensor is much lower than the linear ones, and these cameras can be found in market covering a high variety of spectral range from one to others. And the selection of most convenient sensor turns to be one key thing to do. So that, the first research activity proposed at this point was the technical analysis of all available sensors for selecting the most suitable for the proposed approach.

The main commercial sensors that were studied, and their main technical features, are presented below:

- **Ximea** presents 2 different matricial models: MQ022HG-IM-SM4X4-VIS (16 HSI bands between 470-630 nm) and the MQ022HG-IM-SM5X5-NIR (25 HSI bands between 600-925 nm)
- **BaySpec** proposes 3 different maticial models: OCI-2000HH (20-25 HSI bands between 600-1000 nm), OCI-2000V (16 HSI bands between 470-620 nm) and OCI-D20000 (35-40 HSI bands between 470-875 nm)

New method proposal for sterile quantification in scrap deliveries.

- **SILIOS** Technologies offers 3 hyperspectral sensors: CMS-C1 (9 HSI bands between 400-700 nm), CMS-V1 (9 HSI bands between 550-800 nm) and CMS-S1 (9 HSI bands between 550-950 nm)

Table 9.1 allows doing a compative analysis among the different commercial sensors in order to facilitate the selection of the most convenient one for he proposed application.

Supplier	Sensor	Model	Type	Spectral range	# Bands	Spatial resolution	Communications	SDK	Price
Infaimon	Specim	sisuCHEMA	Linear	1000-2500	256	320x1	LVDS/Camera LINK	NI	Available
Infaimon	Specim	PFD-CL-65-V10E	Linear	400-1000	1040	1312x1	GigE	NI	Available
Infaimon	Specim	FX 10	Linear	400-1000	224	1024x1	Camera LINK	LUMO tool	13k€
Infaimon	Specim	FX 10e	Linear	400-1000	224	1024x1	GigE	LUMO tool	14.1k€
Infaimon	Specim	FX 17e	Linear	900-1700	224	640x1	GigE	LUMO tool	43.7k€
Infaimon	BaySPEC	BayOCI-D2000	Matricial	475-875	35	500x270	GigE / USB	Yes	59.2k€
Infaimon	BaySPEC	Bay OLI2000	Matricial	600-1000	25	400x200	GigE / USB	Yes	36.1k€
Ximea	XiSpec	MQ022HG-IM-SM4X4-VIS	Matricial	470-630	16	512x272	USBVision/GernICam	Yes	14.8k€
Ximea	XiSpec	MQ022HG-IM-SM5X5-NIR	Matricial	600-975	25	409x217	USBVision/GernICam	Yes	15.5 k€
Ximea	XiSpec	MQ022HG-IM-LS100-NIR	Linear	600-975	100	2048x1	USBVision/GernICam	Yes	Available
Ximea	XiSpec	MQ022HG-IM-LS150-VISNIR	Linear	470-900	150	2048x1	USBVision/GernICam	Yes	Available
SILIOSTech	CMS	CSM-C	Matricial	400-700	9	1280x1024	GigE / USB	Yes	7.5k€
SILIOSTech	CMS	CSM-V	Matricial	550-800	9	1280x1024	GigE / USB	Yes	8.3k€
SILIOSTech	CMS	CSM-S	Matricial	550-950	9	1280x1024	GigE / USB	Yes	8.5k€

Table 9.1: Comparative analysis among commercial sensors

9.3.1.2 Technical analysis of the sensors

The simplest comparative analysis that can be done as a first step for the sensor technology selection is the analysis of the pros and cons between linear and matricial sensors. In this regard, the following should be highlighted:

- Linear sensor: The main advantage of this technology is a high spectral resolution which allows to have an enormous amount of information of the captured image. On the other hand, Linear sensors present as main disadvantage the necessity of moving the scene in front of the camera to reconstruct a 2D image.

  These features make linear sensors the most convenient solution for laboratory tests, in which it is easy to build a laboratory set-up for sample displacements in front of the camera allowing understanding the capabilities of the technology due to the high amount of spectral data.

New method proposal for sterile quantification in scrap deliveries.

- Matricial sensor: This technology offers the possibility of generating quick snapshots of the region of interest but, its main drawbacks are the low number of spectral channels available and the higher cost.

  Another advantage is that, by having a lower spectral resolution, the system generates smaller files which facilitates information processing (disk space, memory required, processing times and analysis).

  Considering that in the industrial application of the proposed system we will probably have static scenes, matricial sensors would be the only possible solution for scrap deliveries analysis in site.

The main question to be resolved at this point is whether the spectral resolution is critical or not for the application to be developed. This question arises due to the fact that there may be similarity to what happens with a natural image in which with 16 visible bands 99% of the information is obtained.

Thus, in order to select not only the sensor technology, but also the most appropriate camera option, a preliminary analysis of scrap characterization was carried out with a small group of images. The objective of this initial analysis was to determine if there is any spectral range within the available commercial equipment in the market in which the main features of the ferrous scrap and sterile parts are shown.

To carry out the preliminary analysis, the steps followed are listed below:

1. A dataset of images composed by artificial prepared mixtures of scrap and sterile were captured by the two available hyperspectral linear cameras (JAI from 400 to 1000 and NIR from 970 to 2500). Since the presence of scrap (identified as C) and sterile (identified as A) is exactly known pixel by pixel, a bounding box was created manually labelling each pixel of the image C and A. For doing the Bounding box annotation in images a free python tool utility called Sloth (211) was used.

Fig. 9.17: Examples of artificial prepared mixtures of scrap and sterile

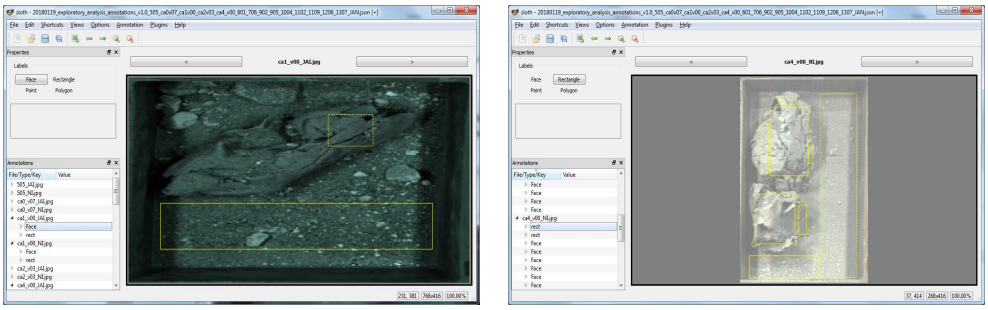

Fig. 9.18: Hyperspectral image acquired with the bounding box for JAI (left) and NI (right) cameras

2. Additionally, prior to each capture, the "dark current" and "reference white" signals are acquired for each of the image:

    a. In the "dark current" signal case, an acquisition is done with the sensor objective blocked. Once dark signal file is generated, 1000 points are randomly selected in the space and the average is calculated and used as Dark for captures calibration for the 1040 (JAI) or 256 (NI) wavelengths.

    b. In the case of "white reference", the Spectralon patterns were captured and the area in with the whitest pixels are detected is recorded as reference for calibration.

3. Once the images are acquired, a data matrix (DataFrame) containing the wavelengths (X axis) and the classification of the pixels at A and C and sensor type (Y axis) is available.

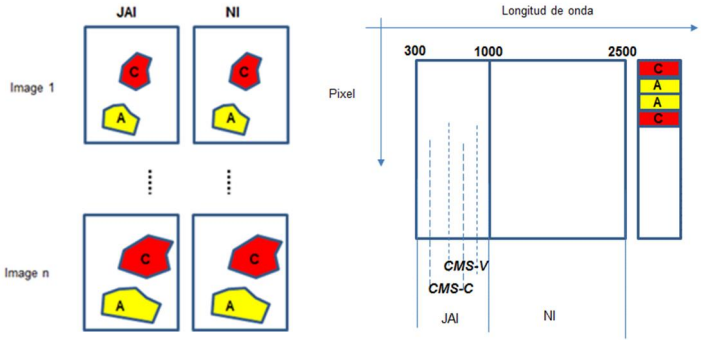

Fig. 9.19: Data set available in sensor selection analysis

4. The spectra corresponding to each of the classes (scrap as C and sterile as A) are drawn in different colours to analyse if differences are observed between the two cameras (Vis + IR and SWIR).

    In Fig. 9.20:, samples that have been processed are displayed for the entire spectral range (400nm – 2500 nm):

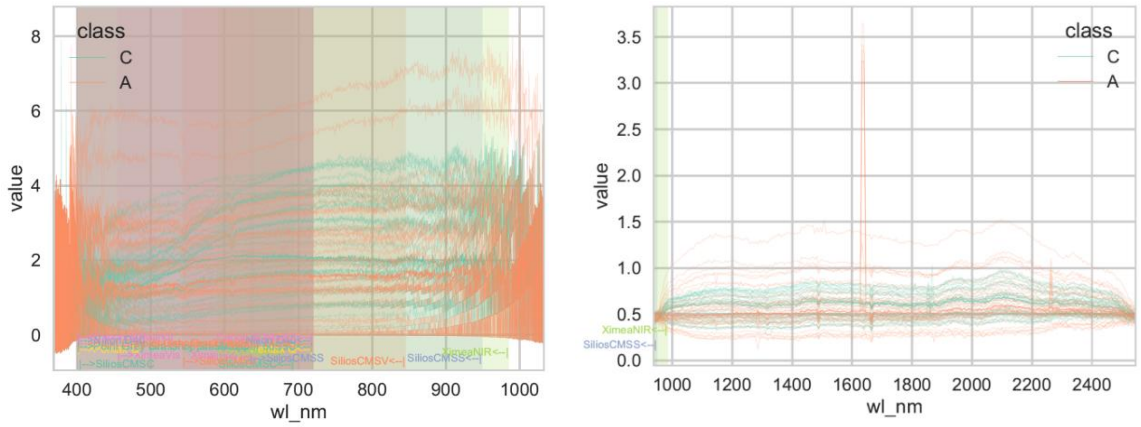

Fig. 9.20: Raw spectral data acquired with JAI (left) and NI (right) sensors

The following graph shows the median of the values and the standard deviation:

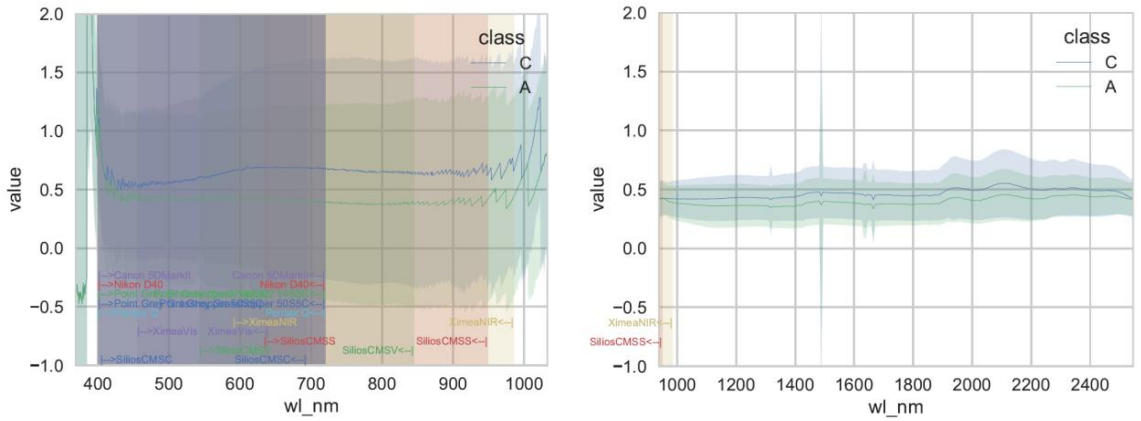

Fig. 9.21: Median of spectral data acquired with JAI (left) and NI (right) sensors

Finally, to simplify the analysis of the acquired information, Fig. 9.22: and Fig. 9.23: represent the pixels values as a median of the raw values captured. In the X axis the wavelength corresponding to different cameras ranges analysed in the previous section according to their specifications have been drawn in different colours.

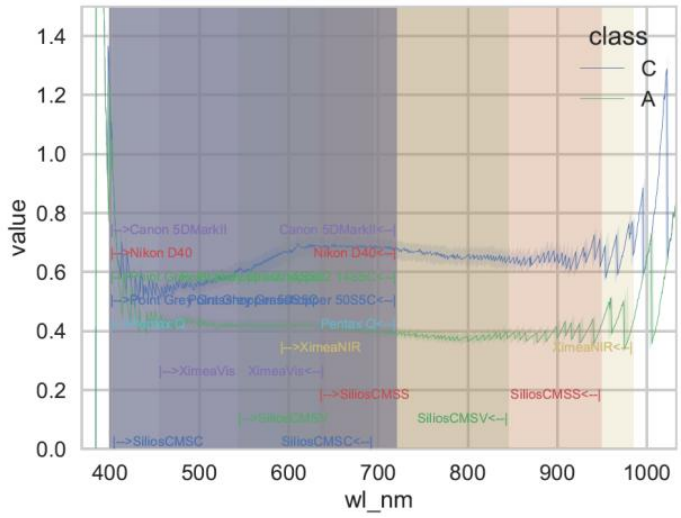

Fig. 9.22: Normalized (white_ref) of spectral data acquired with JAI sensors

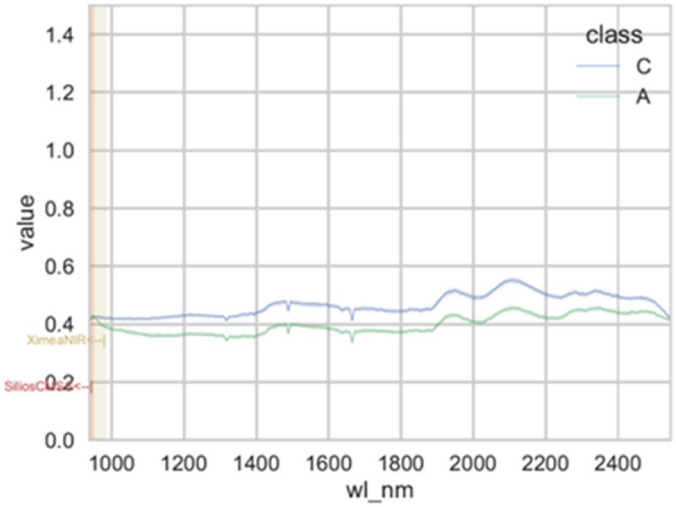

Fig. 9.23: Normalized (white_ref) of spectral data acquired with NI sensors

5. Once the spectral data obtained in the visible spectrum with the linear sensors are available (the cost of the matricial sensors in the IR range is so high that it is not even considered in the present project), the behaviour of the different commercial matricial sensors are simulated and presented in Fig. 9.26. To do this, the spectral responses shown in in Fig. 9.24 (wavelengths to which they are sensitive), the FWHM (Full Width at Half Maximum) and the standard deviation of each FWHM for each sensor was used.

   For the low resolution hyperspectral cameras, to obtain the spectral response o sensibility curves, each band is modelled with the central frequency of the band given by the suppliers' technical specification (wl_nm) and their bandwidths in nanometers (bw_nm) given. i.e. for XimeaVIS sensor, these values are:

```
wl_nm = [465, 474, 485, 496, 510, 522, 534, 546, 548,
562, 578, 586, 600, 608, 624, 630]
bw_nm = [20]*16
```

   JAI camera output signal (Fig. 9.25) is transformed by these values, generating a representation of what each specific camera would see. To do so, the JAI signal (read from a series of samples) is multiplied by the graphs generated above

   In the case of hyperspectral cameras that information is obtained from the technical specifications offered by the manufacturer, and in the case of the visible cameras, the file "camspec_database.txt" (212) has been used. This file specifies the response to RGB at wavelengths between 400 and 720 every 10 nm for several colour cameras.

New method proposal for sterile quantification in scrap deliveries.

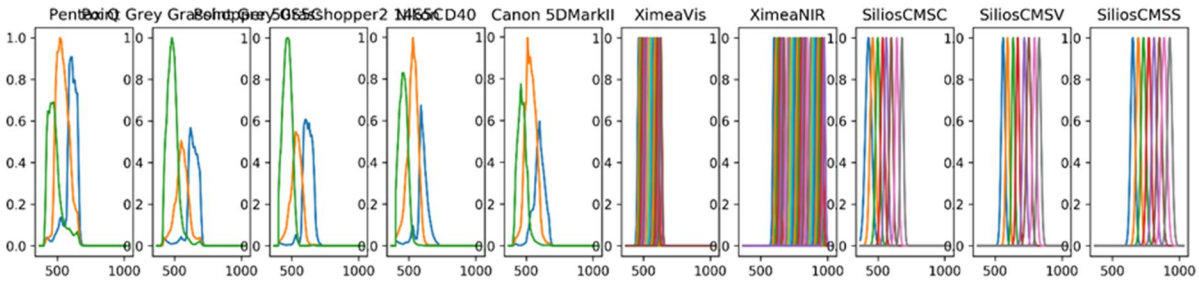

Fig. 9.24: Spectral sensitivity of simulated cameras

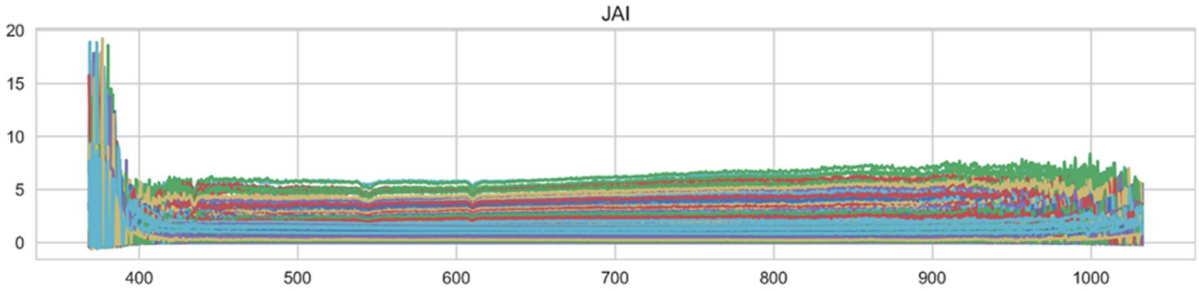

Fig. 9.25: JAI camera output signal

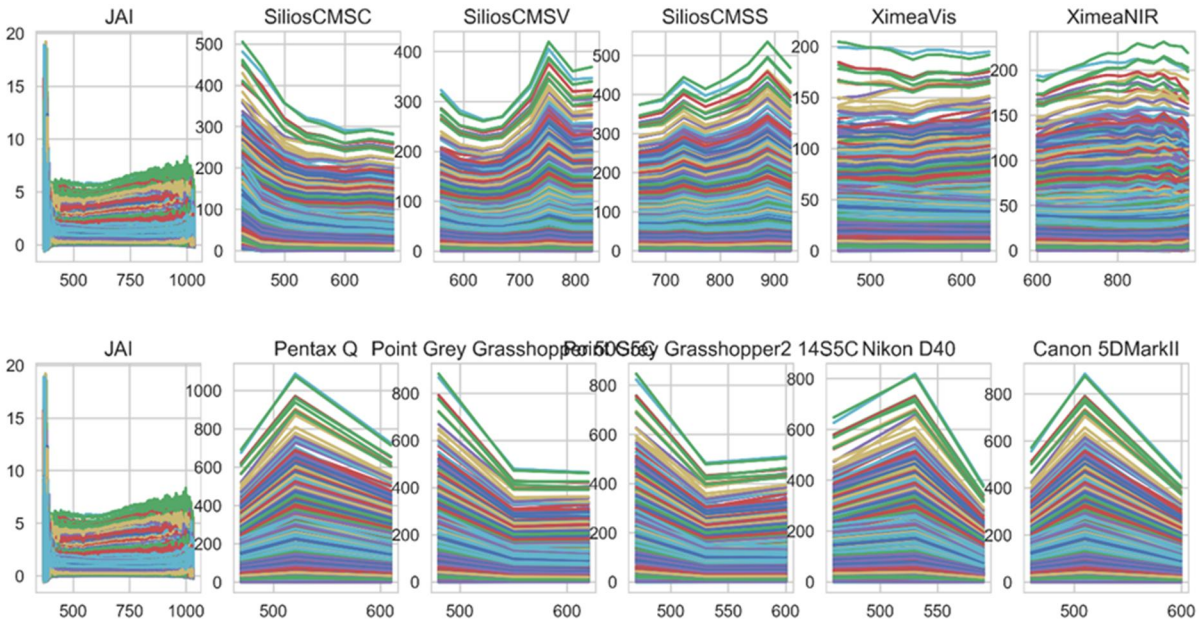

Fig. 9.26: Signal reconstruction for simulated cameras

For each multispectral matricial camera (which present a low spectral resolution), The sensitivities of each band are modelled using the centre frequency of the band provided by the technical specifications of the sensor and a bandwidth in manometers (bw_nm) given or estimated, then the JAI signal, which has a very high spectral resolution, is filtered by each of these filters to obtain the corresponding response.

The obtained information shown the theoretical response that each matricial camera (X values) would have for each of the different samples acquired with JAI camera after applying the analytical methodology proposed.

6. Then, for camera convenience evaluation purpose, the samples were divided into two groups, 50% the samples were used for training and the rest were used for testing, and the following classifiers were applied:
    a. XGBOOST Clasiffier (eXtreme Gradient Boosting package): This is an ensemble method (It supports various objective functions, including regression, classification and ranking) that seeks to create a strong classifier (model) based on “weak” classifiers. By adding models on top of each other iteratively, the errors of the previous model are corrected by the next predictor, until the training data is accurately predicted or reproduced by the model
    b. RANDOM FOREST Classifier: This is a popular ensemble method that can be used to build predictive models for both classification and regression problems. Random Forest algorithm creates an entire forest of random uncorrelated decision trees to arrive at the best possible answer.
    c. SVM Classifier (Support Vector Machines): This is a supervised machine learning algorithm which can be used for both classification or regression challenges. The algorithm plots each data item as a point in n-dimensional space (where n is number of features you have) with the value of each feature being the value of a particular coordinate. Then, the classifier performs classification by finding the hyper-plane that differentiate the two classes very well.
7. Subsequently, and using the same classifiers, a Cross Validation was carried out for each model (5 K-folds) and the average score was calculated.
8. A PCA (Principal Component Analysis) for dimensional reduction is performed for the data generated by each of the cameras twice; Reducing to 8 component and 3 components (instead of the 1040 channels provided by the JAI camera)
9. Finally, a t-SNE (t-distributed Stochastic Neighbour Embedding) is used for results visualization: This tool allows to reduce data dimensionality and visualize high dimensionality data based on the probability distribution of the neighbours (manifold) (213). This algorithm uses the "perplexity" parameter to adjust the number of neighbours used in the reduction. The results of t-SNE analysis is depicted in Fig. 9.27:

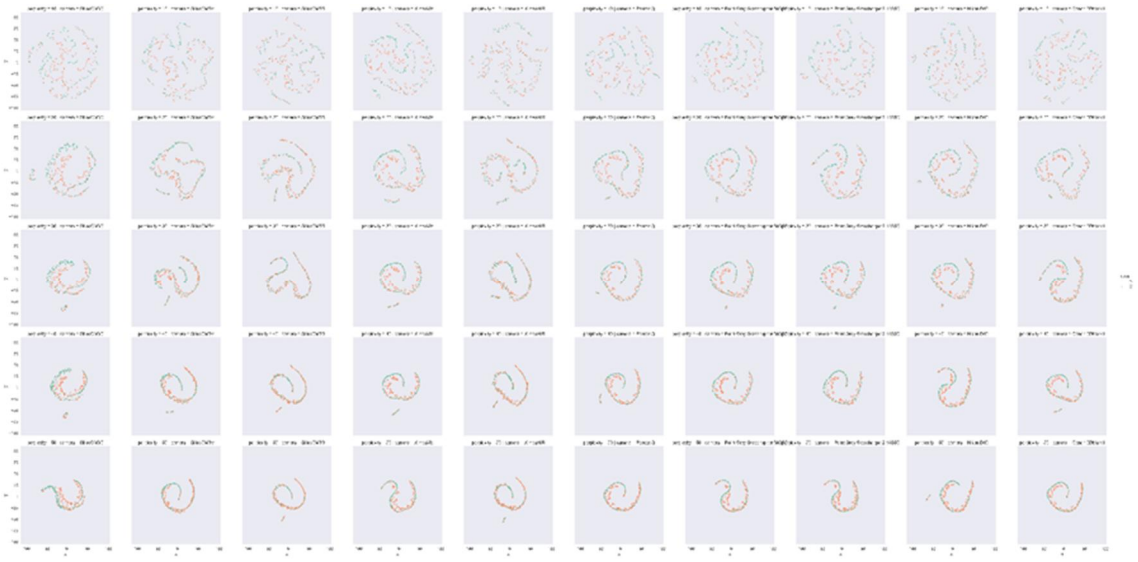

Fig. 9.27: tsne analysis on 10_samples using Ximea sensor data (2 upper lines) and Silos sensor data (3 lower lines).

Since t-SNE models each high-dimensional object by a two-dimensional point, in such a way that similar data are modelled by nearby points, and dissimilar objects are modelled by distant points with high probability, it is a good technique for creating a single map comparing estimation between sterile and scrap data in the images. As it is observed in Fig. 9.27, the points that represent data of sterile and scrap are more separated in the case of the Ximea VIS and CMS-C, which shows that these sensors are the most likely to succeed if they are used for the development of a classification application between both.

The following table shows the results generated by the different classifiers. To do so, the average output value of each of the three tested classifiers were calculated and a color-coded matrix has been applied according to the highest and lowest value.

	rf	svm	xgboost	Mean	PCA dims
Canon 5DMarkII	0,7330	0,7375	0,6907	0,7204	0
Nikon D40	0,7323	0,7316	0,6937	0,7192	0
Pentax Q	0,7328	0,7316	0,6940	0,7195	0
Point Grey Grasshopper 50S5C	0,7500	0,7444	0,7067	0,7337	0
Point Grey Grasshopper2 14S5C	0,7404	0,7335	0,7033	0,7257	0
SiliosCMSC	0,7412	0,7102	0,6833	0,7116	0
SiliosCMSS	0,6779	0,6960	0,6293	0,6677	0
SiliosCMSV	0,7016	0,7212	0,6870	0,7033	0
XimeaNIR	0,6758	0,7007	0,6339	0,6701	0
XimeaVis	0,7925	0,7825	0,7189	0,7646	0
Canon 5DMarkII	0,7482	0,7375	0,7223	0,7360	3
Nikon D40	0,7400	0,7316	0,7156	0,7291	3
Pentax Q	0,7482	0,7316	0,7298	0,7365	3
Point Grey Grasshopper 50S5C	0,7700	0,7444	0,7647	0,7597	3
Point Grey Grasshopper2 14S5C	0,7395	0,7335	0,7244	0,7325	3

SiliosCMSC	0,6942	0,6989	0,6974	0,6968	3
SiliosCMSS	0,7079	0,6932	0,6782	0,6931	3
SiliosCMSV	0,7567	0,7200	0,7530	0,7432	3
XimeaNIR	0,6674	0,6812	0,6511	0,6665	3
XimeaVis	0,7968	0,7593	0,7900	0,7820	3
SiliosCMSC	0,7912	0,7102	0,8096	0,7704	8
SiliosCMSS	0,7326	0,6960	0,7128	0,7138	8
SiliosCMSV	0,8004	0,7212	0,8168	0,7795	8
XimeaNIR	0,7070	0,7137	0,7067	0,7091	8
XimeaVis	0,8484	0,7791	0,8681	0,8319	8

Table 9.2: Matricial hyperspectral sensors analysis

On the other hand, if we analyse the spectral behaviour of the acquired data throughout the analysed spectral range, it was noticed that between 450 and 650 nm, the spectral signature corresponding to sterile shows a horizontal trend and the spectral signature corresponding to scrap shows some ascending slope.

Given that the final objective of the presented development is the discrimination by means of image classification of the two components, this observed difference can be very useful.

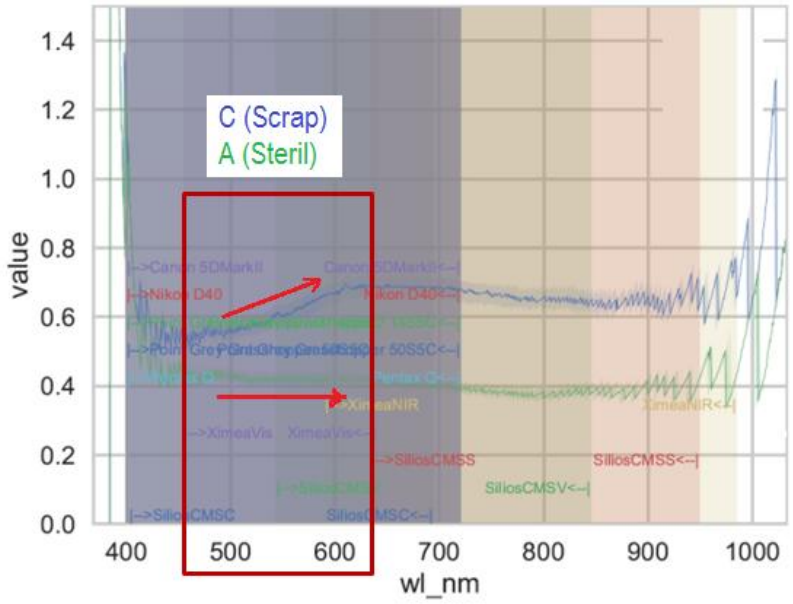

Fig. 9.28: Analysis of the spectral range of interest

According these results, the most convenient camera for the proposed application seems to be the sensor provided by **Ximea in the visible range**

New method proposal for sterile quantification in scrap deliveries.

9.3.2 Data processing algorithms

The data processing procedure proposed in this work can be summarized as follow:

- To define the problem as a scalar regression in which the amount of sterile, scrap and their relationship are predicted starting with Hyperspectral image (HIS) information as input data. It is based on the hypothesis that the outputs can be predicted from the inputs and that there are enough samples to learn the relationship between inputs and outputs. An analysis of the captured samples and the ground truth will be carried out
- To define a general protocol to determine which part of the samples will be used for the training and which ones for the validation of the results.
- Definition of the metrics to determine how good the prediction is.
- To identify a base model that will serve as a reference for predicted results comparison (Baseline).
- Development of new regression models able to improve the predictions of the previously defined base model. For this case, the convolutional neural networks (CNN) offer the most appropriate framework for merging spatial and spectral information features.

Table 9.3 shows a list of the mathematical processing solutions proposed for the project's objectives, together with the type of computer vision task that must be solved for its implementation.

Computer vision task	Input	Output	Description
Regression (Real value estimation)	HyperSpectral Imaging (HSI)	Percentage $p_k \in \mathbb{R}^1$ of estimated weight for each component $k = \{A, C\}$ in the global image.	By regression (full image mapping to a value of p_A and p_C) via Deep learning, learning spectrum-spatial representations, starting from the HSI as input. The convolutional neural networks (CNN) offer the most appropriate framework for the joint analysis of spatial and spectral information. Architectures for encoder type classification (e.g. [28], [29]) will be tested, adapting their last layers to the regression problem. The training can be done: • From scratch (i.e. with the network weights initialized in a pseudo-random way). It requires many input images. • Using fine-tuning or transfer learning techniques (i.e. starting from pre-trained weights for a different database [30] and training only part of the network). In this case it is a complex process, since the network is preloaded on RGB images and the weights must be transferred to HSI type data.
Regression (Real value estimation)	HyperSpectral Imaging (HSI)	Percentage $p_k \in \mathbb{R}^1$ of estimated weight for each component $k = \{A, C\}$ in the global image.	Similar approach as in the previous case but with the RGB type entry. This makes the fine-tuning option simpler, since the input data is RGB-type in both tasks (training and validation).

New method proposal for sterile quantification in scrap deliveries.

Regression (Real value estimation)	HyperSpectral Imaging (HSI)	Percentage $p_k \in \mathbb{R}^1$ of estimated weight for each component $k = \{A, C\}$ in the global image.	Similar approach as in previous cases, but with a gray scale entry. In this case it would be dismissed the spectral information, and only the spatial features are exploited. Both training from scratch and fine tuning training can be carried out, although in the latter case the luminance channel must be replicated three times in order to apply the trained weights on RGB images.
Regression (Real value estimation)	HyperSpectral Imaging (HSI)	Percentage $p_k \in \mathbb{R}^1$ of estimated weight for each component $k = \{A, C\}$ in the global image.	Multitasking Neuronal Convolutional Network (CNN) for joint estimation (Scrap and sterile) on HSI image of the previous outputs

Table 9.3: Analytical mathematical approaches to be tested

- As shown in the table above, one of the key pre-processing tasks of the acquired information prior to the proposed analysis is, in most of the cases, obtaining an image in RGB space from a spectral image. For this processing methodology Color Matching Functions (CMF) are used (214).
- Modification, regularization and adjustment of the hyperparameters of the previously developed models until a satisfactory model is achieved.

Since the objective of this work is the estimation of a series of real values extracted from an input image (weight as absolute data and weight ratios as relative data), the problem should be considered as a regression task, so the metrics proposed for conducting the algorithms analysis are the following:

- Absolute Error (AE): absolute value of the difference between the predicted value and the real value for each quantity.
- Absolute Percentage Error (APE): AE divided by the actual value for each quantity, so as to provide a measure of the relative error of the estimation.

Both magnitudes are calculated for each sample and are averaged for the entire training or testing datasets. This generates the values of MAE and MAPE (Mean AE and Mean APE, respectively) for the magnitude of the aggregate percentage ratio:

$$MAE = \mathcal{L}_{1_{gr\_aridos\_perc}} = \left\| \widehat{gr\_aridos\_perc} - gr\_aridos\_perc \right\|_1 = \frac{1}{M}\sum_{i=1}^{M} \left| \widehat{gr\_aridos\_perc}_i - gr\_aridos\_perc_i \right| \quad \textbf{(9.1)}$$

$$MAPE = \frac{1}{M}\sum_{i=1}^{M} \frac{\left| \widehat{gr\_aridos\_perc}_i - gr\_aridos\_perc_i \right|}{gr\_aridos\_perc_i} \quad \textbf{(9.2)}$$

When reporting results, the complete distributions of AE and APE are shown for the magnitudes to be predicted, as well as their mean values (MAE, MAPE), medians and standard deviations of the errors.

New method proposal for sterile quantification in scrap deliveries.

9.4 Sterile estimator developed at Laboratory scale

In previous sections, Linear sensors were identified as the most convenient solution for laboratory tests, and within market available sensors, SisuCHEMA sensor by SPECIM and V10E by SPECIM seem to be the suitable for covering the spectral range between 400-2500 nm. This section describes, not only the activities related to the laboratory set up design, samples preparation and DeepLearning architectures designs, but also the obtained results to assess whether it is worthy to going on with the proposal in a more industrial approach.

9.4.1 Laboratory set up design

The main objective of this laboratory stage was to well understand the real capabilities of combining DeepLearning methodologies with hyperspectral technologies, in order to propose an industrial solution composed by the optimal network architecture with the best images acquisition and data processing of a defined wavelength range.

One of the critical points to achieve the objectives defined in this laboratory phase is the design of a hyperspectral images acquisition station under very controlled conditions. The main criteria used for the design of the capture station are listed below:

- Necessary to extract as much spectral information as possible → High linear spectral resolution sensor using linear cameras.
- A 2D image is needed → A close control push broom system for sample displacements in front of the camera
- Well-known Lighting system → to ensure the right calibration procedures
- Camera aberrations control → Dark current and White current measuring procedure
- ROI on Samples clearly defined → drawers for sterile / scrap mixes
- Dedicated Software for acquiring, pre-processing, post-processing and data analysis → Use commercial software

Based on these criteria, the laboratory set up design was developed (see Fig. 9.29) containing the following elements:

- A conveyor belt driven by a servo motor and controlled by a FESTO CMMP-AS system. This system allows setting a starting and ending point for the tray displacement path containing the sterile / Scrap samples.
- Linear hyperspectral optical sensor composed by a spectrometer (Specim V10_04204) combined with a scientific CMOS camera (JAI-TM-1327GE) in the VNIR range (400-1000nm) providing 768 spectral bands and a hyperspectral camera in the SWIR range

by sisuCHEMA (1000-2500nm). Two hyperspectral linear cameras have been placed and adjusted in such a way that both collect the information from the same line.

- Lighting system composed by 2 Halogen lamps with a nominal power of 50W each.
- A PC in which a capture SW has been developed that collects the information from each of them and displays it on the UI screen.

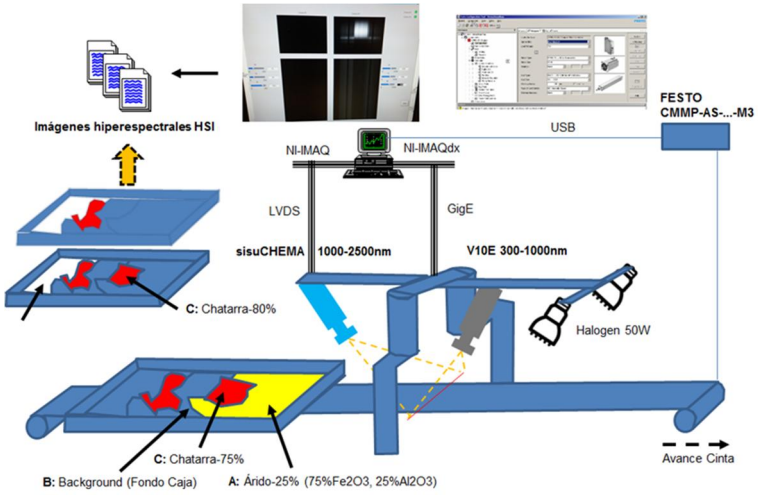

Fig. 9.29: Conceptual architecture of laboratory prototype

Fig. 9.30 shows the final prototype implemented in laboratory according the architecture proposed in Fig. 9.29 :

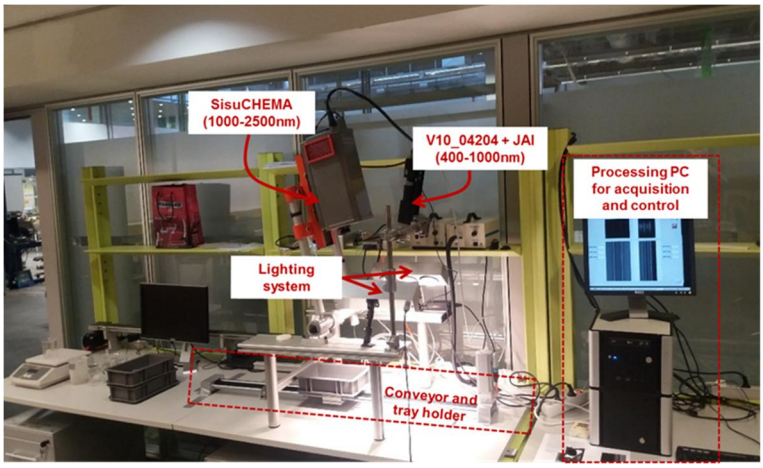

Fig. 9.30: Laboratory prototype

9.4.2 Samples selection for dataset definition

9.4.2.1 Samples preparation

As shown previously in Fig. 8.1, around 60% of the materials contained in E1 scrap sterile correspond to 4 basic compounds (35% SiO_2, 20% Fe oxides, 4% CaO, 2% Al_2O_3). Although this compounds distribution is quite conditioned by the origin and nature of each scrap type. These 4 main components can be considered as the principal ones.

In order to simulate different potential sterile mixtures in industrial materials, some kg of those pseudo-pure materials were collected to be used for samples preparation.

Fig. 9.31: Collected pure materials for sterile simple preparation

In addition to the materials for preparing sterile samples, different elements for sample preparation and mixtures control were also available:

- A scale with weighting range between 1 and 3,000 gr.
- Several plastic trays (weight 320 gr) for sample allocation.
- A Homemade hopper that can be attached to the trays and facilitates samples loading during mixtures preparation.

Fig. 9.32: Hopper for trays preparation

- Different sterile components: Al_2O_3, CaO, SiO_2 and Fe_2O_3,
- Regular E40 Scrap processed in a scrap shear for obtaining samples with different shapes and weights.

New method proposal for sterile quantification in scrap deliveries.

Fig. 9.33: left) E40 scrap and right) shear for small pieces preparation

- Several reflectance patterns manufactured by Spectralon: materials with known Diffuse reflectance (12%, 25%, 50% and 99%).

With all needed materials, needed for conducting the proposed experiment according to the defined methodology in laboratory conditions, it was also necessary to determine the number and the nature of samples to be used for generating the scrap mixtures dataset, ensuring variability requirements to guarantee a representative population of samples. In this sense, a first analysis is made following this approach:

- An empty tray weighs 315 gr.
- Several pieces of scrap are put in a tray and weighed; It is estimated that the total amount of scrap used in each weighing should weigh between 1000 and 2000 gr.
- The regular sterile content present in shredded scrap (E40) is around 10%.
- For the compound combinations of the aggregates, the calculation unit is set at 20 gr.
- Tests are done with iron oxide (5.7 gr / cm^3), lime (1.1 - 1.3 gr / cm^3), alumina (3.5 gr / cm^3) and with silica (0.2 – 0.3 gr / cm^3), verifying the great density difference. These big differences in density, made necessary to define carefully the sterile components in the mixture to be sure that a 10% over the total sample weight is representative of a real situation.

Next, the criteria for elaborating the physical samples to be acquired are detailed. The methodology proposed attempt to guarantee enough data variability for learning, while maintaining an operative number of samples.

Focusing on the preparation of sterile variants (the amount of scrap in the sample was not considered.), the problem to be solved is considered as a combinatorial problem with selection of M = 4 elements (i.e. endmembers or components of the aggregate: {Silica, Iron Oxide, Alumina, CaO}) of a group of N = 2 elements (we define them as presence, 1, or absence, 0 of a given unit of volume, so that for each endmember we can select any of the values of N = {0,1}), where the number of combinations corresponding to this scenario is given by the formula M^N (215).

The volume associated with the components of each combination should then be multiplied by a factor l = {1,2,3,4 ... L}, in order to obtain several combinations with the same relative

abundance but different volumes / weights added in absolute terms. Thus, the CA number of aggregate combinations, would be:

$$C_A = L \times N^M \tag{9.3}$$

It should be noted that the output of the regression network must predict one of these values for the case of sterile, so it is convenient that the resulting number is high enough for well representing the existing variability in the samples. In this work, it was proposed values of N = 2, M = 4 and L = 4 / 5, and a unit of volume to be determined based on the density of the endmembers.

All mentioned so far corresponds to the creation of high variability for sterile. With regard to the scrap part, it was proposed to prepare a fixed number T of aggregate mixtures and different scrap fragments for each of the aggregate combinations, so that:

- Each sample presents the same materials mix amount and sterile mixture
- A random subset of all available scrap fragments is selected for the different samples
- An approximate scrap weight to be included in each sample is fixed, so that random scrap pieces are selected until the target weight is reached.

The total number of samples to be captured would be:

$$C = T \times C_A \tag{9.4}$$

As a general rule, it must be considered that the cost of increasing T is lower than increasing L, which is lower than increasing N (CT < CL < CN)

```
for C_Ai in C_A:  #de forma previa a la elaboración de cada mezcla de áridos:
    Medir el volumen de cada componente del árido
    Medir el peso de cada componente del árido
    Medir el volumen total del árido
    Medir el peso total del árido
    for t in T: # para cada mezlcla áridos + chatarra
        Seleccionar el subconjunto de fragmentos de chatarra
        Pesar dicho subconjunto
        Mezclar, volcar y capturar
        Retirar chatarra y conservar áridos
```

Fig. 9.34: Pseudocode of the sample creation procedure

Fig. 9.35 shows a scheme of the complete procedure.

New method proposal for sterile quantification in scrap deliveries.

Fig. 9.35: Sample preparation procedure (up) and 2 different Sterile + scrap samples (down)

An Excel sheet was generated with random combinations of quantities of each of the basic compounds that form the sterile part of the mix (silica, lime, alumina and iron oxide). This mixture was denominated as aggregate_id. For each of these combinations within an agregate_id, 10 equal mixture inputs were generated to combine them with 10 different amounts of scrap, which was defined as volquete_id. Each of them were tested to get the sample_id.

In addition to the amounts in grams of the different compounds present in the mix, the volume (in ml) of each sample was measured to facilitate the weighing operation.

Fig. 9.36 shows several lines of the sample preparation sheet:

	aggregate_id	volquete_id	sample_id	Silice_gr	Cal_gr	Alumina_gr	Ferroso_gr	Silice_ml	Cal_ml	Alumina_ml	Ferroso_ml	gr_arido	ml_arido	chatarra_gr	total_gr
0	0	0	ca0_v00	90.0	50.0	50.0	60.0	153.0	140.5	118.8	50.1	250.0	462.4		
1	0	1	ca0_v01	90.0	50.0	50.0	60.0	153.0	140.5	118.8	50.1	250.0	462.4		
2	0	2	ca0_v02	90.0	50.0	50.0	60.0	153.0	140.5	118.8	50.1	250.0	462.4		
3	0	3	ca0_v03	90.0	50.0	50.0	60.0	153.0	140.5	118.8	50.1	250.0	462.4		
4	0	4	ca0_v04	90.0	50.0	50.0	60.0	153.0	140.5	118.8	50.1	250.0	462.4		
5	0	5	ca0_v05	90.0	50.0	50.0	60.0	153.0	140.5	118.8	50.1	250.0	462.4		
6	0	6	ca0_v06	90.0	50.0	50.0	60.0	153.0	140.5	118.8	50.1	250.0	462.4		
7	0	7	ca0_v07	90.0	50.0	50.0	60.0	153.0	140.5	118.8	50.1	250.0	462.4		
8	0	8	ca0_v08	90.0	50.0	50.0	60.0	153.0	140.5	118.8	50.1	250.0	462.4		
9	0	9	ca0_v09	90.0	50.0	50.0	60.0	153.0	140.5	118.8	50.1	250.0	462.4		
10	1	0	ca1_v00	15.0	90.0	30.0	120.0	25.5	252.9	71.2	100.2	255.0	449.8		
11	1	1	ca1_v01	15.0	90.0	30.0	120.0	25.5	252.9	71.2	100.2	255.0	449.8		
12	1	2	ca1_v02	15.0	90.0	30.0	120.0	25.5	252.9	71.2	100.2	255.0	449.8		
13	1	3	ca1_v03	15.0	90.0	30.0	120.0	25.5	252.9	71.2	100.2	255.0	449.8		
14	1	4	ca1_v04	15.0	90.0	30.0	120.0	25.5	252.9	71.2	100.2	255.0	449.8		
15	1	5	ca1_v05	15.0	90.0	30.0	120.0	25.5	252.9	71.2	100.2	255.0	449.8		
16	1	6	ca1_v06	15.0	90.0	30.0	120.0	25.5	252.9	71.2	100.2	255.0	449.8		
17	1	7	ca1_v07	15.0	90.0	30.0	120.0	25.5	252.9	71.2	100.2	255.0	449.8		
18	1	8	ca1_v08	15.0	90.0	30.0	120.0	25.5	252.9	71.2	100.2	255.0	449.8		
19	1	9	ca1_v09	15.0	90.0	30.0	120.0	25.5	252.9	71.2	100.2	255.0	449.8		
20	2	0	ca2_v00	63.0	0.0	54.0	36.0	107.1	0.0	128.2	30.1	153.0	265.4		
21	2	1	ca2_v01	63.0	0.0	54.0	36.0	107.1	0.0	128.2	30.1	153.0	265.4		
22	2	2	ca2_v02	63.0	0.0	54.0	36.0	107.1	0.0	128.2	30.1	153.0	265.4		
23	2	3	ca2_v03	63.0	0.0	54.0	36.0	107.1	0.0	128.2	30.1	153.0	265.4		
24	2	4	ca2_v04	63.0	0.0	54.0	36.0	107.1	0.0	128.2	30.1	153.0	265.4		
25	2	5	ca2_v05	63.0	0.0	54.0	36.0	107.1	0.0	128.2	30.1	153.0	265.4		
26	2	6	ca2_v06	63.0	0.0	54.0	36.0	107.1	0.0	128.2	30.1	153.0	265.4		
27	2	7	ca2_v07	63.0	0.0	54.0	36.0	107.1	0.0	128.2	30.1	153.0	265.4		
28	2	8	ca2_v08	63.0	0.0	54.0	36.0	107.1	0.0	128.2	30.1	153.0	265.4		
29	2	9	ca2_v09	63.0	0.0	54.0	36.0	107.1	0.0	128.2	30.1	153.0	265.4		

Fig. 9.36: Material weights definition before sample preparation

New method proposal for sterile quantification in scrap deliveries.

9.4.2.2 Methodology for Samples acquisition

The initial equipment preparation procedure followed at the beginning of each capturing day is described below:

1. Place the lenses caps on the optics of the two hyperspectral cameras and acquire a "black" capture. The files are referenced as "dark_DDMMYY"
2. Place the spectralon patterns on a tray and acquire reflective references. The files are referenced as "patron_DDMMYY"
3. Quick analysis of the files acquired by HDRCrop free application.
    a. Check that the images are well generated
    b. Check that the assembly is centred.
    c. Check the focus of the cameras.

As described in the previous section, the procedure of each trial for aggregate_id sample generation was:

1. Take an empty matrass, place it on the scale and set it to 0.
2. Take the amount of the different compound of the sterile sample specified in the test.
3. Once all the compounds are available, put them in the bucket for mixing.

Once the sterile mixtures are obtained, the following procedure was followed for the elaboration of the final samples identified as volquete_id:

1. Several pieces of scrap were selected and weighed (weights between 500 and 2,000 gr.).
2. Place the pieces of scrap in the mixing bucket and mix it with the sterile.
3. Pour the contents of the bucket into the capturing tray supported by the hopper, making sure that the scrap does not overcome too much.
4. The final mixture is weighed.
5. The tray is placed on the base of the acquiring belt.
6. Start acquisition model in the capturing software.
7. Initialization of FESTO system for tray displacement.
8. When the acquisition is completed, the tray is removed
9. This operation was repeated 10 times for each aggregate_id, trying to modify the scrap weights among captures.
10. Repeat same operation for all aggregate_id combination.

New method proposal for sterile quantification in scrap deliveries.

According to the defined procedure, a total of 440 samples were collected. Each acquisition generated 4 different files (2 files per cameras): one containing the data, in .raw format, and the other containing the header in .hdr format

The acquisition SW was programmed to stop capturing after 500 lines, which coincides with the end of the tray at the programmed forward speed of the conveyor. So, it was important to manually activate the trigger capturing event.

Fig. 9.37 depicts all JAI - Hyperspectral captures done in Lab conditions

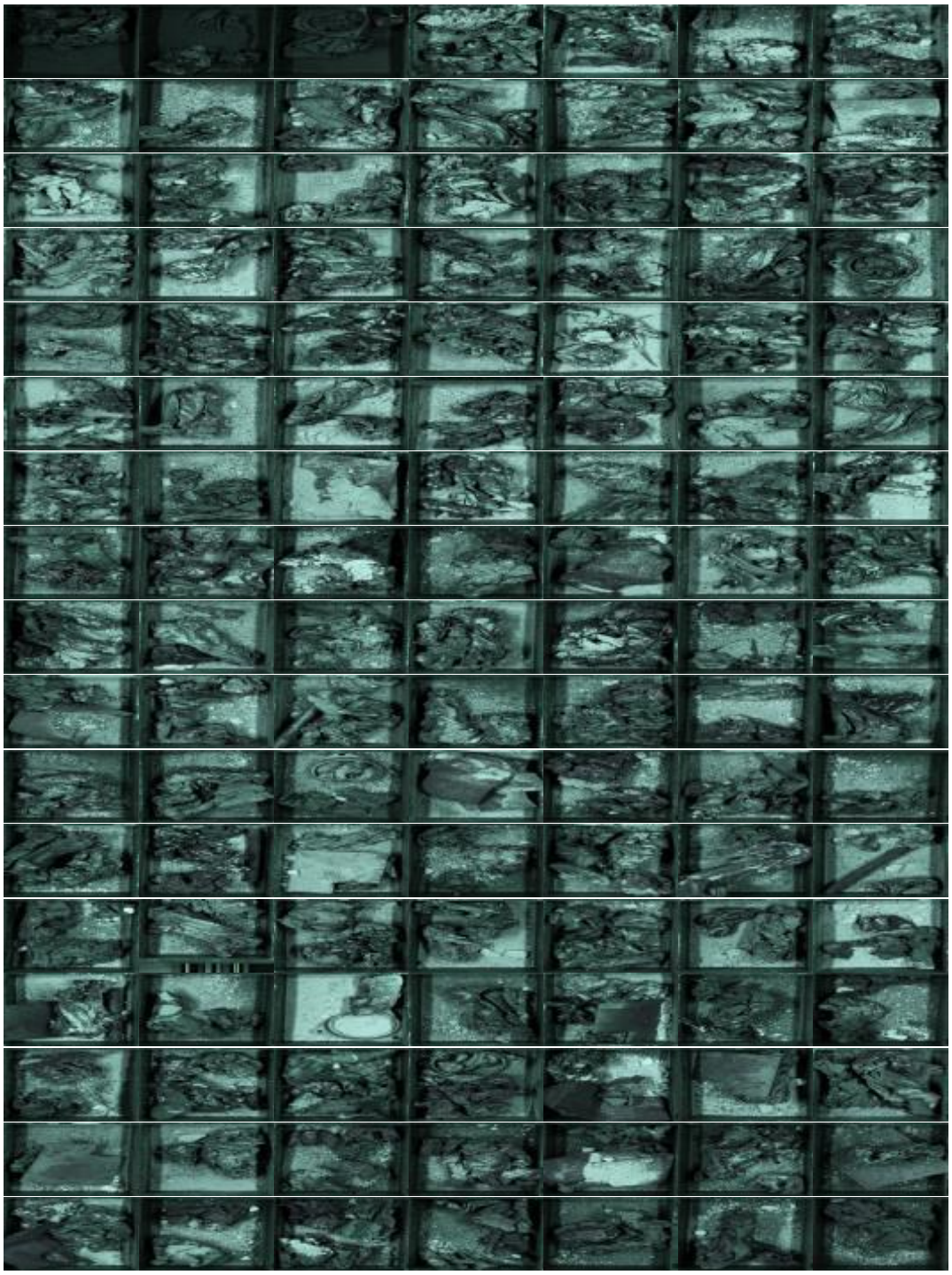

New method proposal for sterile quantification in scrap deliveries.

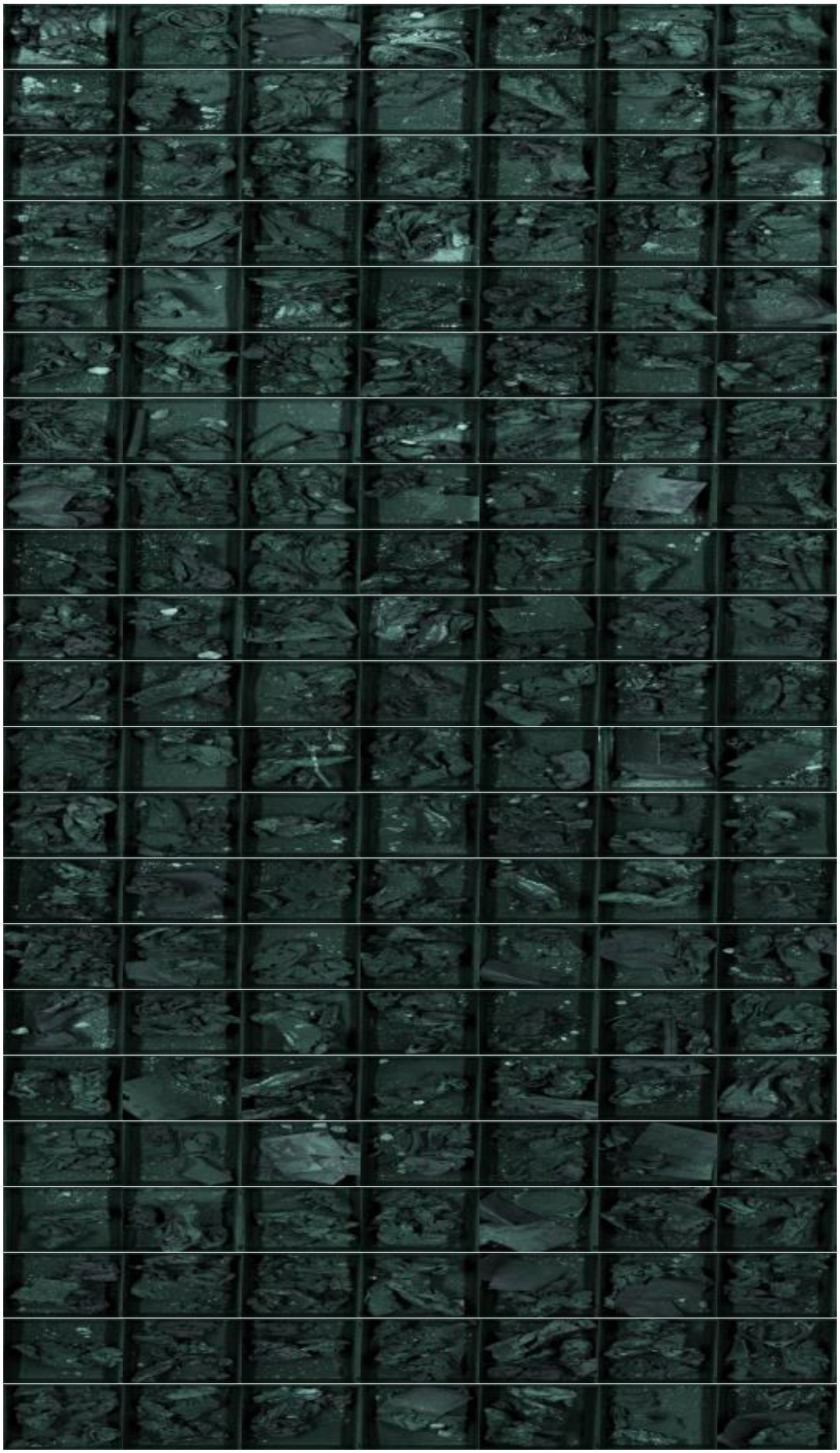

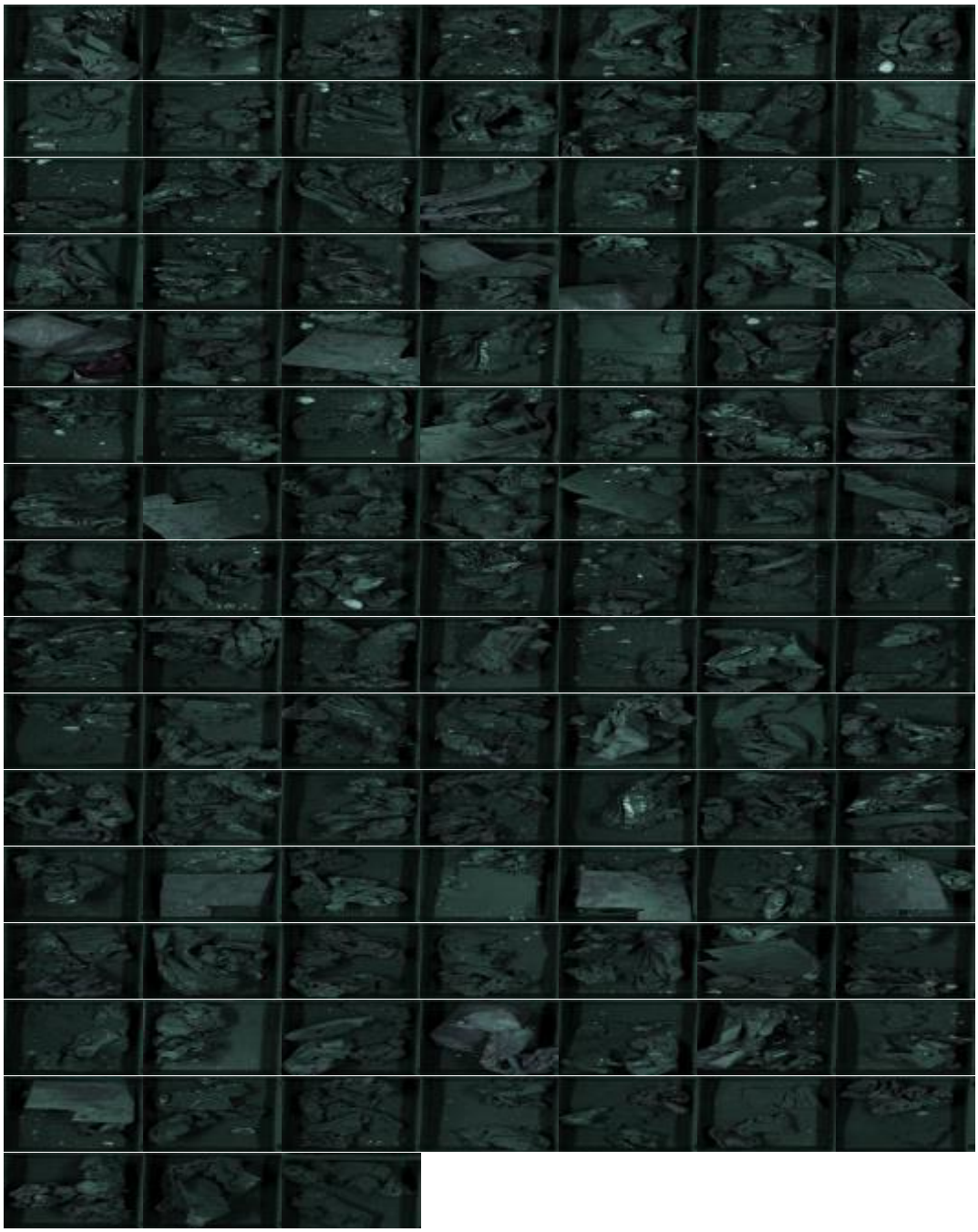

Fig. 9.37: The 440 Scrap / Sterile mixtures acquired in the VIS-NIR spectral range (JAI)

Fig. 9.38 shows all NI- Hyperspectral captures in Lab conditions

New method proposal for sterile quantification in scrap deliveries.

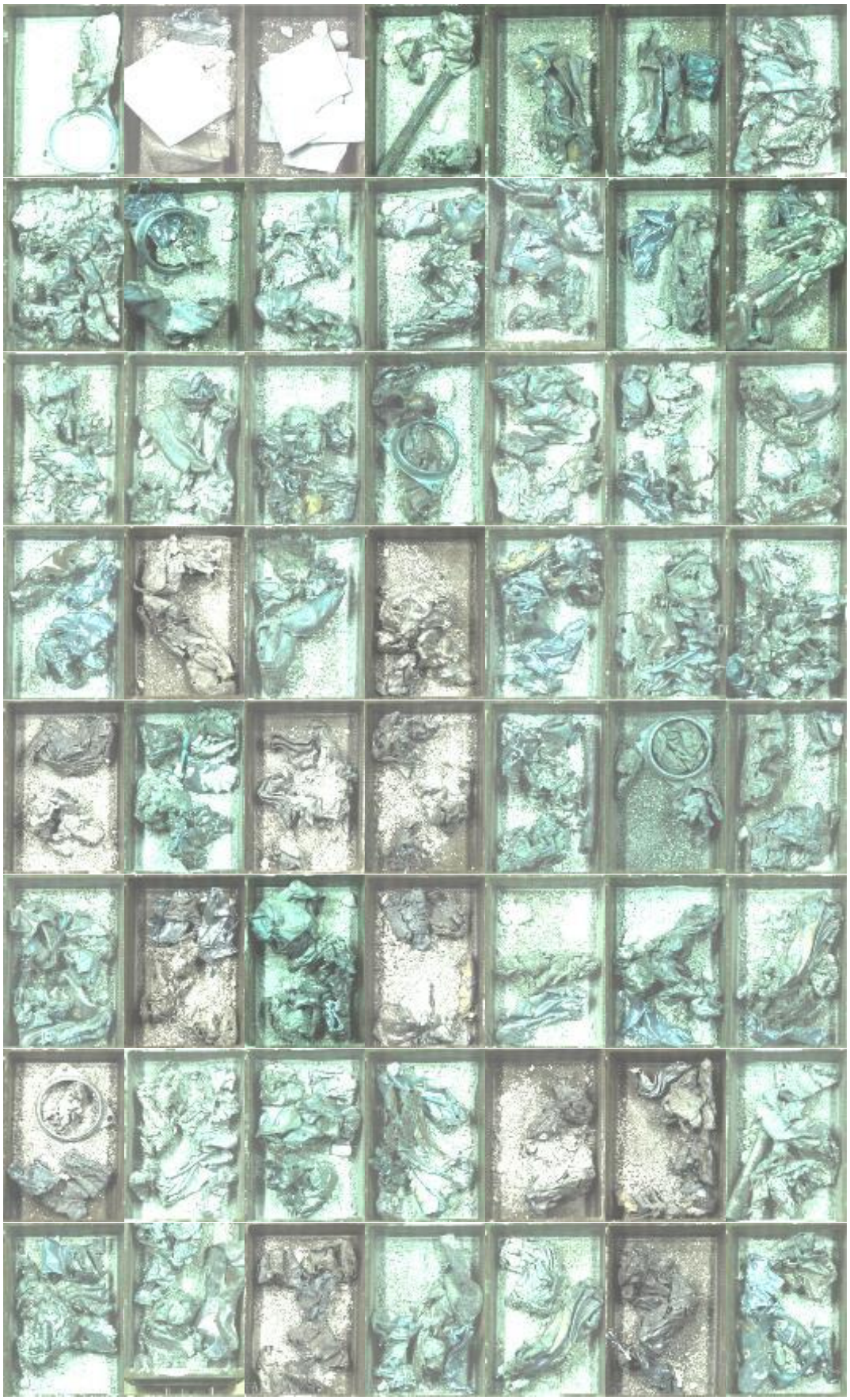

New method proposal for sterile quantification in scrap deliveries.

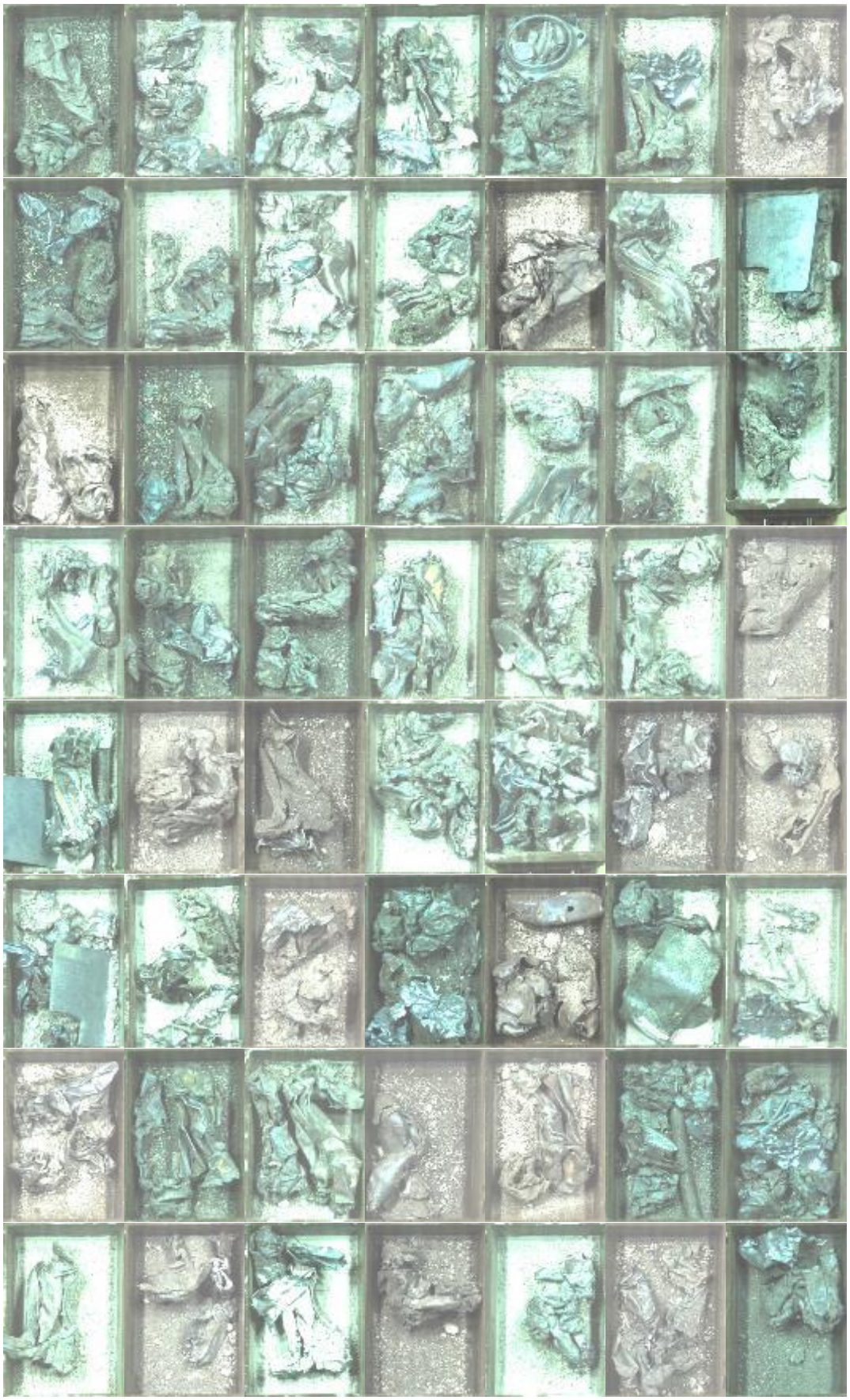

New method proposal for sterile quantification in scrap deliveries.

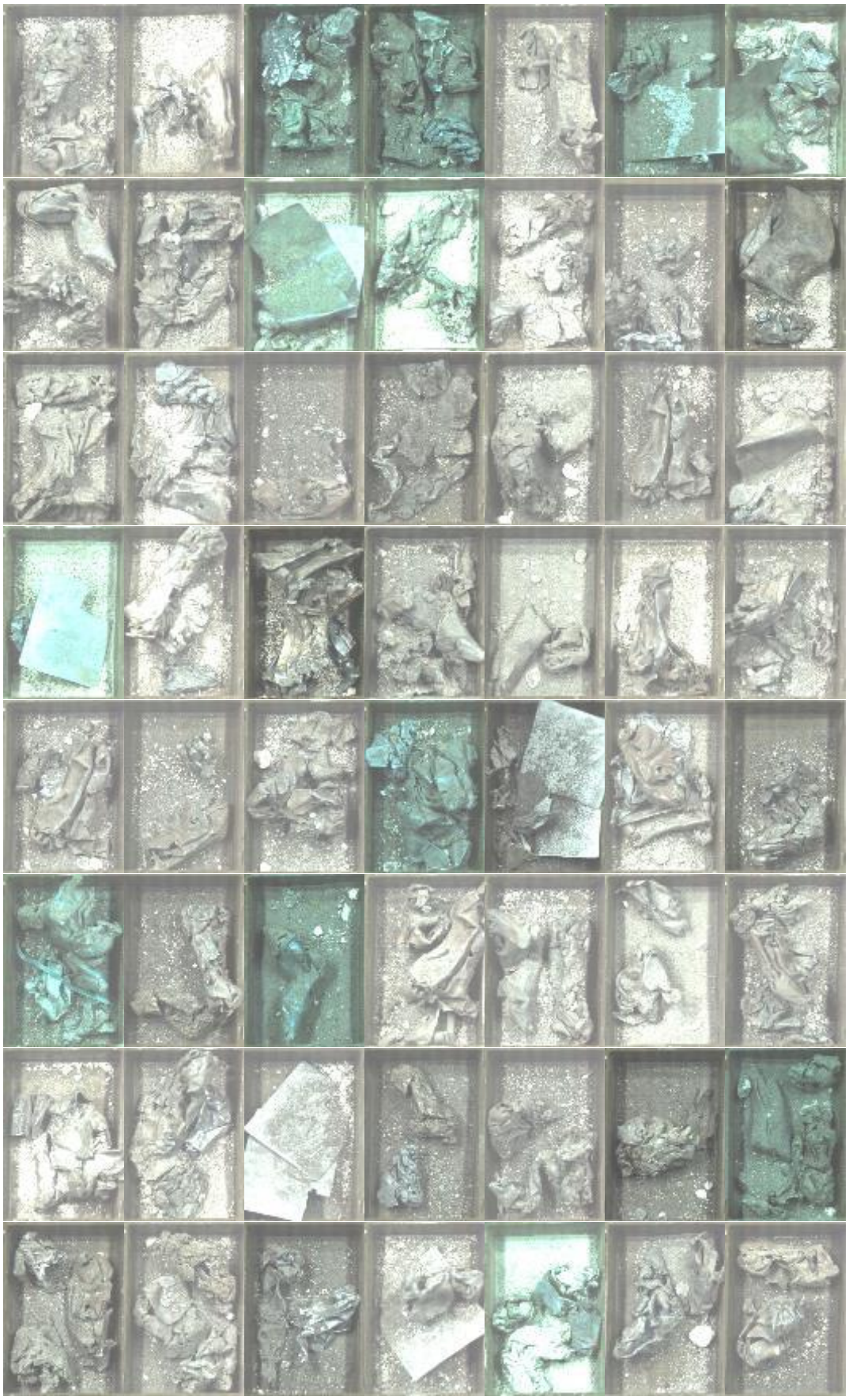

New method proposal for sterile quantification in scrap deliveries.

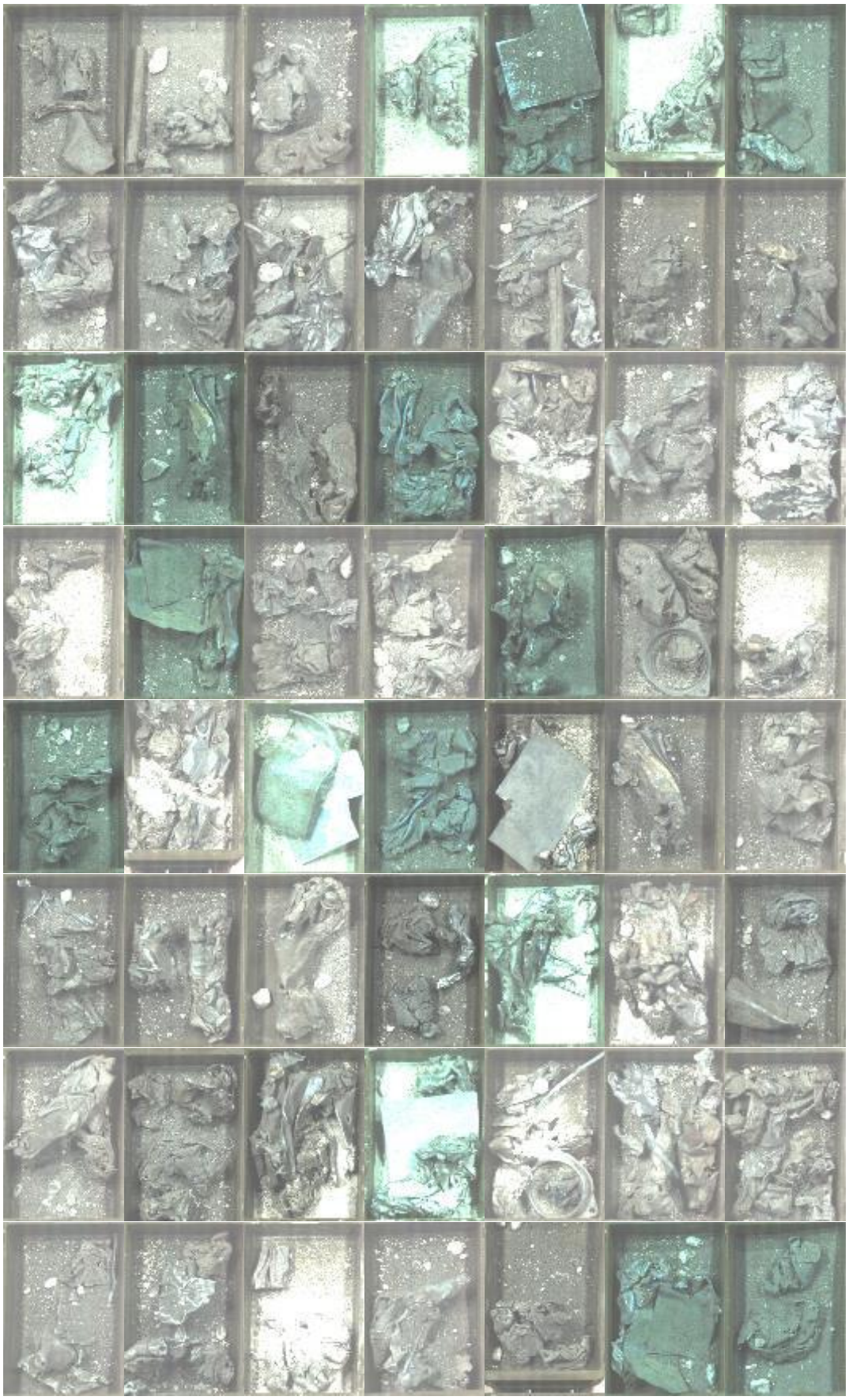

New method proposal for sterile quantification in scrap deliveries.

New method proposal for sterile quantification in scrap deliveries.

New method proposal for sterile quantification in scrap deliveries.

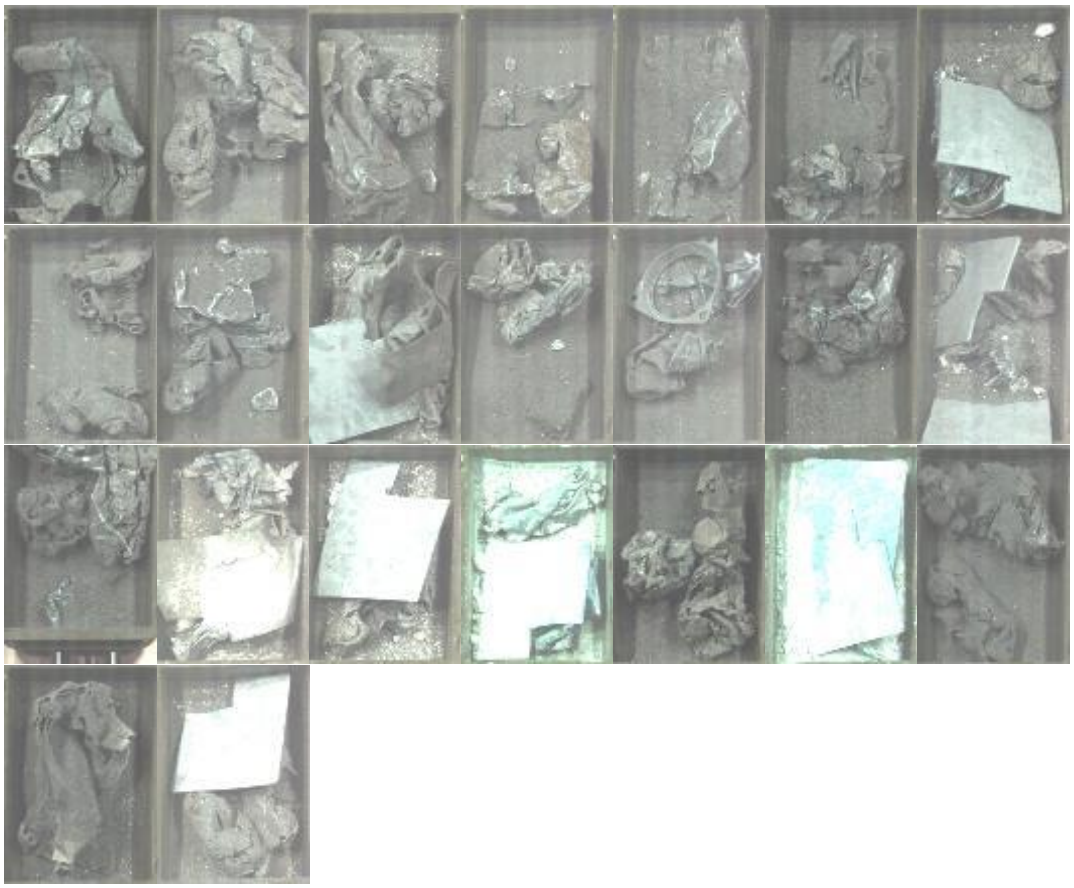

Fig. 9.38: The 440 Scrap / Sterile mixtures acquired in the NIR spectral range (SisuChema)

9.4.2.3 Ground truth analysis

The second step after acquiring the samples in the proposed laboratory set up was to do an analysis of the distributions of the different features to be extracted in the images contained in the database.

Fig. 9.39 and Fig. 9.40 show, respectively, the distributions (in the form of non-normalized histograms) of the weights of aggregates and scrap for the entire samples database available. As mentioned in previous sections, this database contains 440 samples, corresponding to 44 mixtures of aggregates with different percentages of the four components used as sterile, and different sets of scrap fragments in each of them, with a maximum limit of 10 samples taken by each aggregate mixture. This is why, the gr_aggregate histogram presents intervals with numbers samples around 10 or 20. Both distributions present very different mean values and ranges: [50, 380] gr for aggregates, [500, 2000] gr for scrap. In the case of scrap, the histogram also contains a graph showing the location of the quartiles, as well as mean, median and standard deviation values.

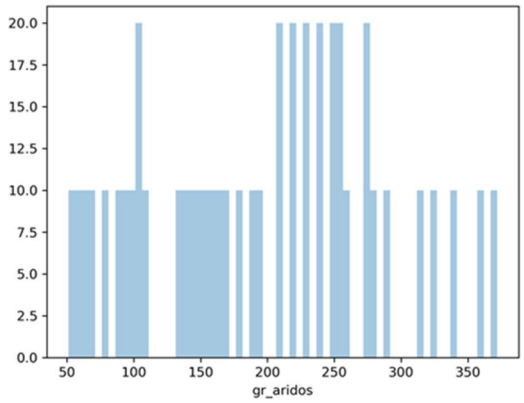

Fig. 9.39: Aggregate weight distribution [gr_aggregates] of the set of samples captured

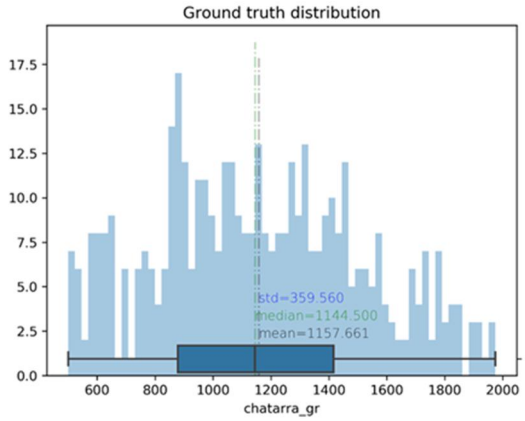

Fig. 9.40: Scrap weight distribution [gr_scrap] of the set of samples captured

Fig. 9.41 shows the weight ratio distribution between aggregates and the total weight of the mixture (aggregates + scrap) in parts per unit. It is thus observed that the aggregates constitute, on average, 15.2% of the total weight of the sample mixture.

It is important to highlight that when designing the experiment, laboratory samples were designed for achieving mixture ranges ratios consistent with the regular scrap deliveries in the scrap yard.

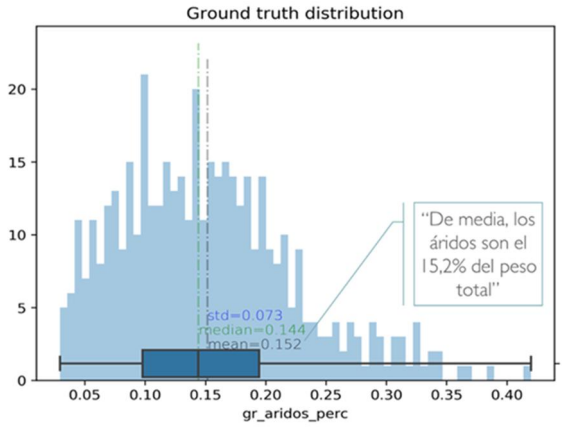

Fig. 9.41: Distribution of aggregates weight with respect to the total weight of the samples in p.u [gr_aggregate_perc]

Finally, in Fig. 9.42 several samples examples are included to the weight histogram (one per camera). In this picture it can be clearly intuited that, as we move to the right, the amount of scrap decreases progressively in proportion to aggregates amount (different material densities must be considered). It is also observed a great variety of appearances of the artificially created mixtures, because of a mixing design in which the variability in the composition has prevailed against variations in its physical appearance and density, aiming to obtain an estimator as robust as possible.

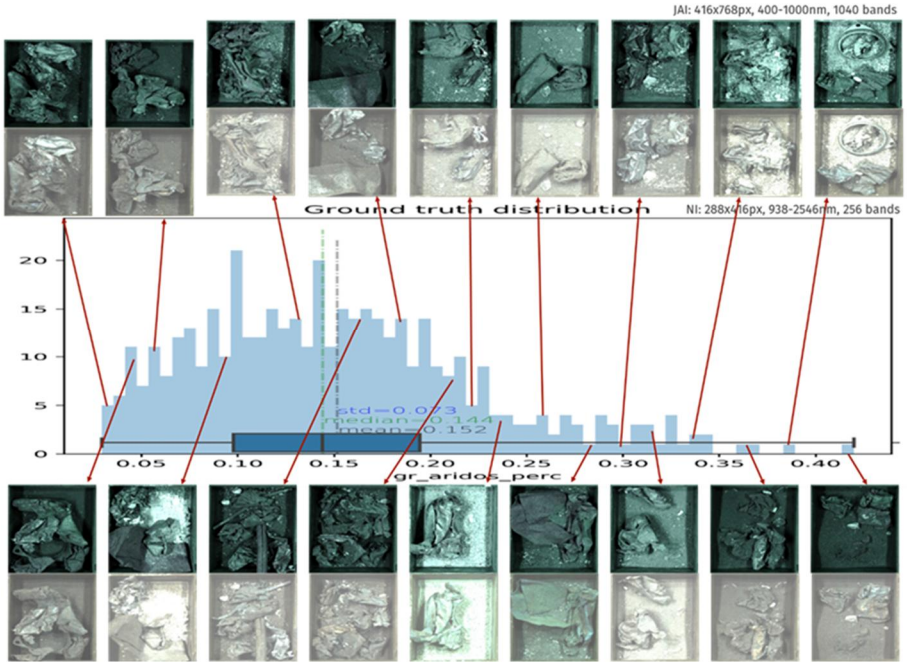

Fig. 9.42: Samples (renderizations corresponding to 3 unique bands for each of the two cameras used in the capture, and rebuilt to generate images in square format) extracted from different intervals of the distribution histogram

The analysis over the ground truth of the whole dataset (train + test) allows to stablish a simple baseline like "always predict the average" in equal conditions with Deep Learning models.

9.4.3 Baseline for analysing image database

From image database management point of view, the set of 440 acquired samples were divided in two sets:

- Training set: set of samples used to train the predictive models to be tested. This data set represents 80% of the total available samples (#350).
- Testing set: set of samples used to objectively evaluate the performance (in terms of predictive capacity) of the trained model. This data set represents 20% of the available samples (#90).

Note that, deliberately, the creation of a third validation set is omitted (this third data set is commonly used to choose the optimal model among a set of them or to optimize the hyperparameters of the network), since the objective of this phase is only to check the capabilities of deep learning techniques for the proposed task, and not to find the optimal model architecture. In this way, the process is simplified.

On the other hand, it is necessary to set a basic baseline to evaluate the real prediction outcomes of the different tested models over each sample (simple method of predicting the magnitudes under study that allows to establish a lower numerical reference to beat using the most advanced techniques). For this particular case, the baseline is defined as predicting always the average value of the whole dataset composing the ground truth. As shown in Fig. 9.41 this baseline value is 14.4%.

Fig. 9.43 shows the error distribution result. If the model always predicts a sterile amount percentage equal to 0.144, the MAE is 0.058. This means that, on average, there are 5.8 percentage points of difference between the estimated percentage of aggregates over the total weight of the sample and the real percentage. While it might seem a low value, it must be considered that the low average ratio in percentage of sterile in the database (15.2%), represents 52.3% in terms of MAPE.

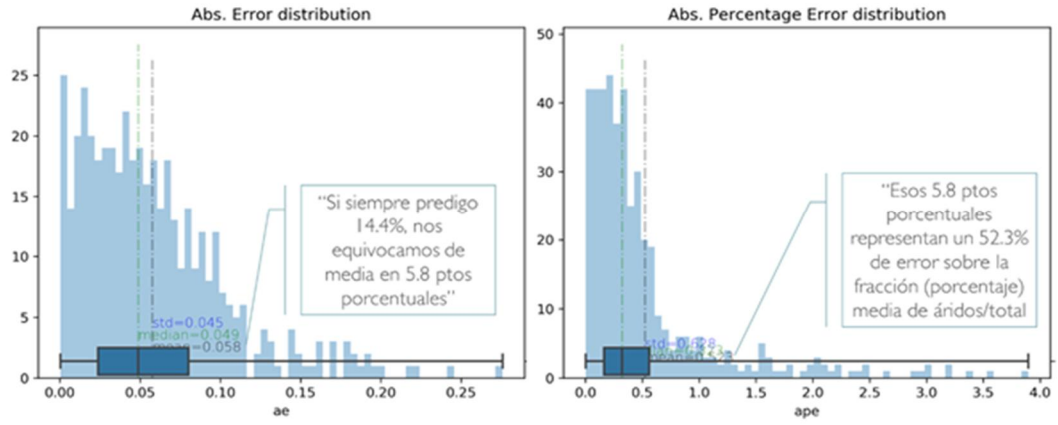

Fig. 9.43: Error distribution (left) AE, right), APE) for Baseline 0 consisting in always predicting the mean value for [gr_aridos_perc] magnitude

New method proposal for sterile quantification in scrap deliveries.

9.4.4 Network architecture design: Models based on Convolutional Neural Networks (CNN)

Regarding the type of network to be used, and well aligned with reasoning given in the state-of-the-art analysis section, it was decided to use CNN (Convolutional Neuronal Network) as the most convenient model architecture to perform the estimation of the magnitudes to be described. These networks allow efficient and optimal fusion of high-density spectral information with local spatial information to make the prediction, enabling:

- Flexible integration of inputs of different types
- The simultaneous prediction of several magnitudes by reusing the learned parameters.

9.4.4.1 Data loading and pre-processing

In order to make suitable the available hyperspectral images, some data loading and image pre-processing operations are required:

- Camera selection and spectral range: According to the results of the sensor selection analyses included in section 9.3.1.2, the classifiers gave better results to the information existing in the Visible + NearIR range (1040 bands generated by the JAI camera). Because of this, only hyperspectral data generated by the JAI sensor was used for the sterile estimator design
- Spatial resolution: The first image pre-processing activity corresponded with an initial fixed-size cut of each image from a variable length (cropping). The initial size reduction generates an image of 416 rows and 768 columns that contain an adjusted view of the content of the tray.

  After loading the entire cropping image in memory, asymmetric spatial decimation is performed, resulting in a 128x128 pixels image. Then, after each epoch a second fixed size cut (114x114) but randomly located for each image is carried, in order to contribute to regularization and increase the invariability to translation.

  Other cropping sizes were tested but the non-used spatial information was high. However, the chosen configuration allows to make use of a relatively simple network reducing the overfitting risk
- Spectral resolution: In order to allow adopting an approach based on fine-tuning (from a RGB model pre-trained from Imagenet images (205)), different options that generate a representation of the original hyperspectral image on the basis of three channels were considered. All these options ensure to generate a dataset compatible with architecture used in the pretraining phase:

New method proposal for sterile quantification in scrap deliveries.

- Selection of three unique bands (3 out of 1040), one in the lower range, one in the mid-range and the last one in the higher range of the VIS+NIR spectrum. This is the simplest and fastest alternative (in terms of data loading and implementation speed) and, although limited in terms of expressiveness and lost information, it is a useful baseline and with low risk of overfitting. This is the first option for setting a lower performance limit in the initial stages of development. The bands selected corresponded to positions 100 (at 428,3 nm), 400 (at 614,1 nm) and 700 (at 806,6 nm).
- Full spectrum loading and conversion to real colour (RGB) using colorimetry techniques like colour matching functions - CMF (i.e.; Spectral sensitivity curves that modify the response of the Human Visual System (HVS) to impulses at different wavelengths to convert the hyperspectral input into an independent representation of the device, such as the XYZ triestimulus values, through the integration of the hyperspectral image on CMF). The main disadvantage of this approach is that the part of the infrared spectrum (above 700 nm) is discarded, although the semantics of each channel coincide with RGB representation used for the pre-training dataset.
- Full spectrum loading and implementation of classic dimensionality reduction techniques (not based on deep learning), to generate 3 channels without a physical interpretation. The simplest case would be principal component analysis (PCA).
- Full spectrum loading and implementation of a first convolutional layer performing the dimensionality reduction to 3 channels in an optimum way, as described in (190), to continue using a network trained in Imagenet

In addition to the proposed image loading and processing options, there is also the possibility of working with the full spectrum as input and applying a first 3x3x1040 channel convolutional layer. Despite being the option that uses the largest amount of original information, there is a greater risk of overfitting, and does not allow the use of pre-trained network architectures in Imagenet, so it would require a greater number of images than the previous alternatives.

9.4.4.2 Data normalization

To keep this research as simple as possible, the initial normalization of hyperspectral images carried out was to contain them in a [0,1] range. However, as described in previous sections, the acquisition procedure was conceived to apply additional normalizations based on reference reflectance patterns and black current correction. Applying any of these normalizations would probably result in lower prediction error rates.

New method proposal for sterile quantification in scrap deliveries.

9.4.4.3 Network architecture design

This section describes the architecture or topology of the developed network. After several initial experiments, the selected network architecture consists of a backbone and a series of input and output modules / branches.

9.4.4.3.1 Network input branch

As mentioned in section 9.4.4.1, and considering the positive results obtained, the choose option was to load only three bands of the original hyperspectral image. Due to this, the proposed architecture lacks any additional input branches. The three mentioned bands generate a three-channel image which is directly loaded to the backbone.

9.4.4.3.2 Backbone

For the backbone of the network, a CNN based architecture designed to do image classification tasks was used. However, the last layers are adapted to convert it into a regression network with multiple outputs. The RGB images classification problem is probably the most classic problem within the Computer Vision community, so there are a variety of architectures whose behaviour for this task is well studied and that present a great robustness when used;

- To conduct classification tasks on images of a different nature to those for which the network was conceived
- To perform tasks different to image classification (i.e. semantic segmentation, regression).

In both cases, the network weights initialization can be done randomly (from scratch), or by using the values resulting from the pre-trained network from Imagenet images.

During this research, three well-known architectures were selected from Resnet (209) and Densenet (210) families (Resnet50, Densenet40 and Densenet121), since all of them have demonstrated excellent performance in classification / regression tasks.

As described in the literature review, the main conceptual innovation of Resnet family architectures, compared to previous designs, was the implementation of residual modules, which contain, in parallel, a path without any type of processing and another path with several convolutional layers, nonlinearities and normalization. This approach allows the input signal always having a path without any type of processing, while each of the different modules allows to add a residual processing component to it.

New method proposal for sterile quantification in scrap deliveries.

This structure facilitates the gradients flow when architectures present a large number of layers, thus avoiding the problem of vanishing gradients and allowing the use of deeper and, therefore, more complex models.

The densely connected networks (Densenet) are built on residual type connections, but generating a dense mesh of connections between the different layers, to offer a more efficient representation (see Fig. 9.44).

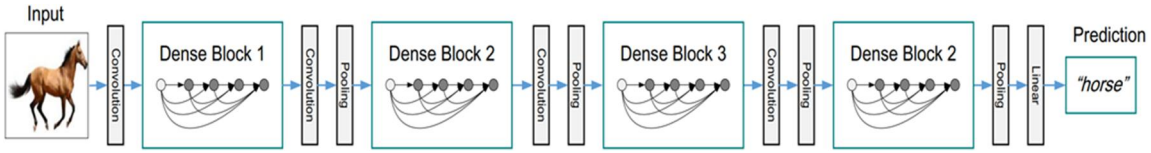

Fig. 9.44: Densenet architecture for image classification tasks

Finally, and considering that network overfitting effect was not observed, the Densenet121 topology was chosen. This architecture corresponds with the 121-layer version of Densenet family which is one of the more efficient and tested architectures for classification problems.

9.4.4.3.3 Network output branch

Starting from a 121-layer Densenet image classification architecture, the network is adapted for a real number regression task (aggregate weight ratio over the total weight, i.e. gr_aridos_perc). To do this, the layers after the last "dense block" were removed. Next, a GlobalAveragePooling layer was added (i.e. aggregation of the activation maps resulting from the last convolutional layers via global average) and a 50 neurons layer with dense connections, followed by an activation layer with a ReLU type non-linearity.

Finally, a last dense connections layer and a single output neuron is added, without any activation. This will avoid limiting the output range but ensuring non-negative quantities estimations.

All attempts to train the network with this type of unique output resulted in errors over the validation set, generating results very close to the baseline consisting of predicting the average.

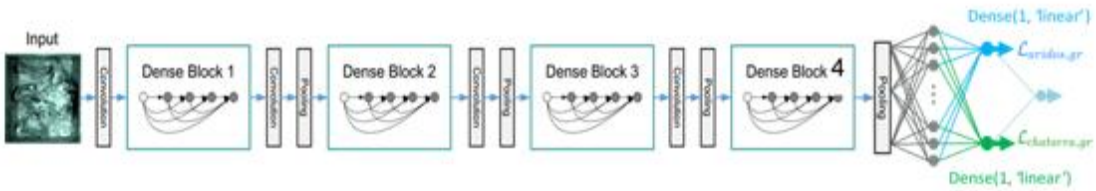

Fig. 9.45: Modified Densenet for multi-task regression

The poor results of the previous experiments indicate that by using a single branch that directly estimates the percentage of aggregates, the network is not able to model the logic that generate the actual values that must be predict. Therefore, and given that during the

acquisition phase of the experiment, special care was taken to systematically measure the sample composition of the scrap + sterile mix (weights of sterile and scrap separately, distribution ratio, aggregate chemical composition and aggregate volume), it was decided to make a design on the upper layers of the network (substitution of the single output branch but maintaining the dense layer of 50 neurons) that allows to take advantage of this information. Fig. 9.45 shows the resulting modified Densenet-121 network architecture, while Fig. 9.46 shows the detail of its last layers and the multitask objective function

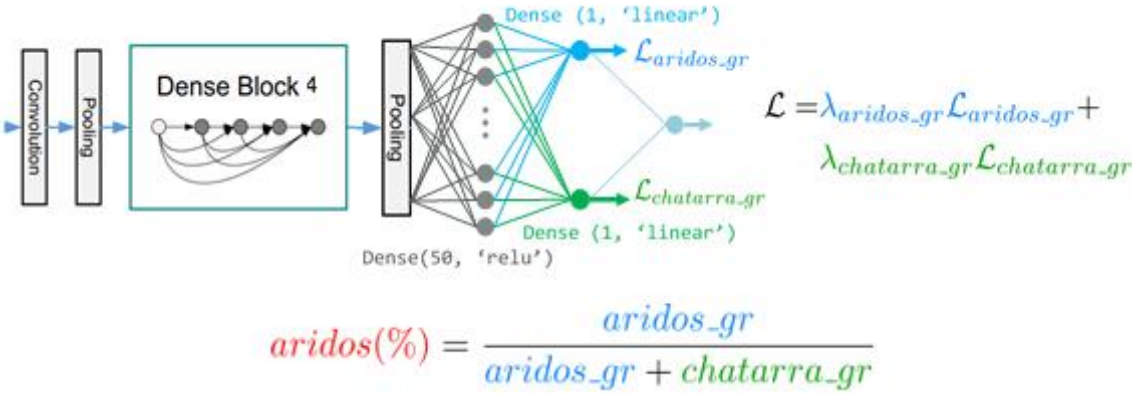

Fig. 9.46: Detail of the output layers of the proposed multi-task Densenet architecture

The network output represented in Fig. 9.46, is described as follow:

- Branch 1 (blue) of a single neuron (51 parameters) and without activation function that estimates the absolute weight of the aggregates, and which has associated a cost function term that will optimize the network (L_ (aridos_gr).
- Branch 2 (green) of a single neuron (51 parameters) and without activation function that estimates the absolute weight of the scrap, and it has a second term associated with the cost function that will optimize the network (L_ (scrap_gr)
- A deterministic type layer (without trainable weights) that computes the ratio between both estimated quantities. Since it contains redundant information already present in the two previous outputs, it was decided not to incorporate this third term to the cost function and produce this output only for informational purposes and for qualitative evaluation of the network

For the proposed network architecture, most of the model's weights are the result of minimizing, jointly, the error made when making both predictions simultaneously. The aim of this multi-task design is to provide the network with a more explicit indication of how the aggregate/scrap ratio magnitude is defined. By having the disaggregated information on aggregate and scrap quantities and by estimating both separately too, we are providing the network with a much more powerful and efficient monitoring signal than if the network had to learn it by itself.

Although there was the possibility of continuing to delve into this line by disaggregating the aggregate branch into independent branches for the estimation of the weights of each of its

components (since such information was available as ground truth), it was decided not to do it because the results obtained at this point were already very promising.

9.4.4.4 Network training

This section describes some of the main design parameters and decisions considered during the training process of the network, as well as the network design elements not defined in previous sections.

9.4.4.4.1 Loss function

As specified in section 9.4.4.3.3, the cost function that optimizes the network is composed by two terms, each of them penalizing the error in the estimation of the aggregate and scrap weights:

$$\mathcal{L} = \lambda_{aridos_{gr}}\mathcal{L}_{aridos_{gr}} + \lambda_{chatarra_{gr}}\mathcal{L}_{chatarra_{gr}} \quad \textbf{(9.5)}$$

Where:

- $\lambda_{aridos_{gr}}$ and $\lambda_{chatarra_{gr}}$ are two scalar coefficients that weigh the importance of both terms. Since the ranges and average values of both magnitudes differ by approximately one order of magnitude (see figures Fig. 9.39, Fig. 9.40 and Fig. 9.41), it was decided to make both terms contribute equally, to which lambda values are set inversely proportional to the average of their corresponding magnitude, calculated for the training dataset.
- $\mathcal{L}_{aridos_{gr}}$ and $\mathcal{L}_{chatarra_{gr}}$ are the loss function associated with the estimation of the absolute weight of aggregates and scrap (in gr), respectively. In both cases two different functions are tested (Mean Absolute Error – MAE and Mean Squared Error – MSE), yielding both satisfactory results.

9.4.4.4.2 Network initialization

Although several initial experiments were done with a random initialization of all the weights of the model (from scratch), all of them were run for the first network designs proposed (single-branch architecture design for direct estimation of the percentage of aggregates) and none of them converged. On the other hand, using same architecture, but with a fine tuning weights initialization approach, there was not convergence either, so it is not possible to attribute the convergence or not to the initialization process.

New method proposal for sterile quantification in scrap deliveries.

All the experiments launched for the three branches architecture (indirect estimation of the aggregate ratio) offered a good convergence when the initialization was based on a pre-trained Densenet-121 network over Imagenet, only the last layers were randomizing initialized for all its branches.

Using this fine-tuning configuration, different strategies for layer “defrosting” were proposed. Generally, in a first phase the weights of the pre-trained layers are frozen and those weights randomized initialized are left opened for free learning. This approach resulted in training curves whose error did not decrease until defrosting the lower layers, so it was decided to perform fine-tuning in a single phase in which all layers had their weights unlocked for training.

9.4.4.4.3 Image argumentation

When training deep neural networks, the use of data augmentation techniques is frequent, these techniques consist of introducing random changes in the appearance of the images, but without affecting the label or the ground truth value. Thus, at each epoch the model observes a slightly modified version of each sample, so that robustness of the model increases. In this research work, the following combined random modifications for image argumentation were included:

- Horizontal and vertical flips
- +/- 90º rotations

9.4.4.5 Workflow for Network set up

This section includes, on the one hand, all the complementary information related to the programming language and the development environment that has been used for generating the different experiments, and on the other hand, the detailed description of the activities carried out throughout all the experiments and that have turned into the final architecture proposed in this investigation.

9.4.4.5.1 Programming environment

The development language used for acquiring, processing and the analysis of all information contained in the samples images has been Python. PyCharm is the “Python IDE for Professional Developers” that has been used to generate, debug and run programs. Throughout the research, different libraries and strategies have been used.

New method proposal for sterile quantification in scrap deliveries.

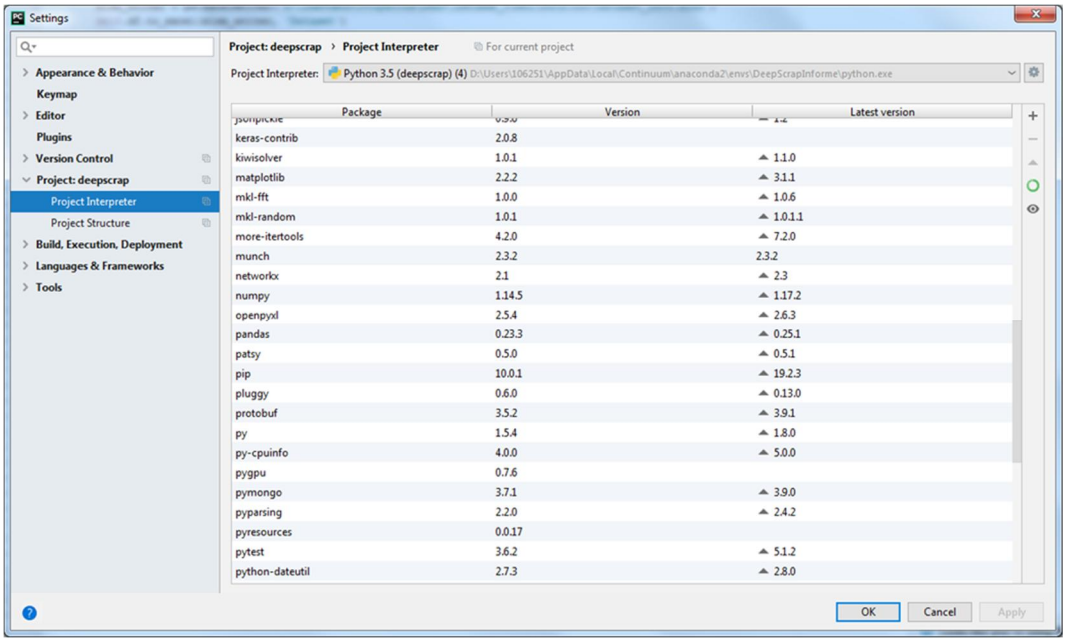

Fig. 9.47: Python Libraries used in this research

As for the Hardware platform, a server with Intel Xeon 6-core processor and Pascal Titan X GPU was employed.

The features offered by the PyCharm environment were used to execute the scripts under development on the infrastructure servers and visualize the results on personal work computers.

9.4.4.5.2 DeepLearning architecture design RoadMap

The data analysis process was iterative and guided by the results of the different experiments. This workflow has allowed developing the final algorithms able to offer valid results on the posed problem. This section presents the chronological description of the research work carried out in this phase.

The initial tests were focused on creating the “SW infrastructure” necessary for data management. These initial tasks were oriented to the generation of the data set that was used later on in the analysis process. The challenge for this first phase laid on the fact that Hyperspectral images are not conventional image formats but are schemes to store the actual pixel values of an image in a file. There are three common methods of organizing hyperspectral data (216); Band-Interleaved-by-Line or Row-Interleaved (BIL), Band-Interleaved-by-Pixel or Pixel-Interleaved (BIP) and Band-Sequential or Band-Interleaved (BSQ).

These files support a simple and multiband images visualization, and handle black and white, grayscale, pseudocolor, true colour and multispectral image data. The BIL, BIP and BSQ files are binary files (they have been generated with the raw extension) and must have an associated ASCII header file so they can be interpreted. This header file contains secondary

New method proposal for sterile quantification in scrap deliveries.

data about the image such as the number of rows and columns in the image, the binary format, etc. (they have been generated with the extension hdr)

In the present work the hyperspectral images are encoded according to a Band-Interleaved-by-Line or Row-Interleaved.

The first prediction tests carried out were launched with an initial spatial decimation at 200x200 pixels (both in the training phase and in the test phase) for two different networks architectures: Resnet50 (209) and Densenet121 (210). The training was done from scratch with the available images. Only images from the JAI camera (Visible + Near Infrared range) were used. As data input, all available spectral channels were utilized, as it was the configuration which presented the best results in the camera selection tests. Below are some basic diagrams of both networks in their original configuration (initially developed for solving general image classification task)

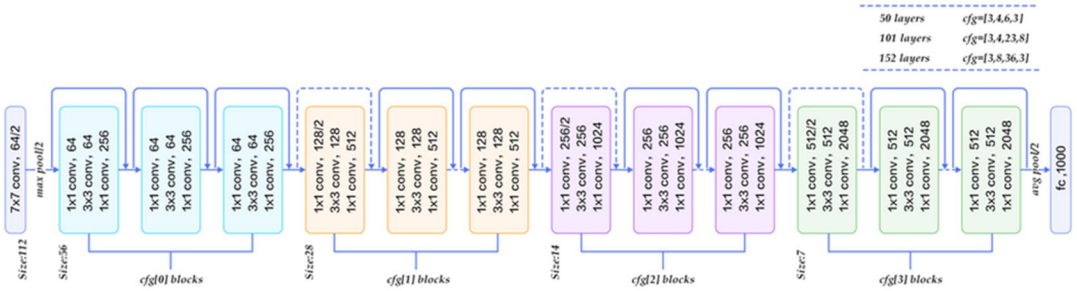

Fig. 9.48:General overview of ResNet50 architecture

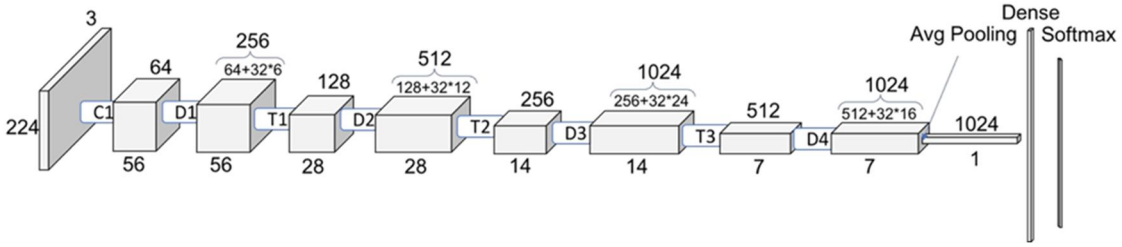

Fig. 9.49: General overview of Densenet121 architecture

To undertake the objective task, the modifications described below were initially made on the base architectures presented in Fig. 9.48 and Fig. 9.49:

- Last layers adaptation to a regression problem for a single output branch (estimation of the percentual weight of aggregate); Removal of the dense layer of 1000 neurons and the output Softmax layer and replacement by a 50 neurons dense layer with a ReLU activation function (for replacing negative values by zeros) and a new single neuron layer without activation function.
- Adaptation of the first convolutional layer of the network to support 1040 channel inputs instead of the 3 commonly used for RGB images.

New method proposal for sterile quantification in scrap deliveries.

The issues encountered in these first attempts were, on one hand that the network results did not converge, and on the other hand, the tests carried out in the network for hyperparameters adjusting took a long time to complete since 1040 channels were used

It was decided to reduce the number of spectral channels from 1040 to 3. This had a double aim: to reduce the processing times and to be able to use pre-trained weights in the networks facilitating a fine-tuning process. This also allows to define the spectral reduction strategy described before (first select three channels throughout the entire spectrum, then to move to real RGB color and finally to make a dimensionality reduction to the 3 main channels).

There are many network hyperparameters tested during the network developing phase. To facilitate these hyperparameters configuration, a config file was generated. One example of the config.json file is depicted (it corresponds to experiment 328):


```
{
  "architecture": "densenet_imagenet121",
  "batch_size_train": 24,
  "bottleneck": true,
  "computing_device": "/gpu:0",
  "dataset_partition_seed": 666,
  "depth": 121,
  "divide_by_std": false,
  "dropout_rate": 0.0,
  "earlystopping_patience": 100,
  "exp_dir": "results/BORRAME",
  "exp_hierarchy": null,
  "full_img_dim": [
    416,
    768,
    3
  ],
  "growth_rate": 32,
  "img_channels": 3,
  "img_cols": 768,
  "img_rows": 416,
  "learning_rate": 0.01,
  "load_crop_size": [
    416,
    768
  ],
  "name_optimizer": "Adam",
  "nb_dense_block": 4,
  "nb_epochs": 100,
  "nb_filter": 64,
  "nb_layers_per_block": [
    6,
    12,
    24,
    16
  ],
-→
-→
  "nb_threads_loader": 10,
  "reduction": 0.5,
  "remove_mean": true,
  "results_dir": "results",
  "scratch_or_finetuned": "finetuned",
  "seed": 455916186,
  "spatially_downsampled_crop_size": [
    80,
    80
  ],
  "spectral_downsampling_method":
"3bands",
  "subsample_initial_block": true,
  "test_is_actually_validation_set":
true,
  "train_as_classifier": false,
  "train_crop_size": [
    64,
    64
  ],
  "train_set_fraction_used": 1.0,
  "train_split": 0.8,
  "use_lr_finder": false,
  "use_sgdr": true,
  "weight_decay": 1e-05
```


Fig. 9.50: Hyperparameters config file for experiment 328

Next, the main network hyperparameters tested during this research are described:

- **computing_device:** The training Process of the model Will be executed in the selected card (CPU or GUP).
- **architecture:** This hyperparameter was set to load several network architectures. The tested architectures were ResNet50 and Densenet121, both of them able to select between pretrained weights (from Imagenet database) or from scratch options when

the training process is launched, according the value of scratch_or_finetuned hyperparameter.

- **scratch_or_finetuned:** this hyperparameter is combined with architecture hyperparameter to define the network architecture and type of training.
- **train_split:** This hyperparameter defines the image dataset ratio between training and validation.
- **dataset_partition_seed:** it is used for random generation of images subsets for training and validation.
- **nb_epochs:** This is the number of epochs that the network training process will last. One epoch is concluded when the whole dataset (all available images) have gone through the network. This hyperparameter defines the number of times the network processes all images in the dataset. In each epoch, the samples feed the network in a different order (the images are mixed) and as part of different batches. In addition, if some type of train-time image augmentation is carried out, each time the network observes a modified version of the same original image, without modifying the label.
- **batch_size_train:** This hyperparameter defines the branch size. As mentioned before, one epoch corresponds with the processing of the whole dataset. Since it is not possible to introduce all images at once, they are grouped in branches according the batch size value. The more memory there is, the higher that value can be and fewer iterations will be needed. Typical values are usual 8, 24, 32, 64, 128, etc.
- **name_optimizer:** To minimize the error that occurs in each pass between the predicted value by the network and the actual value, an optimizer is used. The usual ones are:
    - Stochastic Gradient Descent (SGD) is an algorithm that allows iteratively reducing the error committed by the network (the result of the cost function used). For this, at each step, the gradient of the error with respect to each of the (thousands of) weights of the network is calculated using the backpropagation algorithm. Then, each of these coefficients are updated according to the gradient value. In this way, it is determined to what extent each of these weights contributes to the error, and each of them are corrected so that the error decreases as quickly as possible.
    - Adam (which was the used optimizer in the final proposal) adjusts the learning speed of the parameters based on the first and second *momentum* of the gradients.
- The number of samples used for each calculation is defined by the **lot size, bs_train**
- **Learning_rate, momentum:** The learning rate is a network parameter that controls how the model weights should change (value and direction) in every step according the gradient generated by the backpropagation algorithm.

Small values in the leraning_rate leads to longer time to lower the error (and the process is more likely to converge to a higher local minimum), while large learning-rate values may cause the process to diverge or the error fails to descend to low enough, and to produce significant fluctuations in the error values.

In short, the learning_rate controls how quickly the network adapts to the problem. To consider the historical or inertia of the previous changes, the momentum parameter is also added. This hyperparameter smooths the changes of the parameters, causing them to remain in the same “direction”.

- **weight_decay:** This hyperparameter adds a regularization to the optimizer to avoid overfitting. The regularization is a L2 type and it forces the weights values to be small, avoiding high values to be concentrated in a few coefficients, adding a cost proportional to the square of the weights.

Within the configuration file, the PC folder where all the data associated with the experiment are stored is also defined. It stores results that can be used for debugging process. For example, during the experiment 316 the following graph was generated, which shows the non-convergence of the network.

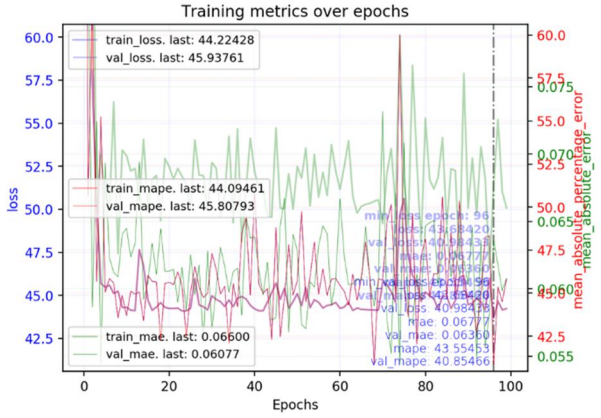

Fig. 9.51: Convergence analysis for Experiment 316 network set up

Many experiments have been done. The main milestones of the network development process were three bands analysis (instead of the whole spectrum) and, the multi-task.

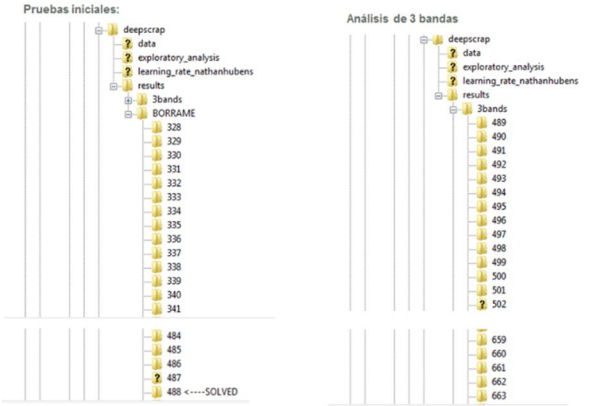

Fig. 9.52: Snapshot of experiments storing methodology

New method proposal for sterile quantification in scrap deliveries.

After several attempts, positive results were obtained with Densenet121 network architecture (pre-trained with Imagenet and with all the layers released during training) and making an initial spatial transformation (decimated) at 128 pixels. Due to the image augmentation, a second random cut at 114 pixels is made.

Below, some MAE graphs for sterile percentage estimation (gr_aridos_perc) are shown for three different experiments. These figures show the evolution of the network adjustment process:

- **Experiment 607** (3bands No augm. Densenet121.Pretrained on Imagenet. Orig size -> 128-> 114px. L1 loss.): At the epoch 172 it was proven that the network converges.

  As shown in Fig. 9.53, for experiment 607, the training was stopped prematurely because a pre-established stop condition was reached. This stop condition consisted on stopping the training if the cost function for the validation set stopped improving within certain number of epochs. Since experiment 621 allowed to lower the error by training up to 1000 epochs. This stopping condition was proved to be too low.

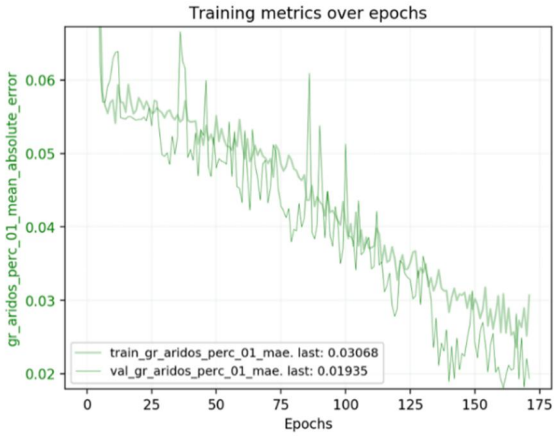

Fig. 9.53: Results on experiment 607 after 172 epochs

- **Experiment 621,** using similar network set up than in experiment 607 (3 bands No augm. Densenet121.Pretrained in Imagenet. Original size -> 128-> 114px. L1 loss). At the epoch 1000 it was proven that the network converges.

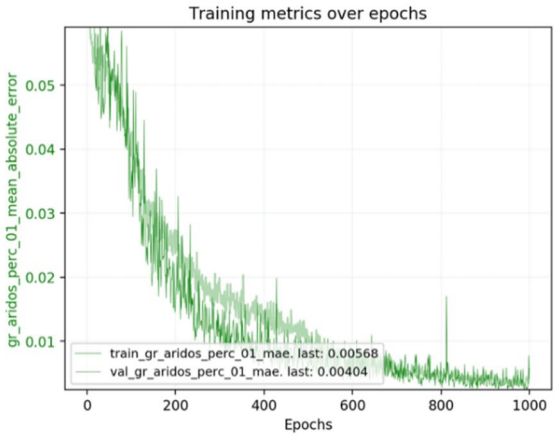

Fig. 9.54: Results on experiment 621 after 1000 epochs

- **Experiment 624** (3bands No augm. Densenet121.Pretrained on Imagenet. Orig size -> 128-> 114px. L2 loss): At the epoch 1000 it was proven that the network converges

  In experiment 621 good results with the L1 loss function (minimization of the absolute error between predicted and true values) were obtained. Experiment 624 proposed replacing L1 by L2 (minimization of the mean square error between predicted and true values). In regression problems, L2 can lead to great instabilities during the training process. However, in experiment 624 the curves evolution suggested that this is not the case, and the obtained errors were even lower than those obtained through the L1 loss.

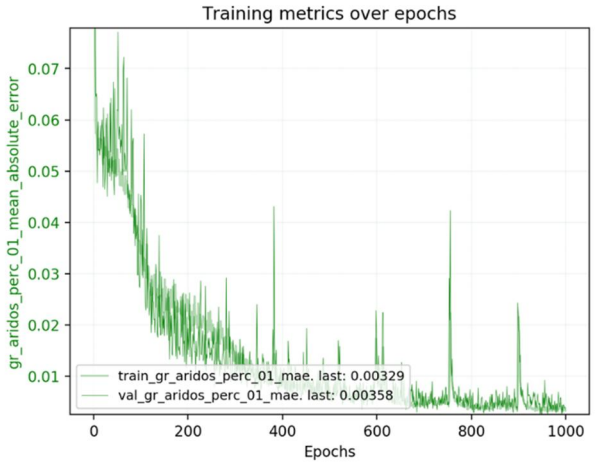

Fig. 9.55: Results on experiment 624 after 1000 epochs

New method proposal for sterile quantification in scrap deliveries.

9.4.5 Results on laboratory set up

The main objective of the laboratory stage was to well understand the real capabilities of combining DeepLearning methodologies with hyperspectral technologies to develop an automatic tool for sterile quantity estimator in ferrous scraps. In order to propose an industrial solution, it is necessary to identify or develop the optimal network architecture through the most convenient images acquisition and data processing at a defined wavelength range. So that, at this stage of research, it is crucial to keep the approach as simple as possible to ensure to master the technology, in well controlled conditions, before going to "demanding" industrial conditions.

The work done in the laboratory phase can be summarized as follow:

- A simple laboratory set up was built for easily controlling all experiment aspects
- The selected sensor for image acquisition corresponds with a linear hyperspectral camera in the Visible Near Infrared range (400 - 1000nm) with a high spectral resolution
- Around 500 different samples composed by a mixture of E40 with common oxides compounds (SiO_2, Fe_2O_3, CaO, Al_2O_3) were manually prepared for generating a large dataset.
- DeepLearning Network architecture development, which can be described as follow:
    - Data input based on an RGB model pre-trained from Imagenet (Selection of three unique bands at 428,3 nm, at 614,1 nm and at 806,6 nm).
    - Network architecture (backbone) based on DenseNet 121
    - Output layers composed by two branches aiming to perform multitasks analysis

Once defined the laboratory set up and the network structure, different experiments were conducted varying the value of several main network hyperparameters. Experiment 621 offered the best results regarding MAE and MAPE (as described in section 9.3.2,MAE and MAPE are used as network results assessment method).

Fig. 9.56 shows the training curves of all the objective functions mentioned, in which the semi-transparent thick lines correspond to the training set and the solid thin lines to the validation set (one sample by epoch is represented):

- In green: MAE values for sterile ratio estimation over the total weight of material in the sample (left), absolute weight of sterile in the sample (middle) and absolute scrap weight in the sample (right).
- In red: MAPE values for the same estimated quantities.
- In blue: value of the compound error function.

New method proposal for sterile quantification in scrap deliveries.

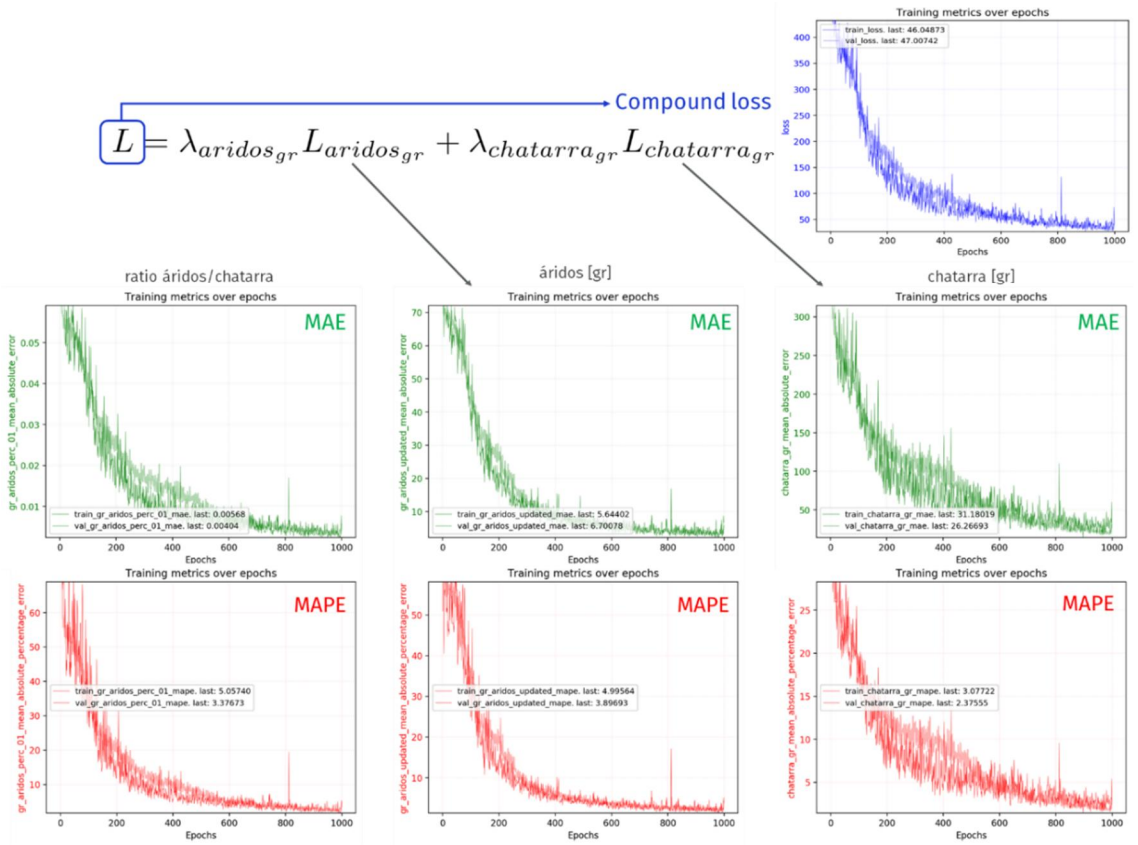

Fig. 9.56: exp 621 train-test curves

It should be noted that (as expected) the network architecture consisting of three branches obtained consistent and very robust results with respect to the variations in these hyperparameters.

For the network architecture design and the hyperparameters setup proposed, graphs and figures corresponding to L1 loss function are shown. After results analysis, it is observed how the error converges to very low values by means of a decreasing exponential curve. Also, there is no significant gap between both curves, so it can be concluded that there is no overfitting or overtraining, meaning that the model generalizes properly.

Fig. 9.57, Fig. 9.58, Fig. 9.59 and Fig. 9.60 depict the numerical output of the model (MAE and MAPE) for training and test datasets:

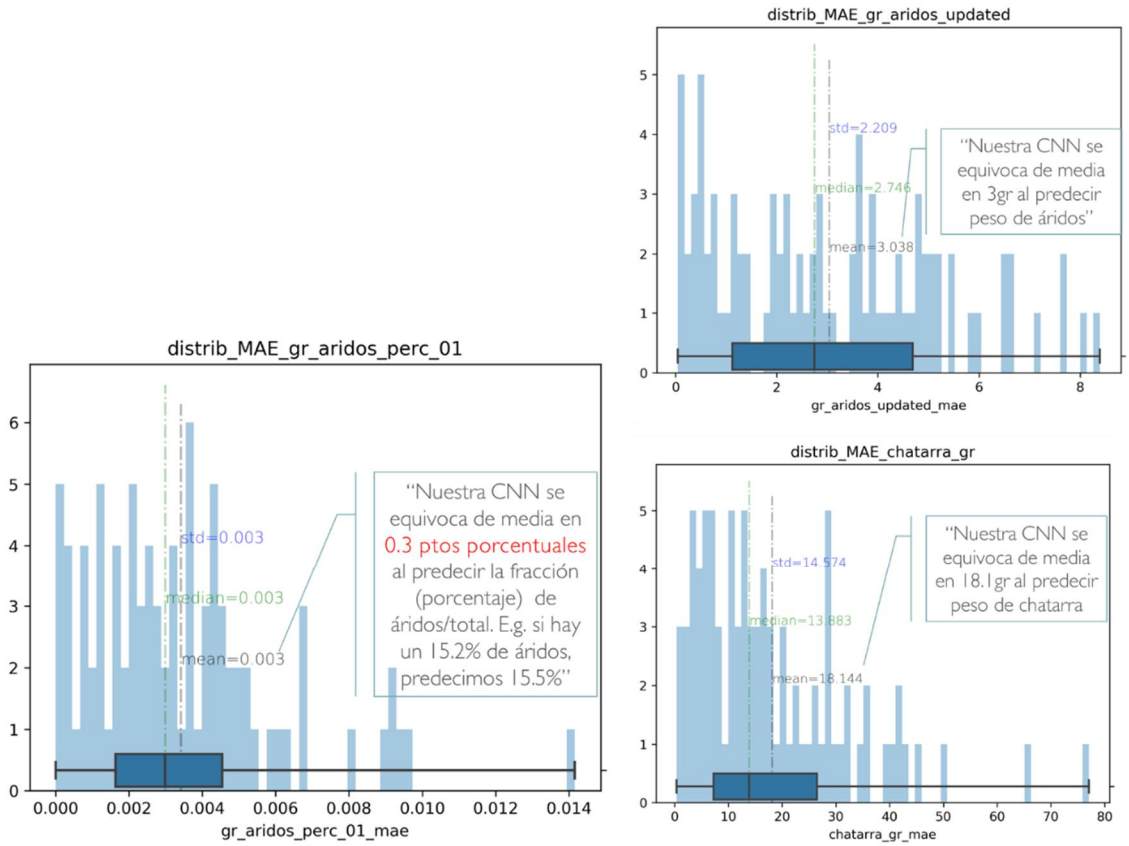

Fig. 9.57: exp 621 MAE test set

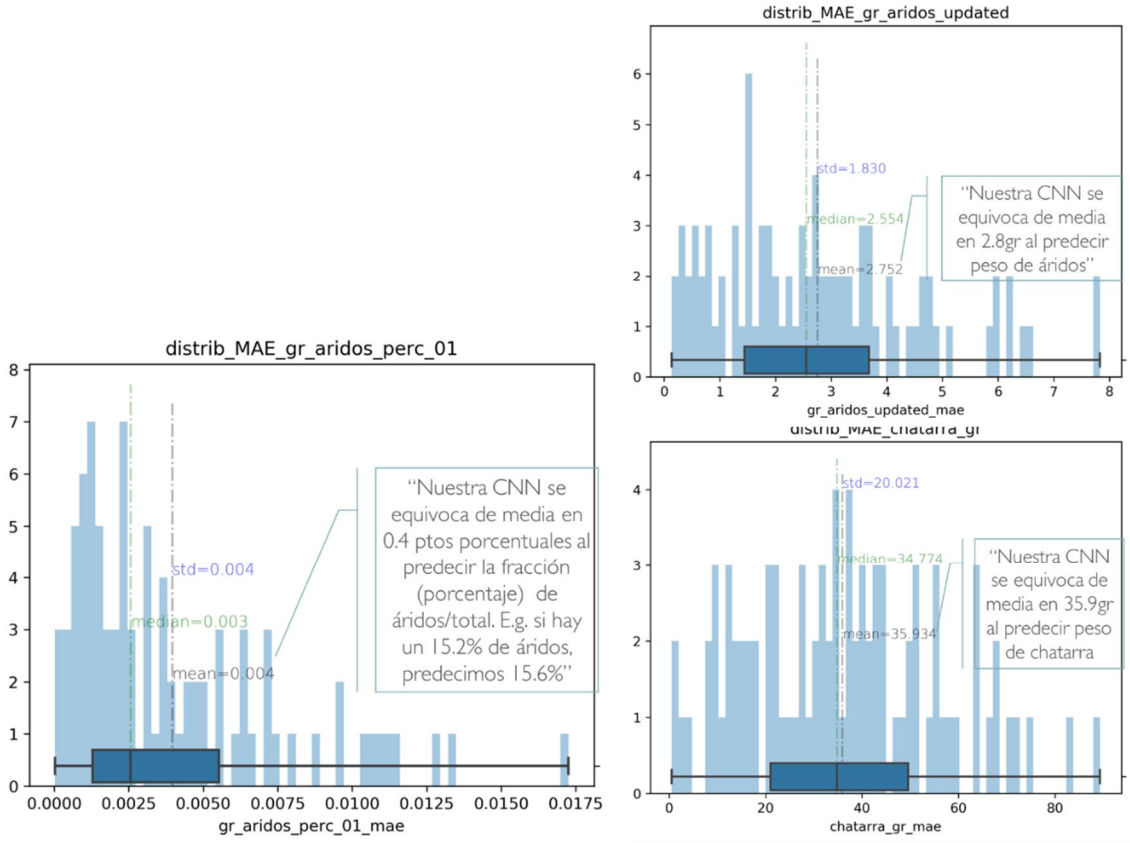

Fig. 9.58: exp 621 MAE train set

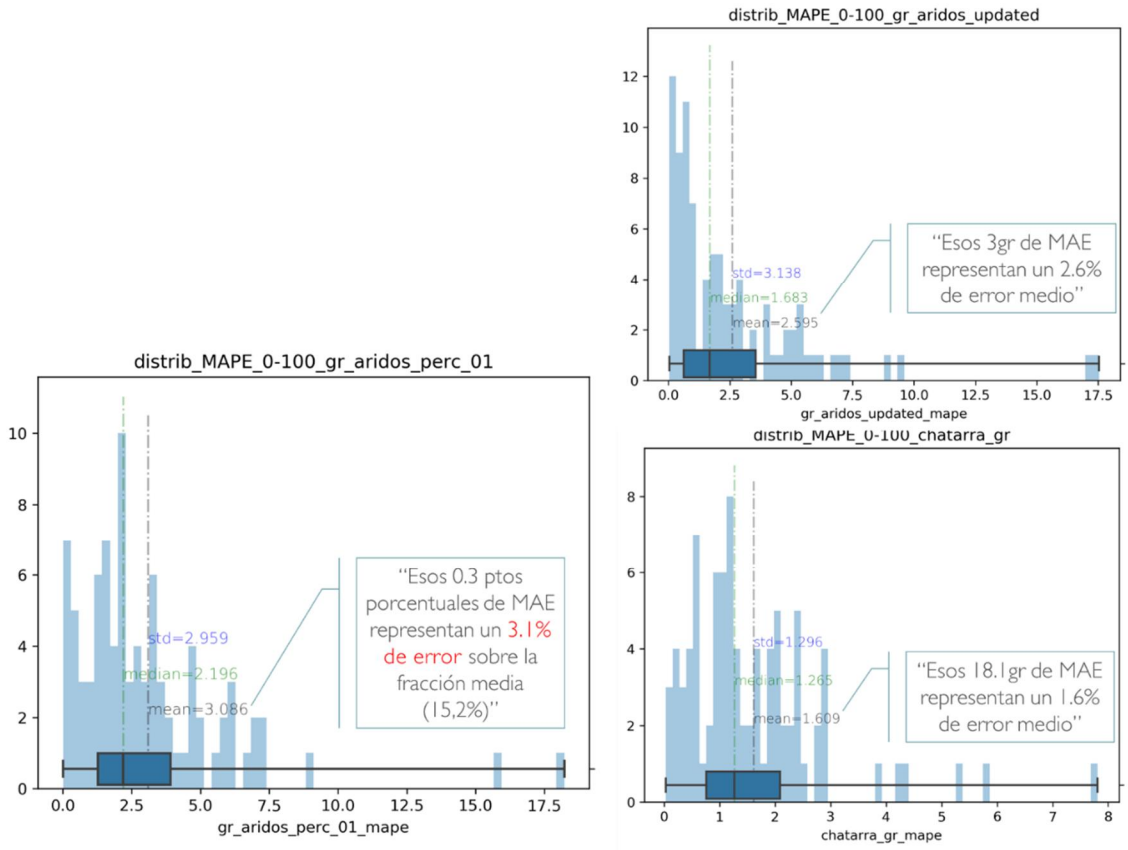

Fig. 9.59: Exp 621 MAPE test set

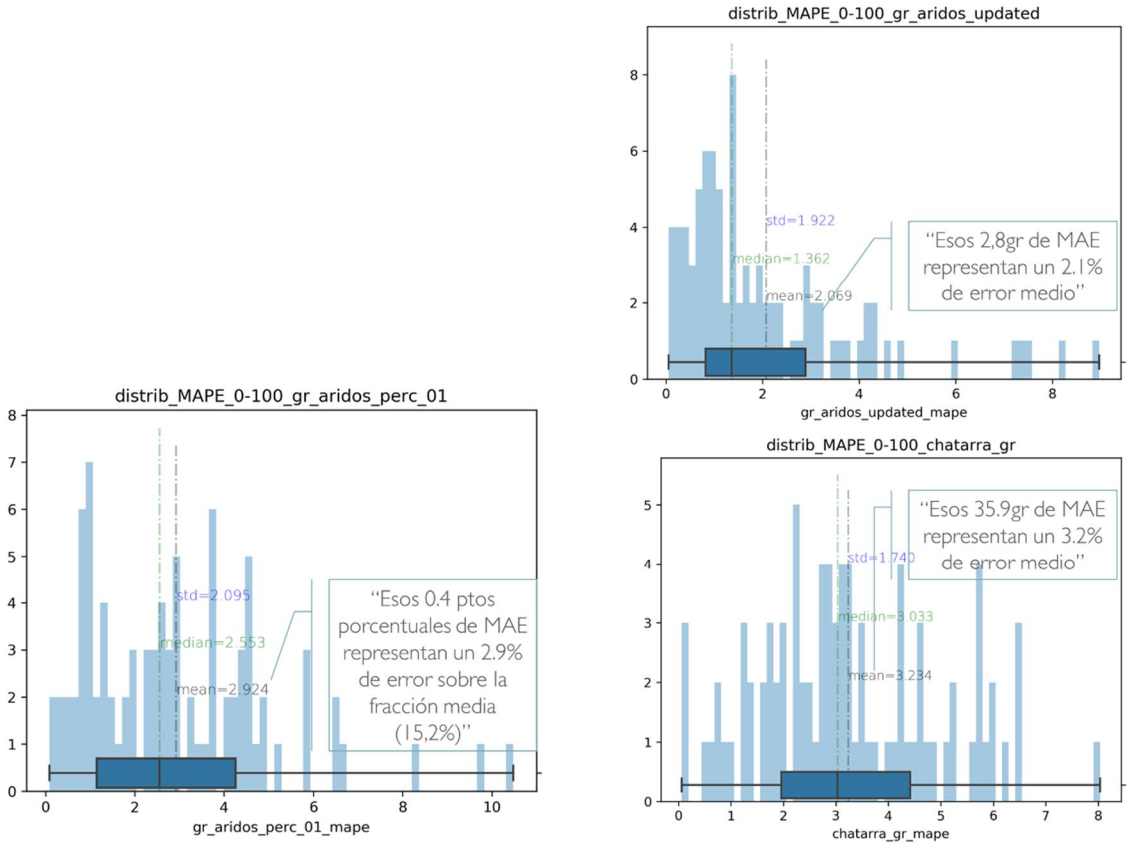

Fig. 9.60: Exp 621 MAPE train set

New method proposal for sterile quantification in scrap deliveries.

After analyzing the results, the following conclusions are reached:

- The average error made by the proposed Deep model is 0,3 %in the aggregate / total weight fraction prediction for the test dataset (this value is even lower for the training set, reaching 0,4%). It is important to highlight that the baseline showed an average error close to 5,8% when predicting always the mean value. Considering absolute quantities, the average absolute error corresponds to 3,0 gr for aggregates and 18,1 gr for metal scrap for the case of the test data set.
- Those absolute errors (MAE) corresponds with a relative error (MAPE) of 3,1% for the case of the test dataset in the aggregate percentage ratio prediction and 2,9% for the validation dataset. It represents errors of 2,6% and 1,6% in the estimation of absolute aggregate and scrap weights respectively.

These results proved that the proposed approach can be considered as valid solution for solving this problem.

New method proposal for sterile quantification in scrap deliveries.

9.4.6 Conclusions on laboratory set up

The aim of the work presented in this section was to propose the necessary laboratory experiments that will allow demonstrating the applicability of the joint approach of hyperspectral imaging and data classification through DeepLearning.

One of the critical points to achieve this objective was to design of a hyperspectral images acquisition station under very controlled laboratory conditions. The core element of sample acquiring station is a hyperspectral sensor composed by a spectrometer in the VNIR range (Specim V10_04204) combined with a scientific CMOS camera (JAI-TM-1327GE).

Using the laboratory set up, around 500 samples were manually prepared (mixing E40 with SiO_2, Fe_2O_3, CaO and Al_2O_3) a captured with the acquiring station.

Then, using the DenseNet network architecture proposed in the ILSVRC challenge, and after several experiments with different modifications in the network architecture in laboratory conditions, the following architecture designed for sterile quantification purpose is proposed:

- A DenseNet121 network was used a backbone
- Adaptation of the first convolutional layer of the network to support 1040 channel inputs instead of the 3 commonly used for RGB images.
- Last layers adaptation to a regression problem for a single output branch; Removal of the dense layer of 1000 neurons and the output Softmax layer and replacement by a 50 neurons dense layer with a ReLU activation function and a new single neuron layer without activation function.

The results obtained in laboratory conditions can be summarized as follow:

- The average error made by the proposed Deep model is 0,3% and 0,4% in the aggregate / total weight fraction prediction for the test and training dataset respectively. These results improve drastically the baseline selected for performance assessment based on predicting always the mean value.
- Considering absolute quantities, the average absolute error corresponds to 3,0 gr for aggregates and 18,1 gr for metal scrap for the case of the test data set.
- With the proposed design, the new sterile estimator based on Hyperspectral imaging is generating errors of 2,6% and 1,6% in the estimation of absolute aggregate and scrap weights respectively.

These results proved that the proposed approach can be considered as valid solution for solving this problem.

New method proposal for sterile quantification in scrap deliveries.

9.5 Sterile estimator development at Industrial scale

In previous sections it was proved that feeding the proper DeepLearning architecture with enough visual information of scrap / sterile mixtures, allow estimating the weight ratio between them.

However, this solution has been developed in laboratory conditions and cannot be used directly to solve the identified problematic, mainly because

- In industrial conditions, dozens of daily trucks are delivering scrap to the scrap yard. It is not technically feasible to move all the scrap that enters the factory in front of a linear sensor for building 2D images, so it is necessary to change the approach to image acquisition towards a matrix sensor (spectral resolution 2 orders of smaller magnitude than linear sensors)
- The acquired samples in laboratory conditions were not real; neither the scrap material used has same morphology than the real scrap materials, nor the sterile compound chemistry are the same.
- The sterile is not heterogeneously distributed is the scrap delivery; some materials present dirt stick to the surface, the material rust varies from one deliver to another, in some cases visual appearance of scrap is similar to sterile. Some examples of these effects are shown in Fig. 9.61

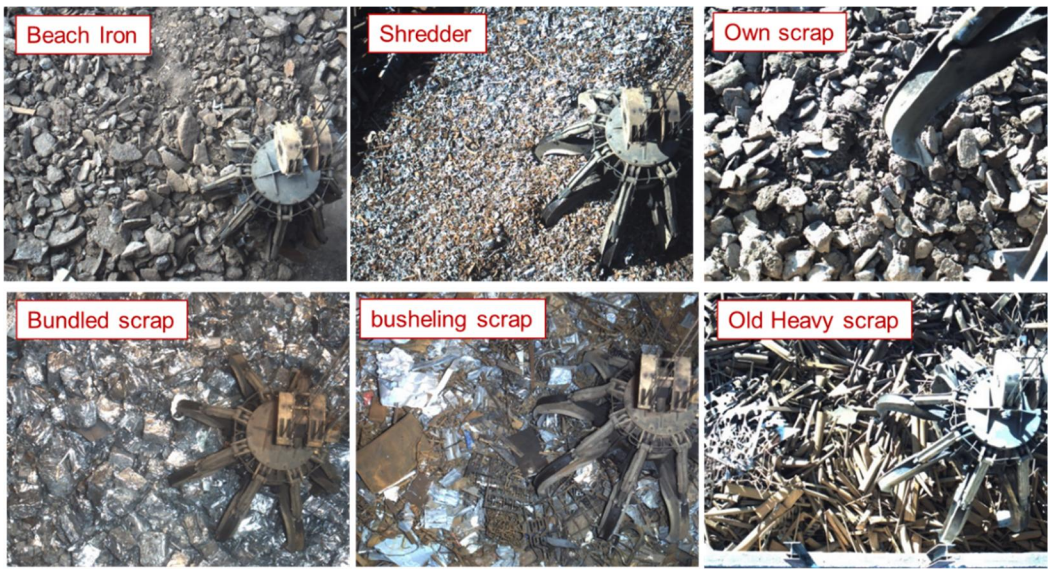

Fig. 9.61: Examples of scrap materials delivered to the scrap yard

Laboratory work was a crucial step to develop a valid solution for industrial conditions, however, an intermediate step is needed to master these industrial conditions before generalizing the solution.

In this sense, as described in section 9.1, scrap cleaning machines can be used for checking, truck by truck, the quantity of sterile present in each scrap deliver to the scrap yard.

New method proposal for sterile quantification in scrap deliveries.

By installing the new system developed in laboratory in a scrap cleaning machine, almost all required data for adapting the new system to industrial conditions is available (in green in Fig. 9.62); the total amount of sterile contained in the truck, the total material weight contained in the truck and the network architecture proposed in laboratory conditions.

The only missing information to complete the tuning and the final training of the network (in red in Fig. 9.62) is the hyperspectral images data set using the matricial sensor

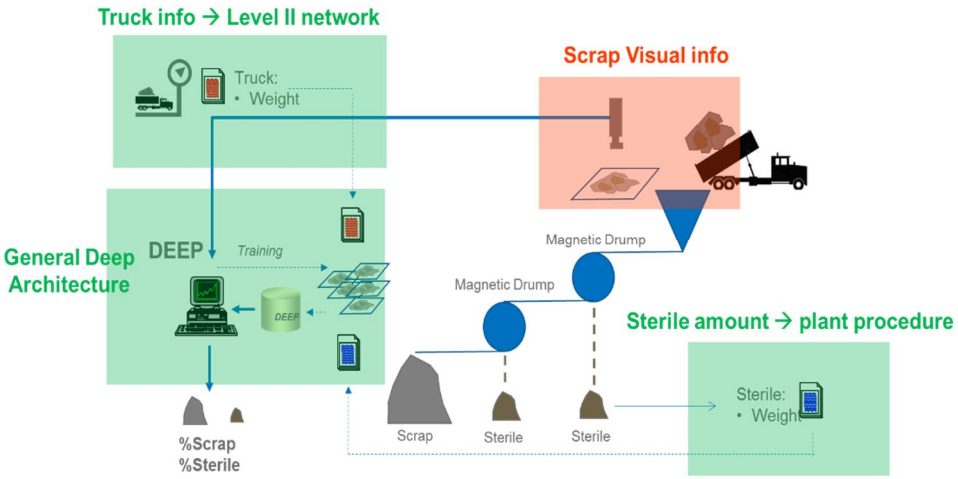

Fig. 9.62: Proposed approach for industrial implementation of sterile quantity estimator in scrap

The methodology proposed in Fig. 9.62 will allow creating a new image dataset composed by:

- Trucks discharging hyperspectral images
- Scrap amount by truck
- Sterile amount by truck

The new dataset can be used for network hyperparameters optimization and for elaborating the industrial model valid only for the scrap type feeding the cleaning machine

Adapt the model to other scrap grades to, later on, generalize this network to other types of scrap types will be also required in the solution industrialization phase.

New method proposal for sterile quantification in scrap deliveries.

9.5.1 Semi-Industrial preliminary tests

Although the final development of an industrial solution for estimating the quantity of sterile materials in the scrap deliveries to steelmaking scrap yards is not included in the scope of this thesis, this work should pose the general technical requirements of the industrial concept for allowing to continue with this work in a sort future

9.5.1.1 Camera selection:

To apply hyperspectral imaging to industrial environment, for extracting useful scene information, represents the main challenge of this research work. This makes sensor selection one of the critical tasks in the proposed development. On the other hand, the system proposed for the final industrial application must be based on a matricial sensor that captures the scene of the scrap unloading in a static way. This requirement presents as key disadvantage the poor spectral resolution offered by matricial hyperspectral sensors

Due to this, the research work described in section 9.3.1.1, was devoted to determine whether the commercially available hyperspectral matricial sensors, in both spectral range and sensibility, were suitable for the proposed application, as well as to select the most convenient sensor for the purpose of this investigation.

Based on the findings reported in section 9.3.1.1, the sensor chosen was Ximea´s model MQ022HG-IM-SM4X4-VIS, which offers 16 spectral bands in the 470-630 nm range

9.5.1.2 System installation:

To move the development phase from laboratory conditions to real industrial conditions, it is necessary to adapt the laboratory solution to the new industrial boundary conditions in a very controlled manner. In order to do it scrap cleaning machine was identify as the ideal industrial facility. Fig. 9.63 proposed a basic Lay-Out of the ideal semi-industrial set up.

According to the proposed Layout, the camera is installed on an elevated platform several meters above the trucks discharging hopper. Also, and considering that the spectral images require occupy excessive memory resources on the PC, an electrical control panel is installed at Hopper level. This panel is composed be 2 buttons (acquisition ON and acquisition OFF) that generate the start and end triggers of image capturing. These buttons must be operated by the truck driver before starting the download (Start button) and after finishing the operation Stop button).

New method proposal for sterile quantification in scrap deliveries.

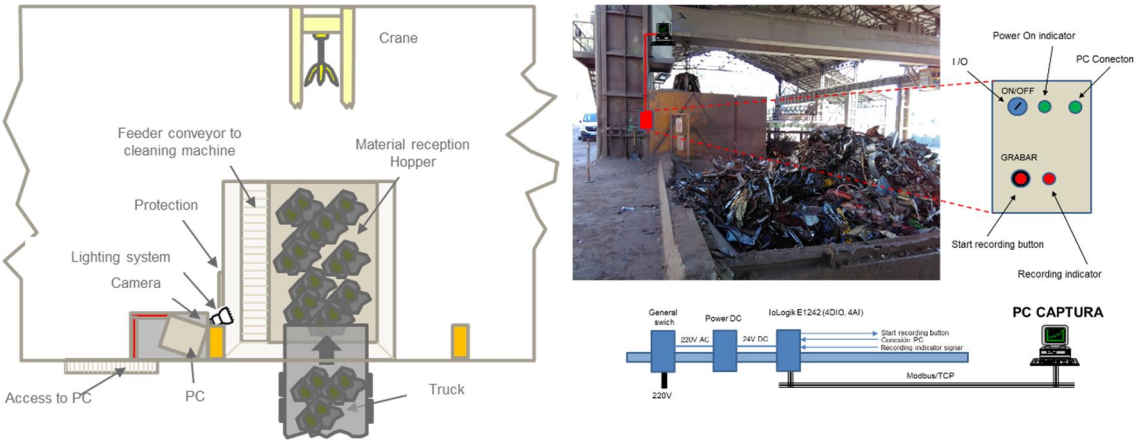

Fig. 9.63: Proposed semi-industrial system lay-out

This layout, together with the start/stop procedure, will ensure that the generated image sequence dataset corresponds only to discrete scrap downloads, and therefore, it can be linked to the truck ID data (scrap and sterile weights) available in factory databases.

9.5.1.3 Environmental conditions control (lighting and calibration):

In order to evaluate the scene changes in a non-controlled environment (industrial scrap yard), the selected sensor was installed in one cleaning machine at one ArcelorMittal Steelshop in Spain. Fig. 9.64 depicts the camera installation location:

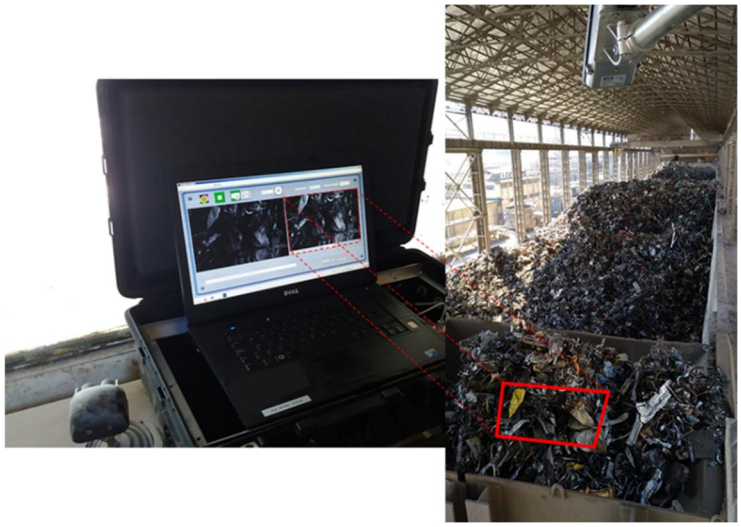

Fig. 9.64: Region of Interest (ROI) of camera over the cleaning machine feeding conveyor

In the case of scrap yard, the facility illumination system is based on different type of lamps distributed for the whole area, just for ensuring enough light for operating the machinery in safe conditions. This causes that the incident radiance over the sample changes along the day depending, not only on the day/night periods, but also due to sunny/cloudy days.

New method proposal for sterile quantification in scrap deliveries.

The lighting changes effects on acquired images are demonstrated in the 24 hours capturing campaign shown in Fig. 9.65:

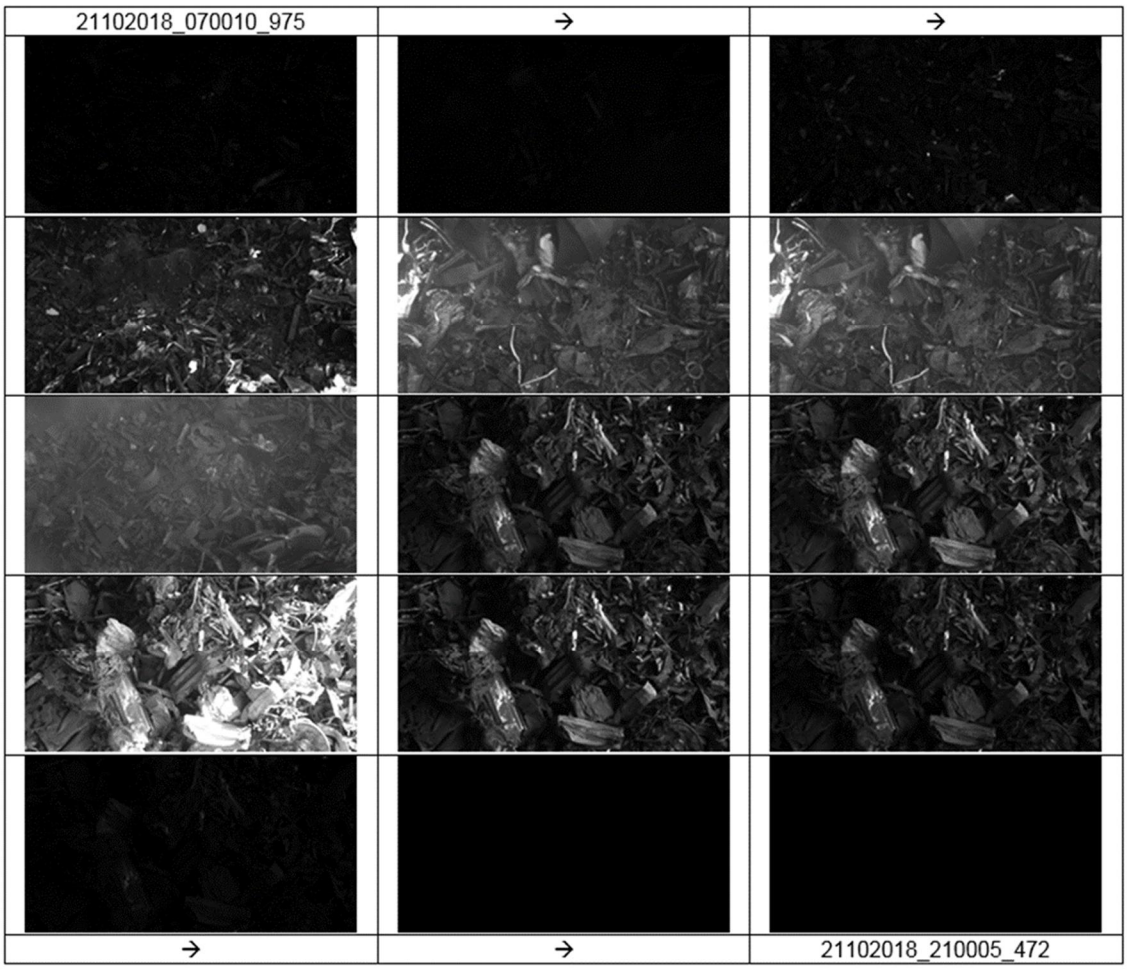

Fig. 9.65: Day light influence on hyperspectral images

Additionally, a calibration solution based on Spectralon material (apart for the initial calibration) is not applicable any more due to the quick degradation of the patterns in such aggressive environment.

The proposed calibration methodologies for the new industrial conditions are:

- Dark current calibration: same procedure that the one described in section 8.2.6.1 can be used. The dark current calibration should be done periodically
- Reflectance reference: A fixed white painted pattern should be installed in the camera ROI (between the camera and the scrap discharging hopper) to be used as reference of the image for normalization purposed (as described in section 8.2.6.1)

New method proposal for sterile quantification in scrap deliveries.

9.5.1.4 Dataset composition: Spectral image capture and processing

The most critical difference between the solution developed in laboratory conditions and the solution proposed for industrial conditions is the dataset morphology:

- Laboratory dataset: the dataset is composed by one 2D hyperspectral image (1040 spectral bands) per data (scrap + sterile mixture)
- Industrial dataset: the dataset is composed by a sequence of 2D hyperspectral images (16 spectral bands) per data (scrap + sterile mixture)

Each data in the industrial data set is composed by a sequence of images per each of the 16 spectral chanes. Fig. 9.66 shows the spectral information of one truck discharging operation over the cleaning machine at 638 nm spectral channel:

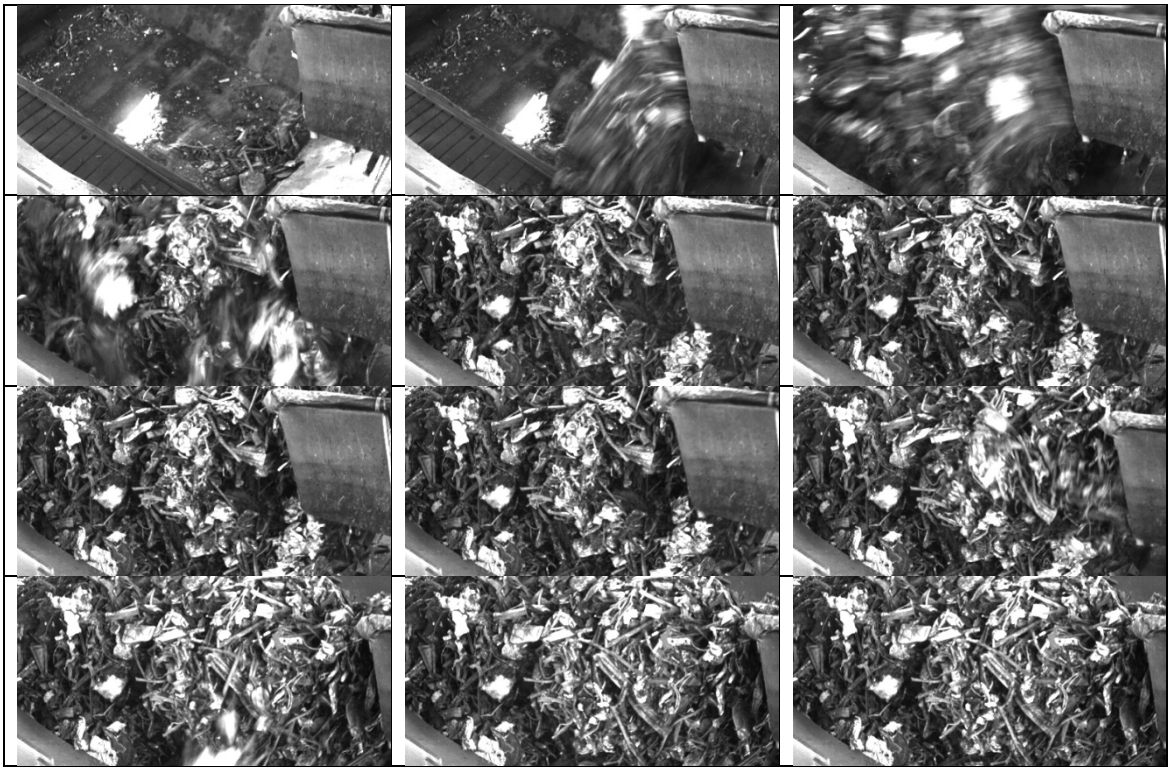

Fig. 9.66 :Scrap discharging sequence acquired at 638 nm

As shown in Fig. 9.66, the scrap/sterile relation that will be reported by the scrap cleaning machine during one dumping has to be related to a great number of images. And all the images in one discharge are linked by a temporal chain, that is, there is some sort of dependence through time between the inputs and the desired output. One of the possible ways of solving this case with Deep Learning is using a Recurrent Neural Network (RNN), which is a kind of Neural Net specifically design for working with sequences of data.

Another additional challenge to be addressed is how the spectral dimension of the captured data will be handled and processed. Samples created for the laboratory tests were recorded using cameras with high spectral resolution (1024 spectral bands). During analysis, the number of channels was reduced to 3 in order to make it faster (load of data and development). The

selected camera to be used in the scrap cleaning machine at ArcelorMittal was a XIMEA SM4X4-VIS that has 16 channels. Several spectral processing approaches can be followed:

- To reduce hyperspectral image to 3 channels by using a classical dimensionality reduction (Principal Component Analysis).
- To make a spectral to RGB conversion of all the spectral data laying in the visible range applying colorimetric techniques. This would imply discarding the spectral information, but it would be optimal from the data-efficiency perspective, as the input would be readily adapted to be fed to a standard classification network backbone pretrained on Imagenet (since the semantics of the 3 channels would be identical for both the pretrained and new data).
- To use a first convolutional layer that reduces the dimensionality to 3 in an optimal way, although this would increase the amount of required training data.

All previous spectral reduction alternatives are posed as potential research lines to be developed after the completion of this thesis.

New method proposal for sterile quantification in scrap deliveries.

9.5.2 Network architecture design for industrial conditions

The spectral nature of the input data and the fact that one sample (i.e. discharge) is defined as a sequence of images rather than just with a unic 2D image are the two main factors that drive and condition the design the deep Convolutional Neural Net (CNN) architecture being trained for the prediction of the scrap/sterile weight relation.

The handling of the spectral data affects primarily to the design of the first layers of the network. Each of the three options mentioned in the previous section requires one particular design element, either as part of the network (e.g. to take 16 channels as input and convert them, via convolution, to 3 channels so as to use a pretrained net, or to 32/64 so as to train it from scratch) or as an out of the network pre-processing step (e.g. an offline process to convert the spectral data to a representation based on the first three eigenvectors given by the PCA algorithm).

As for the temporal dependency, there is no single standard procedure to handle image sequences as input, particularly so for the task of multiple real value regression (following the approach designed in lab tests; try to predict sterile and scrap weights independently and perform a deterministic ratio computation). Most of the existing CNNs working over videos focus on activity classification tasks, and, as was done with the laboratory data. Some potential ideas to be explored are the following:

- Single frame-based predictions have shown to work well for video activity classification (217) using a standard classification net as backbone. This option could be considered as a potential baseline.
- Probably the approach that makes more sense is to use a standard single-image classification network (e.g. Resnet18, Resnet50, Densenet121) as backbone for the extraction of a compact, 1-dimensional representation of each frame, and feed these into a RNN component, such as a GRU (Gated Recurrent Unit (218)) or LSTM (Long-Short Term Memory (219)) layers. The latter would take care of modelling the temporal dependencies and its output would be the base for the two prediction branches. See Fig. 9.67 for a diagram of the envisioned solution.
- There have also been advances in RNN-free architectures for video classification. We will consider the appropriateness of purely convolutional variants such as those in (220), which propose different ways of incorporating the temporal dimension into convolution operations.

New method proposal for sterile quantification in scrap deliveries.

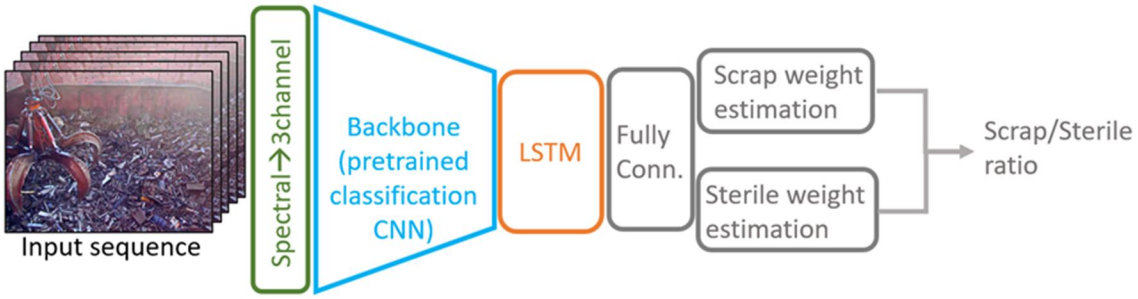

Fig. 9.67: Design of the proposed LSTM-based CNN for hyperspectral image sequence-based sterile/scrap ratio estimation

New method proposal for sterile quantification in scrap deliveries.

9.5.3 Next steps for industrial implementation

The research work of this thesis cannot go further without the involvement of Steelshop technicians since, for the industrial implementation of the solution developed in laboratory conditions, several tasks must be done.

- From the Data Set Generation point of view:
    - Develop and Test Plant Integration
    - Test camera exposure times and software recording capabilities
    - Find solutions to the white reference procedure
    - Test several illumination possibilities
    - Make an image capture validation campaign to ensure Data Set Capture System
- From the Deep Leaning point of view:
    - Complete the recurrent neural network definition and architectures to be tested
    - Start coding the data set loading functions
- Once the Data Set Capture System is working:
    - Record all possible information
    - When a data set of 400 complete discharging samples are recorded, start Deep Leaning parameters fine tuning and architecture adjustment
    - When a data set of 1000 discharging complete sequences are reached use them to start the analysis
    - Continue recording as much as possible

New method proposal for sterile quantification in scrap deliveries.

9.6 Conclusions

Nowadays, it can be usually found that many scrap suppliers do not meet the minimum requirements defined in standard scrap specifications (Mixture of materials with different qualities, inadequate dimensions, Forbidden elements, contamination with other elements such as earth, slag or grease). However, since the complexity of ferrous materials recycling processes is clear, that non-compliance (if they occur within reasonable limits) can be assumed. Nevertheless, the presence of sterile materials mixed with scrap penalizes twice to steelmakers:

- Dirt is paid as scrap when in the purchasing process (100% of the material is assumed to be Iron)
- Nonferrous materials contained in scrap negatively affect to the EAF process performance due to a worsening in the material Value In Use.

For steelmakers is crucial to closely control the quantity of nonferrous materials contained in each scrap delivery to the scrap yard, in order to do scrap suppliers quality tracking and optimize the two above-mentioned penalties

For decades, the most extended practice for sterile quantification consists on the visual inspection of each scrap delivery. Then a very experienced scrap yard operator, based on subjective criteria, estimates the quantity of sterile present as well as other possible non-compliance with the scrap quality specifications. Subsequently the scrap yard operator applies an economic penalization the supplied. It is clear that this methodology strongly depends on the operators skills and so that, it is far from been an optimal procedure.

In the 21st century, with the explosion of complex artificial intelligence algorithms, coupled with the drastic increase in computational capabilities and the democratization of complex vision technologies, new methods can be proposed for estimating sterile / scrap ratio in scrap deliveries.

In the case of sterile estimation, and since the scrap quantity assessment is done by visual appreciation, it is clear that machine vision techniques should extract some features in scrap material to be used for material quality analysis. In this sense, in Machine Learning there are many algorithms which helps discover the underlying physical process under the available data. However, the choice of an algorithm depends on the characteristics of the data. In order to extract as much information as possible, Hyperspectral cameras seems to be the most suitable sensor for this purpose.

The aim of the work presented in this chapter was to propose the necessary laboratory experiments that will allow to, firstly demonstrate the applicability of the joint approach of hyperspectral imaging and data classification through DeepLearning, and secondly, establish the basic requirements of a system that must subsequently be functional in extreme industrial conditions

New method proposal for sterile quantification in scrap deliveries.

One of the critical points to achieve the objectives was to design of a hyperspectral images acquisition station under very controlled laboratory conditions. The main criteria used for the design of the capture station are listed below:

- Necessary to extract as much spectral information as possible; High linear spectral resolution sensor using linear cameras. The sensor is composed by a spectrometer in the VNIR range (Specim V10_04204) combined with a scientific CMOS camera (JAI-TM-1327GE).
- A 2D image is needed; A close control push broom system for sample displacements in front of the camera
- Well-known Lighting system; to ensure the right calibration procedures
- Camera aberrations control; Dark current and White current measuring procedure
- ROI on Samples clearly defined; drawers for sterile / scrap mixes
- Dedicated Software for acquiring, pre-processing, post-processing and data analysis

After developing the laboratory set up, around 500 samples were manually prepared, mixing E40 with 4 basic sterile compounds (SiO_2, Fe oxides, CaO, Al_2O_3).

On the other hand, the ILSVRC challenge has opened infinite options for developing classification / Regression models for image understanding. Taking the ILSVRC challenge as starting point of this research, and after several experiments with different DeepLearning network architectures in laboratory conditions, the following architecture designed for sterile quantification purpose is proposed:

- A DenseNet121 network was used a backbone
- Adaptation of the first convolutional layer of the network to support 1040 channel inputs instead of the 3 commonly used for RGB images.
- Last layers adaptation to a regression problem for a single output branch; Removal of the dense layer of 1000 neurons and the output Softmax layer and replacement by a 50 neurons dense layer with a ReLU activation function and a new single neuron layer without activation function.

The results obtained in laboratory conditions can be summarized as follow:

- The average error made by the proposed Deep model is 0,3% and 0,4% in the aggregate / total weight fraction prediction for the test and training dataset respectively. These results improve drastically the baseline selected for performance assessment based on predicting always the mean value.
- Considering absolute quantities, the average absolute error corresponds to 3,0 gr for aggregates and 18,1 gr for metal scrap for the case of the test data set.
- With the proposed design, the new sterile estimator based on Hyperspectral imaging is generating errors of 2,6% and 1,6% in the estimation of absolute aggregate and scrap weights respectively.

New method proposal for sterile quantification in scrap deliveries.

These results proved that the proposed approach can be considered as valid solution for solving this problem. However, it is worth mentioning that:

- The reported errors were obtained without performing a thorough network hyperparameter optimization, so there may be some room for improvement.
- The results have been obtained through pre-trained models and using three unique bands of the spectrum (since only 500 samples were available), it is also worth mentioning that, when larger volumes of data are available, the whole spectral information available in hyperspectral images should be exploited.

Once the initial analysis with the laboratory data has been concluded, the next step is to gather real data. The industrial scenario raises a number of challenges that need been addressed; Image sequences as input, Spectral image acquisition and processing in industrial conditions and new network (RNN)architectures designs.

In this chapter, the workflow for industrially implementation the solution developed in laboratory has been also proposed.

10 Conclusions and future research lines

In this concluding chapter the final remarks on the work done are presented. This chapter also proposes new potential research lines that could be opened to continue with from the findings reached.

10.1 Conclusions

Before presenting the final conclusions drawn from the findings of this research, the study of the steelmaking sector and its state-of-the-art processing techniques has raised the following general points, which may be noted:

- Around 85% of the total costs incurred by the EAF plant are associated with the Steelshop activities, and the ferrous scrap can represent up to 60% of the total production costs.
- Currently, Europe, NAFTA, Africa and most of the Middle East are heavily dependent on scrap and rely on EAF technology for its processing. Additionally, some authors have forecast a significant rise in EAF production in the medium and long-term, linked to the fact that the integral steelmaking route is increasing average scrap consumption, in response to evident environmental pressures. In consequence, steelmakers are investing immense effort in the development of new technologies that may be used with great precision to analyze the content of ferrous raw materials.

Ferrous scrap products are extremely complex materials. In addition to the ferrous matrix of iron and other metallic elements, scrap also contains coatings, dirt, sterile, foreign materials (plastics, wood, glass) and oxidized layers. If the overall EAF process is to be optimized, detailed information will be needed on the quality of the raw material inputs

In the literature, many research works have studied scrap pre-processing technologies and future availability and access to scrap materials, as feasible improvements to the steelmaking processes. However, although non-quality of scrap strongly influences the variable process costs of steelmaking, scientific papers that propose industrial methods for the characterization of scrap remain scarce.

In this sense, if the material is properly characterized, there are tools (Specifications and standard classifications for ferrous metal scrap or Total Cost of Ownership) that the scrap recycling center can use for the definition of scrap purchasing and management strategies.

If those approaches are to be applied, then the most critical point is the need for tools/methods that can quickly and efficiently provide information (chemical composition, distribution, physical morphology, material degradation, presence of moisture, ...) on the ferrous materials whenever they are to be used.

- **In relation to sterile matter:**

  Steel treatment techniques within the recycling sector are at present quite efficient. However, each of those different technologies was developed and optimized to address very specific problems associated with material morphologies. The processing of iron scrap is much more complex than merely selecting one of the available technologies.

  A potential steel-scrap treatment scheme may consist of an initial size reduction process, followed by several cleansing and separation processes, to upgrade the ferrous raw material for use in the steelmaking processes.

- **In relation to sterile characterization:**

  The various technologies that are currently used in steelmaking for the characterization of ferrous materials can be grouped into four main categories: industrial methods, mathematical methods, chemical analyses, and physical analyses. The literature review of this thesis was employed as background material for a set of discussions with 8 different EAF steelmakers on the weaknesses of current methods, based on their actual industrial interest. The topics of most interest to steelmakers were;

  - Scrap Cleaning technologies,
  - Automatic scrap control
  - Methodologies for scrap management optimization
  - Sterile characterization.

As described in the first chapters of the thesis, the presence of sterile in ferrous scrap is the most important factor in non-quality scrap. In view of the current state of the art, the presence of these types of materials mixed with scrap cannot be completely eliminated. It is therefore necessary to develop technologies, so that scrap recycling plants have the tools for their measurement and control. In this doctoral thesis, different approaches have been proposed for both the qualitative and the quantitative control of sterile.

The main pillar for the development of the thesis, as stated in the conclusions, is the characterization of sterile. It has three main research lines: a new empirical method for estimating VIU loss, due to storage degradation; a new method for the chemical

characterization of sterile material in scrap; and, a new method for sterile quantification in scrap deliveries.

This research work is proposing new methods for the characterization of ferrous scraps. As a first step, an analytical approach based on Value In Use (VIU) methodology has been proposed as a general tool for assessing the real value of non-quality scrap. By applying the VIU method, the general equations in (4.5), (4.6) and (4.7) have been proposed.

- **New empirical method for estimating VIU loss due to storage degradation:**

  The atmospheric degradation process of ferrous material has been widely reported in the literature, but it is mainly focused on metallic structure integrity analysis. Degradation processes affect the material quality of ferrous scrap, the main steelmaking raw material, greatly influencing the operative performance of an EAF, which can be noted by applying the Value In Use concept.

  Knowledge of the chemical composition of ferrous materials and their reactions over time will facilitate estimates of the economic penalty attached to any loss of quality in the EAF smelting process for producing steel. However, current methodologies (and only in the case of HBI / DRI materials) include spot sampling and subsequent laboratory analysis with conventional analytical techniques. There are currently no methodologies to conduct these analyses in a quick and easy manner, nor procedures to quantify how the loss in quality will, in both economic and ecological terms, affect the process.

  The material degradation processes of different ferrous scrap materials have been extensively studied in this work, leading to the development of a model for estimating the variations of Fe and iron oxide compounds in the materials throughout their storage period. By grouping ferrous materials into two categories (HBI and ferrous scrap) during the experimental analysis, an analytical procedure for obtaining the VIU loss of the ferrous material, due to the degradation produced by the atmospheric corrosion, has been developed. The equations upon which the procedure is based have been explained in (7.11), (7.12), (7.29) and (7.30)

  The results of the above equations will help to define the purchasing strategies of the scrap recycling center, in terms of material purchasing volumes, considering that a lengthier storage period will result in worse degradation of ferrous material quality at higher processing costs.

- **New method for the chemical characterization of sterile material in scrap:**

  The very varied sources of ferrous scrap mean that the non-ferrous materials contained in scrap materials will also vary. Gathering reliable information on the chemical distribution of the scrap mixtures is therefore a complex procedure. There are moreover other circumstances that increase the dispersion of the sterile and its chemical distribution, such as mixtures of scrap classes and contamination during manipulation, which should be measured to maximize the efficiency of the subsequent

steel manufacturing processes, as well as unscrupulous trading practices where scrap labelled from one source is in fact from various sources.

The standard state-of-the-art procedure for the determination of the chemical composition of sterile materials is based on X-Ray fluorescence spectroscopy. However, XRF technology presents certain limitations for mass analysis whenever huge piles of scraps are characterized; tests need to be performed under laboratory conditions, and tedious sampling and sample preparation is required for spot analyses.

Several well-known spectroscopy techniques and their performance when estimating the chemical composition of foreign material attached to the ferrous scraps have been evaluated in this study under laboratory conditions.

In the case of Raman spectroscopy, well-defined spectra for iron oxides and calcite compounds have been generated, with reasonable sensor exposure times and laser power levels. However, whenever amorphous SiO_2 was present in the samples, the spectral signatures were saturated by the SiO_2 signal.

Tests with hyperspectral spectroscopy have demonstrated that the SWIR sensor (2300-2400 nm) could be used to arrive at rough estimates of iron oxide (Fe_2O_3) levels within sterile samples, while the VIS+NIR sensor offered quantitative information on the presence of CaO in the samples. Spectral information on the presence of silica can be extracted from both ranges (VIS+NIR and SWIR).

FTIR spectroscopy has generated very clear and well-defined spectral absorption signals for individual compounds of CaO and SiO_2. However, in a similar way to the analysis of silica with Raman technology, the iron-oxide signals were completely blocked by the presence of other compounds.

In this thesis, the architecture of a new matrix sensor has been proposed, as well as a methodology for analyzing the nature of the scrap sterile. Having identified the main compounds, the spectral signatures from the right-hand-side spectrometers could be analyzed to identify the spectral signatures.

- **New method for sterile quantification in scrap deliveries:**

Nowadays, the sorting procedures of many scrap metal suppliers fail to meet the minimum requirements defined in standard scrap specifications, in terms of impurities and properly sorted scrap. However, the complexity of ferrous material recycling processes means that non-compliance (if within reasonable limits) is to some extent expected. The presence of sterile materials mixed with scrap penalizes the steelmaker in two ways:

- If 100% of the material is delivered as iron, then the purchasing process applies the same rates for both impurities and scrap.
- Non-ferrous materials contained in scrap negatively affect EAF process performance, due to a worsening of the Total Cost of Ownership (TCO) of the material.

Tight controls over the quantity of non-ferrous materials contained in each scrap delivery are crucial for steelmakers, in order to track the material quality of scrap from suppliers and to mitigate the two above-mentioned penalties

For decades, the most extensive practice for sterile quantification has consisted of a visual inspection of each scrap delivery, in which an experienced operator at the scrap yard arrives at an estimate based on subjective criteria of the quantity of sterile that is present, as well as other possible issues of non-compliance with the scrap quality specifications. Subsequently the scrap recycling center will adjust the rate per ton paid to the supplier. It is far from the most optimal procedure, as it clearly depends on operator expertise alone.

In the 21st century, the multiplication of complex artificial intelligence algorithms, coupled with the drastic increase in computational capabilities, and the development of vision-based analytical chemistry all offer new methods that can be proposed for estimating the sterile/scrap ratio in scrap deliveries.

The aim of this section of the thesis is to set out the necessary laboratory experiments that will firstly demonstrate the applicability of the joint approach of hyperspectral imaging and data classification through DeepLearning, and secondly, that will establish the basic requirements of a system that must subsequently be functional under extreme industrial conditions

The analytical method, mastered in a laboratory set up under controlled conditions, has served to analyze ±500 samples composed of a mixture of E40 with 4 basic sterile compounds (SiO_2, Fe oxides, CaO, Al_2O_3).

Taking the ILSVRC challenge as the starting point of this research, a valid processing architecture has been designed for sterile quantification, following several experiments with different DeepLearning network architectures under laboratory conditions.

The results have shown that the proposed laboratory set up is a valid method for automatic estimation of the quantity of sterile materials mixed in with scrap, which could be up-scaled for an industrial application.

Certain assumptions must nevertheless change, when moving from the laboratory to an industrial context (outdoor systems, machine activity levels, dust, temperature variations, vibration…): sensors based on linear technology are no longer applicable. The system proposed for the final industrial application will be based on a matrix sensor that performs static monitoring of the site where the scrap is unloaded (so that the Push-Broom effect, easily generated under laboratory conditions, will not occur).

The main challenge of the industrial proposal was the spectral resolution, as the matrix sensor has a much lower resolution than the linear sensors. Bearing in mind that differentiation between steel and sterile will generally be clearer between a spectral range 450 and 650 nm, the most suitable spectral range had to be defined for the proposed approach.

A final proposal is the industrial adaption of the DeepLearning architecture, the validity of which has been proven under laboratory conditions.

The findings reached in the research presented in this thesis have resulted in three innovative methodologies for characterizing the sterile that is present in the scrap materials. With the detailed information gathered through the proper application of those methodologies, strategies will be developed for the optimization of scrap purchasing and the EAF smelting process.

.

10.2 Original contributions and future steps

Within the scope of this doctoral thesis, and based on the feedback from 8 steelmaking companies, three new methodologies for characterizing sterile present in scrap materials have been developed:

1. None of the companies reported methods for quantifying the degradation of materials while in storage. In this thesis, **an empirical model for estimating VIU losses due to storage degradation** has been proposed. The equations from the model can be applied, both to analyze the degradation in material quality and to estimate the economic penalties.

   The new model is also useful for spot analysis of stocked material at the scrap recycling center. Nevertheless, the integration of this model with other models for defining scrap purchasing strategies would result in a highly valuable tool for optimizing the TCO scrap mix at the recycling center.

2. Chemical characterization of the sterile content of scrap material has been restricted to spot analysis under laboratory conditions. Three spectroscopy technologies for facilitating onsite analysis of sterile scrap were investigated: Raman scattering, Hyperspectral imaging, and FTIR. In this research work, light has been shed on the limitations of these **technologies and their efficiency at performing sterile characterization**. With that knowledge, the architecture of a new sensor has been integrated within each of the three new technologies, in addition to the spectra analysis methodology workflow.

   The next step in this research activity will be to prepare a portable analytical device incorporating the various spectrographs, with which it has been demonstrated that relevant chemical information can be extracted from the sample of sterile.

   New processing algorithms for extracting quantitative information from the portable analytical device are still under development and will need to be tested.

3. Last but not least, a **new tool for sterile quantification in scrap deliveries** has been developed. It is relevant, because it moves beyond current practice, which is dependent on the subjective expertise of trained operators whose estimates of the sterile quantity in each scrap delivery depend on a visual inspection.

   Throughout the laboratory phase of this research, a deep-learning architecture applied to the results of hyperspectral imaging has demonstrated that discrimination between ferrous scrap and sterile material in terms of weight fractions is a feasible option.

   However, work on adapting the tool developed in the laboratory and the production of a portable analytical device for use in industry has yet to be completed. An industrial system will be required to continue with the proposed development, so an intermediate step at a theoretical level is proposed in these conclusions. It will involve the redesign of the network architecture to adapt the 2D static input data at a high

spectral resolution to a multi-image input. The image sequence will consist of a recently discharged scrap pile following delivery that will be processed together with data from image recording devices installed within a scrap cleaning system to generate the dataset (images, scrap weight and sterile weight) that will be required for training the new network architecture.

10.3 Published work

The following scientific papers are outcomes of this thesis:

1) A. Vicente, I. Macaya, J. A. Sainz, M. Linares, A. Picon, J. A. Arteche. New sensor for Electric Arc Furnaces arc stability control. 7th international congress on science and technology of steelmaking (2018). Venice – Italy.
2) A. Vicente, I. Macaya, J. A. Sainz, M. Linares, A. Picon, J. A. Arteche. Magnetic field-based arc stability sensor for electric arc furnaces. Measurement 151 (2020) 107134
3) A. Vicente, E. Barco, A.Picon. New method for estimating economic penalties on Hot Briquetted Iron (HBI) due to material degradation during storing. Steelmaking and Ironmaking (2019).
4) A. Vicente, E. Barco, A.Picon. New method for estimating steelmaking economic penalties of Ferrous scraps due to material degradation during storing in scrap yards. Steelmaking and Ironmaking (2020).
5) A. Vicente, I. Macaya, A.Picon, J. A. Arteche.Fast method for slag characterization during ladle furnace steelmaking process based on spectral reflectance. 9th European Slag Conference (2017) Metz – France.
6) A. Picon, A. Vicente, S. Rodriguez-Vaamonde, J. Armentia, J. A. Arteche, I. Macaya. Ladle Furnace Slag Characterization Through Hyperspectral Reflectance Regression Model for Secondary Metallurgy Process Optimization. IEEE Transactions on Industrial Informatics (2017) Vol 14 issue 8 (pag. 3506 – 3512)
7) A. Vicente. Novel tools for scrap yard management in steelmaking facilities. Workshop ESTEP – Green Steel by EAF route (2019) Bergamo – Italy.
8) A. Vicente. New tools for automatic scrap quality assessment in in steelmaking facilities. 1st Jornadas DeepLearning Tecnalia (2019) Derio – Spain

For all papers, the first author contributed with the conceptual design of the research, performing the necessary literature review, analysing the data as well as interpreting the results and drawing the conclusions.

11
Bibliografía

1. ArcelorMittal. http://spain.arcelormittal.com/who-we-are/management.aspx.

2. Worldsteel association. *World Steel in Figures reports from 2000 to 2018.* 2018.

3. Worldsteel. www.Worldsteel.org.

4. InternationalRecycling, Bureau of. *World steel recycling in figures.* 2016.

5. *Long-Term global availability of steel scrap.* al, J. Oda et. 2013, Resources, Conservation and Recycling 81, págs. 81-91.

6. ArcelorMittal. *Global corporate responsibility report 2014.* 2015.

7. ArcelorMittal, Philippe Russo -. *The steel recycling rate.*

8. ISRI. http://www.isri.org.

9. Federación española de la recuperación y el reciclaje. www.recuperacion.org.

10. EUROFER. *Steel's contribution to a low-Carbon Europe 2050; Technical and economic analysis of the sector's CO2 abatement potential.*

11. http://www.eurofer.org/Facts&Figures/Scrap price index.fhtml.

12. ISRI. http://www.isri.org/recycling-industry/commodities-specifications/ferrous-scrap.

13. *Factors Influencing Total Energy Consumption In Arc Furnaces.* Graphtech. Phoenix, Arizona, : s.n., 2001. 59th Electric furnace conference.

14. ArcelorMittal. *Steelmaking: EAF (TCO & Quality training).* s.l. : ArcelorMittal University, 2010.

15. Arana., J. L. *Fundamentos de la fabricacion de acero en EAF.* Bilbao : s.n., 2005 .

16. *Automotive shredder residue (ASR): Reviewing its production from end-of-life vehicles (ELVs) and its recycling, energy or chemicals' valorisation.* I. Vermeulen, J. Van Caneghem, C. Block, J. Baeyens, C. Vandecasteele. Journal of Hazardous Materials. s.n., 2011, pág. 8/27.

17. SEAISI. http://www.seaisi.org .

18. J.-P. Birat, X. Le Coq, P. Russo, E. Gonzales, J.J. Laraudogoitia. *Quality of heavy market scrap: development of new and simple methods for quality assessment and quality improvement* . s.l. : RFCS, 2002 .

19. Russo, Philippe. *Scrap Quality & Steel Recycling: Scrap VIU.* s.l. : ArcelorMittal Unniversity, 2010.

20. Group, Otua. http://www.grupo-otua.com/es/.

21. SteelBenchmaker. *Price Hystori. Tables and charts.* 2019.

22. *Recovery of metals and non-metals from electronic waste by physical and chemical recycling processes.* Kaya, M. 2016, Waste management , Vol. Volume 57, págs. Pages 64-90.

23. *Looking at Shredding Plant Configuration and Its Performance for Developing Shredding Product Stream (An Overview).* Manouchehri, H.R. 2007..

24. Schubert, G. *Aufbereitung metallischer Sekundärrohstoffe.* s.l. : Springer, 1984.

25. Tarantola, A. *The worlds biggest auto shredder eats 450 cars an hour.* 2012.

26. allegro. www. archiwum.allegro.pl.

27. Balasubramanian, A. *Overview of Mineral Processing Methods* Centre for Advanced Studies in Earth Science. Universty of Mysore. 2015*. https://www.911metallurgist.com/blog/primary-crushing.*.

28. Greatwallcrushers. www.greatwallcrushers.com.

29. Shubert, H. *Aufbereitung fester mineralischer Rohstoffe.* s.l. : Leipzig, 1989.

30. METSO. www.metso.com.

31. *Composition and size distributions of particles released in refuse incineration.* Greenberg, R. R., Zoller, W. H., & Gordon, G. E. 5, 1978, Environmental Science & Technology, Vol. 12, págs. 566-573.

32. Trennso-technik. https://www.trennso-technik.de/en/.

33. Cometel. http://www.cometel.net/productos/recycling-4/instalacion-cizallado/separacion-5.

34. Mailx. http://www.mailxmail.com/curso-ciclones/introduccion.

35. Wemco. http://www.innovaenergy.es/two/129254/celdas/de/flotacion/wemco/de/alta/eficiencia/.

36. Hamos. https://www.hamos.com/front_content.php.

37. Hermion. www.hermion.nl.

38. Haith-recycling. www.haith-recycling.com.

39. Eurohansa. www.eurohansa.com.

40. Domenechmaquinaria. www.domenechmaquinaria.com.

41. Flottweg. www.flottweg.com.

42. Navarini. www.navarini.com.

43. Urbar. http://www.urbar.com/mesas-densimetricas-espana/.

44. Yang, D. A New Packed Column Flotation System. s.l. : K. V. S. Sastry., 1988.

45. Bakkermagnetics. https://bakkermagnetics.com/en/recycling-and-metal-separation-systems/.

46. Buntingeurope. https://www.buntingeurope.com/.

47. *Separation of small nonferrous particles using an angular rotary drum eddy-current separator with permanent magnets.* Lungu, M. 2005, International Journal of Mineral Processing, Vol. 78(1), págs. 22-30.

48. *Metal enrichement of Finely Ground Electronic Waste using Eddy Current Separation.* Subrata Roy, V. A. 2012, Separation Science and Technology, Vol. 47, págs. 1777-1784.

49. Goudsmitmagnets. https://www.goudsmitmagnets.com/industrial-magnetic-systems/.

50. Wögerer, C. Separation and recycling technologie of mixt Al and Mg scrap. 2007.

51. Steinert. https://steinertglobal.com/magnets-sensor-sorting-units/magnetic-separation/.

52. Interempresas. www.Interempresas.net.

53. Uned. https://www2.uned.es/cristamine/mineral/minbas_mrc.htm.

54. Tomra. www.Tomra.com.

55. Steinert. https://steinertglobal.com/es/reciclaje-de-metales/.

56. Steqtech. https://steqtech.com/technology/.

57. Sandberg, Erik. *Valorization and dissemination of EAF technology – VALEAF: Road Map for future EAF technology - Scrap control.* s.l. : RFS2-CT-2014-00002, 2014.

58. Marique, C. *2nd ECSC WORKSHOP ON STEELMAKING "Technological Problems Related to Scrap Utilization: Product Quality Demand.* s.l. : ISBN 92-827-4225-3, 1995.

59. *Liquid Steel level measurement at Electric Arc Furnaces without increasing the power off time.* A. Vicente, I. Macaya, J.A. Gutierrez, J.A. Arteche. Venice (Italy) : s.n., 2016. 11th EEC 2016 – ISBN 978-88-98990-06-1.

60. Köhle, S. *Improving the productivity of electric arc furnaces.* s.l. : Bericht 2.32.007, Betriebsforschungsinstitut, 2003.

61. *Mathematical Modeling of the Argon-Oxygen Decarburization Refining Process of Stainless Steel: Part I. Mathematical Model of the Process.* Wei, J.H. and Zhu, H.L. 2002, Metall. Mater.Trans.B, Vol. Vol.33B, págs. pp.111-119.

62. *Preliminary Investigation of Mathematical Modeling of Stainless Steelmaking in an AOD Converter: Mathematical Model of the Process.* Zhu, H.L., Wei, J.H., Shi, G.M., Shu, J.H., Jiang.Q.Y. and Chi,.H.B. 2007, Steel Res.Int., Vol. Vol.78, págs. pp.305-310.

63. *Mass and Heat Balance of Steelmaking in BOF as Compared to EAF Processes.* Lotfy, M. M., Hafiz.A.Ahmed, and Fawzi.A.Elrefaie. 2015.

64. *Thermodynamic analysis of EAF energy efficiency and comparison with a statistical model of electric energy demand.* H. Pfeifer, M. Kirschen. Birmingham : s.n., 2005. 8th EEC 2005 .

65. Julio Astigarraga Urquiza, Juan Vicente Martín Zorraquino. *Hornos de arco para fusión de acero. Teoría, cálculo y aplicaciones.* s.l. : 84-481-1728-X, 1995.

66. *Classification of steel scrap in the EAF process using Image analysis methods.* T. Wieczorek, M. Pilarczyk. 53, 2008, Archives of metallurgy and materials, Vol. 2.

67. *A review of recent application of near infrared spectroscopy to wood science and technology.* Tsuchikawa, S. & Kobori, H. J Wood. 213, 2015, Sci, Vol. 61.

68. *Research of process and development of separator for metal recovery from metallurgical slags.* VN, Vlasov. 213-225, s.l. : Mag electr, 1996.

69. LLC, Phoenix Services. *Water displacement test procedure .*

70. Naiyang Ma, D. G. Hill, L. A. Wood, J. B. Houser and R. W. Lewis. *Fast assessment of total iron contents in steelmaking slags by means of water displacement test for recycling of iron in the iron making and steelmaking process.* s.l. : The minerals, Metals & Mateals society, 2017.

71. E. Martonne, G. Bomben, L. Martonne , G. Calvagno, P. Ronchese, G. Zumerle,. *Muons scanner to detect radioactive sources hidden in scrap metal containers (MU-STEEL).* ISBN 978-92-79-38537-7.

72. Vasco., Asociación de análisis químico siderúrgico del País. *Recepción, preparación y análisis de materias primas por vía húmeda.*

73. Broek, Wienke, et al. *Plastic material identification with spectroscopic near infrared imaging an artificial neural networks.* 1998.

74. *Fuzzy Spectral and Spatial Feature Integration for Classification of Nonferrous Materials in Hyperspectral Data.* A. Picon, O. Ghita, P. F. Whelan, P. M. Iriondo. 4, 2009, IEEE Transactions on Industrial Informatics, Vol. 5, págs. 483-494.

75. Real-time hyperspectral processing for automatic nonferrous material sorting. Artzai Picón, Ovidiu Ghita, Aranzazu Bereciartua, Jone Echazarra, Paul F. Whelan, Pedro M. Iriondo. J. Electron. Imaging. 21(1), 013018 (Apr 04, 2012). .

76. A. Vicente, A. Picon, S. Rodriguez. *METHOD OF DETERMINING A CHEMICAL COMPOSITION OF A SLAG PORTION. WO 2016/181185* 2015.

77. D.Jacquet, P. Tepola, G. Grundmeier, X. Li, T.Jacquot and D. Glijer. *Online chemistry of steel surfaces.* ISBN: 978-92-79-29040-4.

78. S. J. Mannanal, S. Dehnhardt, T. Eickmeyer, K. Fußholz, A. Gesser, S. Tiedke, A. Bostonne , J. McGrath, P. Nolan, G. Monfort, Ph. Desneux, J. Sved, N. Menduev, F. Koehrmann,P. Russo and B. Husson-Tissier. *On-line bulk composition analysis of steel scrap using PGNAA (SCRAP PROBE).* ISBN 978-92-79-33243-2.

79. R. Noll, A. Bengtson, J. Gurell, U. Chiarotti, R. Grieco, V. Volponi, M. Zani, A. Appell, M. Brunk. *Inline elemental characterisation of scrap charging for improved EAF charging control and internal scrap recycling .* ISBN 978-92-79-47471-2.

80. Swerea KIMAB, Fraunhofer ILT, CSM, Univ. Malaga, ORI Martin, Arcelor Mittal Research, Stena Stainless. *Laser Induced Breakdown Spectroscopy for Advanced Characterization and Sorting of Steel Scrap.* ISBN 978-92-79-21545-2.

81. Oxford-instruments. https://www.oxford-instruments.com/products/spectrometers/optical-emission-spectroscopy.

82. *A review of pXRF (field portable X-ray fluorescence) applications for applied geochemistry.* Lemière, Bruno. 350-363, 2018, Journal of Geochemical Exploration, Vol. 188.

83. Garces, R.C. *Evaluacion de la corrosión atmospherica del acero expuesto en diversas atmospheras.* s.l. : Doctoral Tesis- universidad autónoma de nuevo león., 2002 .

84. Tomashov, N. D. *Theory of Corrosion and Protection of Metals.* Nueva York : MacMillan Co, 1966. 367.

85. S.E. Lara, C. Moreno, D. Sanchez. *Efectos de la corrosion atmosferica sobre la corrosion de materiales ferrosos (Aceros) de sider–Peru. Modelo Matematico.* s.l. : NACIONAL DEL SANTA - Departamento de agroindustria Facultad de Ingeniería, 2010.

86. Corsa, Gerdau. El acero Hoy: Principios de proteccion de estructuras metálicas en situación de corrosión y fuego. Gerdau Corsa. www.gerdaucorsa.com.mx.

87. M. TULLMIN, P. R. ROBERGE. *Atmospheric Corrosion.* Ontario, Canada) : s.n.

88. *Atmospheric Corrosion Behavior of Weathering Steel in Periodically Changed Environment.* Xu ZHANG, Shanwu YANG, Hui GUO and Xinlai HE. No. 4, s.l. : ISIJ International, 2014, Vol. Vol. 54. 909–915.

89. Revie, R. Winston. *Uhlig's Corrosion Handbook, Second Edition.* s.l. : John Wiley & Sons, Inc, 2000. ISBN 0-471-15777-5 .

90. *Ensayos para determinación de la corrosion de metales en diferentes ambientes de lima y callao.* Pizarro-Cabrera R, Anaya-Pajuelo A. 1, 1999, Revista Peruana de Química e Ingeniería Química., Vol. 2, págs. 63–71.

91. www.metallics.org. www.metallics.org. https://www.metallics.org/hbi.html.

92. www.aemet.es. www.aemet.es. http://www.aemet.es.

93. Fundacion del metal para la formacion, cualificacion y empleo. *EL SECTOR DE RECICLAJE DE METALES EN ESPAÑA.* Diciembre 2010.

94. *Recycling of construction and demolition waste via a mechanical sorting process.* W. Huang, D. Lin, N. Chang, K. Lin. 2002, Vol. 37.

95. Euric. www.euric-aisbl.eu.

96. Wikipedia. www.wikipedia.es.

97. *Surface-Enhanced Raman Spectroscopy (SERS) for Environmental Analyses.* Halvorson, R. A. y Vikesland, P. J. 44, 7749-7755., s.l. : Environmental Science & Technology, 2010, Vol. 20.

98. Inc, B.VCH publishers. *Infrared and Raman spectroscopy.* New York : s.n., 1995.

99. handbook, Agriculture. *Methods for Soil Characterization.* s.l. : U. S. Dept. of agriculture, 2016. 60.

100. F. Trolard, M. Abdelmoula, G. Bourril, B. Humbert, A. Herbillon. *Identification of a green rust mineral in a reductomorphic soil by Massbauer and Raman spectroscopies.* France : INRA-U.R, de Science du Sol et de Bioclimatologie, F 35042 Rennes Ceclex, 1996.

101. Zhe Xing, Changwen Du, Yin Zeng, FeiMa a, Jianmin Zhou. *Characterizing typical farmland soils in China using Raman spectroscopy.* Nanjing : Institute of Soil Science, Chinese Academy of Sciences, 2008.

102. Keidel A, von Stetten D, Rodrigues C, Máguas C, Hildebrandt P.. J. *Discrimination of Green Arabica and Robusta Coffee Beans by Raman Spectroscopy.* s.l. : Agric Food Chem, 2010.

103. *Shell thickness-dependent Raman enhancement for rapid identification and detection of pesticide residues at fruit peels .* Liu B, Han G, Zhang Z, et al. (1) 255–61, s.l. : Anal Chem, 2012, Vol. 84.

104. M. St. Luce, N. Ziadi, B. J. Zebarthb, C. A. Grant, G. F. Tremblay, E. G. Gregorich. *Rapid determination of soil organic matter quality indicators using visible near infrared reflectance spectroscopy.* Canada : Soils and Crops Research and Development Centre, 2014.

105. Wang., Qi. *Raman spectroscopic characterization and analysis of agricultural and biological systems.* Iowa State University : s.n., 2015.

106. Lee., Alison J. Wright1 and Martin R. *The use of Raman spectroscopy to characterize biological and biomineralic crusts.* s.l. : University of Glasgow - School of Geographical and Earth Sciences, 2012.

107. *The use of Raman spectroscopy in the detection of counterfeit and adulterated pharmaceutical products.* MR, Witkowski. s.l. : Amer Pharma , 2005, Vols. Rev. 56–62.

108. J. Sun, Z. Wua, H. Cheng, Z. Zhang, R. L. Frost. *Raman spectroscopic comparison of calcite and dolomite .* China : Datang International High Alumina Coal R&D Center, 2013.

109. Geophysics, Department of Oceanography and Hawaii Institute of. *Carbonate ion disorder in synthetic and biogenic magnesian calcites: a Raman spectral study.* s.l. : Department of Oceanography and Hawaii Institute of Geophysics , 1985.

110. Miller, Jeri Ropero. *Landscape Study of Handheld and Portable Raman Spectrometers.* s.l. : Forensic Technology Center of Excellence, Sept 2014.

111. *Identification of shredded plastics in milliseconds using Raman spectroscopy for recycling.* Tsuchida A, Kawazumi H, Kazuyoshi A, Yasuo T. 1473., s.l. : IEEE Sensors 2009 , 2009 .

112. C. J. Atkinson, D. Dugwell, S. Dong, R. Kandiyoti, A. Di Donato, J. Gelli, M. De Santis, O. Kerkkonen, G. Harp, G. Stubbe. *Minimising environmental emissions by optimised reductant utilisation (MEORU).* s.l. : European Commission RFCS. . ISBN 978-92-79-21721-0.

113. I. A. Jelonek, K. J. Kruszewska, S. Czudek, M. A. Gómez, A. Kožušníková, H. Liszio, E. Zmuda. *Improvement of coal carbonization through the optimization of fuel in coking coal blends (RATIO-COAL).* s.l. : European Commission RFCS. . ISBN 978-92-79-52048-8.

114. geologie-lyon. http://www.geologie-lyon.fr/Raman/. http://www.geologie-lyon.fr/Raman/.

115. rruff. http://rruff.info/. http://rruff.info/.

116. sdbs. http://sdbs.db.aist.go.jp/sdbs/cgi-bin/direct_frame_top.cgi. http://sdbs.db.aist.go.jp/sdbs/cgi-bin/direct_frame_top.cgi.

117. models.life.ku.dk. http://www.models.life.ku.dk/~specarb/specarb.html. http://www.models.life.ku.dk/~specarb/specarb.html.

118. N. Buzgar, A. I. Apopei. *The Raman study of certain carbonates.* s.l. : University of Iaşi, 2009. Tomul LV, nr. 2.

119. *Influence of water vapour and carbon dioxide on free lime during storage at 80 °C, studied by Raman spectroscopy. .* Dubina, E, Plank, J, Korat, L, Strupi-Šuput, J and Black, L. 299 - 303, s.l. : Spectrochimica Acta - Part A Molecular and Biomolecular Spectroscopy, 2013, Vol. 111. ISSN 1386-1425.

120. Leontakianakos G., Baziotis I., Profitis E., Chatzitheodoridis E. and Tsimas S. *Assessment of the quality of calcination of marbles from Thassos island using Raman spectroscopy and X-Ray diffraction.* s.l. : Bulletin of the Geological Society of Greece, 2013.

121. W.D. Bischoff, S. K. Sharma, F. T. Mackenzie. *Carbonate ion disorder in shyntetic and biogenic magnesian calcites: A Raman spectral study.* s.l. : American Mineralogist. , 1985. Volume 70, 581-589.

122. Adar, Fran. *Molecular spectroscopy workbench – Raman spectra of metal oxides.* October 2014.

123. Pat Henson, Joe Hodkiewicz, Tim Deschaines. http://www.spectroscopyonline.com. *Characterization of Amorphous and Microcrystalline Silicon Using Raman Spectroscopy.* 2019. http://www.spectroscopyonline.com.

124. Pastor, Jose Antonio Moreno. *Analisis de oxidos de silicio y estructuras multicapa para aplicaciones microelectronicas.* . s.l. : Universitat de Barcelona, Sept 2000.

125. Colomban, Philippe. *Potential and Drawbacks of Raman (Micro)Spectrometry for the Understanding of Iron and Steel Corrosion.* France : Université Pierre-et-Marie-Curie.

126. *Quantitative approach in iron oxides and oxihydroxides by vibrational analysis.* A. F. Betancur, F. R. Perez, M. del M. Correa, C. A. Barrero. s.l. : III Conferencia Andina y del Caribe en Optica y sus aplicaciones, 2012.

127. Legodi, M A. *Raman Spectroscopy Applied to Iron Oxide Pigments from Waste Materials and Earthenware Archaeological Objects.* s.l. : Uniiversiity of Pretoria etd, 2008.

128. *The preparation of magnetite, goethite, hematite and maghemite of pigment quality from mill scale iron waste.* M.A. Legodi, D. de Waal. 161 - 168, s.l. : Dyes and Pigments , 2007, Vol. 74 .

129. wikipedia. https://en.wikipedia.org/wiki/Savitzky%E2%80%93Golay_filter. https://en.wikipedia.org/wiki/Savitzky%E2%80%93Golay_filter.

130. mathworld. http://mathworld.wolfram.com/FrobeniusNorm.html. http://mathworld.wolfram.com/FrobeniusNorm.html.

131. *Joint Bayesian endmember extraction and linear unmixing for hyperspectral imagery.* Dobigeon N, Moussaoui S, Coulon M, Tourneret J-Y, Hero AO. 4355–4368, s.l. : IEEE Transactions on Signal Processing, 2009, Vol. 57(11).

132. Halimi A, Altmann Y, Dobigeon N, Tourneret J-Y. Nonlinear unmixing of hyperspectral images using a generalized bilinear model. IEEE Transactions on Geoscience and Remote Sensing. 2011;49(11):4153–4162.

133. *Using color to separate reflection components.* Shafer, S. 210–218, s.l. : Color Research and Applications, Vol. vol. 10.

134. *Separating reflection components based on chromaticity and noise analysis.* R. T. Tan, K. Nishino, and K. Ikeuchi. 1373–1379, s.l. : IEEE Trans. Pattern Anal. Mach. Intell., 2004, Vols. vol. 26, no. 10.

135. *Detection and classification of hyperspectral edges.* Gevers, H. Stockman and T. 643–655, s.l. : inProc. 10th British Mach. , 1999.

136. *Compression technique for plume hyperspectral images.* B.K. Feather, S.A. Fulkerson, J.H. Jones, R.A. Reed, M. Simmons, D. Swann, W.E. Taylor, and L.S. Bernstein. s.l. : Algorithms and Technologies for Multispectral, 2005, Vol. Hyperspectral and Ultraspectral Imagery .

137. *Application of neural networks in optical inspection and classification of solder joints in surface mount technology.* G. Acciani, G. Brunetti, and G. Fornarelli. 200-209, s.l. : IEEE Transactions on Industrial Informatics, 2006, Vols. vol. 2, no. 3 .

138. *Floating search methods in feature selection.* P. Pudil, J. Novovicova, and J. Kittler,. 1119-1125, s.l. : Pattern Recognition Letters, 1994, Vols. vol. 15, no. 11.

139. *Generic Wavelet-Based Hyperspectral Classification Applied to Vegetation Stress Detection.* P. Kempeneers, S. De Backer, W. Debruyn, P. Coppin, and P. Scheunders. 610-614, s.l. : IEEE Transactions on Geoscience and Remote Sensing, 2005, Vols. vol. 43, no. 3.

140. *A review of recent near infrared research for wood and paper. .* Tsuchikawa., S. 43-71, s.l. : Applied Spectroscopy Reviews, 2007, Vols. Vol. 42, No. 1.

141. *Industrial application for inline material sorting using hyperspectral imaging in the NIR range.* P. Tatzer, M. Wolf, T. Panner. 99-107, s.l. : Real-Time Imaging, 2005, Vol. Vol. 11.

142. Marcus Groinig, Markus Burgstaller and Manfred Pail. *Demand for Processed Potato Products and Processing Quality Potato Tubers in India.* 2010.

143. *Bell. Recent applications of Chemical Imaging to pharmaceutical process monitoring and quality control.* A.A. Gowen, C.P. O'Donell, P.J. Cullen, S.E.J. 10-22, s.l. : European Journal of Pharmaceutics and Biopharmaceutics, 2008, Vol. 69.

144. *Spectral reflectace of carbonate minerals in the visible and near infrared (0.35-2.55 microns): Calcite, aragonite and dolomite.* Gaffey, S. J. Pag 151-162, s.l. : American Mineraligist, 1986, Vol. Volume 71.

145. *Determination of Carbonate rock chemistry using laboratory-based hyperspectral imagery.* N. Zaini, F. Van der Meer, H. Van der Werff. 4149-4172, s.l. : Remote Sens , 2014, Vol. 6.

146. *Effect of Grain Size and Mineral Mixing on Carbonate Absorption Features in the SWIR and TIR Wavelength Regions.* N. Zaini, F. Van Der Meer and H. Van Der Werff. 987-1003, s.l. : Remote Sensing, 2012, Vol. 4.

147. *Preparation and Characterization of Silica Material from Rice Husk Ash – An Economically Viable Method .* A. Ananthi, D. Geetha1, P. S. Ramesh. No.6 , s.l. : Chemistry and Materials Research, 2016, Vol. Vol.8 .

148. Lun, Leong Tuck. *Effects of rice husk ash (rha) produced from different temperatures on the performance of concrete.* s.l. : Faculty of Engineering and Green Technology Universiti Tunku Abdul Rahman, May 2015.

149. *Structural, physical and optical properties of rice hush ash derived glass/ceramics.* Sharma., Gaurav. s.l. : School of physics & materials science Thapar Uniersity, 2013.

150. *Mapping the distribution of ferric iron minerals on a vertical mine face using derivative analysis of hyperspectral imagery (430–970 nm).* Richard J.Murphy, Sildomar T. Monteiro. 29-39, s.l. : ISPRS Journal of Photogrammetry and Remote Sensing , January 2013, Vol. Volume 75.

151. G.R. Hunt, J.W. Salisbury. Visible and near-infrared spectra of minerals and rocks; II, Carbonates. : Modern Geol., 1971, Vol. 2 .

152. *Applications of hyperspectral mineralogy for geoenvironmental characterisation. .* N. Fox, A.Parbhakar-Fox, J. Moltzen, S.Feig, K.Goemann, J.Huntington. Pages 63-77, s.l. : Minerals Engineering , June 2017, Vol. Volume 107.

153. *Fast method for slag characterization during ladle furnace.* A. Vicente, I. Macaya, A. Picon, J. A. Arteche. Metz : 9th Euroslag conference, 2018.

154. *Use of Spectralon as a diffuse reflectance standard for in-flight calibration of earth-orbiting sensors.* Bruegge, C. J., Stiegman, A. E., Rainen, R. A., & Springsteen, A. W. 805-814, s.l. : Optical Engineering, 1993, Vol. 32(4).

155. *Hyperspectral imaging: calibration problems and solutions. .* Geladi P, Burger J, Lestander T. 209–217, s.l. : Chemometrics and intelligent laboratory systems, 2004, Vol. 72(2).

156. *Ladle furnace slag characterization through hyperspectral reflectance regression model for secondary metallurgy process optimization.* Artzai Picon, Asier Vicente, Sergio Rodriguez-Vaamonde, Jorge Armentia, Jose Antonio Arteche, Iñaki Macaya. s.l. : IEEE Transactions on Industrial Informatics., 2017. TII.2017.2773068.

157. Smith, Brian C. *Fundamentals of Fourier Trnasform Infrared Spectroscopy.* 2011. ISBN 978-1-4200-6930-3.

158. piketech. https://www.piketech.com/files/pdfs/EducationalPoster.pdf. https://www.piketech.com/files/pdfs/EducationalPoster.pdf.

159. *Characterization of the solid-state: spectroscopic techniques. .* BUGAY, David E. p. 43-65, s.l. : Advanced Drug Delivery Reviews, 2001, Vols. vol. 48, no 1.

160. *Pharmaceutical applications of Mid-IR and Raman spectroscopy. .* WARTEWIG, Siegfried y NEUBERT, Reinhard HH. p. 1144-1170., s.l. : Advanced drug delivery reviews, 2005, Vols. vol. 57, no 8.

161. *Solution concentration prediction for pharmaceutical crystallization processes using robust chemometrics and ATR FTIR spectroscopy. .* TOGKALIDOU, Timokleia, et al. p. 317-322., s.l. : Organic Process Research & Development , 2002, Vols. vol. 6, no 3.

162. *The evaluation of cosmetic and pharmaceutical emulsions aging process using classical techniques and a new method: FTIR. .* Masmoudi, H., Le Dréau, Y., Piccerelle, P., & Kister, J. 117-131, s.l. : International journal of pharmaceutics, 2005, Vols. 289(1-2).

163. *Application of attenuated total reflectance FTIR spectroscopy to the analysis of mixtures of pharmaceutical polymorphs. .* Salari, A., & Young, R. E. 157-166, s.l. : International journal of pharmaceutics, 1998, Vols. 163(1-2).

164. SEYMOUR, Raymond B. y CARRAHER, Charles E. *Polymer chemistry.* New York : Marcel Dekker, 1981.

165. CHANDA, Manas y ROY, Salil K. *Plastics technology handbook.* s.l. : CRC press,, 2006.

166. *Characterization and properties of natural fiber polymer composites: A comprehensive review.* Sanjay, M. R., Madhu, P., Jawaid, M., Senthamaraikannan, P., Senthil, S., & Pradeep, S. 566-581., s.l. : Journal of Cleaner Production, 2018, Vol. 172.

167. *Using Raman spectroscopy to characterize biological materials.* Butler, H. J., Ashton, L., Bird, B., Cinque, G., Curtis, K., Dorney, J., ... & Walsh, M. J. 664, s.l. : Nature protocols, 2016, Vol. 11(4).

168. *ATR-FT-IR spectroscopy in the region of 550–230 cm− 1 for identification of inorganic pigments. .* Vahur, S., Teearu, A., & Leito, I. . 1061-1072, s.l. : Spectrochimica Acta Part A: Molecular and Biomolecular Spectroscopy, 2010, Vol. 75(3).

169. *Characterizing surface properties of oxidized coal using FTIR and contact angle measurements. .* Zhou, Y., Albijanic, B., Wang, Y., & Yang, J. 1559-1564, s.l. : Energy Sources, Part A: Recovery, Utilization, and Environmental Effects, 2018, Vol. 40(12).

170. *Emissivity correction using spectrum correlation of infrared and visible images. .* Gao, Y., & Tian, G. Y. 8-17, s.l. : Sensors and Actuators A: Physical, 2018, Vol. 270.

171. *Effect of P 2 O 5 and Fe t O on the viscosity and slag structure in steelmaking slags. .* Wang, Z. J., Shu, Q. F., Sridhar, S., Zhang, M., Guo, M., & Zhang, Z. T. 758-765, s.l. : Metallurgical and Materials Transactions B, 2015, Vol. 46(2).

172. *FTIR, Raman and NMR investigation of CaO–SiO2–P2O5 and CaO–SiO2–TiO2–P2O5 glasses. .* Sun, Y., Zhang, Z., Liu, L., & Wang, X. 26-33, s.l. : Journal of Non-Crystalline Solids, 2015, Vol. 420.

173. *Analysis of Slag Chemistry by FTIR-RAS and Raman Spectroscopy: Effect of Water Vapor Content in H2 H2O CO CO2 Mixtures Relevant to a Novel Green Ironmaking Technology.* Mohassab, Y., & Sohn, H. Y. 740-75, s.l. : Steel research international, 2015, Vol. 86(7).

174. *An infrared spectroscopic study of non-metallic portion of Linz-Donawitz slag fines generated at Tata Steel, Jamshedpur.* Ashrit, S., Chatti, R. V., Sarkar, S., Venugopal, R., & Nair, U. G. 608, s.l. : Metallurgical Research & Technology, Vol. 115(6).

175. *Effect of steelmaking dust characteristics on suitable recycling process determining: Ferrochrome converter (CRC) and electric arc furnace (EAF) dusts. .* Omran, M., & Fabritius, T. 47-60, s.l. : Powder technology, 2017, Vol. 308.

176. *Asphalt modified with superfine electric arc furnace steel dust (EAF dust) with high zinc oxide content. .* Loaiza, A., Cifuentes, S., & Colorado, H. A. 538-547, s.l. : Construction and Building Materials, 2017, Vol. 145.

177. *Infrared Studies of Aragonite, Calcite, and Vaterite Type Structures in the Borates, Carbonates, and Nitrates. .* C. E. Weir C. E., Lippincott E.R. s.l. : JOURNAL OF RESEARCH of the National Bureau of Standards-A. Physics and Chemistry, 1961, Vol. Vol. 65A.

178. Jones, G. C., & Jackson, B. *Infrared transmission spectra of carbonate minerals.* s.l. : Springer Science & Business Media, 2012.

179. *Infrared Transmission Spectra of Carbonate Minerals. .* Braithwaite, R. S. W. GC Jones and B. Jackson. 523-524, s.l. : Mineralogical Magazine , 1994, Vol. 58(392).

180. *Infrared study of the carbonate minerals. .* Huang, C. K., & Kerr, P. F. 311-324, s.l. : American Mineralogist: Journal of Earth and Planetary Materials , 1960, Vols. 45(3-4).

181. *Assessing and calibrating the ATR-FTIR approach as a carbonate rock characterization tool. .* Delano G. Henry, Jonathan S. Watson, Cédric M. John. 36–52, s.l. : Sedimentary Geology , 2017, Vol. 347 .

182. *FTIR techniques in clay mineral studies. .* Madejová., J. Pages 1-10, s.l. : Vibrational Spectroscopy , 2003, Vols. Volume 31, Issue 1.

183. *Quantitative analysis of iron oxides using Fourier transform infrared spectrophotometry. .* H. Namduri, S. Nasrazadani. Pages 2493-2497, s.l. : Corrosion Science , 2008, Vols. Volume 50, Issue 9.

184. *The Iron Oxides, .* R.M. Cornell, U. Schwertmann,. s.l. : Weinheim, 1996.

185. *Spectroscopic characterization of iron ores formed in different geological environments using FTIR, XPS. .* Walid S., Mourtada El A, Reinhard G. Pages 1816-1826, s.l. : Molecular and Biomolecular Spectroscopy , 2015, Vol. Volume 136 .

186. *Infrared and Raman spectroscopic studies on iron oxide magnetic nano-particles and their surface modifications. .* Ying-Sing Li, Jeffrey S. Church, Andrea L. Woodhead. s.l. : Journal of Magnetism and Magnetic Materials , 2012, Vols. Volume 324, Issue 8.

187. labea. www.labea.com. https://www.labea.com.

188. www.erogol.com. www.erogol.com. http://www.erogol.com/brief-history-machine-learning/.

189. Russell, Stuart y Norvig, Peter. *Artificial Intelligence: A Modern Approach (2nd ed.). .* s.l. : Prentice Hall, 2003 .

190. Brownlee, Jason. Machine Learning Algorithms: Discover how they work and implement them from scratch. *Blog.* 2017.

191. *Intelligent Decision Technologies 2018: Proceedings of the 10th KES International Conference on Intelligent Decision Technologies (KES-IDT 2018).* Ireneusz Czarnowski, Robert J. Howlett, Lakhmi C. Jain, Ljubo Vlacic. s.l. : Springer, 2018.

192. *Deepdriving: Learning affordance for direct perception in autonomous driving.* Chen, C., Seff, A., Kornhauser, A., & Xiao, J. 2722-2730, s.l. : IEEE International Conference on Computer Vision 2015., 2015.

193. *Visual SLAM for Automated Driving: Exploring the Applications of Deep Learning.* Milz, S., Arbeiter, G., Witt, C., Abdallah, B., & Yogamani, S. s.l. : In Proceedings of the IEEE Conference on Computer Vision and Pattern Recognition Workshops , 2018 , Vols. 247-257.

194. *Using convolutional networks and satellite imagery to identify patterns in urban environments at a large scale. .* Albert, A., Kaur, J., & Gonzalez, M. C. 1357-1366, s.l. : Proceedings of the 23rd ACM SIGKDD International Conference on Knowledge Discovery and Data Mining, 2017.

195. *Developments in Artificial Intelligence and Opportunities and Challenges for Military Modeling and Simulation.* Fawkes, A. J. 2017. Proceedings of the 2017 NATO M&S Symposium.

196. *A survey on deep learning in medical image analysis.* Litjens, G., Kooi, T., Bejnordi, B. E., Setio, A. A. A., Ciompi, F., Ghafoorian, M., Sánchez, C. I. 60-88., s.l. : Medical image analysis, 2017, Vol. 42.

197. *Deep learning as a tool for increased accuracy and efficiency of histopathological diagnosis.* Litjens, G., Sánchez, C. I., Timofeeva, N., Hermsen, M., Nagtegaal, I., Kovacs, I., Van Der Laak. s.l. : Scientific reports 26286, 2016, Vol. 6.

198. *Deep Learning Smart Microscope.* Jalali, B., Mahjoubfar, A., & Chen, C. L. s.l. : CLEO: Science and Innovations-Optical Society of America, 2018 .

199. *Computer vision techniques for construction safety and health monitoring. .* Seo, J., Han, S., Lee, S., & Kim, H. 239-251, s.l. : Advanced Engineering Informatics , 2015, Vol. 29(2).

200. *A deep hybrid learning model to detect unsafe behavior: integrating convolution neural networks and long short-term memory. Automation in Construction.* Ding, L., Fang, W., Luo, H., Love, P. E., Zhong, B., & Ouyang, X. 118-124, s.l. : Automation in Construction, 2018, Vol. 86.

201. *Overview of the CPS for smart factories project: deep learning, knowledge acquisition, anomaly detection and intelligent user interfaces.* Sonntag, D., Zillner, S., van der Smagt, P., & Lörincz, A. s.l. : In Industrial Internet of Things, Vols. 487-504.

202. *Deep learning for acoustic modeling in parametric speech generation: A systematic review of existing techniques and future trends.* Ling, Z. H., Kang, S. Y., Zen, H., Senior, A., Schuster, M., Qian, X. J., ... & Deng, L. 35-52., s.l. : IEEE Signal Processing Magazine, 2015, Vol. 32(3).

203. Deng, L., & Liu, Y. *Deep Learning in Natural Language Processing.* s.l. : Springer, 2018 .

204. *Gradient based learning applied to document recognition.* Y. LeCum, L. Bottou, Y. Bengio, P. Haffner. 2278-2324, s.l. : IEEE , (1998), Vol. 86(11).

205. *Imagenet classification with deep convolutional neural networks .* Krizhevsky, A., Sutskever, I., & Hinton, G. E. s.l. : In Advances in neural information processing systems, 2012, Vols. 1097-1105.

206. Zeiler, M. D., & Fergus, R. *Visualizing and understanding convolutional networks.* s.l. : Springer, 2014. European conference on computer vision (pp. 818-833).

207. Simonyan, K., & Zisserman, A. Very deep convolutional networks for large-scale image recognition. 2014 arXiv:1409.1556 : s.n., 2014 . arXiv:1409.1556.

208. *Going deeper with convolutions.* Szegedy, C., Liu, W., Jia, Y., Sermanet, P., Reed, S., Anguelov, D., Rabinovich, A. 1-9, s.l. : Proceedings of the IEEE conference on computer vision and pattern recognition.

209. *Deep residual learning for image recognition.* He, K., Zhang, X., Ren, S., & Sun, J. 770-778, s.l. : Proceedings of the IEEE conference on computer vision and pattern recognition, 2016.

210. *Densely Connected Convolutional Networks.* Huang, G., Liu, Z., Van Der Maaten, L., & Weinberger, K. Q. No. 2, p. 3, s.l. : CVPR , 2017, Vol. Vol. 1.

211. cvhci.anthropomatik. https://cvhci.anthropomatik.kit.edu/~baeuml/projects/a-universal-labeling-tool-for-computer-vision-sloth/. https://cvhci.anthropomatik.kit.edu/~baeuml/projects/a-universal-labeling-tool-for-computer-vision-sloth/.

212. gujinwei. http://www.gujinwei.org/research/camspec/db.html. http://www.gujinwei.org/research/camspec/db.html.

213. *Visualizing data using t-SNE.* Maaten, L. V. D., & Hinton, G. 2579-2605, s.l. : Journal of machine learning research, 2008, Vol. 9.

214. *Calculation of the color matching funtions of digital cameras from their complete spectral sensivities.* F. Martinez, J. Pujol, P. Capilla,. s.l. : Journal of imaging science and technology. , 2002, Vols. Vol 46, 1 .

215. numberempire. http://es.numberempire.com/combinatorialcalculator.php. http://es.numberempire.com/combinatorialcalculator.php.

216. *Real-Time Recursive Hyperspectral Sample and Band Processing: Algorithm Architecture and Implementation. .* Chang, Chein-I. s.l. : Springer, 2017 , Vols. (398-399). ISBN 3319451715, 9783319451718.

217. A. Karpathy, G. Toderici, S. Shetty, T. Leung, R. Sukthankar, and L. Fei-Fei, “Large-scale Video Classification with Convolutional Neural Networks (CVPR 2014),” 2014. Available: http://cs.stanford.edu/people/karpathy/deepvideo/. A. Karpathy, G. Toderici, S. Shetty, T. Leung, R. Sukthankar, and L. Fei-Fei. *Large-scale Video Classification with Convolutional Neural Networks (CVPR 2014).*

218. *Learning Phrase Representations using RNN Encoder-Decoder for Statistical Machine Translation.* K. Cho, B. van Merrienboer, C. Gulcehre, D. Bahdanau, F. Bougares, H. Schwenk, and Y. Bengio,. 2014. Conference on Empirical Methods in Natural Language Processing, Doha, Qatar.

219. *Long Short-Term Memory.* Schmidhuber, S. Hochreiter and J. s.l. : Neural Computation, 1997, Vols. vol. 9, no. 8, pp. 1735–1780.

220. *A Closer Look at Spatiotemporal Convolutions for Action Recognition.* D. Tran, H. Wang, L. Torresani, J. Ray, Y. LeCun, and M. Paluri. pp. 6450–6459, s.l. : IEEE Conference on Computer Vision and Pattern Recognition, D. Tran, H. Wang, L. Torresani, J. Ray, Y. LeCun, and M. Paluri, "A Closer Look a2018, .

221. *Fuzzy spectral and spatial feature integration for classification of nonferrous materials in hyperspectral data.* Picón, Artzai, Ovidiu Ghita, Paul F. Whelan, y Pedro M. Iriondo. 483–494, s.l. : IEEE Transactions on electronic, 2009, Vol. 4.

222. Sharma, Gaurav. *Structural, physical and optical properties of rice hush ash derived glass/ceramics.* Patiala : School of physics & materials science Thapar Uniersity, July 2013.

Bibliografía